

Structural and Sedimentological Controls on the Evolution of Carbonate Platforms on Equatorial Margins

Roberto Loza Espejel

PhD Thesis in Earth Sciences,

October 2021





Structural and Sedimentological Controls on the Evolution of Carbonate Platforms on Equatorial Margins

Roberto Loza Espejel

Thesis submitted in fulfilment of the requirements for the degree in

Doctor of Philosophy (Earth Sciences)

at the

3D Seismic Lab Group,

Cardiff School of Earth and Environmental Sciences

October 2021

Structural and Sedimentological Controls on the Evolution of Carbonate Platforms on Equatorial Margins

Ph.D. project sponsored by the Mexican National Council of
Science and Technology (CONACYT) and the hydrocarbon
Secretariat of Energy (SENER)

Roberto Loza Espejel



Dedicated to my grandpa and grandma, Roberto and Nice.

*“If you have a dream, you have a responsibility to yourself to make it come
true...”*

“Because if you don’t, you’re just a dreamer”

Marco Pierre White

Statements and declaration

Statement 1

This thesis is being submitted in partial fulfilment of the requirements for the degree of Doctor of Philosophy (Earth Sciences).

Signed _____ (candidate) Date _____

Statement 2

This work has not been submitted in substance for any other degree or award at this or any other university or place of learning, nor is it being submitted concurrently for any other degree or award (outside of any formal collaboration agreement between the University and a partner organisation).

Signed _____ (candidate) Date _____

Statement 3

I hereby give consent for my thesis, if accepted, to be available in the University's Open Access repository (or, where approved, to be available in the University's library and for inter-library loan), and for the title and summary to be made available to outside organisations, subject to the expiry of a University-approved bar on access if applicable.

Signed _____ (candidate) Date _____

Declaration

This thesis is the result of my own independent work, except where otherwise stated, and the views expressed are my own. Other sources are acknowledged by explicit references. The thesis has not been edited by a third party beyond what is permitted by Cardiff University's Use of Third Party Editors by Research Degree Students Procedure.

Signed _____ (candidate) Date _____

Word count _____ ~57,300 words_____

(Excluding summary, acknowledgements, declarations, contents pages, appendices, tables, diagrams and figures, references, bibliography, footnotes and endnotes).

Abstract

Carbonate platforms are common features on Cenozoic Equatorial Margins. The growth and development of carbonate platforms and their associated depositional settings depend on a series of controlling factors. This thesis analyses the structural and sedimentological factors controlling four different study areas with carbonate platforms, utilising a variety of datasets. Study areas include the Vulcan Sub-Basin, Bonaparte Basin (Northwest Shelf of Australia), the Cariatiz carbonate platform in the Sorbas Basin (SE Spain), the Pernambuco Basin (Eastern Brazil), and the Pará-Maranhão Basin (Equatorial Brazil). Datasets include 2D and 3D seismic data, wellbore data, airborne LiDAR maps, outcrop maps and multispectral satellite imagery, spanning multiple scales of observation. This thesis aims to improve the current understanding of shallow- and deep-water carbonate depositional and structural settings, aiding industry and academia in prospect identification and reservoir characterisation.

A comprehensive analysis of fault evolution and its relationship with the distribution of isolated carbonate platforms is investigated in the Vulcan Sub-Basin, Northwest Australia, using 3D seismic and borehole data. Detailed fault-throw measurements along arrays of normal faults were completed to generate throw-depth (T-Z) and throw-distance (T-D) profiles, as well as fault-throw maps. The results obtained were useful to determine the fault styles and timing(s) of fault initiation in the Vulcan Sub-Basin, and data were compared to the growth rates of isolated carbonate platforms (ICPs). Three types of ICPs were defined: one in which fault-throw is larger than carbonate productivity (type 1), a second type in which fault-throw is equal or lower than carbonate productivity (type 2), and ICPs where fault-throw postdates the growth of carbonate platforms (type 3).

An integrated method to characterise fracture networks and their scale relationships is proposed using multi-scale datasets from the Cariatiz and Pernambuco carbonate platforms. Small fractures are obtained via detailed outcrop mapping, while intermediate-scale fractures are mapped from airborne LiDAR imagery. Large-scale fractures are measured from 3D seismic data. Geometrical and topological data are acquired to demonstrate that fracture properties behave differently depending on their size, and that particular fracture types correlate to specific scales of observation. The key result in this Chapter is that small-scale fractures strike in all directions, and are highly connected in the two study areas. However, intermediate- and large-scale fractures strike predominantly parallel to the platform margin and have lower connectivity rates than small-scale fractures. Understanding sub-seismic fracture networks is therefore critical to quantify fluid flow and permeability in carbonate reservoirs.

Toward the end of this thesis, deep-water depositional settings from the Pará-Maranhão Basin, Equatorial Brazil, are studied utilising 2D and 3D seismic, borehole and multispectral satellite data to better understand platform-to-basin sedimentary processes. Neogene calciclastic submarine fans and channel-levee systems are analysed, and a comprehensive geomorphologic analysis is undertaken with the ultimate aim of finding similarities (or major contrasts) with their siliciclastic counterparts. Mixed calciclastic and siliciclastic sediment was transported from shallow waters into deep and ultra-deep waters by turbidity flows. Of importance is the confirmation that the pre-existing palaeotopography - such as terraces and gullies - was key to funnel sediment and create distinct types of channel-levee systems in Equatorial Brazil. Three types of channels are recognised: channels related to calciclastic submarine fans (type 1), low-sinuosity, aggradational channels (type 2), and high-sinuosity channels (type 3).

Author note and status of publications

The results chapters presented in this thesis have been prepared as scientific papers for publication in international journals. The present status of publication at the time of thesis submission is as follows:

Chapter 4 has been published as:

Loza Espejel, R., Alves, T.M., and Blenkinsop, T.G. 2019. Distribution and growth styles of isolated carbonate platforms as a function of fault propagation. Marine and Petroleum Geology, 107, pp. 484-507.

Available at: <https://doi.org/10.1016/j.marpetgeo.2019.05.020>.

Chapter 5 has been published as:

Loza Espejel, R., Alves, T.M., and Blenkinsop, T.G. 2020. Multi-scale fracture network characterisation on carbonate platforms. Journal of Structural Geology, 140. Available at: <https://doi.org/10.1016/j.jsg.2020.104160>.

Chapter 6 has been published as:

Loza Espejel, R., Alves, T.M., and Caçador Martins-Ferreira, M.A. 2021. Depositional and geomorphic patterns of mixed calciclastic-siliciclastic systems on a deep-water Equatorial Margin. Basin Research, 00, 1-27.

Available at: <https://doi.org/10.1111/bre.12604>.

Although the articles are jointly co-authored with the project supervisors and other authors, the work presented in the publications is that of the lead author, Roberto Loza Espejel. Editorial work was provided by the project supervisors in accordance with a normal thesis chapter.

Acknowledgements

I would like to express my gratitude to all the people who have contributed in some way to the completion of this thesis and supported me throughout my PhD journey.

First and foremost, I am deeply grateful to my PhD supervisor Tiago Alves, for all the priceless guidance, support, enthusiasm, and motivation that I received from the time I applied for my PhD programme until the completion of this thesis. I am grateful with Tiago for always reading my drafts promptly and the continuous advice and countless discussions about research ideas that helped my development as a researcher. Thank you for the great time throughout my PhD including multiple field and pub trips like the time in Cariatiz, Spain.

I also would like to thank my second supervisor Tom Blenkinsop for the constant support and constructive advice as to improve my research. Thank you for your time and insightful conversations. Thanks to Marco Antonio Caçador Martins-Ferreira for his help and motivation to improve the last data chapter of this thesis and providing me with well data. Gwen Pettigrew is thanked for being always available to help with IT issues in the 3D Seismic Lab.

The Mexican National Council of Science and Technology (CONACYT) and the hydrocarbon Secretariat of Energy (SENER) are acknowledged for funding this PhD project. Geoscience Australia is thanked for providing the Karmt 3D seismic volume and well data interpreted in this work. CGG and Polarcus are also acknowledged for the provision of the Pernambuco and the Pará-Maranhão 3D seismic volumes, respectively. The Brazilian National Agency of Petroleum, Natural Gas and Biofuels (ANP) is acknowledged for providing well data for the Pará-Maranhão Basin.

I am thankful for the AAPG Grants-in-Aid General Fund Award 2018 and the Duncan A. McNaughton Memorial Grant 2020 to cover fieldwork expenses to Cariatiz, Spain. Schlumberger (Petrel®), ESRI ArcGIS® and CorelDRAW® are acknowledged for granting academic licenses to Cardiff's 3D Seismic Lab.

Furthermore, I am thankful with editors and reviewers of the published manuscripts included in this thesis for their comments and criticisms that improved the quality of this thesis: Peter Burgess, Dan Bosence, David Sanderson, Cees Passchier, Lorena Moscardelli, Xavier Janson and anonymous reviewers.

Many thanks to my fellow 3D Seismic labbers past and present - in particular, Chantelle, Lilly, Nick, Nathalia, Cerys, Song and Qiang for all the fun time and interesting - and sometimes bizarre - talks during lunchtime, Christmas dinner, etc.

Thank you to all the amazing friends I was fortunate to make in Cardiff: my best mate Will, Kim, Edith, María, Víctor, Haydeé, Diego, Ana, Alex, Claudia and Silvia. Thank you for all those parties, dances, and food preparations that we do. I also would like to thank my best friend since our undergraduate degree in Mexico, Dino, for always being there for me despite the distance. Without all these friends, my PhD experience would have definitely not been the same.

A special thanks to Charis for encouraging me to start my PhD and for the good times doing either ordinary things or exploring new places and having great adventures. Thank you to all my family in Mexico and my new family in the UK.

Last but definitely not least, I am deeply grateful to both my grandparents Roberto and Nice, for all their unconditional love and care, for encouraging me to pursue science and for always being there for me. Abuelito, te extraño mucho, pero estoy seguro de que desde el cielo puedes ver todos mis logros.

Table of contents

Statements and declaraction.....	iv
Abstract.....	v
Author note and status of publications.....	vii
Acknowledgements.....	viii
Table of contents.....	ix
List of figures.....	xviii
List of tables.....	xlvi
Chapter 1: Introduction and literature review	1
1.1 Rationale and aims.....	2
1.1.1 Rationale	2
1.1.2 Aims of this research	7
1.2 Thesis layout	12
1.3 Carbonate-grain associations	13
1.3.1 Photozoan carbonates.....	13
1.3.2 Transitional carbonates	14
1.3.3 Heterozoan carbonates	16
1.4 Carbonate factories.....	19
1.4.1 Photozoan T-factory	20
1.4.2 Biochemical T-factory.....	21
1.4.3 Photo-C-factory	21
1.4.4 Heterozoan C-factory	22
1.4.5 Automicrite factory.....	22
1.4.6 Seep and continental factory	24
1.4.7 Carbonate productivity and sigmoidal growth.....	24

1.4.8	Sedimentation rates and growth potential.....	26
1.5	Environmental controls of carbonate development	28
1.5.1	Light	28
1.5.2	Water temperature	28
1.5.3	Latitudinal zonation of skeletal production.....	31
1.5.4	Salinity	31
1.5.5	Nutrient concentration.....	31
1.6	Limestone classification.....	32
1.6.1	Dunham classification	32
1.7	Carbonate platforms.....	33
1.7.1	Attached carbonate platforms	35
1.7.2	Rimmed carbonate platforms	35
1.7.3	Carbonate ramp.....	37
1.7.4	Isolated carbonate platform	37
1.8	Carbonate slopes	42
1.8.1	Geometrical profile and terminology	42
1.8.2	Types of slope carbonate deposits	44
1.8.2.1	Debris deposits.....	44
1.8.2.2	Grain-dominated deposits.....	45
1.8.2.3	Mud-dominated deposits	45
1.9	Spatial architecture of slope deposits	47
1.9.1	Strike-continuous aprons	47
1.9.1.1	Gullied upper slope/lower slope aprons	47
1.9.1.2	Grain-dominated slope aprons	47
1.9.1.3	Debris-dominated slope aprons	48
1.9.2	Strike-discontinuous accumulations.....	48
1.9.2.1	Foreslope megabreccia	48
1.9.2.2	Isolated basinal megabreccia.....	48
1.9.2.3	Basinal channel-fan complexes.....	49
1.10	Carbonate porosity and permeability.....	49
1.10.1	Choquette and Pray porosity classification	50

1.10.2	Primary porosity	52
1.10.3	Secondary porosity	52
1.10.3.1	Porosity by dissolution	52
1.10.3.2	Porosity by dolomitization.....	52
1.10.3.3	Porosity associated with breccias	53
1.10.4	Porosity associated with fractures	53
1.10.5	Diagenesis and porosity	54
1.11	Fault and fracture analysis.....	54
1.11.1	Fault linkage.....	55
1.12	Scaling laws	59
1.12.1	Sampling effects	62
1.12.1.1	Truncation effect	62
1.12.1.2	Censoring effect.....	62
1.12.2	Sampling effects when measuring fault throws	63
Chapter 2:	Geological settings of the studied areas	65
2.1	Introduction	66
2.2	Bonaparte Basin, Northwest Shelf of Australia	66
2.2.1	Tectono-stratigraphic evolution	68
2.2.2	Stratigraphic setting.....	69
2.3	Cariatiz carbonate platform, Sorbas Basin, SE Spain	73
2.4	Pernambuco Basin, East Brazil	77
2.4.1	Tectono-stratigraphic evolution	77
2.5	Pará-Maranhão Basin, Equatorial Brazil.....	80
2.5.1	Tectono-stratigraphic setting	82
2.5.2	Regional stratigraphy.....	85
2.5.3	Carbonate platform development off PAMA	86
Chapter 3:	Data and methods	88
3.1	Introduction	89
3.2	Seismic reflection data.....	89

3.3	2D and 3D seismic	90
3.4	Acquisition of seismic reflection data.....	92
3.4.1	Seismic resolution	95
3.4.1.1	Vertical resolution	96
3.4.1.2	Horizontal resolution	96
3.4.2	Marine surveys.....	97
3.5	Seismic processing	100
3.5.1	Data preparation	100
3.5.2	Data correction.....	102
3.5.2.1	Amplitude corrections	102
3.5.2.2	Noise attenuation	102
3.5.2.3	Static corrections.....	102
3.5.2.4	Velocity analysis.....	104
3.5.2.5	Migration.....	104
3.5.3	Data reduction and enhancements	105
3.5.3.1	Multiple attenuation and deconvolution	105
3.5.3.2	Filtering and scaling	105
3.6	Challenges of seismic imaging on carbonates	107
3.6.1	Seismic velocity on carbonates	107
3.6.2	Porosity and its seismic response on carbonates.....	107
3.6.3	Karst features	108
3.7	Datasets in this study	110
3.7.1	Seismic data	110
3.7.1.1	Bonaparte Basin, Northwest Shelf of Australia	110
3.7.1.2	Pernambuco Basin, east Brazil	110
3.7.1.3	Pará-Maranhão Basin, Equatorial Brazil.....	111
3.7.2	Borehole data	112
3.7.2.1	Bonaparte Basin, Northwest Shelf of Australia	112
3.7.2.2	Pará-Maranhão Basin, Equatorial Brazil.....	112
3.7.3	Outcrop data	113
3.7.4	LiDAR data	113

3.7.5	Satellite data	113
3.8	Methods.....	114
3.8.1	Seismic interpretation and visualisation	114
3.8.1.1	Seismic attribute analysis.....	117
3.8.1.2	Multiattribute displays.....	121
3.8.1.3	Fault and fracture mapping.....	122
3.8.1.4	Horizon mapping.....	122
3.8.2	Fault-throw measurements.....	127
3.8.3	Field methodology	130
Chapter 4:	Structural controls on isolated carbonate platforms	133
4.1	Abstract.....	134
4.2	Introduction	135
4.3	Chapter specific datasets and methods.....	137
4.3.1	Physiography of the Karmt Shoals	143
4.3.2	Seismic interpretation	145
4.3.3	Fault-throw measurements.....	151
4.3.4	ICP fault and area distribution.....	158
4.4	Seismic stratigraphy	162
4.4.1	Unit 1: Early Eocene-Paleocene	162
4.4.2	Unit 2: Oligocene-middle Eocene.....	163
4.4.3	Unit 3: Miocene	163
4.4.4	Unit 4: Pliocene	164
4.4.5	Unit 5: Pleistocene	164
4.5	ICP geometries and fault distribution	165
4.5.1	Zone 1	168
4.5.2	Zone 2	169
4.5.3	Zone 3	169
4.5.4	Zone 4	169
4.6	Fault-throw analysis	170
4.7	Fault-propagation styles	175

4.8	Chapter-specific discussion	177
4.8.1	Relationship between carbonate deposition and fault growth....	177
4.8.2	Implications for petroleum systems on continental margins	182
4.9	Chapter-specific summary	184
Chapter 5: Fracture network characterisation on carbonate platforms.		186
5.1	Abstract.....	187
5.2	Introduction	188
5.2.1	Challenges and limitations	189
5.3	Chapter specific datasets and methods.....	196
5.3.1	Topological sampling	198
5.3.2	Geometrical sampling	202
5.3.3	Cariatiz platform.....	203
5.3.3.1	Outcrop data - Field procedure	203
5.3.3.2	LiDAR data - GIS analysis	208
5.3.4	Pernambuco carbonate platform	210
5.3.4.1	Seismic data - seismic interpretation	210
5.3.5	Statistics and data analyses	213
5.4	Fracture network characterisation	216
5.4.1	Fracture complexity	216
5.4.2	Fracture network geometry	217
5.4.2.1	Fracture length	217
5.4.2.1.1	Cariatiz platform - outcrop data	217
5.4.2.1.2	Cariatiz platform - LiDAR data	218
5.4.2.1.3	Pernambuco platform - seismic data	219
5.4.2.2	Fracture orientation	220
5.4.2.2.1	Cariatiz platform - outcrop data	220
5.4.2.2.2	Cariatiz platform - LiDAR data	221
5.4.2.2.3	Pernambuco platform - seismic data	221
5.4.3	Fracture network topology	222
5.4.3.1	Cariatiz platform - outcrop data	222
5.4.3.2	Cariatiz platform - LiDAR data	224
5.4.3.3	Pernambuco platform - seismic data	224

5.5	Chapter specific discussion	225
5.5.1	Fracture attribute relationships at different scales	225
5.5.1.1	Fracture geometry	226
5.5.1.1.1	Orientation	226
5.5.1.1.2	Scale gap	229
5.5.1.1.3	Branch length	232
5.5.1.2	Fracture topology	233
5.5.2	Implications to naturally fractured reservoirs	235
5.6	Chapter-specific summary	237
Chapter 6:	Deep-water depositional systems	240
6.1	Abstract.....	241
6.2	Introduction	242
6.3	Chapter specific datasets and methods.....	248
6.3.1	Seismic interpretation and channel definition	248
6.3.2	Geomorphic parameters	256
6.3.3	Statistical analysis	260
6.4	Physiography and sedimentary environment	263
6.5	Borehole stratigraphic interpretation	265
6.6	Seismic-stratigraphic framework of PAMA	267
6.6.1	Unit 1 - Lower Miocene	268
6.6.2	Unit 2 - Middle Miocene	269
6.6.3	Unit 3 - Upper Miocene-Pliocene	269
6.6.4	Unit 4 Pleistocene to Recent.....	269
6.7	Morphology of calciclastic submarine fans and levee-channels	270
6.7.1	Calciclastic submarine fan a	270
6.7.2	Channel b	271
6.7.3	Channel c	271
6.7.4	Channels d, e and f	272
6.7.5	Channel x	272
6.7.6	Channel y	272

6.8	Channel morphometric relationships	273
6.9	Chapter specific discussion	274
6.9.1	Mixed calciclastic-siliciclastic depositional systems in the deep and ultra-deep PAMA Basin.....	275
6.9.2	Geomorphic characteristics of carbonate deep-water levee-channels	281
6.9.2.1	Type 1 - channels related to calciclastic submarine fans	282
6.9.2.2	Type 2 - low sinuosity, aggradational channels.....	283
6.9.2.3	Type 3 - high-sinuosity channels	283
6.10	Chapter specific summary	285
Chapter 7:	Discussion and conclusions	287
7.1	Preamble	288
7.2	Summary of scientific results.....	289
7.2.1	Chapter 4: Structural controls on isolated carbonate platforms..	289
7.2.2	Chapter 5: Multi-scale fracture network characterisation on carbonate platforms	290
7.2.3	Chapter 6: Deep-water depositional systems.....	291
7.3	Integration and wider implications	293
7.3.1	Structural controls on shallow-water carbonate settings	293
7.3.2	Fracture types and reservoir properties.....	298
7.3.3	Importance of fracture types to fluid flow.....	303
7.3.4	Structural and sedimentological controls on deep-water carbonate settings	304
7.3.4.1	Sediment type	305
7.3.4.2	Palaeotopography and funnelling mechanisms.....	306
7.3.4.3	Sea-level fluctuations.....	307
7.3.4.4	Oceanic currents	308
7.3.5	Deep-water exploration play types	308
7.4	Limitations of this research.....	312
7.5	Future work	314

Chapter 8: References.....	316
Appendix A: Fracture branch length distribution histograms.....	361
Appendix B: Rose diagrams showing fracture branch orientation	364
Appendix C: Ternary plots showing detailed topological analyses	367
Appendix D: Fracture topological data	369

List of figures

Chapter 1

Figure 1.1. World map of carbonate rock outcrops. Modified from Williams, P. and Fong, Y.T. 2010. World map of carbonate rock outcrops v. 3.0. Available at <https://www.fos.auckland.ac.nz/our_research/karst/index.html#karst1>

(accessed 16/08/2020)..... 4

Figure 1.2. Oceanographic world map showing the distribution of modern shallow-water marine carbonate factories. The green lines are isotherm lines dividing warm water zones around the Equator from cool water zones. Red stars show the location of the different study areas analysed in this thesis. Modified from Laugié et al.

(2019)..... 5

Figure 1. 3. Graphical diagram showing the scale of observation for different data types that are commonly used to study structural and sedimentological features in the surface and subsurface. Note the scale gap between wellbore data and seismic data at the intermediate scale. Modified from Gutmanis and Ardèvol i Oró (2015). 6

Figure 1. 4. Summary of Cenozoic carbonate assemblages based on benthic (skeletal and non-skeletal) components. Assemblages are grouped in photozoan, heterozoan and transitional associations after James (1997). Figure from Kindler and Wilson (2010). 15

Figure 1.5. Schematic diagram of the carbonate factory classification proposed by Michel et al. (2019) relating carbonate deposits with oceanographic parameters. 23

Figure 1.6. Sigmoidal growth curve explaining carbonate productivity. Figure from Schlager (2005)..... 25

Figure 1.7. Sedimentation rates of different types of carbonate factories plotted against the length of time-interval of observation. Modified after Schlager (2005).
..... 27

Figure 1.8. Carbonate production profile in a tropical setting. Maximum production is related to the upper part of the photic zone before light saturation decreases exponentially with depth. In areas above the sea level (terrestrial), production is negative as carbonate rocks are dissolved. Figure from Schlager (2005).
..... 29

Figure 1.9. World map showing the position of modern tropical and cool-water carbonates based on the latitude zonation. Modified from Schlager (2005). 30

Figure 1. 10. Dunham (1962) textural classification of limestones. Figure from Schlager (2005). 34

Figure 1.11. Schematic diagram showing the different types of depositional profiles on carbonate platforms, from homoclinal ramps to flat-topped rimmed shelves. Figure from Pomar (2001). 36

Figure 1.12. Schematic cross section of the Florida Shelf showing the main depositional environments commonly seen on a rimmed carbonate shelf: lagoon, back reef, barrier reef, fore reef and slope. Figure from Bosence (2005a). 38

Figure 1.13. Schematic cross section of the Arabian Gulf showing the main depositional environments commonly seen on a carbonate ramp: inner, mid-, and outer ramp. Figure from Bosence (2005a). 39

Figure 1.14. Schematic cross section of the Great Bahama Bank showing the main depositional environments commonly observed on a rimmed isolated carbonate

platform: lagoon, barrier reef, oolitic shoals and slope. Figure from Bosence (2005a).
 40

Figure 1.15. (a) Schematic diagram showing the geometry and internal depositional environments of an isolated carbonate platform. (b) Ancient example of an ICP from the Triassic Sella Group, Dolomites, Italy. Figure from Rusciadelli and Shiner (2018). 41

Figure 1.16. Schematic diagrams showing the different types of carbonate margins (accretionary and escarpment margins) and the major terms related to shelf-to-basin depositional systems. Figure from Playton et al. (2010). 43

Figure 1.17. Schematic diagrams of carbonate slope and basin spatial architecture showing different strike-continuous aprons and strike-discontinuous tongues and channel-fan complexes. Figure from Playton et al. (2010). 46

Figure 1. 18. Choquette and Pray (1970) classification of carbonate porosity. Figure from Moore (1970). 51

Figure 1.19. Schematic diagram of fault trace structures with interacting faults. (a) fault bend, (b) transfer fault, and (c) overlap zone. Figure from Childs et al. (1995). 56

Figure 1.20. Schematic diagram of a relay ramp structure showing the connection between the hanging wall and footwall through the ramp. Relay ramps form when two faults overlap spatially, also overlapping their two strain envelopes. A single, isolated fault is shown to the left. Figure from Fossen and Rotevatn (2016). 56

Figure 1.21. Outcrop example of a relay structure from Canyonlands National Park (Devils Lane), USA. Faults and fractures are observed within the relay ramp area. Figure from Fossen and Rotevatn (2016). 57

Figure 1.22. Diagram showing the stress zonation (drop or increase) around a normal fault in overlay zones. Figure from Fossen and Rotevatn (2016). 58

Figure 1.23. Frequency plot with logarithmic axes showing different statistical distributions. The graph shows (1) an ideal power-law, (2) exponential, (3) log-normal, and (4) normal, Gaussian distribution. Figure from Torabi and Berg (2011). 60

Figure 1.24. Cumulative frequency plot showing the sampling biases (truncation and censoring) that affects the distribution of fault and fracture attributes, causing a deviation of a distribution from a straight line. Figure from Torabi and Berg (2011). 61

Figure 1.25. Schematic diagram showing isolated and segmented-linked faults with their respective T-D profiles showing the impact of data sampling. At coarser sampling intervals: 1) fault geometry changes from symmetric to asymmetric. 2) Fault linkage geometry changes. 3) Fault segment geometry changes. 4) Fault-linkage zone geometry and width change. 5) Fault segments are not discerned. Figure from Tao and Alves (2019). 64

Chapter 2

Figure 2.1. a) Location map of the Bonaparte Basin with an enlarged image (b) showing the seismic volume Karnt 3D and exploration wells utilised in this thesis. c) Bathymetric map showing the study area in the Westralian Superbasin (WASB). The studied Karnt 3D volume is located in the western part of the Sahul Flamingo Nancar

Area. Bathymetric data provided by Geoscience Australia. Basin boundaries are modified from Longley et al. (2002). 67

Figure 2.2. Cenozoic stratigraphic chart of the north-western Bonaparte Basin and its seismic stratigraphic units. Modified from Willis (1998) and Saqab and Bourget (2015a). The seismic section in the figure crosses the Ludmilla-1 well for reference. 71

Figure 2.3. Two-way time (TWT) arbitrary seismic profile, with a NE-SW orientation, across the Ludmilla-1 and Nancar-1, ST1 wells. Main seismic-stratigraphic markers are shown in the figure: Seafloor (SF), Base Pleistocene (H₆), Base Pliocene (H₅), Base Miocene (H₄), Mid Eocene (H₃), Top Paleocene (H₂), Base Paleocene (H₁). 72

Figure 2.4. a) Location of the study area in SE Spain. b) Regional map of the Sorbas Basin showing the Messinian Reef Unit, and the area of interest at Cariatiz. Modified after Reolid et al. (2014). 74

Figure 2.5. Cariatiz facies model. Modified after Braga and Martín (1996) and Reolid et al. (2014). 76

Figure 2.6. a) Location map of the Pernambuco Basin showing the study area in a red circle. b) Seismic section across the Pernambuco Platform showing its internal geometry and seismic facies, as well as the presence of normal faults. *Sequence numbers after Buarque et al (2017). Scale and exact location cannot be given due to data privacy. 79

Figure 2.7. a) Location map of the Brazilian Equatorial Margin highlighting the study area in the Pará-Maranhão (PAMA) Basin. Red rectangle shows the location of the studied 3D seismic survey. Green lines mark basin limits. b) Enlarged figure

showing the different 2D, 3D seismic datasets and exploration wells utilised in this thesis. 81

Figure 2.8. Regional seismic sections depicting the regional stratigraphic units and seismic facies of the PAMA Basin. a) Reinterpreted 2D seismic profile GB1-4500 from Henry et al. (2011) and Zalán (2015). A red rectangle shows the portion of the basin studied in this work. b) Schematic section of the PAMA Basin outlining the distribution of the different geological formations. P-O=Paleocene-Oligocene, M-R=Miocene-Recent. Modified after Brandão and Feijó (1994). 84

Figure 2.9. Cenozoic lithostratigraphic chart of the PAMA Basin and its main seismic stratigraphic units. *Comparable sequences, unconformities and lithostratigraphy taken from Soares et al. (2007). 87

Chapter 3

Figure 3.1. Schematic diagram showing an example of how the acoustic impedance relates to changes in lithological layers. Figure from Brown (2011). .. 91

Figure 3.2. Schematic diagram showing the different types of seismic waves. (a) compressional P waves, (b) shear S waves, and (c) boundary, Rayleigh waves. Figure from Cox et al. (2020). 93

Figure 3.3. Schematic diagram showing wavelet types and their display. A) measurable characteristics of a wavelet. B) different elements of a seismic wave. C) polarity conventions used for displaying seismic data. Figure from Cox et al. (2020). 94

Figure 3.4. Schematic diagram of a 2D marine survey. The acoustic pulse created by airguns travels into the subsurface and reflects the main geological boundaries.

Reflected energy is then recorded by hydrophones within a streamer cable and relayed back to the vessel. Figure from Cox et al. (2020). 98

Figure 3.5. Schematic diagram of a 3D marine survey showing how 3D seismic reflection data is collected. Data contained within the bins is processed as traces for each individual bin. Figure from Cox et al. (2020). 99

Figure 3.6. Workflow summarising the general steps followed on seismic processing from field seismic data to the generation of an interpretable seismic image. Figure from Cox et al. (2020). 101

Figure 3.7. Schematic diagram showing the velocity analysis and normal move-out (NMO) correction. A) Diagrams showing the use of common midpoint (CMP) gathers, source and receiver pairings during acquisition. b) Graphs displaying the distance from the source and the time recorded for both field data and CMP-sorted wavelets. A hyperbolic curve is observed due to the delay in the wavelet. NMO returns the reflection into its correct position for any given time and offset. c) Equations for the hyperbolic reflection and NMO. Figure from Cox et al. (2020). 103

Figure 3.8. Seismic cross section showing an example of a seabed multiple created as a result of the returning seabed reflection, reflecting downwards. Figure from Cox et al. (2020). 106

Figure 3. 9. Graph showing the wide seismic velocity ranges of different types of rocks reported by Birch (1966). Note the higher velocities of limestone and dolomite compared to shale and sandstone. Figure from Telford et al. (1990). 109

Figure 3.10. 3D visualisation showing how seismic data can be displayed including a 3D seismic probe and typical intersections such as In-line, X-line, Z-slice and an arbitrary line. Example from the 3D PAMA seismic volume. 115

Figure 3.11. Series of seismic displays showing (a and c) variable-area wiggles and (b and d) variable amplitude spectrums using different colour schemes. The red-white-black colour scheme is used for the Karmst 3D seismic volume and Pernambuco 3D seismic volume. Seismic default colour scheme is used in the 3D PAMA volume. I Seismic polarity diagram showing peaks and troughs in the wiggles. 116

Figure 3.12. Seismic sections showing seismic attributes that were useful for horizon interpretation as the continuity of reflectors is enhanced. Example from the 3D PAMA volume. 118

Figure 3.13. Seismic depth slices and seismic sections showing the different attributes calculated in this thesis. Seismic overlay enhances visualisation as it combines two seismic attributes. Example from the 3D PAMA volume. 119

Figure 3.14. Example of the autotracking window showing the different parameters that can be constrained for a better interpretation. 124

Figure 3.15. 3D view showing how seismic horizon interpretation was performed. (1) Seeded 2D autotracking along inlines and crosslines to generate a grid. (2) Seeded 3D autotracking along inlines and crosslines. (3) Paintbrush 3D interpretation on map view. 125

Figure 3.16. Example of a seismic section from the Karmt3D, Northwest Shelf of Australia (Chapter 4) showing how the interpreted horizon maps relate to different levels on the seismic line. 126

Figure 3.17. Schematic cross sections showing the different types of normal faults and their characteristic fault-throw profile with the growth index curve. Modified from Hongxing and Anderson (2007). 128

Figure 3.18. A) Schematic diagram showing the geometrical features of a fault and an example of a seismic section showing how fault-throw is measured (b and c). 129

Figure 3.19. Example of the circular scanline methodology followed in this thesis. a) Field photograph with measured fracture branches. b) Rectified photo to perform fracture measurements digitally. c) Circular scanline image showing all the obtained data. r =circle radius, n =number of fractures intersecting the circle line, N_I =number of isolated nodes, N_Y =number of single connected nodes, N_X =number of double connected nodes, $I-I$ =number of isolated branches, $I-C$ =number of single connected branches, $C-C$ =number of double connected branches..... 132

Chapter 4

Figure 4.1. Three-dimensional (3D) seismic display of seismic amplitude corendered with the variance attribute at IL 5333, XL 3335, and a time slice at $T=-932$ ms. Velocity pull-up effects are observed as fault shadows or fault-like structures (green arrow) and false “uplifted” strata (red arrow) as a result of spatial changes in V_p across the ICPs. These effects are also observed in time slices as sub-circular features creating false outlines below ICPs (green arrows). Real faults (blue arrows) present continuity in both the time slices and vertical sections, as well as clearly offsetting continuous seismic reflectors. 139

Figure 4.2. Well correlation panel for the study area showing main stratigraphic units, stratigraphic boundaries, and corresponding seismic horizons as interpreted on seismic data. The correlation was performed considering Ludmilla-1 as the principal well in the study area based on its complete gamma-ray (GR) and sonic (DTC) logs, later integrating biostratigraphic (foraminifera and nannoplankton) data

taken from raster composite well logs and micropalaeontological reports available for the four wells shown in the figure (Rexilius et al., 1998a, 1998b; Willis, 1998, 1999a, 1999b, 1999c; Rexilius and Powell, 1999a, 1999b). See Fig. 4.9 for well locations and corresponding transect. 140

Figure 4.3. Composite log showing GR, RT, NPHI, RHOB and DTC curves for the Ludmilla-1 well. Integrated biostratigraphic data from sidewall core and cutting samples is presented here with foraminifera and nannoplankton zones and their respective ages. Interpreted seismic markers correspond to main seismic horizons considered in this work. Composite log data is taken from Willis (1998). 141

Figure 4. 4. Three-dimensional (3D) perspective of the seafloor as interpreted from the Karmt3D seismic volume. The map displays the Karmt Shoals with several isolated carbonate platforms (ICPs). (1) Moat channels surrounding ICPs, (2) interior patch reefs, (3) interplatform channels, (4) lagoon, (5) platform rim, (6) steep platform slope. 144

Figure 4.5. Isochron maps showing the TWT thickness of different seismic-stratigraphic units. (a) Isochron map of Unit 5 from the Seafloor to horizon H₆. (b) Isochron map of Unit 4 from horizons H₆ to H₅. (c) Isochron map of Unit 3 from horizon H₅ to horizon H₄. (d) Isochron map of Unit 2 from horizon H₄ to horizon H₃. 146

Figure 4.6. Time structure map of the base Pleistocene (horizon H₆) showing the major fault arrays (white dashed lines) in the study area with a general trend NE-SW. ICPs (blue dashed lines) are identified with their types for reference. Thick black line indicated the well correlation shown in Figure 4.2. 148

Figure 4.7. Variance map of the base Pleistocene (horizon H₆) showing the four structural zones (separated by green solid lines) identified in the study area. Large

(light pink polygons) and small (purple polygons) relay ramps are mapped to show their relation to ICPs. The red rectangle represents the area of interest in which detailed throw measurements were undertaken to generate T-Z plots (Figure 4.11), T-D plots (Figure 4.12) and the high-resolution contour fault-throw map in Figure 4.13. 149

Figure 4.8. Diagrams summarising the methodology adopted to collect T-Z and T-D data across the Karmt3D seismic volume. (a) Map view of a fault on a hypothetical time slice. Seismic sections used to compile T-Z and T-D data were perpendicular to the strike of a given fault at each discrete measuring point, as most faults are slightly curved in the study area. Inlines (IL) and cross-lines (XL) are not useful as they cut the fault at an arbitrary angle β . (b) Three-dimensional (3D) view showing a fault with two intersecting sections; one perpendicular to strike in which the fault dip (α_1) can be taken, and a second section intersecting the fault at an arbitrary angle to its strike. This latter section will only provide the apparent dip of the fault. . 150

Figure 4.9. (a) Uninterpreted NW-SE seismic profile and (b) corresponding interpretation showing four different zones in the SW of the study area. Zone 1 shows no faulting. In zone 2, there are two different fault systems: one Neogene-Quaternary and an older Paleogene in age. An ICP developed above the Neogene-Quaternary faults. Zone 3 presents highly faulted Neogene-Quaternary strata with faults propagating to the surface, as well as Paleogene faulting. Within zone 4, there is only one small fault offsetting Neogene-Quaternary strata. 152

Figure 4.10. (a) Uninterpreted NW-SE seismic profile and (b) corresponding interpretation showing three different zones in the centre of the study area. Zone 1 shows normal fault systems. This zone is characterised by the absence of ICPs. Zone

2 shows the presence of the two fault systems: Neogene-Quaternary and Paleogene. There are faults below the two ICPs in this zone. Zone 3 contains the major fault in the area (F1), which propagates to the surface; and minor Neogene-Quaternary normal faults. Zone 4 includes a large fault area with synthetic and antithetic faults. 153

Figure 4.11. (a) Uninterpreted NW-SE seismic profile and (b) corresponding interpretation showing three different zones in the NE of the study area. Zone 1 does not reveal faulting. In zone 2 there are antithetic faults in Neogene-Quaternary strata. Zone 3 is highly faulted and the ICP is underlain by a major fault (F1). .. 154

Figure 4.12. Fault-throw (T-Z) profiles (black curves) and growth index plots (orange curves) with corresponding seismic profiles showing specific measurement points in a direction perpendicular to the strike of fault array F1. Profiles were taken at various distances along F1, from southwest to its northeast (see distances above each of plots shown). For the location of the lines along the fault plane, see Figure 4.13c. Across the study area there are two throw maximas (red circles), indicating a period of fault initiation. The first period of faulting occurred during the Late Paleocene-Early Eocene with downward fault propagation (dotted arrow line) into Unit 1 and upward fault propagation (solid arrow line) into Unit 2. There is a period of fault inactivity between Units 2 and 3, which is represented by an almost constant throw (dashed arrow line). The second period of faulting occurred during the Late Miocene-Early Pleistocene with a downward fault propagation into the base of Unit 3 (dotted arrow line) and upward syn-depositional fault propagation into Units 4 and 5 (solid arrow line). The rapid decrease in throw near the seafloor reflects the presence of a growth sequence. It can also be observed in the form of values greater

than 1.0 on the growth index plot. Horizontal lines indicate the interpreted seismic horizons. 155

Figure 4.13. (a) Uninterpreted and (b) interpreted variance data for the area of interest recognised on the time-structure map of horizon H₆. Different fault segments, displayed as solid red lines, are identified along fault F1 - thus identifying it as a ~50 km long fault array. ICP outlines are shown in blue. Symbols α, β, γ and δ represent the ICPs crossing fault array F1. The bright yellow solid line indicates the position of the cross section. (c) Maximum fault-throw profile (T-D Plot) of fault array F1 in Neogene-Quaternary strata showing different fault segments with a red line. The blue dashed lines represent the boundaries of the ICPs, and the green dashed lines indicate the position of the T-Z plots displayed in Figure 4.12. Relay ramps are located where two different fault segments intersect and throw values are relatively small. These relay ramps are shown in pink. (d) Uninterpreted NW-SE seismic profile and I corresponding interpretation showing fault segments F1a and F1b and a relay ramp in-between. 156

Figure 4.14. High-resolution fault-throw surface map along the strike of fault array F1, shown with a 3x vertical exaggeration. Cold colours represent the smallest throw values, whereas warm colours indicate relatively large throws. The hanging-wall levels of the interpreted horizons (H₁ to H₆) are displayed for reference. The position of the ICPs is drawn with red lines. White line ellipses represent the interpreted individual fault segments. Pink dashed lines represent the large-scale fault segments. The areas with small throw values between the individual fault segments coincide with relay ramps, which are plotted as pink zones. The presence of two faulting events (Paleogene and Neo-Quaternary) separated by horizon H₄ is

clear in the fault surface map. The position of Quaternary ICPs is also shown in the figure and related to the presence of relay ramp zones. 157

Figure 4.15. Variance time slices across the Karmt3D seismic volume, with a spacing of 64 ms, from the base Pleistocene to -216 ms. ICPs are highlighted by the light blue outline. 159

Figure 4.16. Histogram and scatter plots showing (a) the multimodal area distribution of ICPs; (b) ICP area against the number of crossing faults; and (c) ICP area vs. the number of faults around ICPs within 500 m. 161

Figure 4.17. Selected seismic profiles showing the detailed geometry of the different types of ICPs. The variance map of horizon H₆ in (a) shows the location of the seismic profiles. (b) The large ICP ϵ appears as type 3 or (c) a combination between type 2 and 3. This suggests that large platforms can contain ICPs that grew by a combination of any of the types interpreted in this work. (d) ICP η reveals its development as a type 2 platform on an inner relay ramp. e) ICP γ as a type 2 platform with a faulted internal structure. (f and g) Different ICPs developed on a structural high and showing relatively intact internal structures. 166

Figure 4.18. Schematic diagrams illustrating the position of ICPs over relay ramp structures as interpreted in this work. (a) ICPs located over growing fault tips; (b) development of an ICP inside a relay ramp; (c) relay ramp formed by several fault segments on a larger scale where ICPs can develop close to fault tips, or on the relay ramp per se. 178

Figure 4.19. Schematic diagram summarising the relative position of ICPs as a function of fault-throw rates (T) and carbonate productivity (P). Type 1 ICPs develop on structural highs and they remain relatively intact. Type 2 ICPs develop in areas

of antecedent faulting, such as on a relay ramp, and where carbonate productivity exceeds fault-throw rates. Type 3 ICPs develop initially on a non-faulted zone. Once formed, faults can cross-cut the ICP, fracturing them internally. 181

Chapter 5

Figure 5.1. A) Location of the study area in SE Spain. B) Regional map of the Sorbas Basin showing the Messinian Reef Unit, and the area of interest at Cariatiz. Modified after Reolid et al. (2014). C) Topographic map showing the field sites where fracture network mapping was performed using the augmented circular scanline method of Watkins et al. (2015). Rose diagrams show the main fracture orientation at each site. 193

Figure 5.2. A) Location map of the study area in the Pernambuco Basin. b) Variance depth slice (-1720 m) showing the area (yellow line) where fracture characterisation was performed. C) Seismic section across the Pernambuco Platform showing its internal geometry and seismic facies, as well as the presence of normal faults. *Sequence numbers after Buarque et al (2017). Scale and exact location cannot be given due to data privacy. 194

Figure 5.3. Flowchart summarising the methodology used in this work to obtain fracture data from different datasets. Three different input datasets with distinct scale-resolution were utilised (outcrop: small scale, LiDAR: intermediate scale, seismic: large scale). *Consider suggestions by Rohrbaugh et al. (2002) and Watkins et al. (2015) to determine the radius (r). See more details in the text. 195

Figure 5.4. Outcrop images and facies model showing the complexity of structural and depositional attributes in the Cariatiz fringing reef unit. A) Outcrop image showing large fractures across the platform edge. B) Enlarged photo showing circular

shapes of Porites on a horizontal section. C) Fracture swarms along the platform margin. See Figure 5.7a for location. d) Facies model of Cariatiz, modified after Braga and Martín (1996) and Reolid et al. (2014). E) Outcrop photo showing vertical Porites. See Figure 5.1c for location..... 197

Figure 5.5. Schematic diagrams showing the topological analysis and sampling effects of fracture networks. a) Fracture traces (A-B and C-D) and their node and branch association with intersecting fractures (dashed lines). I-nodes (green circles); Y-nodes (blue triangles); X-nodes (orange diamonds); I-I or isolated branch (I-I nodes with no fracture intersection); I-C or partly connected branch (I-Y or I-X node intersection); and C-C or doubly connected branch (Y-Y, Y-X, or X-X node intersection). Modified from Sanderson and Nixon (2015). B) Erroneous recognition of fracture traces occurs as they can be interpreted differently depending on the criteria used, leading to inconsistent trace lengths and orientations depending on the interpreter. C) By utilising fracture branches as a result of topological analyses, the fracture segments can be identified easier, resulting in reliable measurements of geometrical characteristics. d) Truncation effects occur due to limits in data resolution, and it is present regardless of the use of branches or traces. E) Censoring effects occur as the fractures extend the observable area. f) Censoring effects can be minimised by the use of fracture branches as they do not include the entire trace; rather only one segment of the trace. 200

Figure 5.6. Rectified photographs of circular scanlines showing the fracture networks collected at outcrop in Cariatiz. A-j) Digitised fracture networks showing the topological parameters. Circular scanline (red line), fracture intersections with the sampling circle (yellow circle), I nodes (green triangles), Y nodes (blue squares),

X nodes (orange hexagons). k) Field photograph showing the grid used to rectify the perspective of the circle. l) Rectified photo where geometrical and topological analyses can be performed..... 204

Figure 5.7. LiDAR map of the study area in the Cariatiz carbonate platform with the slope attribute highlighting discontinuities. Fractures present high slope values. Site locations are shown with red circles. A) Uninterpreted 3D visualisation of the LiDAR map, useful to locate outcrop localities and perform fracture interpretation in the intermediate scale. B) Interpreted map showing fracture branches as black lines as well as fracture nodes. The map was divided into three zones to analyse fracture variability. 206

Figure 5.8. Seismic depth slices of the Pernambuco carbonate shelf on the variance attribute computed in this work. Fracture interpretation was performed within an area of interest every 100 m in depth from Z=-1020 m to Z=-2020 m. Topological analyses were also carried out to better understand the fracture network. Fractures are represented with continuous pink lines. I nodes are represented by green triangles, Y nodes by blue squares, and X nodes by orange hexagons. Seismic images are rotated and therefore not in their original orientation due to data protection. 211

Figure 5.9. Statistical plots showing fracture branch length distribution from three scale datasets. Outcrop data from the Cariatiz carbonate platform is plotted in yellow. LiDAR data from the Cariatiz carbonate platform is plotted in green. Seismic data from the Pernambuco carbonate platform is plotted in blue. A), f) and k) Histograms showing a positive skew distribution. B), g) and l) Box plots showing the concentration of branch lengths. Q1, Q2 and Q3 are the values for the lower quartile,

median and upper quartile. Box represents the interquartile range, thick solid grey line represents the minimum and maximum values (whiskers), and dotted line shows the outliers of the data. c), h) and m) Cumulative percentage plotted against fracture branch length; note good fit to a straight line for small branch lengths. D), i) and n) Log (cumulative percentage) plotted against fracture branch length, with straight line indicating negative exponential distribution. E), j) and o) Log (cumulative percentage) plotted against log (fracture branch length), with straight line indicating power-law distribution. Straight red line indicates a good fit. 214

Figure 5.10. Bi-directional moving average rose diagrams and numerical cluster analysis showing fracture orientation and fracture sets from (a and d) outcrop, (b and e) LiDAR, and (c and f) seismic data. Rose diagrams were generated as equal area with a weighting factor of 0.9 and aperture of 9°. Equal area rose diagrams are used to visualise results from the cluster analyses. 215

Figure 5.11. Triangular plots showing detailed topological analyses of nodes and branches and resulting parameters from different scales of observation. A) to f) Outcrop and LiDAR topological results from the Cariatiz Fringing Reef Unit. G) to l) Seismic topological results from the Pernambuco carbonate platform. Yellow area represents the variation in results from outcrop data. Green area represents the variation in results from LiDAR maps. Similarly, blue area represents the variation in results from seismic data. *Purple area is an interpretation of topological values expected with branch lengths observable at seismic scale in Cariatiz. **Orange area is an interpretation of expected values at sub-seismic scale in Pernambuco assuming that fracture connectivity increases at a smaller scale, similarly to the observed trend in Cariatiz. A, g) Fracture network node classification. Yellow circle: average

value from outcrop data; green triangle: average value from LiDAR data; and blue square: average value from seismic data. b, h) N_B/N_L ratio shows values of 3 for outcrop data, 2 for LiDAR data, and 2.5 for seismic data. c, i) Average number of connections per line (C_L) shows a value of 3.4 at outcrop level, a value of 2 from LiDAR data, and a value of 2.6 from seismic data. d, j) Average number of connections per branch (C_B) with a value of 1.82 at outcrop scale, 1.49 at LiDAR scale, and 1.66 at seismic scale. E, k) Branch classification with I-I isolated branches, I-C partly connected branches, and C-C doubly connected branches. f, l) Dimensionless intensity of branches at percolation (B_{22C}). 223

Figure 5.12. Multi-scale statistics of fracture branch lengths and figures showing different fracture types with associated datasets depending on scale. A) Outcrop photos with associated datasets and box plots showing the distribution of fracture branch lengths between different datasets. It is observed from the box plots that there is no overlap between datasets (outcrop - airborne LiDAR and airborne LiDAR - seismic). Large fractures with a scale between outcrop and airborne LiDAR were recognised in the field and can be mapped with the use of ground LiDAR or drone imagery. Fractures observed at each scale are mainly of a different type. Veins and joints can be mapped at outcrop; fracture swarms can be mapped with airborne LiDAR maps; and large kilometre faults can be mapped by using seismic data. Fractures with a branch size in between the scale of the three studied datasets can be mapped with data of different resolution such as drone imagery and higher resolution seismic. B) Cumulative percentage plotted against fracture branch length; note good fit to a straight line for small branch lengths. C) Log (cumulative percentage) plotted against fracture branch length, with straight line indicating negative exponential distribution. D) Log (cumulative percentage) plotted against

log (fracture branch length), with straight line indicating power-law distribution. Straight red line represents a good fit..... 228

Chapter 6

Figure 6.1. A) Location map of the Brazilian Equatorial Margin highlighting the study area in the Pará-Maranhão (PAMA) Basin. Red rectangle shows the location of the studied 3D seismic survey. Green lines mark basin limits. B) Detailed map showing published 2D seismic profiles crossing the study area, used to correlate the stratigraphy of the interpreted horizons. Profile GB1-4500 is from Henry et al. (2011) and Zalán (2015), profile 0222-0837 is from Fabianovicz (2013) and profiles 0270-3010 and 0275-8780 are taken from Da Silva and Riveiro (2018). Exploration wells near the interpreted 3D seismic survey are shown as green dots. For the detailed well correlation, please refer to Figure 6.5. All wells were drilled in shallow waters of the carbonate shelf. C) Multispectral satellite (Sentinel-2) map showing a bathymetric band combination using B4-Red, B3-Green and B1-Ultra blue bands. This map highlights the PAMA offshore areas with suspended siliciclastic sediment and autochthonous carbonate deposits..... 246

Figure 6.2. Seafloor relief map highlighting the depositional setting of the PAMA Basin from the shelf margin to the continental rise. Submarine canyons predominate on the continental slope, whereas there is a major channel-levee system on the continental rise. Different sediment conduits are labelled from a to f. Red arrows indicate sediment funnelling points within the continental slope. Note the high number of funnelling conduits towards channel a. 247

Figure 6.3. Regional seismic sections depicting the regional stratigraphic units and seismic facies of the PAMA Basin. a) Reinterpreted 2D seismic profile GB1-4500 from

Henry et al. (2011) and Zalán (2015) displaying the depositional sequences of the basin at the regional scale. A red rectangle shows the portion of the basin studied in this work, which encompasses the upper section of the Drift Supersequence above the gravitational cell. Refer to Figure 6.1b for location. b) Seismic section of the 3D seismic survey showing the detailed stratigraphy of the PAMA Basin. A gravitational system is observed below the Top Oligocene (TO) unconformity comprising extensional, transitional and contractional sections. Refer to Figure 6.2 for location. c) Schematic section of the PAMA Basin outlining the distribution of the different geological formations. P-O=Paleocene-Oligocene, M-R=Miocene-Recent. Modified after Brandão and Feijó (1994). 249

Figure 6.4. Cenozoic lithostratigraphic chart of the PAMA Basin and its main seismic stratigraphic units. *Comparable sequences, unconformities and lithostratigraphy taken from Soares et al. (2007). **Sea level curve taken from Rossetti et al. (2013) based on data from the Pirabas and Barreiras formations. 250

Figure 6.5. Well correlation panel and seismic sections on the PAMA shelf margin. a) Map of the study area showing the location of wells and seismic data. A blue dashed line shows the shelf margin for reference. B) Well correlation panel for wells 1-MAS-9, 1-MAS-16, 1-MAS-19, 1-MAS-24, 1-MAS-10, 1-MAS-25 and 1-MAS-27A. Well correlation is flattened on the Travosas Formation marker. Information displayed for each well are lithology, Gamma-Ray (GR) and Deep Resistivity (ILD) wireline curves. *Cretaceous ages for well 1-MAS-16 were taken from paleontological data in Piovesan (2008). C) and d) Uninterpreted and interpreted seismic profile 0275-8780 showing the PAMA shelf margin with a thick carbonate platform corresponding to the Ilha de Santana Formation. **Well location is projected. BAS=Basement, EK=Early

Cretaceous, LK=Late Cretaceous, P-O=Paleocene-Oligocene, M-R=Miocene-Recent.
 Modified from Da Silva and Ribeiro (2018). 251

Figure 6.6. Flowchart summarising the methodology used in this work to identify and analyse channel-levee systems. 252

Figure 6.7. 3D views of blended depth and variance horizon maps at different intervals: Seafloor (a, b), horizon H₅ (c, d), and horizon H₄ (e, f). Uninterpreted (a, c, e) and interpreted (b, d, f) maps are shown, and principal morphological features are highlighted in them, including the channel-levee systems interpreted in this work. Red arrows indicate sediment funnelling points on the continental slope. 254

Figure 6.8. Seismic section showing the channel-levee systems in cross-section and the way in which geomorphic data were measured. Lh₁ and Lh₂ are the levee heights, which is the vertical distance between the deepest points (thalweg) of the channel to the two levee crests. Lh_{max} is the maximum levee height, which is measured as the average height between Lh₁ and Lh₂, as there is asymmetry in the channels. The parameter W is the channel width, which is measured between the levee crests. 258

Figure 6.9. Seismic section showing the difference in cross-sectional scale between channel-levee systems. Channel y is only about 0.5 km wide and is buried by a low-amplitude reflection unit. In contrast, channel c is three to five times wider than channel y and reveals an aggradational pattern. Both channels have external levees. 259

Figure 6.10. Cross-sectional distribution box plots of the channel-levee systems in the PAMA Basin. a) Conduit bed slope; b) channel sinuosity; c) meander wavelength; d) meander amplitude; e) cross-sectional area; and f) bankfull width. 261

Figure 6.11. Cross-plots comparing morphometric relationships of calciclastic channel-levee systems of PAMA and siliciclastic sediment conduits taken from Lemay et al., 2020. Power-law equations from Williams et al. (1986), Held (2011) and Lemay et al. (2020) are plotted to compare calciclastic channel-levee systems with the geometries of siliciclastic submarine and fluvial channels. A and b) Mean bankfull depth ($L_{h_{mean}}$) against bankfull width (W); c and d) meander amplitude vs. meander wavelength; e and f) bankfull width vs. meander amplitude; and g and h) bankfull width vs. meander wavelength. 262

Figure 6.12. Summary diagram of 3D seismic data showing the main types of channel-levee systems occurring in the mixed carbonate-siliciclastic depositional system of the PAMA Basin. 284

Chapter 7

Figure 7.1. Diagram summarising the key results of this thesis. Chapter 4 investigates the fault growth and linkage associated with ICPs in the Northwest Shelf of Australia. Fault-throw maps and T-Z plots are useful to understand the relationship between distribution and development of ICPs with the presence of fault arrays. Three types of ICPs are found, based on the carbonate growth ratio vs. fault-throw. Chapter 5 investigates the challenges to characterise multi-scale fractures in carbonate platforms. The study suggests that each scale of observation is associated to a particular fracture type, such as joints, fracture swarms and faults. To adequately characterise fracture networks, it is key to combine geometrical and topological analyses of fracture branches utilising various datasets. Chapter 6 investigates the calciclastic submarine fans and channel-levee systems of the PAMA Basin, Brazil as an example of a mixed carbonate-siliciclastic system in deep and

ultra-deep-waters. Geomorphic measurements are analysed, resulting in the classification of three types of channel-levee systems, depending on their sinuosity and depositional patterns. 292

Figure 7.2. Variance map of the base Pleistocene horizon, Bonaparte Basin, NW Australia. Shaded orange area represents a structural high bordered by normal faults. Blue dashed lines indicate the outlines of ICPs..... 295

Figure 7.3. Variance map of the base Pleistocene horizon showing the different types of ICPs observed in the Karmt3D study area of the Bonaparte Basin, NW Australia. Shaded green areas represent Type 1 ICPs, shaded red areas represent Type 2 ICPs, and shaded green areas represent Type 3 ICPs. Small relay ramps are coloured in purple and large relay ramps are coloured in pink. Note that only major faults and associated relay ramps are mapped. Blue dashed lines indicate the outlines of ICPs..... 296

Figure 7.4. Middle Miocene regional map showing the distribution of isolated carbonate platforms in Central Luconia offshore Sarawak, NW Borneo. Note how densely faulted is the area, and that not all ICPs have hydrocarbon accumulation. Modified from Kosa et al. (2015). 297

Figure 7.5. Types of structural and depositional fabrics at Cariatiz, SE Spain. a) Outcropping section of the Cariatiz Fringing Reef Unit showing large vertical fractures and karsts. b) Fracture swarms. c) Open fractures (joints). d) Closed fractures (veins). e) Vertical Porites and a small karst cave. f) Pseudo-bedding surfaces. 302

Figure 7.6. Schematic diagrams of redeposited carbonate play types. Type 1 include reef upper slope (a) and toe-of-slope apron (b). Type 2 include calciclastic

submarine fans (c) and channel-levee systems (d). Modified after Janson et al.
(2012)..... 311

List of tables

Chapter 4

Table 4.1. Seismic character and lithologies of the seismic units interpreted in the study area. The table correlates the seismic horizons in this work with the horizons defined by Willis (1998). 142

Chapter 5

Table 5.1. Summary of topological parameters, notation and key equations. Modified from Sanderson and Nixon (2015, 2018). 201

Chapter 1: Introduction and literature review

1.1 Rationale and aims

1.1.1 Rationale

Carbonate systems are a major component of the Earth, covering over ~13% of the Earth's surface (Fryar, 2021) (Figure 1.1). Modern shallow-water marine carbonate factories are distributed around the world, hosting 25% of the marine life and constituting a major carbon sink. They account for 25% of the global CO₂ trapped in marine sediments (Laugié et al., 2019) (Figure 1.2). The study of carbonate rocks represents an important subject area for many disciplines because of their unique and complex compositional, depositional and structural characteristics. Carbonate rocks represent major reservoir intervals for water and hydrocarbon resources (Laugié et al., 2019), they supply drinking water to approximately 25% of the world's population (Medici et al., 2021) while accounting, in other regions and geological settings, for nearly 50% of the hydrocarbon production around the world. Carbonate rocks have also recently increased the scientific and industry interest in geothermal and carbon sequestration projects (Wu et al., 2021).

The reason why carbonate rocks are effective reservoirs is mainly related to their heterogeneous nature. Carbonate rocks can develop porosity and permeability as a result of diagenetic processes, dissolution, recrystallisation or chemical replacement via dolomitization, and fracture development. For the case of naturally fractured reservoirs, the presence of open and connected fracture networks allow the development of major conduits to fluid flow. However, fractures within carbonate rocks pose a blessing and a challenge for geologists who are in charge of characterising carbonate reservoirs. Fractures undoubtedly enhance permeability and create pathways (or, instead, barriers) to fluid flow, but their natural

complexity - associated with limitations in the data available to characterise them - often result in demanding modelling tasks and predictions of the properties and distribution of subsurface fracture networks. In addition, their compositional and diagenetic nature allows rock dissolution, leading to fracture enlargements and karstification, complicating their modelling. There are also different fracture types in nature, with variable sizes ranging from mm to km in length, that require analyses of multiple datasets (e.g. seismic, wellbore, outcrop) with specific resolutions in order to measure and interpret them exhaustively. Unfortunately, the availability of data crossing distinct scales of analysis is commonly limited, causing difficulties to perform a thorough evaluation of fracture networks. This caveat results in incomplete and ambiguous fracture models.

Data availability at different scales is not just solved by acquiring additional data. The resolution of each dataset is a limitation factor. It is known that in industry, the two main datasets used to analyse subsurface reservoirs are wellbore data and seismic data (Figure 1.3). Wellbore data such as cores and well logs provide information of small-scale features from millimetres to centimetres in length. Seismic data instead, provide information of large-scale features in the range of hundreds of metres to kilometres. A combined analysis of both types of data is important to study the subsurface. However, metre-long features cannot be observed with these datasets in the subsurface, which results in having an observational gap at the intermediate scale (Figure 1.3). This intermediate scale can only be observed on the surface from outcrop exposures or LiDAR imagery.

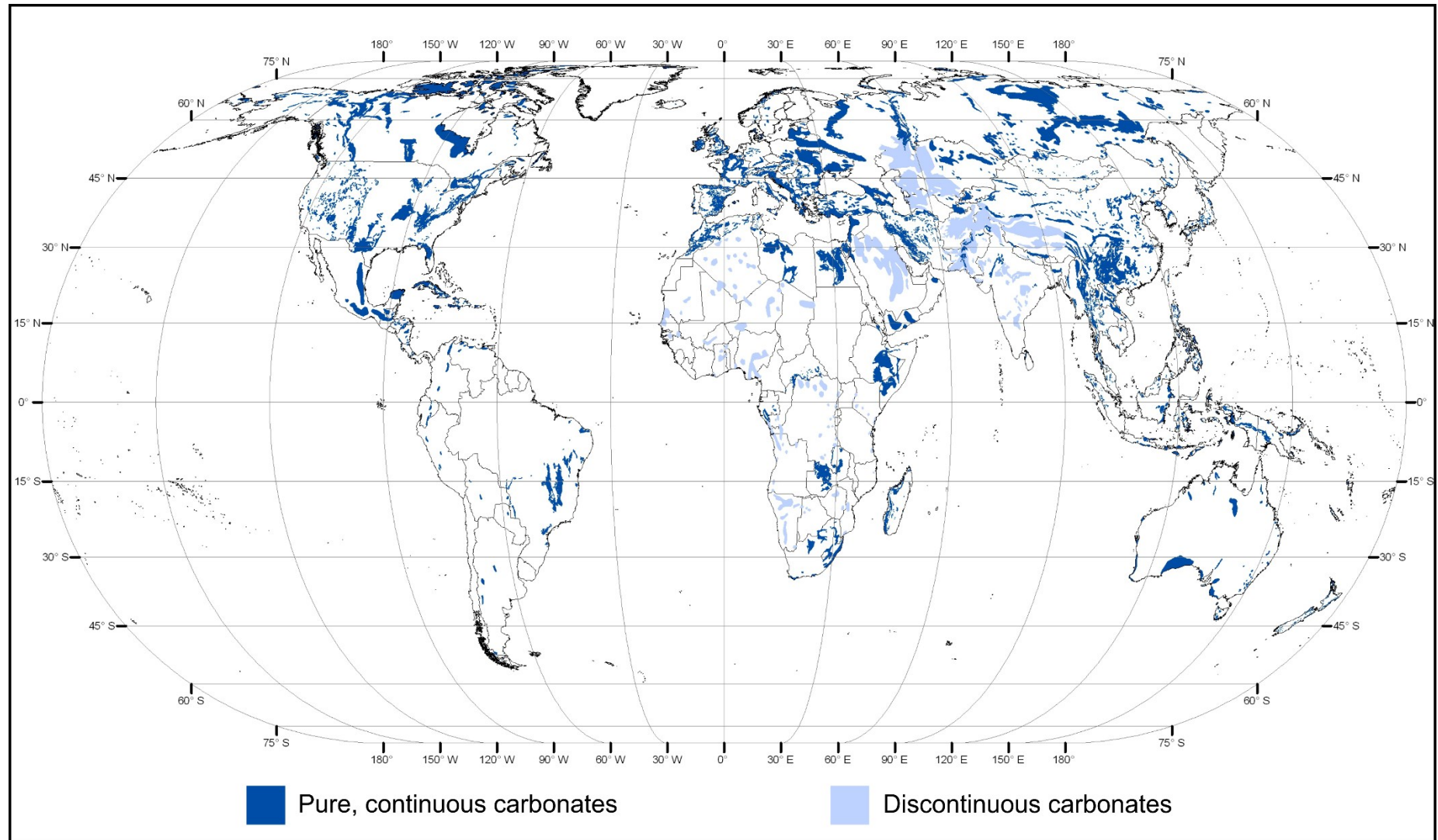


Figure 1.1. World map of carbonate rock outcrops. Modified from Williams, P. and Fong, Y.T. 2010. World map of carbonate rock outcrops v. 3.0. Available at < https://www.fos.auckland.ac.nz/our_research/karst/index.html#karst1 > (accessed 16/08/2020).

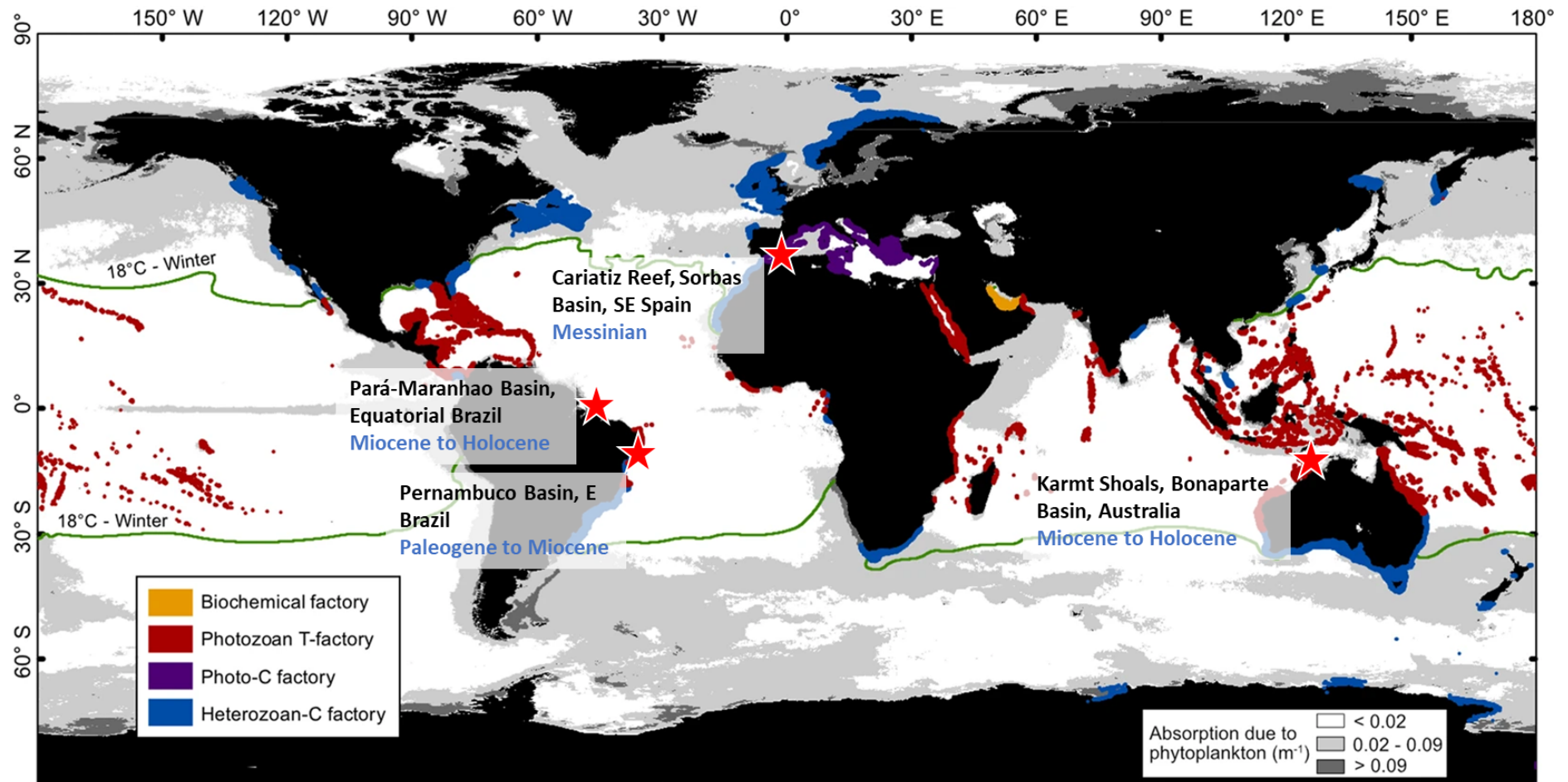


Figure 1.2. Oceanographic world map showing the distribution of modern shallow-water marine carbonate factories. The green lines are isotherm lines dividing warm water zones around the Equator from cool water zones. Red stars show the location of the different study areas analysed in this thesis. Modified from Laugié et al. (2019).

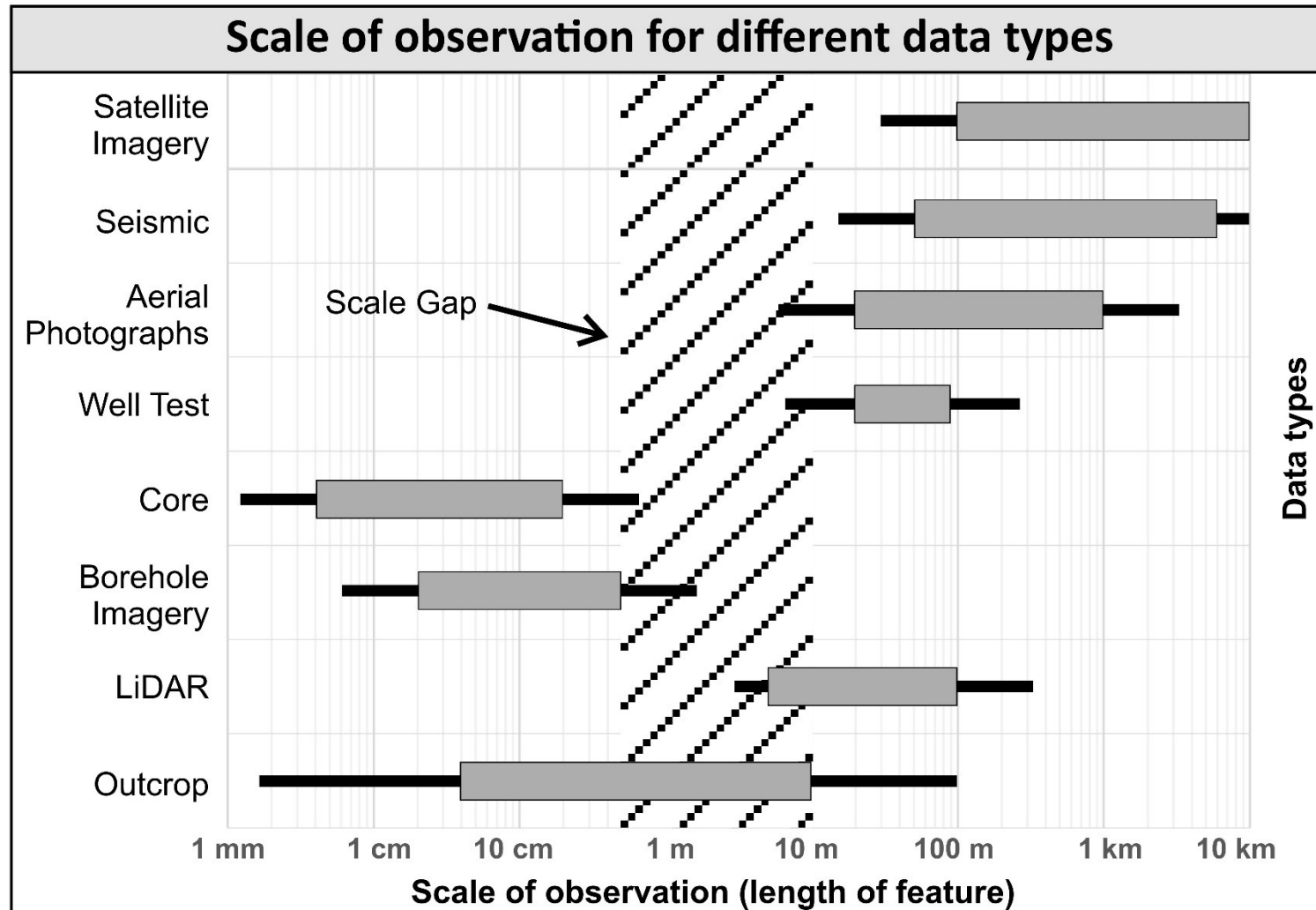


Figure 1. 3. Graphical diagram showing the scale of observation for different data types that are commonly used to study structural and sedimentological features in the surface and subsurface. Note the scale gap between wellbore data and seismic data at the intermediate scale. Modified from Gutmanis and Ardèvol i Oró (2015).

A final aspect relates to the distinctive architectural and geometrical elements of carbonate depositional systems - such as the development of isolated carbonate platforms (ICPs) on shallow waters, or deep-water depositional systems in the form of calciclastic submarine fans and channel-levee systems - all of which provide suitable stratigraphic configurations to trap fluids. Despite the advances in conceptual models of carbonate depositional systems, challenges remain in the literature regarding the relationship between shallow- and deep-water depositional systems.

To improve the understanding of carbonate systems at different scales, it is key to create conceptual models based on multiple datasets with different resolutions. This can be achieved by the combination of outcrop studies, 3D seismic data and borehole data. Improving our knowledge of the controlling parameters of carbonate depositional systems such as syn-depositional deformation, tectonism, sea level changes, type of carbonate factory, amongst others, is key to adequately delineate carbonate reservoirs and evaluate their potential.

1.1.2 Aims of this research

This thesis presents a comprehensive analysis of carbonate depositional systems on equatorial margins by investigating structural and sedimentological characteristics of various types of carbonate platforms and continental shelves, transitioning from shallow- to deep- and ultra-deep waters. Study areas include the Northwest Shelf of Australia, the East and equatorial margins of Brazil, and SE Spain. The selection of these study areas is partly driven by data accessibility and the unique imaging of different types of carbonate platforms on equatorial margins of

Cenozoic ages. An integration of a diverse, multi-scale dataset comprising high-quality 3D seismic volumes, wellbore logs, outcrop maps and aerial LiDAR maps is presented.

This study aims to discuss carbonate sedimentological and structural properties that are important during the exploration, production and development of carbonate reservoirs. During the exploration stage, a key goal is to find structures with economic potential. This can be tackled by the effective identification of a potential structure or depositional system that can accumulate hydrocarbons, such as isolated carbonate platforms or channel-levee systems. Understanding the structural and sedimentological controls that influence the development and distribution of carbonate systems is key to categorize what are the most suitable places to drill. Moving onto the production stage, in which fractures play an important role to develop permeability and fluid flow, the challenge is to model and predict fracture networks at different scales based on a limited and incomplete dataset. Outcrop analogue studies containing detailed observations of the various fracture types formed throughout the development of the carbonate system is key at this stage. Finally, as a result of technological advances, deep- and ultra-deep-water deposits are having an increase of interest in recent years. Calciclastic submarine fans and channel-levee systems are analysed.

This thesis addresses a number of hypotheses that initially started with scientific questions developed during the working experience of the author in multiple carbonate reservoirs in the Gulf of Mexico. The challenges related to understand fault distributions and fracture network modelling set a starting point to this research with an initial aim to quantitatively understand fault displacements. As the

research progressed and results were analysed, research opportunities arose with the necessity to update hypothesis and to provide further scientific evidence, which in occasions, the obtention of additional datasets was crucial. The final hypotheses of this thesis being tested in the following chapters are presented below:

- 1. Fault linkage controls the growth and distribution of isolated carbonate platforms (ICPs) on equatorial margins.** If true, fault-throw measurements from seismic data are expected to show a direct correlation between the position of relay ramps and the development of ICPs. If false, no correlation between the two will be observed, with an independent distribution of ICPs occurring regardless of fault linkage styles observed. See Chapter 4.
- 2. ICPs controlled by fault linkage and relay ramps have a greater reservoir potential than ICPs developed on non-faulted areas.** If true, growth of strata will be documented from seismic data at a concurrent time to fault growth, suggesting syn-tectonic growth of the ICPs. Faults and associated relay ramps developed underneath ICPs will show fluid migration pathways, being connected to the ICPs. If false, fluid migration pathways will not be associated to the position of ICPs and relay ramps on a continental shelf or slope. See Chapter 4.
- 3. Permeability and fluid flow in naturally fractured carbonate reservoirs varies as a function of the size and type of fractures.** If true, a correlation between fracture size and connectivity will be established. Small fractures will appear to be better connected than large fractures, being small fractures the major contributors to fluid flow. Topologic and geomorphic properties of fracture networks analysed from a multi-scale dataset will show characteristic properties at each scale of observation, in order to

differentiate fracture types. If false, fracture properties at different scales will not show a clear correlation and, therefore, fracture sizes will not be useful to predict a relative permeability. See Chapter 5.

4. **Fracture scale gaps due to data resolution can be bridged by a scaling distribution model in order to predict sub-seismic fracture networks.** If true, fracture network properties (i.e. fracture branch length) analysed at different scales will fit a distribution model such as power law or negative exponential, facilitating prediction of multi-scale fracture networks. If false, fracture properties will plot away from a straight line in a distribution model, signifying no correlation of different fracture sizes. See Chapter 5.
5. **Seismic-scale fracture networks are not representative of reservoir-scale properties. Therefore, calibration with outcrop analogues is critical for a detailed reservoir evaluation.** If true, small fractures observed at the outcrop scale will differ from large fractures observed at the seismic scale, as different types of fractures occur at sub-seismic scale. If false, similar fracture types to those observed at outcrop, will be visible and quantifiable from seismic data. See Chapter 5.
6. **A mixed calciclastic-siliciclastic depositional system can develop important sediment conduits off carbonate shelves in deep and ultra-deep waters.** If true, the development of multiple calciclastic submarine fans and channel-levee systems will be observed from seismic data. Sedimentological data from well logs will provide evidence for the presence of a carbonate and siliciclastic input source. If false, well logs

will not identify siliciclastic input from the shelf, suggesting a pure carbonate depositional setting. See Chapter 6.

- 7. Geomorphologic features of calciclastic channel-levee systems show similarities with modern siliciclastic submarine channels.** If true, geomorphologic features of calciclastic channel-levee systems such as mean bankfull depth, bankfull width, meander amplitude and meander wavelength, will have similar distribution models to those of siliciclastic sediment conduits. If false, relationships of calciclastic morphometric features will plot differently when compared to siliciclastic morphometric models. See Chapter 6.

The following section includes a literature review of the major topics studied in this thesis. Descriptions of carbonate depositional systems, fracture analysis, scaling relationships and seismic interpretation are detailed as to provide a relevant background to understand the results chapters. Chapter specific research aims are outlined in each results chapter (4, 5 and 6).

1.2 Thesis layout

This thesis is split into seven chapters. Chapter 1 provides an overview of the thesis and summarises published literature on shallow and deep-water carbonate depositional systems, fracture analyses and scaling relationships, and naturally fractured reservoirs.

The geological settings of the four study areas are summarised in Chapter 2. The 3D seismic datasets and main methodologies used are described in detail in Chapter 3, followed by the results of the studies in Chapters 4, 5 and 6.

The structural controls of the growth and development of isolated carbonate platforms in the Northwest Shelf of Australia are investigated in Chapter 4. Chapter 5 investigates the scaling relationships of different fracture and fault sizes based on outcrop and seismic data from SE Spain and east Brazil. Chapter 6 investigates deep-water depositional systems of the Neogene carbonate shelf of Equatorial Brazil in the Pará-Maranhão Basin. The results are gathered and discussed in Chapter 7, providing a general synthesis of the research presented in this thesis.

1.3 Carbonate-grain associations

Over the last 70 years since the pioneering work of Purdy (1963), many authors have grouped different carbonate grains into carbonate assemblages as a useful measure to classify carbonate factories. Carbonate assemblages have been updated with additional categories throughout the time. Distribution of different carbonate assemblages is subject to different components such as environmental factors like water temperature, salinity, nutrient content, light penetration, etc. Latitude and depth also impact the type(s) of carbonate assemblage together with other factors such as water circulation, river discharge and suspended sediment (Carannante et al., 1988). The following section summarises and explains the carbonate grain association compiled by Kindler and Wilson (2010) (Figure 1.4).

1.3.1 Photozoan carbonates

Photozoan carbonates mostly occur in tropical waters where bottom-water temperatures are $>22^{\circ}\text{C}$, and restricted to low latitudes such as coral reefs (James, 1997). Photozoan carbonates groups skeletal grains that are derived from warm-water, light-dependent organisms (e.g. scleractinian corals, green algae, larger benthic foraminifera); and non-skeletal particles such as ooids, aggregates and peloids (Kindler and Wilson, 2010).

Coralgal assemblage: it can also be known as chlorozoan and it is characterised by hermatypic corals (e.g. *Zoantharia*, *Porites*, *Tarbellastrea*) and calcareous green algae (e.g. *Chlorophyta*, *Halimeda*) in association with molluscs, benthic foraminifers, echinoids, bryozoans, sponges and coralline algae. It has been defined

by Purdy (1963) and Lees and Buller (1972). This assemblage is typical of shallow-water tropical areas with well-developed coral reefs, often associated with non-skeletal grains such as ooids, grapestones, botryoidal grains and pelletoids. Representative examples occur in the Miocene of eastern Spain (Carannante et al., 1988).

Chloralgal assemblage: it is dominated by the presence of calcareous green algae with no hermatypic corals. It was initially defined by Lees (1975). This assemblage is present in tropical-subtropical zones where coral reefs cannot develop. Examples are found in the northern sector of the Brazilian shelf and locally in the shallow Mediterranean Sea (Carannante et al., 1988).

LB-foralgal assemblage: it is characterised by large benthic foraminifera (perforate or imperforate) together with coralline algae and *Halimeda*. They are typical of low light levels (oligophoty) with diverse imperforate large benthic foraminifera together with algae in shallow-water environments, such as sea-grass meadows. It was initially defined by Kindler and Wilson (2010). A modern example is the equatorial region of SE Asia (Wilson and Vecsei, 2005).

1.3.2 Transitional carbonates

Transitional carbonates are used to designate sediments characterised by low (1-20%) percentages of phototrophic organisms.

		Skeletal components					Associated Non-skeletal components						Principal reference									
		Tropical >22°C	Subtropical 22-18°C	Temperate 18-10°C	Sub-polar 10-5°C	Polar <5°C	Herm. Coral	Chlorophyte	LB Foraminifera	Rhodophyte	SB Foraminifera	Mollusc		Echinoderm	Bryozoan	Barnacle	Aherm. Coral	Ooids	Peloids	Aggregates		
Carbonate grain association, province or factory	(Chlorozoan)	—————					●	●	●	●	●	●	●	●	●			▲	▲	▲	Lees & Buller (1972)	
	Photozoan	-----					●	●	●	●	●	●	●	●	●			▲	▲	▲	James (1997)	
	<i>Tropical</i>	—————					●	●	●	●	●	●	●	●	●			▲	▲	▲	Schlager (2003)	
	Assemblage	Coralgal	—————					●	●	●	●	●	●	●	●	●						Purdy (1963)
		Chloralgal	----- often high salinity						●	●	●	●	●	●	●	●						Lees (1975)
		LB-foralgal	----- High Diversity					●	●	●	●	●	●	●	●	●						Wilson & Vecsei (2005)
	Transitional	-----					●	●	●	●	●	●	●	●	●				▲		Halfar <i>et al.</i> (2006)	
	<i>Warm temperate</i>	-----					●	●	●	●	●	●	●	●	●				▲		Betzler <i>et al.</i> (1997)	
	(Foramol)	-----							?	●	●	●	●	●	●	●	●		▲		Lees & Buller (1972)	
	<i>Cool water</i>	-----							?	●	●	●	●	●	●	●	●				Schlager (2003)	
<i>Non-tropical</i>	-----							?	●	●	●	●	●	●	●	●				Nelson (1988)		
Heterozoan	-----								●	●	●	●	●	●	●			▲		James (1997)		
Carbonate assemblage or facies	Rhodalg	-----							●	●	●	●	●	●	●						Carannante <i>et al.</i> (1988)	
	Bryomol	-----								●	●	●	●	●	●						Nelson <i>et al.</i> (1988)	
	Barnamol	-----								●	●	●	●	●	●						Hayton <i>et al.</i> (1995)	
	Rhodechfor	-----								●	●	●	●	●	●						Hayton <i>et al.</i> (1995)	
	Echinofor	-----								●	●	●	●	●	●						Hayton <i>et al.</i> (1995)	
	Bimol	-----								●	●	●	●	●	●						Hayton <i>et al.</i> (1995)	
	Bryorhodalg	-----								●	●	●	●	●	●						Carannante <i>et al.</i> (1988)	
	Molechfor	-----									●	●	●	●	●						Carannante <i>et al.</i> (1988)	
	Ahermacor	-----										●	●	●	●	●	●				Kindler and Wilson (2010)	
Reef/Platform	Rimmed shelf	-----																				
	Reefs	----- Ahermatypic																				
	Open shelf	-----																				
	Ramp	-----																				

Figure 1. 4. Summary of Cenozoic carbonate assemblages based on benthic (skeletal and non-skeletal) components. Assemblages are grouped in photozoan, heterozoan and transitional associations after James (1997). Figure from Kindler and Wilson (2010).

Foramol assemblage: it is characterised by blankets of skeletal carbonates in shallow shelves (0-150 m) that do not contain hermatypic corals nor calcareous green algae. It also contains encrusting coralline algae, bryozoans, echinoids, barnacles and serpulids associated with molluscs and benthic foraminifers. They are not associated with non-skeletal carbonate grains (Carannante et al., 1988). The foramol assemblage was first described by Lees and Buller (1972) as this assemblage does not fit with the coralgal category.

1.3.3 Heterozoan carbonates

Heterozoan carbonate sediments are composed by skeletal grains of heterotrophic biota (i.e. feeding on organic matter) and phototrophic red algae (i.e. using light as source of energy) (Michel et al., 2018). They include carbonate particles produced by light-independent benthic organisms (e.g. bryozoans, barnacles) and fragments of coralline algae (Kindler and Wilson, 2010). This type of sediment can occur in a wide spectrum of climatic zones, making them heterogeneous in terms of sedimentary deposits and oceanographic realms. Heterozoan sediments are present in subtropical (18-22°C) and cool temperate (5-10°C) areas (James, 1997).

Rhodalgal assemblage: it is dominated by crustose calcareous red algae (*Rhodophyta*), often in the form of rhodoliths. It was initially defined by Carannante et al. (1988). Rhodalgal assemblage typically forms in shallow agitated waters in the photic zone with <50 m depth. A high-energy environment is required to restrict the development of other skeletal component and maintain the subspherical shape of

the rhodoliths (Hayton et al., 1995). An example is the central sector of the Brazilian shelf (Carannante et al., 1988).

Bryomol assemblage: it describes carbonate sediments that are dominated by bryozoans with common bivalve molluscs. It was initially defined by Nelson et al. (1988). Bryozoan-rich sediments are common on parts of high-energy, open shelves. Bryozoans are suspension feeders and sensitive to the amount of sediment in suspension, suggesting an environment with relative low terrigenous supply for their dominance (Hayton et al., 1995). Bryozoans live at various depths on the shelf, in which massive and encrusting forms preferentially grow in turbulent shallow waters, and delicate forms have a preference on deeper and calmer conditions (Hayton et al., 1995).

Barnamol assemblage: it is dominated by barnacles (mainly plates) and common bivalve molluscs. It was initially defined by Hayton et al. (1995). Barnacle growth is dominated in environments with strong currents, such as tide-dominated seaways as it prevent burial of the filter-feeding organisms by removal of fine sediments while ensuring a high nutrient supply (Hayton et al., 1995).

Rhodechfor assemblage: it is characterised to be composed of calcareous red algae co-dominating with echinoderms and/or benthic foraminifera, with bryozoans also being an important constituent. It was initially defined by Hayton et al. (1995). Rhodechfor assemblage usually occurs at depths of <50 m within the photic zone due to the presence of calcareous red algae. The presence of other skeletal components

suggest the development around lower sections of isolated structural highs where conditions are not favourable to only develop calcareous red algae such as in the rhodalgal assemblage (Hayton et al., 1995).

Echinofor assemblage: it describes carbonate sediments that are dominated by echinoderms and/or benthic foraminifera. It was initially defined by Hayton et al. (1995). This assemblage is recognised in sandy substrates of modern non-tropical shelf carbonate environments (Hayton et al., 1995).

Bimol assemblage: it is dominated by bivalves, including non-tropical carbonate facies rich in bivalve molluscs, typically forming more than 50% of the skeletal fraction. It was initially defined by Gillespie (Gillespie, 1992) and updated by Hayton et al. (1995). The bimol assemblage is commonly associated with shallow waters on the shelf in areas with relatively higher sedimentation rates of fine terrigenous material, which are less favourable for other assemblages (Hayton et al., 1995).

Nannofor assemblage: it recognises the prevalence of nannofossils and planktonic foraminifera. It was initially defined by Hayton et al. (1995). This assemblage is most typical of off-shelf waters, although it can occur at shallow depths in partly enclosed basins with low-energy zones. Nannofor dominates where there is minimal turbulence, allowing the accumulation of nannofossil- and planktonic foraminifer-rich ooze (Hayton et al., 1995).

Molechfor assemblage: it is characterised by abundant mollusc fragments, benthic foraminifers and echinoids. Barnacles can be main constituents and serpulids and bryozoans can be present. It was initially defined by Carannante et al. (1988). This assemblage commonly occurs in cold-temperate carbonate shelves but can also develop in tropical-sub-tropical shelves. An example is the southern sector of the Brazilian shelf (Carannante et al., 1988).

Thermacor assemblage: it is dominated by azooxanthellate corals building extensive reefs such as those forming offshore Norway in the North Atlantic. In addition to abundant, low-diversity ahermatypic corals, the presence of particular genera of serpulids, bryozoa or moluscs define the thermacor assemblage. It was initially defined by Kindler and Wilson (2010). The thermacor assemblage is associated with sediments forming extensive deposits and develop in cold waters, perhaps promoted by nutrient upwelling along bathymetric highs or associated with methane seeps (Kindler and Wilson, 2010).

1.4 Carbonate factories

Modern and ancient marine carbonates can develop under various environmental conditions, from tropical waters to the poles, showing different associations with biota, sedimentary facies and stratigraphic architectures. Over 90% of carbonate sediments found in modern environments are biological in origin, although it is possible to precipitate carbonates directly from sea water as a result of abiotic chemical processes (Schlager, 2005). A carbonate factory is a carbonate precipitation mode that is defined by an ecosystem (i.e., carbonate producing

organisms and related environment), the sediments which are produced in situ and the early modification of these sediments (Michel et al., 2019). Describing and characterising carbonate factories is a challenging task due to the infinite variety of carbonate rocks (Pomar and Hallock, 2008). Many geologists have been occupied for more than two centuries trying to present a comprehensive classification, being Schlager's (2005) the most used in the literature, dividing carbonate factories into: T-tropical warm water, C-cool-water, and M-microbial, or mud-mound.

The most up to date classification of carbonate factories is the one proposed by Michel et al. (2019), in which four marine and neritic main carbonate factories are defined based on stratigraphic architectures and environmental features, combining the classifications of James (1997), Schlager (2005) and Dupraz et al. (2009). The classification divides them into (1) photozoan T-factory, (2) marine biochemical T-factory, (3) photo-C-factory, and (4) heterozoan C-factory (Figure 1.5). The distribution of these carbonate factories is presented in Figure 1.2.

1.4.1 Photozoan T-factory

This factory corresponds to tropical carbonate shelves or detached rimmed platforms, both characterised by phototrophic skeletal grains and reefs, and presenting the highest rates of carbonate production in nature (Schlager, 2005; Michel et al., 2019). The most common organisms in this factory are corals, stromatoporoids, green algae, sponges and photosymbiotic benthic foraminifers (James, 1997; Michel et al., 2019). Light and temperature are the main controlling factors for the development of the photozoan factory, restricting its distribution to low-latitude, warm and clear ocean waters (Michel et al., 2019). Modern examples

include the Great Barrier Reef in Australia and the Red Sea. Examples of ancient platforms include the Carboniferous platforms in Kazakhstan and the Cretaceous Golden Lane platform in Mexico.

1.4.2 Biochemical T-factory

This factory is typically a tropical carbonate ramp with a characteristic low-angle of repose (i.e. homoclinal ramp) and non-skeletal grains components. This type of platform encompasses extensive evaporitic (sabkha), peritidal, and shallow-water microbial deposits such as stromatolites, shells (e.g. molluscs), ooids, peloids, algal mats and muds (Michel et al., 2019). Carbonate saturation is the main control of its biochemical factory, itself occurring in a marine setting with high temperatures and salinities. A modern example is the Persian/Arabian Gulf, whereas an ancient example is the Asmari Formation from the Zagros Basin in the Middle East.

1.4.3 Photo-C-factory

Distally steepened ramps are typically formed in photo-C-factories, being composed of proximal seagrass-derived bioclastic sediments and distal red algal accumulations such as rhodoliths. This type of factory commonly occurs in warm-temperate or subtropical provinces with a relatively low primary productivity. Light is a major factor controlling its distribution, although the photo-C-factory tolerates turbidity currents and marine productivity. Deep-water factories are possible, but with the highest production rates being clearly recorded in well-illuminated settings (Michel et al., 2019). The Mediterranean Sea is a representative example of this

factory. Oligo-Miocene ramps from the northern Mediterranean show characteristic features of the photo-C-factory with grain associations of red algae and foraminifers.

1.4.4 Heterozoan C-factory

The heterozoan C-factory forms ramps with characteristic heterotrophic biota such as bryozoan- and mollusc-accumulations. The heterozoan factory can occur in mixed carbonate-siliciclastic environments (Michel et al., 2019). Food created by marine productivity is the main source of energy in this type of factory, leading it to occur in nutrient-rich, organic-rich, and plankton-rich marine realms such as upwelling areas and coastal zones influenced by fluvial runoff. Modern examples of this factory include highly mesotrophic to eutrophic settings such as the Gulf of California and South Australia. An ancient example is the Cretaceous Basco-Cantabrian Basin.

1.4.5 Automicrite factory

This type of factory was defined by Schlager (2005) as an M-factory, and it is characterised to produce cohesive sediments building carbonate platforms with very steep slopes. Microbial activity degrading large amounts of organic matter on the seafloor under sub-oxic conditions is typical in the automicrite factory. Organic matter content and oxic conditions appear to constitute the main controls of this factory. However, there are no examples in the modern ocean. During the Early Mesozoic, automicrite factories were related to the Tethyan seaways in which massive sponge/microbe boundstones formed steep, massive progradational slopes and mud-mounds (Pomar and Hallock, 2008; Michel et al., 2019).

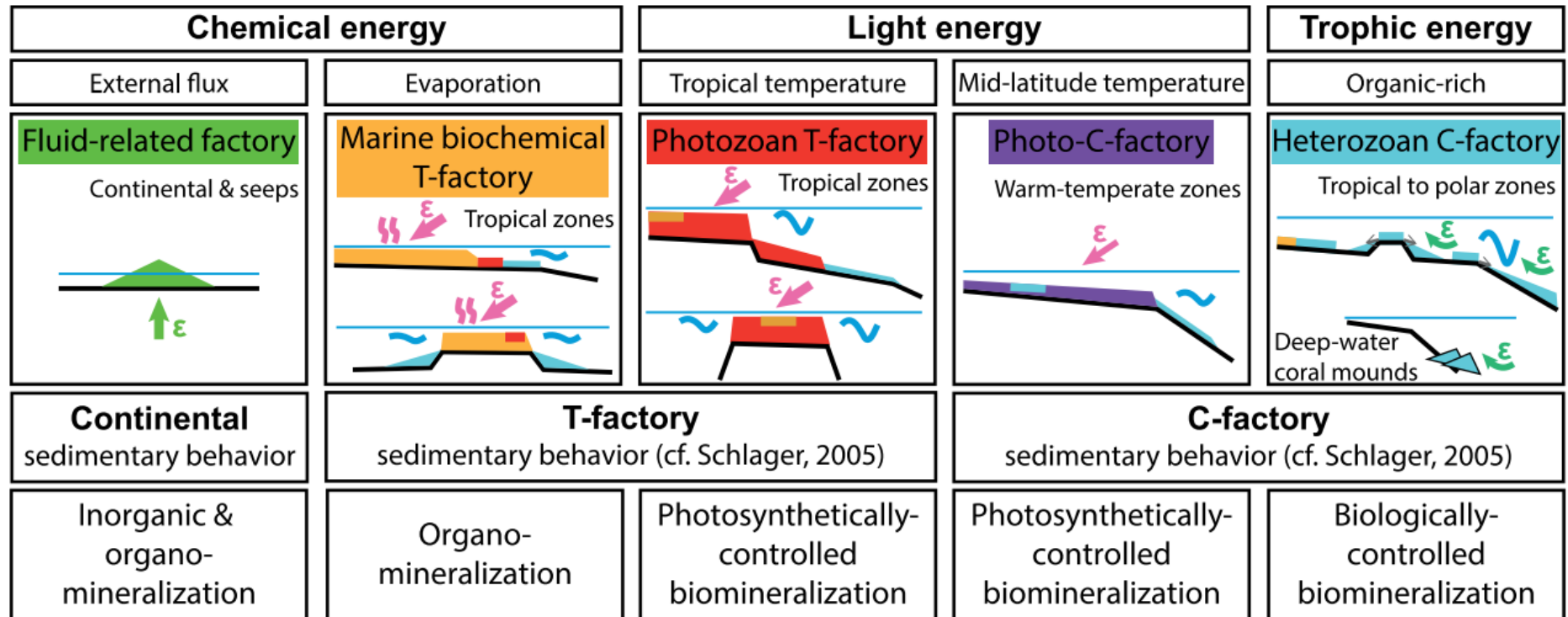


Figure 1.5. Schematic diagram of the carbonate factory classification proposed by Michel et al. (2019) relating carbonate deposits with oceanographic parameters.

1.4.6 Seep and continental factory

Seep carbonates are produced at abyssal depths due to microbial activity and chemosymbiotic organisms such as bivalves and worms. Methane is the most common element to source the energy of these organisms (Michel et al., 2019).

1.4.7 Carbonate productivity and sigmoidal growth

A common pattern in carbonate production is a sigmoidal growth curve. Growth curves are not only used in carbonates, they can be applied to many disciplines including Demography, Biology and Marketing. Their use is to understand an increase in populations, whether of people, viruses, corals, plants, etc. Growth curves are used to describe how a variable increases over a time interval until it approaches its saturation value (Carrillo and González, 2002). Because in nature an indefinite growth is not physically viable, the curve representing the growth has the characteristic elongated S shape, known as sigmoidal (Carrillo and González, 2002).

The sigmoidal curve can be divided into three segments or phases. With respect on the development and growth of organisms on carbonate systems these phases are: (1) start up - slow starting growth, (2) catch up - rapid growth, and (3) keep up - final phase of slow down (Schlager, 2005) (Figure 1.6).

The initial phase or start-up refers to a relatively slow growth over time. At early stages of growth, living space is virtually unlimited and as the population continues to reproduce, the growth accelerates exponentially within the catch-up phase. A decrease in growth in the final phase is observed with an upper asymptotic pattern that is set by an upper limit defined by the capacity of the living space (Schlager, 2005). The living space is constraint by environmental factors such as the sea level.

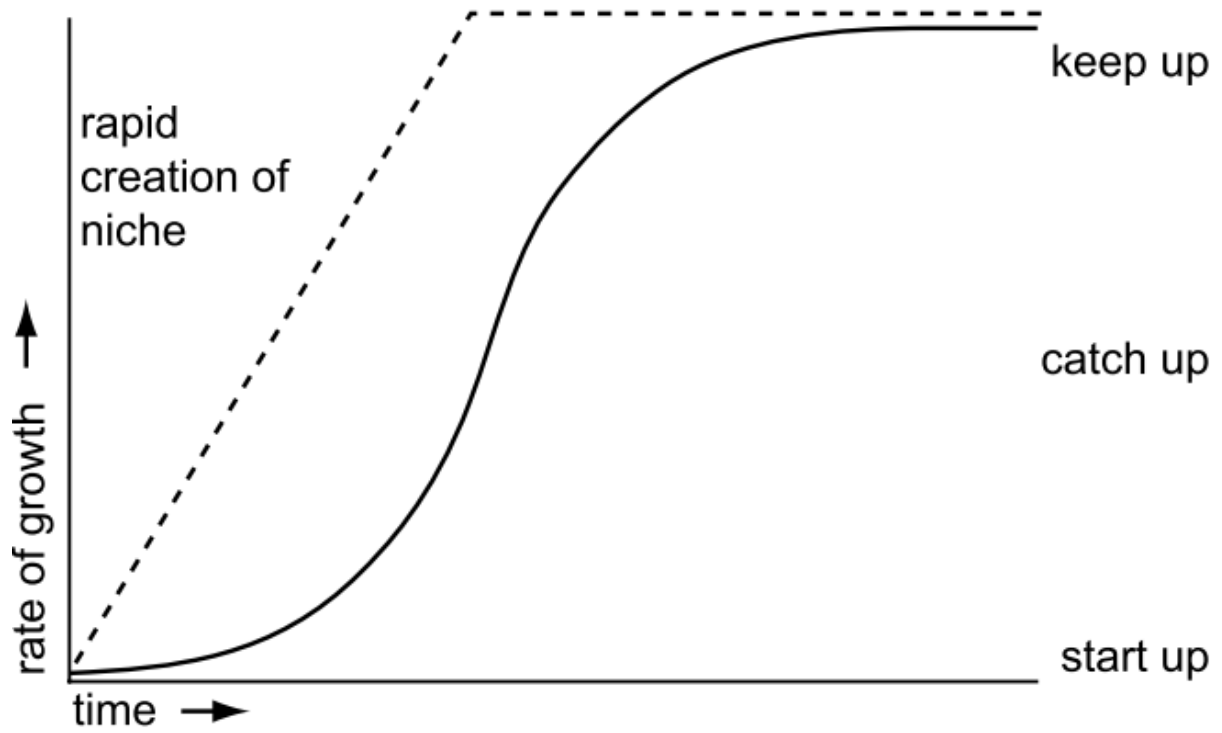


Figure 1.6. Sigmoidal growth curve explaining carbonate productivity. Figure from Schlager (2005).

1.4.8 Sedimentation rates and growth potential

Carbonate factories have the intrinsic property to grow upward and produce sediment. Due to this property, it is common to document the growth of carbonate factories by tracking changes in sea level or their growth potential by determining aggradation rates (Schlager, 2005). However, it is important to note that carbonate growth rates are different depending on the type of carbonate factory and their age (Figure 1.7).

Sedimentation rate is an important characteristic to understand carbonate depositional settings as it provides information about the growth potential of a carbonate system and determines whether the system can keep up with a given relative rise of sea level or leave accommodation unfilled and eventually drown (Schlager, 2000). Sedimentation rates of different carbonate factories calculated from thickness and stratigraphic ages of ancient deposits are observed in Figure 1.7, showing that the sedimentation rates decrease with increasing length of time (Schlager, 2000, 2005). Tropical rates are the highest and better documented, being $10^4 \mu\text{m a}^{-1}$ at 10^3 years and decreasing to $10^2 \mu\text{m a}^{-1}$ at 10^7 years (Figure 1.7). In contrast, cool-water rates are lower overall, amounting to only 25% of the tropical standard in the domain of 10^6 - 10^7 years (Figure 1.7). Mud-mound rates are similar to tropical rates in the domain of 2×10^5 - 10^7 years, however, it exports less sediment laterally into the adjacent basins (Schlager, 2000, 2005) (Figure 1.7).

When comparing rates of carbonate factories, it is important to do it over similar lengths of time. For instance, it would not be meaningful to compare rates of Holocene tropical reefs that were measured in the thousand-year domain with rates of ancient deposits that were averaged over millions of years.

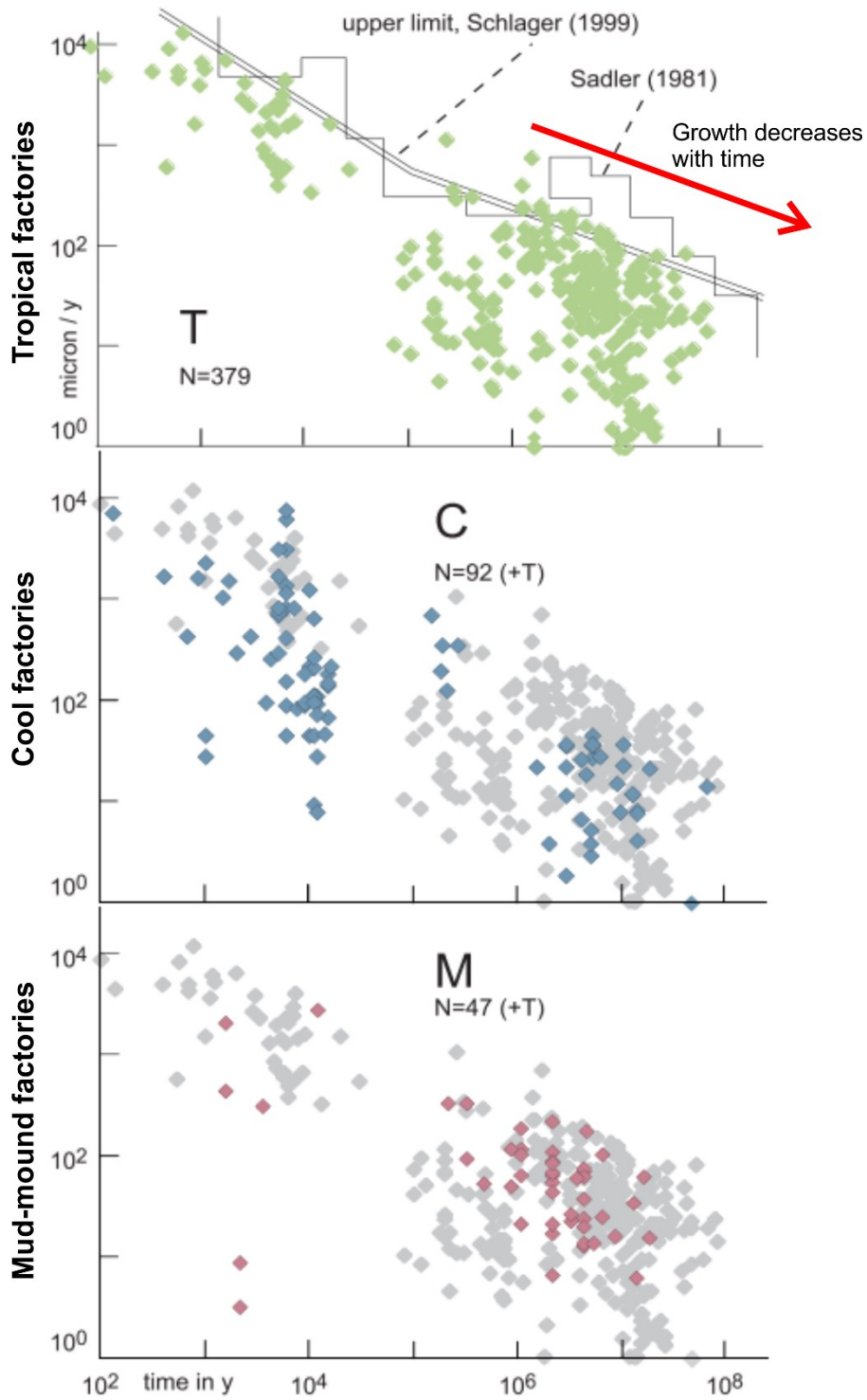


Figure 1.7. Sedimentation rates of different types of carbonate factories plotted against the length of time-interval of observation. Modified after Schlager (2005).

1.5 Environmental controls of carbonate development

The majority of carbonate material in modern oceans is precipitated as highly structured skeletons of organisms and micrite. Organisms such as algae, foraminifera or corals are influenced by the conditions of the sea they live in. Therefore, carbonate productivity is mostly controlled by the type of organisms and the environmental parameters favouring carbonate precipitation such as temperature, salinity, nutrients and light in the sea water (Schlager, 2005).

1.5.1 Light

Light is an important control on skeletal carbonate precipitation as it allows photosynthetic organisms to extract CO₂ from the sea water, thus increasing its carbonate saturation and facilitating precipitation of carbonate minerals (Schlager, 2005) (Figure 1.8). A decrease of light with water depth is related to a decrease in carbonate productivity, being the photic zone the ideal for most benthic carbonate production. The euphotic zone is the water layer in which photosynthesis can occur, having high rates of oxygen production. Its base ranges from 30 m to over 150 m.

1.5.2 Water temperature

Most carbonates occur in warm waters in which carbonate saturation is high, however, there are some temperature limits depending on the type of carbonate-secreting organisms. Most hermatypic (i.e. symbiotic) corals thrive in water temperatures ranging between 20-30 °C. Higher temperatures limit carbonate production, particularly in restricted lagoons where there are temperatures exceeding 30 °C (Schlager, 2005).

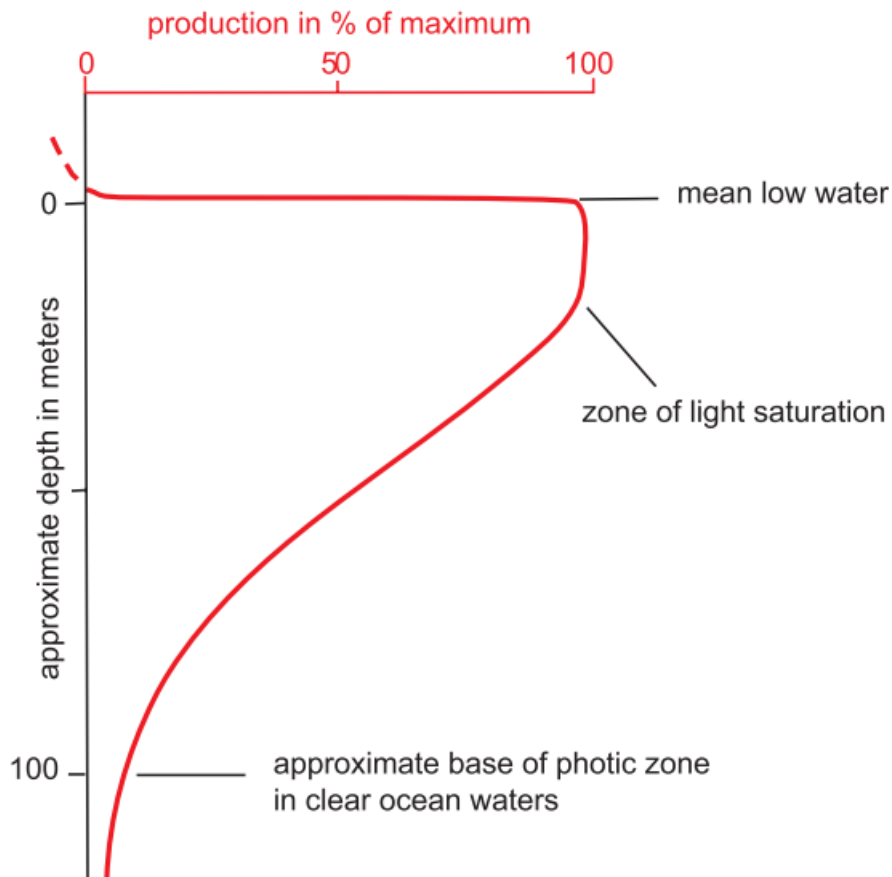


Figure 1.8. Carbonate production profile in a tropical setting. Maximum production is related to the upper part of the photic zone before light saturation decreases exponentially with depth. In areas above the sea level (terrestrial), production is negative as carbonate rocks are dissolved. Figure from Schlager (2005).

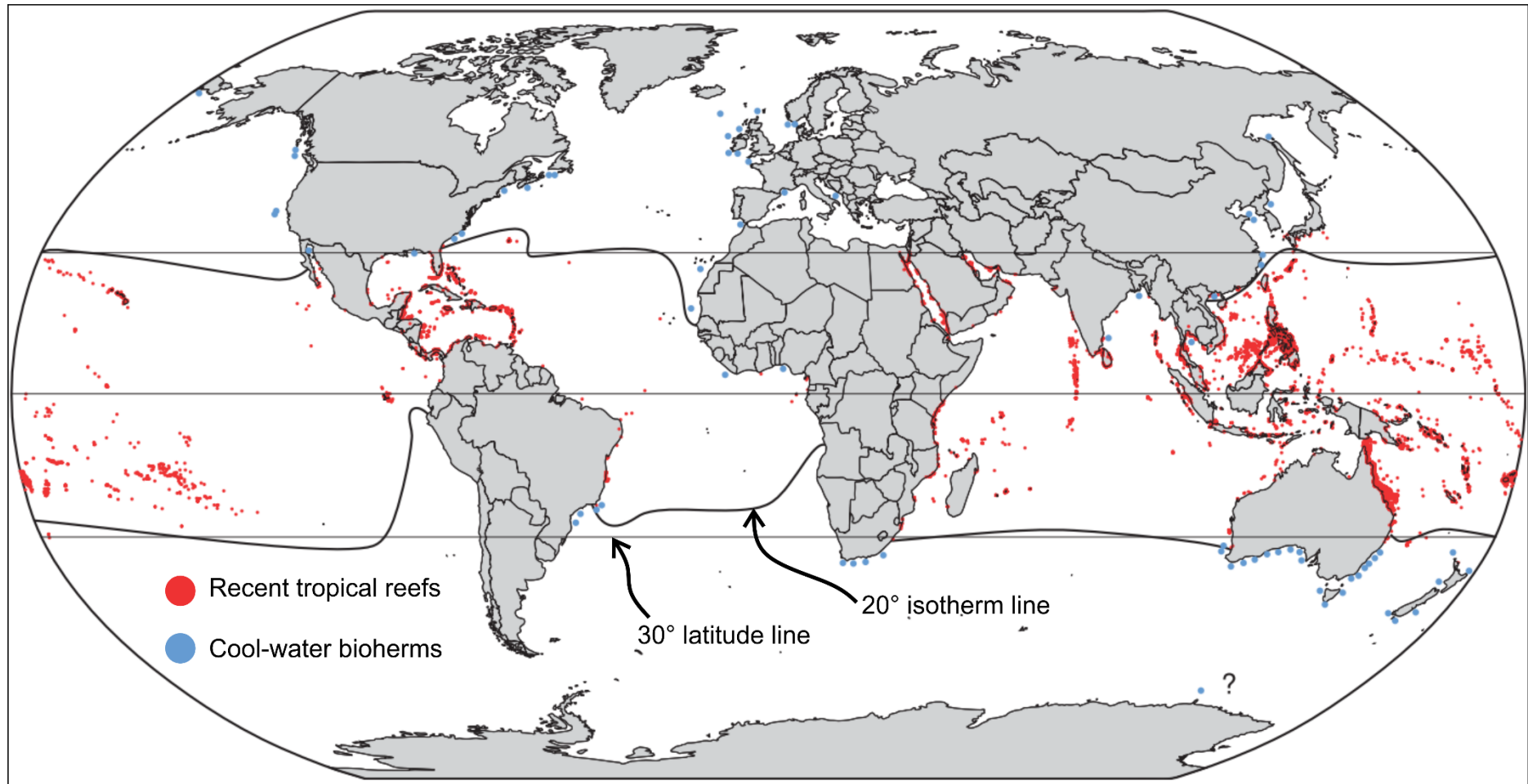


Figure 1.9. World map showing the position of modern tropical and cool-water carbonates based on the latitude zonation. Modified from Schlager (2005).

1.5.3 Latitudinal zonation of skeletal production

Although latitude alone is not a direct control on carbonate development, isotherm lines are important to differentiate between tropical and cool-water carbonates. Tropical carbonates generally occur in latitudes of 30-35°, while cool-water carbonates extend over several climate zones, reaching polar regions (Figure 1.9). However, due to processes like upwellings in the West Coast of Africa, cool-water carbonates are observed within the latitudes of 30-35° (Figure 1.9). Photosynthetic organisms dominate tropical carbonates, including metazoan reefs, green algae and larger foraminifera. Cool-water carbonates lack these deposits and consist mainly of skeletal sand and gravel derived from molluscs, bryozoans, smaller foraminifers and red algae (Schlager, 2005).

1.5.4 Salinity

Marine salinity varies relatively little in the open ocean, with subtle variations on carbonate production not well known. In contrast, where access to the open ocean is restricted, salinity varies greatly, affecting the biota diversity.

1.5.5 Nutrient concentration

The relative concentration of nutrients in the water column is vital to the biota development. Planktonic productivity is controlled by the nutrient input within the photic zone, that inhibits light-related benthic organisms. In addition, heterotrophic biota rely on the nutrients coming from the development of organic matter (Michel et al., 2019). However, high-nutrient environments are unfavourable for many

carbonate systems. Carbonate communities dominated by autotrophs, such as reefs, are adapted to life in submarine deserts (Schlager, 2005).

1.6 Limestone classification

Carbonate factories and their grain associations produce a wide spectrum of different sand- and mud-size carbonate sediments that can be described by their texture and fabric using specific classification schemes (James and Jones, 2016). In carbonates, texture refers to the size, shape and arrangement of the constituent elements; and fabric describes the orientation in space of the particles, crystals and cement (James and Jones, 2016).

1.6.1 Dunham classification

Dunham (1962) classification describes carbonate rocks based on textural features distinguishing allochems (grains and carbonate fragments), matrix or micrite, and sparry calcite cement (Figure 1.11). This classification is useful to understand general depositional settings, and it is widely used in the oil and gas industry. The three textural features are the following (Figure 1.11):

1. Presence or absence of carbonate mud - mudstone (mud-supported) and grainstone (grain supported and cement) are the two end members.
2. Abundance of grains - subdivision of muddy carbonates into:
 - a. Mudstone - mud-supported sediments with <10% grains.
 - b. Wackestone - sediments containing 10-50% grains.
 - c. Packstone - sediments with 10-49% interparticle mud.
3. Signs of binding during deposition - a boundstone is characterised.

Dunham (1962) classification is effective as it is based on descriptive components of the rock with no interpretations. Rock names can further recognised by adding the dominant type of grain such as oolitic grainstone or crinoidal wackestone (James and Jones, 2016).

1.7 Carbonate platforms

A carbonate platform is a stratigraphical term related to thick deposits of shallow-water carbonate rocks (Bosence, 2005a). Marine continental shelves provide an adequate environment to create carbonate sediments, and because of that, the terms carbonate platform and carbonate shelf are often used synonymously (Bosence, 2005a). Most carbonate sediments are formed by the accumulation of skeletons and shells constructed by marine organisms through the precipitation of calcium carbonate (e.g. corals, molluscs, and foraminifera) (Bosence, 2005a). In the literature, there are many attempts to classify carbonate platforms based on their morphology, basinal and tectonic settings, depositional features and carbonate producing biota (Pomar, 2001, 2020; Bosence, 2005b, 2005a). The following section presents a basic morphological classification of carbonate platforms.

Carbonates

Dunham (1962)

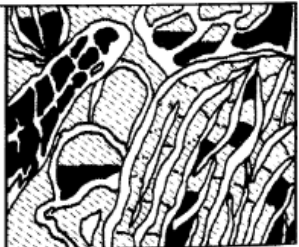
Groundmass:		Fine carbonate matrix		+ spar	sparry cement	Bioconstruction
Matrix-supported		Grain-supported				
Grains: < 10%	> 10%					BOUNDSTONE
MUDSTONE	WACKESTONE	PACKSTONE		GRAINSTONE		
						

Figure 1. 10. Dunham (1962) textural classification of limestones. Figure from Schlager (2005).

1.7.1 Attached carbonate platforms

Attached carbonate platforms are carbonate shelves tied to a continental landmass. The connection to the continent signifies that siliciclastic sediments can be shed to the platform at times, resulting in a mixed carbonate-siliciclastic system (Bosence, 2005a). Carbonate platform successions comprise a wide spectrum of depositional profiles, being divided into ramps or flat-topped platforms (Pomar, 2001) (Figure 1.12). Ramp profiles can be either homoclinal or distally steepened ramps (Pomar, 2001) (Figure 1.12). Flat-topped profiles can be non-rimmed shelves or rimmed shelves (Pomar, 2001) (Figure 1.12).

1.7.2 Rimmed carbonate platforms

The rim surrounding by the carbonate platform is commonly created by the development of reefs or sand shoals, which ultimately partially isolate the inner platform. South Florida is an example of a rimmed carbonate platform that has accumulated carbonate sediments since the Jurassic. The platform comprises a semi-enclosed lagoon, a back reef area protected from high energy waves, the reef and sand shoal margin, and the fore-reef slope (Bosence, 2005a) (Figure 1.13).

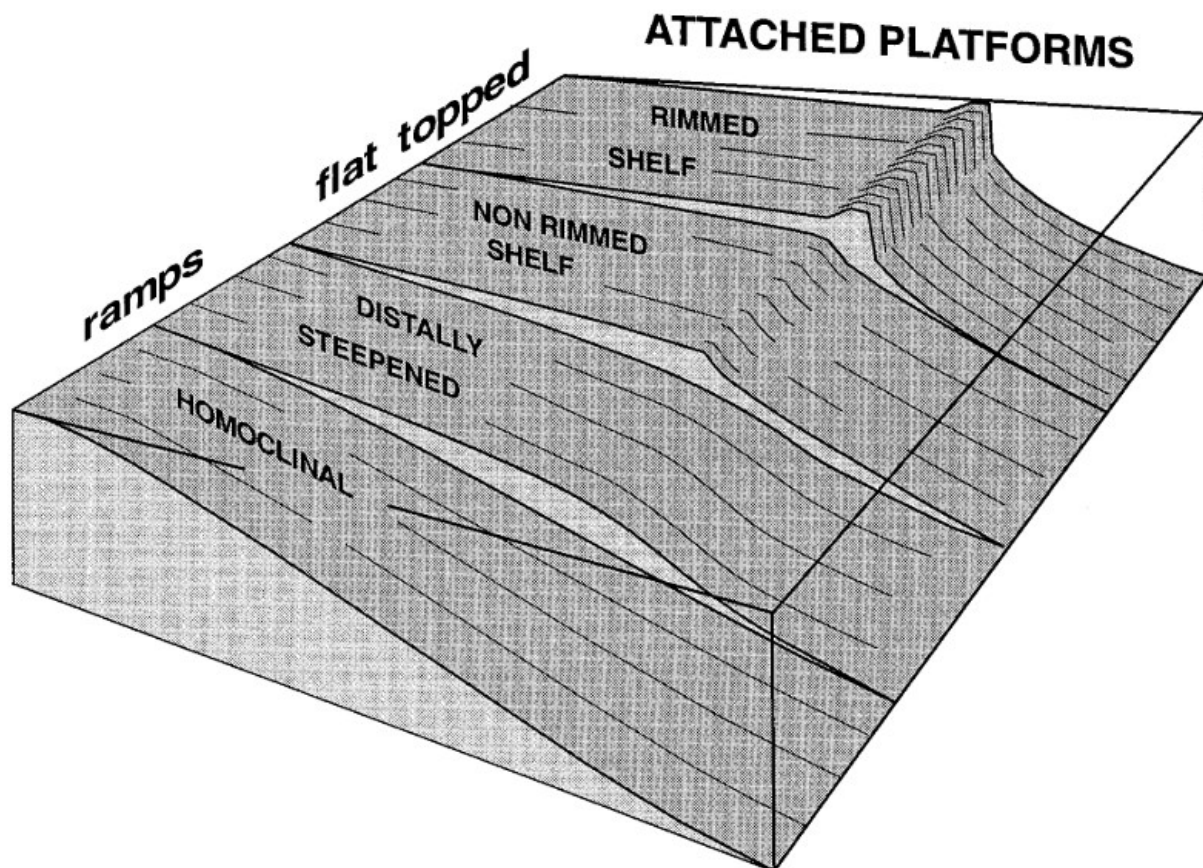


Figure 1.11. Schematic diagram showing the different types of depositional profiles on carbonate platforms, from homoclinal ramps to flat-topped rimmed shelves. Figure from Pomar (2001).

1.7.3 Carbonate ramp

A carbonate ramp commonly has a gentle slope ($<1^\circ$) towards an open sea with no major build-up of reefs or steep slopes. The southern coast of the Arabian Gulf is a good example of a modern carbonate ramp. It is characterised by a gentle slope shelf which gradually transitions from a low-relief desert of the coastal plain to water depths of 100 m over a distance of hundreds of kilometres (Bosence, 2005a) (Figure 1.14). The depositional environments are divided into inner, mid- and outer ramp. The inner ramp is the zone in which waves impinge on the seafloor during normal or “fair-weather” conditions. The mid-ramp is the zone between the fair-weather wave base and the storm wave base (Figure 1.14). The outer ramp is the deep-water zone below the effect of waves (Figure 1.14).

1.7.4 Isolated carbonate platform

An isolated carbonate platform (ICP) is a body of carbonate strata deposited as a geomorphic feature with significant depositional relief relative to adjacent, time-equivalent, deeper-water strata, lacking any significant attachment to a continental land mass, including several depositional environments such as reefs, lagoons, tidal flats and flanking slopes (Burgess et al., 2013; Rusciadelli and Shiner, 2018) (Figures 1.15 and 1.16). The term isolated carbonate platform can also be referred as a carbonate bank, or an atoll when it is formed over a subsiding volcano (Bosence, 2005a). The Great Bahama Bank is an excellent example of an isolated carbonate platform (Figure 1.15).

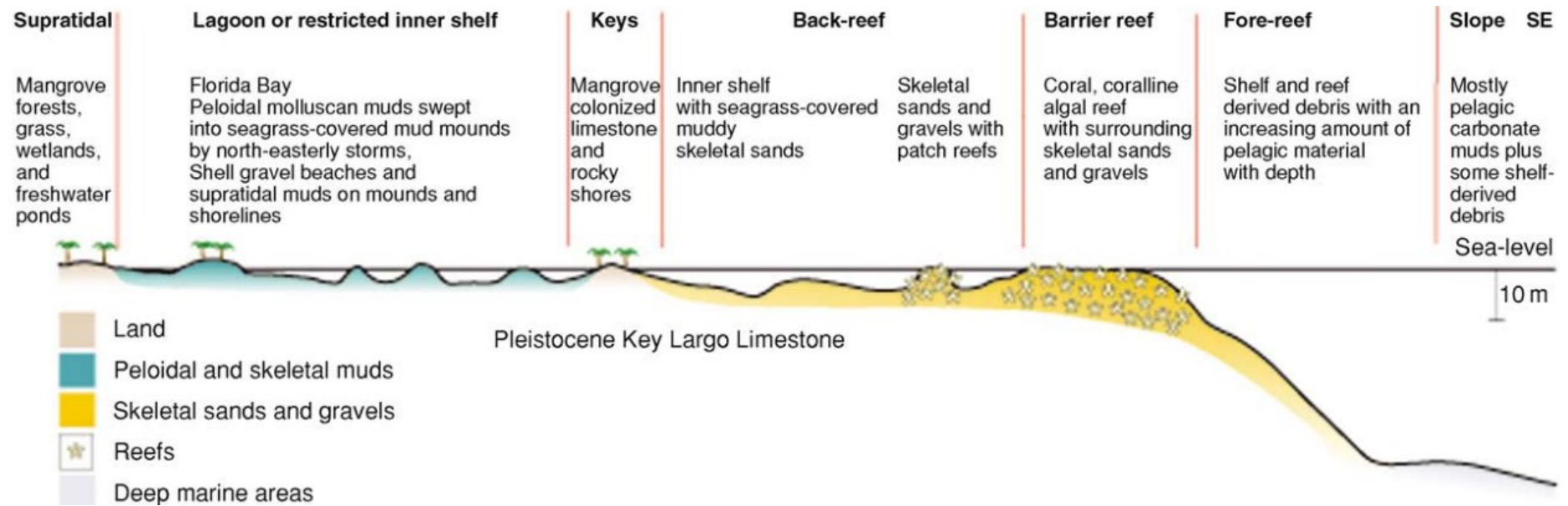


Figure 1.12. Schematic cross section of the Florida Shelf showing the main depositional environments commonly seen on a rimmed carbonate shelf: lagoon, back reef, barrier reef, fore reef and slope. Figure from Bosence (2005a).

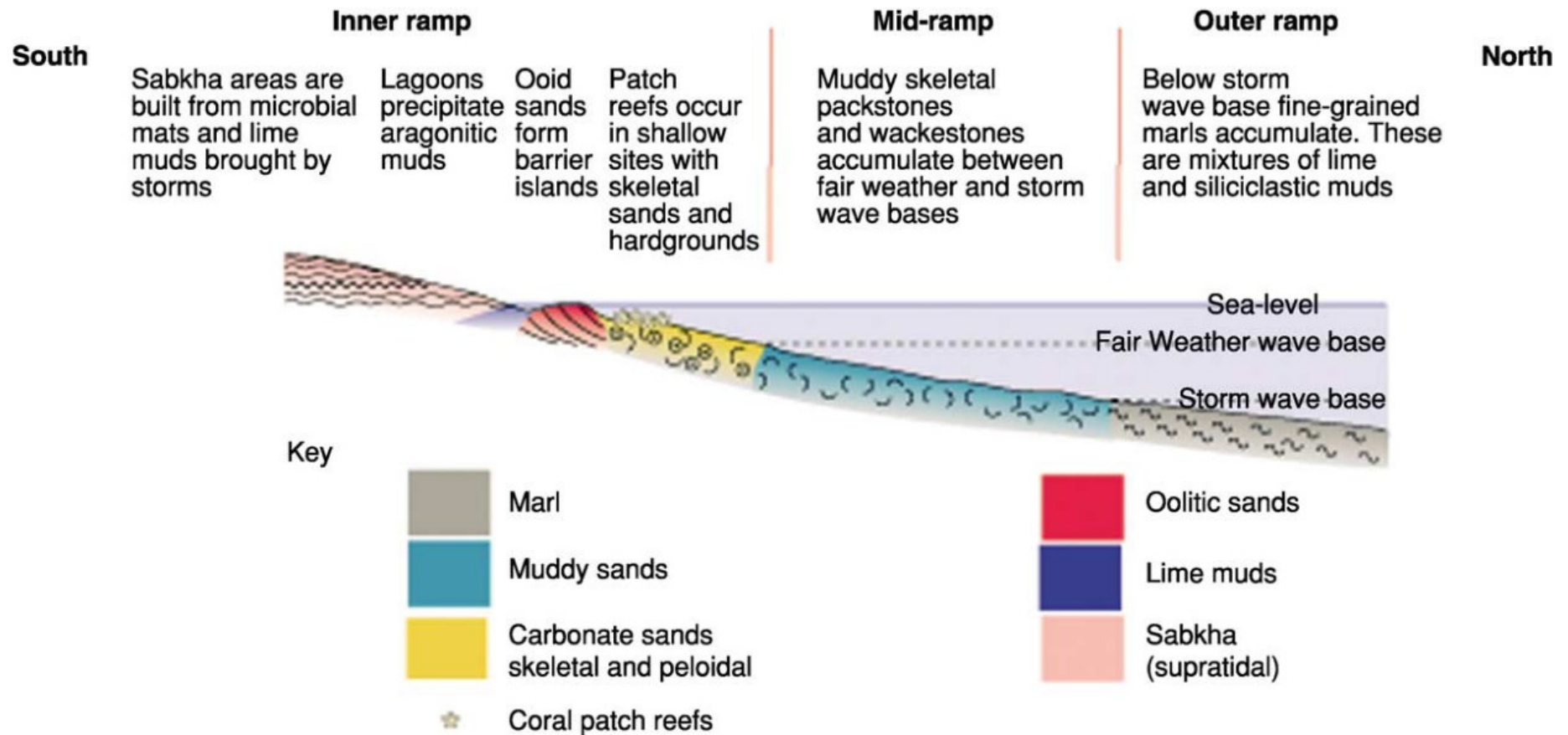


Figure 1.13. Schematic cross section of the Arabian Gulf showing the main depositional environments commonly seen on a carbonate ramp: inner, mid-, and outer ramp. Figure from Bosence (2005a).

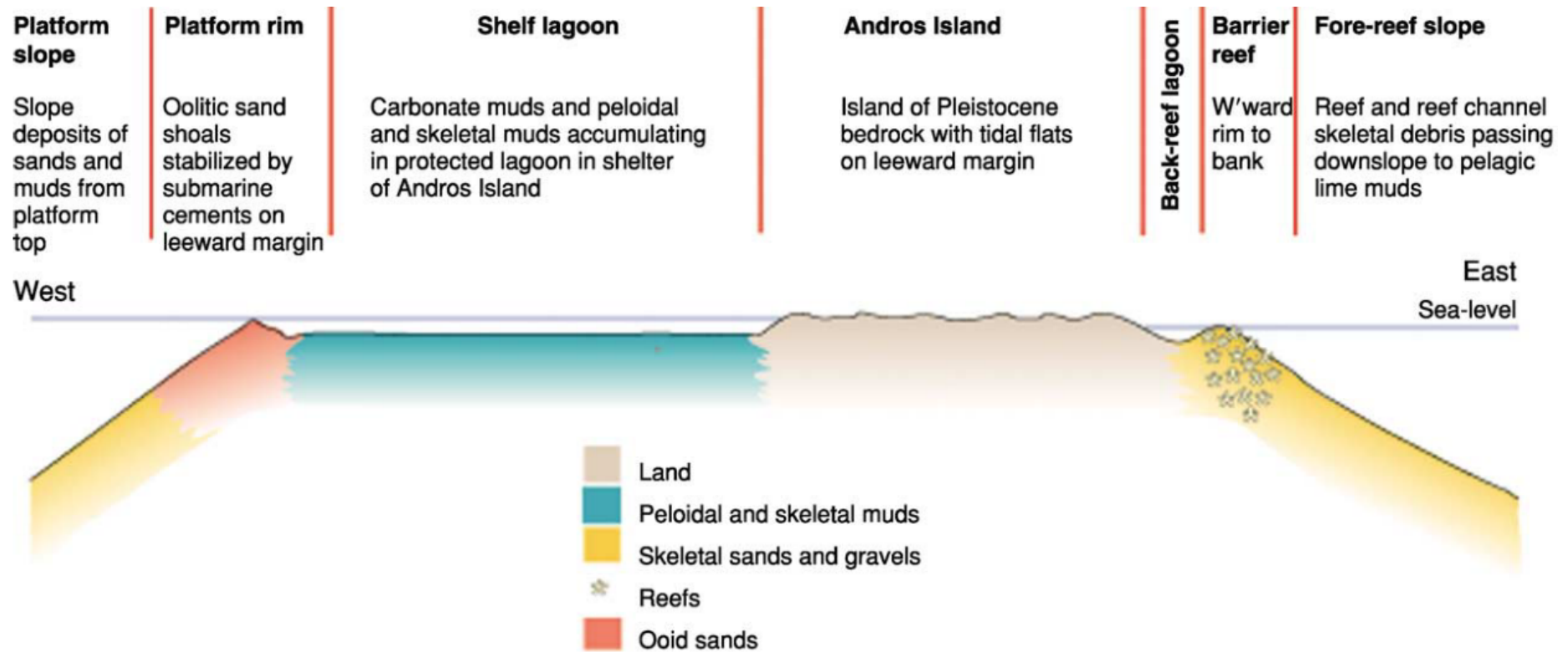


Figure 1.14. Schematic cross section of the Great Bahama Bank showing the main depositional environments commonly observed on a rimmed isolated carbonate platform: lagoon, barrier reef, oolitic shoals and slope. Figure from Bosence (2005a).

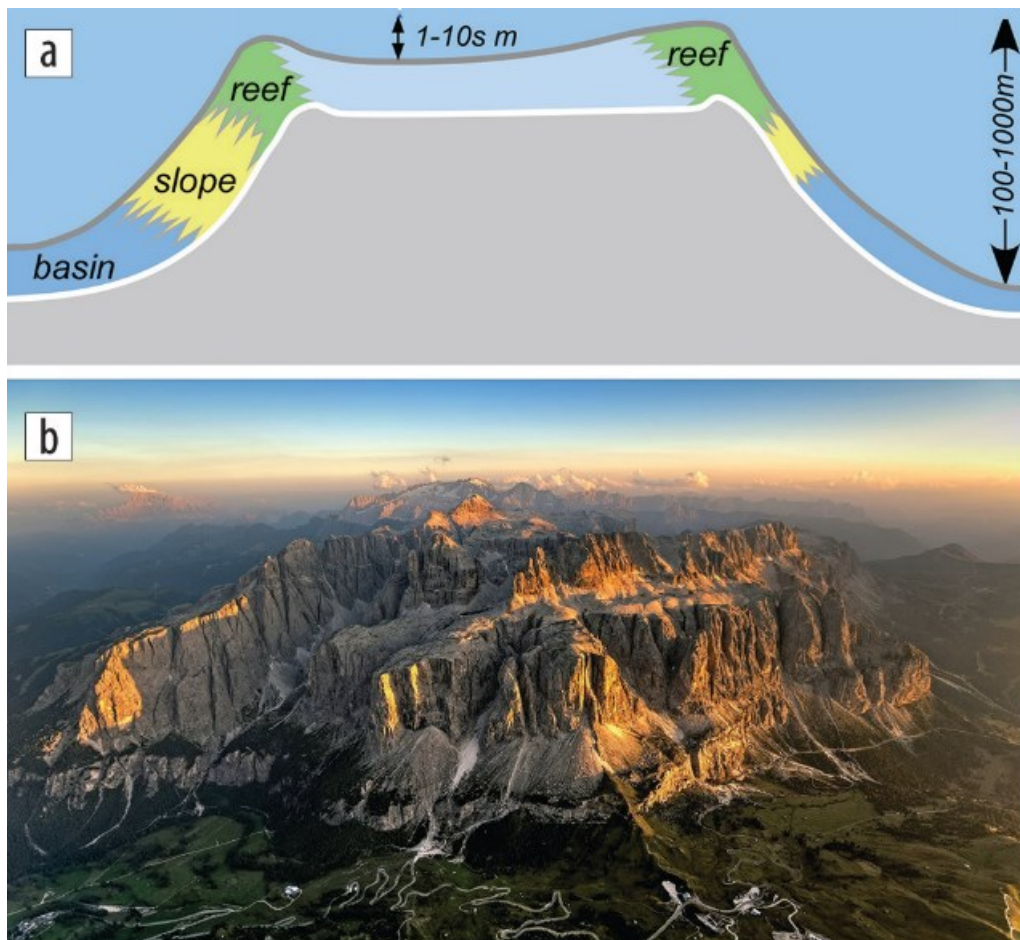


Figure 1.15. (a) Schematic diagram showing the geometry and internal depositional environments of an isolated carbonate platform. (b) Ancient example of an ICP from the Triassic Sella Group, Dolomites, Italy. Figure from Rusciadelli and Shiner (2018).

1.8 Carbonate slopes

Carbonate slopes are valuable architectural and sedimentological features that reflect the growth, evolution and depositional conditions of a carbonate system (Playton et al., 2010). Playton et al. (2010) produced a comprehensive classification of carbonate slope deposits based on their grain size and type of platform margin.

1.8.1 Geometrical profile and terminology

The key nomenclature representing the morphological attributes of carbonate slopes is presented in the following section (Figure 1.17). *Platform edge* is the greatest seaward increase in gradient, *toe-of-slope* is the seaward transition from inclined to flat-lying strata, and the *slope* is the inclined part of the depositional profile (Playton et al., 2010) (Figure 1.17).

Reef is an early lithified, autochthonous biological accumulation occurring around the upper slope, platform edge or on the platform top (Figure 1.17). Reefs are restricted to shallow-water environments (<50 m) composed of skeletal frameworks producing framestone and bafflestone fabrics (Playton et al., 2010).

Margin is the transition from platform-top to re-sedimented foreslope environments, including the interfingering of outer-platform, reef, and upper slope settings (Figure 1.17). *Platform edge* is referred to the central feature of the margin, and *foreslope* is the re-sedimented material along the slope profile (Playton et al., 2010) (Figure 1.17).

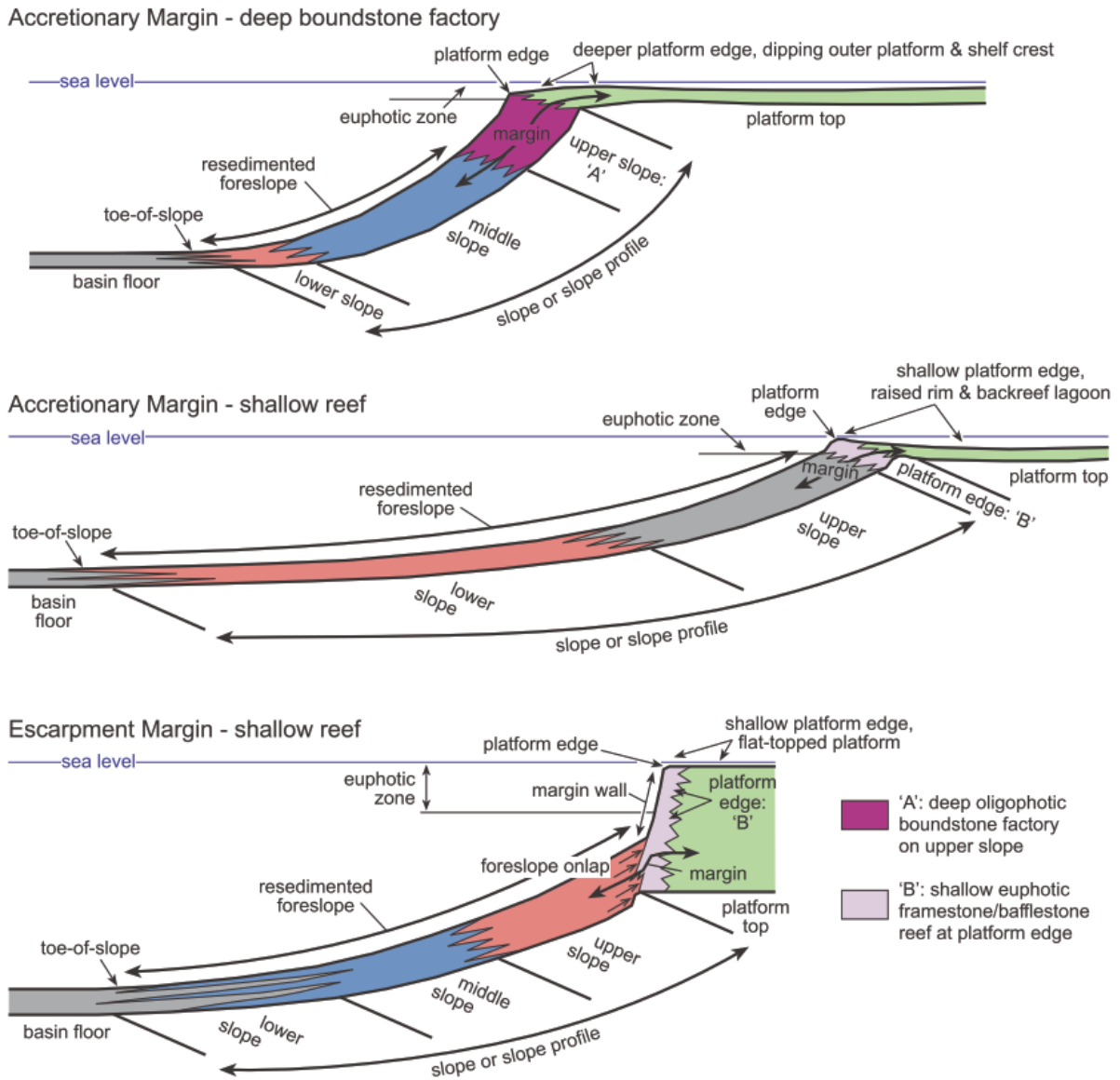


Figure 1.16. Schematic diagrams showing the different types of carbonate margins (accretionary and escarpment margins) and the major terms related to shelf-to-basin depositional systems. Figure from Playton et al. (2010).

Euphotic zone is characterised by shallow-water depths (generally <50 m) where organisms that require light occur (Figure 1.17). *Oligophotic zone* refers to deeper water depth (50 to >100 m) where less light-dependent fauna occurs, and the *photic zone* is the “light penetration zone” comprised by the euphotic and oligophotic zone (Playton et al., 2010).

1.8.2 Types of slope carbonate deposits

Carbonate slopes are highly variable compositionally, architecturally and spatially due to a spectrum of sediment sources, re-sedimentation processes, and controlling factors. Playton et al. (2010) subdivided carbonate slopes in terms of their deposit types, large-scale stratal patterns and spatial architecture, categorising them into debris-, grain-, and mud-dominated deposits.

1.8.2.1 Debris deposits

Debris deposits are generated from gravitational collapse and coherent mass wasting of early lithified material, which is mostly sourced by the platform margin. Debris deposits range in grain size from cobble to boulder (0.1 to >50 m). Transport processes producing these deposits include rockfall, hyper-concentrated flows (producing a grain-rich matrix), and debris flows (resulting in a fine-grained matrix). Debris deposits are generally thick-bedded, and form lenticular channel-form or lobate shapes (Figure 1.18). Debris deposits can also occur as tongues, slope aprons and intercalated lenses on the slope or basin floor (Playton et al., 2010) (Figure 1.18).

1.8.2.2 Grain-dominated deposits

Grain-dominated deposits comprise deposits generated by downslope transport of sand- to gravel-sized particles, mostly derived from platform-top and platform-edge settings. Their size ranges from very fine sand to pebbles (100 μm to cm), consisting of grain-dominated packstones, grainstones, and rudstones. Transporting processes include well-sorted hyper-concentrated flows (true grain flows), pebble-rich hyper-concentrated flows, and concentrated flows when finer grained fractions are present. Grain-dominated deposits are thin- to medium-bedded, tabular to slightly lenticular. Laterally unconfined aprons are common, spanning to the entire slope profile and fining into the basin. Channel-fan complexes also occur in lower slope, toe-of-slope, or basinal settings, indicating sediment bypass (Playton et al., 2010) (Figure 1.18).

1.8.2.3 Mud-dominated deposits

Mud-dominated deposits consist of clay- or silt- sized particles originated from protected platform settings or the water column (pelagic). Their grain size is normally less than 60 μm including mudstone, siltstone, chalk, and argillaceous (marly) textures. Transport processes include pure suspension fallout and fluid turbulence. These deposits are thin bedded or laminated, can drape foreslope topography, and can blanket deep-water seascapes with extensive bed lengths along strike and dip. Gullies and slump/slide features are common (Playton et al., 2010).

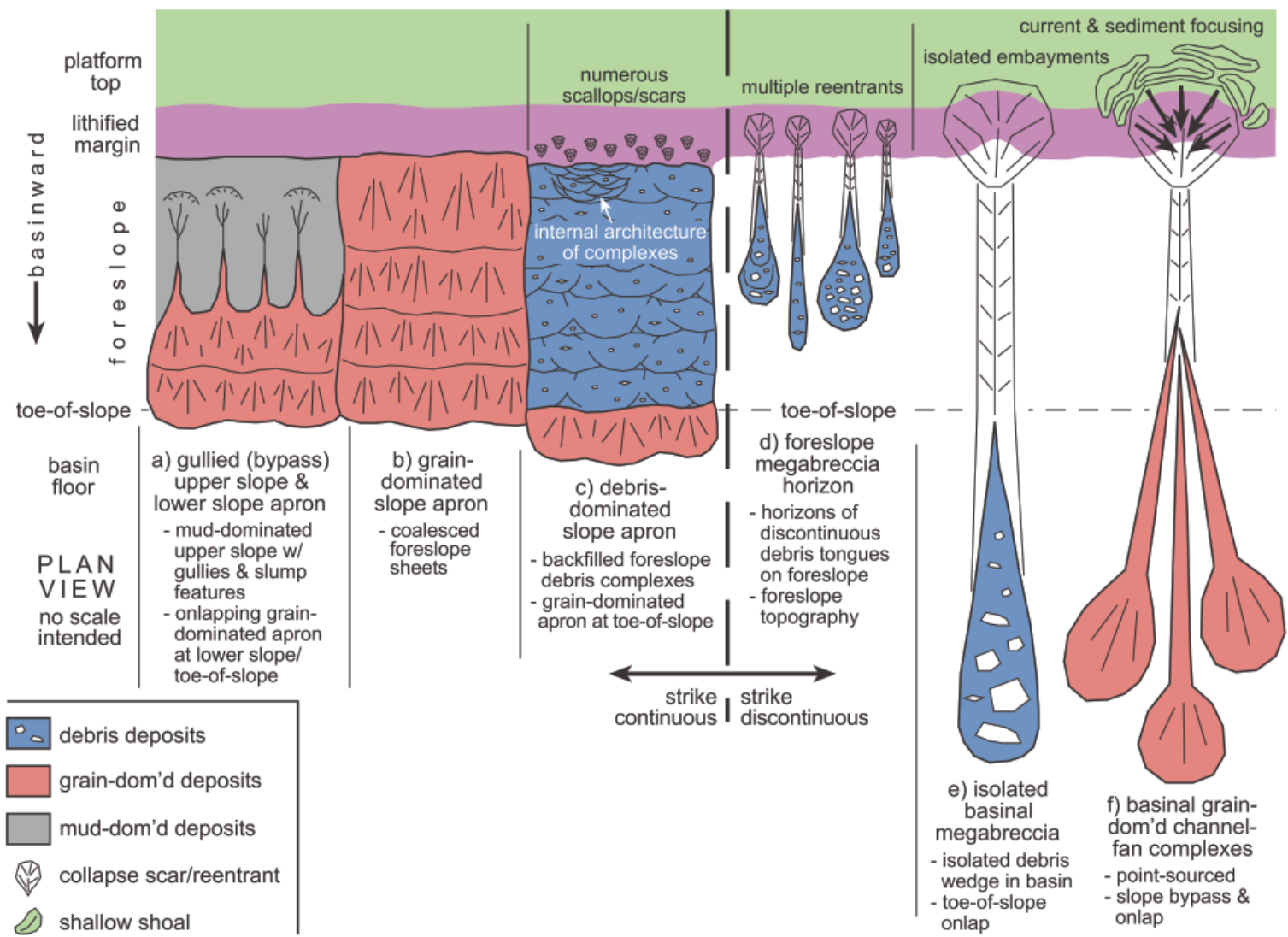


Figure 1.17. Schematic diagrams of carbonate slope and basin spatial architecture showing different strike-continuous aprons and strike-discontinuous tongues and channel-fan complexes. Figure from Playton et al. (2010).

1.9 Spatial architecture of slope deposits

Spatial architecture accounts for the distribution and internal geometries, dividing them into strike-continuous aprons and strike-discontinuous accumulations including channel-fan and debris complexes (Playton et al., 2010).

1.9.1 Strike-continuous aprons

1.9.1.1 Gullied upper slope/lower slope aprons

The upper slope of these systems is a sediment-bypass zone often associated with slump/slide features and numerous gullies or small canyons along the strike (Figure 1.18). The upper slope bypass zone is commonly mud-dominated and prone to early cementation. Sediment derived from the platform top, margin and upper foreslope bypasses via multiple point source gullies along the strike and depositing in areas from the lower slope to the toe-of-slope. Coalesced lobes create aprons typically grain-dominated and rich in debris deposits (Playton et al., 2010) (Figure 1.18).

1.9.1.2 Grain-dominated slope aprons

These deposits are formed by coalesced complexes of sheet-stacked grain-dominated deposits extending from the margin to toe-of-slope environments (Figure 1.18). These complexes merge laterally and along dip to form large-scale aprons with lengths of 10s to 100s of km. A transition from grain- to mud-dominated deposits is common, producing exponential clinoform curvatures (Playton et al., 2010).

1.9.1.3 Debris-dominated slope aprons

From toe-of-slope to margin settings, these aprons characterise to stack debris deposits with lenticular shapes, commonly observed in accretionary margins. The development of a strike-continuous debris apron requires multiple phases of constant small-scale gravitational collapse at multiple points along the strike. As a result, the lithified margin display metre-scale scars and scallops (Playton et al., 2010) (Figure 1.18).

1.9.2 Strike-discontinuous accumulations

1.9.2.1 Foreslope megabreccia

As a result of intermediate- to large-scale collapse, discontinuous debris deposits form on the slope, such as megabreccia channels, isolated blocks and boulder complexes (Figure 1.18). These deposits represent periods of instability. Megabreccias are lenticular and discontinuous along debris horizons forming lateral depositional topography that influences and redirects subsequent grain- or mud-dominated sediment gravity flows (Playton et al., 2010) (Figure 1.18).

1.9.2.2 Isolated basinal megabreccia

Extreme instability and large-scale collapse of the outer platform margin result in this type of deposits. Such events produce high volumes of debris deposits that are generally isolated spatially (spaced 1 to 10s of kilometres apart) (Playton et al., 2010) (Figure 1.18).

1.9.2.3 Basinal channel-fan complexes

These deposits develop in distal settings and are generated from line source carbonate factories that focus downslope through irregularities in the margin such as an embayment (Figure 1.18). The focused flow promotes channelisation, bypass of the slope profile and accumulation of strike-discontinuous sediments at the toe-of-slope or the basin floor (Figure 1.18). Channelisation indicates confined flow and the potential for sediment to transport over great distances. In most distal environments where flow becomes unconfined, fans accumulate, and channel throats backfill to the toe-of-slope. Internal architecture of carbonate channel complexes is similar to that of their siliciclastic counterparts (Playton et al., 2010).

1.10 Carbonate porosity and permeability

Carbonate rocks are hosts of about half of the hydrocarbon reserves in the world and some of the richest metallic ore deposits. The economic importance of carbonate rocks is related to their porosity and permeability. Porosity is the percentage of space in a given rock sample, and permeability is the ability of fluids to flow through a rock. Porosity and permeability are not a function of one another as high porosity does not necessarily mean high permeability.

Porosity in carbonate rocks is complex due to their biologic and heterogenous nature that results from numerous diagenetic cycles at all scales. This complexity is observed as primary porosity (within grains or related to the growth of the reef framework) and the common development of secondary porosity (dissolution and dolomitization, fractures) (Moore, 1989). The interplay between different types of porosity is key to understand carbonate rocks.

An example of high permeability due to intergranular and intercrystalline porosity is the Jurassic Ghawar oil field in Saudi Arabia, which is the largest conventional oil reservoir in the world (James and Jones, 2015). In contrast, an example of high permeability due to highly connected fracture networks and dissolution is the giant Tengiz field in Kazakhstan (Moore and Wade, 2013a).

1.10.1 Choquette and Pray porosity classification

This classification is mostly based on dividing porosity into *fabric selective* and *non-fabric-selective*. Fabric selective refers to solid constituents such as grain type or recrystallisation developed during deposition and diagenesis. If the porosity does not have a relationship to its fabric, then, porosity is classed as *non fabric-selective*, including pores and cavities that cut across grains and depositional fabrics. Choquette and Pray (1970) porosity classification consists of four elements: basic porosity types, genetic modifiers, size modifiers and abundance modifiers (Figure 1.19).

The classification defines 15 types of **basic porosity** based on a descriptive and genetic system (Figure 1.19). The characteristics used to define these types include pore size, shape, genesis, or relationship to other fabrics. **Genetic modifiers** are used to describe processes (i.e. solution, cementation), time of formation (i.e. primary or secondary) whether the porosity has been reduced or enlarged. **Size modifiers** differentiate pore systems into large (megapores) or small (micropores). **Abundance** defines the percentages or ratios of pores in a rock sequence (Moore, 1989).

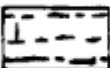
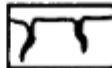
BASIC POROSITY TYPES			
FABRIC SELECTIVE		NOT FABRIC SELECTIVE	
PRIMARY		INTERPARTICLE	BP
		INTRAPARTICLE	WP
		FENESTRAL	FE
		SHELTER	SH
		GROWTH-FRAMEWORK	GF
SECONDARY		INTERCRYSTAL	BC
		MOLDIC	MO
	FRACTURE	FR	
	CHANNEL*	CH	
	VUG*	VUG	
	CAVERN*	CV	
*Cavern applies to man-sized or larger pores of channel or vug shapes.			
FABRIC SELECTIVE OR NOT			
	BRECCIA	BR	
	BORING	BO	
	BURROW	BU	
	SHRINKAGE	SK	
MODIFYING TERMS			
GENETIC MODIFIERS		SIZE*MODIFIERS	
PROCESS	DIRECTION OR STAGE	CLASSES	mm'
SOLUTION	s	ENLARGED	x
CEMENTATION	c	REDUCED	r
INTERNAL SEDIMENT	i	FILLED	f
TIME OF FORMATION		MEGAPORE mg	large lmg 256
PRIMARY	P	small smg	32
pre-depositional	Pp	MESOPORE ms	large lms 4
depositional	Pd	small sms	1/2
SECONDARY	S	MICROPORE mc	1/16
eogenetic	Se	Use size prefixes with basic porosity types:	
mesogenetic	Sm	mesovug	msVUG
telogenetic	St	small mesomold	sms MO
		micropore	mcBP
		*For regular-shaped pores smaller than cavern size	
		+ Measures refer to average pore diameter of a single pore or the range in size of a pore assemblage.	
		For tubular pores use average cross-section.	
		For platy pores use width and hole shape.	
Genetic modifiers are combined as follows:		ABUNDANCE MODIFIERS	
PROCESS + DIRECTION + TIME		percent porosity	(15%)
EXAMPLES: solution enlarged		or	
cement-reduced primary		ratio of porosity types	(1:2)
sediment-filled eogenetic		or	
		ratio and percent	(1:2)(15%)

Figure 1. 18. Choquette and Pray (1970) classification of carbonate porosity. Figure from Moore (1970).

1.10.2 Primary porosity

Primary porosity is the one that can be observed in a rock at the termination of depositional processes, developing pre- and syn-depositional. Interparticle, intraparticle, fenestral and framework are types of primary porosity (Figure 1.19).

1.10.3 Secondary porosity

Secondary porosity develops at any time after the final deposition. In some instances, primary porosity can be progressively lost due to two main processes: (1) dissolution and (2) dolomitization. Fracturing is another important process that generally increases permeability rather than porosity.

1.10.3.1 Porosity by dissolution

Dissolution is generally related to a significant change in the chemistry of the pore fluid such as change in salinity, temperature or partial pressure of CO₂. These changes can occur in relation to meteoric water, hydrocarbon maturation or shale dewatering, or associated to rock exhumation (Choquette and Pray, 1970; Moore, 1989).

1.10.3.2 Porosity by dolomitization

Dolomitization is a common diagenetic process in which calcareous material is partly or wholly transformed into dolomite. The texture and fabric of the rock generally changes, being accompanied by an increase of porosity and permeability (James and Jones, 2015).

1.10.3.3 Porosity associated with breccias

Breccias can be formed as a result of different processes including solution collapse, karst, faulting or hydrothermal processes, and are commonly associated with high porosity (Moore, 1989; James and Jones, 2015).

1.10.4 Porosity associated with fractures

The brittle nature of carbonates facilitates fracturing of carbonate rocks at any time during the diagenetic stage and throughout the burial history of a carbonate sequence. Early lithification of carbonates is a key element controlling fractures in carbonate rocks; and this is one of the main reasons why fractures in carbonates differentiate from the more ductile fine-grained siliciclastics (Moore, 1989). Carbonate materials can be cemented virtually at the same time of deposition, giving rise to syn-depositional faulting and fracturing. When fractures are open, they can provide excellent pathways to fluid flow, such as in the Gaschasan oil field in Iran, where an individual well can produce up to 80,000 barrels of oil per day from the fractured Oligocene Asmari Limestone with a matrix porosity of just 9% (McQuillan, 1985).

Fractures are commonly filled with a variety of minerals including calcite, dolomite, anhydrite, galena, sphalerite, celestite, strontianite and fluorite. These fracture fills are precipitated as the fracture is being used as a fluid conduit (Moore, 1989).

1.10.5 Diagenesis and porosity

Diagenesis can be defined as the chemical and textural changes on carbonate rocks from the time of particle formation and sediment deposition to post-depositional stages as long as active fluids interact with the rock (Mazzullo and Chilingarian, 1992). Composition of fluids can be meteoric or marine (brackish, normal salinity or hypersaline). Porosity has a close relation to diagenesis as it involves processes such as cementation, dissolution, recrystallisation, and replacements including dolomitization and evaporitization (Mazzullo and Chilingarian, 1992).

1.11 Fault and fracture analysis

Fault interactions occur at all scales in many settings, including rock deformation and fracture development (Fossen and Rotevatn, 2016). It is common to see faults interacting in different manners due to their growth history and spacing between them. In an extensional geological setting where normal fault systems develop, fault overlap zones are common. Childs et al. (1995) described overlap zones as the area where the tip lines of two fault traces face each other with a small distance relative to the complete length of the faults. The main structures that can occur are fault bend, transfer fault or overlap zone (Childs et al., 1995) (Figure 1.20).

Displacement areas between the overlapping zones are defined as relay zones (Childs et al., 1995). Relay ramps are the overlap zones where there is interaction between fault tips and where there is transference of displacement from one structure to another (Larsen, 1988; Fossen and Rotevatn, 2016) (Figure 1.21). Bed rotation is common on relay ramps, which suggest that strike and dip of relay ramp sequences have a different orientation from the general trend.

Relay zones experience constant movement and deformation through their development, resulting in highly fractured areas. A relay structure observed in Canyonlands National Park, Utah, USA is a great example of a relay ramp showing high density of fractures within the ramp area (Fossen and Rotevatn, 2016) (Figure 1.22). On a carbonate setting, the Sierra del Carmen in west Texas provides an excellent exposure of relay ramps, which resulted from the linkage of normal faults in the thick, massive Cretaceous Santa Elena Limestone (Ferril et al., 2002). Another good example is the breached relay zone in a layered limestone-shale succession within the Hammam Faraun Fault Block in the Suez rift, Egypt (Bastesen and Rotevatn, 2012). In this example, mechanical stratigraphy between the layers of limestone and shale play an important role on the development of fractures. There is brittle deformation and opening-mode fracturing within the strong limestone, whereas in the mechanically weak shales, deformation is accommodated through folding and bed-parallel shear (Bastesen and Rotevatn, 2012).

1.11.1 Fault linkage

Interactions between faults relate to factors, such as strain, fault density, fault distribution and spatial arrangement of faults in the fault population, and the size of the elastic strain field or stress perturbation around faults (Fossen and Rotevatn, 2016). Development of relay ramps start when the tips of two subparallel fault segments face each other in a relative short distance. Once fault tips are interacting, the pace of fault displacement and growth in the overlapping zone is slowed down. At this stage, relay ramps form, and small-scale structures such as faults, fractures and deformation bands are generated within the ramp (Fossen and Rotevatn, 2016).

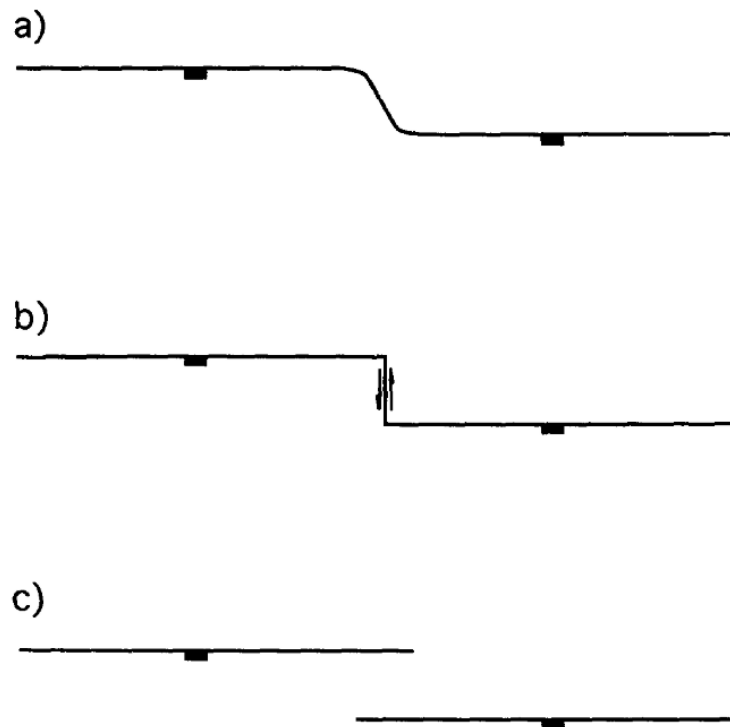


Figure 1.19. Schematic diagram of fault trace structures with interacting faults. (a) fault bend, (b) transfer fault, and (c) overlap zone. Figure from Childs et al. (1995).

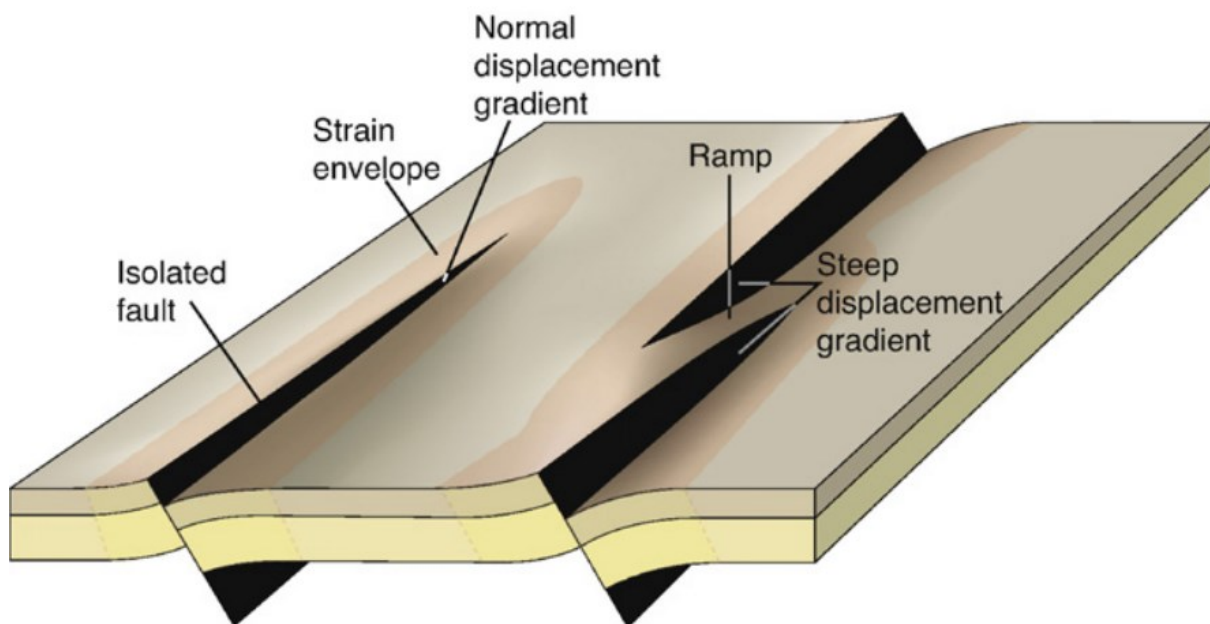


Figure 1.20. Schematic diagram of a relay ramp structure showing the connection between the hanging wall and footwall through the ramp. Relay ramps form when two faults overlap spatially, also overlapping their two strain envelopes. A single, isolated fault is shown to the left. Figure from Fossen and Rotevatn (2016).



Figure 1.21. Outcrop example of a relay structure from Canyonlands National Park (Devils Lane), USA. Faults and fractures are observed within the relay ramp area. Figure from Fossen and Rotevatn (2016).

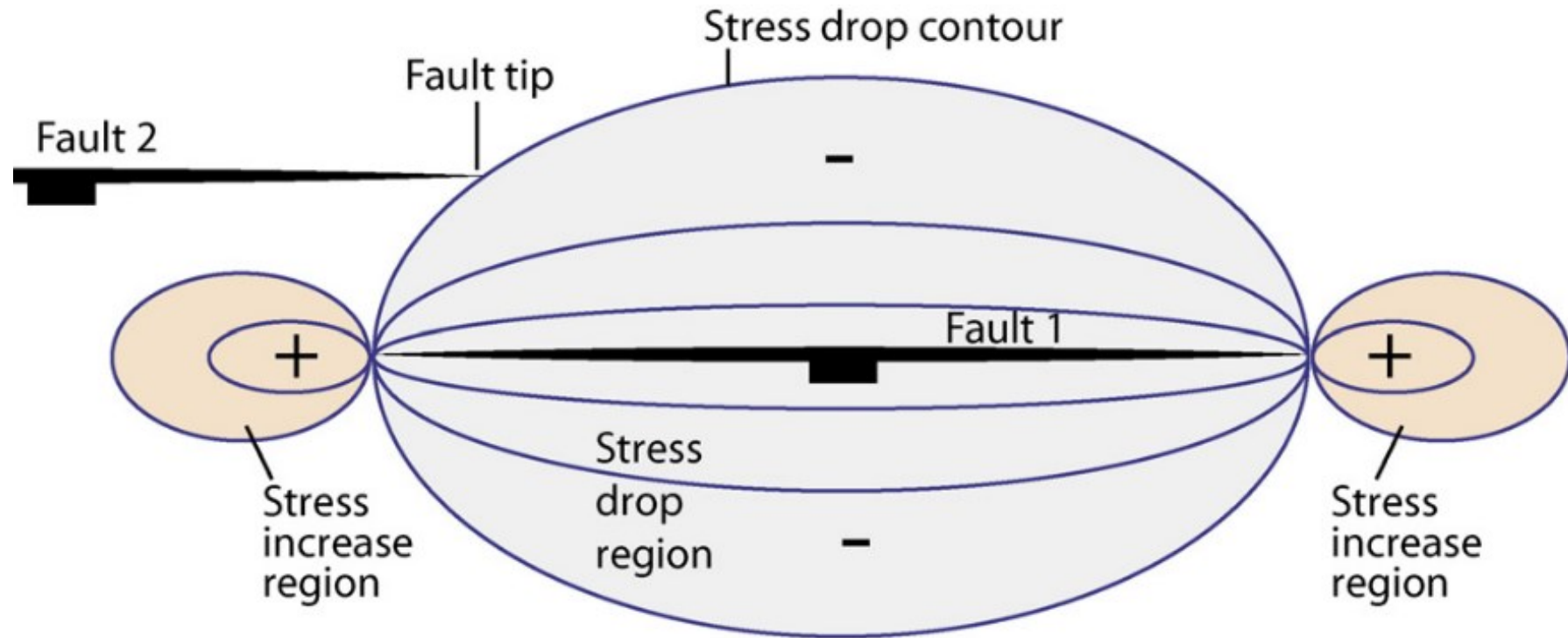


Figure 1.22. Diagram showing the stress zonation (drop or increase) around a normal fault in overlay zones. Figure from Fossen and Rotevatn (2016).

The drop in the pace of fault displacement and growth is the result of mechanical processes creating a stress drop region around overlap zones (Fossen and Rotevatn, 2016). These zones slow down the development of an adjacent fault at the time when the fault tip of the adjacent fault crosses the stress drop contour. In contrast, at the end of the fault tips, small regions of stress increase can develop, which suggests that the fault can expand if there is another adjacent fault (Figure 1.23).

1.12 Scaling laws

Faults and fractures occur in a range of sizes from mm to km structures. Understanding the scale relationship of their multiple attributes is of interest to many disciplines. Predicting sub-seismic faults and fractures from seismically resolvable features is key when modelling fractured reservoirs. Fault and fracture attribute distributions have been studied on scales ranging from drill-core through outcrop to seismic (Torabi and Berg, 2011). Different distributions such as power law or exponential have been previously described to suit specific attributes (Kim and Sanderson, 2005; Soliva et al., 2008).

A power-law distribution implies that there is no characteristic length scale in a dataset, whereas, log-normal and exponential distributions imply that there is a characteristic length scale within which the statistical relationship is valid (Torabi and Berg, 2011) (Figure 1.24).

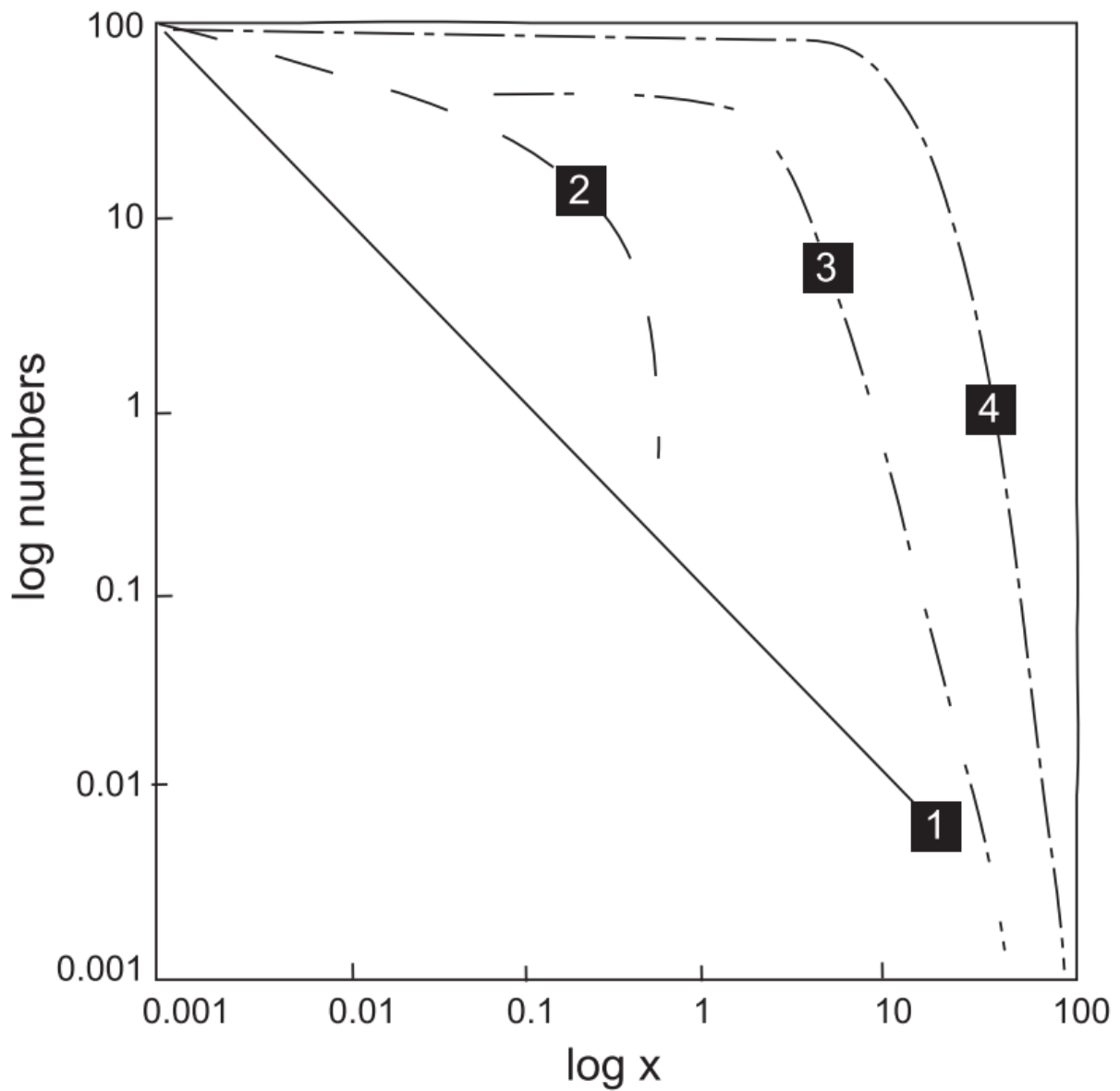


Figure 1.23. Frequency plot with logarithmic axes showing different statistical distributions. The graph shows (1) an ideal power-law, (2) exponential, (3) log-normal, and (4) normal, Gaussian distribution. Figure from Torabi and Berg (2011).

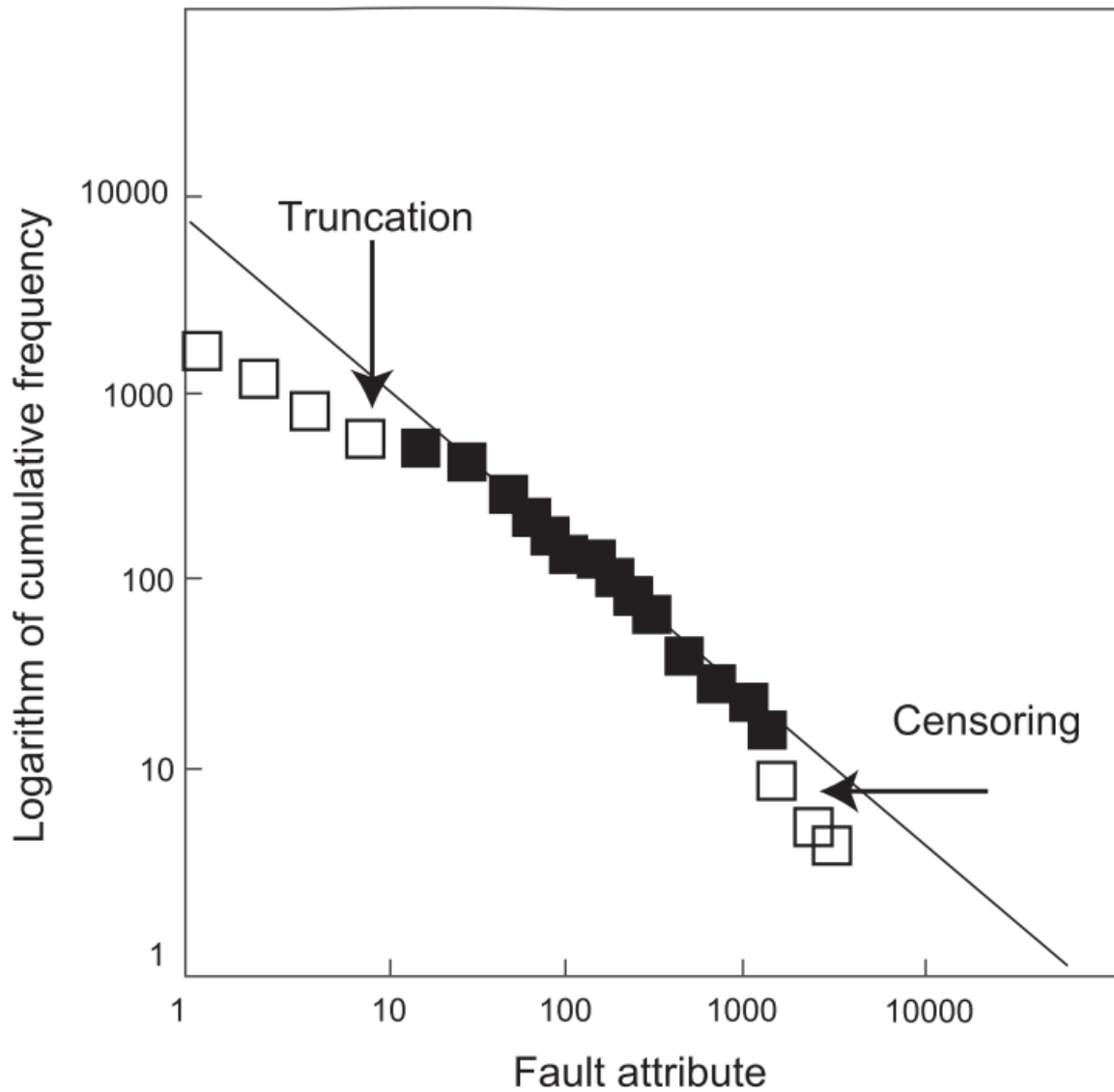


Figure 1.24. Cumulative frequency plot showing the sampling biases (truncation and censoring) that affects the distribution of fault and fracture attributes, causing a deviation of a distribution from a straight line. Figure from Torabi and Berg (2011).

1.12.1 Sampling effects

In nature, attributes that appear to have a power-law, exponential or log-normal distribution are known to have upper and lower bounds as their resolution and size are finite (Pickering et al., 1995; Torabi and Berg, 2011). The finite size of the sampled area and the resolution of the applied technique used to measure fault and fracture attributes affect the sampling at small- and large-scales, and may cause the frequency distribution of a power-law population to deviate from the perfect straight line (Manzocchi et al., 2009; Torabi and Berg, 2011). These effects are called truncation and censoring (Figure 1.25).

1.12.1.1 Truncation effect

Truncation causes underestimation of the frequency of small faults due to the resolution limitation of the sampling method used (Figure 1.25). This effect causes a gradual decrease of power-law slope in the lower bound of the scale range (Torabi and Berg, 2011).

1.12.1.2 Censoring effect

Censoring causes underestimation of the frequency of large faults due to the size limitation of the sample line or subjective choice of the sample region (Figure 1.25), causing an under-representation and under-sampling of large faults. This effect leads to a steepening of power-law trends toward the upper end of the scale range (Torabi and Berg, 2011).

1.12.2 Sampling effects when measuring fault throws

Throw-distance (T-D) and throw-depth (T-Z) plots are useful tools to examine the evolution and growth styles of normal faults. T-D plots comprise systematic measurements of maximum throw along the strike of the full length of faults. T-Z plots comprise systematic measurements of throw along fault dips that are completed across the trace of faults by comparing the relative depth of correlative intervals or reflections across the same fault, providing a record of throw variations at depth from its upper to lower tips (Tao and Alves, 2019).

The reliability of T-D and T-Z plots to exhibit accurate results depends on the sampling interval used when measuring fault throws at any scale. Tao and Alves (2019) introduced two parameters to help interpreters determine the sampling interval when analysing faults, being the sampling interval/fault length ratio (δ) and the module error (ϵ_i). Establishing an appropriate sampling interval is important because the use of coarse intervals result in: a) change of fault geometry; b) underestimation of maximum fault-throw values; c) unrepresentation of fault segments; d) change of fault linkage zones; e) underestimation of width of fault linkage zone; and f) failure to define fault interaction zones (Tao and Alves, 2019) (Figure 1.26).

Tao and Alves (2019) proposed certain threshold values to obtain accurate results when compiling T-D and T-Z data. They calculated that to have reliable data and avoid major caveats associated with poor data sampling, a module error (ϵ_i) should be <0.06 . To accomplish this, they suggest a sampling interval/fault length ratio $\delta = 0.05$ for faults with lengths $< 3,500$ m, which entails that the sampling interval of fault-throw measurements should be $<5\%$ of the total fault length. For faults longer than 3,500 m, a threshold value of $\delta = 0.03$ is suggested (Figure 1.26).

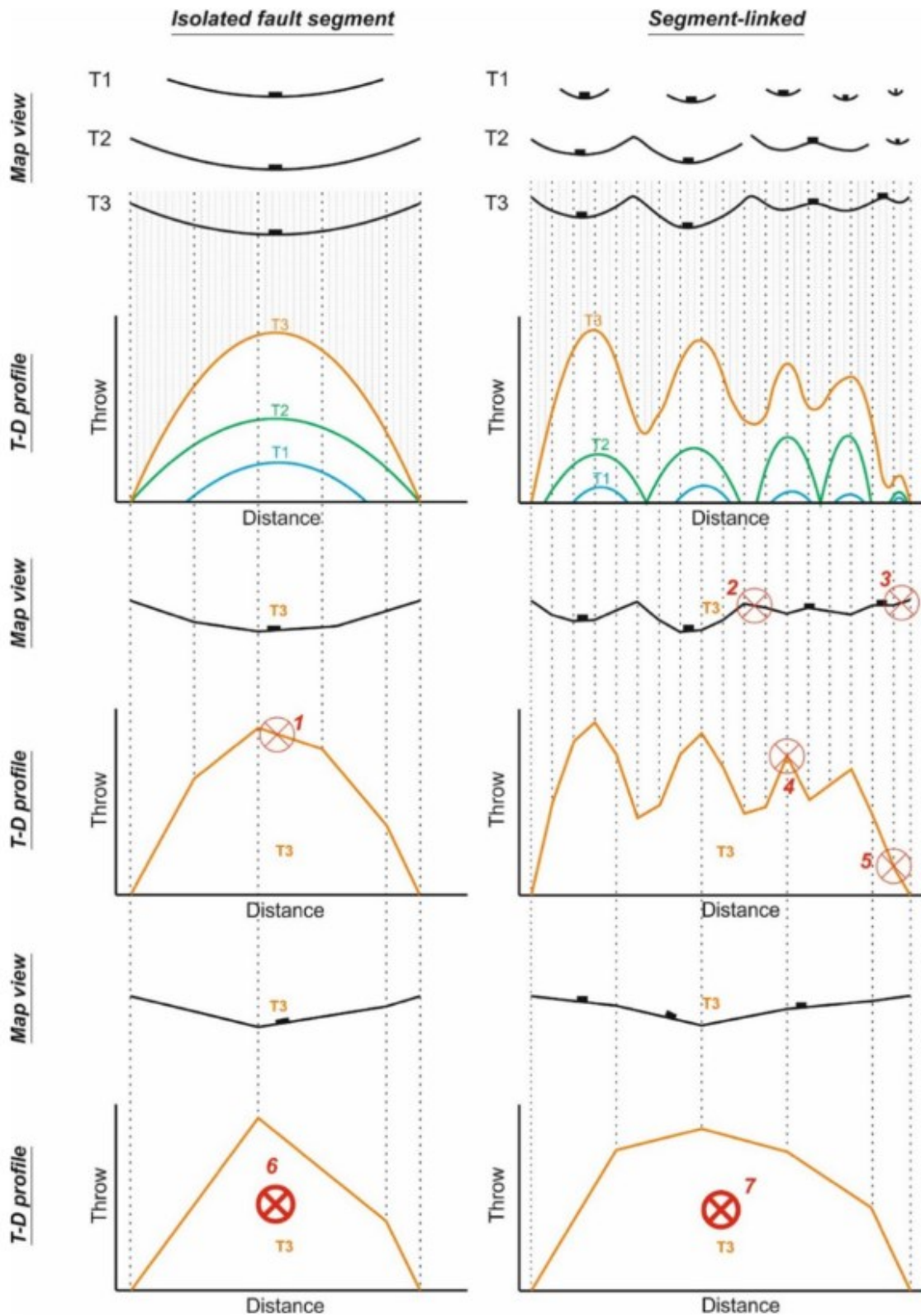


Figure 1.25. Schematic diagram showing isolated and segmented-linked faults with their respective T-D profiles showing the impact of data sampling. At coarser sampling intervals: 1) fault geometry changes from symmetric to asymmetric. 2) Fault linkage geometry changes. 3) Fault segment geometry changes. 4) Fault-linkage zone geometry and width change. 5) Fault segments are not discerned. Figure from Tao and Alves (2019).

Chapter 2: Geological settings of the studied areas

2.1 Introduction

This chapter reviews the geological settings of the four study areas discussed in this thesis, including the Bonaparte Basin, Northwest Shelf of Australia; the Sorbas Basin in SE Spain; the Pernambuco Basin in east Brazil, and the Pará-Maranhão Basin in Equatorial Brazil (Figure 1.2). Each of these study areas was carefully chosen to study a specific topic to help answering the scientific questions raised in this research. All the selected carbonate platforms were developed on equatorial margins and are of Cenozoic ages (Figure 1.2). The location and a brief explanation of why each study area was chosen is presented in each section. Structural and stratigraphic descriptions are presented, in addition to their carbonate depositional setting.

2.2 Bonaparte Basin, Northwest Shelf of Australia

The Bonaparte Basin (Figure 2.1) shows a complex structural evolution; it was subject to variable stress regimes, from predominant extension in the Paleozoic to combined compression and extension in the Mesozoic and Cenozoic. As a result, interesting fault sets are developed in this area. This work focuses on the Nancar Area, which is situated north of the Vulcan Sub-basin (Figure 2.1). This area contains a large number of isolated carbonate platforms (ICPs) known as the Karmt shoals that are exceptionally imaged on 3D seismic data. The relationship between well-developed fault sets and the distribution of ICPs in the north of the Nancar Area, makes this area ideal to quantitatively measure fault displacements to find a link between carbonate growth and fault linkage.

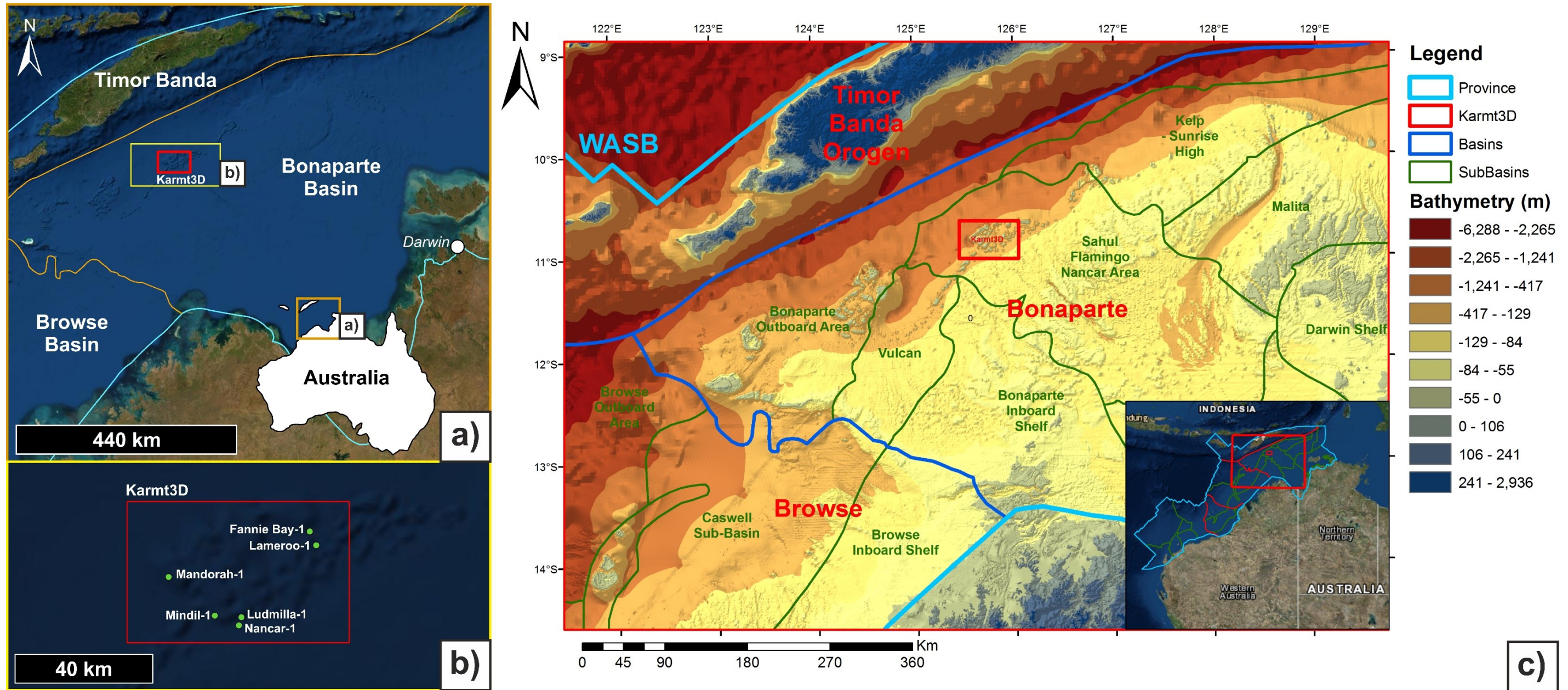


Figure 2.1. a) Location map of the Bonaparte Basin with an enlarged image (b) showing the seismic volume Karmt 3D and exploration wells utilised in this thesis. c) Bathymetric map showing the study area in the Westralian Superbasin (WASB). The studied Karmt 3D volume is located in the western part of the Sahul Flamingo Nancar Area. Bathymetric data provided by Geoscience Australia. Basin boundaries are modified from Longley et al. (2002).

2.2.1 Tectono-stratigraphic evolution

The area recorded different tectonic stresses during its evolution that relate to alternating rifting and compression events. During the Late Paleozoic and Jurassic times, two major episodes of extension occurred (Willis, 1998). In contrast, during the Late Triassic, the Bonaparte Basin was subjected to compressional forces (Longley et al., 2002; Saqab and Bourget, 2015a, 2015b).

Late Paleozoic rifting created NW-trending structures such as the Flamingo and Sahul synclines and the Londonderry High (Willis, 1998). Conversely, NE-SW Jurassic extension resulted with the formation of the Malita Graben and Vulcan Sub-Basin (Willis, 1998). Late Jurassic rifting marks the onset of separation between Greater India and Western Australia, which was completed by ~132 Ma bp, resulting in a basin-wide Valanginian unconformity (Willis, 1998). Subsequent to a later Valanginian transgression, clastic input to the basin became scarce due to flooding of sediment source areas (Willis, 1998). Following continental break-up, the area in which the Bonaparte Basin is included became a passive margin subject to thermal subsidence, with maximum water depths of about 500 m in the basin depocentre (Willis, 1998; Longley et al., 2002; Saqab and Bourget, 2015a).

In the Bonaparte Basin, important climatic changes occurred during the Early Cenozoic due to the progressive drift of Australasia to the north, placing the study area in tropical latitudes within 30° of the Equator, where carbonate factories could develop in areas with low clastic input (Baillie et al., 1994; Longley et al., 2002). In the middle Eocene, a relative realignment of tectonic plates gave place to a marked episode of carbonate progradation that filled the accommodation space provided by underlying rift basins (Baillie et al., 1994). Progradational and aggradational

carbonate ramp settings reflect an Eocene transition phase from siliciclastic to carbonate deposition (Baillie et al., 1994; Willis, 1998; Longley et al., 2002).

Tectonic convergence between the Australasian and SE Asian plates, from Late Miocene (6 Ma) to the Pliocene along the Banda Arc, developed a thrust belt on Timor Island and reactivated pre-existing extensional faults in the study area as left-lateral transtensional structures (Etheridge et al., 1991; Willis, 1998; Saqab and Bourget, 2015a). At present, the Timor Plateau and the Banda Arc converge along the Indonesian Trough at an estimated rate of 7.7 cm/yr, in a NNE direction (Ding et al., 2013; Saqab and Bourget, 2015a). That rate of movement is considered as average, given that the slowest rate in the Arctic Ridge is less than 2.5 cm/yr, and the fastest rate in the East Pacific Rise near Easter Island in Chile is more than 15 cm/yr.

The main fault families (set 1) in the Bonaparte Basin have an average strike of 072° NE and the secondary fault family (set 2) strikes 050° NE. Saqab and Bourget (2015a) suggested, in the study area, that fault displacement occurred from Late Miocene to Early Pleistocene using a different seismic dataset (Vulcan MegaSurvey). They confirmed that a good number of faults terminate just below the seafloor. However, some faults did not reach Pleistocene strata due to a relative quiescence in tectonic activity (Saqab and Bourget, 2015a).

2.2.2 Stratigraphic setting

In the Bonaparte Basin, carbonate sequences are recognised throughout the Cenozoic, with a clear onset in the Eocene (Figure 2.2). The first stage of carbonate deposition records the development of a broad ramp and is characterised by minor terrigenous input in the Early Eocene and Early Miocene (Mory, 1991; Saqab and

Bourget, 2015). This carbonate ramp is 3,000 m thick and mainly composed of calcarenite, calcilutite and marls, with small volumes of chert in the Grebe and Oliver Formations (Figure 2.2). At the base Miocene, a regional unconformity is recognised throughout NW Australia (Longley et al., 2002; Saqab and Bourget, 2015) (Figure 2.3). The interaction between the Australian and Pacific plates during the Middle Miocene caused a transgression, resulting in a regional flooding episode marked by the development of a broad carbonate shelf in the study area (Baillie et al., 1994; Whittam et al., 1996; Longley et al., 2002; Saqab and Bourget, 2015). Periodic lowstands resulted in karstic (subaerial) erosion throughout the Miocene. At the Base of the Pliocene (Figure 2.3), a local unconformity is recognised in the north Bonaparte Basin (Marshall et al., 1994; Saqab and Bourget, 2015a).

From the Late Pliocene to Early Quaternary a tropical, wide, shallow-water platform setting predominated in the Bonaparte Basin. This led to the development of the Malita intra-shelf basin (Bourget et al., 2013). Significant changes in sea level occurred throughout the Quaternary (Yokoyama et al., 2001). The shelf margin of the Bonaparte Basin presents a mixed system with alternating carbonate and siliciclastic sediments (Bourget et al., 2013). Saqab and Bourget (2015a) suggest that the initiation of the ICPs occurred in the Mid Pleistocene due to sea-level fluctuations, oceanographic changes, and variations in the structural shape of the margin.

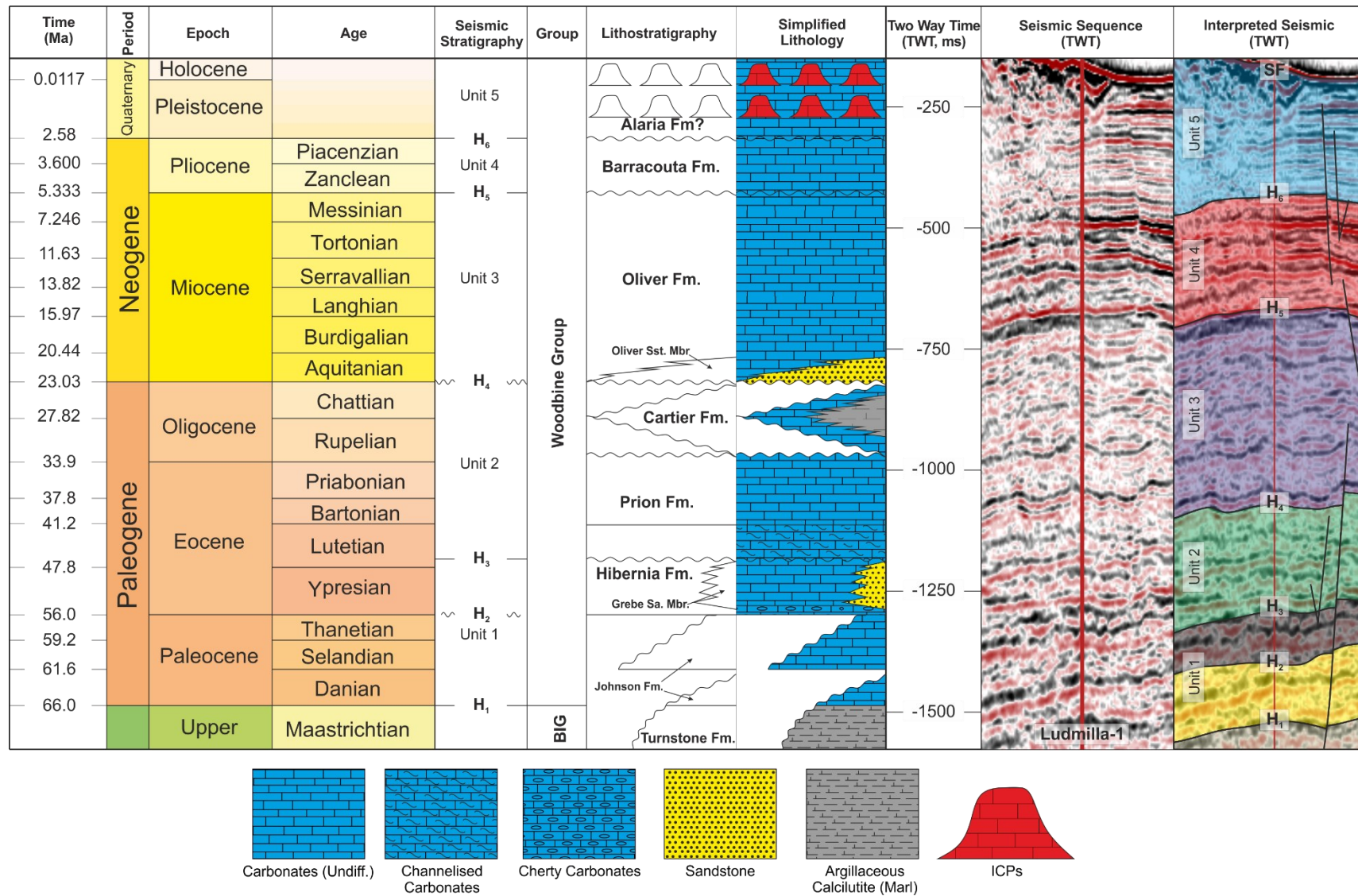


Figure 2.2. Cenozoic stratigraphic chart of the north-western Bonaparte Basin and its seismic stratigraphic units. Modified from Willis (1998) and Saqab and Bourget (2015a). The seismic section in the figure crosses the Ludmilla-1 well for reference.

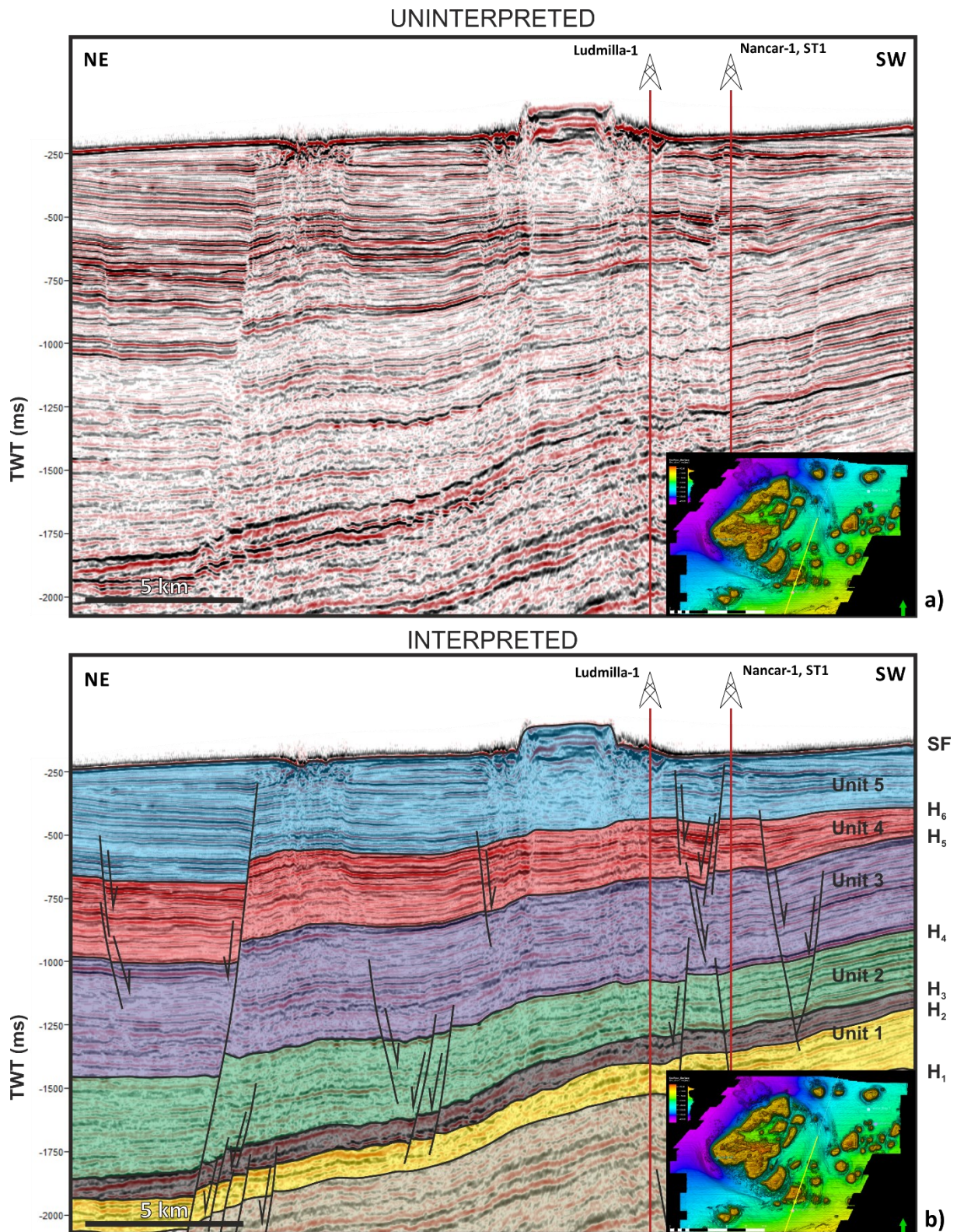


Figure 2.3. Two-way time (TWT) arbitrary seismic profile, with a NE-SW orientation, across the Ludmilla-1 and Nancar-1, ST1 wells. Main seismic-stratigraphic markers are shown in the figure: Seafloor (SF), Base Pleistocene (H₆), Base Pliocene (H₅), Base Miocene (H₄), Mid Eocene (H₃), Top Paleocene (H₂), Base Paleocene (H₁).

2.3 Cariatiz carbonate platform, Sorbas Basin, SE Spain

The focus of this study at outcrop level is on the Cariatiz Messinian carbonate platform, which is one of the pre-evaporitic Messinian sedimentary units in the Sorbas Basin (Martín and Braga, 1994; Braga and Martín, 1996). The Cariatiz platform is located on the northern margin of the Sorbas Basin, close to the village of Los Alías, SE Spain (Figure 2.4). The Sorbas Basin is oriented E-W and it is bordered by the Sierra de los Filabres to the north and the Sierras Alhamilla and Cabrera to the south (Braga and Martín, 1996; Cuevas Castell et al., 2007; Reolid et al., 2014; Nooitgedacht et al., 2018) (Figure 2.4b). The formation of this Neogene basin is linked to strike-slip (Jonk and Biermann, 2002) and extensional tectonism (Meijninger and Vissers, 2006), comprising strata of Middle Miocene to Quaternary ages (Martín and Braga, 1994; Reolid et al., 2014; Nooitgedacht et al., 2018).

The Cariatiz Fringing Reef Unit was chosen in this work because of its unique three-dimensional exposure in which several fracture types with various sizes are recognised at different scales. During platform development, the Sorbas Basin was affected by a regional tectonic uplift with a rate of *ca* 110 m/Myr, imposing a 3° dip to the Cariatiz platform. Different reef growth phases appear as clinoform bodies (Reolid et al., 2014) which, in addition to syn-depositional erosion, influenced the geometry of the platform (Cuevas Castell et al., 2007). Sea-level changes have been reported as the governing mechanism controlling carbonate productivity, reef slope geometry and stacking patterns of the clinoform bodies (Kendall and Schlager, 1981; Braga and Martín, 1996; Reolid et al., 2014).

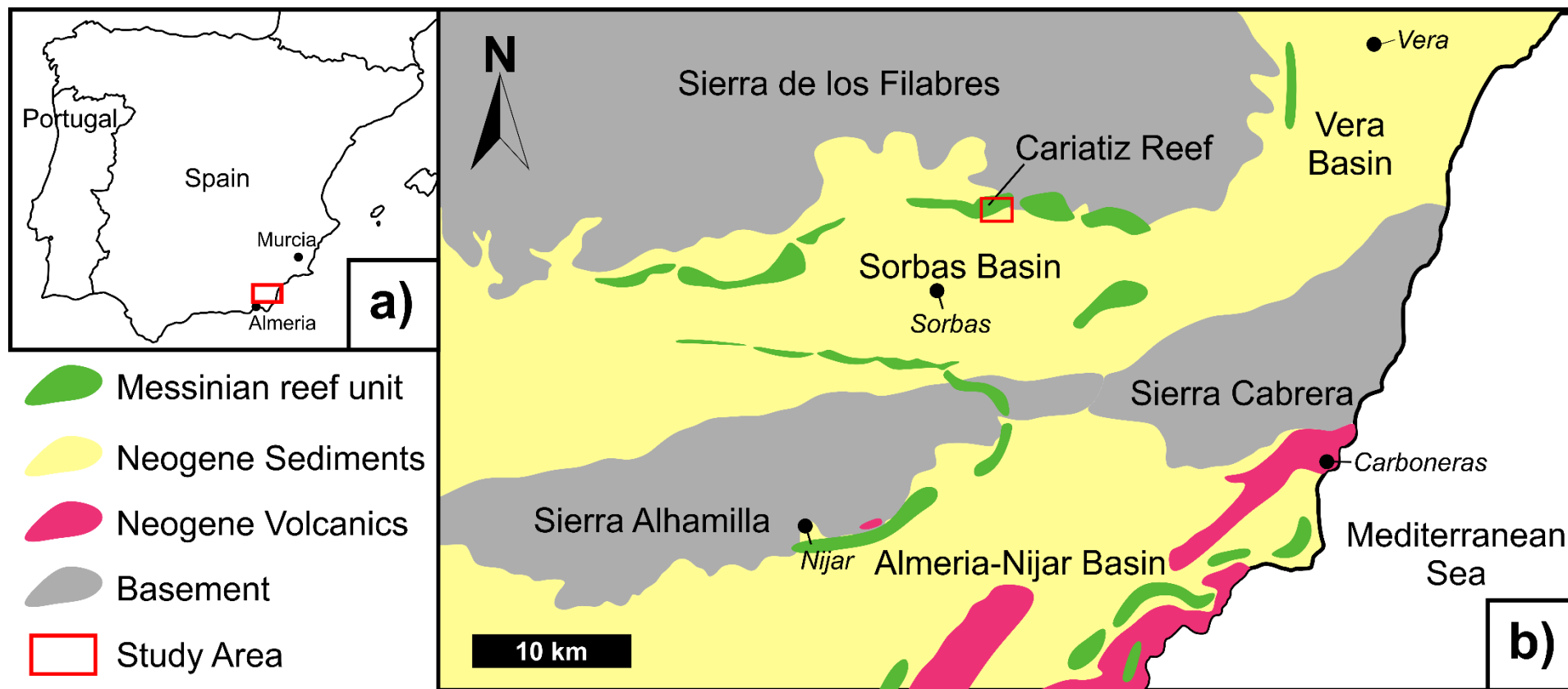


Figure 2.4. a) Location of the study area in SE Spain. b) Regional map of the Sorbas Basin showing the Messinian Reef Unit, and the area of interest at Cariatiz. Modified after Reolid et al. (2014).

The geometry and stratigraphy of the Cariatiz Fringing Reef Unit have been subject of extensive research (Riding et al., 1991; Martín and Braga, 1994; Braga and Martín, 1996; Cuevas Castell et al., 2007; Sánchez-Almazo et al., 2007; Reolid et al., 2014; Nooitgedacht et al., 2018). The Messinian Fringing Reef Unit comprises six distinct depositional facies (Riding et al., 1991; Braga and Martín, 1996) (Figure 2.5). From the platform interior to the basin, these depositional facies are as follows:

1. Lagoon - parallel beds of calcarenites and calcirudites with abundant gastropods, red coralline algae, foraminifera, and mollusc remains. Small coral patches of *Porites* occur near the reef crest. Siliciclastic grains are locally mixed with carbonate sediments. Lagoonal beds dip 3° to the southwest (N216°E).
2. Reef framework - a 20 m thick unit subdivided into three sub-facies from top to bottom:
 - a. Reef crest zone (4-0 m water depth) - laminar to contorted *Porites* colonies with stromatolitic crusts. Contains rudstones with echinoderms and molluscs fill cavities.
 - b. Thicket zone (ca 4-10 m below the reef crest) - vertical corals and continuous lateral coral growth.
 - c. Lower pinnacle zone (ca 10-15 m below the reef crest) - pinnacle morphologies formed by columnar *Porites* connected by vertical and laminar coral growth. Bioclastic matrix fills in remaining spaces.
3. Reef talus slope (uppermost slope) - deposits of reef framework blocks and coral breccia with *Halimeda*, bivalves, molluscs, serpulids and coralline algae. Frequent laminar *Porites* colonies encrusting bioclasts.

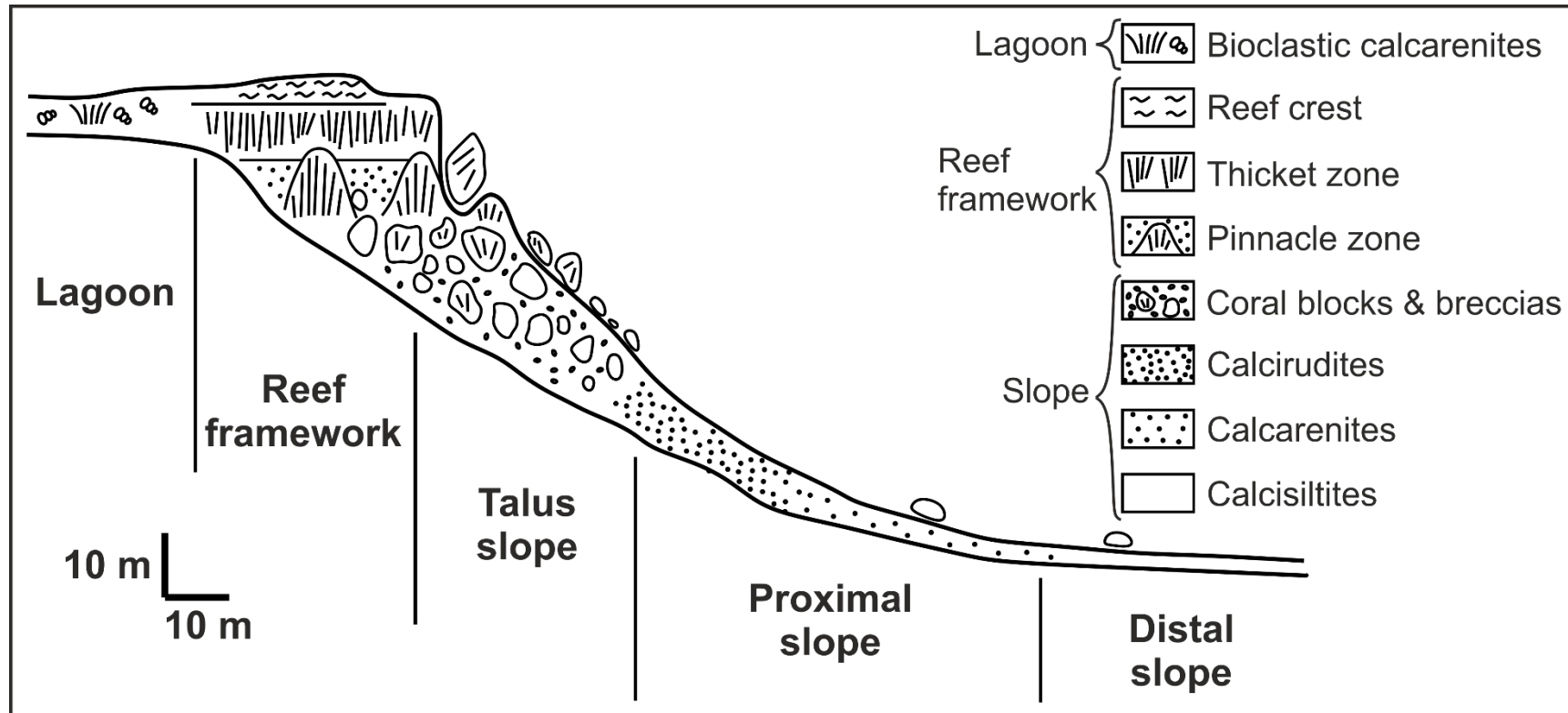


Figure 2.5. Cariatiz facies model. Modified after Braga and Martín (1996) and Reolid et al. (2014).

4. Proximal slope (middle slope) - well-bedded deep water calcarenites and calcirudites with bioclasts of serpulids, coralline algae, molluscs and abundant *Halimeda*.
5. Distal slope (lowermost slope) and basin - calcarenites, silty and sandy marls variably intercalated with basinal marls and diatomites (upper part of the Abad Member).
6. Fan delta - episodic flows of fan delta sediments during carbonate platform growth, alternating with conglomerates and sandstones intervals that interfinger with the carbonate platform.

2.4 Pernambuco Basin, East Brazil

At the seismic scale, the study focuses on the Pernambuco carbonate platform, which is part of the eastern portion of the Brazilian continental platform, an area of stretched continental crust forming the Pernambuco Plateau (Magalhães et al., 2014; Buarque et al., 2017) (Figure 2.6). This platform was chosen because of its distinctive km-long normal faults located along the platform margin and platform interior, revealing a similar setting to the fractures observed on the platform margin in Cariatiz, but at a larger scale (Figure 2.6b). In addition, seismic characteristics (geometries and seismic facies) observed in Pernambuco present similarities to the depositional facies in Cariatiz (Figure 2.6b).

2.4.1 Tectono-stratigraphic evolution

The Pernambuco Basin is part of the Borborema Province, consisting of a complex collage of continental masses (dos Santos et al., 2010; Buarque et al., 2017). This

province was subject of a series of Precambrian orogenic events, prior to late Mesozoic rifting stages that culminated in continental breakup during the Cretaceous (Darros de Matos, 1999; dos Santos et al., 2010; Buarque et al., 2017). The evolution of the basin was initially controlled by NE-SW and E-W Precambrian shear zones that were then reactivated during rifting as strike-slip and normal faults (Buarque et al., 2017). After that, the basin was controlled by NW-SE oblique transfer faults, in addition to N-S, WNW-ESE and NNW-SSE normal faults, during the Aptian-Albian (Buarque et al., 2017).

Buarque et al (2017) recognised five seismic sequences off Pernambuco. Seismic Sequence 1 represents the beginning of a sag phase, comprising Aptian-Albian rift strata and a salt layer. Salt layers generated large halokinetic features, such as diapirs and salt domes that cross-cut Seismic Sequence 2, a unit composed of Cenomanian-Santonian post-rift strata (Buarque et al., 2016, 2017, Fig. 7). Offshore carbonate deposition developed during two main post-rift intervals: the Cretaceous post-rift Seismic Sequence 3 during the Campanian-Maastrichtian, and the Lower Cenozoic post-rift Seismic Sequence 4 from Paleogene to Middle Miocene. Upper Miocene to Recent strata occur in Seismic Sequence 5, described as an Upper Cenozoic post-rift interval (Buarque et al., 2017 Figs. 4 and 5). Sequences 3 and 4 comprise the Pernambuco carbonate platform (Figure 2.6b).

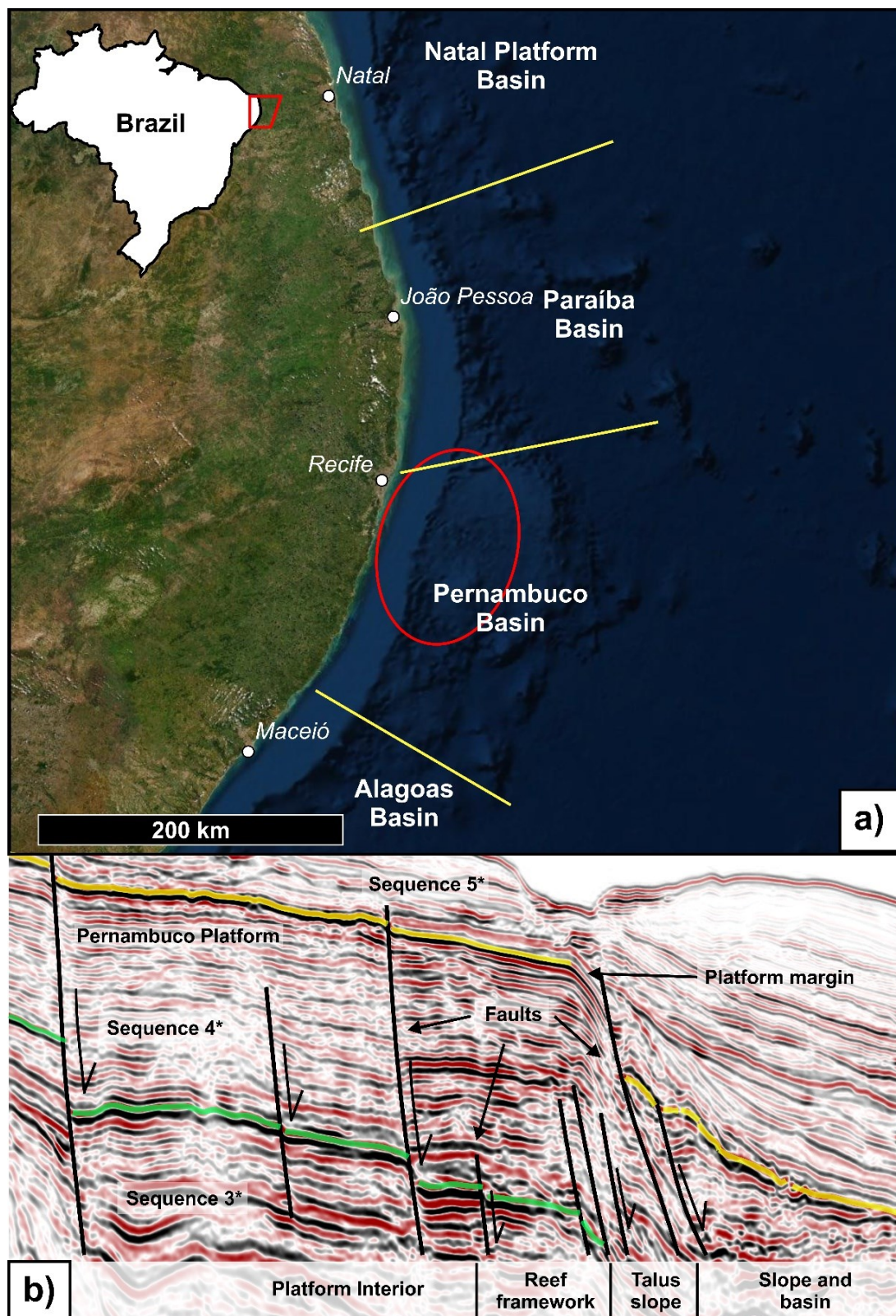


Figure 2.6. a) Location map of the Pernambuco Basin showing the study area in a red circle. b) Seismic section across the Pernambuco Platform showing its internal geometry and seismic facies, as well as the presence of normal faults. *Sequence numbers after Buarque et al (2017). Scale and exact location cannot be given due to data privacy.

Four seismic facies are recognised in Pernambuco from the platform interior to the basin (Figure 2.6b):

1. Platform interior (lagoon) - semi-continuous to discontinuous, low- to medium- amplitude internal reflections capped by a high-amplitude reflector.
2. Reef framework - semi-continuous sub parallel reflections bounded by the platform margin, which coincides with a steep high-amplitude reflector.
3. Talus slope - chaotic, steep reflections with low- to medium- amplitude.
4. Slope and basin (including the proximal and distal slopes) - discontinuous, chaotic reflections with low- to medium- amplitude.

2.5 Pará-Maranhão Basin, Equatorial Brazil

The offshore Para-Maranhão (PAMA) Basin is located on the Brazilian Equatorial Margin and consists exclusively of marine deposits covering an area of about 48,000 km² (Soares et al., 2007) (Figure 2.7). The basin is oriented NW-SE due to the effect of transtensional tectonics in its early development, being bounded by the Foz do Amazonas Basin to the northwest and the Barreirinhas Basin to the southeast (Zalán, 2015) (Figure 2.7).

This study area was chosen to analyse sedimentological patterns beyond the carbonate shelf margin due to the clear exposure of reworked sediments on the continental slope. This area is particularly interesting as it is not a pure carbonate setting such as the Bahamas, since there is a mix with siliciclastic sediments.

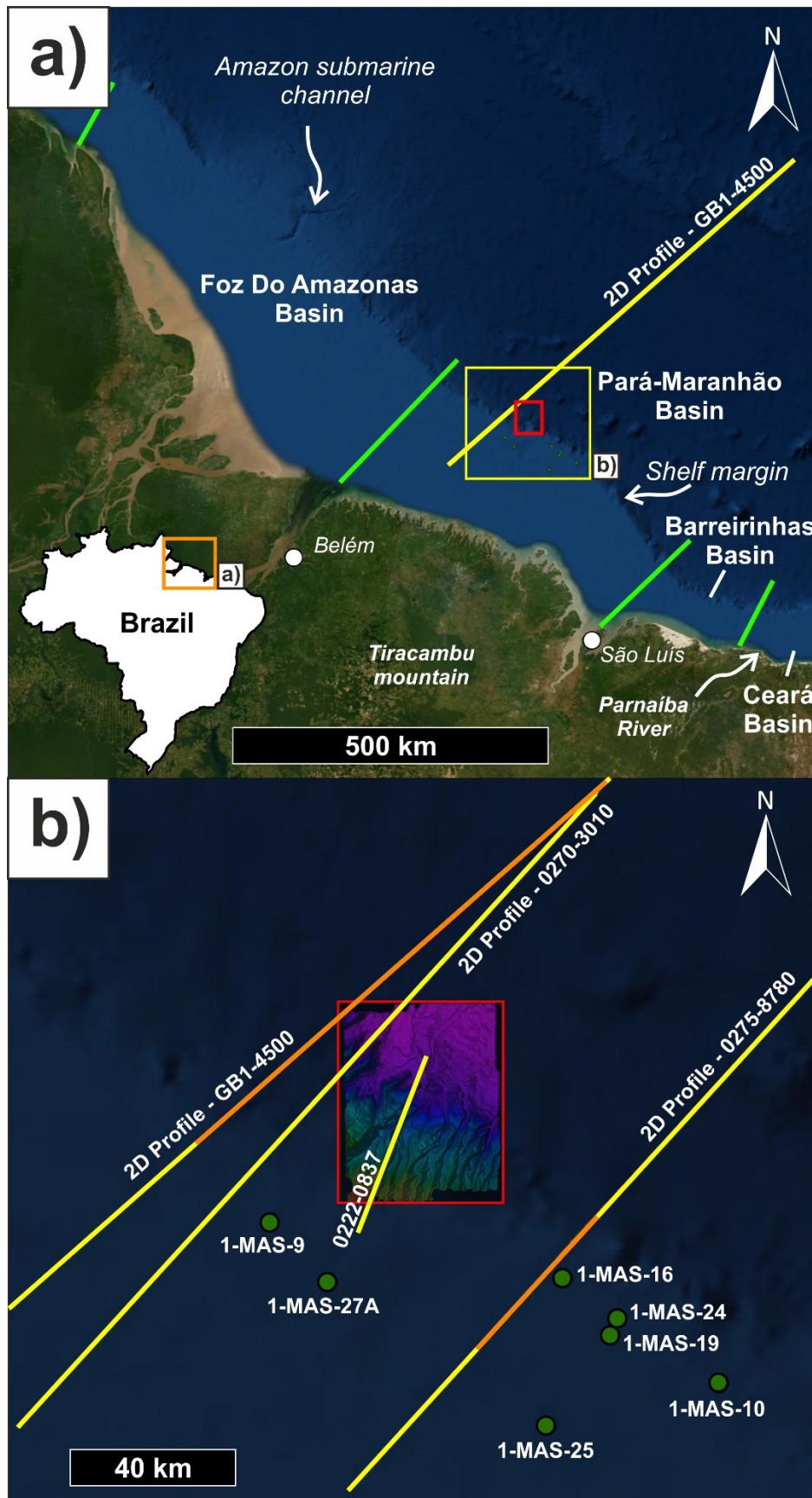


Figure 2.7. a) Location map of the Brazilian Equatorial Margin highlighting the study area in the Pará-Maranhão (PAMA) Basin. Red rectangle shows the location of the studied 3D seismic survey. Green lines mark basin limits. b) Enlarged figure showing the different 2D, 3D seismic datasets and exploration wells utilised in this thesis.

Hydrocarbon exploration started in the PAMA Basin during the 1970s and 1980s, via the acquisition of a series of 2D seismic profiles and the drilling of multiple exploratory wells. Most wells were deemed dry until the year of 1993, with the discovery of a sub-commercial oil show in fractured Cenozoic carbonates in the well 1-PAS-11 (Soares et al., 2007; Zalán, 2015). Interest in the region has increased in the past decade due to the economic potential of deep- and ultra-deep-water basins of Equatorial Brazil.

Large discoveries of oil fields on the conjugate margins of Ghana and Ivory Coast have had a positive impact to exploration in Equatorial Brazil as deep-water basins in West Africa and Equatorial Brazil have similar structural and sedimentary features (Henry et al., 2011; Zalán, 2015; Almeida et al., 2018, 2020; Da Silva and Ribeiro, 2018). In parallel, recent data in Zalán (2015) and Da Silva and Ribeiro (2018) describe a broad gravitational system in the PAMA and Barreirinhas basins, relating this same system to the deposition of overlying turbidites (e.g. GB1-4500, Figure 2.7a).

2.5.1 Tectono-stratigraphic setting

The sedimentary history of the PAMA Basin is complex and started with the deposition of Paleozoic deposits over Precambrian intracratonic sequences (Soares et al., 2007; Zalán, 2015). This basin has been controlled since the Cretaceous by two major oceanic fracture zones, the Romanche and St. Paul; which are still active today (Nemčok et al., 2013). An updated and detailed tectono-stratigraphic chart was published by Soares et al. (2007) in which the PAMA Basin is sub-divided into three supersequences: Pre-Rift (intracratonic), Rift, and Drift (Figure 2.8a). Basal

Paleozoic deposits from the intracratonic Pre-Rift Supersequence are inferred as similar to those in the Parnaíba Basin (Zalán, 2015). The latter basin comprises Paleozoic strata deposited over the São Luís Craton due to the fragmentation and breakup of northwestern Gondwana (Soares et al., 2007; Oliveira et al., 2012).

The Rift Supersequence was deposited under a transtensional tectonic regime and is divided into Aptian and Albian syn-rift (Rift II) and intra-rift (Rift III) deposits (Soares et al., 2007). Syn-rift strata are composed of continental sandstones and shales showing strata pinch-outs in seismic sections. In between the two rift phases (Rift II and Rift III), a sag basin was developed and was filled by the Codó Formation, a unit of lagunar organic-rich shales, anhydrites and calcilutites (Soares et al., 2007). Their seismic response is characterised by parallel reflectors with good continuity. The Albian Rift III sequence is formed by siliciclastic deposits typical of delta fans accumulated in a marine environment (Brandão and Feijó, 1994; Soares et al., 2007). Comparisons with the Ceará Basin (Almeida et al., 2018, 2020) indicate this latter Rift III sequence to be a Breakup Sequence *sensu* Soares et al. (2012) and Alves and Cunha (2018).

The Late Albian to Recent Drift Supersequence comprises the Humberto de Campos Group, and is divided into three units: Areinhas (sandstones), Ilha de Santana (wide carbonate shelf), and Travosas formations (slope and turbidite deposits) (Soares et al., 2007; Zalán, 2015) (Figure 2.8b). In addition, the study area contains gravitational systems in the Drift Supersequence that impose a marked structural zonation in the basin from its proximal to distal parts (Figure 2.8a). As a result; extensional, transitional and contractional zones are identified from the shelf to the abyssal parts of the PAMA Basin (Zalán, 2001; Oliveira et al., 2012; Almeida et al., 2018).

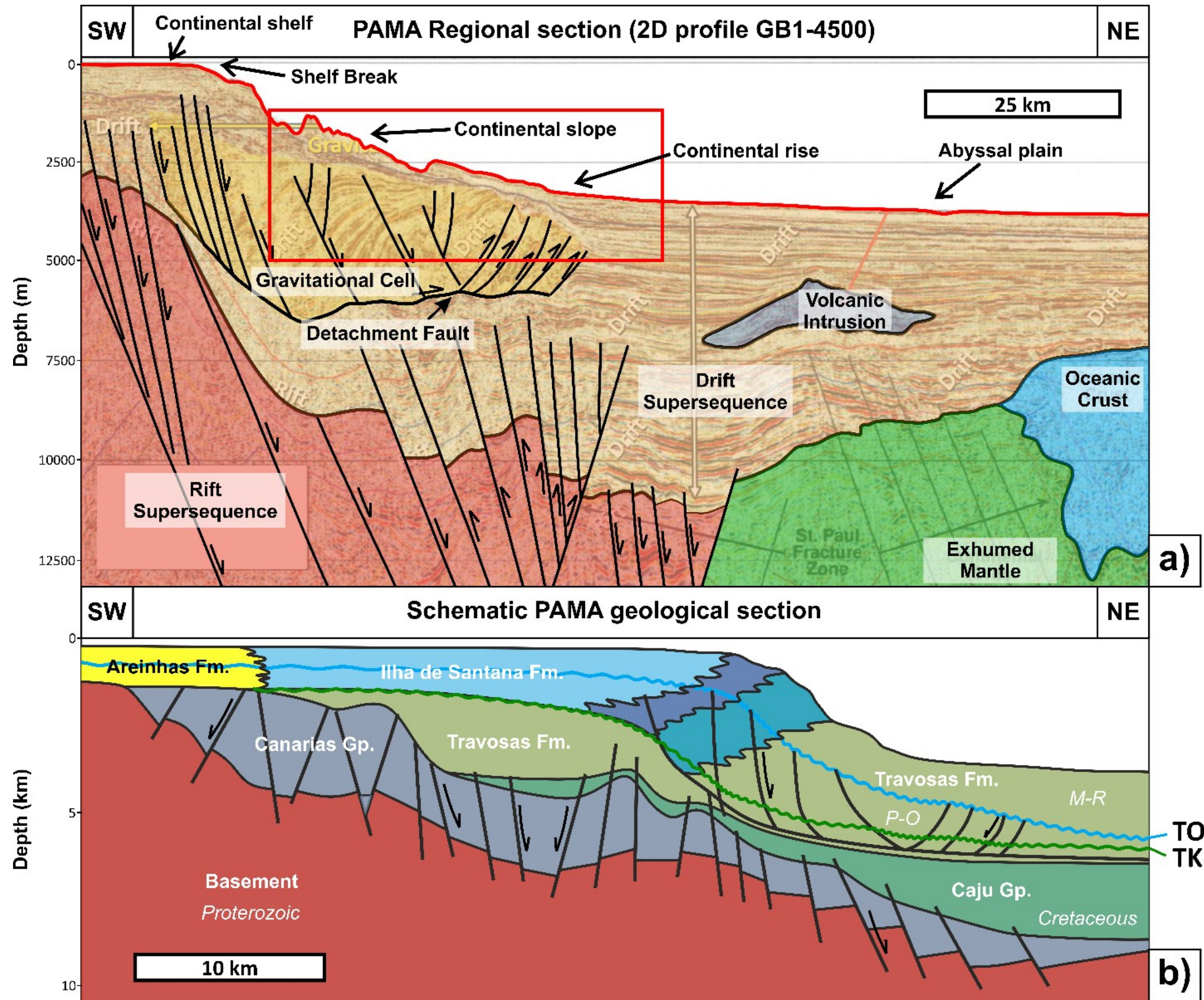


Figure 2.8. Regional seismic sections depicting the regional stratigraphic units and seismic facies of the PAMA Basin. a) Reinterpreted 2D seismic profile GB1-4500 from Henry et al. (2011) and Zalán (2015). A red rectangle shows the portion of the basin studied in this work. b) Schematic section of the PAMA Basin outlining the distribution of the different geological formations. P-O=Paleocene-Oligocene, M-R=Miocene-Recent. Modified after Brandão and Feijó (1994).

2.5.2 Regional stratigraphy

Brandão & Feijó (1994) first described the stratigraphic succession of the PAMA Basin based on data from 29 exploration wells and 45,500 km of 2D seismic profiles, sub-dividing the region into three groups: Canárias, Caju and Humberto de Campos (Figure 2.8b). The Canárias Group consists of sandstones, siltstones and shales deposited by deltaic fans in a marine environment during the Early and Mid- Albian (Brandão and Feijó, 1994). The Caju Group consists of quartzose sandstone, shales and local bioclastic calcarenites accumulated in a neritic environment during the late Albian (Brandão and Feijó, 1994). The Humberto de Campos Group comprises Cenomanian to Recent deposits representative of a divergent margin, and includes the Areinhas, Ilha de Santana and Travosas formations (Figures 2.8b and 2.9). The Humberto de Campos Group extends to the Barreirinhas Basin and its youngest strata are the focus of this work.

The Areinhas Formation is composed of quartzose sandstone packages intercalated with shales, siltstone and calcilutite. The Ilha de Santana Formation comprises a thick carbonate succession with the presence of calcarenites and calcilutites intercalated with shales and marls. Turbidites are common on the continental slope. The Travosas Formation is a typical coastal-platform-slope system and, at its most distal part, is known to comprise deposits of shales and siltstones intercalated with quartzose sandstones (Brandão and Feijó, 1994; De Souza, 2006; Piovesan, 2008). However, based on the well data later described, parts of the Travosas Formation are also dominated by calciclastic deposits. In essence, a mixed calciclastic-siliciclastic system sourced by the Ilha de Santana Platform fed the continental slope and rise as a result of slope instability, turbidity and marine currents.

2.5.3 Carbonate platform development off PAMA

In the latest Cretaceous-earliest Paleogene, the main sediment input to the PAMA Basin was siliciclastic, and the Ilha de Santana Platform was still an emerged area (Soares Júnior et al., 2011). According to Soares et al. (2007), a sea-level lowstand dominated the evolution of the PAMA Basin during the upper Eocene and lower Oligocene, narrowing the carbonate shelf and exposing it to subaerial conditions. This facilitated the development of dolomitic intervals in the Ilha de Santana Formation (Soares et al., 2007).

During the late Oligocene-middle Miocene, the Equatorial Margin of Brazil was dominated by the development of a large carbonate platform in a shallow-water palaeoenvironment (Soares et al., 2007; Soares Júnior et al., 2011; Rossetti et al., 2013; Aguilera et al., 2020). This carbonate platform extended from the Foz do Amazonas Basin (Figueiredo et al., 2007; Aguilera et al., 2020), to the PAMA (Soares et al., 2007), Barreirinhas (Trosdorf Junior et al., 2007) and the Ceará basins (Soares Júnior et al., 2011). In the Foz do Amazonas Basin, carbonate productivity terminated around the late Miocene-Pliocene as a consequence of Andean tectonics, which led to a rearrangement of the palaeo-Amazon River and the subsequent onset of clastic sediment input from both the Amazon delta and coastal plain drainage systems (Figueiredo et al., 2007; Soares Júnior et al., 2011; Aguilera et al., 2020). In the three other basins mentioned above, carbonate productivity continued until the present-day, as recorded in well data crossing the Ilha de Santana Formation and published stratigraphic data from the Ceará and Barreirinhas basins (Soares Júnior et al., 2011; Aguilera et al., 2020). In the PAMA Basin, Aguilera et al. (2020) identified minor siliciclastic input near the shore during the Miocene, sourced from small river mouths such as the Gurupí River.

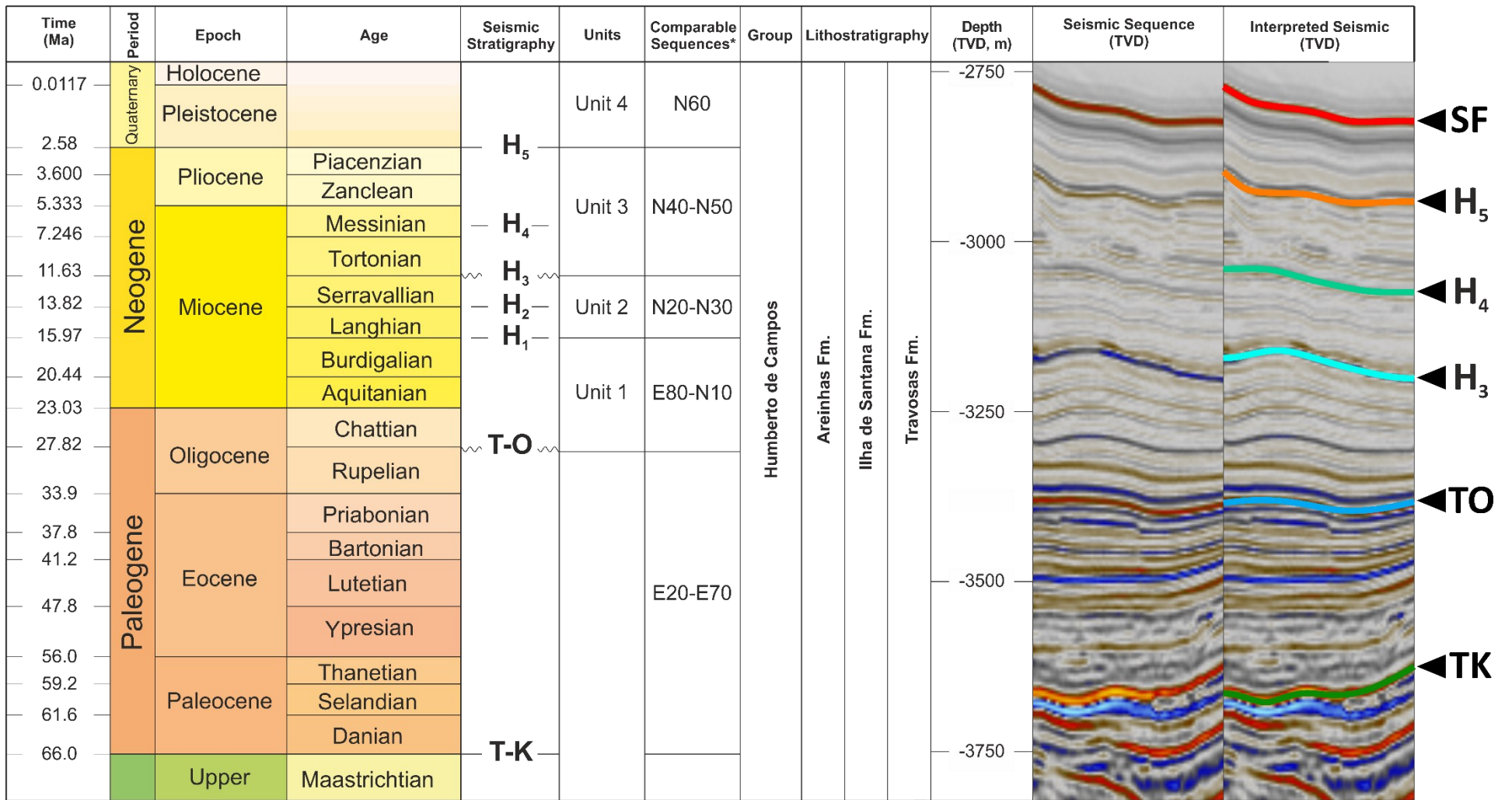


Figure 2.9. Cenozoic lithostratigraphic chart of the PAMA Basin and its main seismic stratigraphic units. *Comparable sequences, unconformities and lithostratigraphy taken from Soares et al. (2007).

Chapter 3: Data and methods

3.1 Introduction

This thesis uses a variety of datasets from multiple study areas, including 2D seismic profiles, 3D seismic volumes, wellbore logs, aerial LiDAR and satellite imagery, and outcrop mapping techniques. Three-dimensional (3D) seismic data is used as the main source of information as to interpret structural and sedimentological features in the subsurface. The 3D seismic volumes used as part of this work were initially acquired by energy companies for hydrocarbon exploration purposes. The data is now being used for research in Cardiff University at the 3D Seismic Lab.

This chapter provides an overview of how seismic data is acquired, processed and interpreted, as well as details on the seismic datasets used. General methodology of seismic interpretation and outcrop mapping is presented here. Specific methods used for the different datasets are discussed in each chapter (4, 5 and 6) as to provide a better context for each study.

3.2 Seismic reflection data

Reflection seismic is a common technique to image the subsurface, and it involves the transmission of sound waves into the subsurface, which is then refracted and reflected at the interface between rocks of different physical properties according to the acoustic impedance contrast and angle of incidence (Herron, 2011; Cox et al., 2020). When the energy returns to the surface, it is recorded and processed to create an image of the subsurface (Herron, 2011; Cox et al., 2020).

Three-dimensional (3D) seismic data has been key to geologists and geophysicists working in hydrocarbon exploration and production, resulting in successful

discoveries around the world. 3D seismic data has been useful to improve the understanding of structural and stratigraphical features in the subsurface, being an important tool for many areas of Earth sciences such as igneous and structural geology (Davies et al., 2004).

Seismic reflections are the result of changes in acoustic properties of the rocks. Acoustic impedance of a rock is the product of the density and velocity of a specific layer of rock in which a reflection is generated by a change in acoustic impedance (Brown, 2011). Impedance and lithology are normally related, suggesting that impedance boundaries are equivalent to lithologic boundaries (Figure 3.1).

3.3 2D and 3D seismic

The ability to acquire and process 2D seismic data was developed in the 1950s, followed by 3D seismic data in the 1980s. 2D surveys provide a key dataset for regional studies as a cross section of the subsurface and are important for initial investigations in a frontier area. 3D seismic data are more expensive to collect, but allow a better mapping of faults, geomorphological features, reservoirs blocks, and so forth (Cox et al., 2020). 3D seismic is distinguished from 2D seismic by the acquisition of multiple closely spaced lines (e.g. 25 m) that provides regular data points that feeds 3D data migration during processing (Davies et al., 2004). The density of subsurface reflection point coverage allows stratal reflections to be mapped using automated or semi-automated trackers to provide continuous mapped surfaces. Features such as fault and fracture networks can be mapped in much detail with 3D seismic data (Davies et al., 2004).

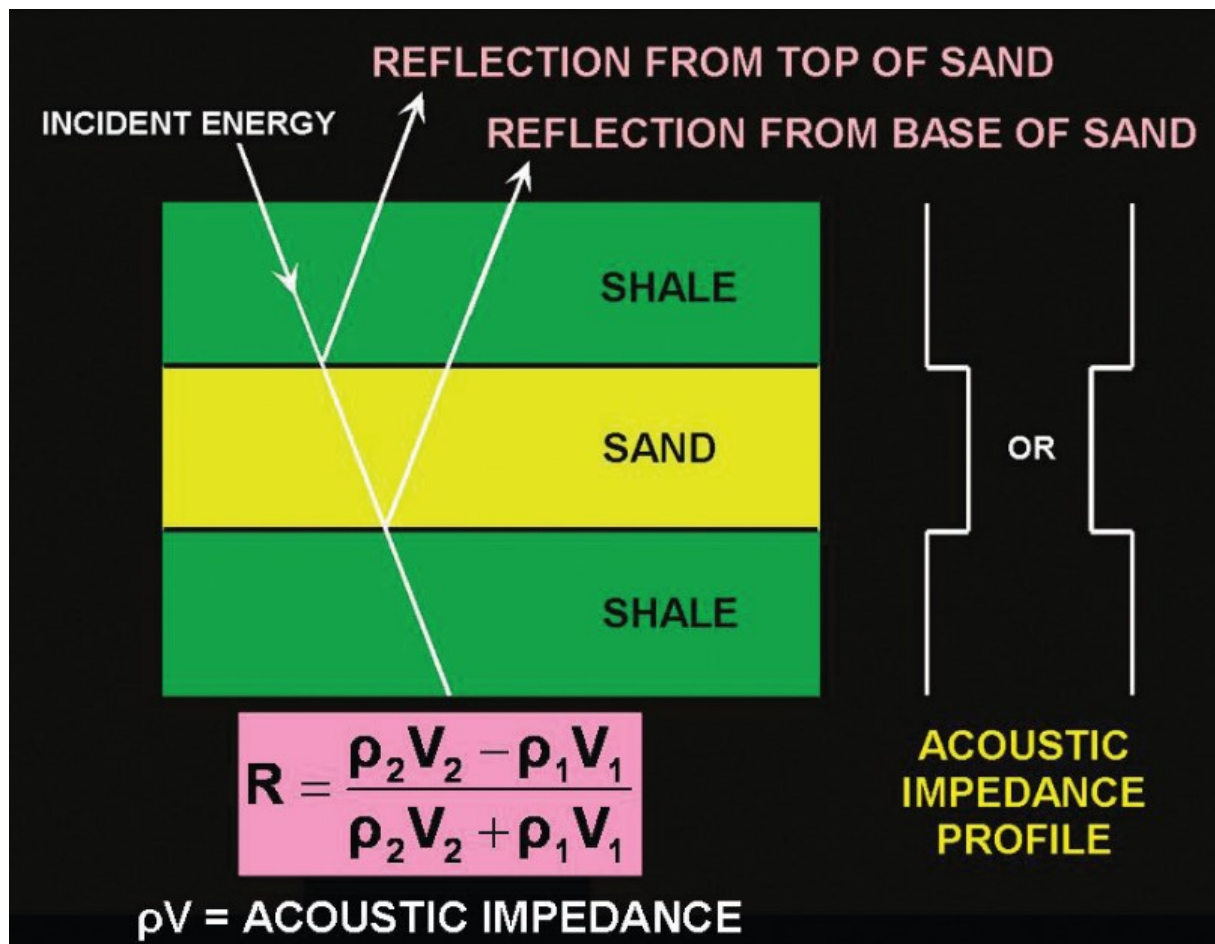


Figure 3.1. Schematic diagram showing an example of how the acoustic impedance relates to changes in lithological layers. Figure from Brown (2011).

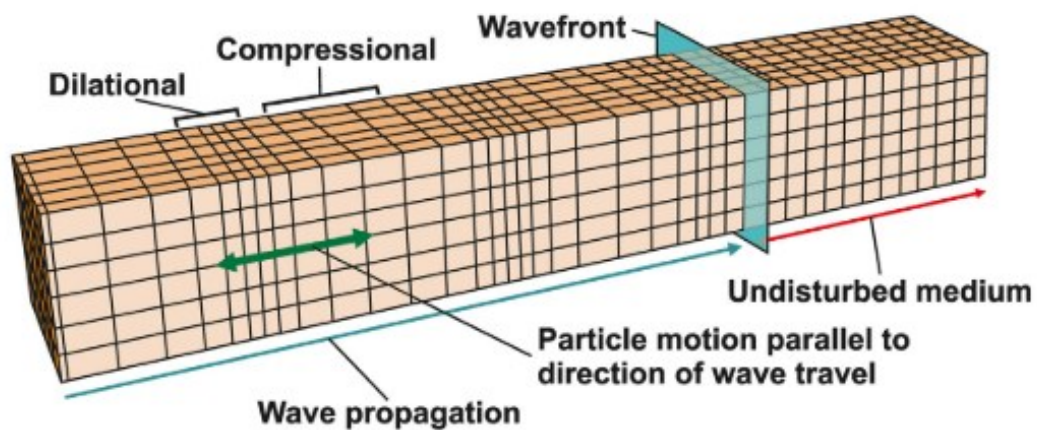
3.4 Acquisition of seismic reflection data

The process of creating an interpretable seismic image starts generating sound waves transmitted into the subsurface, which are then returned to the surface as reflections from boundaries (reflectors) that represent changes in the physical properties of layers of rock or anomalous fluid accumulations. Reflected waves are detected by receivers that measure the energy and arrival time (Wencai, 2013; Cox et al., 2020). There are three types of waves generated by the source: P (longitudinal) waves, S (transverse) waves and boundary waves (Figure 3.2).

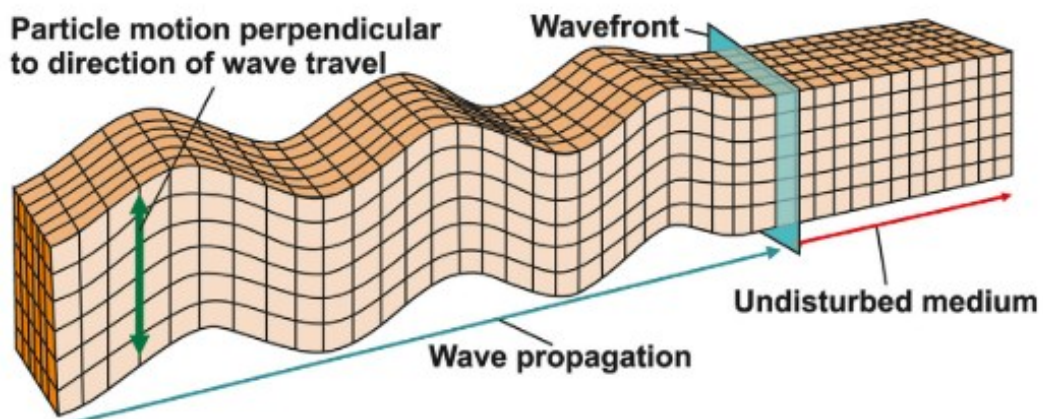
Compressional waves (P-waves) have a backward and forward particle motion and propagate in a compressional and dilational uniaxial strain, parallel to the wave propagation direction (Bolt and Bolt, 1982; Cox et al., 2020) (Figure 3.2a). Shear waves (S-waves) have a side to side particle motion with propagation perpendicular to the direction of wave travel (Bolt and Bolt, 1982; Cox et al., 2020) (Figure 3.2b). Boundary waves are low-velocity, low-frequency surface waves with a complex particle motion (Bolt and Bolt, 1982; Cox et al., 2020) (Figure 3.2c).

Propagation of seismic waves can be visualised as wavefronts or raypaths in which each point of the wavefront is represented by a seismic wavelet. A wavelet is a one-dimensional (1D) pulse generated by the seismic source that has a measurable amplitude, frequency, period and phase (Figure 3.3). Amplitude is the maximum extent of the oscillation (vibration through the Earth). Frequency is the number of crests of a wave that move in a given unit of time. Period is the time taken for a complete oscillation to pass a given point. Phase is the angular difference between peak amplitude of a seismic wavelet and reference time, usually 0 (Cox et al., 2020; Gluyas and Swarbrick, 2021).

(A) **P-waves (Compressional)**



(B) **S-waves (Shear)**



(C) **Boundary waves (Rayleigh)**

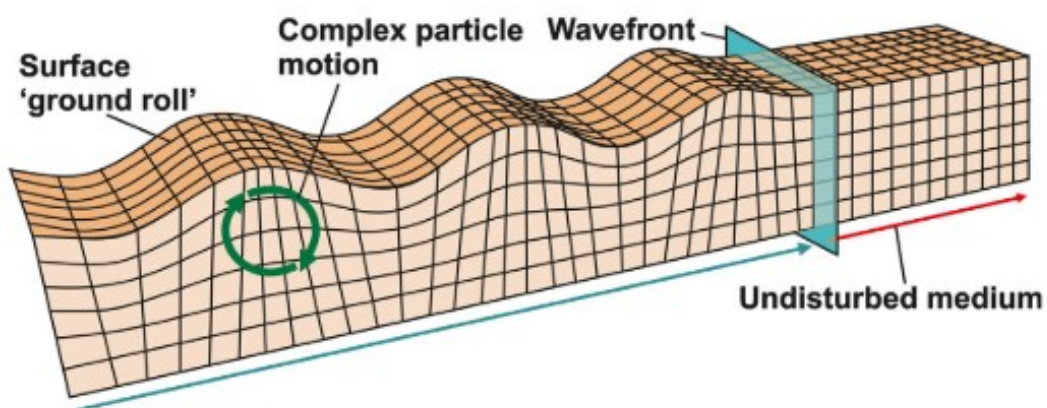


Figure 3.2. Schematic diagram showing the different types of seismic waves. (a) compressional P waves, (b) shear S waves, and (c) boundary, Rayleigh waves. Figure from Cox et al. (2020).

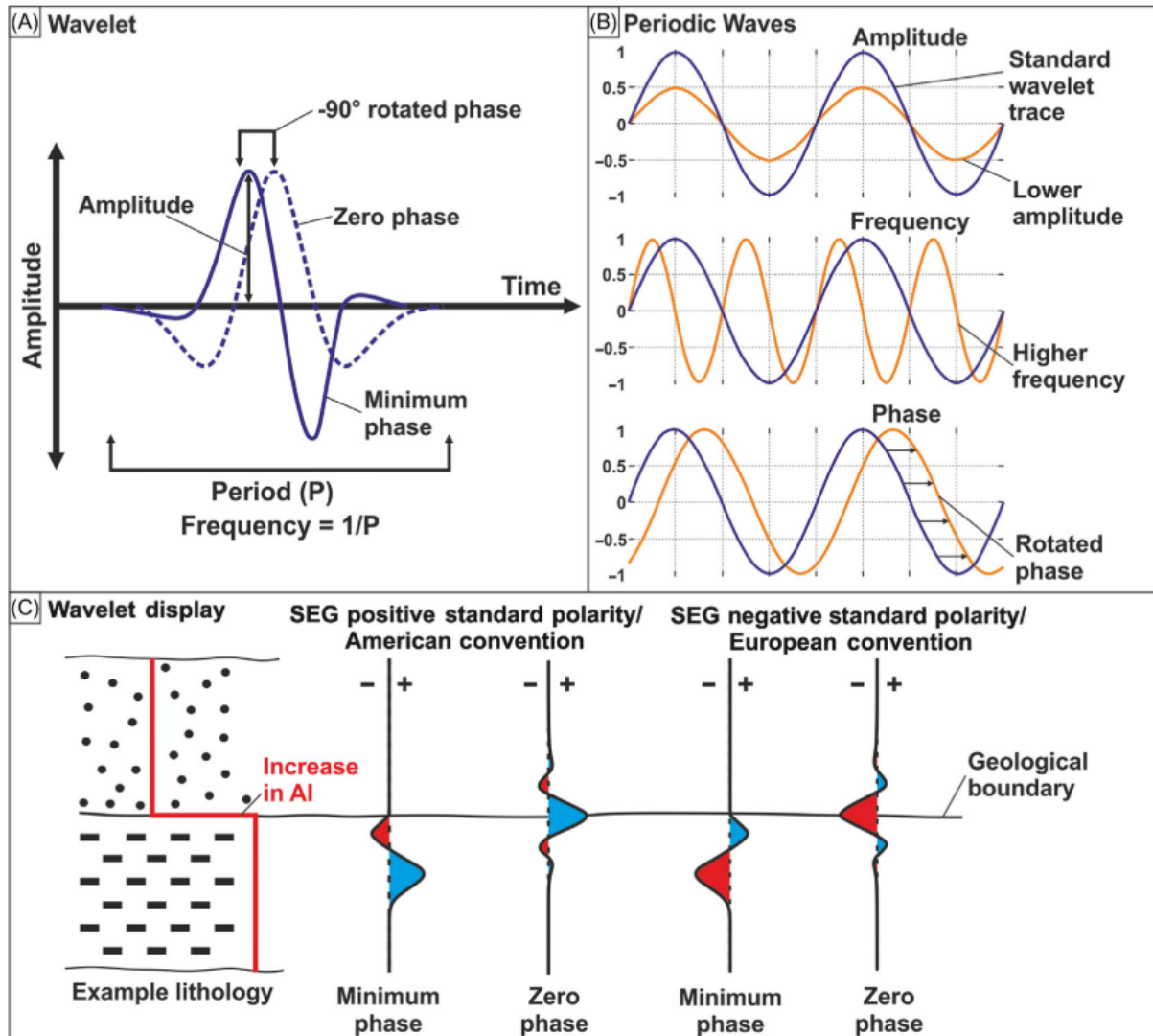


Figure 3.3. Schematic diagram showing wavelet types and their display. A) measurable characteristics of a wavelet. B) different elements of a seismic wave. C) polarity conventions used for displaying seismic data. Figure from Cox et al. (2020).

The Society of Exploration Geophysicists (SEG) defines two types of polarity convention used for displaying seismic data. For an American positive polarity, an increase in acoustic impedance with depth (such as water bottom) will be registered as negative reflection amplitudes and therefore display the onset of compression as a trough to the left of the central trace line (Figure 3.3). For a zero-phase wavelet, an increase in acoustic impedance is represented by a central positive peak. In contrast, for the European negative polarity, the onset of compression from an increase in acoustic impedance is displayed as a positive peak, with a zero-phase wavelet displaying a central negative trough (Figure 3.3). Polarity conventions are also defined by the colours used. A peak in the American convention is coloured in blue or black, with a trough coloured in red. For the European convention, it is the opposite, peaks being displayed in red colours and troughs in blue or black (Cox et al., 2020). The seismic data presented in this thesis have different polarities depending on the convention utilised for each company.

3.4.1 Seismic resolution

Seismic resolution is an important parameter used as a measure of quality of seismic data. It controls the spacing at which it is possible to detect and resolve two individual geological features, and controls what the interpreter is able to visualise (Brown, 2011). Both vertical and horizontal resolution are related to the wavelengths of the seismic energy being imaged. Since wavelength is inversely proportional to frequency, higher frequency data is expected to have better resolution.

3.4.1.1 Vertical resolution

Wavelets are important components to determine the vertical resolution of seismic data, being the measure of how far two geological boundaries have to be in order to be detected as separate events. Resolution limit is often one-fourth of the dominant wavelength, which is determined by the frequency of the wavelet and the velocity of the rock unit (Kearey et al., 2002; Brown, 2011; Cox et al., 2020).

Wavelength: $\lambda = V/F$ (wavelength=velocity/frequency)

Vertical seismic resolution: $\lambda/4$ (wavelength/4)

Vertical resolution decreases with depth due to a reduction of the wavelength frequency (high frequencies are reflected by shallow reflectors) and an increase in velocity (often due to compaction). The thickness at which two geological boundaries are no longer recorded as separate events is termed the “tuning thickness” (Brown, 2011; Roden et al., 2017; Cox et al., 2020).

3.4.1.2 Horizontal resolution

Horizontal resolution is coarser than vertical resolution due to acquisition effects. The area in which energy is reflected is known as Fresnel zone (Kearey et al., 2002). The Fresnel zone is an indicator for horizontal resolution and depends on the wavelength. In the case of perfect 3D migration, the migrated Fresnel zone width is $\lambda/2$. The horizontal resolution of high-quality 3D migrated data is thus limited to $\lambda/2$ or the acquisition line spacing (Brown, 2011; Roden et al., 2017).

3.4.2 Marine surveys

The most common marine seismic source is produced from airguns, which release a shot of compressed air into the water every 4-8 seconds. Typically, this involves an array of different sized guns that are fired at the same time to reduce potential noise in the data. A hydrophone receiver converts changes in water pressure, after signal generation, into an electrical voltage. Extensive lengths of cables are required to collect the data that is normally recorded at intervals of 2-4 milliseconds. In marine surveys, these are called streamers and can be several kilometres long. (Dondurur, 2018; Cox et al., 2020). Each streamer contains many individual hydrophones that are arranged into receiver groups. At the end of the streamer, a buoy with a GPS unit marks the end of the equipment array. The streamer and airguns trail behind the boat as it moves through the water and collects data for set time intervals (Dondurur, 2018; Cox et al., 2020) (Figure 3.4).

In marine 3D seismic surveys, data are collected in swaths a few hundred metres wide, oriented in the direction of the vessel (Figure 3.5). Commonly, several streamers behind the vessel are spread out by vanes. In order to image a “true” 3D geometry of the subsurface, the seismic survey is subdivided into smaller cells known as “bins” that are usually square (e.g. 25 by 25 m or 12.5 by 12.5 m) or rectangular (e.g. 18.75 by 37.5 m). Traces generated during acquisition are gathered in a specific bin depending on the common midpoint (CMP) between the source and the receivers (Dondurur, 2018; Cox et al., 2020) (Figure 3.5).

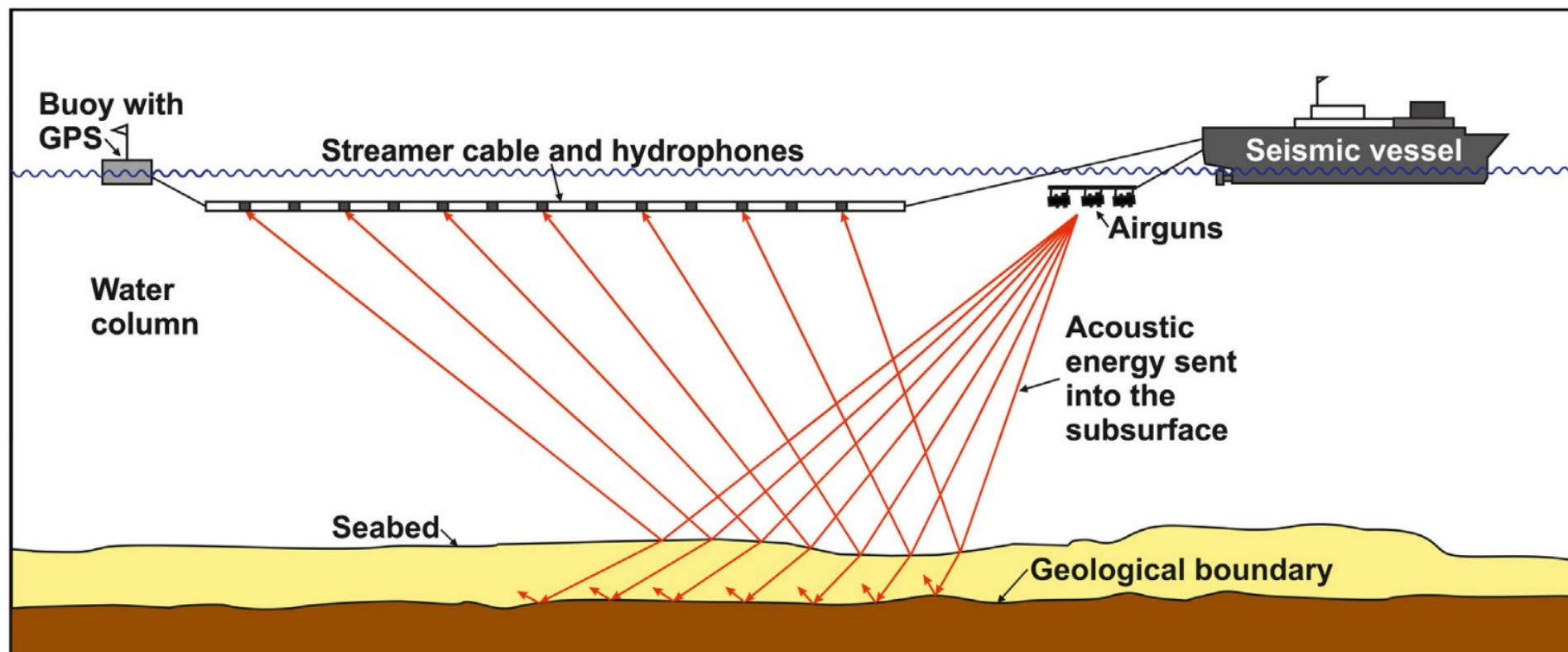


Figure 3.4. Schematic diagram of a 2D marine survey. The acoustic pulse created by airguns travels into the subsurface and reflects the main geological boundaries. Reflected energy is then recorded by hydrophones within a streamer cable and relayed back to the vessel. Figure from Cox et al. (2020).

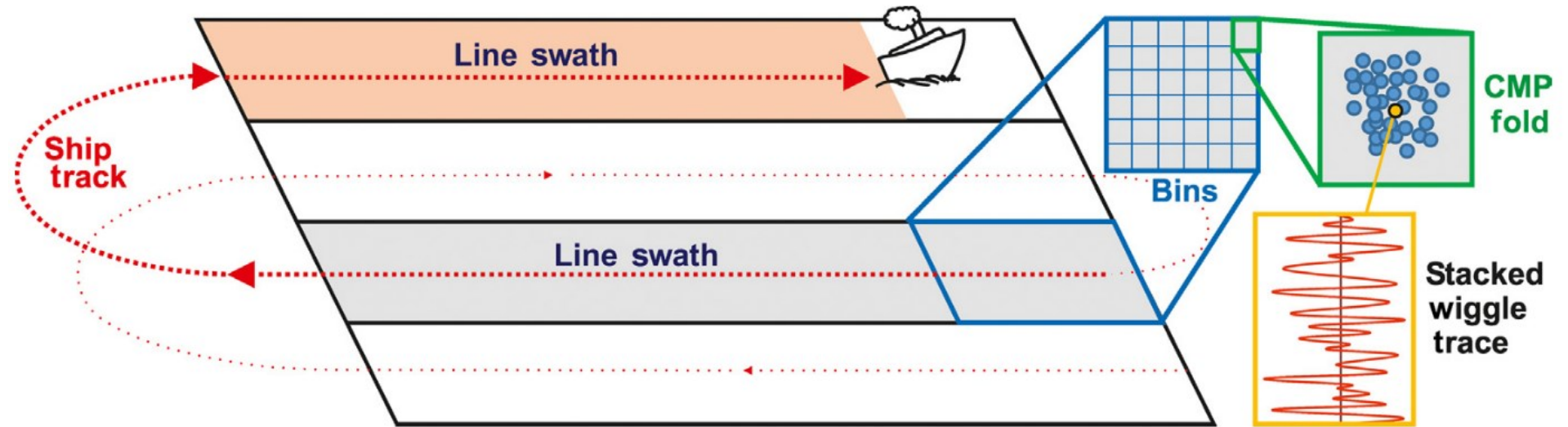


Figure 3.5. Schematic diagram of a 3D marine survey showing how 3D seismic reflection data is collected. Data contained within the bins is processed as traces for each individual bin. Figure from Cox et al. (2020).

3.5 Seismic processing

The raw recorded data provided by reflection seismic acquisition are not immediately suitable for interpretation. Data processing involves different steps in which noise is removed, artefacts are minimised, resolution is improved, and data is simplified to create an accurate and interpretable image. Modern processing workflows are often highly iterative and require multiple, repeated (and refined) stages of model building and correction to ensure a best possible final image. The basic seismic processing steps can be categorised into four functions: data preparation, data correction, data reduction and data enhancement (Cox et al., 2020) (Figure 3.6).

3.5.1 Data preparation

Seismic data is often transferred from the field in a format called multiplexed (SEG-A or SEG-D), which refers to the combined seismic traces being in time order from all the receivers at a given time. A trace sequential format (SEG-Y or SEG-X) is needed, which can be accomplished by demultiplexing the traces for all the times for each given receiver (Dondurur, 2018; Cox et al., 2020).

Some traces need to be flagged for editing due to errors during recording, storage or transfer, including noisy traces, duplicated traces, data spikes, dead traces with no signal or polarity reversals (Dondurur, 2018; Cox et al., 2020).

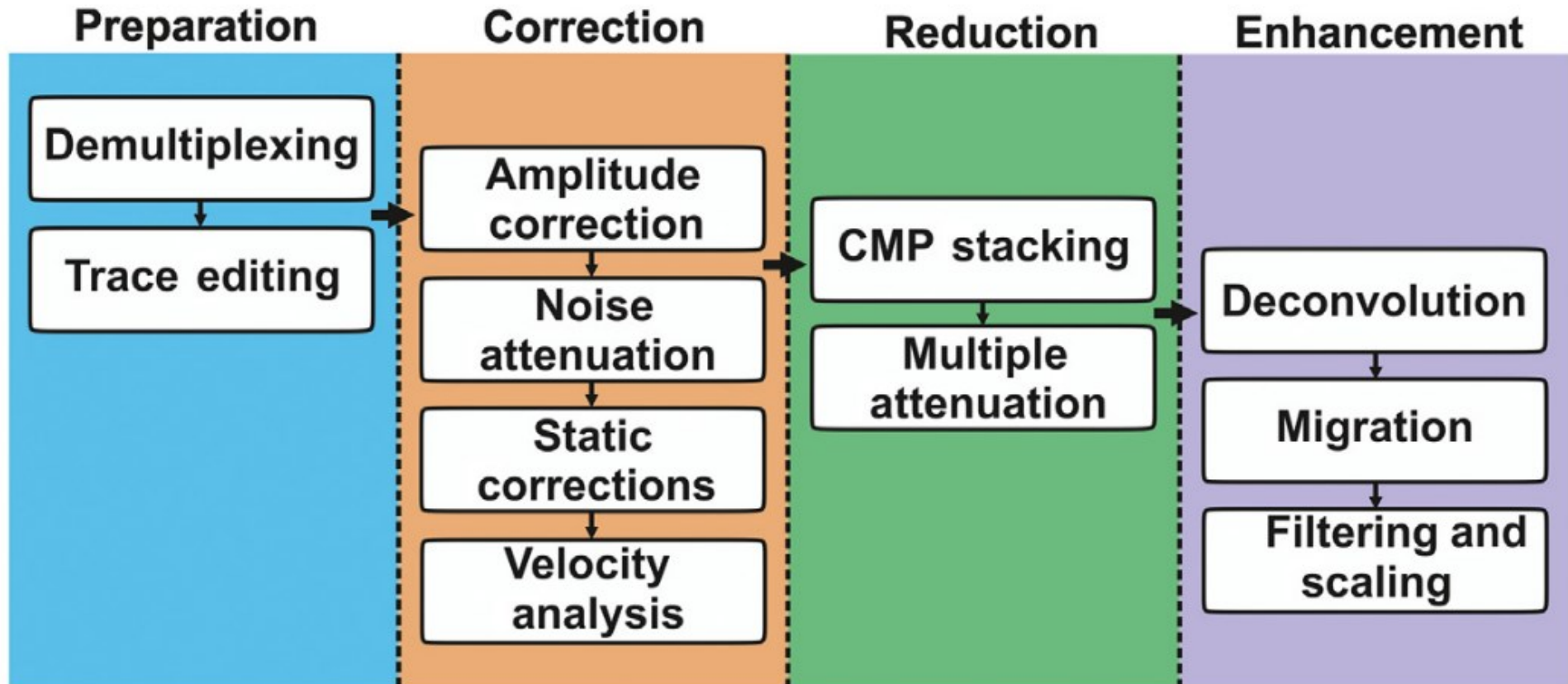


Figure 3.6. Workflow summarising the general steps followed on seismic processing from field seismic data to the generation of an interpretable seismic image. Figure from Cox et al. (2020).

3.5.2 Data correction

3.5.2.1 Amplitude corrections

Degradation of wavelets through time in the subsurface causes a weak reception of the reflection amplitude. This degradation can be caused by several factors such as divergence of sound waves, energy absorption, internal reflecting between rock layers (multiples) and unreturned reflections (scattering). Therefore, correction of these errors is therefore crucial (Yilmaz, 2001; Cox et al., 2020).

3.5.2.2 Noise attenuation

Noise can be produced by natural or anthropogenic sources; certain coherent and linear noise sources can be anticipated and removed in initial field processing or via automatic noise removal software packages. However, additional noise attenuation steps are often required (Yilmaz, 2001; Cox et al., 2020). The most common method of random noise attenuation is a bandpass filter which removes unwanted low- and high- frequencies prone to noise.

3.5.2.3 Static corrections

Static corrections involve a bulk time shift of certain seismic traces to allow accurate comparison of traces throughout a survey. Static corrections are usually required due to alterations in gun and streamer depths, or tidal changes during marine acquisition. Effects on velocity caused by shallow unconsolidated layers found above the bedrock, also requires static corrections (Yilmaz, 2001; Cox et al., 2020).

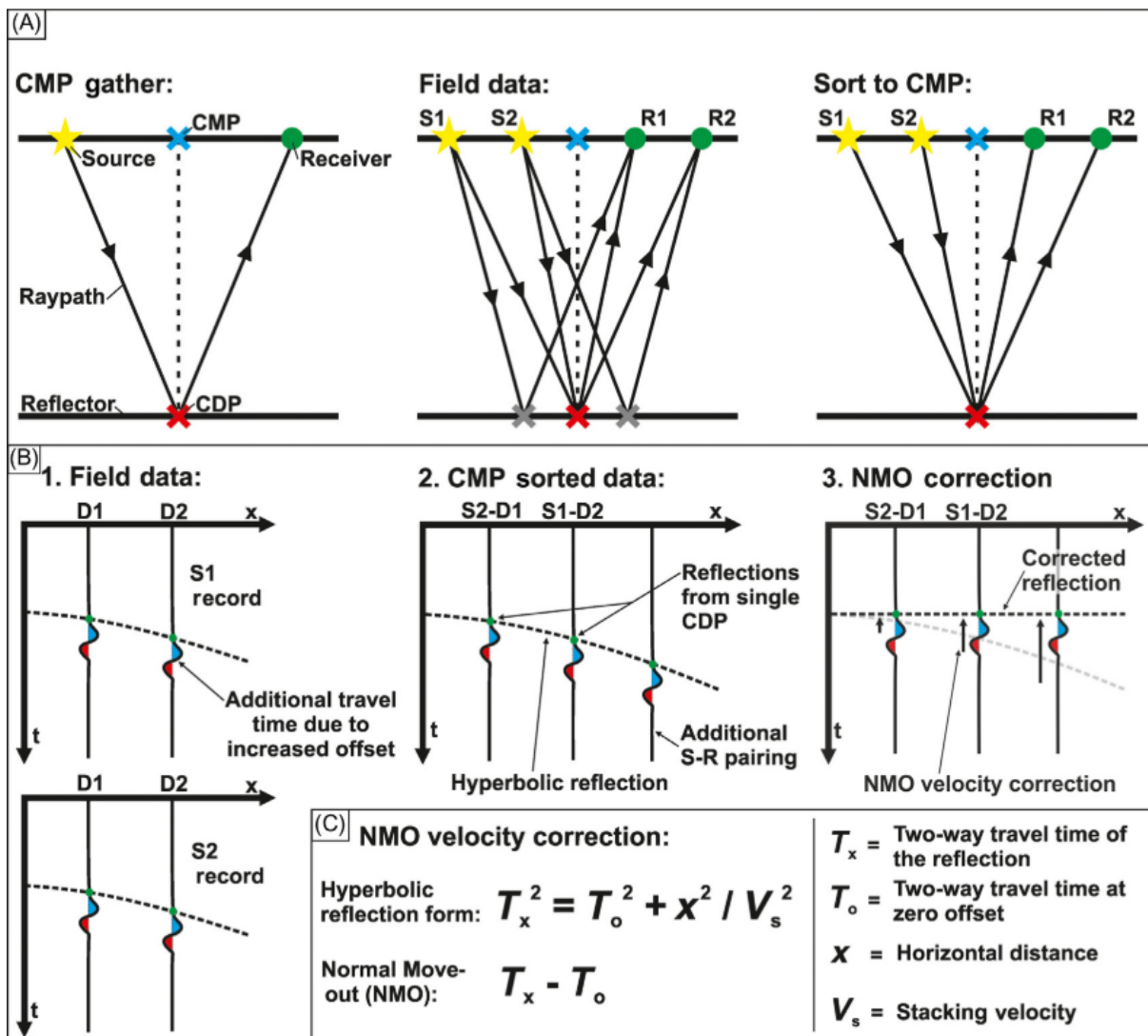


Figure 3.7. Schematic diagram showing the velocity analysis and normal move-out (NMO) correction. A) Diagrams showing the use of common midpoint (CMP) gathers, source and receiver pairings during acquisition. b) Graphs displaying the distance from the source and the time recorded for both field data and CMP-sorted wavelets. A hyperbolic curve is observed due to the delay in the wavelet. NMO returns the reflection into its correct position for any given time and offset. c) Equations for the hyperbolic reflection and NMO. Figure from Cox et al. (2020).

3.5.2.4 Velocity analysis

Velocity corrections of deep reflections involve the process termed normal move-out (NMO). Common mid-point (CMP) gathers record nonzero offset data and NMO corrections allow the data to be corrected to the plane of zero offset. This removes the effect caused by increased travel time due to increased offset between source and receiver. The CMP is the point on the surface equidistant between the source and receiver. The point directly below this at the reflector depth is known as the common depth point (CDP) (Yilmaz, 2001; Cox et al., 2020) (Figure 3.7).

A sampled reflection forms a hyperbolic curve due to the increase in time taken for the sound to reach distant receivers. The mathematical form of the reflection hyperbola allows the calculation of the stacking velocity. The stacking velocity is calculated from the geometric information known from the acquisition geometry and two-way travel time (TWT) recording for each trace and the time shift necessary to correct the reflection hyperbola to its horizontally aligned position for any given time and offset. This correction is known as NMO. Once applied, reflections appear horizontal on a “corrected gather” (Yilmaz, 2001; Cox et al., 2020) (Figure 3.7).

3.5.2.5 Migration

Complex geological features in the subsurface such as folds or faults can cause differences between the true location of a reflector and its representation on a seismic reflection section. The reflected and refracted reflections of variable dip rock layers can have differing angles towards the receiver, misplacing the reflectors. Seismic migration is useful to geometrically relocate seismic events in space and time to their true subsurface position. One of the most common migration algorithms

is known as Kirchhoff. When migration is not completely successful, prestack depth migration (PSDM) is used, commonly in areas of salt diapirism (Yilmaz, 2001).

3.5.3 Data reduction and enhancements

3.5.3.1 Multiple attenuation and deconvolution

Multiple reflections can be created by the downward reflection of the primary reflected source at shallower acoustic impedance contrasts. If the secondary reflected wavelet is reflected again at a deeper acoustic impedance boundary and returns to the receiver, it will be recorded as a multiple reflector (Telford et al., 1990; Yilmaz, 2001; Cox et al., 2020) (Figure 3.8).

Deconvolution is the method to convolve the seismic trace with the predicted noise, or multiple signals, to remove it, only leaving the primary reflection signal as main output in seismic data. Wavelet deconvolution is useful to change the trace signal from minimum to zero phase as to ensure the peak amplitude of the recorded reflection occurs at the point of impedance contrast, which is the lithological boundary (Sheriff and Geldart, 1995; Yilmaz, 2001; Cox et al., 2020).

3.5.3.2 Filtering and scaling

A frequency filter is commonly the last processing step as to reduce the effect of white noise on the signal. Different types of frequency filters can be applied, being the bandpass filter one of the most used, filtering frequencies outside a desired range. During seismic interpretation, a number of parameters can be adjusted on the workstation to better display the seismic, such as gain correction (Yilmaz, 2001; Cox et al., 2020).

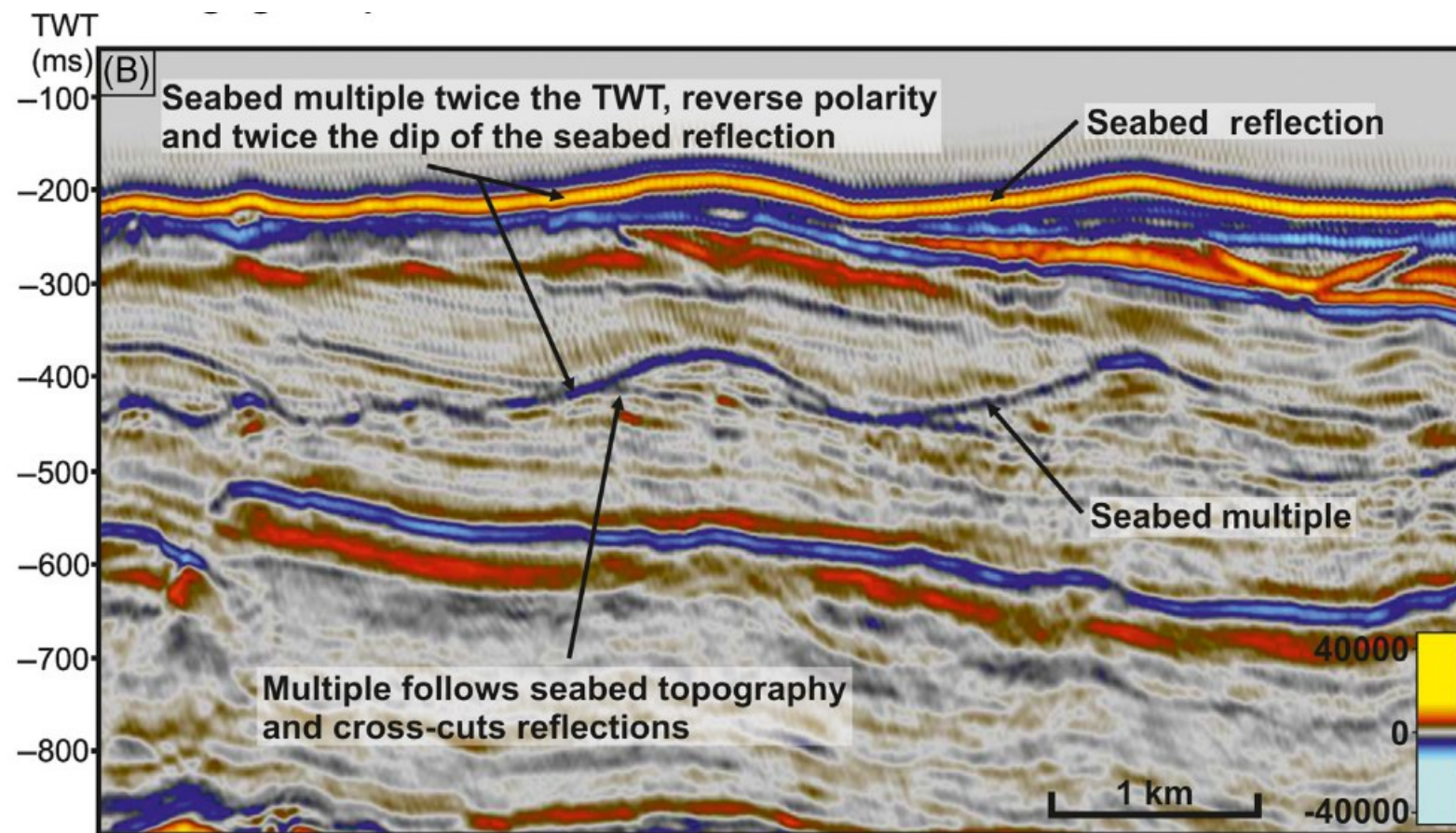


Figure 3.8. Seismic cross section showing an example of a seabed multiple created as a result of the returning seabed reflection, reflecting downwards. Figure from Cox et al. (2020).

3.6 Challenges of seismic imaging on carbonates

3.6.1 Seismic velocity on carbonates

Compared to siliciclastic sequences, carbonate rocks have greater densities and faster seismic velocities than most siliciclastics (Telford et al., 1990) (Figure 3.9). This generally results in lower vertical and spatial resolution in carbonate strata versus siliciclastics of comparable thickness (Palaz and Marfurt, 1997). High velocities in carbonates can also affect how to recognise target horizons in a reservoir as the reflectivity between formations is low, resulting in a near transparent appearance (Palaz and Marfurt, 1997).

3.6.2 Porosity and its seismic response on carbonates

To add more complexity, variations in texture, fabric, porosity, fractures, cementation and fluid fill lead to highly variable carbonate rock properties that affect seismic wave velocities (Wang, 1997). In Chapter 1, the carbonate porosity classification of Choquette and Pray (1970) was introduced, defining 15 basic types of porosity. In principle, seismic velocities should decrease as porosity increases. However, the shape, type and amount of porosity directly affect seismic velocities, as this is a measure of deformability (compressibility and rigidity) of a rock. A flat, thin pore is easy to deform, resulting in low seismic velocities even though porosity may be low. Intercrystalline, interparticle and fenestral porosities are generally related to low seismic velocities. In contrast, round and circular cavities are hard to deform, resulting in high seismic velocities (Wang, 1997). Moldic and vug porosity are generally related to high seismic velocities.

When it comes to fractures, seismic velocities depend on the direction of wave propagation relative to the orientation of the fractures. The rock will behave anisotropically because the rock is most compliant in the direction perpendicular to the fracture. When fractures are randomly oriented and abundant, the rock will behave isotropically in terms of seismic properties (Wang, 1997).

3.6.3 Karst features

Repeated exposure and diagenetic changes of carbonate platforms have a major impact on porosity evolution and reservoir quality. Irregular karstified terranes with vugs, caves and collapse features are a challenge for seismic imaging. These features are rarely observed on seismic, large-scale dissolution features can reflect seismic waves in a chaotic manner (Eberli et al., 2004).

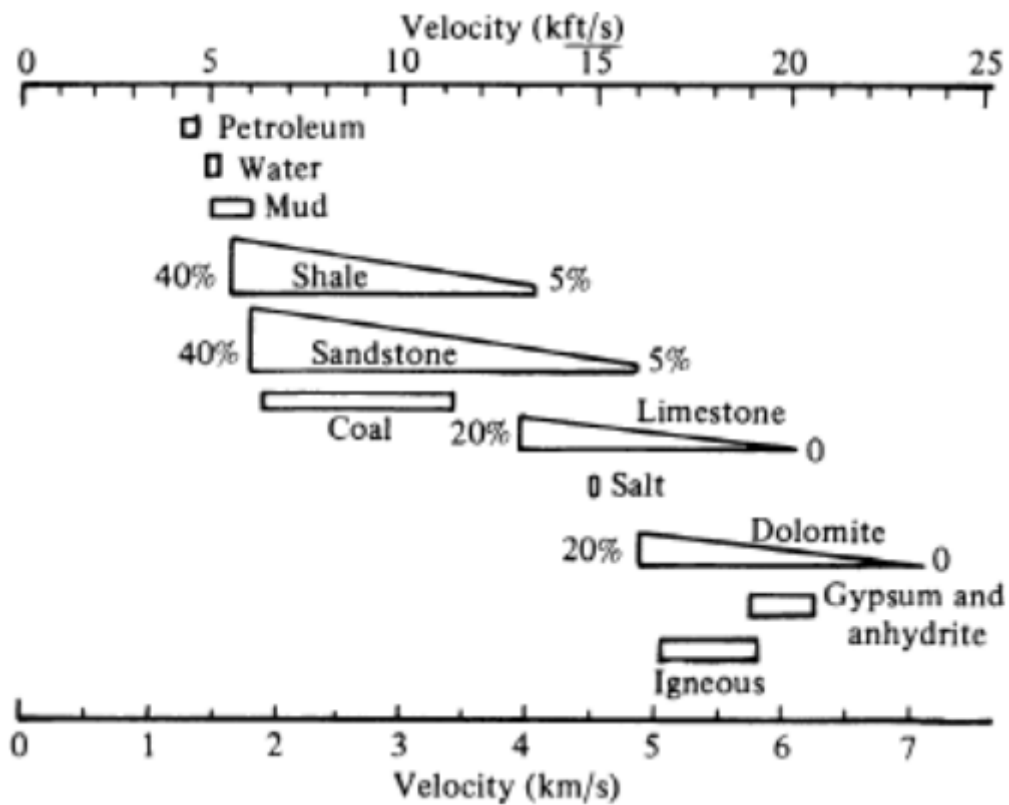


Figure 3. 9. Graph showing the wide seismic velocity ranges of different types of rocks reported by Birch (1966). Note the higher velocities of limestone and dolomite compared to shale and sandstone. Figure from Telford et al. (1990).

3.7 Datasets in this study

3.7.1 Seismic data

This thesis focuses on three study areas from the Northwest Shelf of Australia, eastern and equatorial Brazil. The details of each 3D seismic dataset used herein are provided below.

3.7.1.1 Bonaparte Basin, Northwest Shelf of Australia

The seismic data used in this study includes a 3D seismic volume (Karnt3D AGC Time) located in the northern part of the Vulcan Sub-Basin, Timor Sea (Figure 2.1). The seismic volume was acquired by Geco-Prackla in 1996 for Woodside Offshore Petroleum, covering more than 2000 km² with a 6 s vertical penetration (Carenzi and Cazzola, 2008). The volume was provided by Geoscience Australia and comprises 3334 inlines (IL) and 5191 crosslines (XL) with a 12.35 × 12.50 m line spacing and a vertical sampling interval of 4 ms. The frequency spectrum of the interpreted volume in the first 3,000 ms ranges from 10 to 70 Hz, with an average value of around 20 Hz.

3.7.1.2 Pernambuco Basin, east Brazil

A post-stack depth-converted 3D seismic volume from the Pernambuco Plateau, offshore East Brazil, was used in this study (Figure 2.6a). The seismic volume covers an area of 3,200 km² with a vertical penetration of almost 9 km. The seismic volume was provided by CGG and comprises 2700 inlines (IL) and 1899 crosslines (XL) with a 25 × 25 m line spacing and a vertical sampling interval of 5 m. The interpreted seismic

data is in depth domain with SEG's American polarity, and of good quality, allowing for the detailed analysis of fracture networks on the wide platform margin.

3.7.1.3 Pará-Maranhão Basin, Equatorial Brazil

The 3D PAMA PSDM Full Stack is a full-stack depth-converted 3D seismic volume covering an area of about 1,950 km² in the PAMA Basin, Equatorial Brazil (Figure 2.7). This dataset images the edge of the continental shelf, together with the continental slope and continental rise, in water depths ranging from 100 m to 3,500 m. The seismic volume, provided by Polarcus, consists of 3201 inlines (IL) and 3901 crosslines (XL) with a 12.5 x 12.5 m line spacing and a sampling interval of 5 m. The interpreted seismic data were processed in the depth domain with a SEG positive polarity using the European convention; an increase in impedance is represented by a red (positive) peak. The high-quality seismic data allow for the detailed analysis of stratigraphic and seismic facies to a depth of 7,500 m below the seafloor. This study focuses on the Miocene to Holocene stratigraphic successions of the PAMA Basin.

In addition to 3D seismic data, public 2D seismic profiles were used to complement this study. The regional 2D seismic profile GB1-4500 was reinterpreted from Henry et al. (2011) and Zalán (2015) as to provide information on the PAMA Basin at the scale of the continental margin (Figure 2.7). Regional 2D seismic profile 022-0837 (Fabianovicz, 2013), and seismic profiles 0270-3010 and 0275-8780 (Da Silva and Ribeiro, 2018), were used to correlate the seismic stratigraphy of the study area with main depositional sequences recognised on borehole and outcrop data (Figure 2.7).

3.7.2 Borehole data

3.7.2.1 Bonaparte Basin, Northwest Shelf of Australia

Completion data and proprietary geological reports from four different wells (Mandorah-1, Ludmilla-1, Lameroo-1 and Fannie Bay-1) were used in seismic-well correlations (Figure 2.1). Seismic well-ties were performed using check-shots and time-depth (TWT-Z) tables published with the well reports. Completion data include stratigraphic and lithological descriptions based on cuttings and sidewall core samples (Woodall, 1990; Rexilius et al., 1998a; Willis, 1998, 1999a, 1999b, 1999c, 2000). Wireline logs (gamma ray, resistivity, density, sonic) were digitised from raster composite well logs and used to correlate stratigraphic surfaces and depositional units across the study area. Digitalisation of the well logs was performed using CorelDraw based on raster images. Geological reports from Geoscience Australia include micropaleontological analyses of benthonic and planktonic foraminifera, as well as calcareous nannoplankton of three wells (Mandorah-1, Ludmilla-1 and Fannie Bay-1), which allowed correlations between wells and provided age controls to the interpreted seismic-stratigraphic units (Rexilius et al., 1998a, 1998b; Rexilius and Powell, 1999a, 1999b).

3.7.2.2 Pará-Maranhão Basin, Equatorial Brazil

Well data are scarce in the PAMA Basin, with only a few exploration wells spudded in shallow waters of the carbonate shelf margin. No wells have been drilled on the continental slope and rise within the interpreted seismic survey. Composite data from seven (7) exploration wells, provided by the Brazilian National Agency of Petroleum, Natural Gas and Biofuels (ANP) were used to correlate seismic

interpretation. The exploration wells are located near the edge of the PAMA continental shelf and document shallow-water depositional systems transporting sediment into deep waters (Figure 2.7). Well data include gamma-ray, deep-resistivity and lithological logs.

3.7.3 Outcrop data

The outcropping Cariatiz carbonate platform in SE Spain was used to map fracture networks on the reef framework zone (Figure 2.4). Traditional field mapping techniques were utilised to define the extent of the platform margin. An enhanced circular scanline methodology was used to adequately map the geometry and topology of the fracture networks in Cariatiz.

3.7.4 LiDAR data

Airborne LiDAR imagery from the Cariatiz carbonate platform permitted the collection of fracture measurements at an intermediate scale. Data was provided by the Instituto Geográfico Nacional (IGN) and the Centro Nacional de Información (CNIG) of Spain. The airborne LiDAR map was acquired with a density of 0.5 points/m² with a 5 m grid size. After processing for slope, a resolution of about 5 m is suggested for the airborne LiDAR dataset.

3.7.5 Satellite data

For the PAMA Basin, this work utilises a combination of multispectral satellite imagery with bands B4-Red, B3-Green, and B1-Ultra blue (coastal aerosol) provided

by the Sentinel-2 mission. Sediment suspended in water can be traced by using the coastal aerosol band (B1), as this band reflects the blue and violet colour spectra displaying subtle differences in the colour of water (Hedley et al., 2018).

3.8 Methods

3.8.1 Seismic interpretation and visualisation

Different types of datasets are used for each result chapter of this thesis. However, 3D seismic data was used in all of the studied areas. Therefore, seismic interpretation is one of the most significant methods employed in this thesis. Schlumberger Petrel® 2019 was the primary software to complete seismic interpretation in the 3D Seismic Lab at Cardiff University. This is a specialised industry software installed on high performance workstations that allows an integrated and comprehensive analysis of seismic and wellbore datasets.

Data can be visualised as 2D vertical profiles, representing shot line (inline) or recording line (crossline) directions. 3D seismic probes and horizontal depth slices can also be made to display the pattern of seismic reflections at any time or depth plane. Arbitrary lines are useful to visualise a section in any desired direction (Figure 3.10).

Seismic data is visualised as a series of wavelets that reflect the amplitude peaks and troughs with specific colours, depending on the polarity of the seismic and the colour palette utilised (Figure 3.11). Seismic data of the Karmst3D and Pernambuco volumes was displayed with a red-white-black colour scheme. The PAMA seismic volume was displayed with a default seismic colour scheme (Figure 3.11).

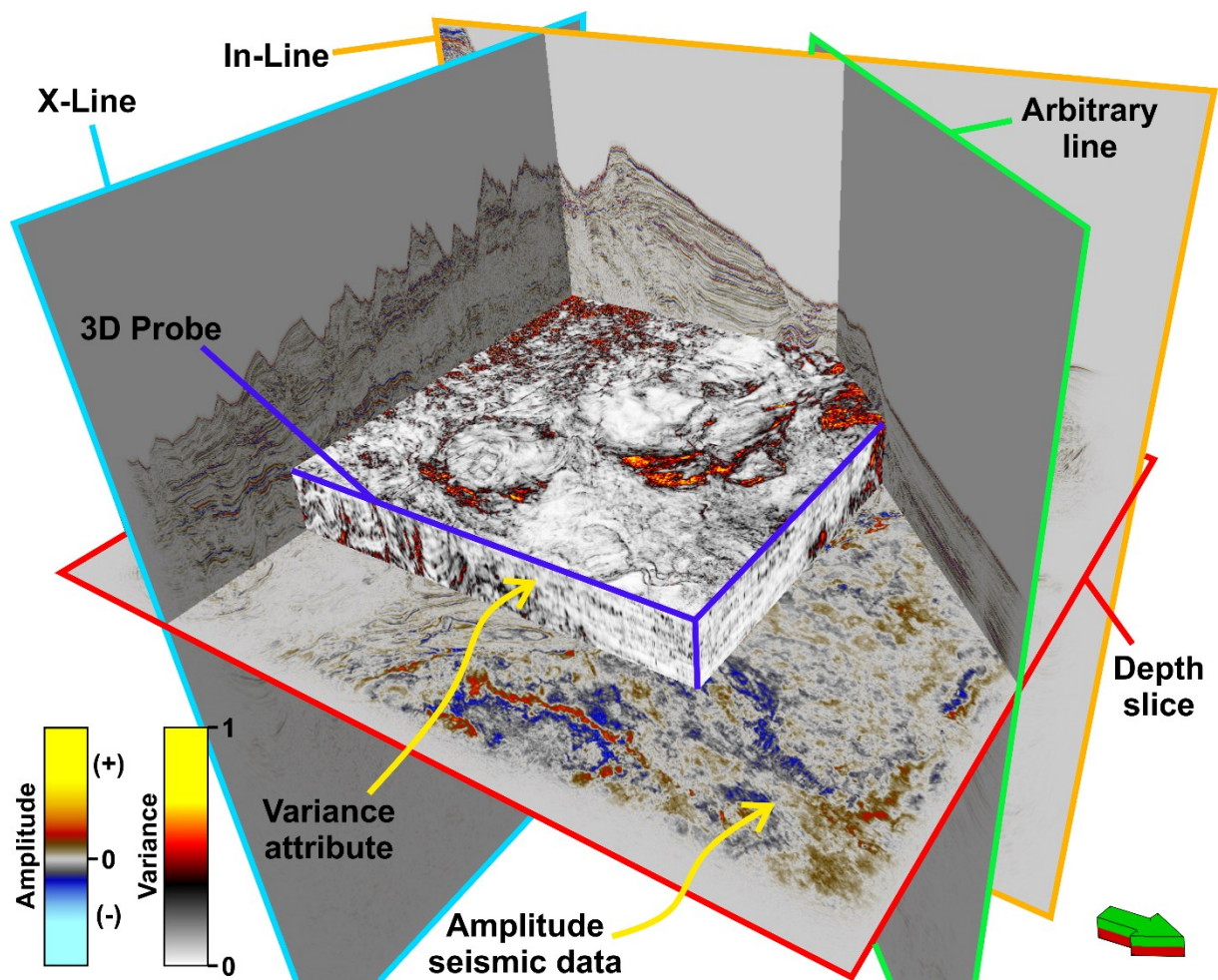


Figure 3.10. 3D visualisation showing how seismic data can be displayed including a 3D seismic probe and typical intersections such as In-line, X-line, Z-slice and an arbitrary line. Example from the 3D PAMA seismic volume.

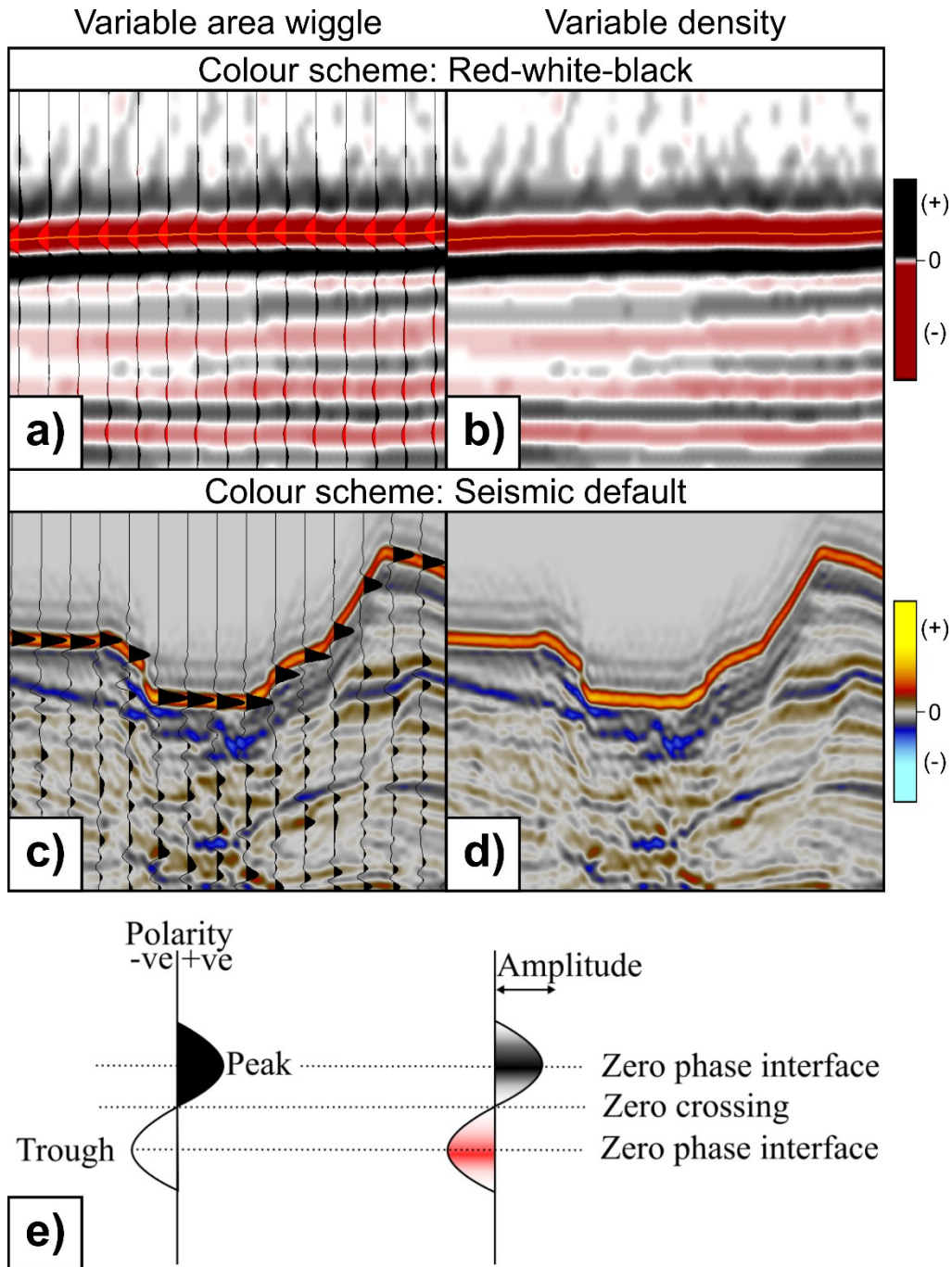


Figure 3.11. Series of seismic displays showing (a and c) variable-area wiggles and (b and d) variable amplitude spectrums using different colour schemes. The red-white-black colour scheme is used for the Karmst 3D seismic volume and Pernambuco 3D seismic volume. Seismic default colour scheme is used in the 3D PAMA volume. | Seismic polarity diagram showing peaks and troughs in the wiggles.

3.8.1.1 Seismic attribute analysis

Seismic attributes can be used to better visualise and constrain interpretations in three dimensions in structural or stratigraphic studies based on derivatives of basic seismic measurements such as time, amplitude, frequency or attenuation (Brown, 2011). A wide variety of seismic attributes are available to use in Petrel®. A broad generalisation is that time- or depth-derived attributes provide structural information and amplitude-derived attributes provide stratigraphic information. Although attributes like variance can be used for both purposes. Studies in this thesis included a range of attributes to facilitate fault and horizon interpretation, although the variance attribute is the most used. Other attributes included are cosine of phase and chaos. Attributes are normally calculated and extracted from the data volume.

Amplitude: seismic reflection amplitude is normally the first volume used to visualise data and perform seismic interpretation as it is the default setting of a seismic section from which other seismic attributes can be extracted. It denotes the value measured of the largest displacement of a seismic wavelet at its crest, recording a positive or negative amplitude. Seismic amplitudes change laterally due to differences in acoustic impedance across a geological interface. These changes can be interpreted as lithology variations or the presence of fluids (Brown, 2011). These characteristics are useful to understand stratigraphic variations and initial fault recognition (Figures 3.12a and 3.13a, b).

Instantaneous frequency: this is a time or depth derivative of phase, calculated from the change of instantaneous phase. This is a useful attribute to identify seismic attenuation caused by oil and gas reservoirs and to measure cyclicity of geological intervals for cross-correlating strata across faults (Figure 3.12d and e).

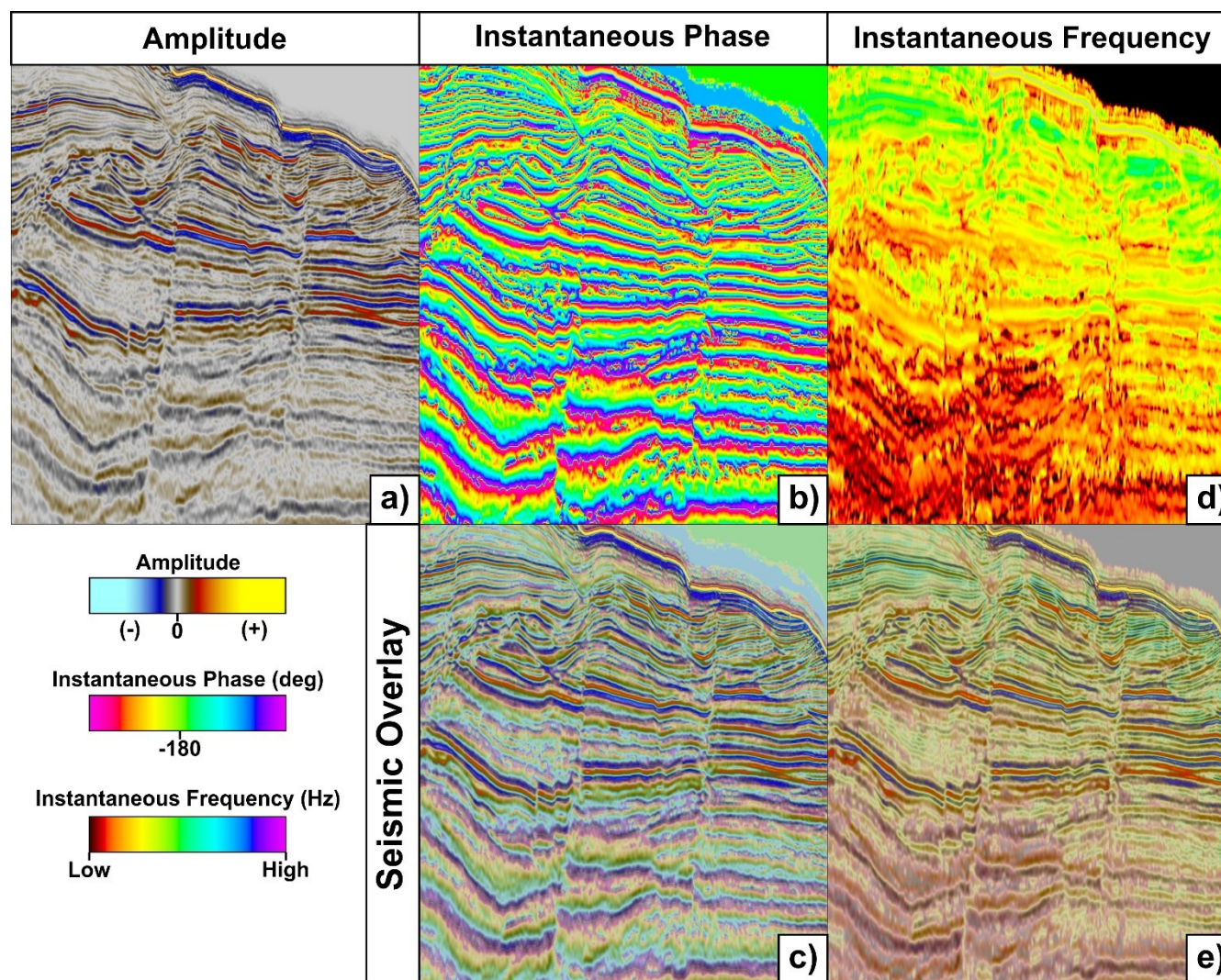


Figure 3.12. Seismic sections showing seismic attributes that were useful for horizon interpretation as the continuity of reflectors is enhanced. Example from the 3D PAMA volume.

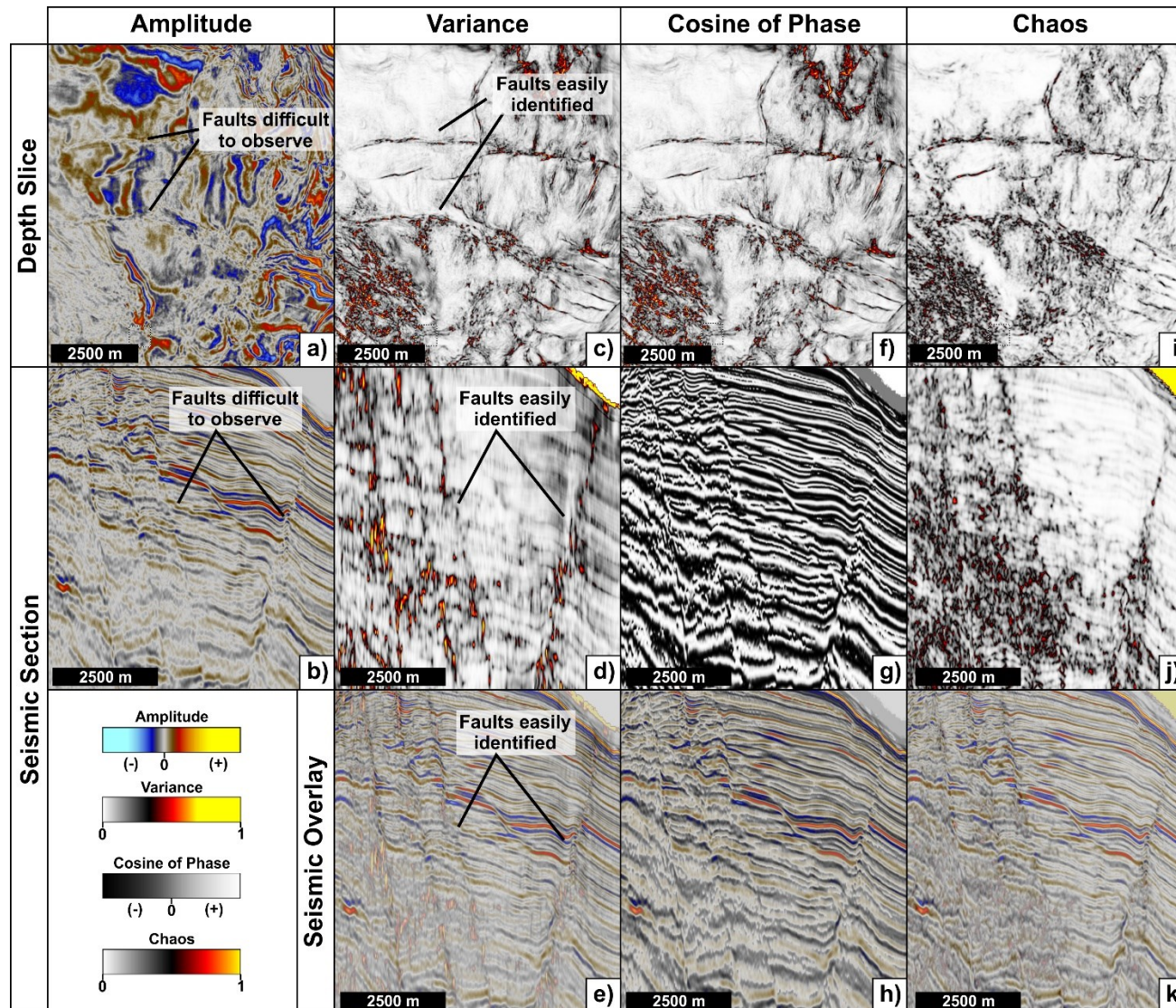


Figure 3.13. Seismic depth slices and seismic sections showing the different attributes calculated in this thesis. Seismic overlay enhances visualisation as it combines two seismic attributes. Example from the 3D PAMA volume.

Instantaneous phase: this attribute shows the continuity of seismic reflections that vary in amplitude. It emphasises spatial continuity or discontinuity of reflections by providing a way for weak and strong events to appear with equal strength. This attribute is calculated on a sample-by-sample basis with no regard for the waveform, and it is a good indicator of pinch-outs, bed interfaces, sequence boundaries and regions with onlapping reflection patterns. This attribute was considerably helpful in Chapter 6 as a guide for the different stratigraphic features observed offshore PAMA (Figure 3.12b and c).

Cosine of phase: this attribute is similar to instantaneous phase as it is calculated independently from the amplitude and facilitate bedding interpretation. The additional benefit is that the attribute is continually smooth. This attribute is useful for structural and stratigraphic analyses (Figure 3.13f-h).

Chaos: this attribute maps the “chaos” of the local seismic signal from statistical analyses of dip and azimuth estimates. It is useful to identify faults and fractures as well as channel infill, reef internal textures and discriminate facies analysis (Figure 3.13i-k).

Variance or coherence: coherence is a measure of similarity between waveforms or traces. Geologically highly coherent seismic waveforms indicate laterally continuous lithologies; in contrast, abrupt changes in the waveform can indicate faults and fractures (Chopra and Marfurt, 2007). This attribute integrates information of adjacent traces and samples in a nonlinear manner. Coherence volumes are extremely useful in structural and stratigraphic studies facilitating 3D interpretation of faults, fractures and channel geometries (Chopra and Marfurt, 2007). In general, structural features that cut across stratigraphy, such as vertical faults, are seen best on constant-time (or depth) slices, which lack the interpreter

bias that would be present on horizon-based extractions. This approach was followed in Chapters 4 and 5 to perform fracture interpretation (Figure 3.13c-e). In contrast, stratigraphic features, such as the channels observed in Chapter 6, are shown best on horizon slices using a vertical analysis window that is approximately equal to the period of the dominant frequency (Chopra and Marfurt, 2007).

Isochron: this is a thickness map that shows the time difference between two given horizons or surfaces. In Chapter 4 it was used to define the thickness of isolated carbonate platforms and better understand their distribution.

3.8.1.2 Multiattribute displays

Seismic attributes are usually displayed in colour to capture as much detail as possible. Often, attribute calculations are meaningful only if the underlying seismic data are sufficiently strong and coherent. An effective combination of more than one attribute into a single display allows interpreters to better visualise, analyse and present the data by linking key attributes (Figures 3.12 and 3.13). The most commonly used techniques include seismic overlays and blended or mixed maps. Seismic overlays plot an attribute in colour to form a background, and a second attribute in variable area format to overlay the background attribute with a given transparency (Chopra and Marfurt, 2007). In contrast, blended displays attempt to render two seismic attributes simultaneously at all points (Chopra and Marfurt, 2007). Seismic overlays were used in Chapter 6 as to better identify stratigraphic features on the interpreted horizons. A blended display was used in Chapters 4 and 5 as to better visualise faults and fractures on seismic sections and time or depth slices.

3.8.1.3 Fault and fracture mapping

One of the main tasks in this thesis is to measure and analyse faults and fractures resolved at the seismic scale. A good practice is to combine the interpretation of amplitude seismic in 2D sections and the variance attribute in time or depth slices. Fault interpretation involves mapping the breaks or displacements in seismic reflections that appear to be linear, cross-cut and offset packages of seismic reflections (Figure 3.13). Faults map the offset of seismic reflections until the offset ceases or is not visible on the fault tips.

Faults are first mapped on plan view using time or depth slices with the calculated variance attribute. Once the faults are mapped on plan view, those segments can be used as a guide to interpret the full extent of faults using 2D amplitude sections. These sections should preferably be oriented perpendicular to each fault strike in order to visualise the real maximum dip and facilitate interpretation. Interpreting faults on inlines and crosslines can be problematic as they can show apparent dips in which faults are more difficult to visualise. The faults are picked manually both vertically and laterally at intervals ranging from 150 m to 500 m as to capture structural complexity and generate an accurate 3D representation of the fault plane.

3.8.1.4 Horizon mapping

Key seismic reflectors were mapped following sequence stratigraphy principles (Catuneanu, 2006). Stratigraphic data from exploration wells were tied to seismic data in Chapters 4 and 6 as to correlate major stratigraphic units to their corresponding seismic reflections. Reflection interpretation was performed using the autotracking horizon interpretation tool in three general steps. This option allows to

perform seismic interpretation in 3D by clicking on a specific event. This tool constrains the interpretation depending on the confidence and correlation parameters previously set (Figure 3.14). The seeded autotracking follows the picked event with similar amplitude and phase until it reaches a disturbance such as faults or noise. The initial interpretation was undertaken using the seeded 2D autotracking along inlines and crosslines with a spacing of 50-100 lines depending on the size of the seismic volume (Figure 3.15). The result is a grid map with a preliminary view of the interpreted horizon. The following step was to continue interpretation using the 3D autotracking tool as to populate the mapped grid. In complex areas, spacing between lines increased to every inline and crossline to obtain more detail (Hart, 1999) (Figure 3.15). The final stage was to use the paintbrush 3D autotracking tool on map view as to fill the missing gaps (Figure 3.15). Quality control is then performed to address and amend any erroneous picks in order to produce an accurate structural map (Figure 3.16).

Surfaces were created from the interpreted horizon using the “Make Surface” Tool in Petrel®, from which attributes such as variance could be extracted as to highlight structural discontinuities such as large faults and fractures.

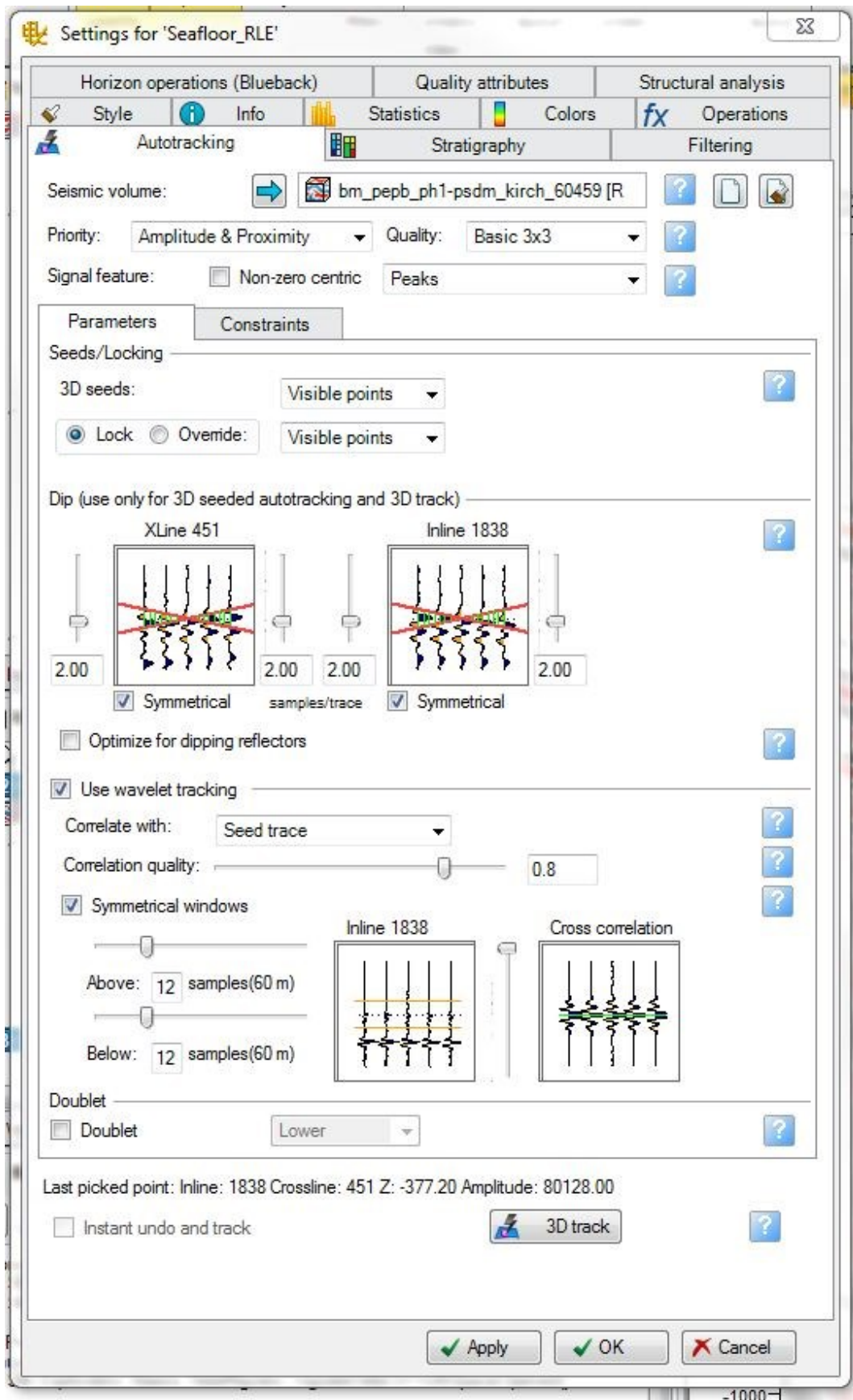


Figure 3.14. Example of the autotracking window showing the different parameters that can be constrained for a better interpretation.

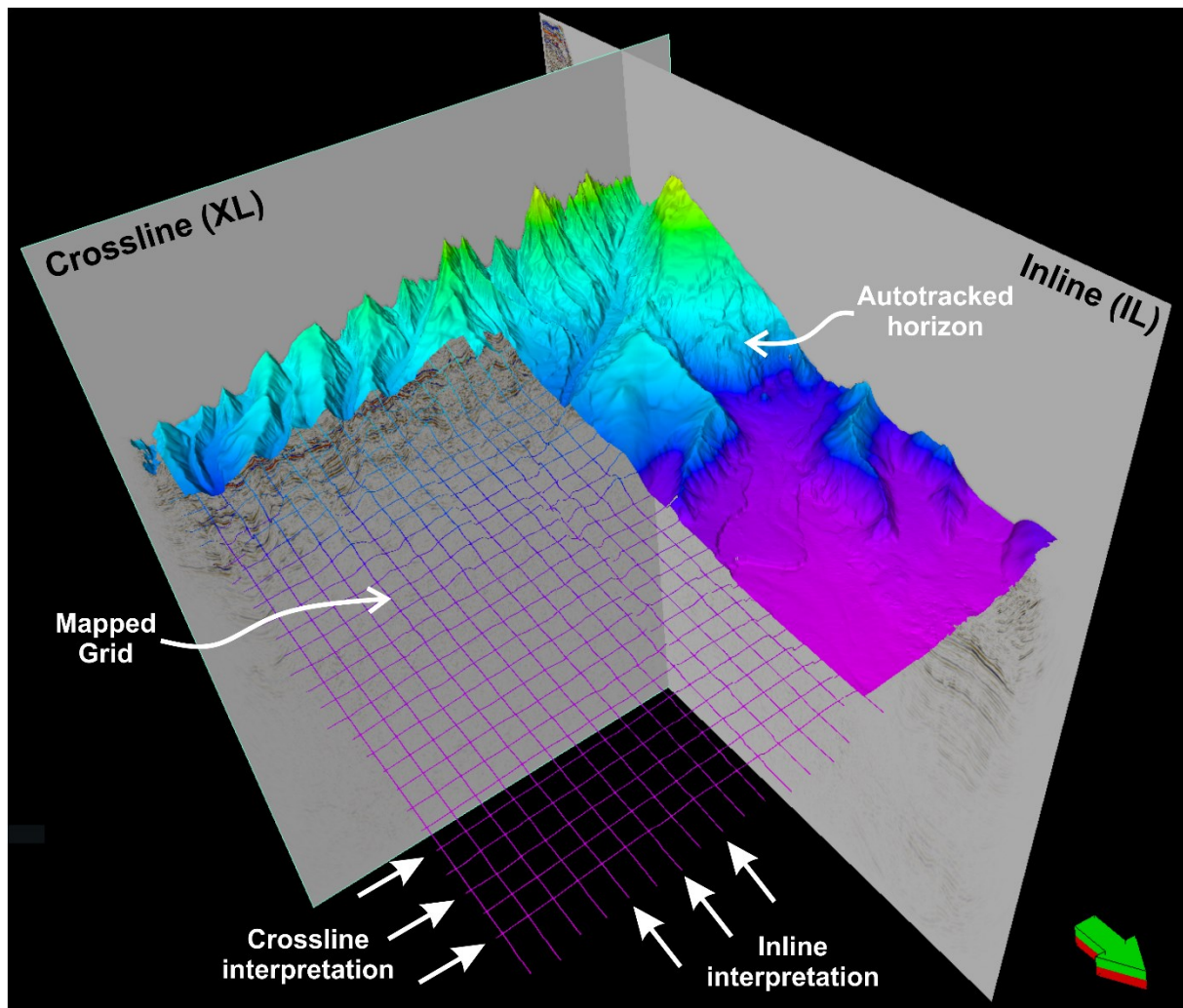


Figure 3.15. 3D view showing how seismic horizon interpretation was performed. (1) Seeded 2D autotracking along inlines and crosslines to generate a grid. (2) Seeded 3D autotracking along inlines and crosslines. (3) Paintbrush 3D interpretation on map view.

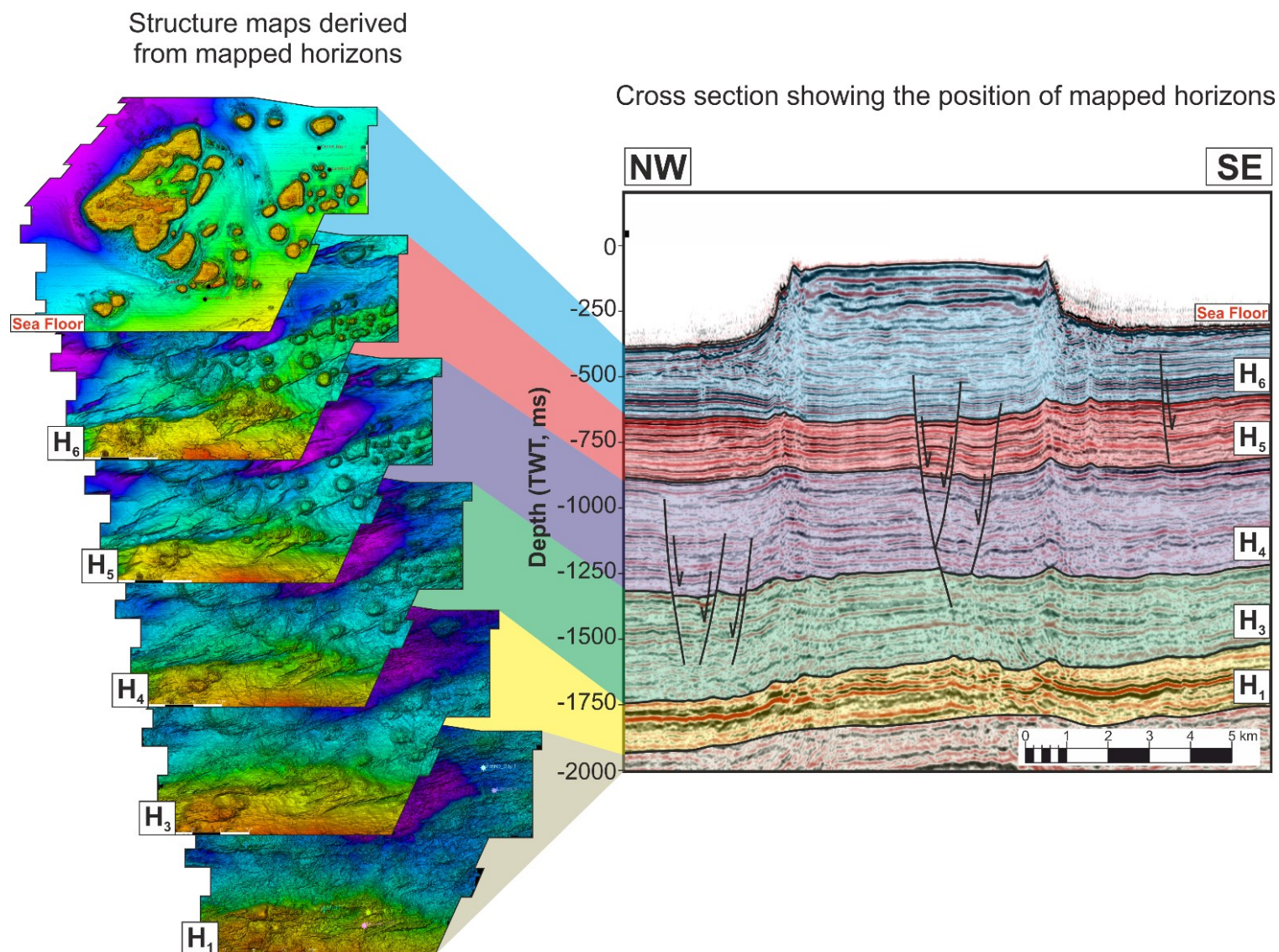


Figure 3.16. Example of a seismic section from the Karnt3D, Northwest Shelf of Australia (Chapter 4) showing how the interpreted horizon maps relate to different levels on the seismic line.

3.8.2 Fault-throw measurements

In a natural fault, displacement from the hanging wall to the footwall varies throughout the fault surface as fault walls do not move perfectly parallel. This displacement is higher at its nucleus and reduces towards the fault tips (Muraoka and Kamata, 1983). Vertical fault-throw measurements plotted against geologic or seismic horizons across a section is known as a fault-throw profile and it can be used to determine the style, time of fault initiation and kinematic history of normal faults (Hongxing and Anderson, 2007). The point in which the plot shows a maximum throw indicates the time in which fault displacement started. Knowing this is important to understand the structural evolution of a basin, and it can be useful to petroleum exploration as it can indicate migration and entrapment systems. Hongxing and Anderson (2007) described three types of normal faults: type 1 or simple post-depositional fault, type 2 or simple post-depositional crestal keystone-stretching fault, and type 3 or simple growth fault.

Type 1 is characterised to be formed after sediment deposition, having a constant or nearly constant throw displacement across the entire stratigraphic section (Figure 3.17). The fault growth index should equal 1 for all layers as there is no thickness variations between the hanging wall and the footwall layer (Figure 3.17). Type 2 is formed after sediment deposition in which the fault starts to grow in the upper part, gradually displacing to deeper strata (Figure 3.17). The maximum throw displacement is seen at the top of the plot, and the minimum at the bottom (Figure 3.17). Type 3 occurs at the same time of sediment deposition, being called syn-depositional normal growth fault. The result is a sedimentary succession that is thicker in the hanging wall (Figure 3.17).

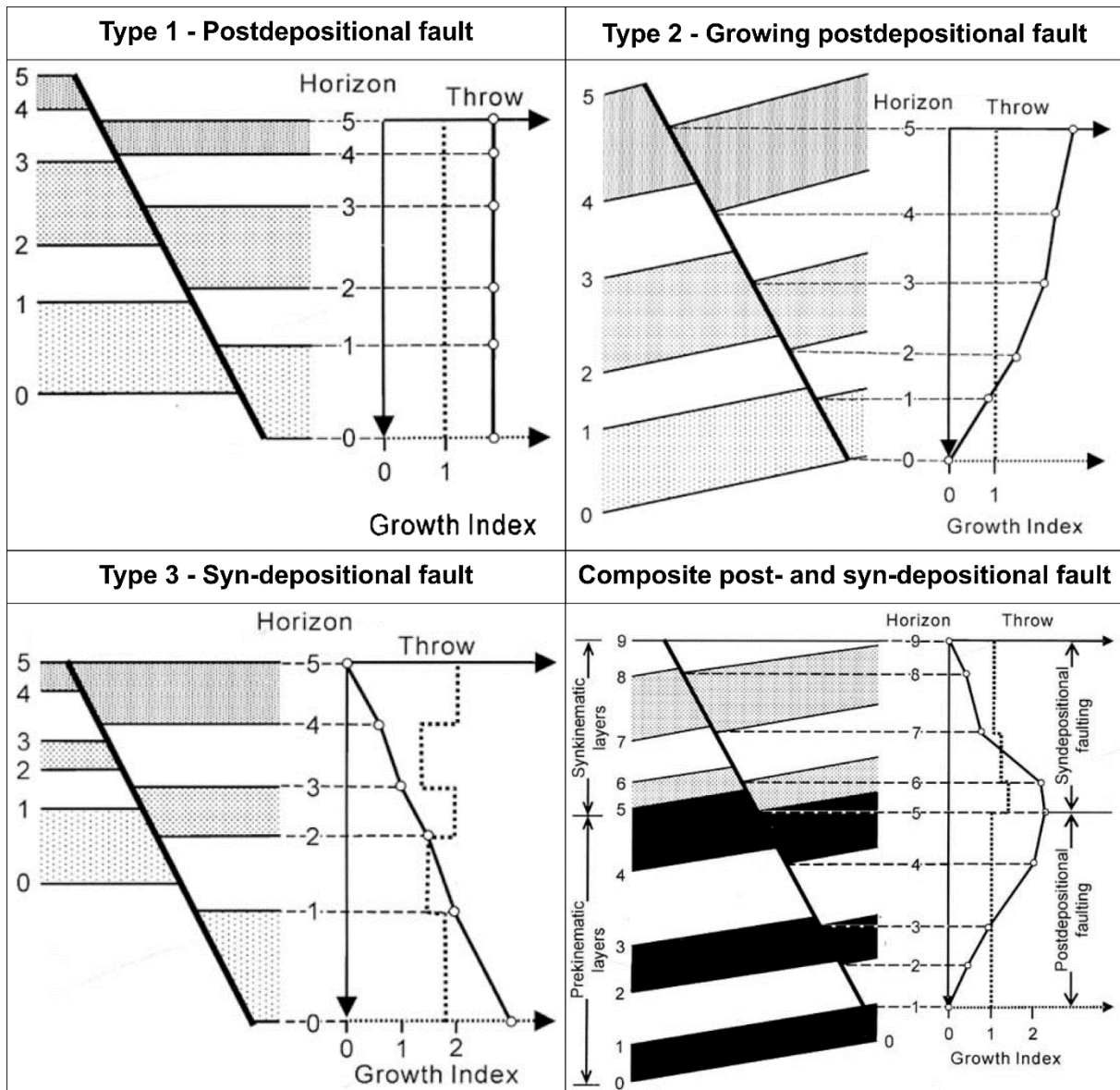


Figure 3.17. Schematic cross sections showing the different types of normal faults and their characteristic fault-throw profile with the growth index curve. Modified from Hongxing and Anderson (2007).

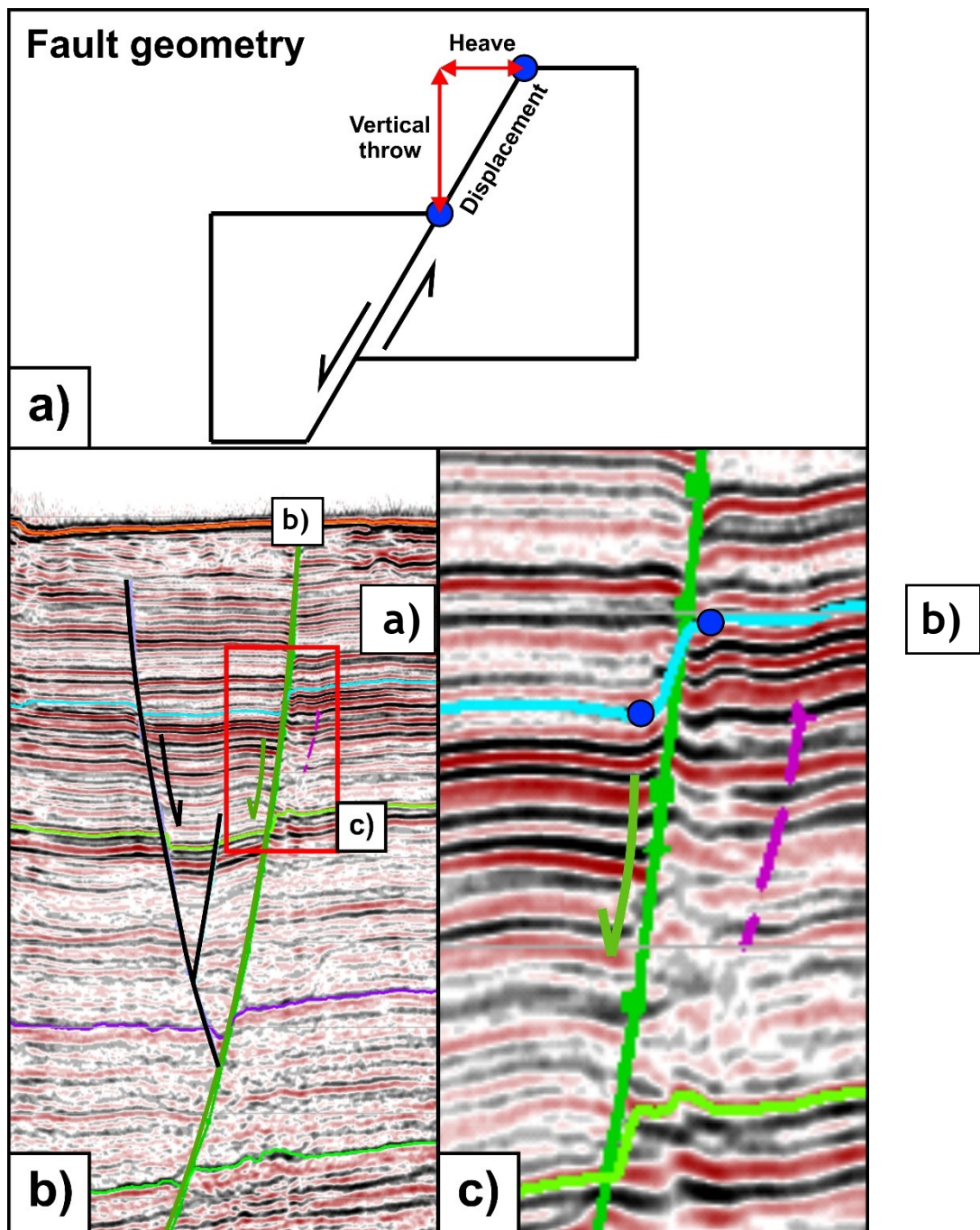


Figure 3.18. A) Schematic diagram showing the geometrical features of a fault and an example of a seismic section showing how fault-throw is measured (b and c).

Because faults are normally complex, a combination between the previous types is commonly observed. One example is a post- and syn-depositional fault in which fault displacement starts after sediment deposition, observed as a fault-throw curve with a positive slope (Figure 3.17). The maximum value indicates the starting point of fault development. When fault displacement continues to propagate at the same time of sedimentary deposition, another fault stage can be observed as a fault-throw curve with a negative slope (Figure 3.17).

In Chapter 4, fault-throw measurements were key to provide information about the evolution history of the faults in the Bonaparte Basin and its relation to the development of isolated carbonate platforms. Exhaustive fault-throw measurements were taken from different faults as to create detailed fault-throw distribution plots and generate a high-resolution contour map. Throw measurements were taken from reflection seismic in sections perpendicular to the strike of the faults with an along-strike spacing of 150 m and along-dip spacing of 25 m (Figure 3.18). Fault-throw is obtained from the difference between the depth of a reflector in the footwall and the depth of the corresponding reflector in the hanging wall (Figure 3.18).

3.8.3 Field methodology

Fieldwork was completed in SE Spain at the Cariatiz reef, a representative unit of the Messinian fringing reef in the Sorbas Basin. Chapter 5 performs a comparison between large-scale fractures observed from seismic data and small to intermediate fractures observed from outcrop data. The use of an outcrop analogue is key to generate predictive models and scale relationships of fracture networks. The work

carried out at Cariatiz includes measurements of different geomorphic and topologic fracture properties such as orientation, length and connectivity.

The methodology used in this thesis follows the technique proposed by Watkins et al. (2015) called augmented circular scanline. The first stage is to adequately select sampling sites to collect fracture data on the field as to obtain suitable outcrops where fracture attributes can be measured. Satellite images from Google Earth were useful to recognise areas where bedding surfaces appear to be exposed.

The circular scanline methodology involves drawing a circle of a known radius l on a bedding surface where fractures will be measured. Fractures intersecting the circle line (n) and the total number of fracture terminations within the circle (m) are measured (Figure 3.19). The circle radius l is determined based on a minimum “ m ” value of 30 as suggested by Rohrbaugh et al. (2002), so that the collected data reflect a good sample of the fractured area.

One of the major contributions of this thesis is to point out the measurement of fracture branches rather than fracture traces to analyse the topology of fracture networks. The number of fracture nodes and fracture branches (isolated, single connected, double connected) within the circle are counted (Figure 3.19). Values obtained using this method can provide key information to determine the connectivity of fracture networks at different scales. In addition, geometric attributes such as fracture strike, dip and dip direction, branch length, aperture, and fracture fill (if it is open or mineralised) are also measured in order to provide a full understanding of the fracture network.

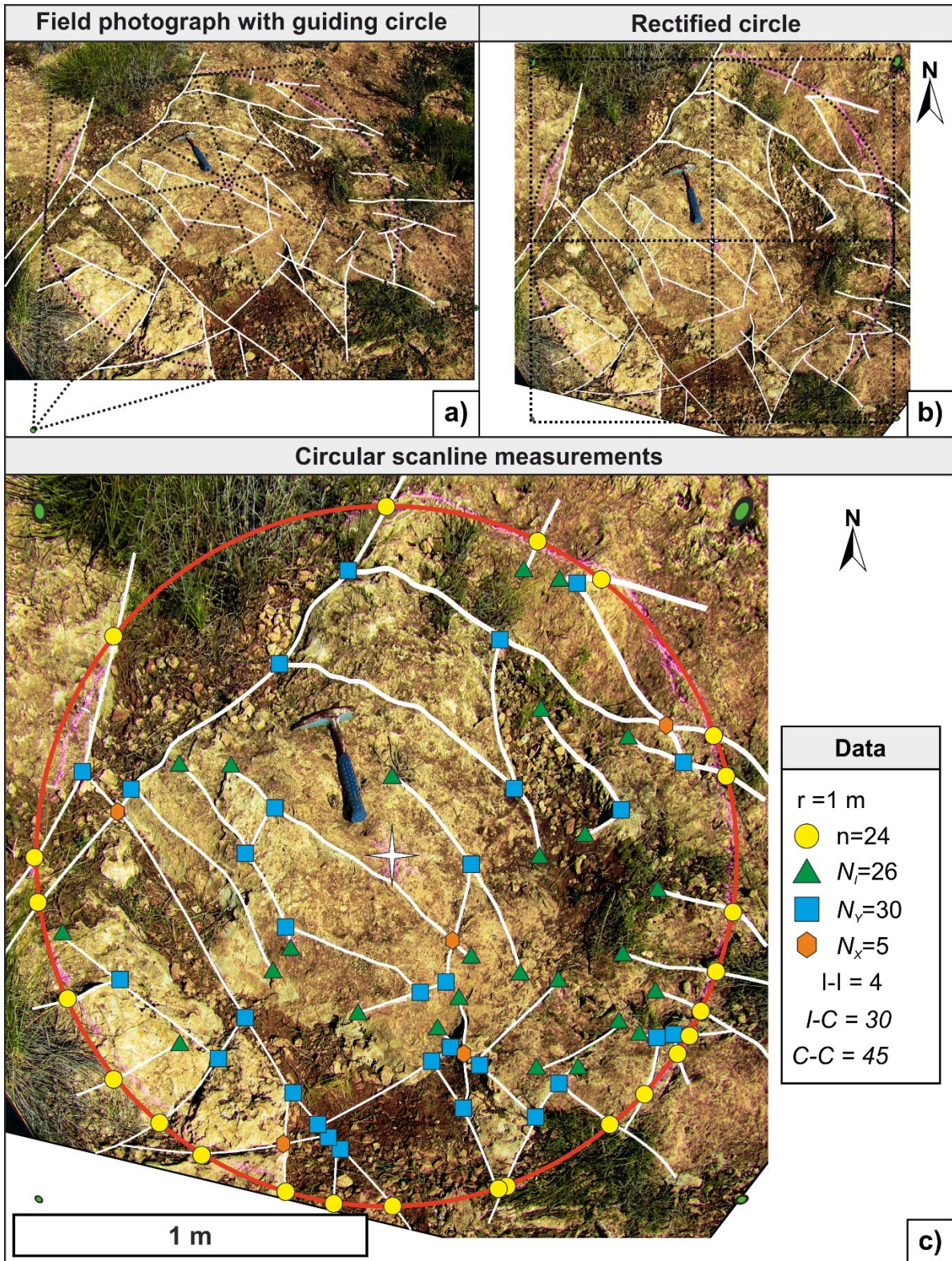


Figure 3.19. Example of the circular scanline methodology followed in this thesis. a) Field photograph with measured fracture branches. b) Rectified photo to perform fracture measurements digitally. c) Circular scanline image showing all the obtained data. r =circle radius, n =number of fractures intersecting the circle line, N_i =number of isolated nodes, N_v =number of single connected nodes, N_x =number of double connected nodes, $|I|$ =number of isolated branches, $I-C$ =number of single connected branches, $C-C$ =number of double connected branches.

Chapter 4: Structural controls on isolated carbonate platforms

An abridged version of this chapter has been published as:

Loza Espejel, R., Alves, T.M., Blenkinsop, T.G., 2019. Distribution and growth styles of isolated carbonate platforms as a function of fault propagation. *Marine and Petroleum Geology*, 107, p.p. 484-507.

<https://doi.org/10.1016/j.marpetgeo.2019.05.020>.

Co-author contributions to the paper:

Tiago M. Alves - checked for grammatical errors, ensured the scientific content was accurate and appropriately presented.

Tom G. Blenkinsop - checked for grammatical errors, ensured the scientific content was accurate and appropriately presented.

4.1 Abstract

Fault control on the position and distribution of isolated carbonate platforms (ICPs) is investigated in Northwest Australia using high-quality 3D seismic and borehole data from the Bonaparte Basin. Specifically, this chapter addresses the relationship between carbonate productivity and fault growth so as to understand what are the primary controls on the growth of isolated carbonate platforms. Throw-depth (T-Z) and throw-distance (T-D) profiles for normal faults suggest they formed fault segments that were linked at different times in the study area. This caused differential vertical movements; some of the normal faults propagated to the surface, while others have upper tips that are 19-530 ms two-way-time below the seafloor, with the largest throw values comprising faults underneath isolated carbonate platforms. As a result, four distinct zones correlate with variable geometries and sizes of carbonate platforms, which are a function of the topographic relief generated by underlying propagating faults. Some relay ramps form preferred locations for the initiation and development of carbonate platforms, together with adjacent structural highs. Due to the complex effect of fault propagation to the palaeo-seafloor, and soft-linkage through relay ramps, three distinct ICP types are proposed: (type 1) fault-throw is larger than carbonate productivity; (type 2) fault-throw is equal or lower than carbonate productivity; and (type 3) fault-throw post-dates the growth of the carbonate platform(s). The analysis of fault propagation vs. carbonate platform growth shown here is important, as the three ICP types proposed, potentially correlate with variable fracture densities and distributions within the carbonate platforms. Based on the results shown in this chapter, types 2 and 3 above enhance fracture- and fault-dominated porosity and permeability to a greater degree, making them favourable targets for hydrocarbon exploration.

4.2 Introduction

Isolated carbonate platforms are of great interest to petroleum exploration due to their reservoir potential. Some of the best examples of such a potential are recorded in the South China Sea (Neuhaus et al., 2004; Ding et al., 2014; Hutchison, 2014), Kazakhstan (Collins et al., 2006, 2016; Kenter et al., 2008), the Middle East (Alsharhan, 1987), the Brazilian Margin (Buarque et al., 2017), the Barents Sea (Blendinger et al., 1997; Elvebakk et al., 2002; Nordaunet-Olsen, 2015; Alves, 2016), amongst others. It is estimated that reserves of about 50 billion barrels of oil equivalent are accumulated around the world within these structures (Burgess et al., 2013), in places such as the Luconia Province and the Malampaya Field in Southeast Asia (Neuhaus et al., 2004; Zampetti et al., 2004; Rankey et al., 2019), or the Karachaganak and Tengiz fields of the Pre-Caspian Basin, Kazakhstan (Elliott et al., 1998; Collins et al., 2006; Borromeo et al., 2010; Katz et al., 2010).

Isolated carbonate platforms accumulate in situ as geomorphic features with a significant topographic expression relative to adjacent, time-equivalent strata (Burgess et al., 2013). They tend to have a flat top as a result of the accommodation space being vertically constrained by relative sea level (Schlager, 2005). They are also characterised by presenting steep margins on their edges (Schlager, 2005). As such, isolated carbonate platforms show no significant attachment to a continental landmass. They can comprise several depositional environments such as reefs, lagoons, tidal flats and flanking slopes (Stanton Jr, 1967; Burgess et al., 2013). Structural elements (such as faults), palaeotopography, environment (penetration of light to the seafloor, temperature, nutrients, salinity) and distinct biologic assemblages are some of the mechanisms that, when combined, influence the timing, location, growth and development of isolated carbonate platforms (Schlager,

2005). For instance, the vertical propagation of a fault can modify the seafloor topography, which in turn can influence carbonate platform development.

Research has been primarily focused on the controls and genesis of isolated carbonate platforms, or ICPs as used herein, on large, regional scales of analysis (Bosence, 2005b; Dorobek, 2007). Additionally, stratigraphic relationships and depositional contacts with adjacent structural features have been somewhat generalised in the published literature (Dorobek, 2007). Detailed structural controls have been previously studied focusing on structural highs of sedimentary basins (Zampetti et al., 2004; Saqab and Bourget, 2015a). In contrast to the published literature, this paper focuses on the Karnt Shoals area to understand how underlying propagating faults can control carbonate growth and the morphology of ICPs in the Bonaparte Basin (Figure 2.1). Saqab and Bourget (2015a) have undertaken an analysis of fault controls on ICPs in this same area, with a focus on the “Big Bank” platform located to the northeast of the Karnt Shoals, using a different seismic and well dataset. However, quantitative fault measurements have not been completed at depth in the Karnt Shoals area, i.e. below the ICPs developed on the present-day seafloor. Understanding the relationship between carbonate productivity and fault history can provide useful information in regions with complex extensional faults such as the Northwest Shelf of Australia, where footwall areas and structural highs (horsts) interact to enhance carbonate productivity, isolating the supply of clastic sediment to the region (Bosence, 2005b). Fault growth history can also be used to provide important insights into the development and timing of ICPs, as well as their relationship with carbonate productivity rates.

The Bonaparte Basin (Figure 2.1) contains Neogene deposits that are mainly composed of carbonate successions over which ICPs have developed since the Pleistocene (Saqab and Bourget, 2015a). Isolated carbonate platforms started to develop in areas recording changes in topography during the early Quaternary (Mory, 1991; Saqab and Bourget, 2015a). Some of these platforms were controlled by structural highs (horsts) in a highly faulted region (Burgess et al., 2013). However, the ICPs in the study area have a much more complex story with different periods of faulting and fault reactivation. Therefore, a simple description relating their initiation to a unique mechanism cannot completely address the geological and oceanographic settings in which they were formed. The observed spatial distribution of ICPs relative to fault position suggests more complex controls than just the faulting. There is a good number of ICPs that are not positioned on structural highs and their interior is cross-cut by faults. In detail, this chapter addresses the following questions:

- a) How does the surface fault propagation influence the growth styles and distribution of ICPs, and what is the relationship between carbonate growth and fault-throw rates?
- b) Can the recognition of ICP types help hydrocarbon prospect identification in ICPs, and to predict the best structures for hydrocarbon accumulation?

4.3 Chapter specific datasets and methods

The seismic data used in this study includes a 3D seismic volume (Karnt3D AGC Time) located in the northern part of the Vulcan Sub-Basin, Timor Sea (Figure 2.1).

For a full description of the data resolution, please see section 3.5.1.1. The focus of this study is the Cenozoic interval allowing a very detailed analysis of the ICPs. (Figures 2.3 and 2.4).

The seismic data is in time domain and of very good quality in the Cenozoic interval, allowing for a very detailed analysis of structures and ICPs (Figures 2.3 and 2.4). The survey has been processed by Veritas DGC in 1997 to correct pull-up effects and poor reflector continuity beneath the ICPs (Ruig, 2000; Carezzi and Cazzola, 2008). These pull-up effects are related to differences in lithology. In general, the carbonates within the ICPs have a higher (V_p) velocity than the surrounding strata. Moreover, the ICPs have steep slope angles, which made the acquisition and processing of data more complex due to the angle in which the acoustic waves penetrated the subsurface in those areas (Figure 4.1). As a result, pull-up effects are observed underneath ICPs, as well as below their rims (Figure 2.4 and 4.1). Despite all the efforts to correct these pull-up effects, they are still present in the interpreted seismic volume (Figure 4.1). On variance time slices below the ICPs, the platform outlines are still observed as a result of the velocity pull-up effects (Figure 4.1). In profile view, these effects could be mistakenly interpreted as faults with sub-circular horst-like structures, but normally the strata is continuous across the pull-up zones (Marfurt and Alves, 2015) (Figure 4.1).

Well completion data and proprietary geological reports from four different wells (Mandorah-1, Ludmilla-1, Lameroo-1 and Fannie Bay-1) were used in seismic-well correlations (Figures 4.2 and 4.3). For full details about well data please refer to section 3.5.2.1. Modern bathymetric data (taken from Geoscience Australia contributed to determine the depth, size, shape and position of the ICPs at present (Figure 2.1).

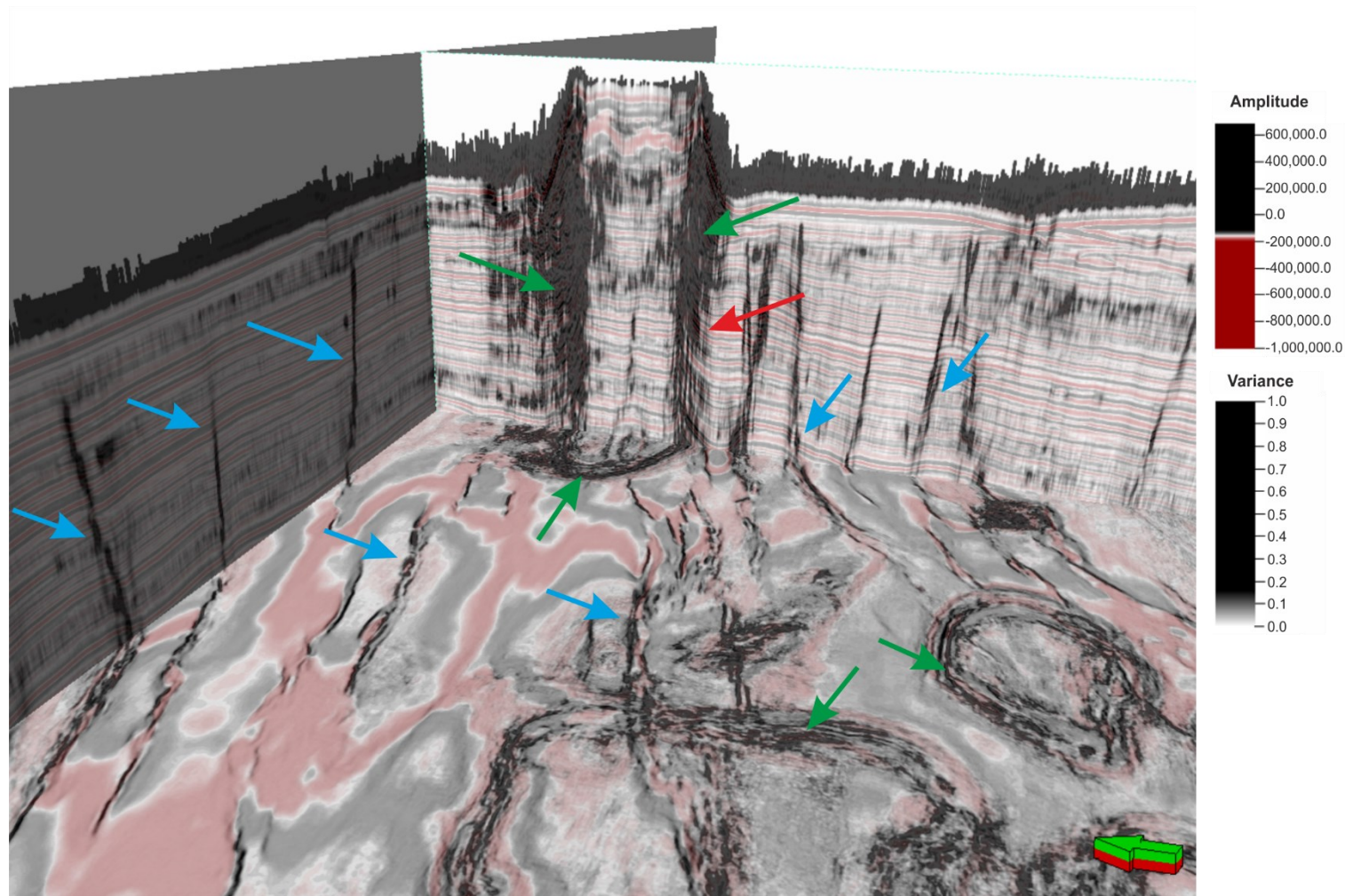


Figure 4.1. Three-dimensional (3D) seismic display of seismic amplitude corendered with the variance attribute at IL 5333, XL 3335, and a time slice at $T=-932$ ms. Velocity pull-up effects are observed as fault shadows or fault-like structures (green arrow) and false “uplifted” strata (red arrow) as a result of spatial changes in V_p across the ICPs. These effects are also observed in time slices as sub-circular features creating false outlines below ICPs (green arrows). Real faults (blue arrows) present continuity in both the time slices and vertical sections, as well as clearly offsetting continuous seismic reflectors.

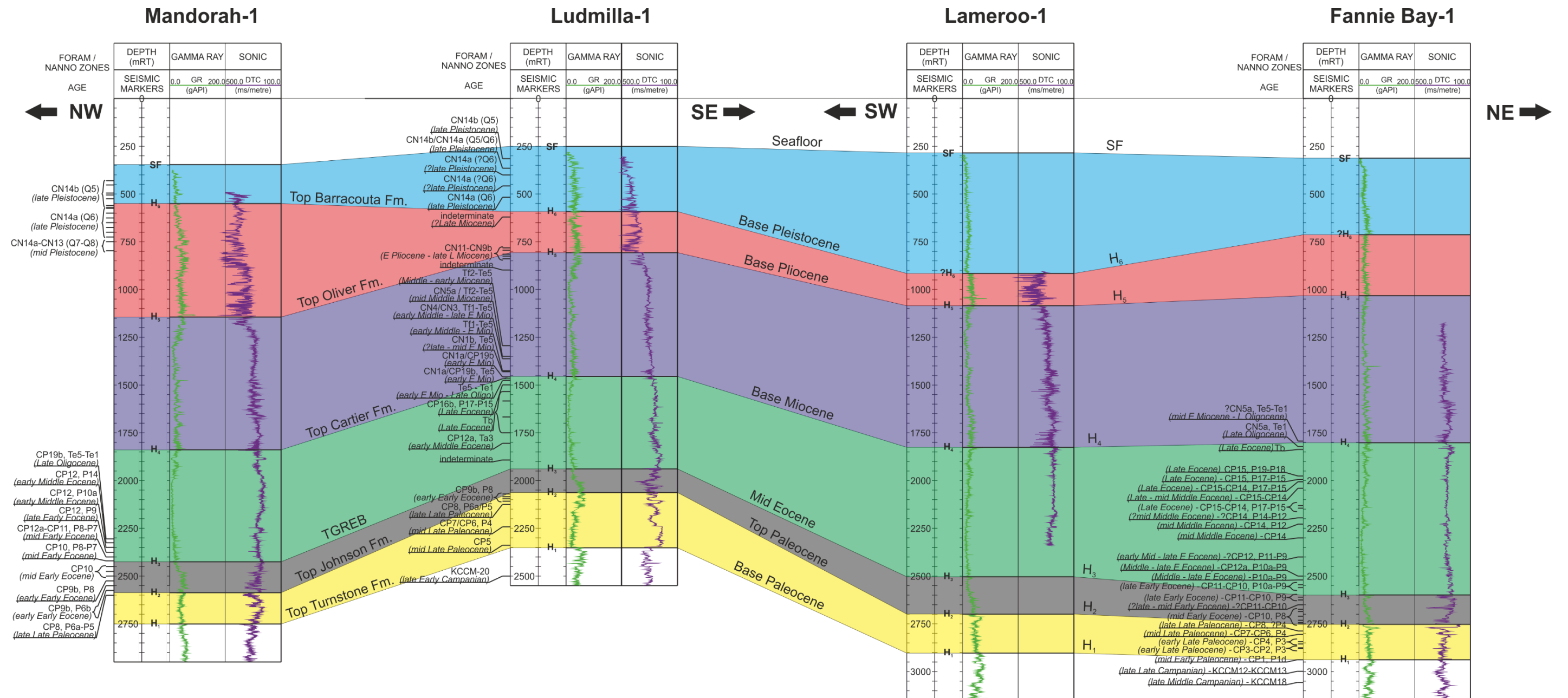


Figure 4.2. Well correlation panel for the study area showing main stratigraphic units, stratigraphic boundaries, and corresponding seismic horizons as interpreted on seismic data. The correlation was performed considering Ludmilla-1 as the principal well in the study area based on its complete gamma-ray (GR) and sonic (DTC) logs, later integrating biostratigraphic (foraminifera and nannoplankton) data taken from raster composite well logs and micropalaeontological reports available for the four wells shown in the figure (Rexilius et al., 1998a, 1998b; Willis, 1998, 1999a, 1999b, 1999c; Rexilius and Powell, 1999a, 1999b). See Fig. 4.9 for well locations and corresponding transect.

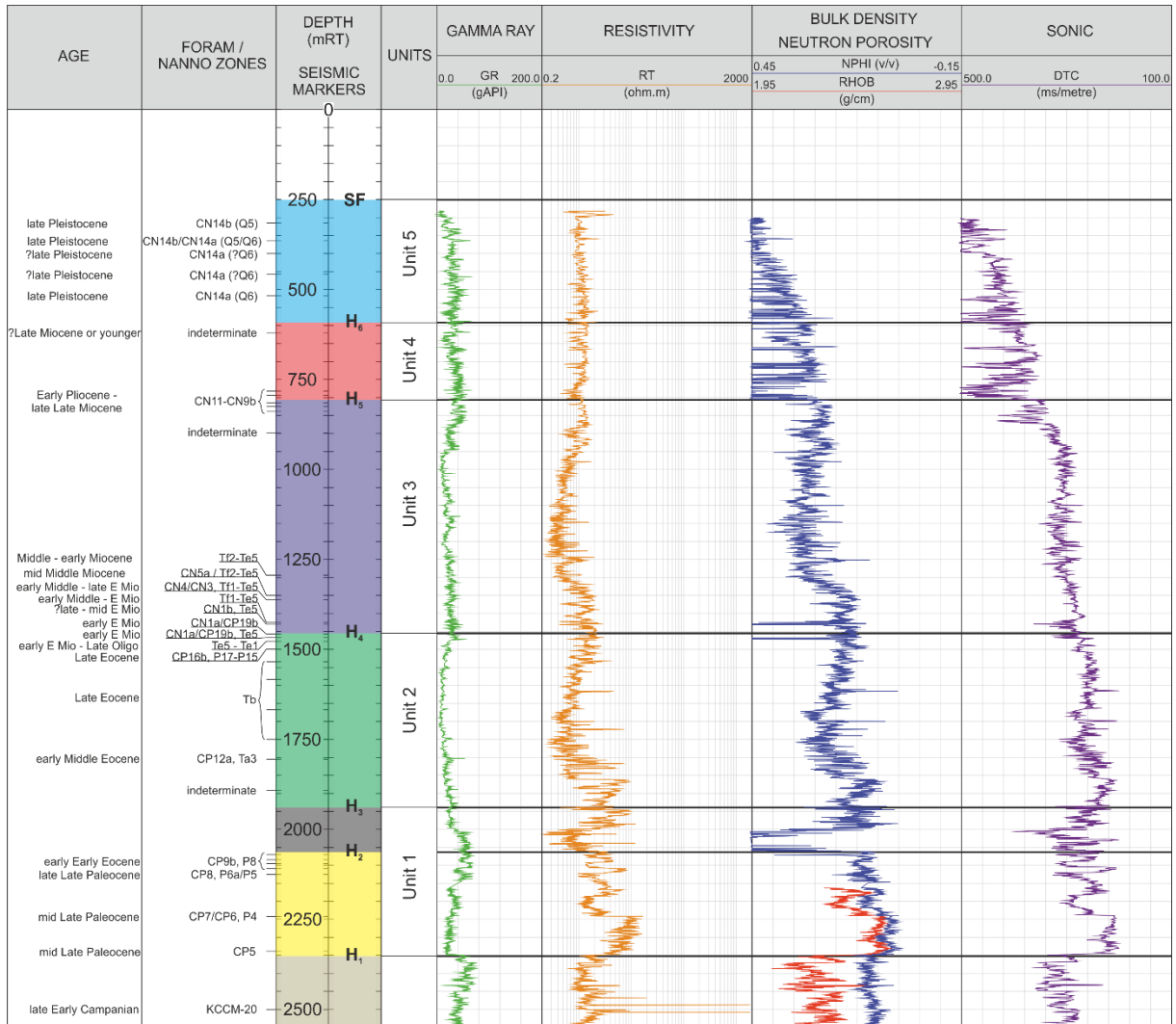


Figure 4.3. Composite log showing GR, RT, NPHI, RHOB and DTC curves for the Ludmilla-1 well. Integrated biostratigraphic data from sidewall core and cutting samples is presented here with foraminifera and nannoplankton zones and their respective ages. Interpreted seismic markers correspond to main seismic horizons considered in this work. Composite log data is taken from Willis (1998).

Table 4.1. Seismic character and lithologies of the seismic units interpreted in the study area. The table correlates the seismic horizons in this work with the horizons defined by Willis (1998).

Epoch	Seismic Unit	Horizon	Comparable horizons	TWT Thickness (ms)	Internal Character, Geometry, and Terminations	Lithology
Pleistocene	5	--Seafloor--	--Sea Bed--	200-650	Moderate- to high- amplitude reflectors. Chaotic under ICBs and parallel to discontinuous in other areas.	Yellowish-grey coarse-grained calcarenites interbedded with silty calcilutites.
Pliocene	4	-- H ₆ --	-- BPLE --	110-350	Moderate- to high-amplitude continuous reflections. Fault offsets present in the reflectors.	Light olive grey calcareous claystone.
Miocene	3	-- H ₅ --	-- BPLI --	350-550	Low- to moderate amplitude internal seismic reflections, subparallel to wavy. Highly faulted reflections.	Greenish grey to light grey calcareous claystone interbedded with greenish grey to very light grey argillaceous calcilutites and light grey arenaceous calcarenites.
Oligocene	2	-- H ₄ --	-- TM3 --	170-550	Low- to moderate amplitude seismic reflections, subparallel to wavy. Seismic reflections intersected by faults.	Light olive-grey calcareous claystone, olive- to yellow-grey argillaceous calcilutites, and yellow-grey to light grey calcilutites with minor yellowish-grey medium to coarse calcarenites.
Late Eocene		-- H ₃ --	-- TGREB --			
Early Eocene	1	-- H ₂ --	-- TE2 --	0-120	Moderate- to high- amplitude internal reflections. Unit truncating to the west.	White to light grey very fine to fine grained sandstones.
Paleocene		-- H ₁ --	-- T --	0-200	Moderate amplitude sub-continuous reflections. Wedge-shaped seismic unit thickening towards the south.	Light olive-grey calcareous claystone and yellow-brown and very light grey medium to coarse grained calcarenites; white to very light calcilutites, interbedded with light grey calcareous claystone.

4.3.1 Physiography of the Karmt Shoals

Carbonate platforms can develop along basin margins on continental shelves (Kendall and Schlager, 1981). ICPs in the Bonaparte Basin are situated on the upper continental slope along the shelf margin (Veevers, 1971) (Figure 2.1). The growth and development of ICPs can be attributed to different factors including tectonic movement, sediment supply, tectonic subsidence, relative sea level changes, amongst others (Wilson, 1999; Pomar, 2001; Zampetti et al., 2004; Dorobek, 2007; Sattler et al., 2009; Ding et al., 2014). For instance, Van Tuyl et al. (2018) have identified ICPs rooted on pinnacle reefs in the Browse Basin, further south, with pinnacles providing shallow areas for the preferential growth of ICPs.

Isolated carbonate platforms in the Bonaparte Basin have a circular and ellipsoidal morphology in map view. Some of the most recognisable features of the ICPs in the Karmt Shoals are interior patch reefs, interplatform channels such as the ones within ICP ϵ , and moat channels (Veevers, 1971; Saqab and Bourget, 2015a) (Figure 4.4).

Moats surrounding ICPs have been interpreted by Veevers (1971) as resulting from subsidence caused by the loading of the same structure over unconsolidated sediment (Figure 4.4). Different platform sizes are observed in the study area, ranging from 500 m to 18,000 m in length. The isolated platforms are aligned along a NE-SE direction (Figure 4.4). This is a similar direction to the shelf margin (Figure 2.1). In bathymetric data, the ICPs are observed as shallow topographic features at a water depth of 20-40 m (Figure 2.1).

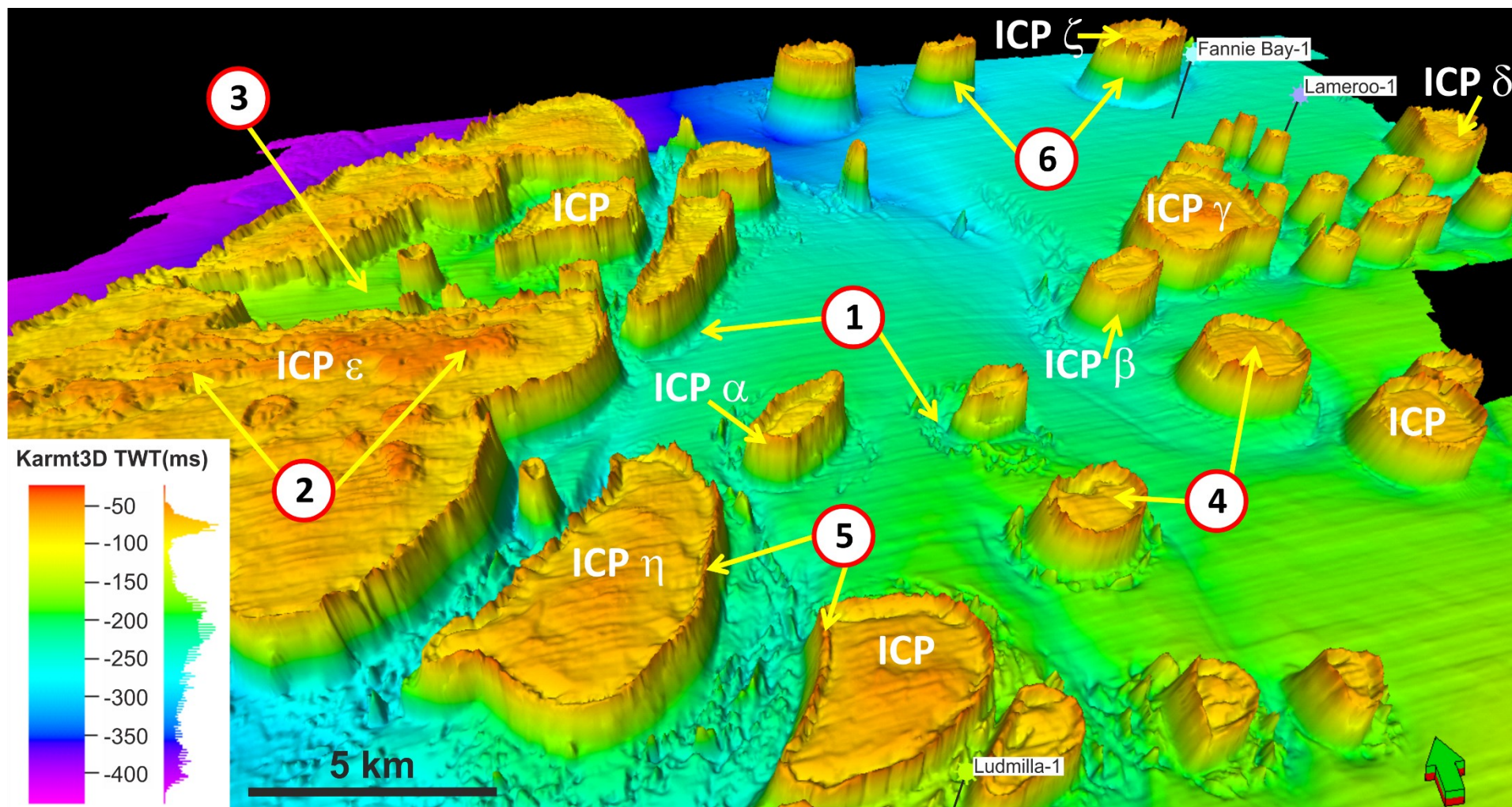


Figure 4. 4. Three-dimensional (3D) perspective of the seafloor as interpreted from the Karmt3D seismic volume. The map displays the Karmt Shoals with several isolated carbonate platforms (ICPs). (1) Moat channels surrounding ICPs, (2) interior patch reefs, (3) interplatform channels, (4) lagoon, (5) platform rim, (6) steep platform slope.

4.3.2 Seismic interpretation

Horizon and fault interpretation were performed in both vertical and map sections using seismic amplitude and variance data (Figure 4.1). Key seismic reflectors were mapped in the 3D volume following basic stratigraphic principles (Alves et al., 2006; Catuneanu, 2006; Mattos et al., 2016) so as to identify the primary stratigraphic events from the Base Paleocene (H_1) to the modern seafloor (SF) (Figures 2.2 and 2.3). Well-log (gamma ray, resistivity, bulk density, neutron porosity and sonic) and biostratigraphic data from four exploratory wells were integrated into the seismic volume (Figure 4.3). The seismic surfaces and units were also compared with previous interpretations by Willis (1998) (Figures 2.2, 4.2, 4.3 and Table 4.1).

Key seismic horizons were mapped every 150 m in NE-SW and NW-SE amplitude seismic sections using strict autotracking parameters on Schlumberger Petrel®. Isochron maps were calculated based on the interpreted horizons in order to determine the variation in thickness of the different units (Figure 4.5). For fault interpretation, a variance attribute was extracted to better define major seismic discontinuities (e.g. fault, channels, karst features) (Figures 4.1 and 4.7). Variance compares the similarity of traces in all directions on an interpreted surface (Chopra and Marfurt, 2007), highlighting prominent discontinuities such as faults and fractures (Brown, 2011; Marfurt and Alves, 2015). Faults were initially mapped on variance time slices to determine their length and strikes. The strikes of the faults do not coincide with the inlines (IL) or crosslines (XL) of the seismic survey (Figures 4.6, 4.7 and 4.8). These sections crosscut the fault with an arbitrary angle (β) between the IL or XL and the strike of the fault.

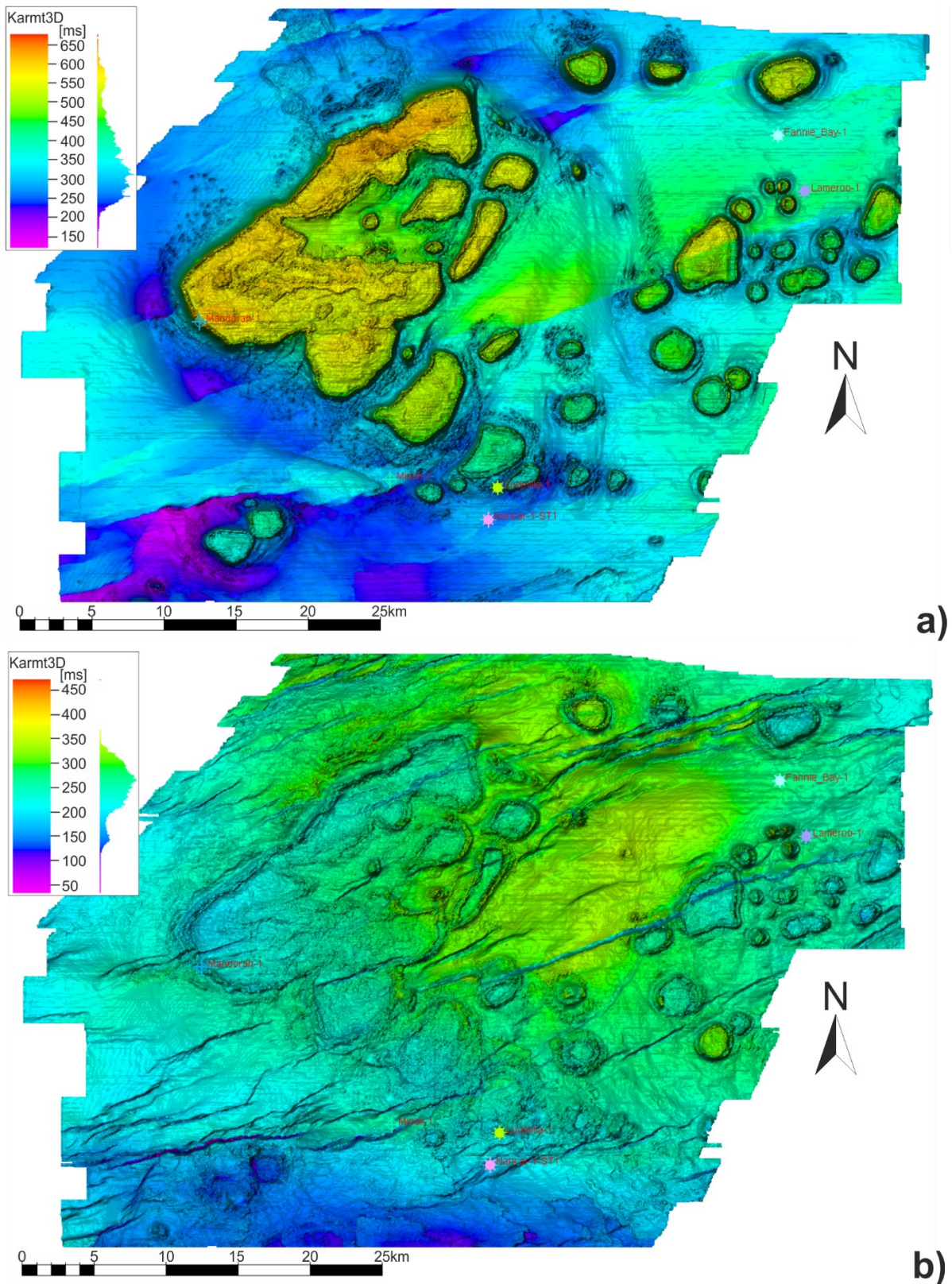


Figure 4.5. Isochron maps showing the TWT thickness of different seismic-stratigraphic units. (a) Isochron map of Unit 5 from the Seafloor to horizon H_6 . (b) Isochron map of Unit 4 from horizons H_6 to H_5 . (c) Isochron map of Unit 3 from horizon H_5 to horizon H_4 . (d) Isochron map of Unit 2 from horizon H_4 to horizon H_3 .

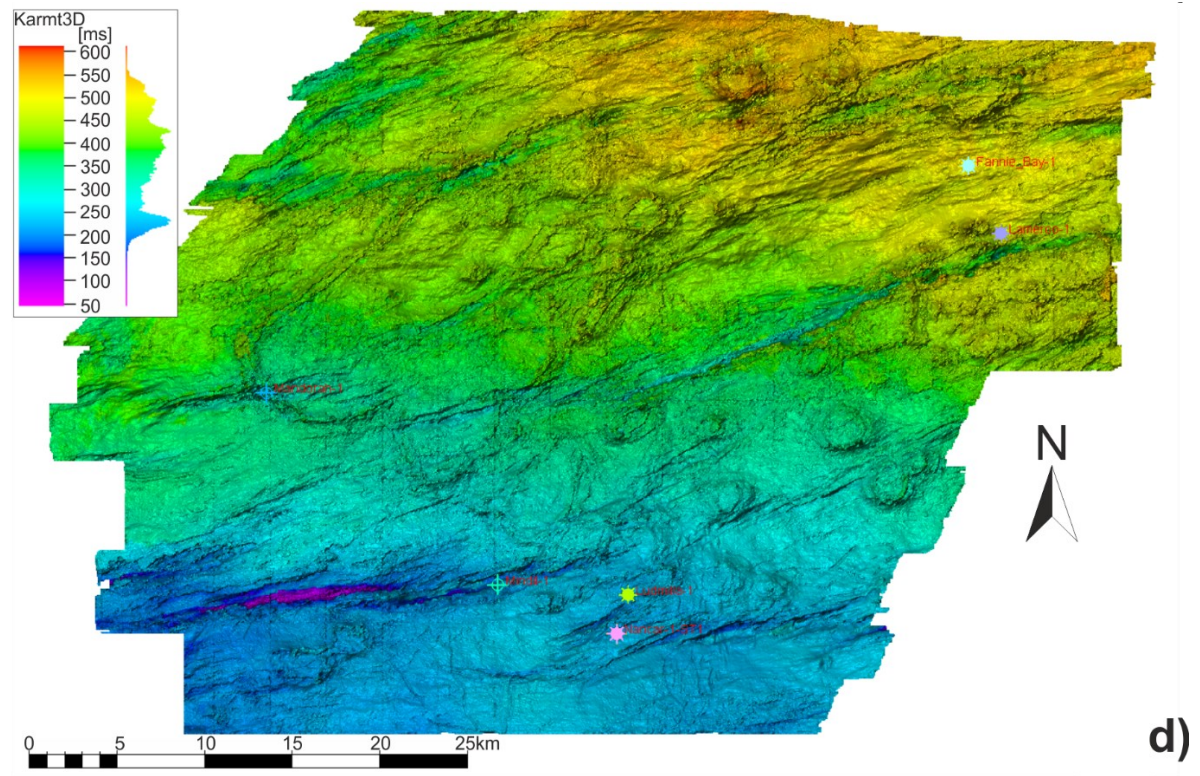
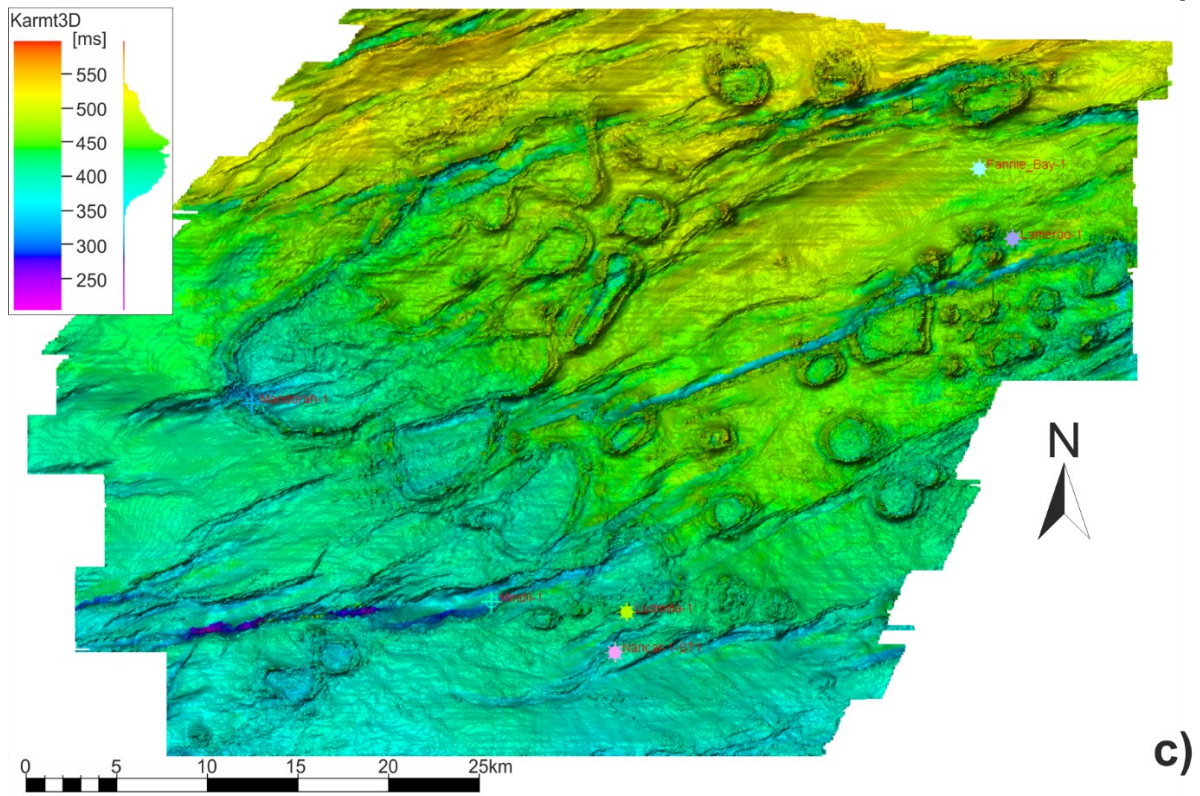


Figure 4.5. Continued.

Base Pleistocene (H_6) - Time Structure Map

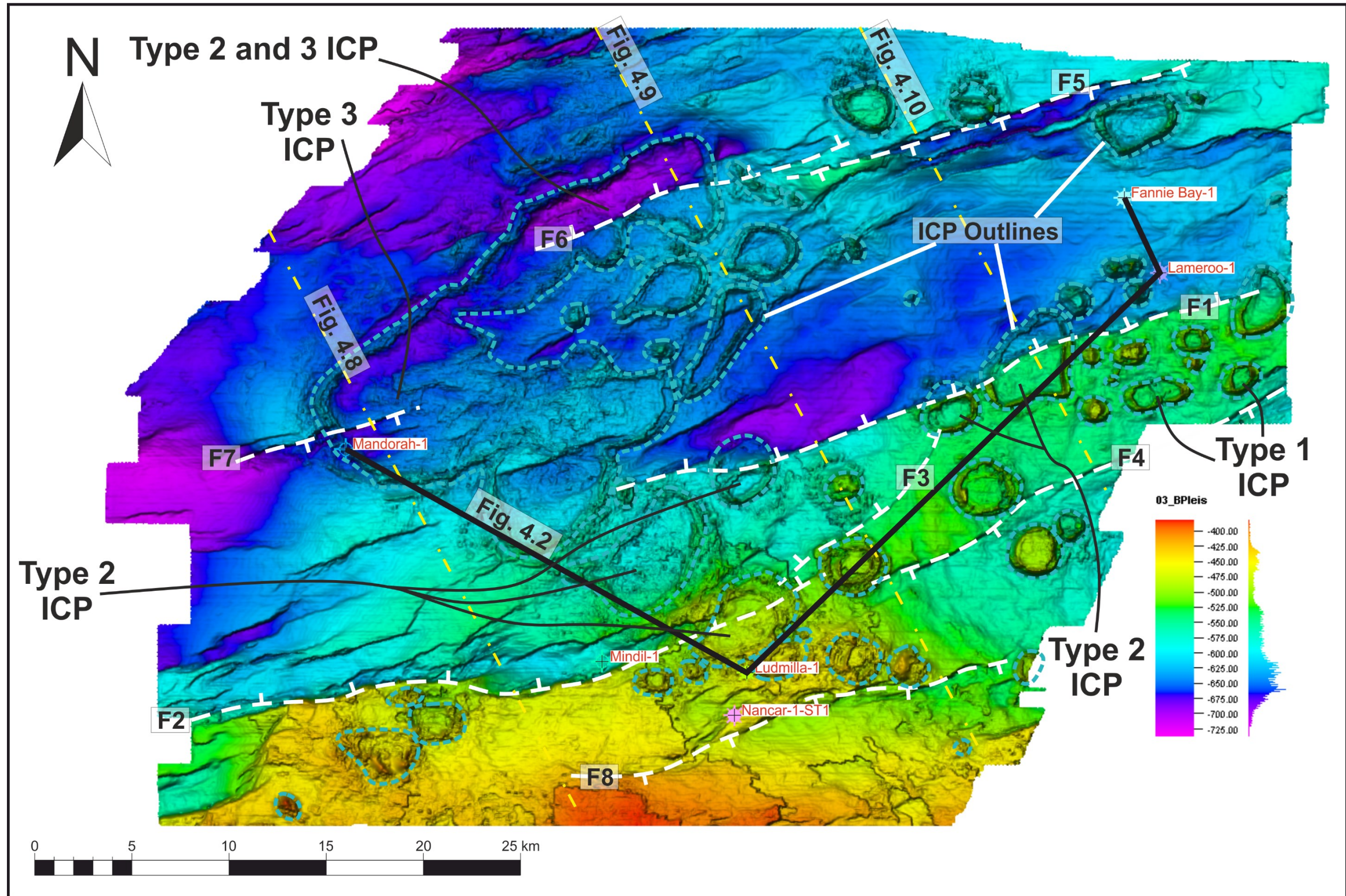


Figure 4.6. Time structure map of the base Pleistocene (horizon H_6) showing the major fault arrays (white dashed lines) in the study area with a general trend NE-SW. ICPs (blue dashed lines) are identified with their types for reference. Thick black line indicated the well correlation shown in Figure 4.2.

Base Pleistocene (H_6) - Coherence Map

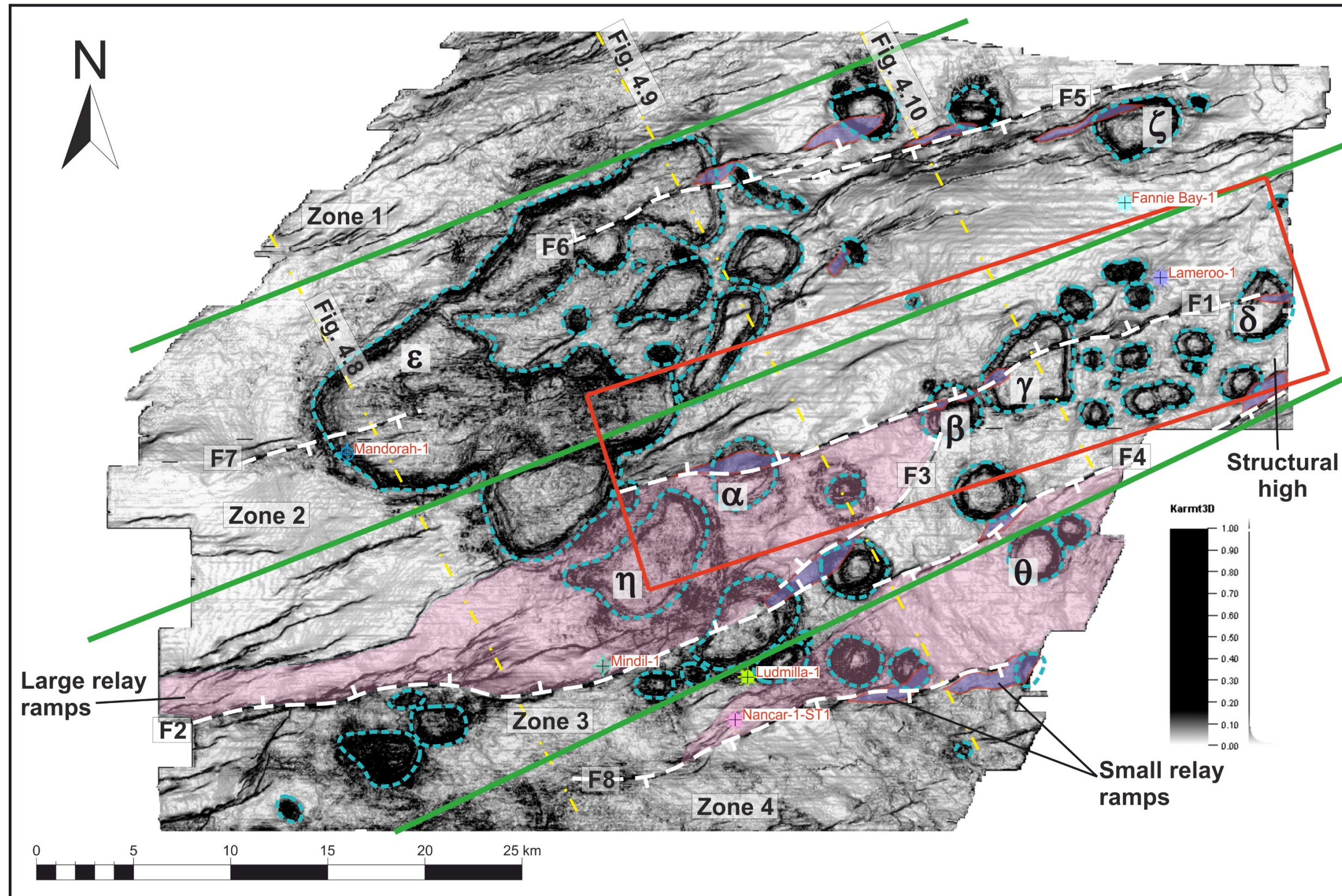


Figure 4.7. Variance map of the base Pleistocene (horizon H_6) showing the four structural zones (separated by green solid lines) identified in the study area. Large (light pink polygons) and small (purple polygons) relay ramps are mapped to show their relation to ICPs. The red rectangle represents the area of interest in which detailed throw measurements were undertaken to generate T-Z plots (Figure 4.11), T-D plots (Figure 4.12) and the high-resolution contour fault-throw map in Figure 4.13.

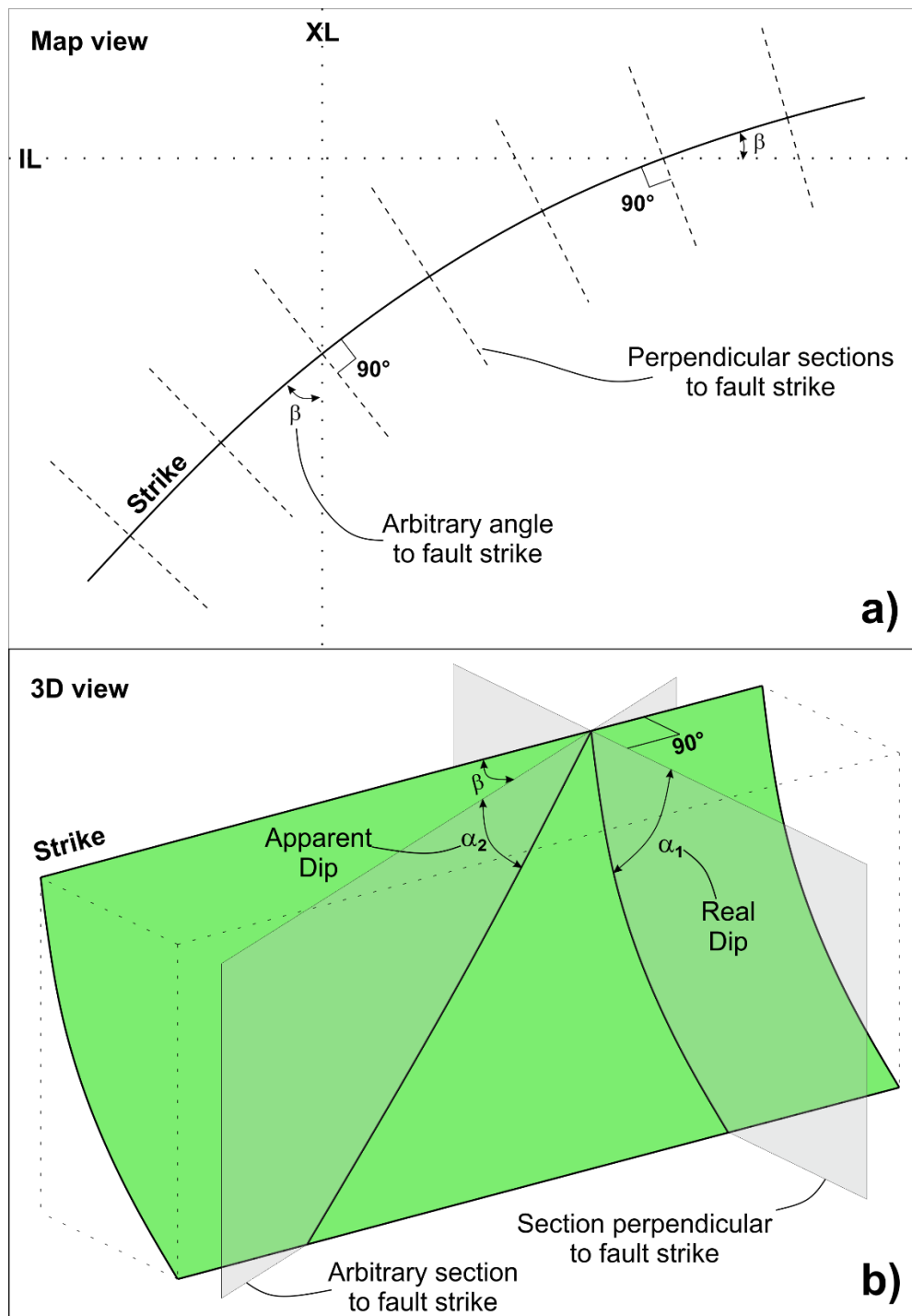


Figure 4.8. Diagrams summarising the methodology adopted to collect T-Z and T-D data across the Karmt3D seismic volume. (a) Map view of a fault on a hypothetical time slice. Seismic sections used to compile T-Z and T-D data were perpendicular to the strike of a given fault at each discrete measuring point, as most faults are slightly curved in the study area. Inlines (IL) and cross-lines (XL) are not useful as they cut the fault at an arbitrary angle β . (b) Three-dimensional (3D) view showing a fault with two intersecting sections; one perpendicular to strike in which the fault dip (α_1) can be taken, and a second section intersecting the fault at an arbitrary angle to its strike. This latter section will only provide the apparent dip of the fault.

Interpreted faults in the interpreted sections show the apparent dip (α_2) of the fault, which is less than the real dip (α_1) (Figure 4.8) and can lead to erroneous throw measurements. For this reason, perpendicular sections to the strike of the fault at each point of interest were created (Figure 4.8a). These sections are key to visualise the real (maximum) dip (α_1) of the fault (Figure 4.8b) and later corroborate the interpretation. They provide the maximum throw values that are required to obtain good quality data for the T-Z and T-D plots. Structures such as relay ramps are observed in the study area, and their recognition was deemed important to understand the way(s) fault segments are linked in the study area. Different zones were established based on features observed on variance data in order to aid a distinction between different fault sets and types of ICPs (Figures 4.7, 4.9, 4.10 and 4.11).

4.3.3 Fault-throw measurements

Fault-throw measurements were taken from different fault segments to create detailed fault-throw-depth (T-Z) (Figure 4.12) and throw-distance (T-D) profiles (Figure 4.13c), and thus generate a high-resolution throw contour map (Figure 4.14). Fault-throws are used instead of total displacements because the faults in the area are steeply dipping and show small heaves. Therefore, the most convenient fault interpretation method is to measure the vertical difference (throw) between correlative seismic reflectors on the hanging-wall and footwall blocks (Cartwright et al., 1998).

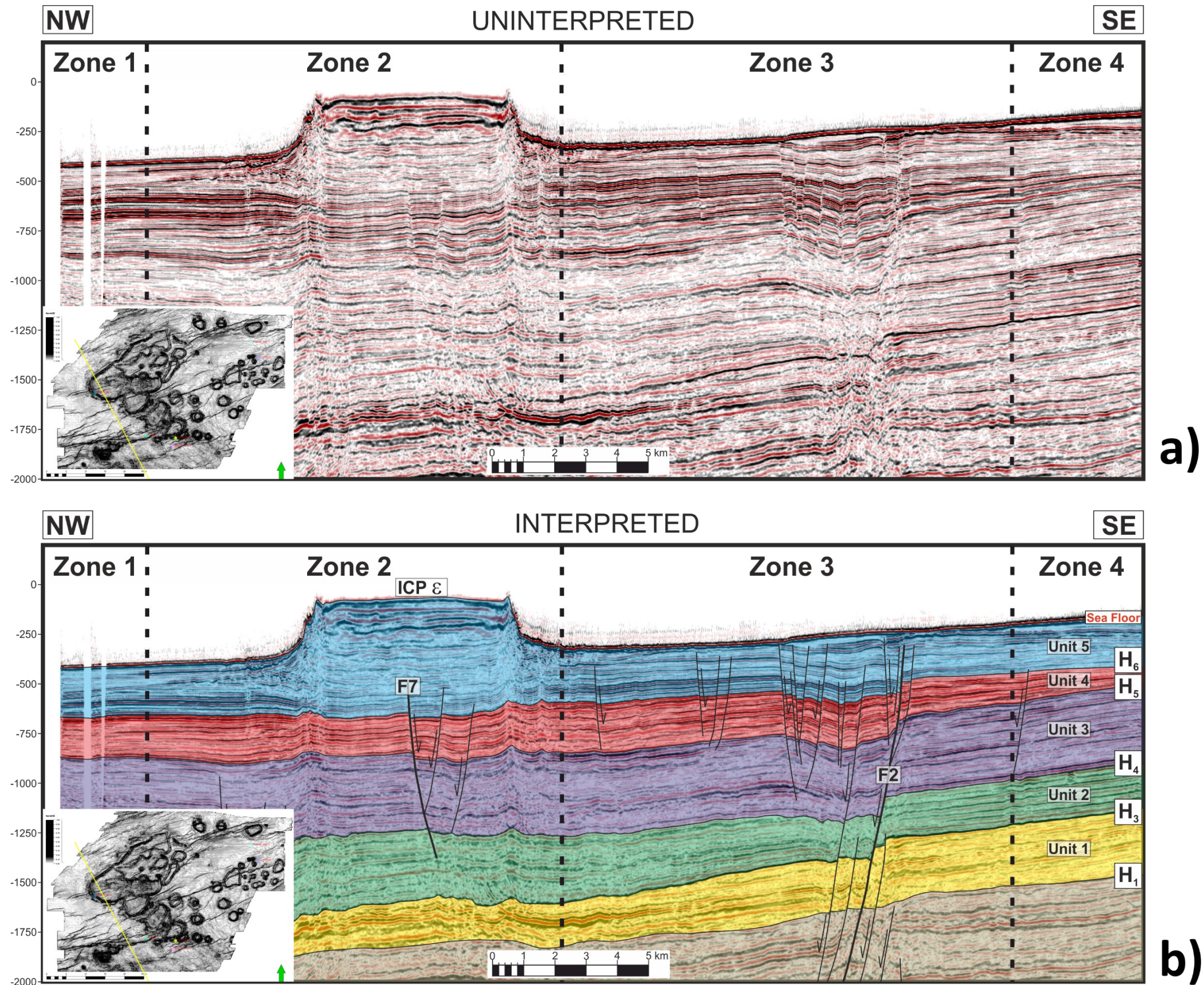


Figure 4.9. (a) Uninterpreted NW-SE seismic profile and (b) corresponding interpretation showing four different zones in the SW of the study area. Zone 1 shows no faulting. In zone 2, there are two different fault systems: one Neogene-Quaternary and an older Paleogene in age. An ICP developed above the Neogene-Quaternary faults. Zone 3 presents highly faulted Neogene-Quaternary strata with faults propagating to the surface, as well as Paleogene faulting. Within zone 4, there is only one small fault offsetting Neogene-Quaternary strata.

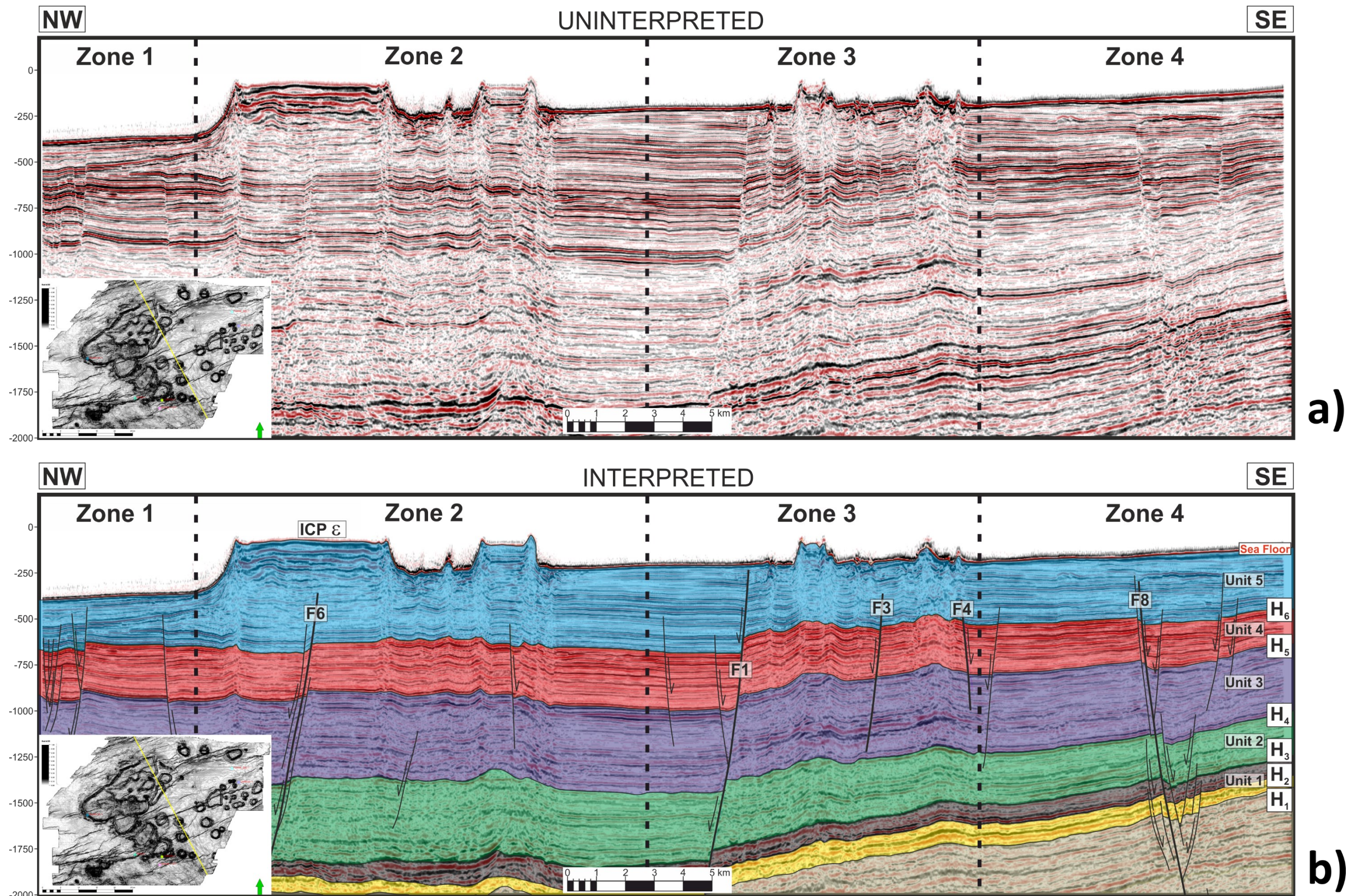


Figure 4.10. (a) Uninterpreted NW-SE seismic profile and (b) corresponding interpretation showing three different zones in the centre of the study area. Zone 1 shows normal fault systems. This zone is characterised by the absence of ICPs. Zone 2 shows the presence of the two fault systems: Neogene-Quaternary and Paleogene. There are faults below the two ICPs in this zone. Zone 3 contains the major fault in the area (F1), which propagates to the surface; and minor Neogene-Quaternary normal faults. Zone 4 includes a large fault area with synthetic and antithetic faults.

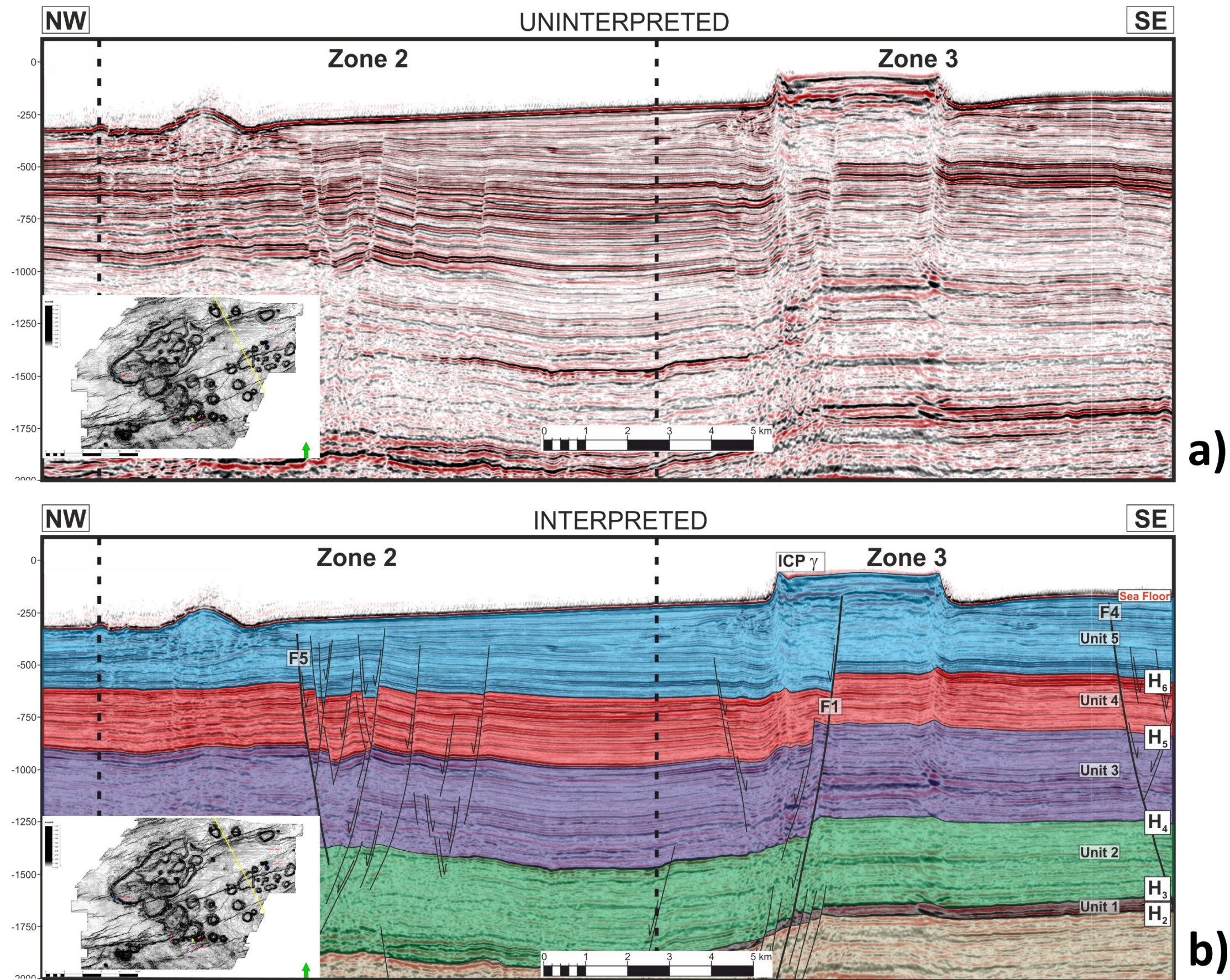


Figure 4.11. (a) Uninterpreted NW-SE seismic profile and (b) corresponding interpretation showing three different zones in the NE of the study area. Zone 1 does not reveal faulting. In zone 2 there are antithetic faults in Neogene-Quaternary strata. Zone 3 is highly faulted and the ICP is underlain by a major fault (F1).

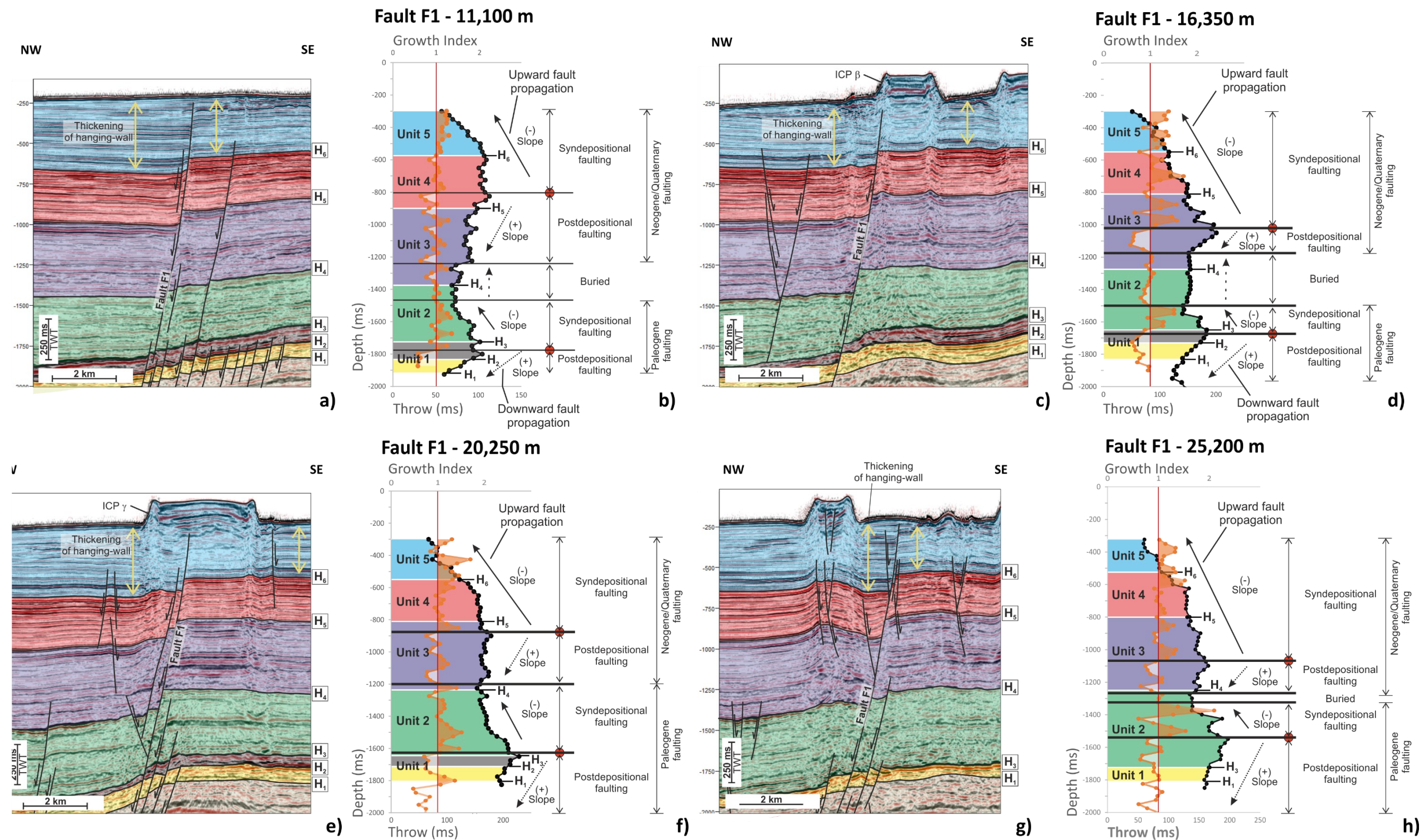


Figure 4.12. Fault-throw (T-Z) profiles (black curves) and growth index plots (orange curves) with corresponding seismic profiles showing specific measurement points in a direction perpendicular to the strike of fault array F1. Profiles were taken at various distances along F1, from southwest to its northeast (see distances above each of plots shown). For the location of the lines along the fault plane, see Figure 4.13c. Across the study area there are two throw maximas (red circles), indicating a period of fault initiation. The first period of faulting occurred during the Late Paleocene-Early Eocene with downward fault propagation (dotted arrow line) into Unit 1 and upward fault propagation (solid arrow line) into Unit 2. There is a period of fault inactivity between Units 2 and 3, which is represented by an almost constant throw (dashed arrow line). The second period of faulting occurred during the Late Miocene-Early Pleistocene with a downward fault propagation into the base of Unit 3 (dotted arrow line) and upward syn-depositional fault propagation into Units 4 and 5 (solid arrow line). The rapid decrease in throw near the seafloor reflects the presence of a growth sequence. It can also be observed in the form of values greater than 1.0 on the growth index plot. Horizontal lines indicate the interpreted seismic horizons.

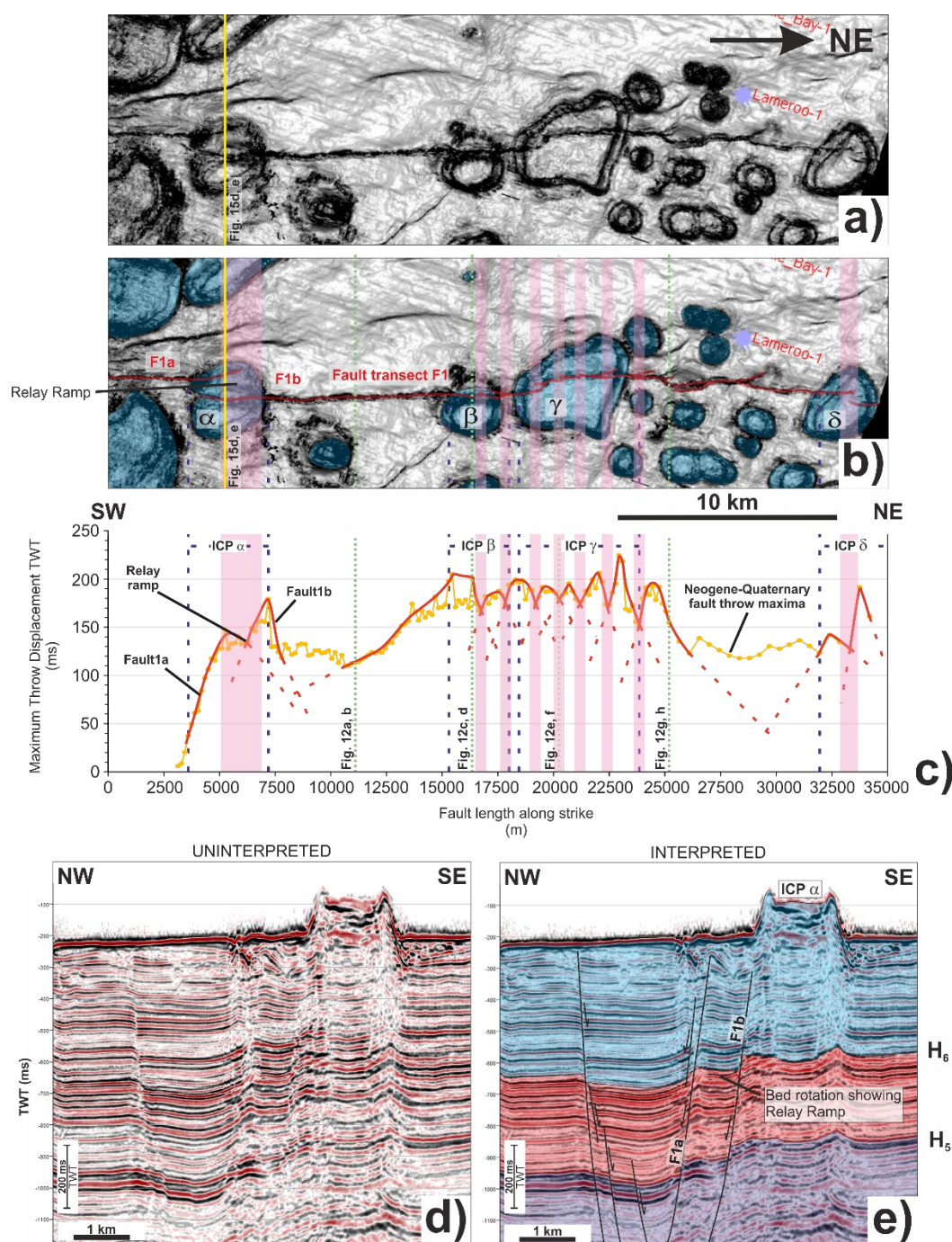


Figure 4.13. (a) Uninterpreted and (b) interpreted variance data for the area of interest recognised on the time-structure map of horizon H₆. Different fault segments, displayed as solid red lines, are identified along fault F1 - thus identifying it as a ~50 km long fault array. ICP outlines are shown in blue. Symbols α , β , γ and δ represent the ICPs crossing fault array F1. The bright yellow solid line indicates the position of the cross section. (c) Maximum fault-throw profile (T-D Plot) of fault array F1 in Neogene-Quaternary strata showing different fault segments with a red line. The blue dashed lines represent the boundaries of the ICPs, and the green dashed lines indicate the position of the T-Z plots displayed in Figure 4.12. Relay ramps are located where two different fault segments intersect and throw values are relatively small. These relay ramps are shown in pink. (d) Uninterpreted NW-SE seismic profile and (e) corresponding interpretation showing fault segments F1a and F1b and a relay ramp in-between.

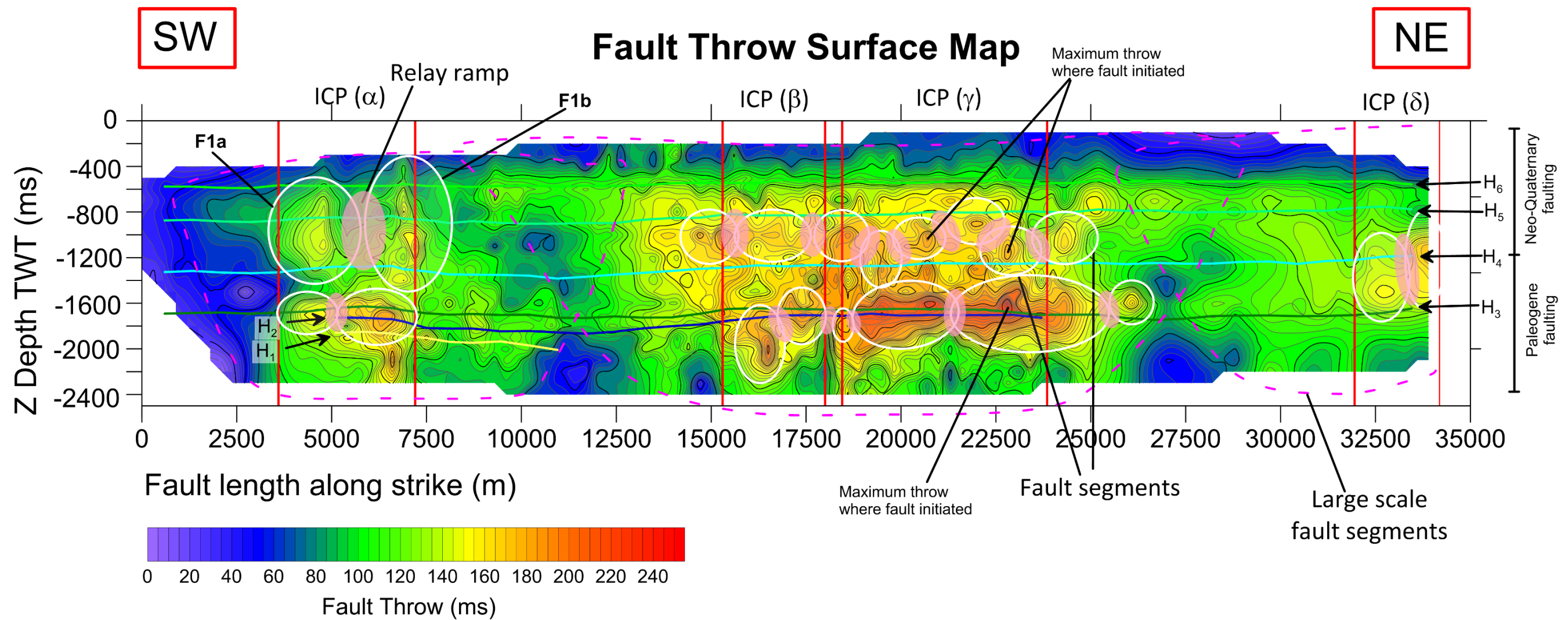


Figure 4.14. High-resolution fault-throw surface map along the strike of fault array F1, shown with a 3x vertical exaggeration. Cold colours represent the smallest throw values, whereas warm colours indicate relatively large throws. The hanging-wall levels of the interpreted horizons (H₁ to H₆) are displayed for reference. The position of the ICPs is drawn with red lines. White line ellipses represent the interpreted individual fault segments. Pink dashed lines represent the large-scale fault segments. The areas with small throw values between the individual fault segments coincide with relay ramps, which are plotted as pink zones. The presence of two faulting events (Paleogene and Neo-Quaternary) separated by horizon H₄ is clear in the fault surface map. The position of Quaternary ICPs is also shown in the figure and related to the presence of relay ramp zones.

Twenty (20) interpreted seismic horizons were used as key markers when collecting throw data. Throw measurements were taken from seismic sections perpendicular to the strike of faults. An along-strike spacing of 150 m was used between each measurement and along-dip spacings of 25 ms, thus complying with the minimum 'delta ratio' of Tao and Alves (2019) necessary to acquire reliable T-D and T-Z data. This degree of detail led to an accurate estimation of fault-throws and to the completion of high-resolution fault map surfaces.

4.3.4 ICP fault and area distribution

The area of each ICP was measured from different time slices (Figure 4.15) to produce a histogram displaying frequency versus ICP area (Figure 4.16a). Detailed analysis was undertaken to determine if there is a correlation between the size of the ICPs and: 1) the number of faults crossing the structures, as well as 2) the number of faults surrounding the ICPs within a radius of 500 m (Figure 4.16b and c). For this analysis, different time slices were taken, from the base Pleistocene horizon to -216 ms with a spacing of 64 ms (Figure 4.15). For each ICP, the number of crossing faults and surrounding faults (where possible) were counted and plotted in Figure 4.16a and b. These analyses were constrained by the inherent vertical and horizontal seismic resolution of the Karmt3D seismic volume. Only large-scale faults visible on seismic data were taken into account in the analysis.

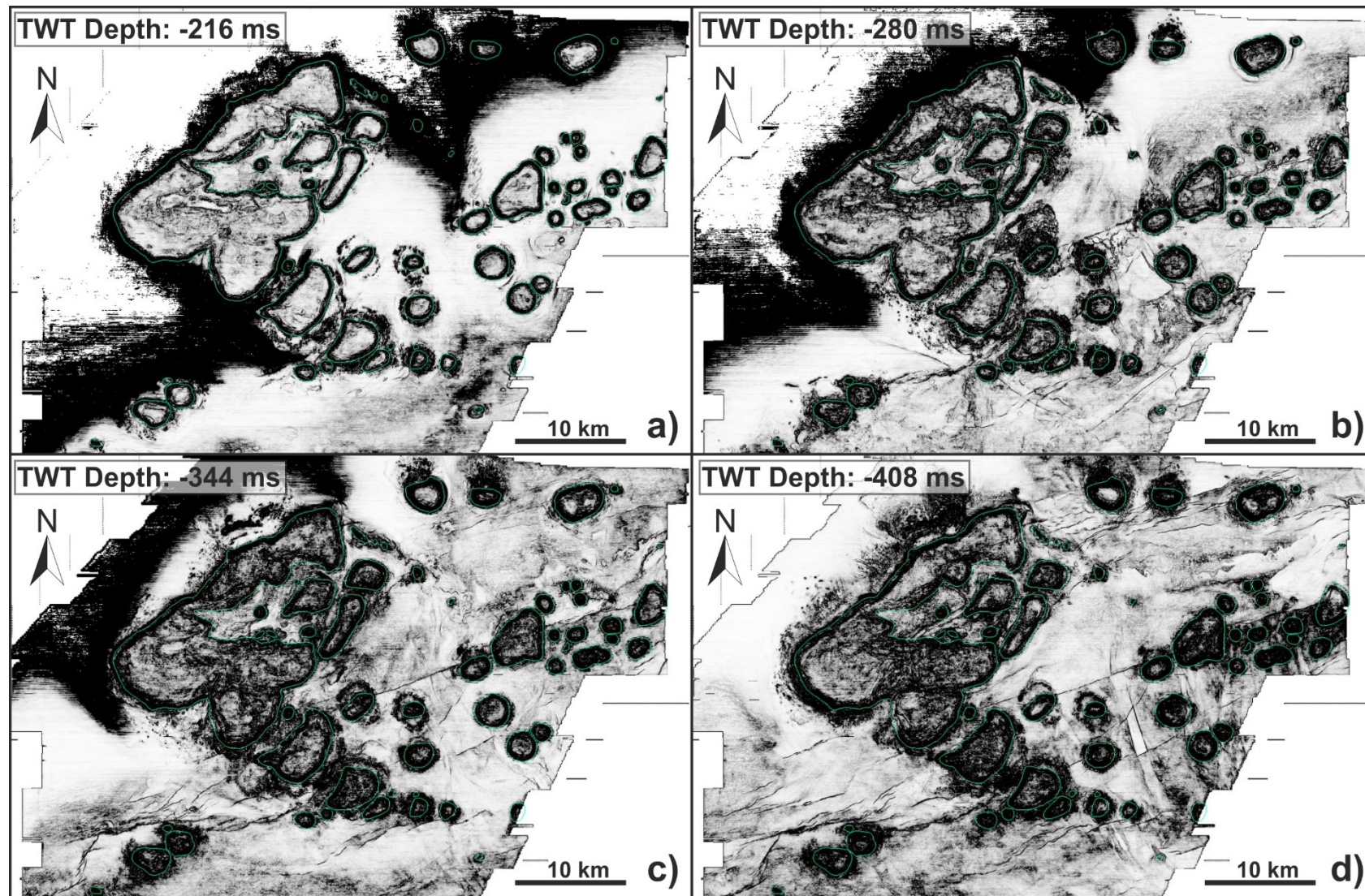


Figure 4.15. Variance time slices across the Karmt3D seismic volume, with a spacing of 64 ms, from the base Pleistocene to -216 ms. ICPs are highlighted by the light blue outline.

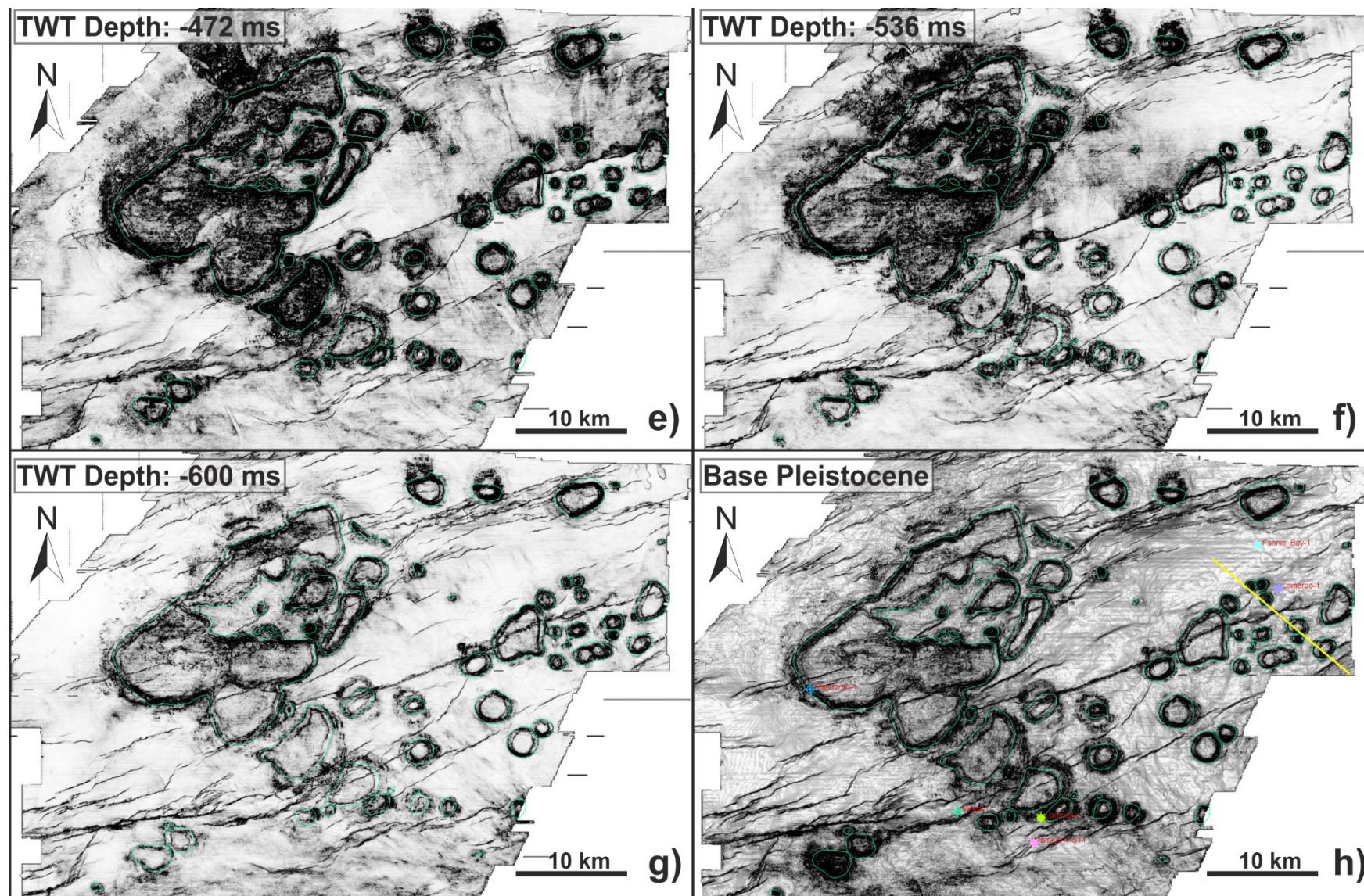


Figure 4.15. Continued.

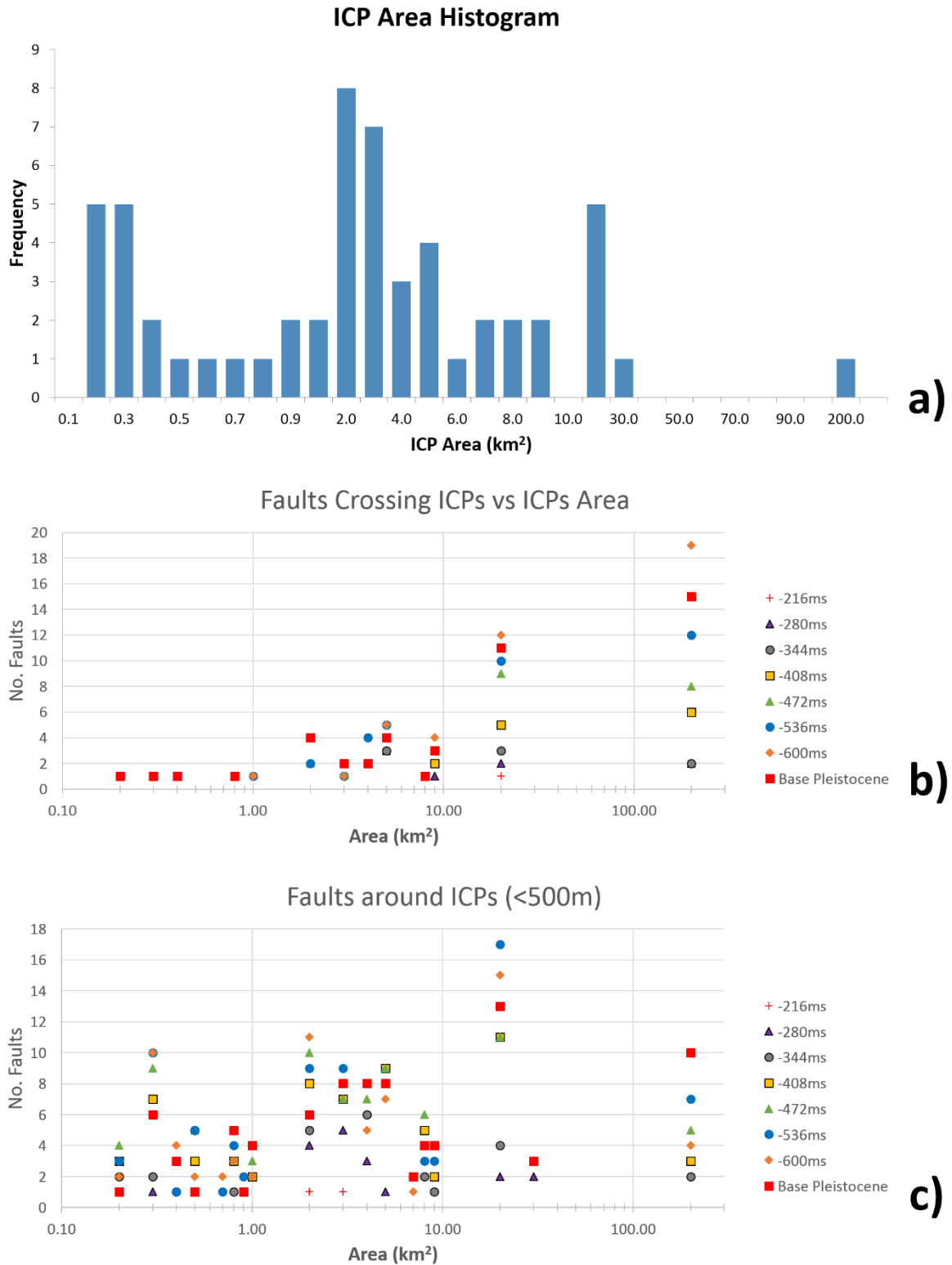


Figure 4.16. Histogram and scatter plots showing (a) the multimodal area distribution of ICPs; (b) ICP area against the number of crossing faults; and (c) ICP area vs. the number of faults around ICPs within 500 m.

4.4 Seismic stratigraphy

Several seismic horizons were identified and mapped within the Karmt 3D survey. In Figure 4.9, seven key seismic-stratigraphic horizons are displayed, ranging in age from the Base Paleocene to the seafloor. These horizons divide Cenozoic strata into six distinct seismic units (Figures 2.2 and 4.2). All seismic-stratigraphic surfaces were correlated with wireline data and biostratigraphic data in order to constrain their ages and thickness (Figures 4.2 and 4.3).

4.4.1 Unit 1: Early Eocene-Paleocene

The lower boundary of Unit 1 coincides with horizon H_1 and comprises Early Eocene-Paleocene strata (Figures 2.2, 2.3 and 4.3). Horizon H_1 coincides with the Top of the Bathurst Island Group ('BIG' in Figure 2.2) at a depth of 2321.5 m in the Ludmilla-1 well (Figure 4.3). Horizon H_1 can only be mapped in the south of the 3D survey, as it pinches out towards the north. Internally, it presents medium to low-amplitude positive seismic reflections. On well-log data, H_1 shows an abrupt change in density with the highest values reaching 2.6 g cm^{-3} (Figure 4.3). Unit 1 has an average thickness of 120 ms and is bounded at its top by H_2 , which correlates to the Top Paleocene (Figure 2.2). This horizon shows a high positive amplitude and pinches out against H_3 towards the north. The lower Unit 1 comprises light olive-grey calcareous claystones and predominantly medium- to coarse-grained yellow-brown and very light grey calcarenites, part of the Johnson Formation (Willis, 1998) (Table 4.1). Horizon H_2 is recognised on well logs as a dramatic change in density with values reaching 1.95 g cm^{-3} . The resistivity values are also low in this unit, ranging from 0.2 to $4 \Omega \text{ m}$ (Figure 4.3).

One of the strongest positive reflections in Unit 1 is horizon H₃, which marks the top of the Hibernia Formation (Figure 2.2). In the Ludmilla-1 well, this reflection correlates with the top of the Grebe Sandstone Member and occurs at a depth of 1908.5 m (Figure 4.3). Horizon H₃ marks the top of the 110 ms-thick upper Unit 1. The predominant lithology of the Grebe Sandstone Member is a white to light grey fine sandstone (Willis, 1998) (Table 4.1).

4.4.2 Unit 2: Oligocene-middle Eocene

Unit 2 has an upper boundary at the top of the base Miocene unconformity (horizon H₄), which coincides with a high to moderate positive amplitude reflection (Figures 2.2 and 2.3). In the Ludmilla-1 well, this reflection corresponds to the top of the Cartier Formation and occurs at a depth of 1424.5 m (Figures 2.2 and 4.3). The lower boundary of Unit 2 coincides with H₃, a Mid-Eocene unconformity. Unit 2 is relatively thick (200 ms-550 ms) and includes the Prion and Cartier Formations (Figure 2.2). Unit 2 is an interval comprising greenish grey calcareous claystones interbedded with olive-grey to yellow-grey, moderately hard argillaceous calcilutites with minor yellowish-grey calcarenites (Willis, 1998) (Table 4.1). This interval is highly faulted across the interpreted seismic survey.

4.4.3 Unit 3: Miocene

The basal surface of Unit 3 corresponds to horizon H₄, whereas its top surface correlates to horizon H₅. Horizon H₅ marks the base of Pliocene strata according to biostratigraphic data and coincides with the top of the Oliver Formation at a depth of 776.5 m in the Ludmilla-1 well (Figures 2.2 and 4.3). On seismic data, horizon H₅

is a high to moderate negative amplitude reflection that is easily mapped across the study area (Figure 2.3). This unit is relatively thin (200-250 ms) to the south and thickens to the north, where it shows an average of 500 ms (Figure 4.5). Unit 3 presents internal reflections with fairly parallel geometries and low to moderate amplitude. On wireline data, H₅ marks an abrupt change in neutron and sonic logs from relatively low values in Unit 3, to high values in Unit 4 (Figure 4.3). The Oliver Formation is mainly composed of light olive-grey calcareous claystones interbedded with greenish argillaceous calcilutites and light grey, dominantly fine to medium grained arenaceous calcarenites (Willis, 1998) (Table 4.1).

4.4.4 Unit 4: Pliocene

Unit 4 is bounded by the base Pliocene (H₅) and base Pleistocene (H₆) horizons (Figures 2.2 and 2.3). The base Pleistocene (H₆) is marked by a high-amplitude, positive reflection at a depth of approximately 561.5 m in the Ludmilla-1 well (Figures 2.2 and 4.3). Strata in this unit consist of light olive grey calcareous claystones (Willis, 1998) (Table 4.1). Unit 4 comprises the Barracouta Formation and varies in thickness from 100 to 350 ms, thickening towards the northwest (Figure 4.5).

4.4.5 Unit 5: Pleistocene

On the interpreted seismic sections, the top of Unit 5 coincides with the modern seafloor at 220 m in the Ludmilla-1 well (Figure 4.3). This Pleistocene interval varies in thickness from 200 to 450 ms in areas with no ICPs (Figure 4.5). Close to ICPs, where thicker intervals are present, the unit varies in thickness from 450 to 650 ms

(Figures 2.3 and 4.5). The base of the unit is horizon H₆, which also coincides to the base of most ICPs. The interior of Unit 5 is composed of high-amplitude reflections (Figure 2.2). Seismic reflections below the ICPs are not continuous, suggesting a change in depositional facies. The seismic response within these areas is characterised by mounded morphologies and internally chaotic to stratified reflections from the margins to the ICPs internal structures, as expected for carbonate platform facies (Burgess et al., 2013). Unit 5 comprises the Alaria Formation, which consist of yellowish-grey coarse-grained calcarenites interbedded with silty calcilutites (Willis, 1998) (Table 4.1). The internal reflections of the biggest ICP ϵ present clinofolds suggesting the coalescence of smaller individual ICPs into a larger feature (Figures 4.6 and 4.17).

4.5 ICP geometries and fault distribution

In the study area there are 51 Quaternary ICPs with different sizes, ranging in area from 0.1 km² to 200 km² (Figures 4.6, 4.7, 4.15 and 4.16a). The histogram in Figure 4.16a shows a multimodal distribution with three distinct peaks. This indicates that there are three groups of ICPs, each showing different areas. The first peak shows a group of ICPs with an area of around 0.2 km², the second peak shows the major frequency with ICP areas of 2 km²; and a third peak shows a distribution of ICPs with an area of 20 km². The higher frequency of ICPs is within the scale range of 2 km². The smaller ICPs are concentrated in the frequency peak of a range of sizes with the order of 0.2-0.3 km². The biggest ICP (ϵ) has an area of about 189 km².

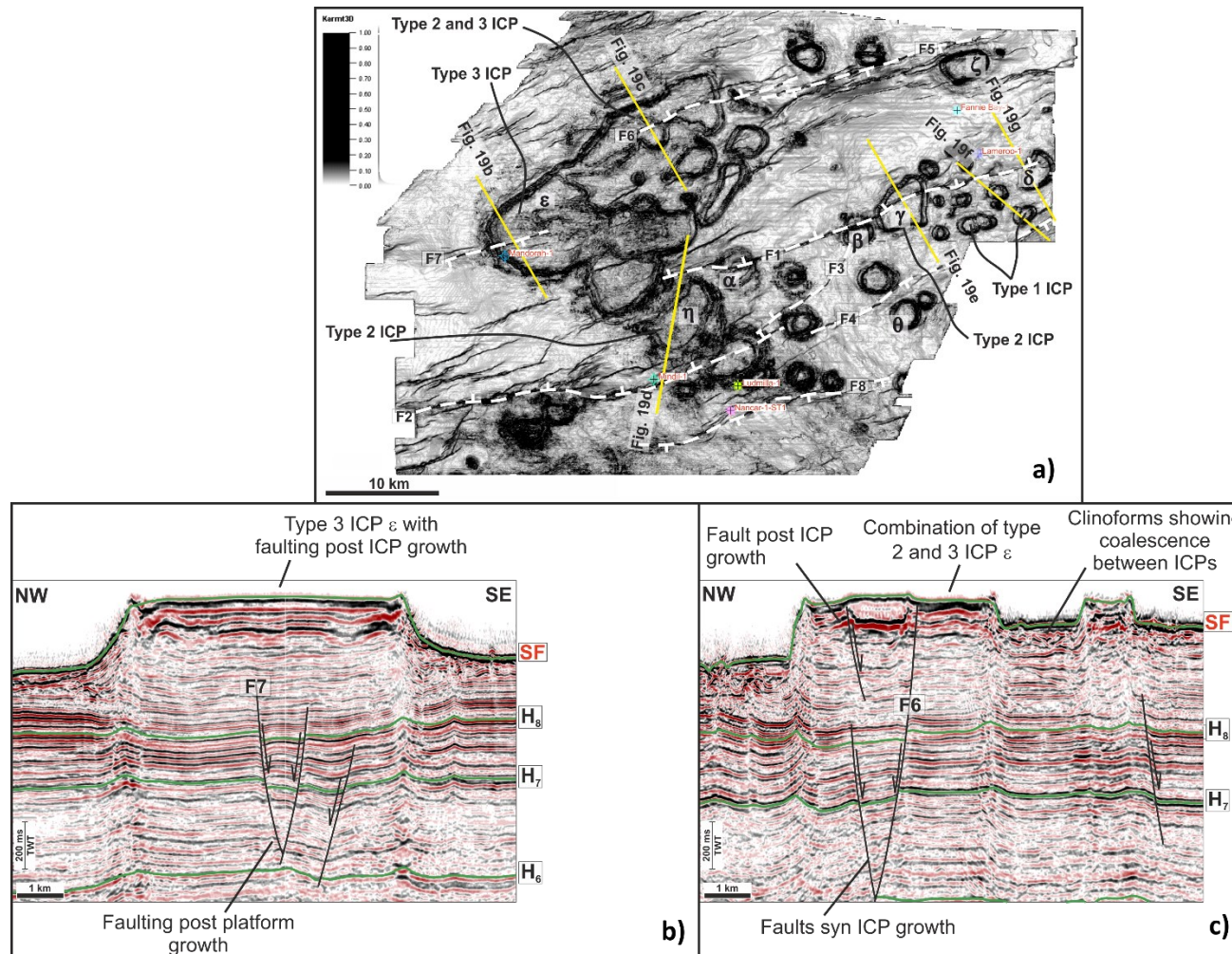


Figure 4.17. Selected seismic profiles showing the detailed geometry of the different types of ICPs. The variance map of horizon H_6 in (a) shows the location of the seismic profiles. (b) The large ICP ϵ appears as type 3 or (c) a combination between type 2 and 3. This suggests that large platforms can contain ICPs that grew by a combination of any of the types interpreted in this work. (d) ICP η reveals its development as a type 2 platform on an inner relay ramp. (e) ICP γ as a type 2 platform with a faulted internal structure. (f and g) Different ICPs developed on a structural high and showing relatively intact internal structures.

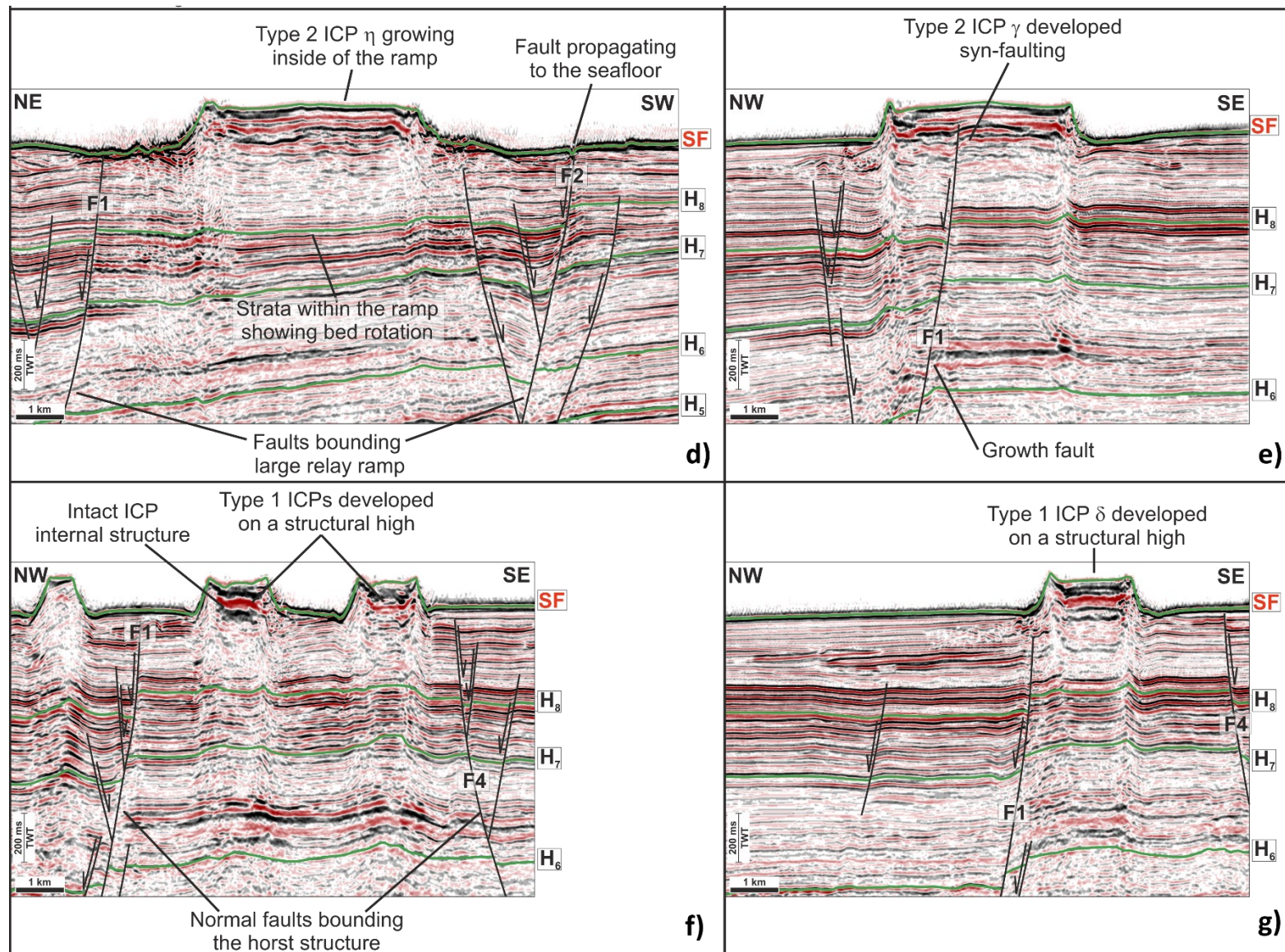


Figure 4.17. Continued.

The incomplete correlation between the ICPs' areas and underlying faults, indicated by the scatter plots (Figure 4.16b and c), suggests that there is no spatial relationship between the size of ICPs and the number of fault segments crossing, or surrounding them. However, the ICPs in the Bonaparte Basin have a sub-circular and ellipsoidal morphology in map view, with a NE long-axis direction that is similar to the orientation of underlying faults (Figures 2.4 and 4.6).

It is observed from the seafloor map (Figure 2.4), and seismic profiles of the Karmt shoals (Figures 4.9, 4.10 and 4.11), that the ICPs could have developed by the coalescence of smaller platforms. For instance, the large platform ϵ is an elongated feature with two main branches (Figures 4.6 and 4.7); this suggests coalescence of smaller platforms. In section view the platform interior is characterised by clinofolds, which indicate the merging and aggradation of distinct ICPs (Figure 4.10). Similar examples include the isolated platforms of the East Natuna Basin (Bachtel et al., 2004) and offshore Madura, Indonesia (Posamentier et al., 2010).

A detailed structural interpretation of the base Pleistocene (H_6) using an extracted variance map resulted in the sub-division of the study area into four distinct zones (Figure 4.7). These zones were defined based on the size, clustering, position and geometry of the ICPs, as well as the type, density, and orientation of faults.

4.5.1 Zone 1

Zone 1 is located in the northwestern corner of the study area (Figure 4.7). This zone is characterised by the absence of ICPs. Zone 1 has a high density of Plio-Pleistocene normal faults striking NE. Faults are synthetic and antithetic, closely spaced (100-300 m) (Figure 4.10). These faults do not propagate to the surface.

4.5.2 Zone 2

Zone 2 covers an area aligned NE-SW, just to the south of zone 1 and comprises the large platform ϵ and 14 smaller isolated platforms (Figure 4.7). Plio-Pleistocene normal faults strike NE-SW with an average of 072° (Figures 4.9, 4.10 and 4.11). The large ICP ϵ includes large fault arrays with a net normal offset, such as F6 and F7, that crosscut the platform as a later event (Figure 4.7 and 4.17c). In contrast, to the northeast, the interior of the ICP ζ is intact and bounded by a fault array that includes F5 (Figure 4.7).

4.5.3 Zone 3

Zone 3 is located to the south of Zone 2 and comprises a large number of ICPs (28). Fault array F1 is located in zone 3 (Figures 4.6, 4.7 and 4.11). There are two fault families in this area; the principal family striking 072° NE (fault arrays F1, F3 and F4) and a secondary family striking around 050° NE (fault array F3). The interaction between faults creates large relay ramp structures such as the one containing ICP η , which is bounded by fault arrays F1, F2 and F3 (Figures 4.6 and 4.7).

4.5.4 Zone 4

Zone 4 occurs in the southeastern part of the study area (Figure 4.7) and it is mainly characterised by its relative scarcity of ICPs. There are only eight small ICPs, including ICP θ with an average area of 1.5 km^2 . This zone presents a major fault zone around fault array F8 (Figure 4.10).

4.6 Fault-throw analysis

In order to better understand the propagation history of the interpreted faults, maximum throw measurements were taken from fault array F1 (Figures 4.12 and 4.13). This fault array was selected for the analysis because it crosses four different ICPs (α , β , γ , δ).

Fault-throw measurements were completed in detail, every 150 m along the strike of the faults, and every 25 ms along their dip, complying with the minimum amount of measurements ('delta ratio') proposed by Tao and Alves (2019). These measurements were used to generate detailed throw-depth (T-Z) plots as well as a maximum throw-distance (T-D) plot (Figures 4.12 and 4.13c). The large amount of data was compiled to generate a high-resolution map of throw displacement (Figure 4.14).

T-Z profiles were useful to investigate the style, timing of fault initiation and the detailed kinematic history of normal faults (Hongxing and Anderson, 2007). Overall, the intention was to analyse the slope of different curve segments and their deflections within the throw profile. The analyses performed here were based on the conceptual models developed by Hongxing and Anderson (2007). A vertical line segment with a constant throw indicates a simple post-depositional fault, cutting the entire pre-kinematic stratigraphic section; it suggests that it was formed after all the sedimentary layers were deposited. Another way to determine the presence of a post-depositional fault is by a constant growth index of 1.0 for all layers because there is no change in the thickness of the strata.

A T-Z profile with a positive slope and throw values decreasing at depth towards older units indicates a post-depositional keystone-stretching fault, where the fault propagates downwards, with the uppermost and youngest units recording the largest

throw values. The growth index of post-depositional stretching faults is also identified by a constant value of 1.0 or less, due to the thinning of the layers by stretching. The timing of fault formation post-dates the deposition of the unit recording the largest fault-throw (Hongxing and Anderson, 2007).

In a given scenario in which the T-Z profile presents a negative slope, with throw values increasing towards the older units, the presence of a syn-depositional normal growth fault is recognised. The sedimentary sections expand on the hanging-wall, leading to growth indexes with values greater than 1.0 (Hongxing and Anderson, 2007).

The combination between throw profiles and growth index are useful to provide information of the time in which a fault first nucleates (Hongxing and Anderson, 2007). A change from post-depositional keystone-stretching fault to a growth syn-depositional fault is given by the deflection of a positive slope curve to a negative curve. The growth index profile in this case, shows a change in values from 1.0 or less to values greater than 1.0. The maximum throw value in the profile along with the change of the growth index corresponds to the initiation of the fault growth (Hongxing and Anderson, 2007).

Several seismic profiles were analysed using T-Z plots in order to determine the growth history of the fault array F1 (Figure 4.12). Across the study area, the results suggest that there were two stages of faulting throughout the Cenozoic. The stages are identified as Paleogene in age, with a maximum throw of 255 ms TWT, and Neogene-Quaternary faulting with a maximum throw of 200 ms TWT (ca. 287 m and 225 m respectively, assuming an average velocity of 2250 m s^{-1}) (Figure 4.12).

Fault-throws decrease towards the base of Unit 1 (Figure 4.12). This segment of the throw profile has a positive slope and the growth index is smaller than 1.0, indicating that Unit 1 was deposited before faulting commenced (Figure 4.12). Unit 1 is considered as a pre-kinematic layer. Maximum throw values are observed around the Middle Eocene horizon (H_3). Above these throw maxima, within Unit 2, throw values start to decrease towards younger strata (Figure 4.12b, d, f and h). The throw profile in this segment has a negative slope and growth index values are greater than 1.0 (Figure 4.12). The change in deflection from a positive to a negative slope, in addition to the change in growth index values from smaller than 1.0 to greater than 1.0, suggest a change from post-depositional to syn-depositional faulting. These two faulting stages are considered to be Paleogene in age (Figure 4.12).

Fault-throw and growth index values are observed to remain relatively constant around the base Miocene horizon (H_4), within the uppermost part of Unit 2 and the lowermost part of Unit 3 (Figure 4.12b, d and h). This can be interpreted as a period of fault inactivity. A change is observed upwards in the form of a positive slope throw profile with values progressively increasing towards the uppermost part of Unit 3, around the base Pliocene horizon (H_5) (Figure 4.12b and f). The growth index profile records values smaller than 1.0. This segment of the throw profile records pre-kinematic strata. This stage is considered to reflect post-depositional faulting due to the cessation of activity of Paleogene faults.

A second throw maximum is recognised in Late Miocene to Early Pliocene strata around horizon H_5 (Figure 4.12). This throw maximum indicates the start of the second faulting period described here as Neogene-Quaternary. Above this maximum, throw values start to decrease towards Quaternary strata, as shown in the throw profiles as a negative slope line (Figure 4.12b, d, f and h). In this segment of the

profile, growth index values are greater than 1.0, suggesting thicker strata in the hanging-wall of a syn-depositional normal growth fault. In some areas (Figure 4.12a and g), the growth fault propagates to the seafloor. However, below the ICPs, fault-throw decreases and stops before reaching the seafloor (Figure 4.12c and e). The presence of growth faults and the relative thickening of hanging-wall strata in Units 4 and 5 (Figure 4.12a, c, e and g) confirm the occurrence of a syn-depositional fault. This suggests that at the time of initiation of the ICPs (Quaternary), the faults were propagating towards the seafloor. The fact that faults do not completely cross-cut all ICPs indicates that carbonate productivity was relatively larger than vertical fault-propagation rates for some of these latter platforms.

The T-D plot in Figure 4.13 shows maximum fault-throw values along the strike of fault array F1 for the Neogene-Quaternary. It shows different throw maxima peaks along the fault array, suggesting the presence of discrete fault segments in fault array F1 (Figure 4.13b and c). These fault segments are indicated by red solid lines in Figure 4.13c along the fault-throw maxima (yellow line). A dashed line was drawn to highlight the interpreted length of each fault segment. It is interpreted that lateral and vertical propagation of these individual fault segments through time led to soft linkage between their fault tips, creating relay ramps. In these relay ramps there is a transfer of displacement from the footwall to the adjacent hanging-wall blocks. The relay ramps are located in areas with relative minimum displacement between segments. These relay ramps are shown in Figure 4.13c as pink rectangle areas. These linked fault segments created a large set of overstepping fault zones along fault array F1 (Larsen, 1988; Fossen and Rotevatn, 2016). This type of fault interaction exists at different scales of observation (Figures 4.6 and 4.7). In the study area, there are relatively small relay ramps (2 km wide) created by individual fault

segments, such as the one located around ICP α (Figure 4.13). There are also larger relay ramp structures (>10 km wide) created by the interaction between large fault arrays such as the relay ramp between fault arrays F1 and F2 (Figures 4.6, 4.7 and 4.17).

Relay ramps can only be observed in seismic data if the ramp is large enough to be clearly imaged (e.g. the relay ramp containing the ICP α , shown as a light purple polygon with a red outline in Figure 4.7b). Relay ramps that are less than 1 km wide are not easily recognised in the Karmt3D volume. For this reason, it is necessary to use T-D plots to accurately identify relay ramps, such as those in ICP γ , which are only clearly recognised by the small throw values documented between adjacent fault segments (Figure 4.13c). For the relay ramps that can be clearly identified in a seismic section, they present rotation of strata between two linked faults (e.g. F1a and F1b), where the strike and dip of the beds are slightly different to the general orientation (Figure 4.13d and e). Relay ramps can be identified from the T-D plot in Figure 4.13c as the intersection between two different fault segments (pink areas), usually occurring in areas with small throw values. Relay ramp structures are not only observed in fault array F1, but also in some other parts of the study area (Figure 4.7). There are some small relay ramps placed close to the largest fault arrays, such as the ones shown in Figure 4.7, shown as light purple polygons with a red outline. There are also some other larger ramps shown as light pink polygons on the map in Figure 4.7, such as that containing ICP η .

Fault-throw measurements, comprising more than 200 T-Z plots taken along fault array F1, were used to generate a high-resolution fault-throw map (Figure 4.14). In contrast to the T-D plot in Figure 4.13c, the geometry of discrete fault segments can be determined in this fault-throw map together with their nucleation depths. The

fault-throw surface map shows the elliptical-like geometry of the fault segments (white ellipses in Figure 4.14). Throw maxima are localised inside the fault segments (warm colours), indicating the depth of fault initiation (Cartwright et al., 1998; Hongxing and Anderson, 2007). The throw values decrease towards the fault tips (cold colours) (Muraoka and Kamata, 1983). One example is observed at about 22,500 m along strike, where there is an area with large throw values around horizon H₃. Fault-throw values decrease laterally and vertically from ~240 ms (orange colour) in the middle of the fault segments to values of ~130 ms (yellow and green colours) towards the fault tips.

Relay ramps can be interpreted in the areas where the two fault tip segments interact and present relatively low throw values. These relay ramps are plotted as pink zones on the fault-throw map, such as the relay ramp between the fault segments 1a (F1a) and 1b (F1b) (Figure 4.14).

The presence of two faulting events is clearly recognised on the T-Z plots (Figure 4.12) and by analysing the fault-throw map (Figure 4.14). The Paleogene fault segments are observed below horizon H₄ between -2000 and -1500 ms TWT (Figure 4.14). The Neogene-Quaternary faulting event is mostly observed above horizon H₄.

4.7 Fault-propagation styles

Paleogene and Neogene faults are NE-striking in the study area (Figures 4.6 and 4.6). They have a net normal component, and fault arrays present discrete fault segments linked to each other (Figures 4.6 and 4.7). The linkage and overlap between several fault segments result in the creation of large fault arrays, a character known as geometric coherence. The displacement of each fault segment accumulates and

creates a large fault (Walsh and Watterson, 1991; Conneally et al., 2014). The formation of the fault arrays F1 to F8 present geometric coherence (Figures 4.6 and 4.7).

Around fault array F1, within the overlap zones between different fault segments, small relay ramps are observed primarily from T-D plots and the throw surface map as well as large relay ramps easily identified in the variance map (Figures 4.6, 4.7, 4.13 and 4.14). In Figure 4.13, where ICP α is located, there is an intact relay ramp with a maximum width of about 2000 m.

Interactions between several fault segments can create a large fault, e.g. fault array F1. These long faults, if interpreted on a regional scale as one large fault, can interact with other large fault arrays in a similar way to individual fault segments. As a result, they can generate large relay ramps such as the 8 km wide relay ramp between F1, F2 and F3 containing ICP η (Figure 4.7). The relay block often shows significant bed rotation and breached strata, even when it is not visible on seismic profiles (Fossen and Rotevatn, 2016). It is inferred that this uneven palaeo-surface is a good substrate for the initiation of ICPs based on the fact that all the ICPs intersected by fault array F1 directly correlate to the position of an underlying relay ramp. However, direct spatial relationship between relay ramps and the position of ICPs has not been recognised in all the isolated platforms in the study area.

4.8 Chapter-specific discussion

4.8.1 Relationship between carbonate deposition and fault growth

In the Bonaparte Basin, there is a high concentration of ICPs across the shelf margin (Figure 2.3). This region is highly faulted as observed on the variance maps in Figure 4.7. Fault-throw data suggests a positive correlation between the position of linked fault segments and developed relay ramps (Figures 4.13 and 4.14). Despite the lack of an absolute spatial relationship for all ICPs and relay ramps in the study area, some of these ICPs (e.g. ICPs α , β , γ , δ , ϵ , ζ , η and θ) occur above or close to underlying relay ramps - as revealed by the T-D plot in Figure 4.13c and the fault-throw map in Figure 4.14. For these same reasons, detailed fault-throw analyses are introduced here as an additional aspect to take into account when characterising (and mapping) ICPs in extensional settings (Burgess et al., 2013; Rusciadelli and Shiner, 2018).

The initiation of ICPs in the Bonaparte Basin has been attributed to antecedent topography, which was able to trigger the preferential settlement of reef building organisms, thus controlling the distribution of ICPs in the Vulcan Sub-Basin (Saqab and Bourget, 2015a). This antecedent topography was tectonically controlled by extensional faults. It is well documented in the literature that ICPs can initiate on horst structures, such as those in the Maldives Archipelago (Paumard et al., 2017). Saqab and Bourget (2015a) have documented the development of the “Big Bank” in an adjacent area to the Karmt Shoals. This ICP was interpreted as controlled by a structural high. However, in the 3D seismic dataset presented here, there are some areas in which ICPs do not grow on structural highs being, instead, cross-cut by normal faults (Figure 4.7).

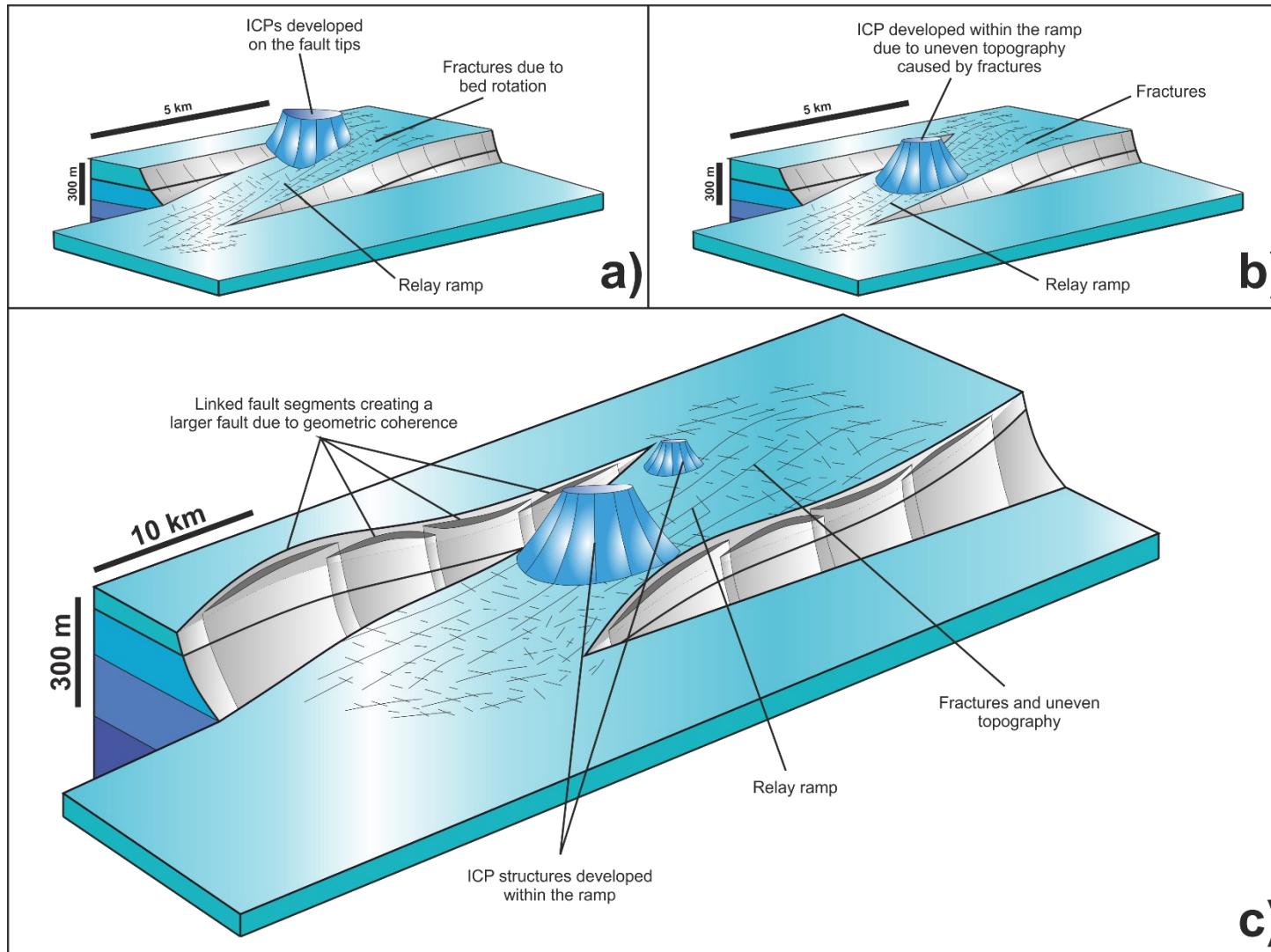


Figure 4.18. Schematic diagrams illustrating the position of ICPs over relay ramp structures as interpreted in this work. (a) ICPs located over growing fault tips; (b) development of an ICP inside a relay ramp; (c) relay ramp formed by several fault segments on a larger scale where ICPs can develop close to fault tips, or on the relay ramp per se.

As recognised from the T-D profile in Figure 4.13c and the fault-throw map (Figure 4.14), the ICPs in the fault array F1 (α , β , γ and δ) are underlain by relay ramps formed between two fault segments. These relay ramps produce local bed rotations that create a local change in bathymetry (Giba et al., 2012). The gradual transition from intact rock to a breached relay ramp develops fractures in the area, even before the two interacting faults are completely breached. Fossen and Rotevatn (2016) have shown a field example from the Canyonlands National Park, USA, in which the ramp is highly fractured. Therefore, a high concentration of fractures is likely to occur in the sub-seismic scale even if the ramp appears to be continuous and unbreached in the seismic data due to its resolution limits. This uneven topography may favour the concentration of opportunist biota and result in the initiation of ICPs (Figure 4.18). However, such a correlation between relay ramps and the development of ICPs is not direct; it is a way of explaining some of the local controls on ICPs locations. Transfer zones including relay ramps (soft-linkage) are known to be important features in controlling basin stratigraphy due to the marked change in relief recorded on both the hanging-wall and footwall blocks associated with the transfer zones (Leeder and Gawthorpe, 1987; Gawthorpe and Hurst, 1993). The Abu Shaar el Qibli carbonate platform in the Gulf of Suez is an example of an ICP positioned in a transfer zone (Gawthorpe and Hurst, 1993; Cross et al., 2008).

Based on the analysis of this chapter, three scenarios are considered, in which faults interact to trigger the initiation and development of ICPs: (1) interaction of single fault segments with the creation of relay ramps (Figures 4.17 and 4.18b); (2) large scale relay ramps created by large fault arrays (Figures 4.17 and 4.18c); and (3) structural highs (Figure 4.17). Furthermore, the ICPs can start on different places

of the relay ramp: (1) close to the fault tips (α , Figures 4.13 and 4.18a) or (2) inside the relay ramp (η , Figures 4.13 and 4.18b).

Carbonate platform growth in the study area can thus be explained by a balance between local carbonate productivity and fault-throw-rates such as: (1) some of the ICPs are affected by fault-throw rates that are larger than carbonate productivity (Figures 4.17 and 4.19); (2) other ICPs were influenced by faults recording throw rates equal or less than carbonate productivity (Figures 4.17 and 4.19); while (3) the remaining ICPs were affected by faults that post-date the growth of the carbonate platform(s) (Figures 4.17 and 4.19).

The study area documents the three scenarios above in the form of three distinct types of ICPs. Type 1 occurs in zone 2 with ICPs presenting intact internal structures, as no faults cross-cut them (Figure 4.17f and g). These ICPs developed on the structural high bounded by fault arrays F1 and F4. There is a cluster of isolated platforms within this block including ICP δ . Type 2 ICPs can also be found within the zone 2. An example of a type 2 platform developed inside a relay ramp is shown in Figure 4.17d, where fault arrays F1 and F2 created a large ramp with a wide rotational surface suitable for the development of ICP η . A type 2 ICP developed between the fault tips of two different individual fault segments is shown in Figure 4.17e. This type of platform is faulted in its interior, as observed on the seismic profile. Type 3 ICPs are characterised by their post-growth faulting. The faults propagate after the growth and deposition of the ICPs such as in the case of ICP ϵ , which was faulted by F6 and F7 (Figures 4.17 and 4.19). ICP ϵ is interpreted as belonging to type 2 to the northeast (Figure 4.18c), where syn-depositional faults propagate to the seafloor. In the same area is observed a shallow fault developed after the growth of ICP ϵ , implying the existence of a type 3 ICP.

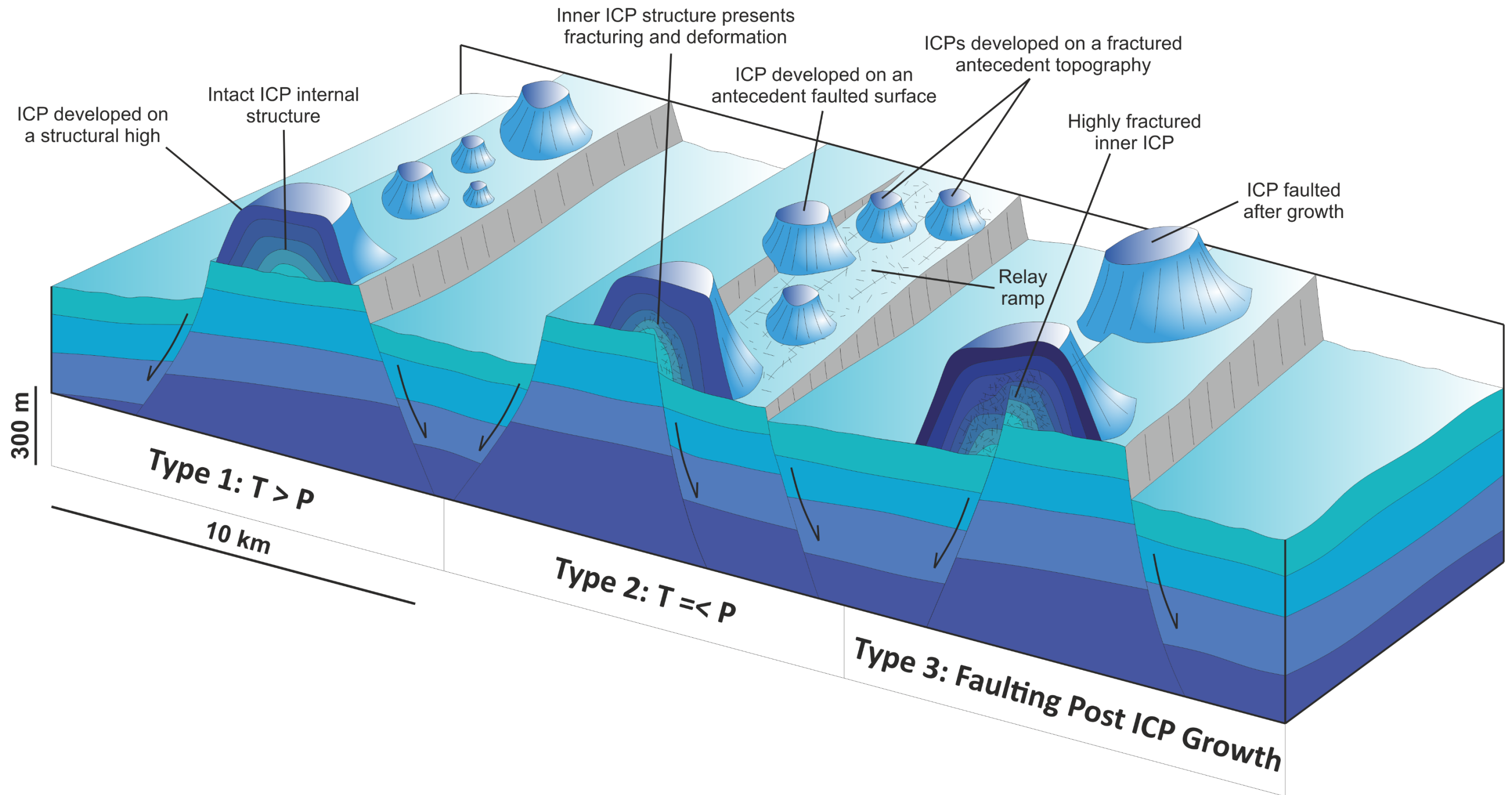


Figure 4.19. Schematic diagram summarising the relative position of ICPs as a function of fault-throw rates (T) and carbonate productivity (P). Type 1 ICPs develop on structural highs and they remain relatively intact. Type 2 ICPs develop in areas of antecedent faulting, such as on a relay ramp, and where carbonate productivity exceeds fault-throw rates. Type 3 ICPs develop initially on a non-faulted zone. Once formed, faults can cross-cut the ICP, fracturing them internally.

4.8.2 Implications for petroleum systems on continental margins

ICPs can trap significant volumes of hydrocarbons, being good targets for exploration. It is estimated that reserves of ~50 billion barrels of oil equivalent presently occur within ICPs (Greenlee et al., 1993). Several super-giant fields are found in ICPs, such as the Tengiz and Kashaghan fields in the Precaspian Basin (Kuznetsov, 1997). Because of their geometry, petroleum system elements can be easily identified in seismic data. Trap geometries and seal properties are usually favourable, developing four-way dip closures sealed by fine-grained marine strata or evaporites (Burgess et al., 2013). Adjacent or underlying strata can form good source rocks with clear migration pathways into ICPs (Burgess et al., 2013). However, not all ICPs have the same potential to store hydrocarbons. For this reason, it is critical to not just identify any ICPs in seismic data, but also to perform a broader evaluation of their reservoir potential before deciding what is the best structure to drill, and therefore guarantee an exploration success.

It is known in the literature that relay ramps represent potential pathways for the vertical migration fluids (Fossen and Rotevatn, 2016). Relay ramps can enhance vertical porosity and permeability due to a range of fluid-rock interactive processes. Breaches in relay structures can develop complex fracture systems that enhance porosity and permeability (Fossen and Rotevatn, 2016). Furthermore, during the development and breaching of relay ramps, faults can create compartmentalised blocks to generate isolated reservoir intervals. These structures can serve as vertical pathways for fluid migration and hydrocarbon accumulation, as exemplified by the Gullfaks Field in the North Sea (Fossen and Hesthammer, 1998; Fossen and Rotevatn, 2016). Hence, one can predict that ICPs located over relay ramps are good reservoir intervals since they comprise a favourable scenario for hydrocarbon migration and

trapping. The hydrocarbon can migrate through the relay ramp to be trapped in the ICP.

Strata in ICPs are known to record early cementation, leading to a rigid structure (Burgess et al., 2013). This early cementation can lead to the significant development of small-scale faults and fractures together with the syn-tectonic deposition of ICPs (Cross et al., 2008). Therefore, it can be inferred that ICPs recording syn-tectonic growth - such as those corresponding to the type 2 proposed here - are significantly fractured in their interior. Similarly, type 3 ICPs may develop fracture networks in their interior as the fault propagates to the platform interior. This induced fracturing can develop secondary porosity within the platform per se, enhancing its reservoir potential (Cross et al., 2008).

Based on the analysis of ICPs in the Karmt Shoals, once the ICPs are identified in seismic data, a way to assess which platform can potentially form the best hydrocarbon reservoir is by identifying those positioned on relay ramps. According to the ICP types proposed here, the platforms with the largest chances of success are found in types 2 and 3 (Figure 4.19). Types 2 and 3 ICPs are developed on relay ramps, which enhance hydrocarbon migration. Furthermore, the ICPs interior should be highly fractured due to a combination of syn- and post-depositional faulting, leading to an enhanced capacity to store hydrocarbons.

4.9 Chapter-specific summary

In this work, fault-throw measurements taken from 3D seismic data allowed the compilation of detailed throw-depth (T-Z) and throw-distance (T-D) profiles, as well as a high-resolution fault-throw surface map. These profiles and maps, tied to well data, were the basis of the analysis of the timing of fault initiation and ICP growth, in the Bonaparte Basin, Northwest Australia.

The Vulcan Sub-Basin presents two Cenozoic stages of faulting: 1) Paleogene faulting and Neogene-Quaternary faulting, which are documented in the form of fault-throw maxima on T-Z plots (Figure 4.12) and fault-throw surface maps (Figure 4.14). A period of fault inactivity is recognised as spanning the Late Oligocene to Early Miocene.

Based on the Karmt3D seismic data, the development of ICPs began in the Pleistocene. At this time, palaeo-bathymetric features were chiefly generated by the vertical propagation of faults towards the seafloor, generating structures such as relay ramps and localised structural highs. As recognised from the distribution analysis of ICPs versus faults (Figure 4.16), the majority of the ICPs does not have a direct relation to the faults. However, some of the ICPs (e.g. α , β , γ and η) relate to the position of relay ramps underneath. For these examples, relay structures play a very important role in the initiation and development of ICPs.

Three different types of ICPs are proposed in this work to document the relationship between these latter platforms and underlying faults. In essence, these types of ICPs reflect the time and spatially variable relationship between fault-throw rates and carbonate productivity. Type 1 ICPs are those formed where fault-throw rates are larger than carbonate productivity. Type 2 ICPs consider fault-throw rates

to be equal or smaller than carbonate productivity, Type 3 ICPs are those in which fault movement and vertical propagation post-date the growth of the carbonate platform(s).

The models proposed in this work are useful to assess the hydrocarbon potential of ICPs in extensional settings using subsurface data, and therefore assist the identification of new hydrocarbon prospects. Types 2 and 3 ICPs are the best features when considering their hydrocarbon potential. They present favourable hydrocarbon migration pathways (relay ramps) and structural traps (platform facies) that can be highly fractured, enhancing their (secondary) porosity. These ICP types are expected to occur on Equatorial Margins around the world.

Chapter 5: Fracture network characterisation on carbonate platforms

An abridged version of this chapter has been published as:

Loza Espejel, R., Alves, T.M., Blenkinsop, T.G., 2020. Multi-scale fracture characterisation on carbonate platforms. *Journal of Structural Geology*, 140.

<https://doi.org/10.1016/j.jsg.2020.104160>.

Co-author contributions to the paper:

Tiago M. Alves - checked for grammatical errors, ensured the scientific content was accurate and appropriately presented.

Tom G. Blenkinsop - checked for grammatical errors, ensured the scientific content was accurate and appropriately presented.

5.1 Abstract

Characterisation of fracture networks at different scales is challenging and important to many fields of geoscience, especially when access to multiple resolution datasets is limited. Here, an integrated analysis of fracture networks on carbonate platforms is developed using three scales of observation: small (outcrop), intermediate (airborne LiDAR) and large (3D seismic). Statistical analyses and ternary diagrams of geometrical and topological data from Cariatiz (Southeast Spain) and Pernambuco (East Brazil) are used to understand the relationships and distribution of fracture networks between multi-scale datasets. A variety of fracture types at each scale of observation reveal how complex fracture networks are on carbonate platforms. The results presented in this chapter demonstrate that fracture network properties behave differently depending on the fracture size, and that transitional scale gaps between datasets constrain fracture characterisation. Airborne LiDAR maps show that intermediate-sized fractures appear to have a better controlled orientation and a lower connectivity than smaller fractures from the same area in Cariatiz. Fracture branch length distributions fit a negative exponential or log-normal distribution for massive non-stratabound units. This work is important as it demonstrates that the use of outcrop data is a good approach to understand fracture complexity of carbonate platforms. Understanding sub-seismic fracture networks is therefore critical in quantifying fluid flow and permeability in carbonate reservoirs.

5.2 Introduction

Fracture networks control many physical properties in rocks, and their characterisation is important in many disciplines of geosciences and engineering, including oil and gas exploration (Nelson, 2001; Sarkheil et al., 2013), geothermal reservoir characterisation (Chen et al., 2018; TerHeege et al., 2018; Vidal and Genter, 2018; Doornenbal et al., 2019), carbon capture and storage projects (March et al., 2018), hydrogeology and environmental geology studies (Abotalib et al., 2019; Medici et al., 2019), as well as mining and tunnelling (Friedman, 1975; Van As and Jeffrey, 2002; Zarei et al., 2012). Fracture networks have a significant effect on porosity, permeability and fluid flow of naturally fractured units. Well-connected open fractures can increase the natural permeability of rocks to provide active conduits for fluid flow (Laubach, 2003; Maerten et al., 2006; Strijker et al., 2012; Gutmanis et al., 2018). Conversely, closed or cemented fractures can act as barriers compartmentalising reservoirs, which is important for field delineation (Bourbiaux, 2010). Examples of fractured carbonate reservoirs can be found worldwide including the Cantarell complex in Campeche (Gulf of Mexico), the Haft Kel field in North Iraq (Middle East), and the Ekofisk complex in the North Sea (Dominguez et al., 1992; Key et al., 1999; Hermansen et al., 2000; Alavian and Whitson, 2005; Mandujano et al., 2005; Bourbiaux, 2010; Santiago et al., 2014; Galvis, 2018).

A key aspect in reservoir characterisation is the need to analyse the interaction between individual fractures and fracture sets, which can be estimated by studying topological attributes such as branch and node types (Strijker et al., 2012; Sanderson and Nixon, 2015). Both geometrical and topological attributes affect the connectivity and permeability of a rock volume. Moreover, natural fractures typically occur over several orders of magnitude; they range from microscopic fissures to kilometre

structures such as fracture swarms or corridors (Bush, 2010). It is therefore crucial to understand the scale dependency of these distribution parameters to characterise sub-surface fluid flow patterns (Berkowitz, 2002; Tao and Alves, 2019).

Fractures can be described by quantifiable geometrical attributes such as their orientation, length, height, spacing, morphology, or some other form of classification involving fracture type and mineral fill (Odling et al., 1999). In this chapter, the term *fracture* is used as any type of discontinuity (joints, faults, etc.) formed in different settings, such as during large-scale tectonic events, local uplift and erosion, slope instability or excess fluid pressure (Peacock et al., 2000, 2016; Berkowitz, 2002; Kim and Sanderson, 2005). The intention is to characterise an entire fracture network, including different fracture types of various sizes that interact between each other within a given rock unit, as all of them may contribute to the connectivity of the fracture network. Specific terms such as fault, joint, fracture swarm, etc. are only used where the fracture type and geological connotation are important to the analysis.

5.2.1 Challenges and limitations

One of the main challenges when characterising fracture networks is to obtain reliable data to analyse fracture networks at different scales. At present, it is still difficult to fully characterise fractures from a single dataset or by utilising data in which fractures of certain sizes cannot be observed due to limited data resolution. Integration of datasets and the knowledge of the capabilities for each type of data are key. Ideally, a carbonate platform with access to an exhaustive dataset, allowing mapping at different scales in both surface (e.g. outcrop mapping, drone imagery,

airborne LiDAR) and sub-surface (e.g. cores, borehole, seismic), would provide a comprehensive setting to fully characterise not just fracture networks, but also additional structural and sedimentological properties. However, availability of such a perfect scenario is rare, and the necessity to work with limited datasets is a daily issue for geoscientists.

Three-dimensional (3D) reflection seismic data is usually the main source of subsurface structural information in industry. Seismic surveys are generally acquired at a line spacing of 25 to 50 m and, depending on the resolution of the seismic volume, faults with throws smaller than 10 to 30 m cannot be resolved (Needham et al., 1996; Lohr, 2004; Maerten et al., 2006). Faults and fractures of sizes below seismic resolution, referred to as sub-seismic, can only be determined using borehole data (e.g. wireline logs, cores, well log images), leading to underestimations of fracture volumes (Maerten et al., 2006). Fracture downscaling or upscaling using discrete stochastic methods is a common practice to populate fractures with a scale that cannot be observed directly from the studied dataset, for example between seismic and borehole data (Cacas et al., 2001; Chilès, 2005). Similarly, fractal analyses have been undertaken to characterise fracture properties (Needham et al., 1996; Nicol et al., 1996; Bonnet et al., 2001). However, their scale invariance is still subject to controversy (Cowie et al., 1996; Needham et al., 1996; Nicol et al., 1996; Gillespie et al., 2001; Guerriero et al., 2010), and extrapolations with limited reliable statistics can lead to important uncertainties (Maerten et al., 2006).

Outcrop analogues play an important role in the evaluation of small- and intermediate-scale fracture parameters that cannot be quantified from seismic and borehole data (e.g. Eberli et al., 2005; Gutmanis et al., 2018, Fig.4). Field analogues can guide the development of conceptual reservoir models and provide spatial and

statistical data to understand inter-well fracture property populations, as techniques are available to cover all scales of observation (Nelson, 2001; Strijker et al., 2012; Gutmanis and Ardèvol i Oró, 2015; Sanderson, 2016). In such analyses, it is important to carefully choose valid field analogues to calibrate them with reservoir data (Cacas et al., 2001; Laubach et al., 2009; Kleipool et al., 2017). If there is sufficient exposure of fracture data, and sampling is undertaken carefully using appropriate methodologies (e.g. circular scanlines), field analogues can provide valuable information to characterise 3D fracture networks in multi-scale scenarios (Bertotti et al., 2007; Strijker et al., 2012).

This study is not an exception of the challenges associated to data limitations; in fact, the aim is to emphasise the issues associated when characterising multi-scale fracture networks. For this reason, an integrated methodology is explained in detail, utilising three scales of observation from two carbonate platforms with similar settings. This approach was useful to characterise fractures at sub-seismic (centimetre to metre) and seismic (kilometre) scales.

The Cariatiz carbonate platform in the Sorbas Basin, SE Spain, which has a unique 3D exposure, was used to analyse the geometry and topology of fracture networks at two sub-seismic scales from outcrop mapping (small scale) and airborne LiDAR (Light Detection and Ranging) maps (intermediate scale) (Figure 5.1). Correlating the two datasets, covering the same carbonate platform, was key to predict trends of fracture properties at different scales. In addition, three-dimensional (3D) seismic studies from the Pernambuco carbonate platform in East Brazil were used to analyse km-long fracture networks (Figure 5.2). Comparison between the two study areas (Cariatiz and Pernambuco) have limitations as they are not in the same region. However, they are of great importance to improve the understanding of multi-scale

fracture networks. Outcrop data provides the opportunity to understand sub-seismic fractures that can be used as conceptual models when only working with seismic data. In contrast, seismic data is useful to understand km-long fractures that are often poorly exposed and can also be used as conceptual models for example, when working with borehole data or surface data.

This study is a novel approach to study multi-scale fracture networks. However, there is indeed the possibility and a call to continue future work to test and apply these observations and conclusions in similar carbonate platforms which might have a more robust dataset covering fracture sizes of several orders of magnitude in the same region. This thesis chapter addresses the following research questions:

- a) How can we improve interpretation techniques combining fracture datasets with different resolutions to predict sub-seismic fractures?
- b) What is the importance of integrating geometrical and topological attributes in the study of fracture networks?
- c) What is the complexity of natural fracture networks at sub-seismic scales?
- d) Do fractures of distinct sizes observed at different scales present different attributes?

In summary, this chapter analyses the relationship between fracture sizes to test if there is a correlation between their size and connectivity. It also aims to show a comprehensive methodology to characterise fracture networks by using geometrical and topological attributes of fractures at different scales of observation (outcrop, airborne LiDAR, seismic) (Figure 5.3).

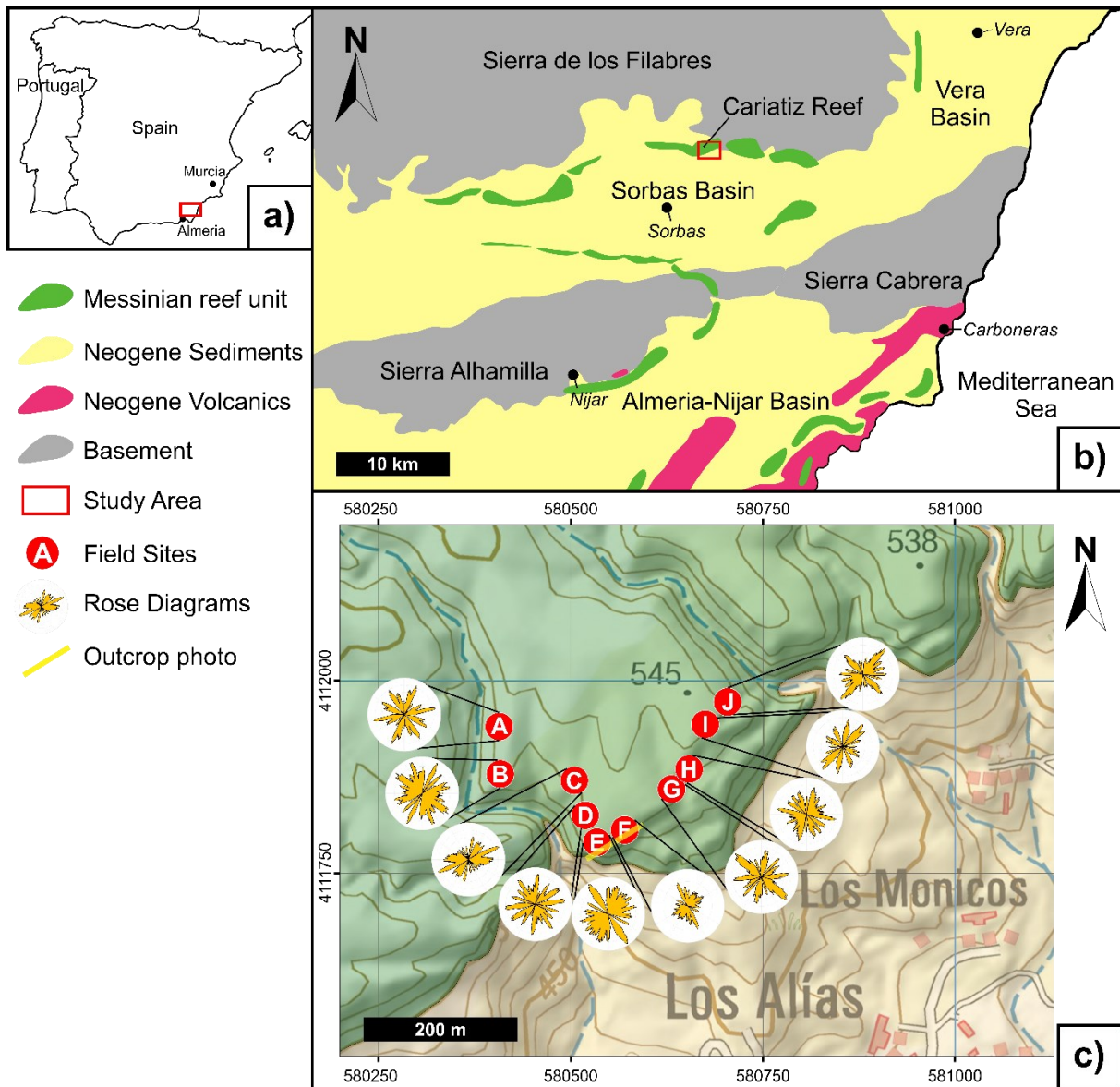


Figure 5.1. A) Location of the study area in SE Spain. B) Regional map of the Sorbas Basin showing the Messinian Reef Unit, and the area of interest at Cariatiz. Modified after Reolid et al. (2014). C) Topographic map showing the field sites where fracture network mapping was performed using the augmented circular scanline method of Watkins et al. (2015). Rose diagrams show the main fracture orientation at each site.

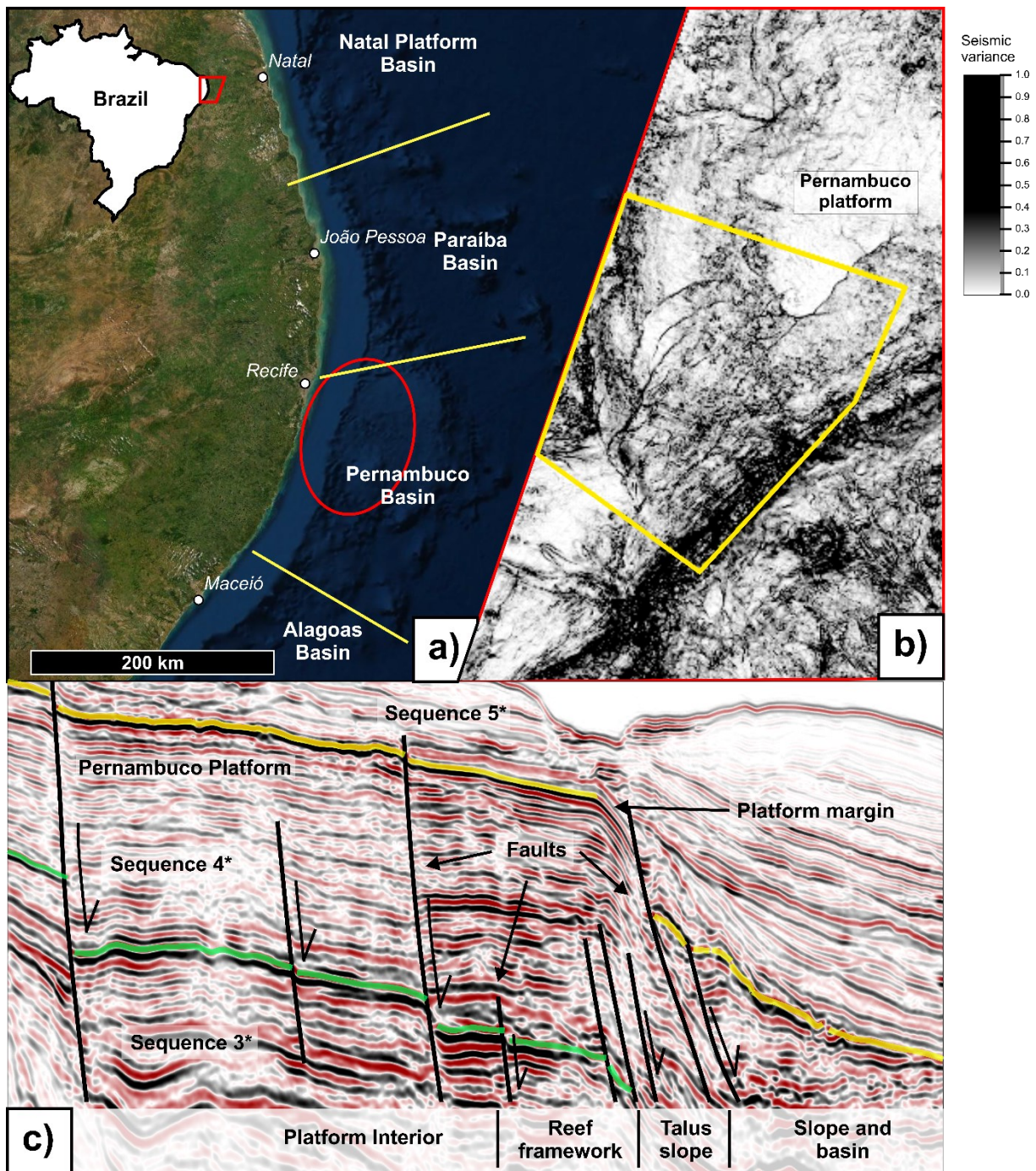


Figure 5.2. A) Location map of the study area in the Pernambuco Basin. b) Variance depth slice (-1720 m) showing the area (yellow line) where fracture characterisation was performed. C) Seismic section across the Pernambuco Platform showing its internal geometry and seismic facies, as well as the presence of normal faults. *Sequence numbers after Buarque et al (2017). Scale and exact location cannot be given due to data privacy.



Figure 5.3. Flowchart summarising the methodology used in this work to obtain fracture data from different datasets. Three different input datasets with distinct scale-resolution were utilised (outcrop: small scale, LiDAR: intermediate scale, seismic: large scale). *Consider suggestions by Rohrbaugh et al. (2002) and Watkins et al. (2015) to determine the radius (r). See more details in the text.

5.3 Chapter specific datasets and methods

Outcrop data from the Cariatiz carbonate platform are interpreted in this study, including ten sampling sites and airborne LiDAR data covering an area of about 0.4 km² (Figure 5.1). Cariatiz is used as an outcrop analogue to understand the complexity of sub-seismic fracture networks as the platform displays a multi-scale system of fractures identified from airborne LiDAR maps down to the outcrop scale. The aim is to correlate fracture networks measured from both field datasets to investigate the relationship between small and intermediate scale of observations. In a later stage, a seismic dataset from the Pernambuco Basin in Brazil was used to analyse fracture networks at a large scale (Figure 5.2). The methodology used in this work is summarised in Figure 5.3.

The main rationale behind the use of datasets from two different localities, and with varied resolutions, was to investigate the effects of scale when characterising multi-scale fracture networks. As observed from platform to basin transects of both platforms, seismic facies and geometries from Pernambuco relate to depositional and structural settings at Cariatiz (Figures 5.2 and 5.4d). In addition, fractures are observed along the platform margin in both Pernambuco and Cariatiz platforms (Figures 5.2c and 5.4d). Nevertheless, each dataset has a distinctive resolution in which a range of specific fracture sizes can be observed. Centimetre-long fractures can be measured from exposure outcrop mapping, whereas fractures with a few metres in length can be mapped from airborne LiDAR datasets, and kilometre fractures can be measured utilising seismic data. This approach was useful to understand which geological features can be observed at each particular scale.

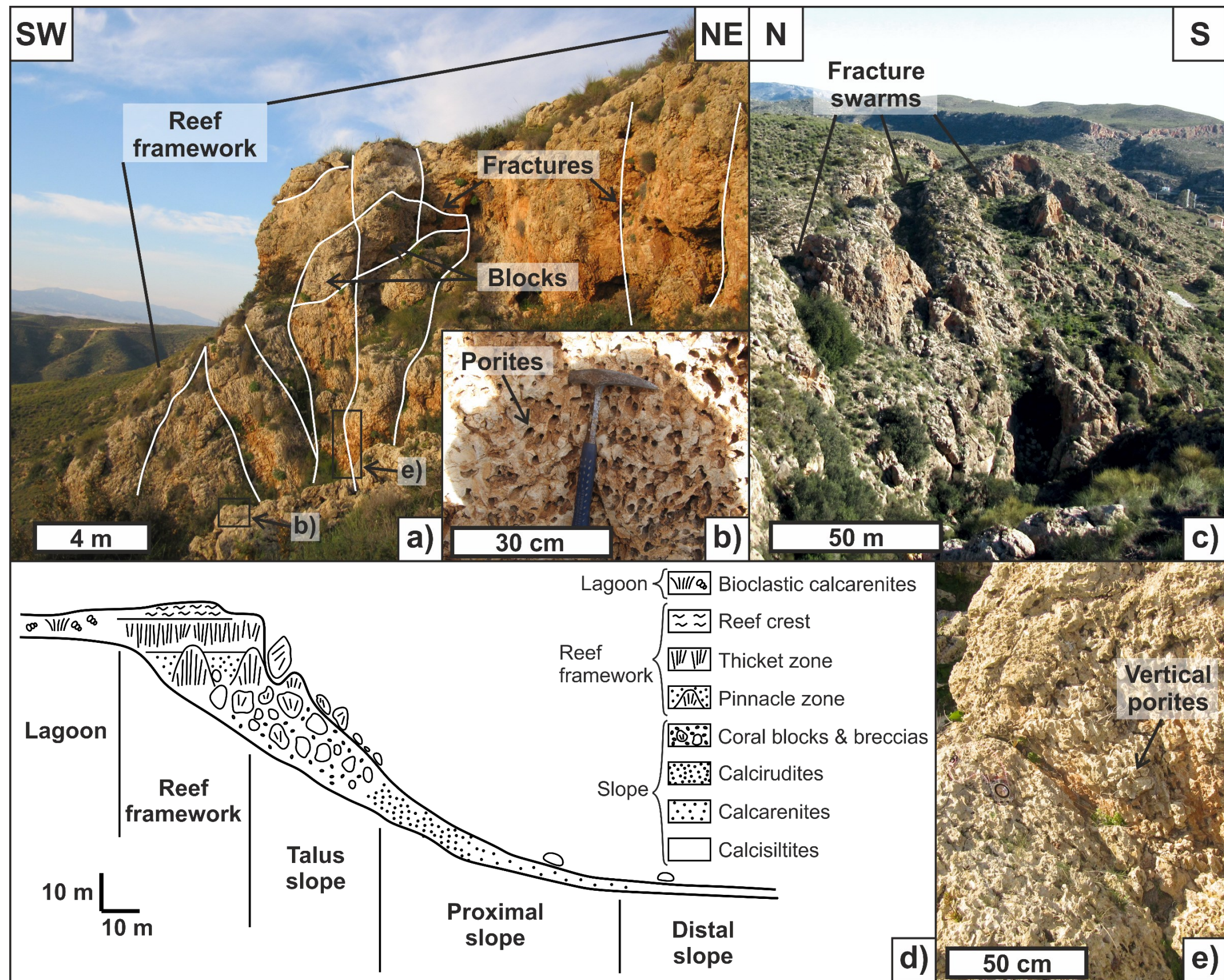


Figure 5.4. Outcrop images and facies model showing the complexity of structural and depositional attributes in the Cariatiz fringing reef unit. A) Outcrop image showing large fractures across the platform edge. B) Enlarged photo showing circular shapes of *Porites* on a horizontal section. C) Fracture swarms along the platform margin. See Figure 5.7a for location. D) Facies model of Cariatiz, modified after Braga and Martin (1996) and Reolid et al. (2014). E) Outcrop photo showing vertical *Porites*. See Figure 5.1c for location.

The analysis discussed in this chapter does not intend to suggest that both platforms have the same fracture network properties, as they have different tectonic histories. In fact, the results demonstrate the differences between the fracture network properties obtained from the two localities. However, the use of outcrop data can help to understand the complexity of fracture networks at different scales of observation, and the amount of detail that is lost due to data resolution.

5.3.1 Topological sampling

A fracture network is defined as a system of fractures developed within the same volume of rock, and may include different fracture sets that could interact by connecting individual fractures (Adler and Thovert, 1999; Sanderson and Nixon, 2015). An important part of the workflow presented in this chapter is to consider the topology of fracture networks from the three studied datasets. Topology is the tool that allows geoscientists to properly characterise the connectivity (and relationships) of a given fractured unit, in addition to geometrical attributes (Manzocchi, 2002; Sanderson and Nixon, 2018). A combined analysis of fracture networks is the best practice, as geometrical data on its own is not sufficient to produce a model reflecting the connectivity of a fractured rock volume. In fact, two fracture networks with the same geometrical properties (orientation, length) can show different connectivity (Sanderson and Nixon, 2018).

This work follows the models of Manzocchi (2002) and Sanderson and Nixon (2015) in which fracture networks are considered in terms of traces (lines) and nodes (fracture intersections and terminations) to form a system of branches between nodes (Figure 5.5a). Fracture network topology is given by the analysis of node types

(I: isolated, Y: abutting or splaying, X: crossing) and branch types (I-I: isolated, I-C: partly connected, CC: doubly connected). It also involves resulting dimensionless parameters such as average number of connections per line (C_L), average number of connections per branch (C_B), and dimensionless branch intensity at percolation (B_{22C}) (Manzocchi, 2002; Sanderson and Nixon, 2015, 2018) (Figures 5.3, 5.5a, and Table 5.1). In order to further differentiate fracture populations, nodal functions such as the N_B/N_L ratio, proportions of connecting nodes (isolated: P_I or connected: P_C) and branches (isolated: P_{II} , singly connected: P_{IC} or doubly connected: P_{CC}) were used in this analysis (Table 5.1).

Topological data and resulting dimensionless parameters are analysed using a series of equations and diagrams from Sanderson and Nixon (2015, 2018) (Table 5.1). A simple approach to assess the topology and connectivity of fracture networks consists of plotting nodal and branch data in ternary plots (Manzocchi, 2002; Sanderson and Nixon, 2015; Morley and Nixon, 2016). Results from each dataset vary between outcrop locations, zones or depths. An area covering the data variability is shown in ternary diagrams in addition to their average values (Figure 5.3). In this work, the Ternary Plot Maker (2019) was used to plot topological data.

As suggested by Sanderson and Nixon (2015, 2018), dimensionless parameters such as C_B , are useful measures to assess the connectivity of a fracture network. Values of C_B range from 0-2. On a ternary diagram, low connected networks with C_B values close to 0, plot towards the I-I corner, whereas high connected networks with C_B close to 2, plot towards the C-C corner with a high proportion of interconnected branches. Furthermore, C_B can be used with B_{22C} to estimate the percolation threshold of a given network topology. Sanderson and Nixon (2018) demonstrated that most percolating systems have values of $C_B > 1.56$.

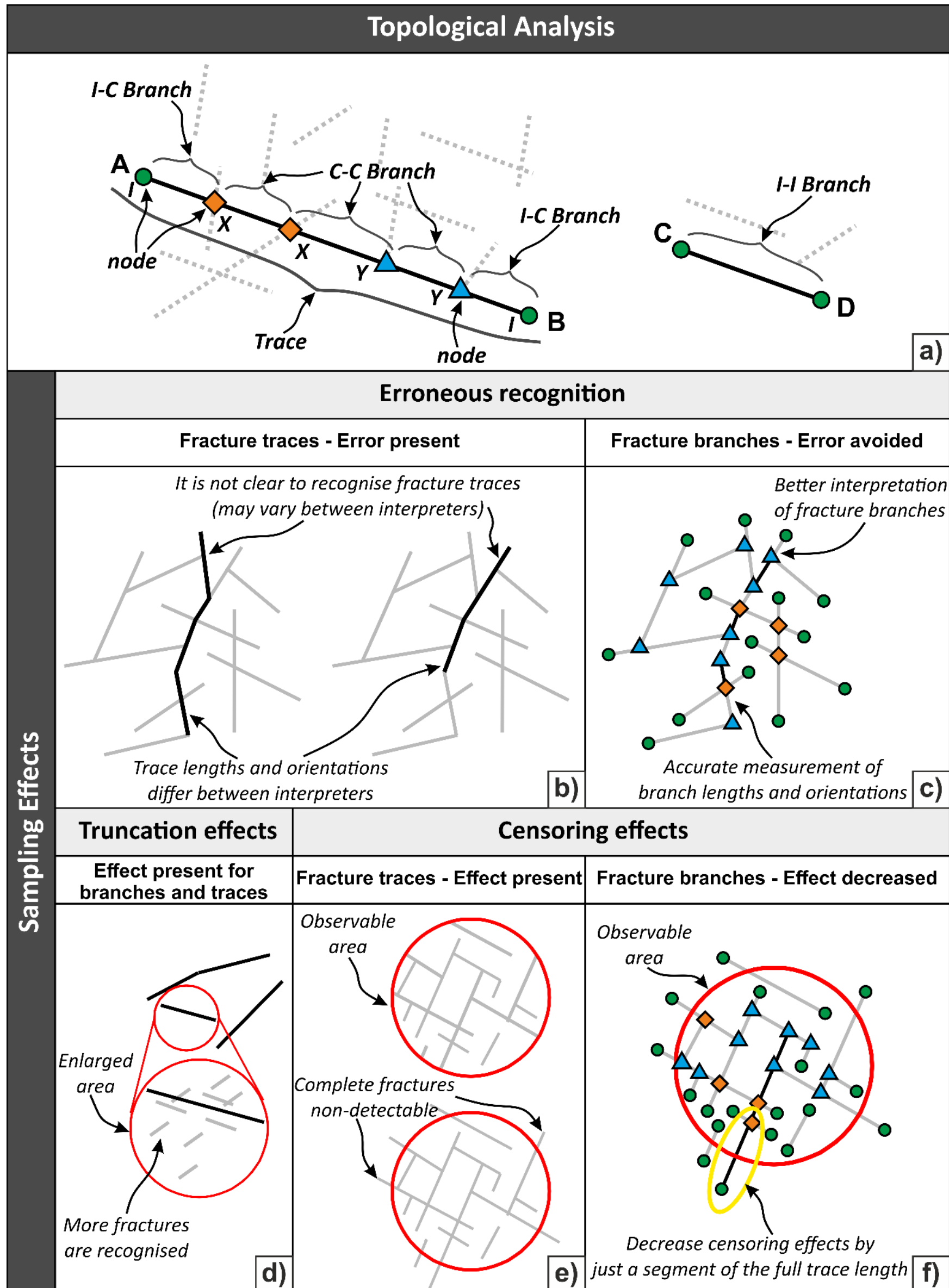


Figure 5.5. Schematic diagrams showing the topological analysis and sampling effects of fracture networks. a) Fracture traces (A-B and C-D) and their node and branch association with intersecting fractures (dashed lines). I-nodes (green circles); Y-nodes (blue triangles); X-nodes (orange diamonds); I-I or isolated branch (I-I nodes with no fracture intersection); I-C or partly connected branch (I-Y or I-X node intersection); and C-C or doubly connected branch (Y-Y, Y-X, or X-X node intersection). Modified from Sanderson and Nixon (2015). b) Erroneous recognition of fracture traces occurs as they can be interpreted differently depending on the criteria used, leading to inconsistent trace lengths and orientations depending on the interpreter. c) By utilising fracture branches as a result of topological analyses, the fracture segments can be identified easier, resulting in reliable measurements of geometrical characteristics. d) Truncation effects occur due to limits in data resolution, and it is present regardless of the use of branches or traces. e) Censoring effects occur as the fractures extend the observable area. f) Censoring effects can be minimised by the use of fracture branches as they do not include the entire trace; rather only one segment of the trace.

Table 5.1. Summary of topological parameters, notation and key equations. Modified from Sanderson and Nixon (2015, 2018).

Parameter	Notation	Equations
Nodes	I, Y, X	Isolated, abutting or splaying, crossing
Number of nodes	N_I, N_Y, N_X	
Branches	$I-I, I-C, C-C$	Isolated, singly-, doubly connected
Total nodes	N_N	$N_N = N_I + N_Y + N_X$
Total lines	N_L	$N_L = (N_I + N_Y) / 2$
Total branches	N_B	$N_B = (N_I + 3N_Y + 4N_X) / 2$
Branches/Lines	N_B / N_L	$N_B / N_L = (N_I + 3N_Y + 4N_X) / (N_I + N_Y)$
Average connections/line	C_L	$C_L = 2 (N_Y + N_X) / N_L$
Average connections/branch	C_B	$C_B = (3N_Y + 4N_X) / N_B$
Branch dimensionless intensity at percolation	B_{22C}	
Probability of isolated nodes	P_I	$P_I = N_I / (N_I + 3N_Y + 4N_X)$
Probability of connected nodes	P_C	$P_C = (3N_Y + 4N_X) / (N_I + 3N_Y + 4N_X)$
Probability of isolated branches	P_{II}	$P_{II} = P_I^2$
Probability of singly connected branches	P_{IC}	$P_{IC} = P_I P_C$
Probability of doubly connected branches	P_{CC}	$P_{CC} = P_C^2$

5.3.2 Geometrical sampling

Geometric parameters considered in this study are branch lengths and branch orientations (strike), as they can be measured at different scales from the three provided datasets. Sanderson and Nixon (2015, 2018) suggested that using branches instead of full traces is a better approach to characterise fracture networks as it can avoid or decrease sampling errors (Figure 5.5b-f). These errors can be related to (1) erroneous recognition, (2) censoring effects, and (3) truncation effects (Manzocchi et al., 2009; Guerriero et al., 2010; Torabi and Berg, 2011 2011; Tao and Alves, 2019).

Due to the complexity of fracture arrangements and the access limitation to entire fracture networks (censoring), it is a challenging task to define the full fracture trace (Figure 5.5b). Erroneous recognition of the full fracture trace is common among interpreters as length and orientation measurements of fracture traces may differ between different interpretations (Figure 5.5b). Variations in the results (e.g. orientation and length) between interpreters can lead to distinct and contrasting conclusions about a given fracture network. Identifying shorter segments (branches) during interpretation is a consistent protocol to measure fracture geometries (Figure 5.5c). Results obtained utilising fracture branches can lead to similarities between interpreters, avoiding the erroneous recognition bias, as the identification of the full trace is not required.

Furthermore, censoring effects occur when a fracture extends beyond the sampling area and the frequency of large fractures is underestimated (Figure 5.5e). This effect can be reduced by the use of fracture branches as the segment outside the sampling area is shorter (Figure 5.5f). On the other hand, truncation effects occur when small fracture frequencies are underestimated as a result of resolution

limitations that cannot be avoided due to data constraints (Figure 5.5d). Therefore, this work stresses the use of fracture branches in all measurements collected, as the obtained values can decrease uncertainties related to fracture sampling and provide more reliable information about the geometrical parameters (length and orientation) (Figure 5.5).

5.3.3 Cariatiz platform

5.3.3.1 Outcrop data - Field procedure

Geometrical and topological attributes were measured from the Cariatiz reef framework zone (Figure 5.4a, d) on 10 outcrop surfaces (a 2D view of a fracture network) using the enhanced circular scanline methodology of Watkins *et al.* (2015) (Figure 5.6). More than 400 fracture traces with ~1000 fracture branches were measured and analysed (Figure 5.6). Topological analyses and field procedures are similar to Sanderson and Nixon (2015) and Procter and Sanderson (2018) in which nodes and branches are defined in the field, followed by rectified outcrop photographs (Figures 5.3, 5.5 and 5.6).

The first stage in the workflow was to select key sampling localities prior to fracture data collection (Figure 5.3). Sampling localities were initially chosen along the platform rim, within the reef framework facies, using aerial photographs and LiDAR maps with elevation and slope attributes (Figure 5.7). This step was crucial to identify accessible areas where the fringing reef could be mapped along exposed outcrop surfaces.

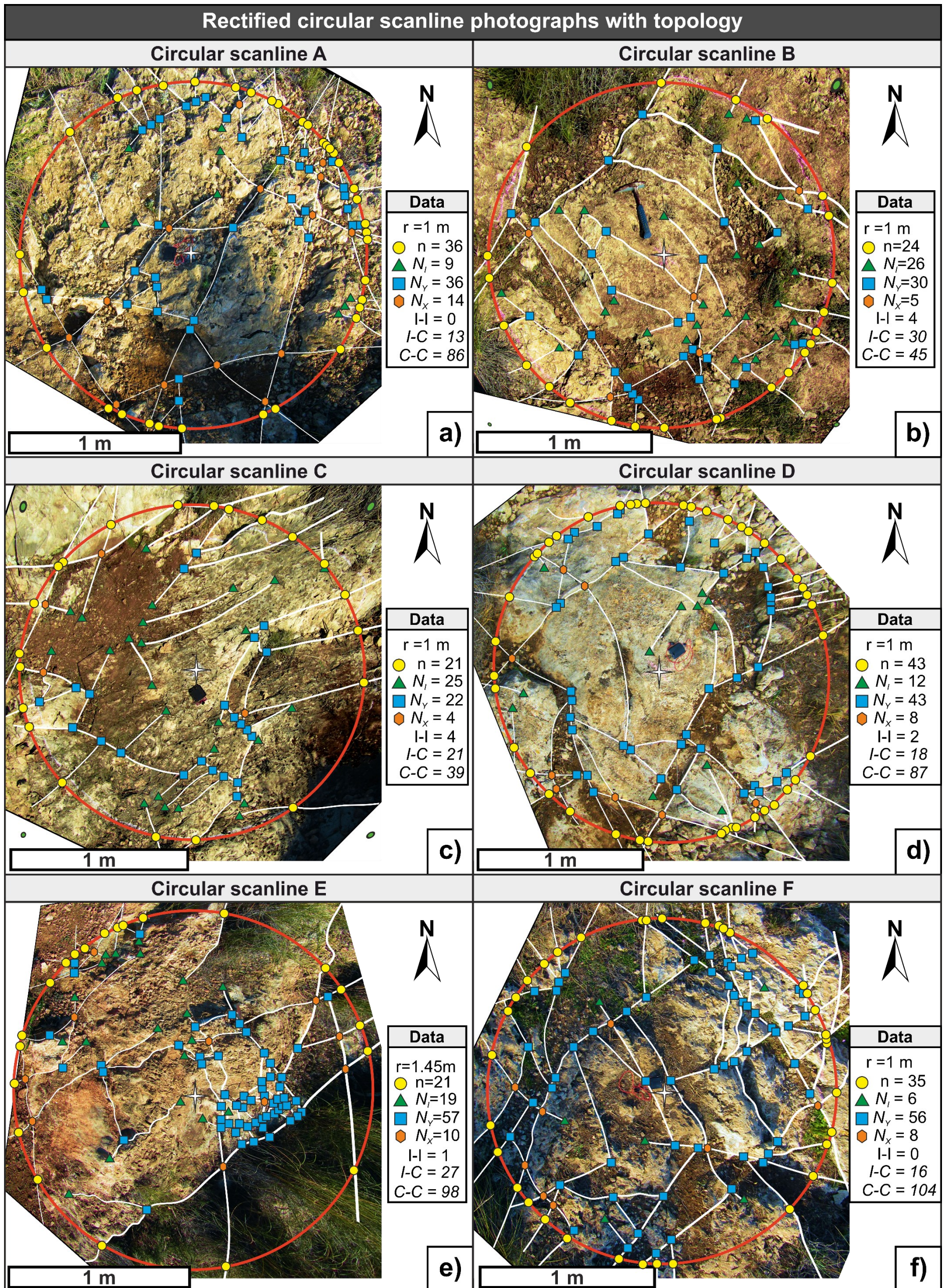


Figure 5.6. Rectified photographs of circular scanlines showing the fracture networks collected at outcrop in Cariatiz. A-j) Digitised fracture networks showing the topological parameters. Circular scanline (red line), fracture intersections with the sampling circle (yellow circle), I nodes (green triangles), Y nodes (blue squares), X nodes (orange hexagons). k) Field photograph showing the grid used to rectify the perspective of the circle. l) Rectified photo where geometrical and topological analyses can be performed.

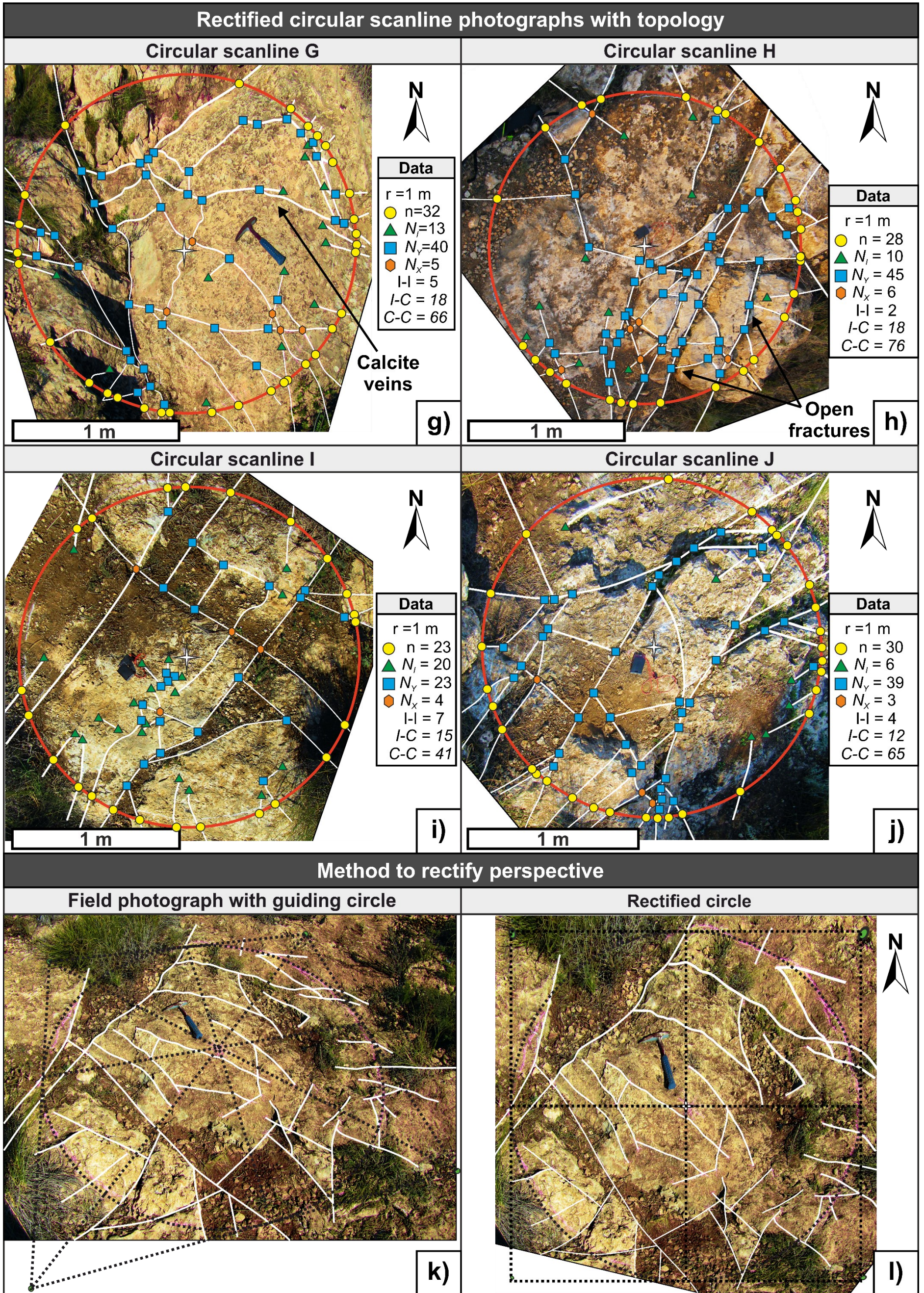


Figure 5.6. Continued.

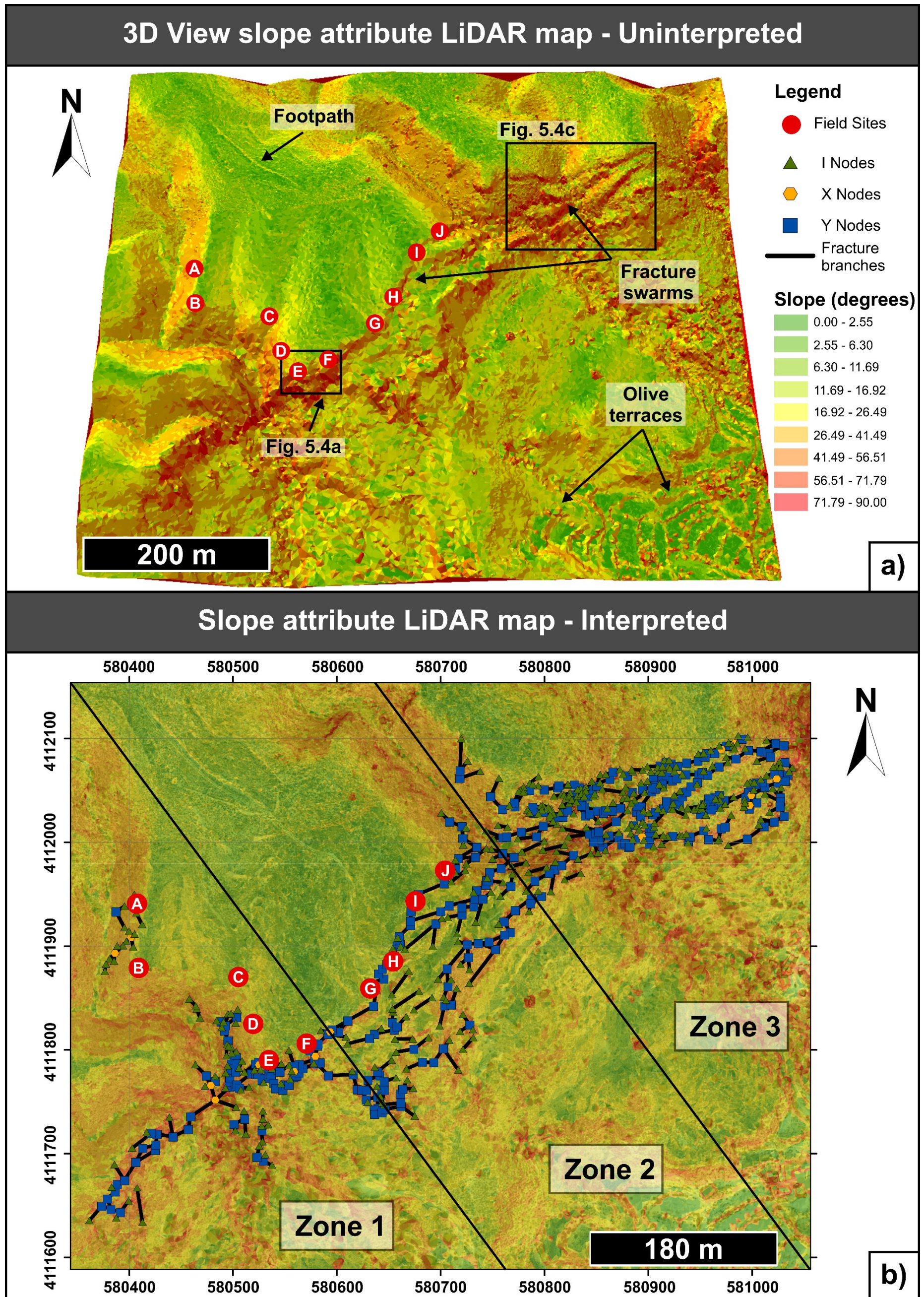


Figure 5.7. LiDAR map of the study area in the Cariatiz carbonate platform with the slope attribute highlighting discontinuities. Fractures present high slope values. Site locations are shown with red circles. A) Uninterpreted 3D visualisation of the LiDAR map, useful to locate outcrop localities and perform fracture interpretation in the intermediate scale. B) Interpreted map showing fracture branches as black lines as well as fracture nodes. The map was divided into three zones to analyse fracture variability.

Field measurements were dependent on how clearly the fractures were exposed at the surface. Vegetation is preferentially localised within fractures, as these are zones of intense weathering where soil accumulates and moisture is retained, especially in arid conditions such as in Cariatiz (Boyer and McQueen, 1964; Aich and Gross, 2008). As a result, soil and vegetation was present at some localities, indicating the presence of open fractures (Figure 5.6b, d). However, prior to fracture measurement, large vegetation was removed, and soil was cleared from the outcrop surface.

The circular scanline sampling method was used to count the number of fracture intersections at the edge of the circle (n) and the number of fracture terminations within the circle (m) (Mauldon et al., 2001; Watkins et al., 2015) (Figures 5.3 and 5.6). At each sampling locality, a circle of known radius was drawn onto the surface using a length of rope with a stick of chalk tied to the end (Figures 5.3 and 5.6). The radius was chosen based on the minimum m and n count (30) of Rohrbaugh *et al.* (2002) and Watkins *et al.* (2015) to ensure reliable fracture estimates and identify individual fracture sets or data clusters (Figure 5.3). Following the method of Procter and Sanderson (2018), every node and branch was marked with chalk of different colours, depending on their type, to help node and branch counting. A sketch of the fracture network was drawn on the go to provide robust documentation of the measured data and to guide digital interpretation at a later stage.

Once fracture nodes and branches were identified within the sampling circle, geometrical measurements were performed in the field. The workflow included measuring fracture branch orientation (strike, dip and dip direction), branch length, as well as identifying aperture and fracture fill. By completion of topological and geometrical measurements, a photograph of the locality was taken for a later use.

Outcrop photographs of the circular scanline were rectified using the graphics suite of CorelDraw and Corel PaintShop Pro in order to remove distortions in 3D perspective (Figure 5.6k, l). This process allows fracture attributes (branches, nodes) to be digitised as a vector graphic image, in order to provide a clear representation to scale of the outcrop fracture networks (Procter and Sanderson, 2018) (Figure 5.6). Topological and geometrical attributes were also measured digitally using the vector lineaments to confirm the values taken in the field (Figure 5.6). This process provides a good quality control of the measured data. Additionally, vector lineaments allow accurate calculations of average orientations and exact length measurements of irregular fracture branches. These latter measurements were the ones used in the subsequent statistical analyses.

5.3.3.2 LiDAR data - GIS analysis

Airborne LiDAR imagery from the Cariatiz carbonate platform permitted the collection of fracture measurements at an intermediate scale. Data was provided by the Instituto Geográfico Nacional (IGN) and the Centro Nacional de Información (CNIG) of Spain (Figure 5.7). The airborne LiDAR map was acquired with a density of 0.5 points/m² with a 5 m grid size. After processing for slope, a resolution of about 5 m is suggested for the airborne LiDAR dataset. As a result, fractures of less than 5 m (below the LiDAR resolution) are subject to truncation effects. Fracture branches ranging from a few metres to tens of metres in length can be resolved from this dataset.

Visualisation and interpretation were carried out using ArcGIS 10.5. A slope attribute was calculated from the LiDAR map to highlight intermediate-scale discontinuities (fractures and fracture swarms) at Cariatiz (Figure 5.7). A 3D visualisation of the LiDAR map, the slope attribute map and aerial photographs were used simultaneously during fracture interpretation, to be confident that the lineaments were real geological fractures and no other elements such as footpaths or agriculture terraces related to abandoned olive fields (Figure 5.7). The LIDAR map was divided into three zones in order to understand spatial fracture variability in Cariatiz (Figure 5.7b).

Each fracture branch was digitised as a single polyline to preserve geometrical characteristics such as fracture branch length and orientation. Guidance from Nyberg et al (2018) was used during the interpretation of fracture branches to avoid topological inconsistencies such as erroneous short isolated fracture branches or overlapping fracture branches. The snapping tool from GIS was crucial in this task. Node counting was performed by digitising points at fracture terminations (I-nodes) or fracture intersections (Y-, X-nodes). Geometrical attributes (length and orientation) were calculated using the “linear directional mean” tool from the “spatial statistics tools” in ArcGIS.

5.3.4 Pernambuco carbonate platform

5.3.4.1 Seismic data - seismic interpretation

The seismic data used in this study includes a depth-converted 3D seismic volume located on the Pernambuco Plateau, offshore East Brazil (Figure 5.2). For full description of the data resolution, please refer to section 3.5.1.2.

Seismic attribute calculation and fracture interpretation were completed using Schlumberger Petrel®. A variance cube was computed for the entire Pernambuco seismic volume to compare the similarity of traces and highlight seismic discontinuities such as faults and fractures (Chopra and Marfurt, 2007; Brown, 2011; Marfurt and Alves, 2015) (Figures 5.3 and 5.8).

Eleven depth slices were analysed and interpreted from $Z = -1020$ to -2020 m at intervals of 100 m (Figures 5.3 and 5.8). Fault interpretation was performed on a portion of the Pernambuco carbonate platform covering the shelf and slope. Faults were interpreted by visualising depth slices and seismic sections simultaneously to make sure that lineaments are real faults with a vertical displacement and avoid interpretation of artefacts (Figure 5.2c). Data was then exported to Esri® ArcGIS Desktop where geometrical (branch length, orientation) and topological (nodal and branch counting) analyses were performed using the same methodology as with LiDAR data (Figures 5.3 and 5.8).

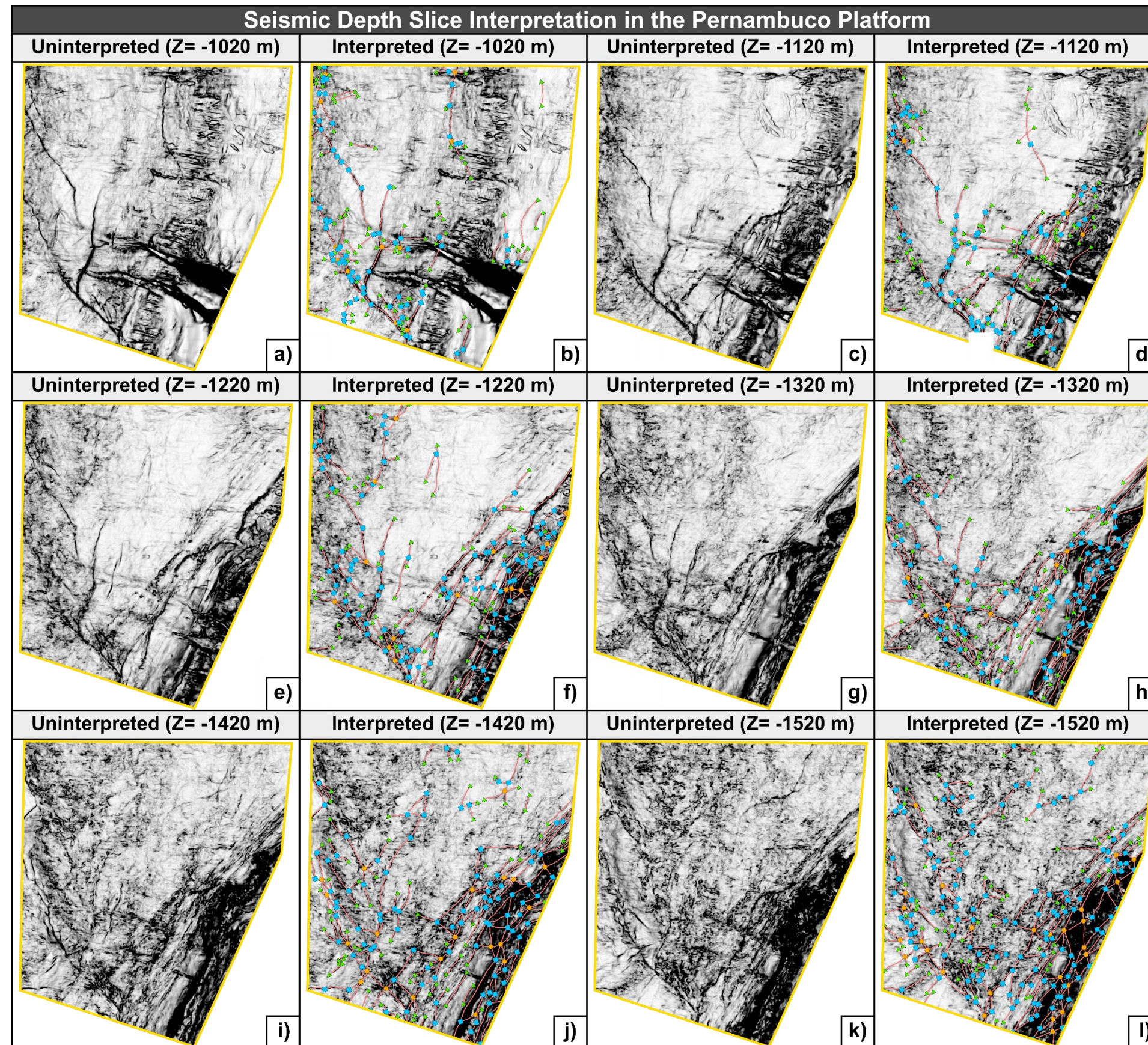


Figure 5.8. Seismic depth slices of the Pernambuco carbonate shelf on the variance attribute computed in this work. Fracture interpretation was performed within an area of interest every 100 m in depth from Z=-1020 m to Z=-2020 m. Topological analyses were also carried out to better understand the fracture network. Fractures are represented with continuous pink lines. I nodes are represented by green triangles, Y nodes by blue squares, and X nodes by orange hexagons. Seismic images are rotated and therefore not in their original orientation due to data protection.

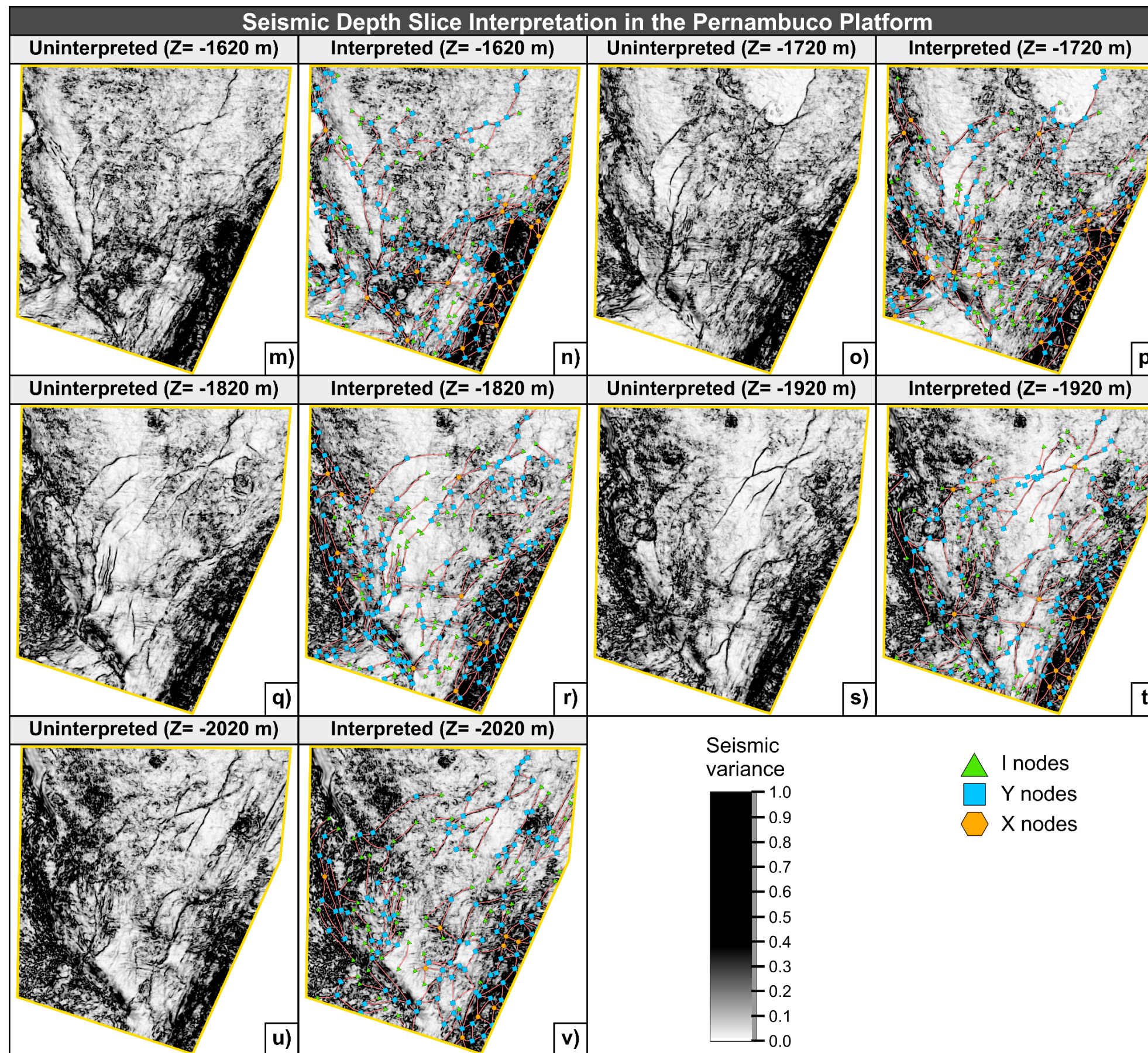


Figure 5.8. Continued.

5.3.5 Statistics and data analyses

A practice to analyse geometrical attributes of a fracture network is to use rose diagrams and frequency distribution plots such as histograms and cumulative plots (Watterson et al., 1996; Odling, 1997; Nyberg et al., 2018). Geometrical data in this work is analysed by equal area rose diagrams and branch length-frequency plots. Branch length measurements were processed using Microsoft Excel, where histograms, box plots, cumulative frequency plots, and tables with statistical data were compiled in order to identify distribution trends (negative exponential, log-normal or power law) in a similar way to Nyberg et al. (2018) (Figure 5.9).

Fracture orientation measurements were processed using the Matlab® version of MARD 1.0 by Munro and Blenkinsop (2012). Rose diagrams were plotted using a bi-directional function with a weighted moving average and equal area. The weighting factor for all plots was 0.9 with a 9° aperture angle for data averaging (Figure 5.10 a-c, B1 and B2). Visual analyses from these rose diagrams suggest that fracture data is multimodal with different fracture sets (Figure 5.10).

Numerical techniques were key in the workflow to define specific fracture sets. Multimodal orientation datasets were divided into clusters utilising the cluster analysis tool in Orient 3.11.1 (Vollmer, 1990, 1995, 2015) (Figure 5.10 d-f). The cluster analysis method included axial data in which the number of clusters (from 2 to 9) is defined by the user. Every data sample was tested using different number of clusters in which the dominant sets were mostly defined regardless of the cluster counts. Visual interpretation of fracture sets based on equal area rose diagrams (Figure 5.10 a-c) was useful in determining the final selection of the number of clusters (Figure 5.10a-c). For every fracture set, the axial mean was calculated using the Statistics Tool within Orient 3.11.1.

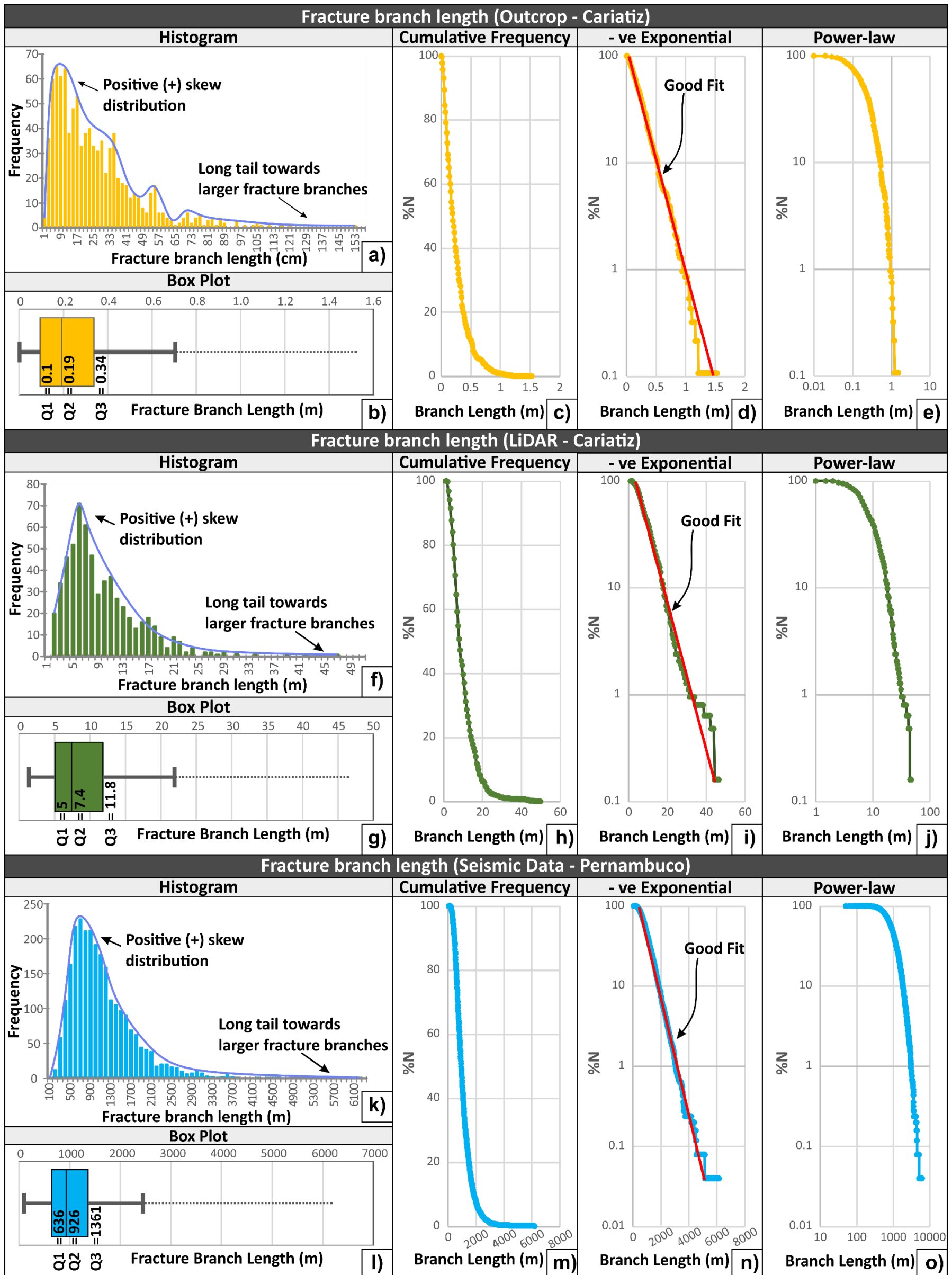


Figure 5.9. Statistical plots showing fracture branch length distribution from three scale datasets. Outcrop data from the Cariatiz carbonate platform is plotted in yellow. LiDAR data from the Cariatiz carbonate platform is plotted in green. Seismic data from the Pernambuco carbonate platform is plotted in blue. A), f) and k) Histograms showing a positive skew distribution. B), g) and l) Box plots showing the concentration of branch lengths. Q1, Q2 and Q3 are the values for the lower quartile, median and upper quartile. Box represents the interquartile range, thick solid grey line represents the minimum and maximum values (whiskers), and dotted line shows the outliers of the data. c), h) and m) Cumulative percentage plotted against fracture branch length; note good fit to a straight line for small branch lengths. D), i) and n) Log (cumulative percentage) plotted against fracture branch length, with straight line indicating negative exponential distribution. E), j) and o) Log (cumulative percentage) plotted against log (fracture branch length), with straight line indicating power-law distribution. Straight red line indicates a good fit.

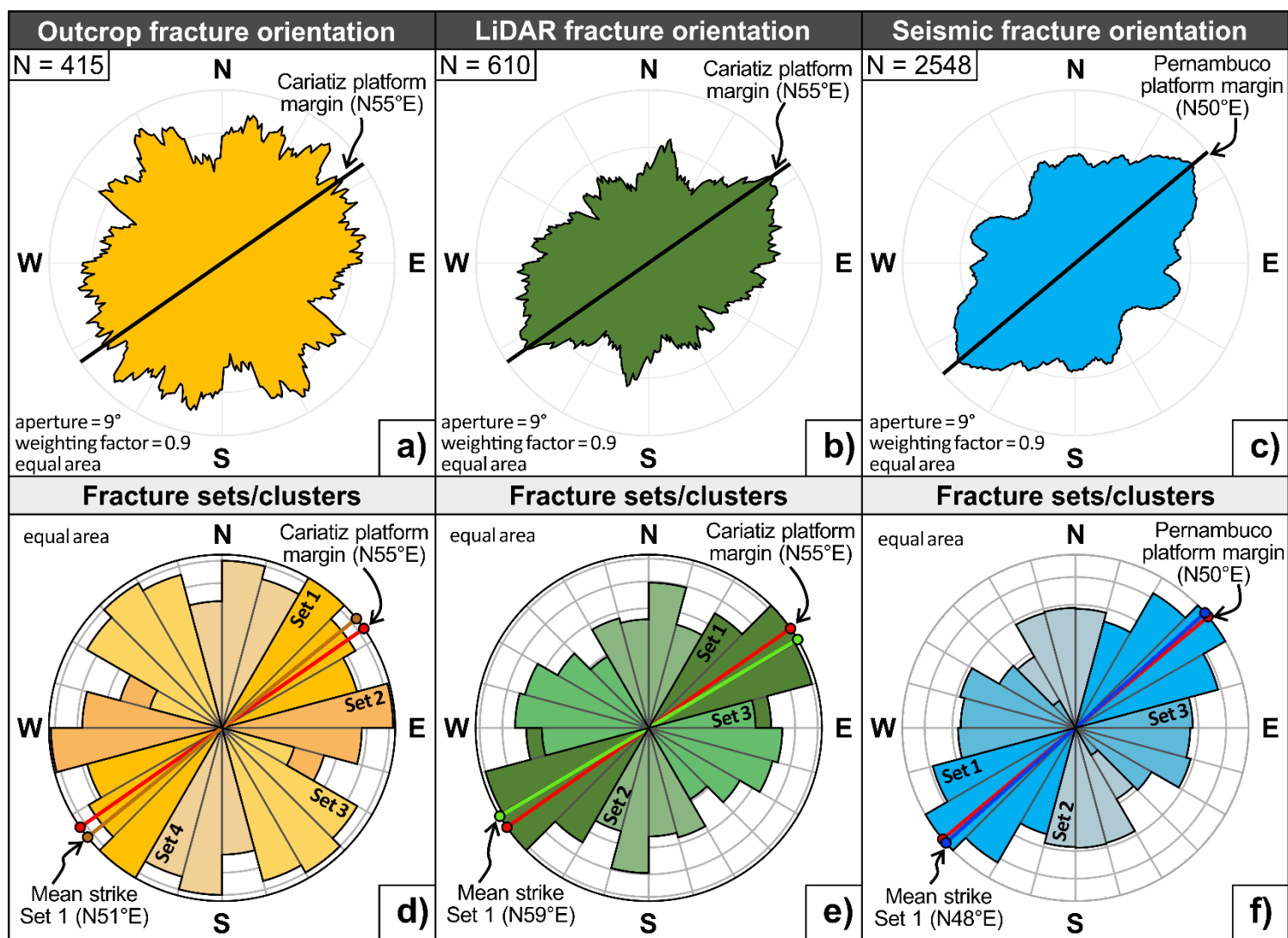


Figure 5.10. Bi-directional moving average rose diagrams and numerical cluster analysis showing fracture orientation and fracture sets from (a and d) outcrop, (b and e) LiDAR, and (c and f) seismic data. Rose diagrams were generated as equal area with a weighting factor of 0.9 and aperture of 9°. Equal area rose diagrams are used to visualise results from the cluster analyses.

5.4 Fracture network characterisation

5.4.1 Fracture complexity

In this study, different fracture types are recognised depending on the scale of observation. At outcrop scale, fracture compartmentalisation, chaotic and curved stylolite surfaces, as well as vertical *Porites* on the platform edge, show how complex the structural and depositional attributes are on carbonate platforms like Cariatiz (Figures 5.4 and 5.6). Open fractures (joints) and veins were recognised across the Cariatiz Reef Unit (Figures 5.4 and 5.6g, h). Veins have calcite infill and can be observed in many of the circular scanlines analysed (Figure 5.6g). Large vertical fractures are visible across the reef framework zone, extending from the reef crest down to the slope facies zone (Figure 5.4a). These fractures create blocks and are related to slope instability.

From airborne LiDAR imagery, the main structures comprise fracture swarms composed of clusters with closely spaced fractures. These fracture swarms are identified in the field (Figure 5.4c) but can be better mapped and measured with slope attribute maps from airborne LiDAR data (Figure 5.7). At the largest (seismic) scale of Pernambuco, normal faults are observed from different depth slices and profile sections (Figure 5.8). These faults have variable throws ranging from a few tens of metres (reaching the data resolution) up to 300 m in some areas (Figure 5.2c). These faults have regional and large-scale tectonic origins in contrast to those observed at outcrop.

5.4.2 Fracture network geometry

5.4.2.1 Fracture length

5.4.2.1.1 *Cariatiz platform - outcrop data*

The length of fracture branches at Cariatiz displays a wide range of sizes (Figures 5.9a, b and A1). However, every site has a similar distribution of fracture branch lengths with a positive skew (Figure A1). Data gathered from the ten field sites also have a positive skew, showing that smaller fracture branches are the most abundant with centimetre lengths (Figures 5.9a and A1). Higher frequencies are observed in fractures ranging from 9.4 cm to 33.8 cm with a medium value of 19.3 cm and a mean of 25 cm (Figure 5.9b).

Sites A and C present a unimodal distribution with a positive skew. The dominant lengths are 3 to 25 cm (Figure A1a, c). Fracture branch length at Sites B and I show a multimodal distribution (Figure A1b, i). There are two dominant peaks with ranges of 3 to 13 cm and 31 to 41 cm (Figure A1b, i). Sites D and G have a bimodal distribution with major fracture length frequencies ranging from 5 to 17 cm and 21 to 39 cm in length (Figure A1d, g). Fracture distribution in Site E shows a large positive skew with the highest frequency observed in fractures ranging from 3 to 11 cm (Figure A1e). Sites F and H present a major peak in fractures ranging from 9 to 21 cm in length (Figure A1f, h). Site J has a positive skew distribution, with a highest peak representing fractures from 3 to 21 cm in length (Figure A1j).

Cumulative percentages of fracture branch lengths were plotted to determine if they fit a distribution trend such as negative exponential, log-normal or power-law distribution models (Figure 5.9c, d, e). Outcrop data is best represented by a negative exponential or lognormal distribution (Figure 5.9d). A deviation from this trend is observed for the longest branches due to truncation effects.

5.4.2.1.2 *Cariatiz platform - LiDAR data*

Airborne LiDAR imagery has a resolution of 5 m, implying that lineaments with sizes below this value, such as centimetre-long fracture branches mapped at outcrop (joints and veins), cannot be identified on the LiDAR map (Figure 5.7). Instead, fracture swarms that are difficult to measure at outcrop (Figure 5.4c), can be easily recognised and measured at this scale (Figure 5.7). Areas that appear to be highly fractured at outcrop, such as Site C (Figure 5.6c), appear as areas with no fractures on the LiDAR map (Figure 5.7), a character related to the absence of fracture swarms in that section of the platform.

The study area was divided into three different zones in order to understand fracture variability along the platform margin (Figure 5.7b). Fracture branch length at the LiDAR scale ranges from 1.4 to 47 m. Data present a positively skewed distribution, similar to outcrop data (Figure 5.9f, g). The higher concentration of fracture branches is observed from 5 m to 11.8 m, with a median value of 7.4 m and a mean of 9.2 m (Figure 5.9f, g). Zones 1 and 3 have a positively skewed histogram (Figure A1k, m). The dominant fracture branch length ranges from 4 to 11 m. Zone 2 has more variability with a less positive skewed histogram and dominant fracture branch lengths ranging from 6 to 20 m (Figure A1l).

Plots of cumulative percentage against fracture branch lengths display a similar pattern to the outcrop data, having the best fit with a negative exponential or log-normal distribution (Figure 5.9h, i, j). A power-law distribution is only representative with fracture branches longer than 10 m.

5.4.2.1.3 *Pernambuco platform - seismic data*

Fractures (faults) in the range of hundreds of metres to a few kilometres predominate on seismic data from Pernambuco. These faults have throws ranging from a few metres up to 300 m (Figure 5.2c). In Pernambuco, the highest fracture frequency is represented by features between 636 m to 1360 m with a median value of 926 m, and a mean of 1064 m (Figure 5.9k, l). Due to its resolution, features that were observed in the field at the Cariatiz platform such as fracture swarms, joints and veins are not visible in seismic data.

Fracture branch length distribution from depth slices at $Z=-1020$ m and $Z=-1220$ show a positive unimodal skew. The major peak is observed with branch lengths of 300 to 700 m (Figure A2a, c). At a depth of -1120 m, fracture branch lengths have a multimodal distribution with a concentration of fractures between 500 to 600 m. Fault lengths range from 200 m to 2500 m (Figure A2b).

The variance slice at a depth of $Z= -1320$ m shows a multimodal distribution with length peaks at 700 m, 1100 m, 1400 m and 1700 m. Most of the data ranges from 200 m to 2600 m with a few outliers (Figure A2d). At $Z= -1420$ m, a slight positive skew with unimodal distribution is observed (Figure A2e). The dominant fracture branch length ranges from 600 m to 1200 m (Figure A2e). Fracture branch length distribution at $Z= -1520$ m ranges from 300 m to 3100 m, with predominant fractures between 700 m to 1100 m (Figure A2f). A unimodal distribution is recognised on the variance slices at $Z= -1620$ m, -1720 m, -1820 m, -1920 m and -2020 m. Fracture branch lengths range from 300 m to 3500 m. At these depths, the dominant values range from 500 m to 1300 m. A positive skew with a long tail towards the larger values is observed in all histograms (Figure A2g, h, i, j, k). A negative exponential or

log-normal distribution plot displays a reasonable fit over most of the data range at seismic scale. A poor fit is observed in longer faults (Figure 5.9m, n, o).

5.4.2.2 Fracture orientation

5.4.2.2.1 *Cariatiz platform - outcrop data*

Fracture strike distributions from field measurements differ slightly from site to site with rose diagrams showing different orientations at each locality (Figures 5.1c and B1). Data gathered from all localities display a multimodal distribution with fractures striking nearly in all directions with similar frequencies (Figure 5.10a). However, four fracture sets are defined based on the cluster analysis (Figure 5.10d). The first two sets strike NE and E-W with an axial mean of N51°E and S89°E, respectively. The third set strikes SE (S38°E) followed by a fourth set striking N-S (S11°W). The axial mean of fracture set 1 is almost parallel to the orientation of the Cariatiz platform margin (Figure 5.10d).

Sites A and B contain fracture sets with a multimodal distribution (Figures 5.1c and B1a, b). Three fracture sets with high frequency are recognised. The first one strikes NE, while the second and third sets strike NW. Site C and D exhibit three fracture sets; the highest frequency coincides with a SW strike, followed by E-W fractures and a set striking to the SSW (Figures 5.1c and B1c, d). Outcrop surfaces at Sites E, F and G have two main fracture sets: a first set with a NW strike, and a second set striking widely NE (Figures 5.1c and B1e, f, g). Fractures at Site H exhibit three main fracture sets, with the most dominant striking NE. The second and third fracture sets strike to the WNW and to the NW (Figures 5.1c and B1h). Fractures at Sites I and J show a dominant NE strike, followed by NW (Figures 5.1c and B1i, j).

5.4.2.2.2 *Cariatiz platform - LiDAR data*

The average orientation of the Cariatiz carbonate platform margin is N55°E, as observed from the aerial and LiDAR maps (Figures 5.7 and 5.10b). Three fracture sets are recognised on LiDAR data along the Cariatiz fringing reef (Figure 5.10e). The dominant Set 1, with the highest frequency, strikes to the NE (N59°E), in a direction similar to the edge of the platform margin (Figures 5.7, 5.10b and e, and B1k, l, m). The second and third minor fracture sets strike to the N-S (N02°W) and SE (S71°E), respectively. The second fracture set is recognised in the three zones, but it is more predominant in Zone 1 (Figure B1k).

5.4.2.2.3 *Pernambuco platform - seismic data*

The orientation of the Pernambuco carbonate platform margin is N50°E as observed from seismic depth slices (Figures 5.2b and 5.10c). Cluster analysis of fault orientation data from the eleven depth slices reveal a major set of faults (Set 1) aligned NE (N48°E), a direction parallel to the platform edge (Figure 5.10c, f). Two minor fracture sets with lower frequencies, striking N-S and E-W, are also recognised with axial means of S09°E and S77°E, respectively (Figure 5.10f).

From each depth of observation, data can be summarised as follows. Fractures at Z=-1020 m depth predominantly strike NW (Figure B2b). Two secondary sets are also recognised with NE and NNW strikes. At depths of Z= -1120 m, -1220 m, -1320 m and -1420 m, there are similar fracture orientations with a dominant set striking to the NE, followed by two minor fracture sets striking NNW and WNW (Figure B2c, d, e). A primary fracture set striking NE is recognised from Z= -1520 m to -2020 m (Figure B2g, h, l, j, k, l).

5.4.3 Fracture network topology

5.4.3.1 Cariatiz platform - outcrop data

Abutting or Y nodes are the dominant type of nodes at the outcropping Cariatiz platform. Nodal data change slightly at each locality, which is observed as a zone of variability on the ternary plots (Figures 5.11a and C1a). Based on average results, the proportion of isolated nodes (P_I) at outcrop is low with a value approaching 9%, whereas the proportion of connected nodes (P_C) is 91% (Table D1). At Cariatiz, from outcrop scale, branch classification shows that isolated branches (P_{II}) are only 0.8%. The highest proportions are related to connected branches with 8.3% being singly connected (P_{IC}) and 82.4% being doubly connected (P_{CC}) (Table D1). The N_B/N_L ratio ranges between 2 to 4, but most values lie around 3, suggesting that small scale-length fracture networks are dominated by abutting or splaying fracture terminations (Figures 5.11b, C1b, and Table D1).

From the connectivity analysis, it was determined that in Cariatiz, the average number of connections per line (C_L) ranges from 2 to 5, with 50% of the data ranging between 3 to 4 (Figures 5.11c, C1c, and Table D1). Moreover, 70% of the outcrop fractures at Cariatiz have a C_B value ranging between 1.8 to 2 (Figures 5.11d, C1d, and Table D1), suggesting that the fracture network is well connected, mostly by Y nodes. High values of C_B also indicate that fracture networks at Cariatiz are above the percolation threshold. The branch classification diagram plots values towards the C-C corner (Figures 5.11e and C1e), stressing the high proportion of interconnected branches at Cariatiz, which can favour fluid flow. Fracture networks from localities B, C and I are less connected than most data and are typical of multimodal joint networks (see Procter and Sanderson, 2018) (Figure C1a). These localities have tree-like geometries based on the average degree $\langle d \rangle$ value from Sanderson et al (2019).

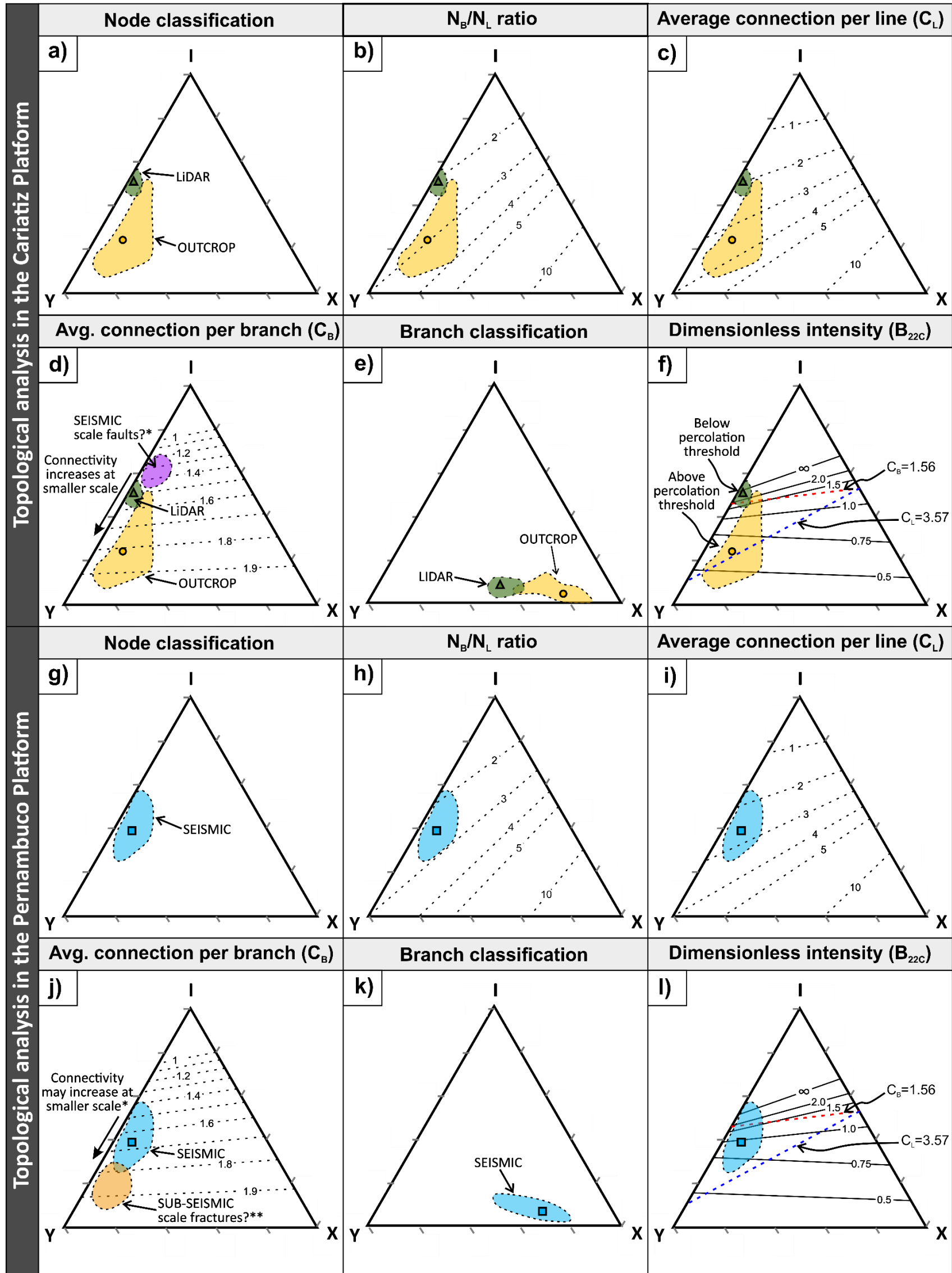


Figure 5.11. Triangular plots showing detailed topological analyses of nodes and branches and resulting parameters from different scales of observation. A) to f) Outcrop and LiDAR topological results from the Cariatz Fringing Reef Unit. G) to l) Seismic topological results from the Pernambuco carbonate platform. Yellow area represents the variation in results from outcrop data. Green area represents the variation in results from LiDAR maps. Similarly, blue area represents the variation in results from seismic data. *Purple area is an interpretation of topological values expected with branch lengths observable at seismic scale in Cariatz. **Orange area is an interpretation of expected values at sub-seismic scale in Pernambuco assuming that fracture connectivity increases at a smaller scale, similarly to the observed trend in Cariatz. A, g) Fracture network node classification. Yellow circle: average value from outcrop data; green triangle: average value from LiDAR data; and blue square: average value from seismic data. b, h) N_B/N_L ratio shows values of 3 for outcrop data, 2 for LiDAR data, and 2.5 for seismic data. c, i) Average number of connections per line (C_L) shows a value of 3.4 at outcrop level, a value of 2 from LiDAR data, and a value of 2.6 from seismic data. d, j) Average number of connections per branch (C_B) with a value of 1.82 at outcrop scale, 1.49 at LiDAR scale, and 1.66 at seismic scale. E, k) Branch classification with I-I isolated branches, I-C partly connected branches, and C-C doubly connected branches. f, l) Dimensionless intensity of branches at percolation (B_{22c}).

5.4.3.2 Cariatiz platform - LiDAR data

LiDAR data indicates that on average, 51% of the nodes are of type I and 47% are of type Y, with only 2% of X nodes (Figure 5.11a and Table D1). It suggests that fracture connectivity at a metre-scale is not as developed as at the centimetre-scale. At an intermediate scale, the proportion of isolated nodes (P_I) is 25% and that of connected nodes (P_C) is 75% (Table D1). Branch classification reveals that proportions of isolated branches (P_{II}) represent 6.5% of the network and singly connected branches (P_{IC}) comprise 19% of the network. Higher proportions relate to doubly connected branches (P_{CC}) with 55.5% (Table D1).

The N_B/N_L ratio has a value of 2, suggesting low proportions of connected branches at the metre-scale (Figure 5.11b and Table D1). The average number of connections per line (C_L) and per branch (C_B) are also lower than at outcrop, with values of 2 and 1.5, respectively (Figure 5.11c, d and Table D1). Despite the observed low values of branch connectivity, single and double connected branches dominate the fracture network at the metre scale (Figure 5.11e and Table D1). These fracture networks are tree-like and multicomponent, which suggest that the fractures observed here are localised and therefore not part of a connected regional system (Sanderson et al., 2019).

5.4.3.3 Pernambuco platform - seismic data

Fracture topology on the Pernambuco carbonate platform is represented on average, by 39% of I nodes, 54% of Y nodes and 7% of X nodes (Figures 5.11a, C1g, and Table D1). The average proportions of having isolated nodes (P_I) is 17%, and the proportion of connected nodes (P_C) is 83% (Table D1). These proportions are similar

to Cariatz, as the proportions of connected nodes are higher than isolated nodes (Table D1). Regarding proportions of branches in Pernambuco, the proportion of isolated branches (P_{II}) are 2.9% (P_{II}) followed by singly connected branches (P_{IC}) with 14%. Higher proportions are observed in doubly connected branches (P_{CC}) with 69.1% (Table D1).

The N_B/N_L ratio ranges from 2 to 3 (Figures 5.11b, C1h, and Table D1). The average number of connections per line (C_L) is 2.64, with a range between 2 and 3. The average number of connections per branch (C_B) has a wider range from 1.4 to 1.8 and a median value of 1.66, suggesting a moderate fracture connectivity at the seismic scale and networks close to the percolation threshold ($C_B = 1.56$) (Sanderson and Nixon, 2018) (Figures 5.11c, d; C1j, l and Table D1). Doubly connected branches dominate the fracture network at seismic scale (Figures 5.11e, C1k, and Table D1).

5.5 Chapter specific discussion

5.5.1 Fracture attribute relationships at different scales

Previous studies have explored the idea of limitations due to data resolution and the effects of scale on the spatial arrangements of fault and fracture networks. For instance, studies such as Strijker et al. (2012) and Gutmanis et al. (2018) have examined the challenges related to the analysis of sub-seismic fracture networks and the presence of an “intermediate” data gap between fractures observed from seismic and borehole datasets. Furthermore, extensive research including Odling (1997) and Watterson et al. (1996) have discussed scaling relationships of fracture networks and the uncertainties related to sampling effects. Pickering et al. (1997) and Nixon et al. (2012) have also suggested that resolution limitations of seismic data

affect the estimation of fault network parameters such as connectivity, as this appears to change depending on the data resolution.

This chapter aims to perform a multi-scale analysis to understand the inherent complexity of natural fracture networks, the existing differences at each scale and their scale dependency. A way to understand sub-seismic features is by using outcrop analogues. For this reason, I used exposure mapping and airborne LiDAR maps from the Cariatiz carbonate platform in SE Spain. In parallel, seismic datasets such as the one from the Pernambuco carbonate platform in Brazil are important to study km-long subsurface features. It is recognised from geometrical and topological analyses of fracture networks from Cariatiz that they have different attributes depending on the scale of observation, which may also be related to the distinct fracture types observed at each scale (Figure 5.12).

5.5.1.1 Fracture geometry

5.5.1.1.1 *Orientation*

The Cariatiz carbonate platform margin is oriented N55° E (Figure 5.10). Fracture branch orientation data differ between centimetre scale-length (outcrop) and metre scale-length (LiDAR) fractures. Rose diagrams from each dataset have different distributions, implying that fracture development may vary depending on scale (Figure 5.10). Equal area rose diagrams show a multimodal distribution of fracture orientations at outcrop (Figure 5.10a and d). These fractures are specifically recognised as open joints and calcite filled veins (Figures 5.6g, h and 5.12a). Numerical methods of cluster analysis were key to divide the data into four fracture

sets with similar frequencies (Figure 5.10d). Fracture set 1 is important as it strikes parallel to the Cariatiz platform margin with an axial mean of N51° E (Figure 5.10d).

At airborne LiDAR scale, the main lineaments comprise large fracture swarms that may be better related to gravitational instability at the edge of the platform margin (Figures 5.4c, 5.7 and 5.12a). Small centimetre-length fractures identified from the outcrop exposure mapping are not visible at LiDAR scale due to limitations in resolution, as the smallest features identified are about 5 m in length (Figures 5.7 and 5.9g). Furthermore, the orientation distribution and cluster analysis of fractures observed from airborne LiDAR data show a clear dominant fracture set striking NE-SW, with an axial mean of N59° E (Figure 5.10e). The orientation of the Cariatiz platform margin (N55° E) is similar to the dominant fracture set 1 identified from LiDAR data (Figure 5.10e), suggesting that intermediate scale-length fractures are dependent on the geometry of the platform (Figures 5.7 and 5.10e).

The orientation of the Pernambuco platform margin is N50° E (Figure 5.10f). Similarly to LiDAR data from the Cariatiz platform, the dominant fracture set recognised from the equal area rose diagrams and cluster analysis, is parallel to the platform margin with an axial mean of N48° E (Figure 5.10c and f). This result suggests that fractures at intermediate and large scales, namely fracture swarms and kilometre faults respectively, are mainly controlled by the geometry of the platform margin (Figures 5.8 and 5.10). Although there is a fracture set recognised at outcrop that also correlates to the Cariatiz platform margin, it is not the most dominant set at the cm scale. This suggests that at outcrop, fracture development is also highly controlled by other processes such as intense weathering, and the uplift of the platform, in addition to gravitational instability at the proximity of the platform edge.

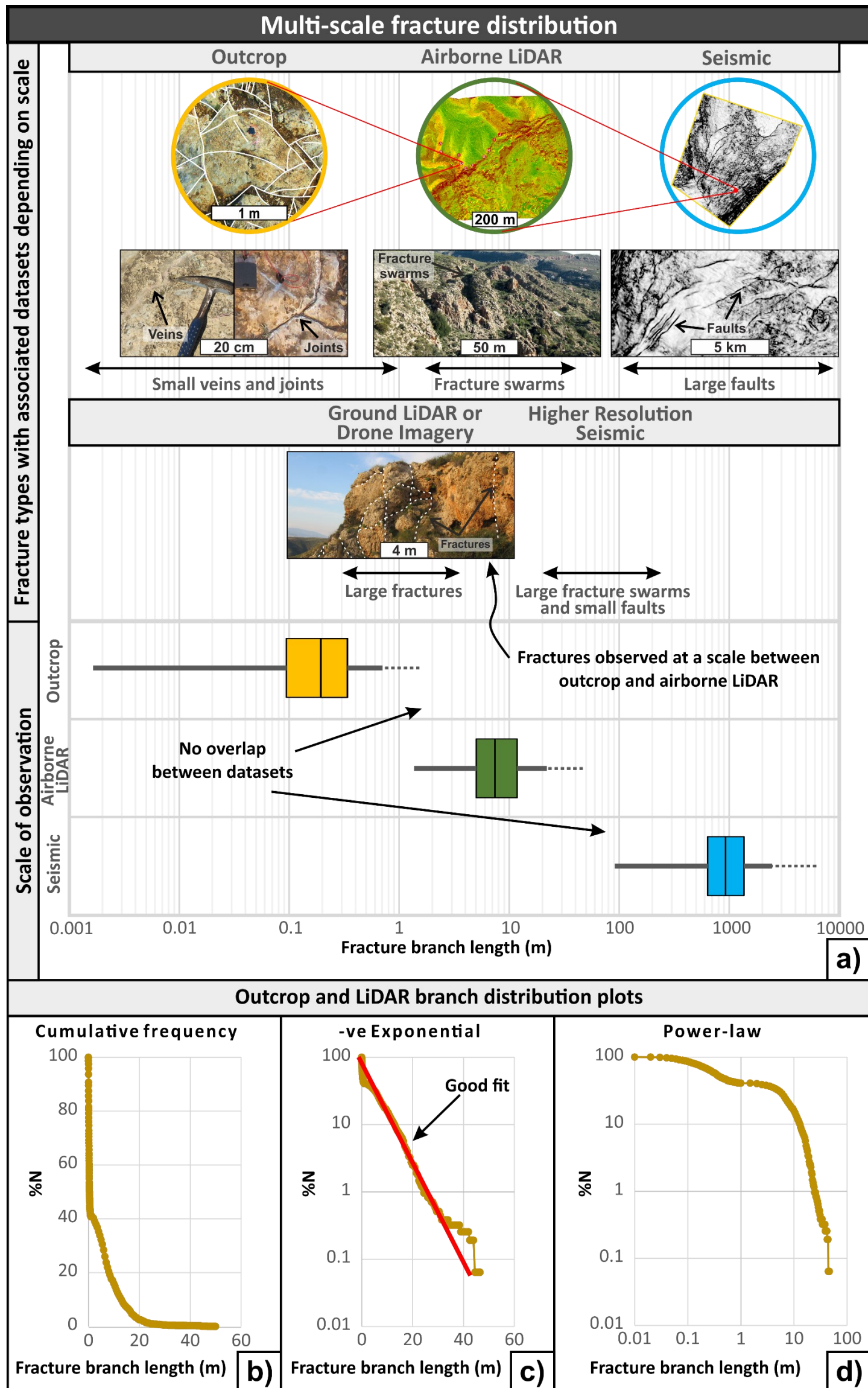


Figure 5.12. Multi-scale statistics of fracture branch lengths and figures showing different fracture types with associated datasets depending on scale. A) Outcrop photos with associated datasets and box plots showing the distribution of fracture branch lengths between different datasets. It is observed from the box plots that there is no overlap between datasets (outcrop - airborne LiDAR and airborne LiDAR - seismic). Large fractures with a scale between outcrop and airborne LiDAR were recognised in the field and can be mapped with the use of ground LiDAR or drone imagery. Fractures observed at each scale are mainly of a different type. Veins and joints can be mapped at outcrop; fracture swarms can be mapped with airborne LiDAR maps; and large kilometre faults can be mapped by using seismic data. Fractures with a branch size in between the scale of the three studied datasets can be mapped with data of different resolution such as drone imagery and higher resolution seismic. B) Cumulative percentage plotted against fracture branch length; note good fit to a straight line for small branch lengths. C) Log (cumulative percentage) plotted against fracture branch length, with straight line indicating negative exponential distribution. D) Log (cumulative percentage) plotted against log (fracture branch length), with straight line indicating power-law distribution. Straight red line represents a good fit.

5.5.1.1.2 *Scale gap*

Studies such as Strijker *et al.* (2012) have identified a scale gap between fractures resolved on seismic and borehole data. Outcrop data from this study are used to describe fractures that occur in this “intermediate” gap. Scale gaps are created by the limited resolution of the imaging methods, and resolution is given by the smallest feature that can be observed and measured in a specific dataset. Exposure mapping from outcrop data can be useful to identify joints and veins (Figure 5.6g, h) covering three orders of magnitude with fracture branches ranging from 10^{-3} to 10^0 m in length (Figure 5.12a). Airborne LiDAR data can cover two orders of magnitude with fracture branches ranging from 10^0 to 10^2 m in length (Figure 5.12a), with the main observed features being fracture swarms. Fracture branch length measurements from outcrop and LiDAR data at Cariatiz, show that the higher frequencies of branch lengths range from 10 to 34 cm and 5 to 12 m, respectively (Figures 5.9b, g and 5.12).

Fracture lengths in both datasets are below seismic resolution. Even the less abundant and largest fracture branches recognised on LiDAR, which are part of the outliers of the data, have lengths of less than 50 m. Given a line spacing of 25 x 25 m on a seismic dataset, these fracture lengths would be subject to truncation effects and not visible from seismic data (Figures 5.9g, d and 5.12). Moreover, the smallest fracture branch length recognised on seismic data is 100 m (Figures 5.9k, l and 5.12). As a result, a scale gap in terms of fracture branch length is observed with no overlap between datasets (outcrop-LiDAR and LiDAR-seismic) due to the fact that resolution limits in the imaging methods constrain reliable fracture characterisation (Figure 5.12a). A fundamental issue when measuring fractures from any source of data is the inherited limitation of the sampling bias due to censoring and truncation effects (Guerriero *et al.*, 2010; Torabi and Berg, 2011 2011) (Figure 5.5). These effects can

cause under- or over- estimation of statistical parameters, compromising the results of fracture characterisation.

As observed in the field, fractures at the “transitional” scale do exist in nature, and the gap can be breached by using a dataset that can cover the resolution of those features. For instance, large vertical fractures are observed at the edge of the Cariatiz platform, creating compartmentalised blocks (Figure 5.4a). Those fractures have high censoring effects at the outcrop scale as they extend outside the observable area, and at airborne LiDAR they are not identified due to truncation effects; therefore their presence is underestimated (Figures 5.5d, e and 5.12a).

The Pernambuco seismic data is useful to understand features (faults) that one can encounter when analysing large carbonate platforms such as Pernambuco's, which is more than 40 km wide and hundreds of kilometres long (Figure 5.2). From this study, it was determined that at this scale, fracture branches can be observed and measured with a range of 10^2 to 10^4 m in length (Figure 5.12a). However, when comparing large carbonate platforms with smaller structures such as isolated carbonate platforms (ICPs), these latter have dimensions ranging from 2 to 18 km, such as those ICPs in the North West Shelf of Australia (Loza Espejel et al., 2019b) and the South China Sea (Zampetti et al., 2004, Fig. 15). Internal fault branches within these structures are a few hundreds of metres long and cannot be fully resolved in seismic data. These types of faults would be part of the “transitional” gap that cannot be resolved by using datasets with comparable scales to either airborne LiDAR maps or seismic data (Figure 5.12a). Only large, regional faults crossing the ICPs can be easily observed in seismic data. This is related to the size of the fractures as well as the seismic response in ICP facies. ICP facies are typically characterised by chaotic and low amplitude reflectors (Burgess et al., 2013; Loza

Espejel et al., 2019b). Any feature below this range is considered as sub-seismic and therefore additional data with higher resolution is required to be able to observe these faults (Figure 5.12a).

The problem of scale gaps between datasets is partly related to the fact that, in all datasets, the highest frequency of fracture branch lengths is concentrated at the smaller lengths of each resolution, which is observed from histograms in the form of a positive skew distribution (Figure 5.9). Even if there is a small overlap and fractures of similar length can be observed from two different scales of observation, those measurements are on the limit of the resolution of both datasets and therefore not representative due to censoring and truncation effects. The gap size will depend on the detail and parameters of the data acquisition for different datasets.

To obtain a better controlled model of the fracture network characterisation, it is critical to bridge those gaps and obtain datasets in which fracture observations considerably overlap from one dataset to another. This can be done by acquiring datasets with higher resolutions. For instance, to link outcrop observations with aerial LiDAR maps, high-resolution drone imagery or ground-based LiDAR mapping could be used (Figure 5.12a). To link LiDAR and seismic datasets, changes to acquisition parameters of LiDAR maps and seismic volumes could be made to increase the data resolution; or if possible, an intermediate-scale high resolution seismic survey could be acquired to bridge the scale gap between the seismic and airborne LiDAR data (Figure 5.12a). This is important, as higher resolution seismic data processed to image a certain depth (and frequency spectrum) can reveal fracture patterns that the original exploration surveys may not have imaged in the first place, as the original interest was to image the entire thickness of sediments on a basin.

5.5.1.1.3 Branch length

There has been much discussion on whether fracture trace length distributions are exponential or power-law (Needham et al., 1996; Nicol et al., 1996; Gillespie et al., 2001; Zeeb et al., 2013; Liu et al., 2016). Studies such as Gillespie *et al.* (2001) and Strijker *et al.* (2012) have analysed fracture trace length distributions from different datasets and concluded that for massive, non-stratabound units, fracture trace lengths can be represented by a power-law distribution, while stratabound units can be represented by a lognormal distribution. Despite the wide range of published work on trace length distribution, there seems to be a lack of knowledge in the literature about branch length distributions.

The Cariatiz platform has a complex geometry in which bedding cannot be observed at the reef framework; instead, massive rock units are intensely fractured to create large blocks and compartmentalise the carbonate unit (Figure 5.4). Branch length analysis from outcrop and LiDAR data suggest that, for massive units like Cariatiz, a negative exponential distribution better represents the fracture distribution, with a deviation for longer trace lengths due to truncation effects (Figure 5.12c). Such a trend can be expected to extend over longer fracture branches, as fracture distribution in Pernambuco with km-long fractures follows the same trend (negative exponential or log-normal distribution; see cumulative plot in Figure 5.9n). This may suggest that, in order to predict smaller scale-length fracture branches when utilising seismic data, a negative exponential distribution can be used. This is of particular importance to reservoir characterisation in which prediction of sub-seismic fractures is key.

5.5.1.2 Fracture topology

Topology is a relevant aspect when characterising fracture networks as dimensionless parameters can be obtained to understand specific attributes such as connectivity (Sanderson, 2016; Sanderson and Nixon, 2018). Exposed outcrops on the Cariatiz carbonate platform allowed a detailed analysis of fracture network distribution (Figure 5.11). Outcrop results show a variability cloud with an average of high proportions of connected nodes (mostly Y) and low proportions of isolated nodes. Conversely airborne LiDAR results demonstrate that larger fracture branches at Cariatiz have less connected nodes with an almost equal proportion of I and Y nodes (Figures 5.11a, C1a and Table D1). The average number of connections per branch analysis (C_B) demonstrates that outcrop data are better connected than LiDAR data with an average of 1.8 and 1.5, respectively (Figures 5.11d, C1d and Table D1).

Branch classification shows that outcrop scale fractures have high proportions of doubly connected branches and low proportions of singly connected branches with almost no isolated branches. LiDAR data is also dominated by doubly connected branches, but with lower proportions than the observed at outcrop as isolated branches have slightly higher proportions (Figures 5.11e, C1e and Table D1). Branch classification thus suggests that smaller fractures have a higher probability to form connected branches (single and double) than larger fractures observed on the LiDAR map. This can be confirmed by the analysis of connections per branch and dimensionless intensity (Manzocchi, 2002; Sanderson and Nixon, 2018).

Sanderson and Nixon (2018) suggested that dimensionless parameters such as the average of connections per branch (C_B) and dimensionless branch intensity (B_{22C}) are useful measures of connectivity. These measures are also related to percolation in which systems with $C_B > 1.56$ can indicate percolation. Topological results from

Cariatiz were plotted using Fig. 10d from Sanderson and Nixon (2018) (Figure 5.11f). From this diagram it is observed that fractures at outcrop are mostly plotted above the percolation threshold, whereas fractures from the LiDAR data plot just below the percolation threshold. When comparing the higher values of C_B for outcrop data ($C_B=1.8$) with those obtained by LiDAR ($C_B=1.5$), the results suggest that small length scale fractures are better connected than intermediate length fractures (Figure 5.11f). These results align with the observations from Nixon et al (2012, Fig. 14), suggesting that for carbonate platforms comparable to Cariatiz, fracture connectivity increases with increasing data resolution. Fault networks appear to be less connected at lower resolutions according to the latter authors.

If the connectivity trend recognised from outcrop and LiDAR continues towards larger fracture lengths, in a similar way to the trend observed by Nixon et al (2012, Fig. 14) as a function of data resolution, longer faults and fractures at Cariatiz, resolvable at seismic scale, would be expected to plot closer to the I node corner (Figure 5.11d). These topological values expected at seismic scale would have lower values of C_B and therefore be less connected (Figure 5.11d). This observation is important as it suggests that topological results at the largest scale analysed (e.g., seismic scale), are expected to have lower values of connectivity than fractures analysed at smaller scales (e.g., outcrop), given that connectivity may increase as the resolution increases and smaller fracture branches are measured. This trend is expected to occur in carbonate platforms with similar settings to Cariatiz, in which connectivity decreases as scale is increased. Further research is however needed to accurately predict the exact range of topological values at a different scale.

At seismic scale in Pernambuco the average proportions of connected nodes are considerably higher than the proportions of isolated nodes. Doubly connected

branches have also higher proportions than singly connected and isolated branches. In Pernambuco, the average number of connections per branch (C_B) is 1.66 (Table D1) and, when analysed together with the dimensionless branch intensity at percolation (B_{22c}), it is observed that the values are on average, well connected and above the percolation threshold (Figure 5.11l). As stated from the Cariatiz topological trend, topological results of large fracture branches from the Pernambuco carbonate platform analysed from seismic scale (large scale) are expected to have lower connectivity values than sub-seismic smaller fractures. Consequently, sub-seismic fractures in Pernambuco are expected to be better connected with values plotted closer to the Y node corner and higher values of C_B (Figure 5.11j).

5.5.2 Implications to naturally fractured reservoirs

Fracture network characterisation plays an important role in hydrocarbon exploration and the development of naturally fractured reservoirs. It is known that the use of outcrop analogues is key to predict sub-seismic fracture networks, particularly when borehole data (e.g. well cores, image logs) are not available and there is the need to estimate the volume capacity and fluid flow of a given unit (Gutmanis et al., 2018). Outcrop analogues can provide valuable information on the behaviour of small (centimetre) and intermediate (metre) scale fracture networks by the combination of outcrop and LiDAR data, respectively. Predicting the geometry (orientation and length) and topology (dimensionless parameters) of fracture networks at sub-seismic scales is crucial to increase the quality of fracture network characterisation. The study from Cariatiz demonstrates that fracture networks at a smaller scale (e.g., outcrop) have a higher level of connectivity than in a larger scale

(e.g., LiDAR) with higher values of C_B . Sub-seismic fractures are predicted to have a better connectivity than seismic fractures. Topological parameters measured from seismic data represent lower values of connectivity compared to smaller fractures expected within the reservoir. Fracture network results obtained from fractures observed at seismic (km long) scale are not representative for the multi-scale fracture system, and only describe the parameters of km-long fracture branches. As a result, fracture reservoir models utilising topological parameters obtained from seismic fractures (km-long) may underestimate the presence of fractures at lower scales of observation. Areas that appear to have no faults on seismic data, might be highly fractured as observed in Cariatiz (Figures 5.6 and 5.7). Consequently, a potential reservoir could be ignored if proper studies are not performed. To fully characterise the fracture system at different scales, including the reservoir, topological and geometrical analyses like those presented for Cariatiz and Pernambuco should be performed. Furthermore, negative exponential or log-normal distribution trends can be used to predict sub-seismic fracture branch lengths. It is advisable to use different resolution datasets such as borehole data and outcrop analogues to calibrate seismic results.

Open small-scale fracture networks mostly control the permeability characteristics of a rock, developing the main conduits of fluid flow (e.g. Bush, 2010; Questiaux et al., 2010). Conversely, when closed or cemented, they can provide barriers or baffles to fluid flow and contribute to reservoir compartmentalisation (Damsleth et al., 1998; Steen et al., 1998; Laubach, 2003; Maerten et al., 2006; Strijker et al., 2012). As suggested by Sanderson and Nixon (2018), topological values of C_B and B_{22C} are important to understand parameters such as permeability in a reservoir as they are related to connectivity and percolation. The permeability of a

rock and resulting fluid flow are mainly dependent on the fracture network with topological values above the percolation threshold, assuming that fractures are conductive (Figure 5.11f, l). In contrast, permeability is dependent on the matrix where connectivity is below the percolation threshold and fracture conductivity is lower than the matrix (Figure 5.11f, l).

The analysis provided in this study is not limited to fractured reservoirs with hydrocarbon accumulations, as the results and methodology shown could also be applied to other geoscience disciplines such as geothermal reservoirs, hydrogeology, or carbon storage projects.

5.6 Chapter-specific summary

Carbonate platforms present complex multi-scale structural and sedimentological characteristics as observed in Cariatiz (Figure 5.4). The integration of fieldwork data with outcrop exposure mapping and airborne LiDAR studies from Cariatiz, Spain, and 3D seismic data from Pernambuco, Brazil, allowed a better understanding of multi-scale fracture networks developed on carbonate platforms. These analyses reveal the complexity of fracture networks at different scales and are useful to predict sub-seismic fractures from seismic datasets that are widely used in industry. Fractures at each scale of observation behave differently, having different geometrical and topological characteristics.

- a) This study presented an integrated geometrical (orientation and branch length) and topological (node, branch counting and dimensionless parameters) analysis of fracture networks using a methodology in which small-, intermediate- and large- scale datasets are combined.

- b) Multi-scale fracture networks in carbonate platforms are complex; different fracture types are identified at each scale of observation. At small scale, cm-long joints and veins are mostly recognised (Figure 5.12a). Fracture swarms are the dominant type observed from airborne LiDAR, whereas km-long faults prevail at seismic scale (Figure 5.12a).
- c) Transitional scale gaps of fracture branch lengths between three scales of observation (outcrop - airborne LiDAR, airborne LiDAR - seismic) are recognised. Fracture branch lengths with sizes falling in these “transitional” gaps cannot be resolved by the resolution of the analysed datasets. However, fractures of these lengths do exist in nature, although datasets such as drone imagery and higher resolution seismic are needed to bridge the gaps and allow fractures of all sizes to be measured (Figure 5.12). This issue is related to censoring and truncation effects.
- d) Fracture branch orientation at intermediate (airborne LiDAR) and large (seismic) scales appear to be controlled by the dominant orientation of the platform margin. Dominant fracture sets observed in Cariatiz and Pernambuco strike parallel to the edge of the platform margin. Fracture branches at outcrop scale (< 1 m) strike in almost all directions, suggesting that different processes control the development of small fractures (Figure 5.10).
- e) Fracture branch length distributions from Cariatiz and Pernambuco fit a negative exponential or log-normal distribution in a massive, non-stratabound unit (Figure 5.12). This trend may be useful to predict sub-seismic branch lengths when working with seismic datasets.
- f) Fracture connectivity changes as a function of scale as it appears to decrease as fracture length is increased (Figure 5.11). This work complements the

conclusions proposed by Nixon et al (2012) in which they studied changes in connectivity at different resolutions. Small-scale fracture branches measured at outcrop present higher connectivity than larger fractures observed in LiDAR data. Fracture networks measured from seismic data may show lower connectivity values compared to smaller fractures expected at reservoir scale. This suggests that sub-seismic fracture networks mainly control the permeability and fluid flow in reservoirs that are dominated by open fractures or, instead, may develop barriers to fluid flow and contribute to reservoir compartmentalisation when fractures are closed or cemented.

- g) Outcrop data are useful to investigate the complexity of fracture networks and fracture types that occur at sub-seismic scale. Understanding these sub-seismic parameters allow us to better characterise fractured reservoirs.

Chapter 6: Deep-water depositional systems

An abridged version of this chapter has been published as:

Loza Espejel, R., Alves, T.M., Caçador Martins-Ferreira, M.A., 2021. Depositional and geomorphic patterns of mixed calciclastic-siliciclastic systems on a deep-water Equatorial Margin. *Basin Research*, 00, 1-27.

<https://doi.org/10.1111/bre.12604>

Co-author contributions to the paper:

Tiago M. Alves - checked for grammatical errors, ensured the scientific content was accurate and appropriately presented.

Marco Antonio Caçador Martins-Ferreira - provided well data and checked for grammatical errors.

6.1 Abstract

Distal slope and basin depositional systems in deep waters of the Pará-Maranhão Basin, Equatorial Brazil, are investigated using a high-resolution 3D seismic volume, borehole data and multispectral satellite imagery. A Neogene calciclastic submarine fan and a series of channel-levee systems are analysed at water depths of 100 m to 3,500 m. Channel-levee systems have sinuous and straight morphologies and are of different sizes. Their origin is related to turbidity flows sourced and funnelled from the carbonate shelf to submarine canyons and gullies, as well as from areas with marked slope instability. A mixed calciclastic-siliciclastic sediment input is recognised with autochthonous calcarenites and calcilutites comprising the bulk of sediment on the mid and outer continental shelf. Minor amounts of siliciclastic sediment sourced from small rivers occur on the inner shelf. Sedimentation processes of a distally steepened carbonate ramp are discussed considering a general depositional setting dominated by fluctuations in relative sea level. Cross-sectional and planar parameters of mixed calciclastic-siliciclastic channel-levee systems are compared to their siliciclastic counterparts. Morphological results show similarities between calciclastic and siliciclastic channel-levee systems. As a corollary, three types of channel-levee systems are described: (1) channels related to calciclastic submarine fans, (2) low-sinuosity, aggradational channels, and (3) high-sinuosity channels.

6.2 Introduction

Deep-water channel-levee systems develop beyond continental shelves (Lemay et al., 2020), where sediment is transported from shallow waters into deep and ultra-deep water basins; described by Pettingill (2006) as ranging in depth from 500 m to 2,000 m, and extending beyond 2,000 m, respectively. Research on siliciclastic depositional systems has been generally the centre of attention in deep-water basins, with studies on calciclastic systems lagging behind the latter (Payros and Pujalte, 2008). Furthermore, when compared to carbonate-platform settings, deep-water carbonate systems are also less documented and poorly understood (Playton et al., 2010). Yet, deep-water calciclastic systems have recently regained interest in industry and academia due to the need of integrating deep-water deposits in global and local models of carbonate depositional systems. Such models are crucial as new hydrocarbon exploration plays are being sought beyond the more-common shallow carbonate depositional settings (Reijmer et al., 2015a).

Deep-water carbonate systems are key to understand the growth, evolution and depositional conditions of carbonate systems as a whole, and can be used to document the relationship between basin and platform settings (Playton et al., 2010). Calcium carbonate (CaCO_3) is a significant source of sediment to the present-day ocean with an estimated discharge of ~5 billion tons (bt) per year, of which 3bt accumulate in sediments, and the other 40% is dissolved (Milliman, 1993; Jorry et al., 2020). Deep-water carbonate depositional systems (i.e. carbonate slopes and basins) can be categorised and subdivided based on their type of deposit, large-scale stratal patterns, and spatial architecture. Playton et al. (2010) grouped deep-water carbonate systems taking into account their dominant type of deposit: debris, grain- and mud-dominated. Spatial architecture in these settings is documented by Playton

at al. (2010) and range from strike-continuous aprons to discontinuous tongues and channel-fan complexes. Calciclastic submarine fans and channel-levee systems are less documented than slope aprons; they have been largely overlooked as they were, thus far, thought to be rare in the stratigraphic record (Payros et al., 2007; Payros and Pujalte, 2008; Back and Reuning, 2015; Dunlap et al., 2018).

Published work aiming to understand deep-water carbonate depositional systems include vintage articles with initial descriptions of carbonate slopes (e.g. Ditty et al., 1977; James and Mountjoy, 1983; Ravenne et al., 1985; Kenter, 1990; Coniglio and Dix, 1992), important compilations (Payros and Pujalte, 2008; Playton et al., 2010; Reijmer et al., 2015a) and recent studies in which depositional models separate carbonate settings from their siliciclastic counterparts (Mulder et al., 2014; Counts et al., 2019; Moscardelli et al., 2019; Jorry et al., 2020). For instance, the modern and ancient Bahamian sedimentary system has been crucial to understand carbonate platform-to-basin sedimentation patterns, and recognise that carbonate-lobe and channel systems are able to develop in deep-water basins (Bornhold and Pilkey, 1971; Crevello and Schlager, 1980; Eberli et al., 1997, 2005; Betzler et al., 1999, 2014; Mulder et al., 2012, 2014; Reijmer et al., 2015a; Wunsch et al., 2017). Ancient outcrop examples have also been used to document calciclastic systems such as the Miocene Azagador Formation in southern Spain (Braga et al., 2001), the Eocene Anotz Formation in the western Pyrenees (Payros et al., 2007), and the Miocene Albacore slope fan in SE Australia (Gallagher et al., 2001).

New investigations based on high-quality seismic data have increased our knowledge of deep-water carbonates in areas such as the Browse Basin, Northwest Shelf of Australia, with carbonate deep-water channel-levee systems having been reported in Miocene strata (Back and Reuning, 2015; Rankey, 2017; Dunlap et al.,

2018; Janson et al., 2018; Rinke-Hardekopf et al., 2018; Tesch et al., 2018; Zeng, 2020). In addition, Mulder et al (2014) and Wunsch et al. (2017) described a modern channel-levee system in the pure carbonate setting of the Bahamas Archipelago. Ultra-deep-water carbonate deposits are relatively less documented, but recent investigations have pointed out their existence in the form of channel-levee complexes and turbiditic lobes at water depths of 2,000 m to 3,400 m around isolated carbonate platforms in the Indian Ocean (Counts et al., 2019; Jorry et al., 2020). Despite these efforts, geomorphological and architectural features of mixed carbonate-siliciclastic systems remain underexplored in the literature, possibly due to incomplete datasets leading to simplistic descriptions (Moscardelli et al., 2019). Mixed calciclastic-siliciclastic systems derive from the interaction between a siliciclastic source (usually river discharge) and a regional carbonate factory (Chiarella et al., 2017). These systems have been studied since the 1970s in regions such as the Hispaniola-Caicos Basin, where siliciclastic and carbonate deposits mix in the form of turbidity currents generating a deep-water fan system. In parallel, Francis et al. (2008) have presented an example of a mixed deep-water calciclastic-siliciclastic system in the Gulf of Papua, northeast Australia and southern Papua New Guinea. Here, mixed sediment derived from two different sources, resulted in the generation of channel-levee systems. More recently, Moscardelli et al. (2019) have documented a mixed siliciclastic-carbonate turbiditic depositional system offshore Nova Scotia (Back and Reuning, 2015; Dunlap et al., 2018).

This study aims to expand the current knowledge about deep- and ultra-deep water carbonate depositional systems (i.e., mixed calciclastic-siliciclastic systems) by using a case study from the Miocene to Holocene Pará-Maranhão (PAMA) Basin in Equatorial Brazil (Figures 6.1 and 6.2). High-quality 3D seismic data are used to

characterise the internal geometry of channel-levee systems formed in a mixed calciclastic-siliciclastic depositional system. Borehole data from the shelf margin document the thickness and composition variability of the so-called Ilha de Santana Platform and the PAMA continental shelf, which provide the main source of sediment to the continental slope and rise (Figures 6.1 and 6.2). Hence, this work investigates the morphological expression of mixed calciclastic and siliciclastic sediment transfer from the PAMA shelf and the Ilha de Santana Platform, via the continental slope, on its way to deep and ultra-deep waters. Details about the Neogene stratigraphic succession of the PAMA Basin aim to provide a better understanding of new exploration plays in Equatorial Brazil. In summary, this paper intends to answer the following questions:

1. What types of depositional features characterise mixed calciclastic-siliciclastic systems in deep and ultra-deep-water environments?
2. Can deep-water channel-levee systems be formed on a carbonate-dominated continental margin recording minor siliciclastic input?
3. How similar are the geomorphic properties of channel-levee systems formed on carbonate-rich margins when compared to their siliciclastic counterparts?

As described in Playton et al. (2010), it is useful and important to understand the relationship between platform and basinal settings. This is because in many cases, platform-derived information is more robust than basin-related data. The study area analysed here is such a case, as the continental slope and rise are imaged in seismic data, while exploration wells were, thus far, only drilled on the shelf margin (Figure 6.1b).

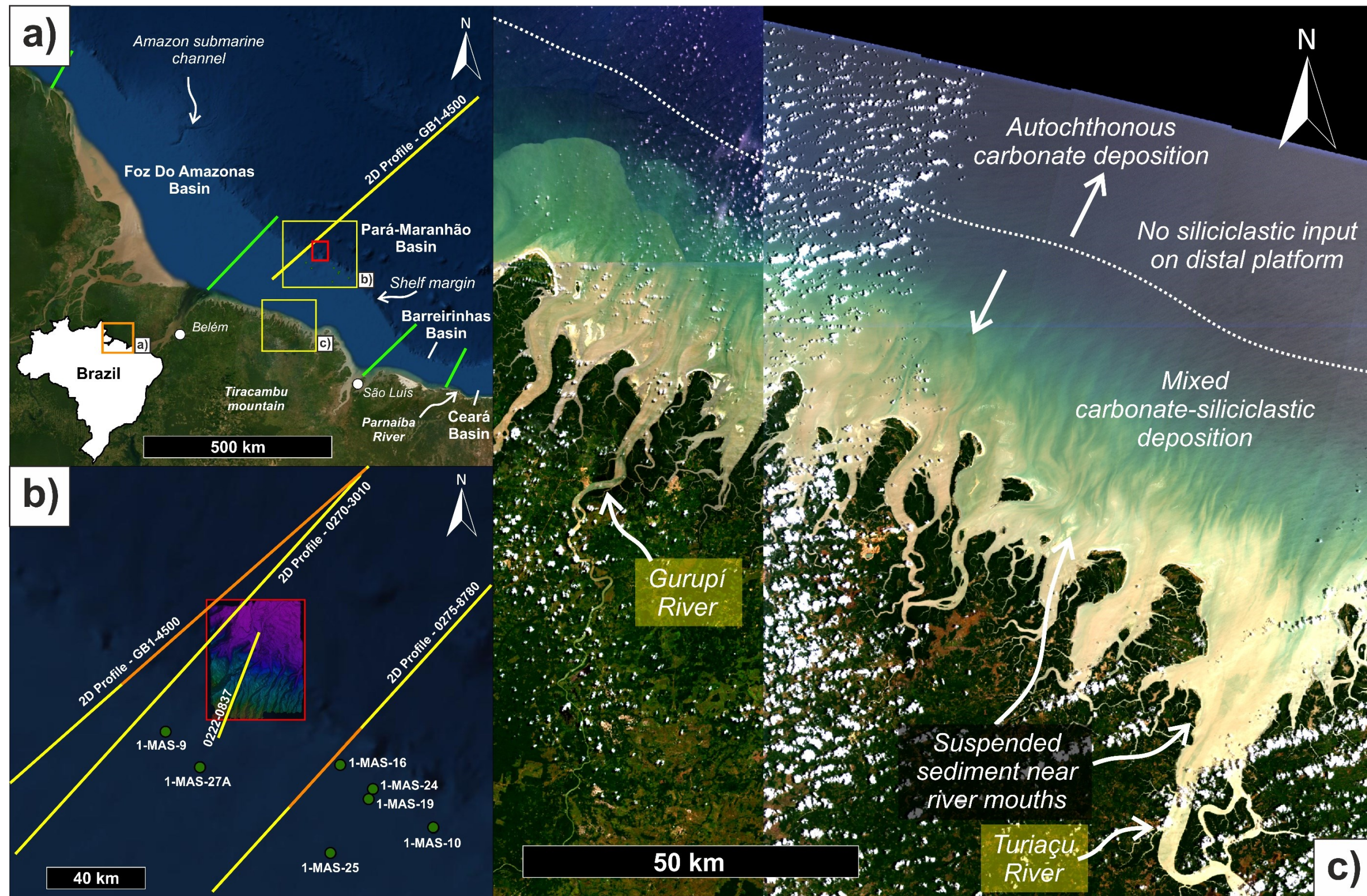


Figure 6.1. A) Location map of the Brazilian Equatorial Margin highlighting the study area in the Pará-Maranhão (PAMA) Basin. Red rectangle shows the location of the studied 3D seismic survey. Green lines mark basin limits. B) Detailed map showing published 2D seismic profiles crossing the study area, used to correlate the stratigraphy of the interpreted horizons. Profile GB1-4500 is from Henry et al. (2011) and Zalán (2015), profile 0222-0837 is from Fabianovicz (2013) and profiles 0270-3010 and 0275-8780 are taken from Da Silva and Riveiro (2018). Exploration wells near the interpreted 3D seismic survey are shown as green dots. For the detailed well correlation, please refer to Figure 6.5. All wells were drilled in shallow waters of the carbonate shelf. C) Multispectral satellite (Sentinel-2) map showing a bathymetric band combination using B4-Red, B3-Green and B1-Ultra blue bands. This map highlights the PAMA offshore areas with suspended siliciclastic sediment and autochthonous carbonate deposits.

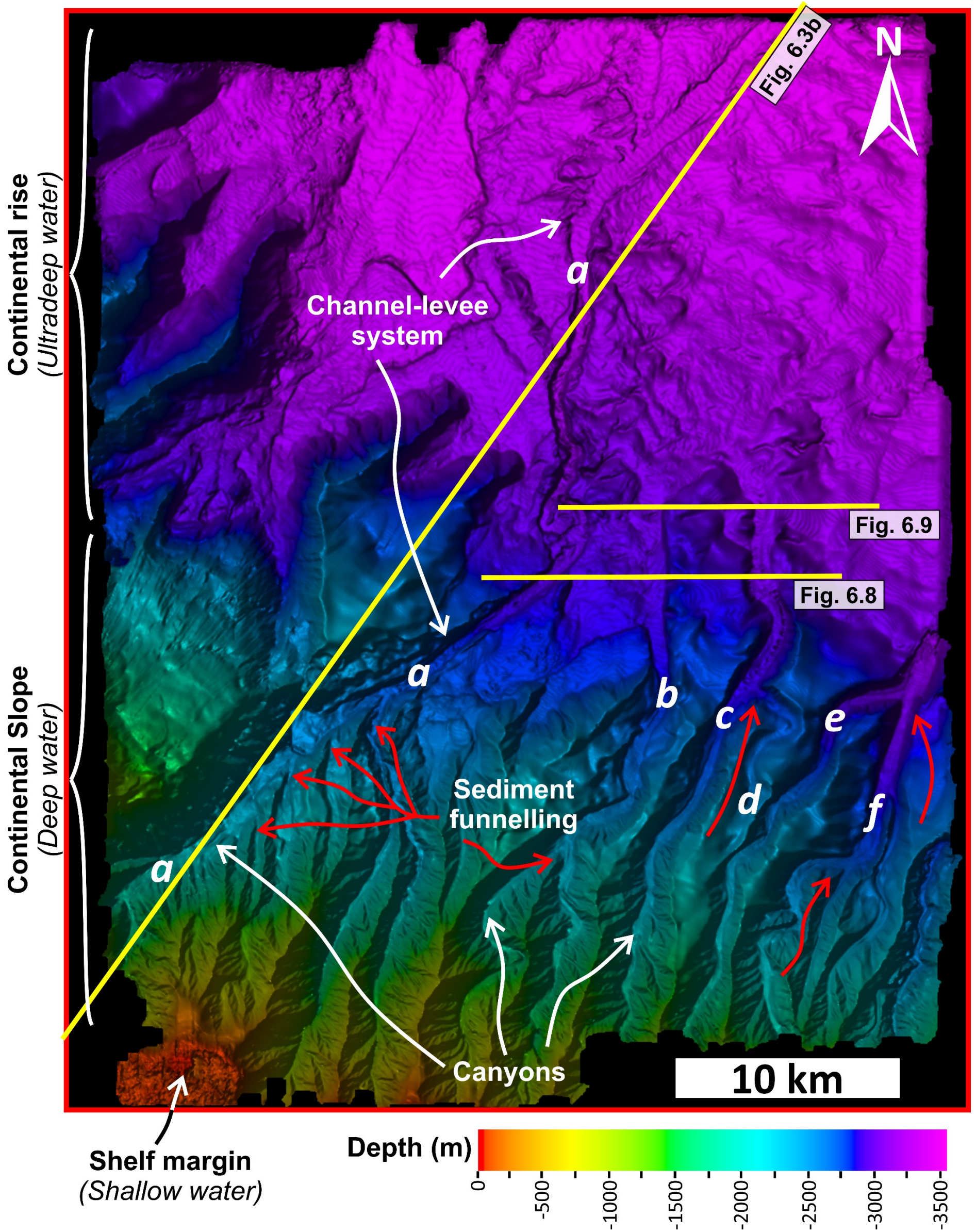


Figure 6.2. Seafloor relief map highlighting the depositional setting of the PAMA Basin from the shelf margin to the continental rise. Submarine canyons predominate on the continental slope, whereas there is a major channel-levee system on the continental rise. Different sediment conduits are labelled from a to f. Red arrows indicate sediment funnelling points within the continental slope. Note the high number of funnelling conduits towards channel a.

6.3 Chapter specific datasets and methods

The seismic data used in this study includes a 3D seismic volume (3D PAMA PSDM Full Stack) located in the PAMA Basin, Equatorial Brazil (Figure 6.1). For a full description of the data resolution, please refer to section 3.5.1.3. The focus of this study is the Miocene to Holocene stratigraphic successions of the PAMA Basin (Figures 6.3 and 6.4), allowing a detailed analysis of the channel-levee systems in deep and ultra-deep waters.

Composite well data from seven exploration wells located near the edge of the continental shelf are used to document the transition of depositional systems from shallow waters to deep waters (Figure 6.5). For full details about well data, please refer to section 3.5.2.2.

6.3.1 Seismic interpretation and channel definition

Seismic-stratigraphic interpretation is based on published literature from Fabianovicz (2013), Da Silva and Ribeiro (2018), and Alves et al. (2020). Stratigraphic data for the basin derive from the work of Brandão & Feijó (1994), Soares et al. (2007) and university theses such as De Souza (2006), Da Silva (2007) and Piovesan (2008). A summary of the methodology used to analyse the depositional systems and geomorphic parameters of channel-levee systems is shown in Figure 6.6.

The offshore PAMA Basin is still an exploration frontier with limited data available in existing publications. However, a few published 2D seismic profiles intersecting the 3D survey were useful to gain a regional understanding of the basin (Figure 6.1b).

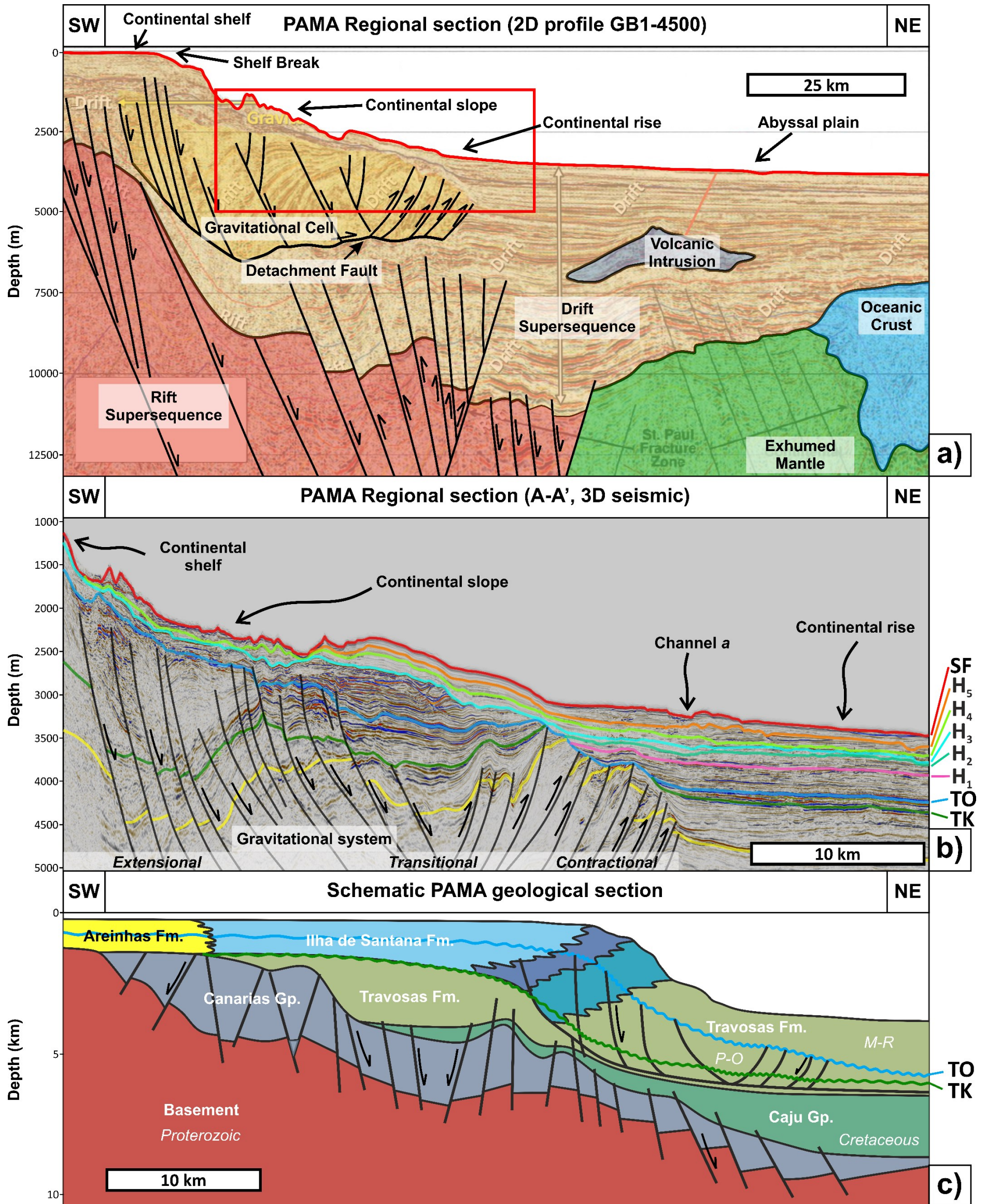


Figure 6.3. Regional seismic sections depicting the regional stratigraphic units and seismic facies of the PAMA Basin. a) Reinterpreted 2D seismic profile GB1-4500 from Henry et al. (2011) and Zalán (2015) displaying the depositional sequences of the basin at the regional scale. A red rectangle shows the portion of the basin studied in this work, which encompasses the upper section of the Drift Supersequence above the gravitational cell. Refer to Figure 6.1b for location. b) Seismic section of the 3D seismic survey showing the detailed stratigraphy of the PAMA Basin. A gravitational system is observed below the Top Oligocene (TO) unconformity comprising extensional, transitional and contractional sections. Refer to Figure 6.2 for location. c) Schematic section of the PAMA Basin outlining the distribution of the different geological formations. P-O=Paleocene-Oligocene, M-R=Miocene-Recent. Modified after Brandão and Feijó (1994).

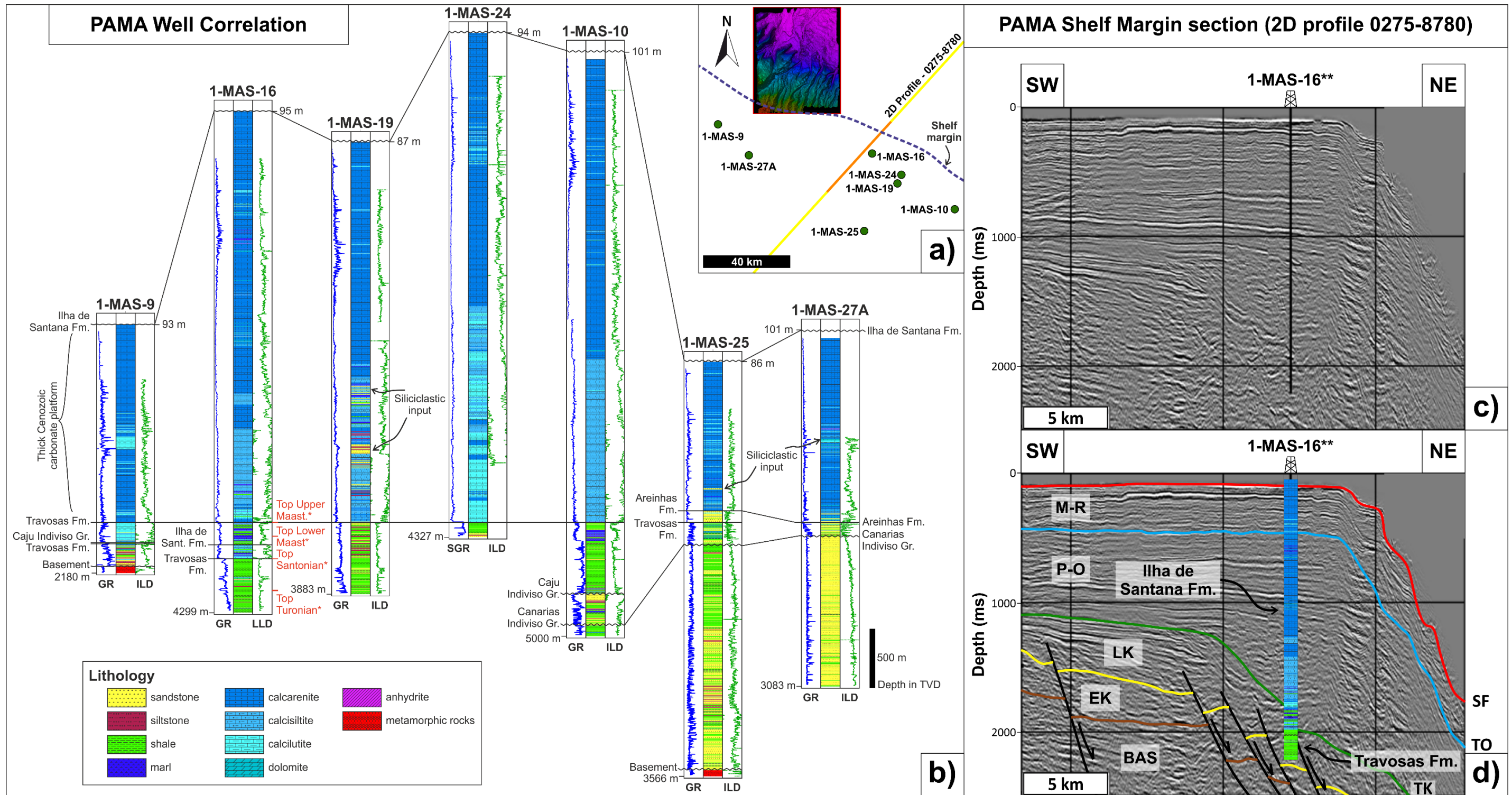


Figure 6.5. Well correlation panel and seismic sections on the PAMA shelf margin. a) Map of the study area showing the location of wells and seismic data. A blue dashed line shows the shelf margin for reference. b) Well correlation panel for wells 1-MAS-9, 1-MAS-16, 1-MAS-19, 1-MAS-24, 1-MAS-10, 1-MAS-25 and 1-MAS-27A. Well correlation is flattened on the Travosas Formation marker. Information displayed for each well are lithology, Gamma-Ray (GR) and Deep Resistivity (ILD) wireline curves. *Cretaceous ages for well 1-MAS-16 were taken from paleontological data in Piovesan (2008). c) and d) Uninterpreted and interpreted seismic profile 0275-8780 showing the PAMA shelf margin with a thick carbonate platform corresponding to the Ilha de Santana Formation. **Well location is projected. BAS=Basement, EK=Early Cretaceous, LK=Late Cretaceous, P-O=Paleocene-Oligocene, M-R=Miocene-Recent. Modified from Da Silva and Ribeiro (2018).

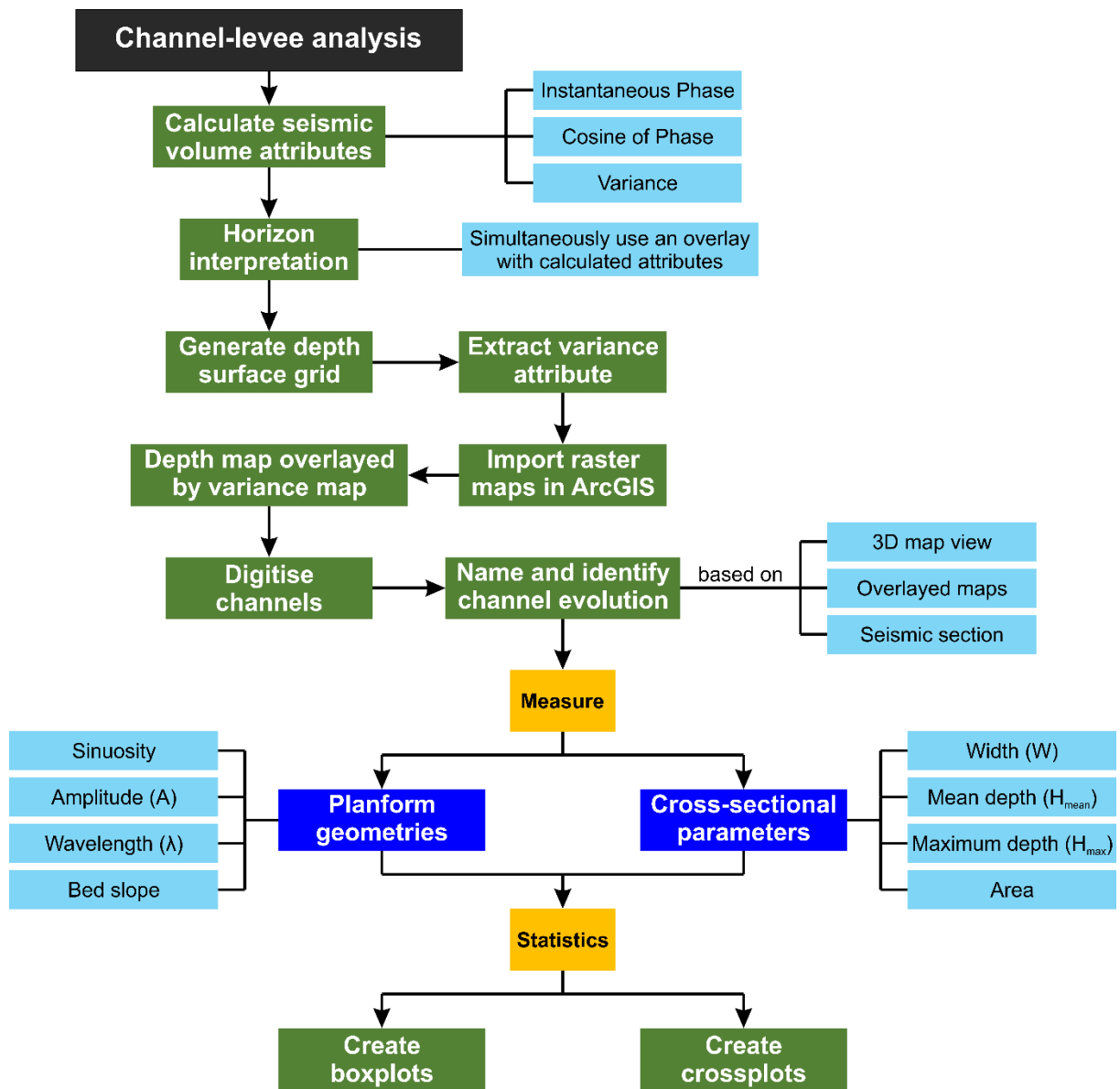


Figure 6.6. Flowchart summarising the methodology used in this work to identify and analyse channel-level systems.

This study includes a reinterpreted portion of the GB1-4500 seismic profile to provide a regional context for the PAMA Basin (Figure 6.3a). This pre-stack depth migrated (PSDM) 2D seismic profile GB1-4500 from ION's Greater Brazil SPAN project has been previously interpreted by Henry et al (2011) and Zalán (2015). Published interpretations of 2D seismic profiles 0222-0837 from Fabianovicz (2013), and 0270-3010 and 0275-0780 from Da Silva et al. (2018), provided us with additional stratigraphic information (Figure 6.1b). A portion of the seismic profile 0275-8780 is shown in Figure 6.5c and d together with a projection of well 1-MAS-16.

Seismic interpretation was completed using Schlumberger's Petrel® and based on the general principles of seismic stratigraphy; hence, reflection terminations, seismic facies and seismic units were interpreted in great detail (Cross and Lessenger, 1988; Catuneanu, 2006). In total, five key seismic horizons (H_1 to H_5) were interpreted, together with the seafloor (SF), in Miocene to Recent strata (Figures 6.3b, 6.4 and 6.7). Two regional unconformities (Top Oligocene and Top Cretaceous) were also interpreted and considered to be key stratigraphic markers in the study area (Figures 6.3b and 6.4). Channel-levee systems were mapped on specific seismic horizons (Figures 6.6, 6.7 and 6.8).

Seismic interpretation near the continental slope and also within channel systems is difficult due to their complex geometries and poor continuity of seismic reflections (Figure 6.8). To tackle this problem, seismic attributes such as instantaneous phase and cosine of phase are computed and displayed with a certain degree of transparency over the amplitude volume, so as to better identify the continuity of particular seismic reflectors (Figure 6.6).

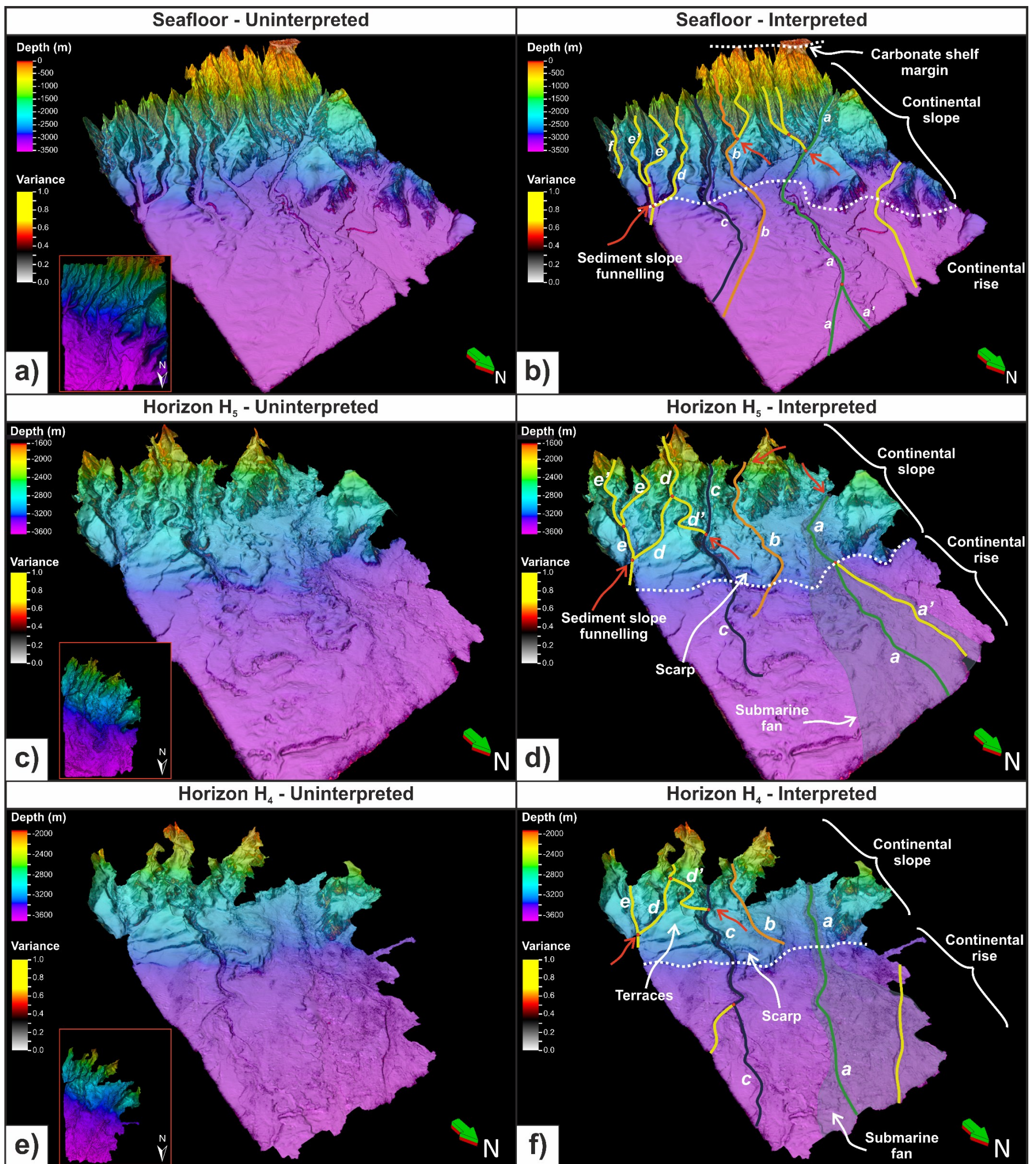


Figure 6.7. 3D views of blended depth and variance horizon maps at different intervals: Seafloor (a, b), horizon H₅ (c, d), and horizon H₄ (e, f). Uninterpreted (a, c, e) and interpreted (b, d, f) maps are shown, and principal morphological features are highlighted in them, including the channel-levee systems interpreted in this work. Red arrows indicate sediment funnelling points on the continental slope.

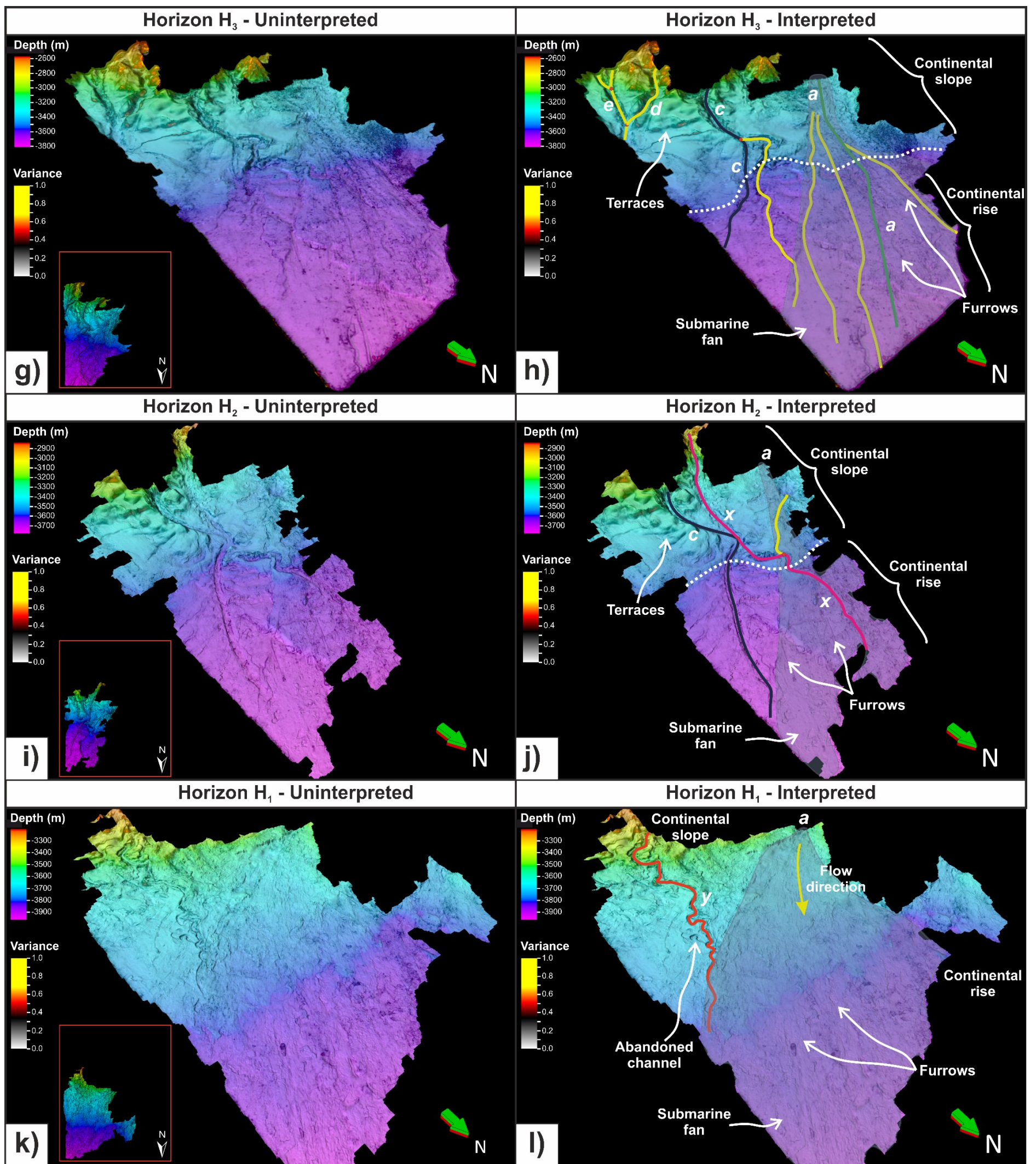


Figure 6.7. (continued). 3D views of blended depth and variance horizon maps at different intervals: horizon H₃ (g, h), horizon H₂ (i, j), and horizon H₁ (k, l). Uninterpreted (g, i, k) and interpreted (h, j, l) maps are shown to highlight main morphological features, including the channel-levee systems interpreted in this work.

A surface grid with a cell size of 25x25 m is used to generate structural maps (Figures 6.6 and 6.7). Based on a previously calculated variance attribute volume, the variance attribute is extracted with a search window of 20 m for every depth map (H_1 to H_5 , and SF) (Figure 6.6). This latter seismic attribute is crucial in this analysis as it highlights discontinuities in each seismic horizon, improving the imaging of stratigraphic features and facilitating channel recognition (Figure 6.7).

Both depth and extracted variance raster maps have been imported into ArcGIS to digitise and delineate discrete channel-levee systems (Figure 6.6). For an enhanced visualisation, depth maps are overlaid by variance maps with a 50% transparency (Figure 6.7). A 3D visualisation of key maps is also useful to better recognise channel-levee systems and other sediment conduits (Figure 6.7).

6.3.2 Geomorphic parameters

A similar methodology to Gee et al. (2007) and Lemay et al. (2020) is adopted in this work to analyse the morphometric parameters of channel-levee systems in the PAMA Basin (Figure 6.6). Lemay et al (2020) introduce a quantitative geomorphic classification and methodology to analyse submarine sediment conduits based on cross-sectional and planform data. Their classification helps to differentiate between sediment conduits with and without the presence of levees. In parallel, Gee et al. (2007) examines and quantifies key geometric parameters in deep-water submarine channels to better understand the main controls on submarine channel geometry, as well as on their initiation and evolution. The latter authors focus on siliciclastic systems, and this work aims to compare and differentiate their models to the calciclastic systems of the PAMA Basin.

Cross-sectional parameters are measured every 3 to 5 km along the channel thalwegs, in perpendicular profiles to these latter. Measurements include width (W), mean depth ($L_{h_{\text{mean}}}$), maximum depth ($L_{h_{\text{max}}}$) and area; parameters used later in this work to classify the interpreted channels (Figure 6.8). The upper limits of asymmetric levees are precisely defined for each channel. In the measurements analysed here, the mean depth ($L_{h_{\text{mean}}}$) is the ratio of the cross-sectional area to the bankfull width of a channel (Figures 6.8 and 6.9).

Parameters used in this work to characterise channel planform geometries include sinuosity, meander amplitude (A) and meander wavelength (λ) and are measured using a Python Jupyter Notebook provided by Lemay et al. (2020). This algorithm is based on Sylverster and Pirmez (2017) script, allowing for consistent measurements of all studied channels. The processing steps of the Lemay et al. (2020) algorithm are as follows: (1) x and y coordinates of the channel centrelines are resampled with a 50 m spacing; (2) centrelines are smoothed out for a given window length using the Savitzky-Golay filter (Savitzky and Golay, 1964). (3) The curvatures of the centreline are computed to determine inflection points in channels; (4) the number of channel bends are defined by computing inflection and apex points; and (5) geometric parameters (sinuosity, λ and A) are computed for each channel bend. In this work, conduit bed slope is measured every 3 to 5 km based on the thalweg depth obtained from seismic profiles. A value of about twice the mean channel width is used in Step 2 above, to scale the window length to the interpreted channels.

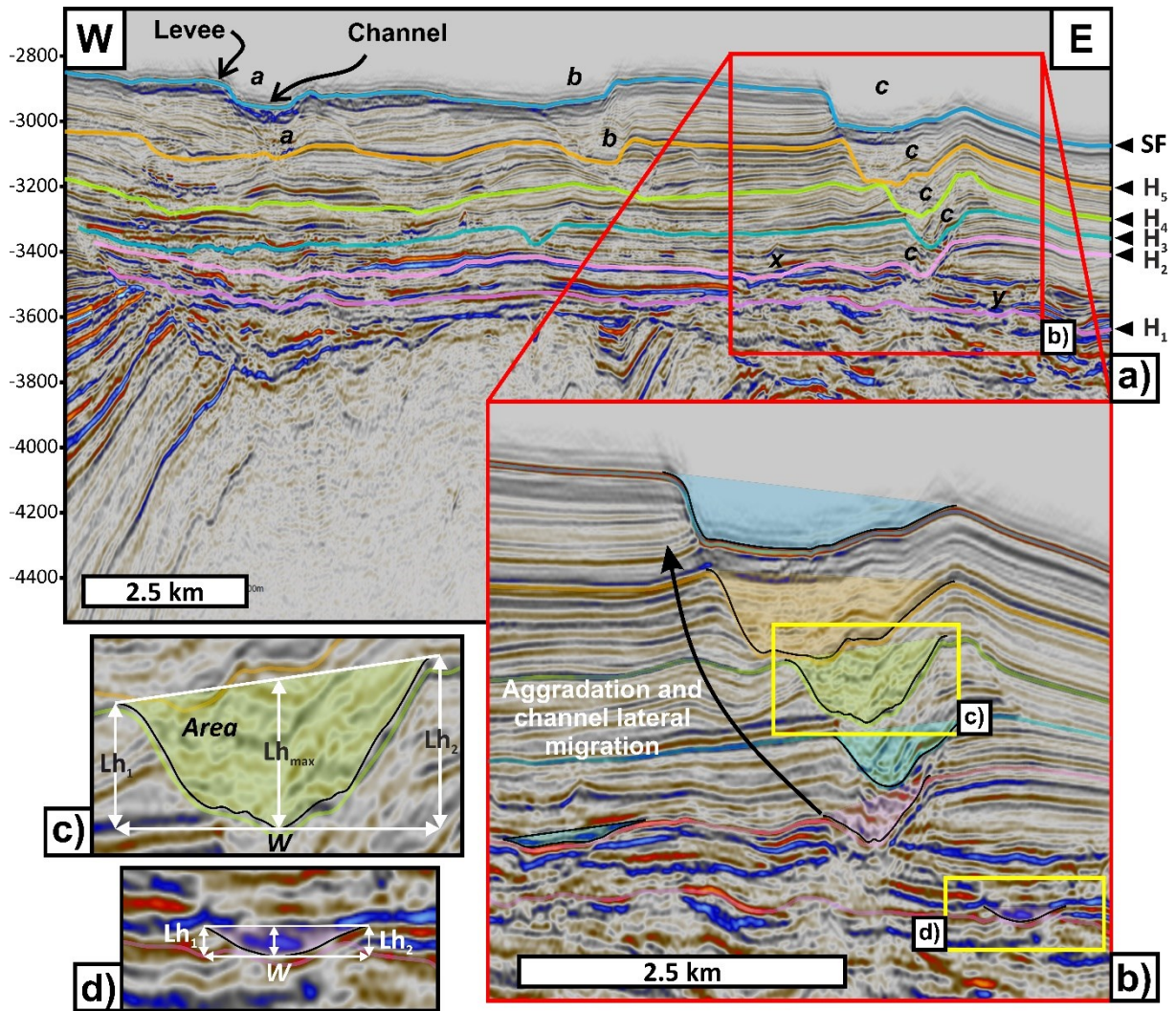


Figure 6.8. Seismic section showing the channel-levee systems in cross-section and the way in which geomorphic data were measured. Lh_1 and Lh_2 are the levee heights, which is the vertical distance between the deepest points (thalweg) of the channel to the two levee crests. Lh_{max} is the maximum levee height, which is measured as the average height between Lh_1 and Lh_2 , as there is asymmetry in the channels. The parameter W is the channel width, which is measured between the levee crests.

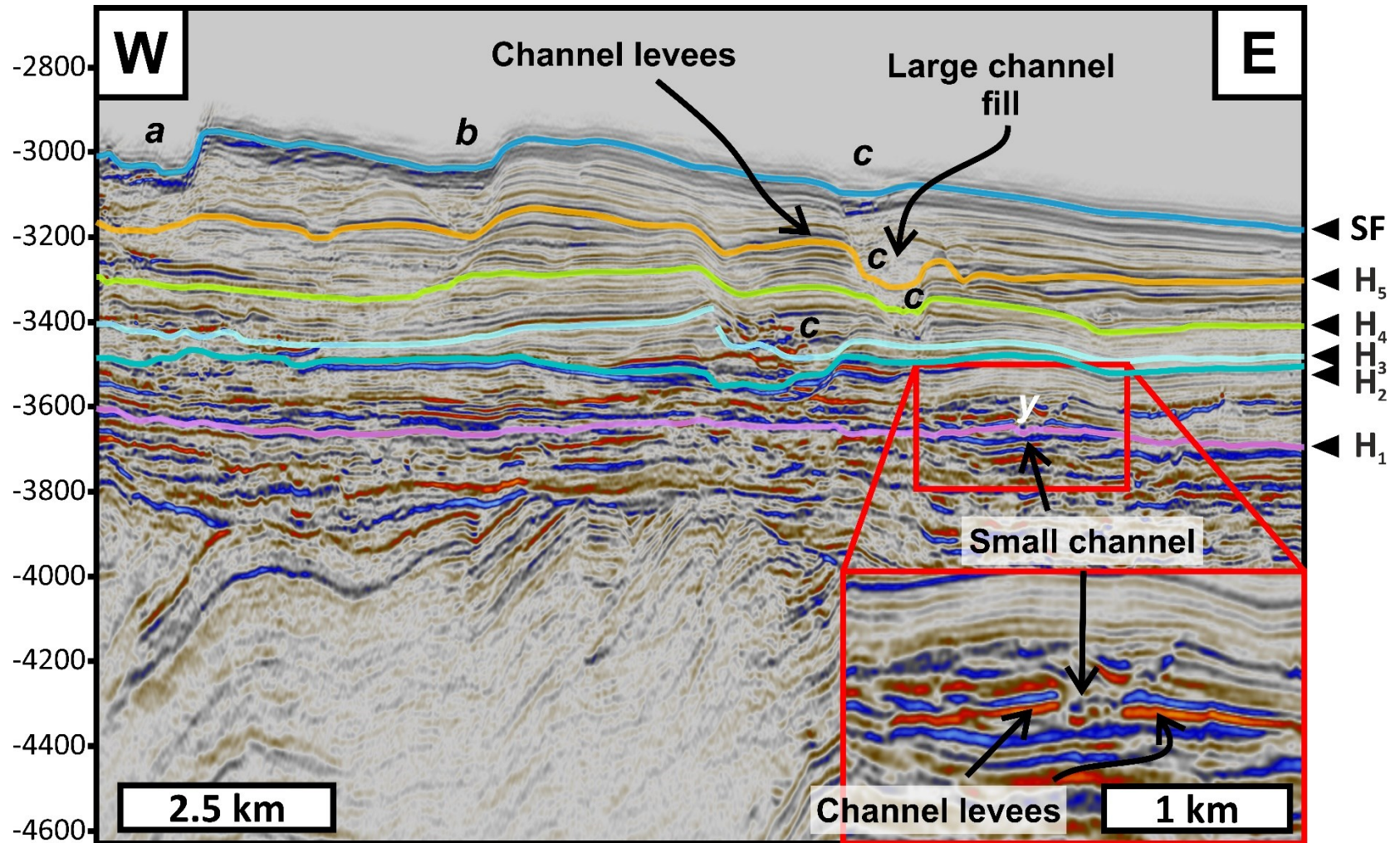


Figure 6.9. Seismic section showing the difference in cross-sectional scale between channel-levee systems. Channel y is only about 0.5 km wide and is buried by a low-amplitude reflection unit. In contrast, channel c is three to five times wider than channel y and reveals an aggradational pattern. Both channels have external levees.

6.3.3 Statistical analysis

The morphometric parameters of the PAMA calciclastic channel-levee systems are plotted on box- and cross-plots (Figures 6.10 and 6.11). Box plots show the statistical distribution of the morphometric parameters for each channel-levee system (Figure 6.10). Cross-plots show the relationships between specific morphometric parameters (i.e. mean bankfull depth, bankfull width, meander amplitude and meander wavelength) (Figure 6.11). Least-square linear regressions were computed on log-transformed data for all calciclastic channel-levee systems together, as to obtain a power-law equation (Figure 6.11). A regression curve with its associated 95% confidence interval is shown only when the coefficient of determination R^2 is higher than 0.1 to avoid non-correlation hypotheses (Figure 6.11).

Calciclastic morphometric relationships are compared to established models (i.e. power-law equations) of siliciclastic submarine conduits from Lemay et al. (2020) and fluvial channels from Williams (1986) and Held (2011) (Figure 6.11). Data from Lemay et al. (2020) are plotted to document the differences between siliciclastic submarine conduits and calciclastic channels (Figure 6.11).

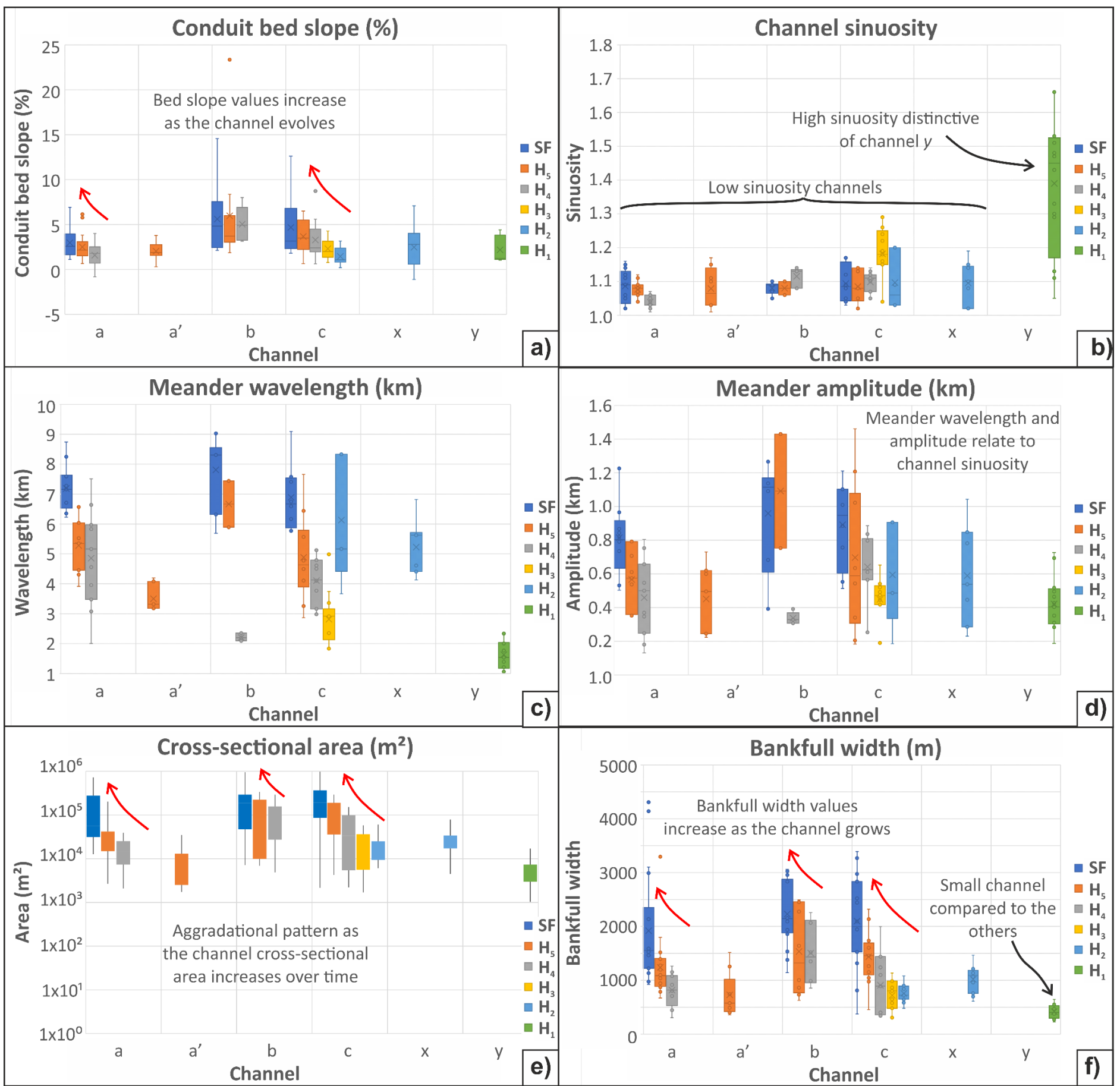


Figure 6.10. Cross-sectional distribution box plots of the channel-levee systems in the PAMA Basin. a) Conduit bed slope; b) channel sinuosity; c) meander wavelength; d) meander amplitude; e) cross-sectional area; and f) bankfull width.

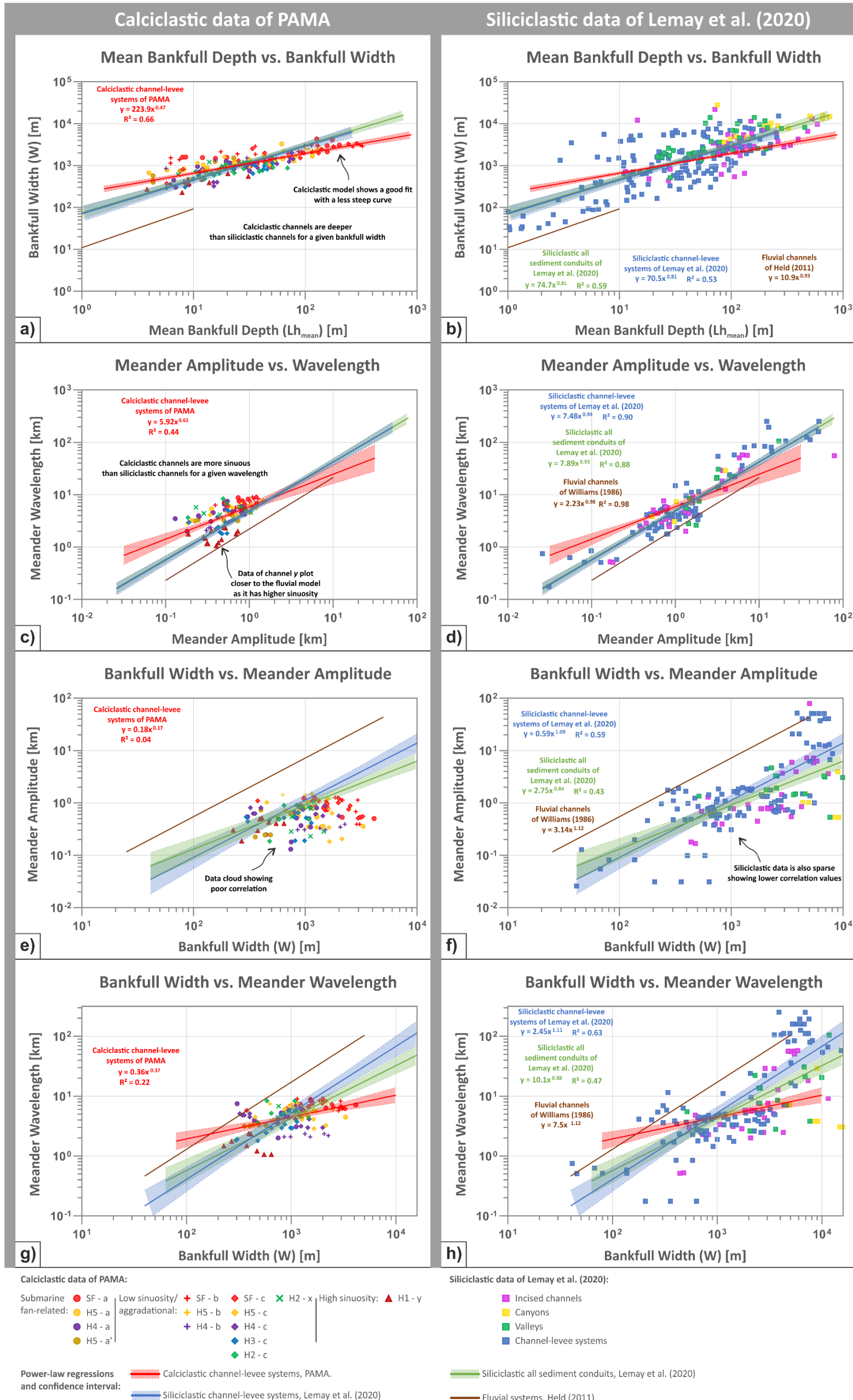


Figure 6.11. Cross-plots comparing morphometric relationships of calciclastic channel-leeve systems of PAMA and siliciclastic sediment conduits taken from Lemay et al., 2020. Power-law equations from Williams et al. (1986), Held (2011) and Lemay et al. (2020) are plotted to compare calciclastic channel-leeve systems with the geometries of siliciclastic submarine and fluvial channels. A and b) Mean bankfull depth (Lh_{mean}) against bankfull width (W); c and d) meander amplitude vs. meander wavelength; e and f) bankfull width vs. meander amplitude; and g and h) bankfull width vs. meander wavelength.

6.4 Physiography and sedimentary environment

The modern PAMA continental shelf is 150 km to 250 km wide. Water depth along the shelf-slope profile transitions from shallow waters with an average depth of 25 m on the continental shelf to 3,500 m in ultra-deep waters (Figures 6.1, 6.2 and 6.3). The PAMA continental shelf is a tectonically steepened carbonate ramp with no rimmed reef along its margin (Alves et al., 2020). The study area has been considered as a mixed carbonate-siliciclastic shelf in all similar to the analogous Ceará Basin (de Morais et al., 2019) (Figure 6.1a).

Recent data from Ceará identified three main depositional systems on its continental shelf: a) siliciclastic, located near the shoreface and river mouths, b) mixed, comprising biolithoclastic and lithobioclastic facies and, c) carbonate, revealing the predominance of an autochthonous carbonate supply, mainly derived from calcareous algae (de Morais et al., 2019). The modern carbonate shelf of Equatorial Brazil is itself considered to be a major supplier of carbonate deposits to more distal regions as its middle and outer parts record typical autochthonous carbonate sedimentation (de Morais et al., 2019). The inner continental shelf is characterised by the mixing of siliciclastic and carbonate sediment, especially during maximum freshwater discharges from suspended sediment released from river mouths (de Morais et al., 2019). An exception to this setting is the Foz do Amazonas Basin, which is dominated at present by the large siliciclastic input from the Amazon River and Delta, feeding sediment into deep waters via a large submarine channel (Figure 6.1a).

Siliciclastic input from rivers such as Gurupí and Turiaçu in PAMA can be compared to the depositional setting observed in Ceará, as they have similar settings (Figure

6.1c). In Ceará, the transporting distance of suspended sediment sourced from near the shoreline have been studied around the Parnaíba and Jaguaribe rivers, where siliciclastic material is transported up to 10 km oceanward from the river mouths (Dias et al., 2013; Aquino da Silva et al., 2015) (Figure 6.1^a). In order to verify how far siliciclastic sediment can travel on the modern PAMA shelf today, a comparable approach to Aquino da Silva et al. (2015) and Morais et al. (2019) was used in this study (Figure 6.1c). Data included a combination of multispectral satellite imagery with bands B4-Red, B3-Green, and B1-Ultra blue (coastal aerosol) provided by the Sentinel-2 mission (Figure 6.1c). Sediment suspended in water can be traced by using the coastal aerosol band (B1), as this band reflects the blue and violet colour spectra displaying subtle differences in the colour of water (Hedley et al., 2018). The interpreted multispectral satellite data prove that sediment from rivers in PAMA is transported 20 km to 50 km off the shoreline (Figure 6.1c). This pattern is similar to that observed on the Ceará continental shelf (de Morais et al., 2019, Fig. 1), suggesting that the inner shelf in PAMA is also dominated by the deposition of siliciclastic sediment (Figure 6.1c).

Well data from PAMA document the presence of calcarenite and calcilutite deposits on the outer continental shelf (Figure 6.5). In PAMA, there are no scuba diving or sedimentary cores such as the ones analysed in Ceará by de Morais et al. (2019), but the well data shown in this paper still reveals similar depositional systems to those recognised in Ceará. On both the PAMA and Ceará basins, the middle and outer continental shelf reveal the predominance of autochthonous carbonate sediment (de Morais et al., 2019).

Based on the observations above, it can be suggested that beyond the inner 50 km zone of the PAMA continental shelf, dominated by episodic siliciclastic input, there

is a healthy development of a carbonate depositional system such as the one observed off Ceará. In PAMA study area, this carbonate system extends up to 150 km to 165 km away from the inner zone and occurs on the herein called middle and outer continental shelf (Figure 6.1c). Beyond the shelf edge, submarine canyons develop on the continental slope and transition to channel-levee systems in ultra-deep waters (Figure 6.2). The outer continental shelf, dominated by carbonate deposition with calcarenites and calcilutites, is the primary sediment source feeding the channel-levee systems recognised beyond the shelf edge. Deep-water depositional systems in PAMA can be considered as pure carbonate systems given the presence of a wide area of carbonate deposition on the Ilha de Santana Platform. However, because of the presence of siliciclastic deposits on the inner continental shelf, it is more conservative to consider these same deep-water depositional systems as mixed calciclastic-siliciclastic. This is because siliciclastic input can be transported away from the inner shelf to the proximity of the shelf break and upper continental slope due to marine currents acting on the shelf, such as the documented in the Gulf of Papua and North Queensland, Australia (Francis et al., 2008). Additional data such as piston core samples would be useful to confirm this interpretation.

6.5 Borehole stratigraphic interpretation

Seven (7) exploration wells provide important stratigraphic data in the study area and complement the stratigraphic column in Soares et al. (2007) (Figures 6.4 and 6.5). Well 1-MAS-9 drilled 1658 m of strata in the Ilha de Santana Formation comprising thick successions of calcarenites with intercalated packages of calcilutites (Figure 6.5). Below this latter unit, Well 1-MAS-9 crossed a thin package of the Travosas Formation consisting of carbonate deposits (calcarenites and

calclutites) intercalated with sandstone intervals up to 3 m-thick (Figure 6.5). This is an important observation because it shows carbonate deposition to predominate on the continental slope of PAMA, a character contrasting with previous interpretations of the Travosas Formation as a siliciclastic-dominated unit (e.g. Brandão and Feijó, 1994; De Souza, 2006; Piovesan, 2008).

Well 1-MAS-16 found 3450 m of Paleogene-Neogene strata in the Ilha de Santana Formation consisting of thick packages of calcarenites intercalated with thin layers of calclutites and calcisiltites with sparse layers of marls and dolomite (Figure 6.5). Towards the base of the formation there are more frequent, and thicker calcisiltite intervals. Well 1-MAS-16 is the only well with available chronostratigraphic data, although only for Cretaceous strata (Piovesan, 2008). Here, the Travosas Formation shows a greater presence of siliciclastic material, mainly intervals of shale and marl intercalated with calcisiltite layers (Figure 6.5). Well 1-MAS-16 is also important as it can be projected and tied to seismic profile 0275-8780 from Da Silva and Ribeiro (2018) (Figure 6.5c, d). Paleocene-Oligocene strata appear to be dominated by the development of a thick carbonate shelf. Miocene to Recent strata reveal the aggradation of a growing, healthy carbonate shelf (Figure 6.5c, d).

Well 1-MAS-19 found 3193 m of strata in the Ilha de Santana Formation, which comprises calcarenites in its upper part (Figure 6.5). Below a depth of 2140 m, the Ilha de Santana Formation reveals significant siliciclastic input in the form of 5 m- to 10 m- thick layers of sandstones and marls (Figure 6.5). Well 1-MAS-19 also drilled through 603 m of intercalated sandstones, siltstones and shales in the Travosas Formation (Figure 6.5).

Wells 1-MAS-24 and 1-MAS-10 respectively drilled 4108 m and 3946 m of the Ilha de Santana Formation in the thickest part of the continental shelf (Figure 6.5). In

contrast, wells 1-MAS-25 and 1-MAS-27A drilled the thinnest portion of the carbonate shelf, recording 1252 m and 1630 m of intercalated calcarenite and calcilutite packages (Figure 6.5). Thin layers of sandstone and shale are observed in these two wells, suggesting episodic pulses of siliciclastic material transported from the inner continental shelf to its outer part. Wells 1-MAS-25 and 1-MAS-27A also reveal the presence of a 97 m and 110 m thick Areinhas Formation, chiefly consisting of sandstone and shale (Figure 6.5).

Well 1-MAS-25 found 183 m of the Travosas Formation with intercalations of sandstone, shales and calcarenites (Figure 6.5). The Travosas Formation in wells 1-MAS-9 and 1-MAS-25 documents that, during the Maastrichtian, there was a mixed carbonate-siliciclastic depositional system on the upper continental slope of the PAMA Basin. In addition, the seven wells interpreted in this work confirm the presence of a thick Cenozoic carbonate shelf in the study area, with thin siliciclastic deposits. This suggests that distal slope deposits in the Miocene to Recent PAMA Basin are mainly dominated by redeposited calciclastic sediments with occasional compositional mixing with siliciclastic deposits (Figure 6.5).

6.6 Seismic-stratigraphic framework of PAMA

Four Miocene-Holocene seismic units were interpreted in the PAMA Basin and named, from the oldest to the youngest, as Units 1 to 4 (Figures 6.3b and 6.4). These stratigraphic units lie on top of the gravitational complex imaged in Figure 6.3b. The Top Cretaceous (TK) horizon was mapped first to provide a key reference to the structural analysis (Figure 6.3b, c). The Top Oligocene (TO) horizon marks a major regional unconformity in the PAMA Basin caused by a global sea-level fall (Gradstein

et al., 2005; Soares et al., 2007) (Figure 6.3b). Faults related to the slope gravitational complex terminate at horizon TO (Figure 6.3b). In the study area, the unconformity forms a high amplitude reflector with onlapping strata above it (Figure 6.3b), as also recognised in the Barreirinhas and Foz do Amazonas Basins (Soares et al., 2007; Da Silva and Ribeiro, 2018). Above the TO unconformity, a general aggradational setting for the PAMA carbonate shelf has been previously suggested by Soares et al. (2007).

Multiple channel-levee systems occur close to or on Miocene to Recent horizons H₁ to H₅ (Figure 6.7). These systems occur in Seismic Units 1 to 4 described below. Based on descriptions in Soares et al. (2007) and Rosetti et al. (2013), seismic units were correlated to the sequences defined in Soares et al. (2007) (Figure 6.4).

6.6.1 Unit 1 - Lower Miocene

Unit 1 is characterised by its high to medium sub-parallel internal reflections. It is bounded at its base by the TO horizon and onlaps this latter unconformity to the southwest (Figure 6.3b). Horizon H₁ marks the top of Unit 1 and comprises a high amplitude, sub-parallel seismic reflector (Figure 6.7k, l).

Unit 1 is correlated with Sequence E80-N10 in Soares et al (2007), recognised as a major Cenozoic transgressive event (Figure 6.3). This event is associated with the maximum expansion of carbonate deposition on the PAMA continental shelf. On the continental slope, horizon H₁ is characterised by the incision of a small and sinuous channel and the formation of a calciclastic submarine fan as shown in Figure 6.7k, l.

6.6.2 Unit 2 - Middle Miocene

Middle Miocene strata in Unit 2 is bounded by horizons H₁ and H₃, and onlaps the Top Oligocene unconformity to the southwest (Figures 6.3b and 6.4). This unit has medium- to high- amplitude reflections, and is correlated with Sequence N20-N30 defined in Soares et al. (2007). Horizon H₂ is observed half-way through Unit 2 as a low- to high- amplitude discontinuous reflection. The formation of a large channel (channel c) is first observed at the level of horizon H₂ (Figure 6.7i, j).

The top of Unit 2 coincides with horizon H₃, a moderate-amplitude reflector (Figure 6.4). This unconformity has been considered as an important feature on Brazil's Equatorial Margin in seismic and well data (Soares et al., 2007). Although its amplitude is not as high as the Top Oligocene (TO) unconformity, horizon H₃ marks a relative sea-level drop across the PAMA Basin (Figures 6.3b and 6.7g, h).

6.6.3 Unit 3 - Upper Miocene-Pliocene

Unit 3 correlates with Sequence N40-N50 in Soares et al. (2007) (Figure 6.4). The unit is bounded at its base by horizon H₃ and at its top by horizon H₅ (Figure 6.4). Strata in this unit mark a phase of progradation of the PAMA continental shelf (Soares et al., 2007). A low- to medium- amplitude, sub-parallel reflector (Horizon H₄) separates Upper Miocene and Pliocene strata within Unit 3 (Figures 6.3b and 6.4). Horizon H₄ is incised by Holocene channels and canyons on the continental slope.

6.6.4 Unit 4 Pleistocene to Recent

Pleistocene to recent strata lie above horizon H₅, a medium-amplitude continuous reflector. The seafloor (SF) bounds Unit 4 at its top. This unit has low-amplitude

continuous reflections and correlates with Sequence N60 in Soares et al. (2007) (Figure 6.4).

6.7 Morphology of calciclastic submarine fans and levee-channels

6.7.1 Calciclastic submarine fan a

Linear features are recognised in horizons H₁, H₂, and H₃, and are interpreted as erosional distributary furrows (Figure 6.7k, l). These furrows suggest the presence of a turbidite system with a sediment flow direction towards the north, which created a large submarine fan. Sediment flow is funnelled by conduit *a*, widely opening from the continental slope onto the continental rise.

Channel-levee systems started to develop within the calciclastic submarine fan at the level of horizon H₃ as a result of the continuing incision of the erosional furrows (Figure 6.7g, h). Channel *a* became, at this time, the major feature at this level (Figure 6.7g, h). In Horizons H₄ and H₅, the submarine fan becomes narrower, but with channel *a* still growing in size (Figure 6.7c-f). The Holocene submarine fan is no longer observed on the modern seafloor but channel *a* has grown considerably when compared with its Miocene and Pliocene counterparts (Figure 6.7a, b). At present, conduit *a* forms a deep, incised canyon at the shelf margin, spanning to the continental rise, where it becomes a channel-levee system (Figure 6.7a, b). Channel *a* is the main feature on the modern seafloor with a minimum length of 56 km, continuing to the north beyond the limits of the seismic data (Figures 6.2 and 6.7a, b).

Morphometric data for channel *a* increase consistently as the channel evolved from horizons H₄ to the seafloor (Figure 6.10). Cross-sectional area and bankfull

width suggest that channel *a* developed over time (Figure 6.10e, f). Similarly, conduit bed slope and sinuosity also increase from H₄ to the seafloor. Mean slope varies from 1.6 at H₄, to 2.5 at horizon H₄, and reaches a value of 3 on the seafloor, a character that proves continuing channel incision (Figure 6.10a). Sinuosity, however, shows that as the channel evolved, its amplitude and wavelength increased, reaching values of 1.04 to 1.09 (Figure 6.10b-d).

6.7.2 Channel b

Channel *b* is first recognised in horizon H₄, developing on the continental slope (Figure 6.7e, f). Similarly to channel *a*, this sediment conduit grew from horizon H₄ to the seafloor (Figure 6.7). An aggradational stacking pattern is recognised in cross-section, suggesting a continuous sediment input to channel *b* through time (Figure 6.8). Area and bankfull width of the channel increase upwards (Figure 6.10e, f). Conduit bed slope and sinuosity do not markedly change, recording mean values of 5.0-6.0 and 1.08-1.12 %, respectively (Figure 6.10a, b).

6.7.3 Channel c

Channel *c* shows flanking levees, a character similar to the previous two channels (Figures 6.8 and 6.9). Planform and cross-sectional parameters of channel *c* are comparable to channels *a* and *b*; they are all aggradational, with area, bankfull width and bed slope increasing as the channel evolved (Figures 6.7-6.10). The difference between channel *a* and *c* is that channel *c* starts as a discrete channel-levee system at the level of horizon H₂ and no submarine fan is observed (Figure 6.7k, l). Cross-sectional area increased from 21217.3 m² in horizon H₂ to 276135.7 m² on the

seafloor. Mean bankfull width values also increase from 756.7 m at horizon H₂ to 2098.1 m on the seafloor. Mean bed slope rises from 1.5% at H₂ to 4.7% on the seafloor. Sinuosity values are similar at different stratigraphic levels, with low mean values ranging from 1.09 to 1.18 (Figure 6.10b).

6.7.4 Channels d, e and f

Channels *d*, *e* and *f* are first observed on the continental slope at the level of horizon H₃ (Figure 6.7g, h). The seismic data in this work only image the development of these conduits as canyons on the continental slope, and they appear to merge into one channel near the limit between the continental slope and continental rise. The funnelled channels *d*, *e* and *f* extend beyond the limits of the seismic data (Figure 6.7 g, h).

6.7.5 Channel x

Channel *x* is only identified in horizon H₂ (Figures 6.7c, d and 6.8). Cross-sectional data show that channel *x* did not evolve beyond horizon H₂ (Figure 6.8). Its mean cross-sectional area is 29111.0 m² and its mean bankfull width is 1019.1 m. Conduit bed slope is 2.5% on average and mean sinuosity is low, reaching a value of 1.1 (Figure 6.10).

6.7.6 Channel y

Channel *y* is only observed in horizon H₁, showing a sinuous morphology that contrasts with the previous channels (Figure 6.7k, l). In cross-section, channel *y* is a

small channel that aggrades a few reflections above horizon H₁, dying out below horizon H₂ with characteristic low amplitude, parallel internal reflections (Figures 6.8 and 6.9). Mean cross-sectional area and mean bankfull width are the smallest recognised when compared to the other channels, with values of 6169.8 m² and 417.6 m, respectively. Its mean conduit bed slope is 2.18% with a high mean sinuosity of 1.39 (Figure 6.10).

6.8 Channel morphometric relationships

Channel morphometric data are here compared to power-law regressions concerning submarine and fluvial channels formed in siliciclastic environments (Williams, 1986; Held, 2011; Lemay et al., 2020). These results confirm that calciclastic channels in the PAMA Basin have a degree of similarity to their siliciclastic counterparts.

Width vs. depth relationships for the interpreted calciclastic channel-levee systems are comparable to the siliciclastic channel models proposed by Lemay et al. (2020), in which channel sizes are similar (Figure 6.11a, b). However, differences in the exponents and coefficients of the power-law distribution display a less steep curve for calciclastic channels (Figure 6.11a, b). The latter have larger levee heights than siliciclastic channels for a given bankfull width (Figure 6.11a, b). Wavelength and amplitude regression data also show a less steep curve (Figure 6.11c, d). Thus, calciclastic channels are slightly more sinuous than siliciclastic channels, as their amplitude is higher for a given wavelength (Figure 6.11c, d). Data from channel y are particularly interesting as they plot closer to the model of fluvial channels of Williams (1986), thus justifying why channel y shows higher sinuosity values than the

other calciclastic channels (*a*, *b*, *c* and *x*) (Figure 6.11c, d). Abandoned channels are also observed from seismic data around channel *y*, revealing another similarity with meandering fluvial channels (Figure 6.6e, f).

Bankfull width vs. meander amplitude and bankfull width vs. meander wavelength relationships for calciclastic channels have low correlation values of the power-law distribution, ranging from 0.04 to 0.22 (Figure 6.11e-h). When compared calciclastic channel data to siliciclastic channel data from Lemay et al. (2020), it is evident that this type of relationship display a lower correlation (Figure 6.11e-h).

6.9 Chapter specific discussion

Oil and gas exploration on continental margins has advanced our knowledge of deep-water depositional systems, as the latter contain large hydrocarbon fields (Weimer and Slatt, 2004; Kang et al., 2018; Lemay et al., 2020). Examples of deep-water basins with hydrocarbons include the Campos Basin in Brazil, the Gulf of Mexico, the Niger Delta Basin and the Congo Fan Basin in West Africa; basins that account for 70% of the global deep-water reserves to date (Kang et al., 2018). Furthermore, it is important to address the evolution and depositional character of deep-water systems in any offshore activity. Gravity flows in deep-water channels can impact to deep-water infrastructure such as submarine cables, pipelines, or the foundations of offshore wind farms (Schneider and Senders, 2010; Baker et al., 2016; Clare et al., 2017).

Calciclastic systems are important to understand sediment transfer off carbonate shelves and isolated carbonate platforms. In the case of isolated carbonate platforms, it is relatively easy to recognise pure carbonate systems in deep waters

as they comprise, locally, the only source of carbonate sediment. An example of this is the Glorieuses archipelago in the SW Indian Ocean, in which around an isolated carbonate platform, channel-levee complexes and turbiditic lobes were developed at water depths of 2000-3400 m (Jorry et al., 2020). In contrast, carbonate shelves have a more complex setting as they often occur adjacently to siliciclastic depositional systems. A well-documented example is the Gulf of Papua between NE Australia and S Papua New Guinea, where siliciclastic material sourced from rivers draining the Papuan Peninsula mix with carbonate deposits from the shelf and isolated carbonate platforms (Francis et al., 2008).

6.9.1 Mixed calciclastic-siliciclastic depositional systems in the deep and ultra-deep PAMA Basin

This work stresses the presence of a mixed calciclastic-siliciclastic depositional system on the distal continental slope in PAMA during the Miocene to Holocene, as revealed by the Travosas Formation. So far, there are no wells drilled on the distal continental slope and ultra-deep waters of PAMA to confirm the latter assumption, but based on well data from the shelf margin, a similar stratigraphy to the one observed in wells 1-MAS-9 and 1-MAS-16 is suggested. In these wells, the Travosas Formation is dominated by carbonate deposits intercalated with minor siliciclastic intervals (Figure 6.5). Throughout the Miocene to Holocene, the PAMA continental shelf has developed a similar environment to what we see today as reported in Soares Júnior (2002) and Soares Júnior et al. (2011). During the Miocene, the Ilha de Santana Platform was submerged forming a wide area with carbonate sediment ready to be redeposited in deep waters (Figs. 14-17 in Soares Júnior et al. 2011). Similarly, the

Tiracambu mountain has sourced the inner PAMA continental shelf with siliciclastic material since the Miocene to Recent via small rivers (Figure 6.1a).

The development of deep-water depositional systems is controlled by multiple factors such as basin tectonics, sea-level fluctuations, and the rates, types and sources of sediment supply (Payros and Pujalte, 2008). According to Payros and Pujalte (2008) the most important factor generating a calciclastic submarine fan is the existence of an efficient funnelling mechanism forcing sediment gravity flows to merge downslope. Despite an initial line-source of sediment gravity flows, the physiographic profile of distally steepened ramp slopes allows the conversion of gullies and canyons to build up a point-sourced sedimentary accumulation. In the study area it can be observed from horizons H_1 to the seafloor that, for the calciclastic submarine fan *a*, there is a relatively line-source of canyons, which merge together on the continental slope to create a point-source and funnel sediment coming from the shelf margin (Figure 6.7). Seafloor maps are the best way to understand this process, as the whole continental slope is better imaged (Figures 6.2 and 6.7a, b). The modern slope shows a wide array of canyons along PAMA's margin and near the border to the continental rise, some canyons merge into a single sediment conduit (Figures 6.2 and 6.7a, b).

The way sea level affects sediment transport is distinct when comparing siliciclastic to carbonate depositional systems (Kendall and Schlager, 1981; Ma et al., 2018; Jorry et al., 2020). It is generally known that siliciclastic sediments can dominate deep-water deposition during a falling-stage or lowstand in sea level, as the inner continental shelf is exposed sub-aerially and usually connected to point-sources of sediment such as rivers, which are thus able to supply sediment directly into deep-water depocentres (Kendall and Schlager, 1981; Ma et al., 2018; Jorry et

al., 2020). Submarine canyons are also commonly formed in falling-stage and lowstand periods in sea level. In contrast, carbonate basins during sea-level lowstands record a decrease in carbonate productivity as the shelf is also sub-aerially exposed and fails to export carbonate sediment into deep waters (Droxler and Schlager, 1985; Glaser and Droxler, 1993; Andresen et al., 2003; Jorry et al., 2008; Ma et al., 2018).

During sea-level transgressions and highstands, the supply of siliciclastic sediment is reduced as river deltas retrograde and the shorelines retreat landward (Droxler and Schlager, 1985; Glaser and Droxler, 1993; Andresen et al., 2003; Jorry et al., 2008; Ma et al., 2018). Sea-level highstands are stages in which organic productivity increases on carbonate shelves allowing for their lateral expansion. The accompanying increase in slope instability has demonstrated that this stage promotes the transport of calciclastic sediment into deep-water basins (Droxler and Schlager, 1985; Glaser and Droxler, 1993; Andresen et al., 2003; Jorry et al., 2008; Ma et al., 2018). Ramp aprons, calciclastic submarine fans, channel-levee systems and elongate lobes of mud-rich calciturbidites are characteristic of transgressive and highstand periods in sea level (Droxler and Schlager, 1985; Glaser and Droxler, 1993; Andresen et al., 2003; Jorry et al., 2008; Ma et al., 2018). As an example, Tournadour et al. (2017) explain that submarine canyons in the Bahamas are related to slope failure followed by different stages of regressive erosion on isolated carbonate platforms.

Recent studies have proven that sea-level lowstand periods contribute to exporting calciclastic material into deep-water basins. Jorry et al. (2020) demonstrate that certain topographic features on the shelf break and leeward slopes play an important role on carbonate shelves by storing sediment that is initially shed

during sea-level highstands to be later re-mobilised during lowstands as calciturbidite deposits. This suggests that some calciturbidites behave like siliciclastic turbidites. Examples include the channel-levee complexes of the Glorieuses archipelago, SW Indian Ocean (Jorry et al., 2020), and calciturbidites in the Northern Nicaragua Rise (Reijmer and Andresen, 2007), the Exuma Sounds, Bahamas (Reijmer et al., 2012, 2015b), and deposited along the Great Barrier Reef (Puga-Bernabéu et al., 2014). Furthermore, Payros and Pujalte (2008) suggest that in carbonate ramps with no rimmed platforms, such as in PAMA, shallow-water sediment production is generally not interrupted in distally steepened ramps during lowstands because productive zones in shallow waters can shift basinwards (Wright and Burchette, 1998; Payros and Pujalte, 2008).

The data in this work reveal a complex scenario when considering the development of calciclastic submarine fans and channel-levee systems in the PAMA Basin during the Miocene to Holocene. The whole Equatorial Margin of Brazil experienced similar conditions, therefore it is common in the literature to correlate observations from adjacent basins (Soares et al., 2007; Piovesan, 2008; Rossetti et al., 2013). Sea-level curves for the PAMA Basin can be extrapolated from outcrop observations of the Pirabas and Barreiras formations (Rossetti et al., 2013) (Figure 6.4). The study from Rossetti et al. (2013) concluded that two major marine transgressive episodes occurred in Equatorial Brazil, one in the Oligocene-Miocene and the other in the early-middle Miocene (Figure 6.4). Both events correlate with sea-level highstands recorded in other South American basins and also worldwide (Rossetti et al., 2013). Oligocene-Miocene marine deposits are represented by the Pirabas Formation, which accumulated at a time when a rise in sea level was recorded in several parts of the world. Rossetti et al. (2013) also reported a sea-

level drop immediately before the start of the late Miocene with no subsequent transgressions being recorded, at least until the late Quaternary. This drop in sea-level is recognised by the development of a regional unconformity and formation of a lateritic soil at the top of the Barreiras Formation.

During the late Oligocene-lower Miocene (Sequence E80-N10), there was a major transgressive event covering all the Brazilian Equatorial Margin, associated with the Pirabas Sea, leading to an expansion of the carbonate shelf (Soares et al., 2007). These observations coincide with the transgressive episode reported in Rossetti et al. (2013) (Figure 6.4). Upper Oligocene-lower Miocene strata are considered part of Unit 1 in this work. At the top of Unit 1 (horizon H₁), a sinuous channel (channel *y*) is recognised as well as several linear furrows forming a calciclastic submarine fan funnelled by sediment conduit *a* (Figure 6.7k, l). Furrows can be related to turbidity flows similar to those recorded in the Little Bahama Bank (Tournadour et al., 2017), and cover a large area with no developed channels at this time (Figure 6.7k, l). This interpretation agrees with the model proposed by Payros and Pujalte (2008) in which the major transport of calciclastic deposits occur during sea-level highstands in the form of turbidity flows.

The shoreline transgression during the Early Miocene, to a position far from the shelf edge restricted the influx of siliciclastic sediment onto the continental shelf, suggesting that carbonate sediment was the predominant type feeding PAMA's deep-water basins at that time. As described earlier, channel *y* is only observed in Horizon H₁ and does not continue upwards in Unit 1. The interpretation provided here is that, unlike the calciclastic submarine fan *a*, there was no effective funnelling system feeding channel *y* above horizon H₁, leading to its abandonment (Figures 6.7-6.9).

Based on the data from Soares et al. (2007) and Rossetti et al. (2013), the middle Miocene (Unit 2) is interpreted as a falling stage in sea level. Soares et al. (2007) suggested that there is an unconformity in well and seismic data correlating with a marked sea level drop that occurred in PAMA before the late Miocene (Rossetti et al., 2013). In the study area, Horizon H₃ is interpreted being the unconformity described in Soares et al. (2007), separating moderate-to-high-amplitude seismic reflections from low-amplitude strata above (Figures 6.3b and 6.9). At the level of horizon H₃, tributary channel-levee systems were first developed within the calciclastic submarine fan, with channel *a* constituting the main sediment conduit (Figure 6.7g, h). The development of tributary channels suggests that sediment supply was significant at the time, although relatively smaller in volume when compared to strata at the level of horizon H₁. This interpretation is also corroborated by a decrease in size of the calciclastic submarine fan in younger strata, until the fan disappears near the modern seafloor. Conversely, a considerable growth of channel *a* is still recorded within the submarine fan until one reaches the modern seafloor, where the channel becomes the predominant feature (Figures 6.2, 6.7 and 6.10).

Channel *c* started developing at the level of horizon H₂ (Figure 6.7i, j). This channel is important as it shows a constant aggradation towards younger strata (Figure 6.8). The aggradation of channel *c*, accompanying its lateral migration, suggests that sediment input to the channel was constant regardless of any relative changes in sea level; geomorphic parameters such as cross-sectional area and bankfull width reveal that channel *c* continued to grow over time (Figure 6.10). Horizon H₃, correlating with the relative drop in the sea level documented in Soares et al. (2007), also reveals that channel *c* did not stop developing at this time, and its

geometry remained constant. In addition, Soares et al. (2007) suggest that at the end of the late Miocene and Pliocene (Sequence N40-N50), both the carbonate shelf and associated coastal depositional systems prograded over the PAMA Basin, a character justifying why channel c remained active during the deposition of Unit 3.

The continuous development of channel c during successive sea-level high- and lowstands, together with its constant sinuosity values through time, prove that calciclastic depositional systems are not primarily controlled by sea-level change, as also suggested in Payros and Pujalte (2008). A possible explanation to the observed aggradation of channel c through multiple fluctuations in sea level is the existence of an efficient funnelling mechanism on the continental slope (Figure 6.7). Additionally, as described in Jorry et al. (2020), calciclastic sediments can be shed to deep-water systems not just during sea-level highstands, but also during lowstands. Calciclastic sediments might have accumulated on terraces at the slope, to be later redeposited during falling-stages and lowstands in sea-level (Figure 6.7).

6.9.2 Geomorphic characteristics of carbonate deep-water levee-channels

Geomorphic analyses of deep-water channel-levee systems fed by siliciclastic sediment have been previously documented in Lemay et al. (2020) and compared to fluvial channels. It was recognised that submarine channels are one to two orders of magnitude wider and deeper than fluvial channels, with the latter being more sinuous than submarine channels (Lemay et al., 2020). This work aims to determine how similar calciclastic levee-channels are in comparison to their siliciclastic counterparts.

Based on the obtained results and comparison with published power-law relationships, it can be confirmed that bankfull width vs. depth relationships of calciclastic channels in PAMA are similar and comparable to siliciclastic channels (Figure 6.11a, b). However, calciclastic channels are deeper than siliciclastic channels for a given bankfull width (Figure 6.11a, b). Calciclastic channels also appear to be slightly more sinuous than siliciclastic channels as the regression curve between meander amplitude and wavelength is less steep (Figure 6.11c, d). Sinuosity values recorded in channel *y* approaches the sinuosity of meandering fluvial channels, marking a distinction with other channels (Figure 6.11c). In fact, three different types of calciclastic sediment conduits have been observed in the PAMA Basin: i) Type 1, which are channel-levee systems related to calciclastic submarine fans (channel *a*), ii) Type 2, comprising low sinuosity channel-levee systems *b*, *c* and *x*, and iii) Type 3, which is represented by highly sinuous channel *y* (Figure 6.12).

6.9.2.1 Type 1 - channels related to calciclastic submarine fans

The early stages of this type of channel are associated with erosive turbidity currents developing furrows within a calciclastic submarine fan (Figure 6.12a). These furrows are recognised in cross-sectional data and on key seismic reflectors as small spikes, which mark the loci of incision of erosive turbidity currents (Figure 6.12b). As the incision of the furrows continues, a channel-levee system may develop, such as channel *a* (Figure 6.12c, d). This type of channel is characterised by its low sinuosity, and by presenting geomorphic features similar to its siliciclastic counterparts (Figure 6.11).

6.9.2.2 Type 2 - low sinuosity, aggradational channels

Type 2 channels record low sinuosity values, usually less than 1.3 (Figures 6.10 and 6.12e). Type 2 channels are not associated with calciclastic submarine fans and originate due to the funnelling of sediment from upper slope canyons to form, downslope, a well-defined sediment conduit (Figure 6.12h). They start as small channels with high-amplitude internal reflections (Figure 6.12f). Due to the characteristic mixing of carbonate and siliciclastic deposits through multiple episodes of sea-level rise and fall, aggradational features are observed in their interior, leading to the generation of large channel-levee systems (Figure 6.12g, h).

6.9.2.3 Type 3 - high-sinuosity channels

The high sinuosity (average of 1.4) of Type 3 channels is comparable to fluvial channels (Figures 6.10b, 6.11b and 6.12i). Channel y shows features such as abandoned channels that suggest a change in its flow direction (Figure 6.12i, j). In contrast to the previous low sinuosity channels (Type 2), the cross-sectional area of Type 3 channels is considerably smaller (Figure 6.10). This type of channel does not aggrade over time, implying that sediment sources were episodic and not continuous.

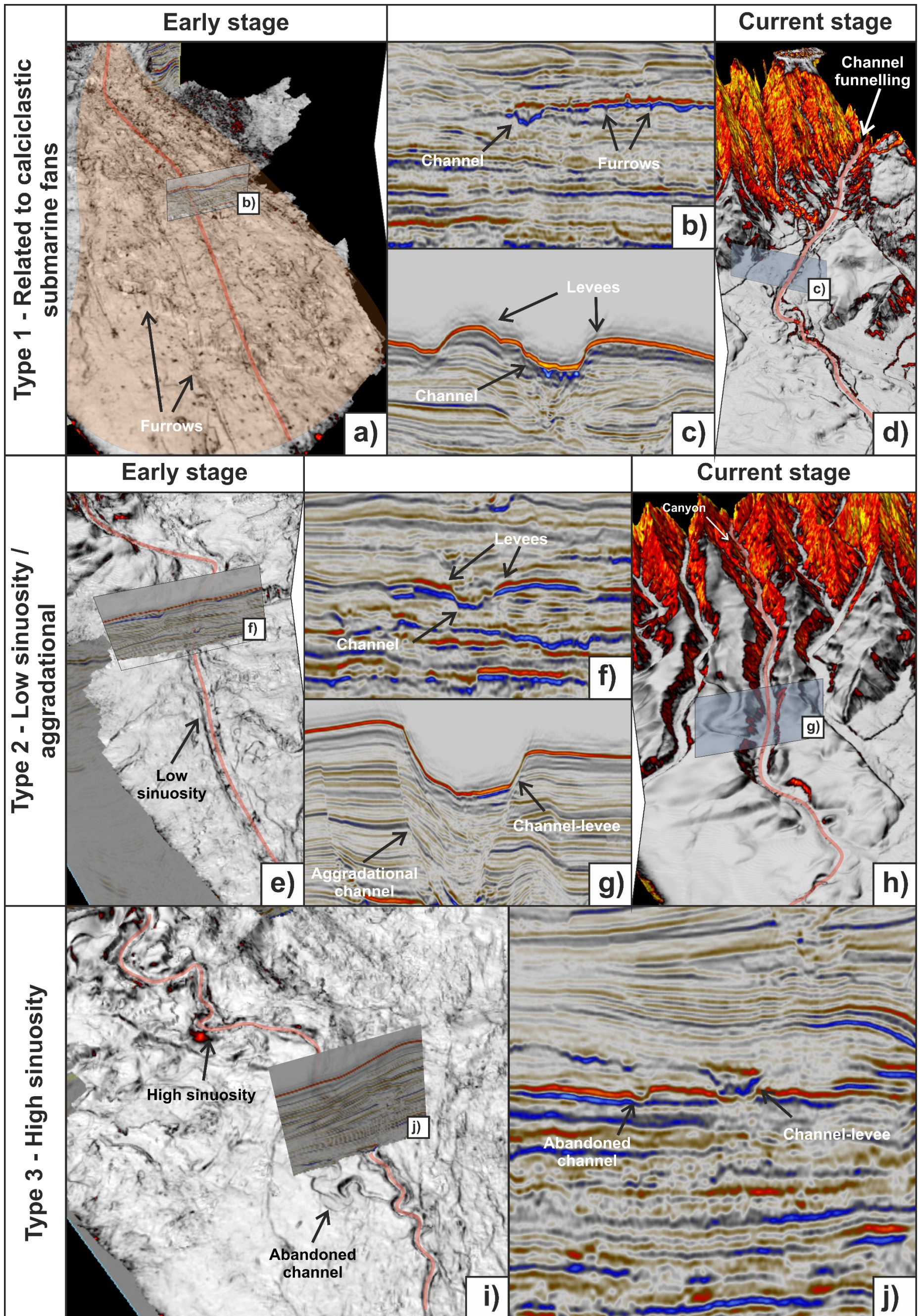


Figure 6.12. Summary diagram of 3D seismic data showing the main types of channel-levee systems occurring in the mixed carbonate-siliciclastic depositional system of the PAMA Basin.

6.10 Chapter specific summary

The main conclusions concerning the deep- and ultra-deep-water mixed calciclastic-siliciclastic depositional systems of the Miocene-Holocene PAMA Basin can be summarised as follows:

- a) A portion of the Miocene-Holocene strata of the Travosas Formation comprises a mixed calciclastic-siliciclastic depositional system recording a dominant carbonate input from the continental shelf. A calciclastic submarine fan and channel-levee systems are identified within deep and ultra-deep waters of the PAMA Basin.
- b) Multispectral satellite data point out to a dynamic sediment transport on a mixed calciclastic-siliciclastic carbonate shelf. The PAMA continental shelf is divided into a mixed carbonate-siliciclastic zone in its inner part, and an autochthonous carbonate zone in its middle and outer zones.
- c) Geomorphologic relationships of the PAMA calciclastic channel-levee systems show similarities with modern siliciclastic submarine channel models previously published by Lemay et al. (2020).
- d) The formation of a large calciclastic submarine fan in the lower Miocene correlates with a period of progradation and lateral growth of the carbonate shelf during a sea-level rise. Erosional furrows are characteristic of distal fans and comprise an effective funnelling mechanism for younger channels forming on the continental slope.
- e) Three different types of deep-water depositional systems are recognised in the PAMA Basin: channels related to calciclastic submarine fans (Type 1), low sinuosity-aggradational channels (Type 2), and high sinuosity channels (Type 3).

- f) Channels related to calciclastic submarine fans (Type 1), such as channel *a*, were initiated by the action of highstand turbidity flows. The continuous erosive turbidite flows led to an increase in the funnelling of sediment, developing a large channel-levee system.
- g) Low-sinuosity channels (Type 2) are not associated with calciclastic submarine fans, are aggradational, and appear to develop through time regardless of any relative sea-level change. This can be explained by the accumulation of sediment in topographic features, such as terraces on the continental slope, which is later redeposited during sea-level lowstands. Furthermore, the presence of a steepened ramp on the PAMA continental shelf provides a continuous supply of carbonate material during sea-level lowstands as the productive zone shifts basinwards.
- h) Highly sinuous channels (Type 3) are characterised by their small cross-sectional area, showing a bankfull wavelength vs. amplitude relationship, and sinuosity values, that are similar to fluvial channels.

Chapter 7: Discussion and conclusions

7.1 Preamble

The results chapters in this thesis are focused on understanding the geological processes affecting the development of isolated carbonate platforms, their internal structure, and later recognise which depositional systems develop beyond carbonate margins in deep and ultra-deep waters. This Chapter aims to integrate the results obtained in this research, discuss wider implications, summarise the limitations, and propose themes for further work related to carbonate exploration and production. The main findings of Chapters 4, 5 and 6 are summarised schematically in Figure 7.1. In Chapter 4, fractured carbonate units are shown to comprise prolific hydrocarbon reservoirs around the world. The challenge of producing hydrocarbons from this type of reservoir is primarily due to scale and resolution limitations when defining and modelling them, as stated in Chapter 5. Understanding the structural and sedimentological components of carbonate platforms, and their scale relationship between different datasets is therefore key in reservoir delineation. In Chapter 6, the relationship between platform top to distal slope and basin depositional settings is explored. This latter approach is important as deep-water exploration is becoming more common due to technological advances on carbonate-rich prospects such as those in Mexico and Brazil.

7.2 Summary of scientific results

7.2.1 Chapter 4: Structural controls on isolated carbonate platforms

The first data chapter in this thesis (Chapter 4) investigates the relationship between the position and distribution of isolated carbonate platforms in relation to distinct arrays of faults in the Timor Sea, Northwest Australia (Figure 2.1). High-resolution 3D seismic and borehole data were used to calculate fault-throws and thus generate throw-depth (T-Z) profiles and throw maps detailing the kinematic history of the investigated faults. An important result in this chapter is the clear correlation amongst certain relay ramps in the study area and the position of isolated carbonate platforms (Figure 7.1). Carbonate productivity vs. fault growth ratios were the primary controls on the growth of isolated carbonate platforms, generating three distinct settings: (1) one in which fault-throw surpasses carbonate productivity, (2) settings in which fault-throw is equal to carbonate productivity, and (3) settings in which faulting post-dates the formation of isolated carbonate platforms (Figure 7.1). The control of such settings on the reservoir potential of carbonate shelves is also addressed in Chapter 4, focusing on the role of faults and associated structures (e.g. relay ramps) in controlling the type of isolated carbonate platforms. Variable fracture densities and distributions within carbonate platforms may favour the accumulation of hydrocarbons. Isolated carbonate platforms of types 2 and 3 are expected to have enhanced fracture porosity and permeability, making them preferential reservoir targets.

7.2.2 Chapter 5: Multi-scale fracture network characterisation on carbonate platforms

Chapter 5 investigates fracture networks formed on carbonate platforms and how complex is to characterise them at multiple scales using distinct datasets. In this chapter, the term *fracture* was defined as any type of discontinuity (joints, faults, etc.) formed because of different stress conditions such as large-scale tectonic events, local uplift and erosion, slope instability or excess fluid pressure. Sub-seismic (small and intermediate size) fractures were studied in the outcropping Cariatiz platform of the Sorbas Basin, southeast Spain, using specific mapping techniques and airborne LiDAR data (Figure 5.1). In addition, large fractures were analysed using 3D seismic data from the Pernambuco Basin in Brazil (Figure 5.2). The complexity of different fracture types was introduced, stressing the fact that different types of fractures can only be recognised at certain scales of observation. Another important aspect discussed in this chapter was the significance of characterising fracture networks based on fracture branches, as well as using a combination between topology and geometry analyses to better demonstrate the connectivity of fracture networks (Figure 7.1). The results of Chapter 5 reveal that fracture network properties behave differently depending on the fracture size, and that transitional scale gaps between datasets do significantly hinder fracture characterisation. A log-normal distribution model was deemed useful to predict fracture branch lengths for massive non-stratabound units, such as the reef and slope facies of the carbonate platform at Cariatiz. This can be applied to reservoir characterisation to fill the gap between wellbore data and seismic data, as intermediate-scale fractures are known to comprise the main conduits for fluid flow.

7.2.3 Chapter 6: Deep-water depositional systems

Chapter 6 is focused on sedimentological aspects beyond the carbonate shelf of the Pará-Maranhão Basin, Equatorial Brazil (Figure 6.1). The rationale behind this chapter is that little is known about deep and ultra-deep-water carbonate environments compared to their shelf and platform counterparts. Understanding the relationship between shallow- and deep-water sedimentation is key to develop valid depositional models on carbonate settings. A mixed calciclastic-siliciclastic sediment input was recognised in PAMA during the Miocene to Holocene. Deep-water calciclastic submarine fans and channel-levee systems were investigated utilising 2D and 3D seismic, borehole data and multispectral satellite imagery (Figure 7.1). In this chapter, the controls of sedimentation processes are related to sea-level fluctuations and sediment-funnelling mechanisms. Cross-sectional and platform geomorphological characteristics were measured on multiple channel-levee systems to compare them with their siliciclastic counterparts, showing similarity to these latter. This chapter is important as it shows different types of depositional systems associated with turbidity flows in a mixed calciclastic-siliciclastic setting. Channel-levee systems, as those analysed in this thesis, are known to be prolific hydrocarbon reservoirs and have seldom been associated to carbonate depositional systems. Because calciclastic channel-levee systems are similar to their siliciclastic counterparts, similar approaches to those followed for siliciclastic depositional systems can be used to study the architecture and sedimentological patterns of deep-water calciclastic depositional systems.

7.3 Integration and wider implications

The results obtained in this thesis show a wide range of carbonate depositional settings, starting from shallow marine settings with isolated carbonate platforms developing on the continental shelf of NW Australia to deep-water settings with re-sedimented calciclastic channel-levee systems in the PAMA Basin, Brazil. This thesis explores different approaches related to the study of carbonate settings from the platform shelf to basin at different scales of observation. The interaction between geometrical patterns, diagenetic processes, and fracture development is important to understand the reservoir potential of carbonate successions. This sets an overview of how complex and diverse the carbonate depositional systems can be, resulting in challenges for geoscientists working in exploration and development.

7.3.1 Structural controls on shallow-water carbonate settings

During the stages of exploration and prospect evaluation, one of the main types of data used to image carbonates is seismic data, in which geometry is the most important information that can be extracted from this dataset (Eberli et al., 2004). This is true when analysing the architecture and heterogeneities of ICPs, such as the ones observed in the Timor Sea, Northwest Shelf of Australia (Chapter 4). Their characteristic round and ellipsoid shape, as well as their steep margins are well-defined by 3D seismic data (Figure 4.4). This characteristic geometry and the common relationship of ICPs to develop on top of structural highs (i.e., horsts) have been useful to find world-class hydrocarbon reservoirs including the Tengiz Field in the Caspian Sea, Kazakhstan (Narr and Flodin, 2013; Kenter et al., 2015) and Central Luconia in NW Borneo (Zampetti et al., 2004; Kosa et al., 2015).

However, the results obtained from the Timor Sea show that distribution and arrangement of ICPs differs from the common model of structural highs in areas with complex fault configurations and high fracture density (Figure 7.2). This is because, as observed from the data of the Timor Sea in Chapter 4, only a small portion of ICPs are placed on structural highs, with the majority of ICPs developing on different settings in relation to the fault distribution (Figure 7.2). A classification of isolated carbonate platforms based on fault linkage and distribution was presented, defining three types of ICPS. Type 1 ICPs develop on structural highs. Type 2 ICPs develop in areas of active faulting, over relay ramps. Type 3 ICPs develop on a non-faulted zone in which the ICP grows, but it is later cut by a fault (Loza Espejel et al., 2019a).

In a complex setting such as in the Timor Sea, a good practice for explorationists is to generate a detailed map characterising ICPs by their type, such as in Figure 7.3. This approach is favourable to obtain additional information and determine the potential of different ICPs to accumulate hydrocarbon. This research is focused on naturally fractured reservoirs, which have an intrinsic implication that fractures influence fluid flow either by enhancing it or by creating barriers or baffles to its movement (Burchette, 2012). However, the biological origin and inherent susceptibility to environmental changes of carbonates plays an important role on carbonate rocks. (Choquette and Pray, 1970). Carbonate reef facies are subject to early lithification, developing brittle mechanical properties in the early stages of diagenesis. These properties result in the ability of carbonate rocks to build steep margins and to fracture almost at the same time of deposition.

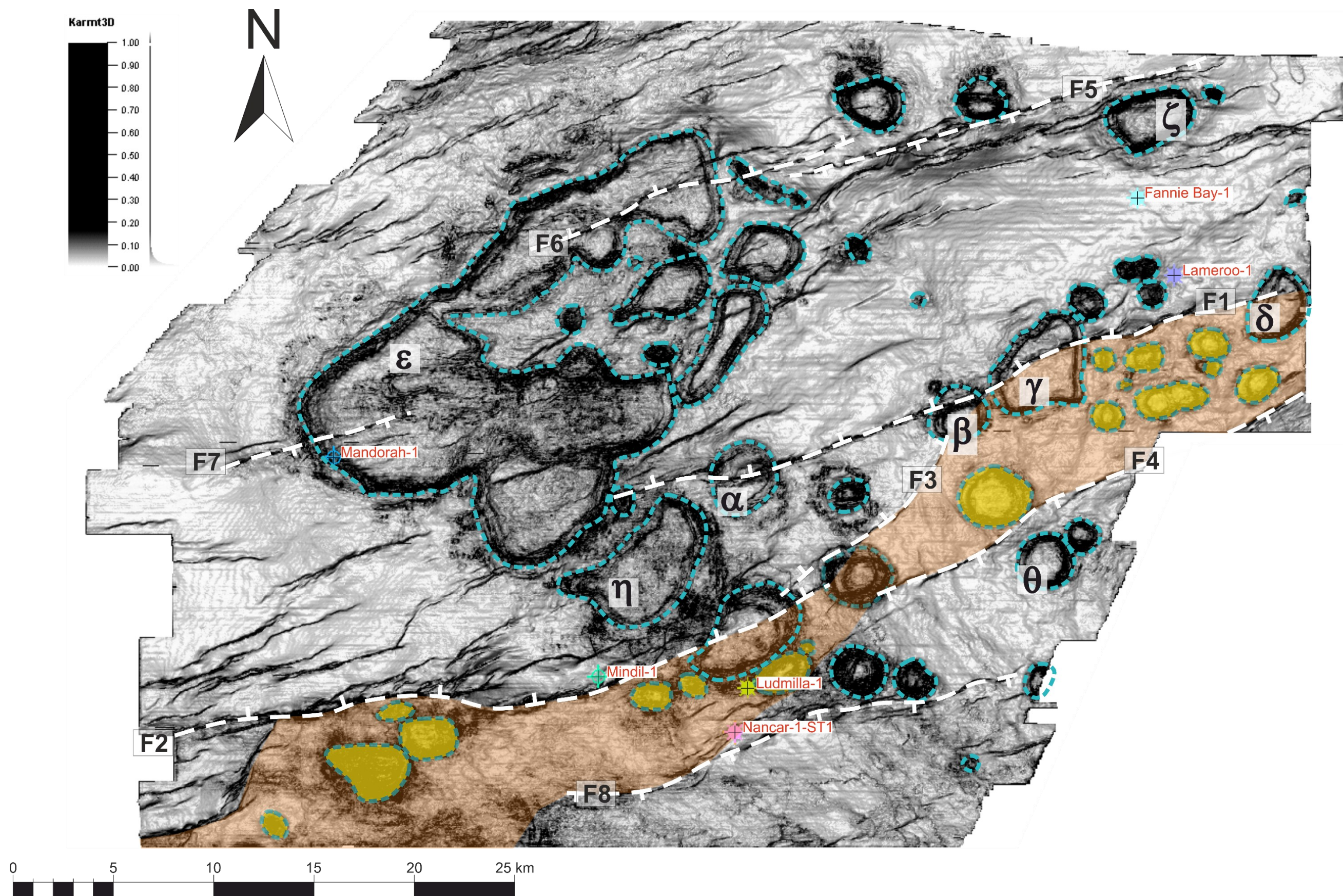


Figure 7.2. Variance map of the base Pleistocene horizon, Bonaparte Basin, NW Australia. Shaded orange area represents a structural high bordered by normal faults. Blue dashed lines indicate the outlines of ICPs.

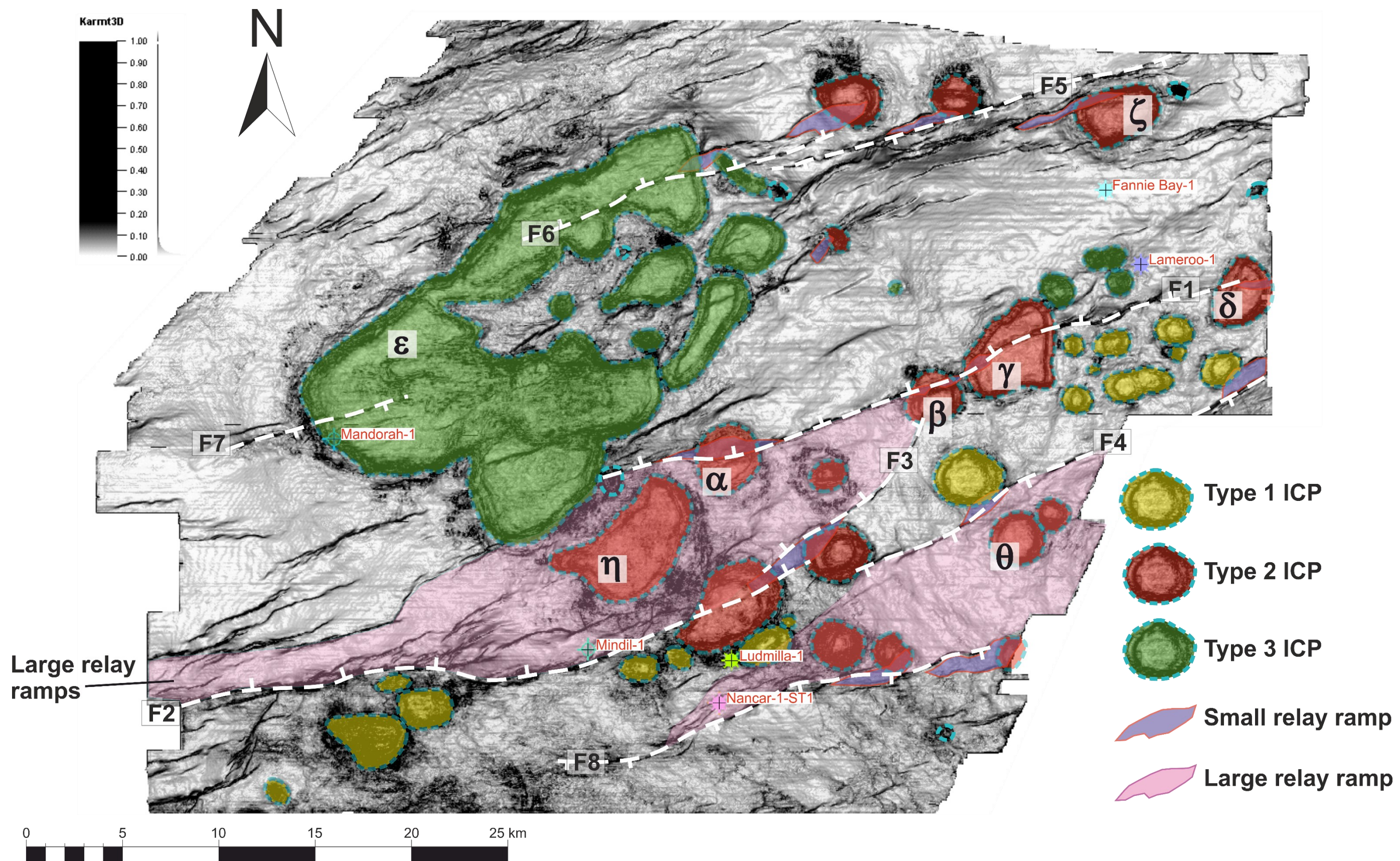


Figure 7.3. Variance map of the base Pleistocene horizon showing the different types of ICPs observed in the Karmt3D study area of the Bonaparte Basin, NW Australia. Shaded green areas represent Type 1 ICPs, shaded red areas represent Type 2 ICPs, and shaded green areas represent Type 3 ICPs. Small relay ramps are coloured in purple and large relay ramps are coloured in pink. Note that only major faults and associated relay ramps are mapped. Blue dashed lines indicate the outlines of ICPs.

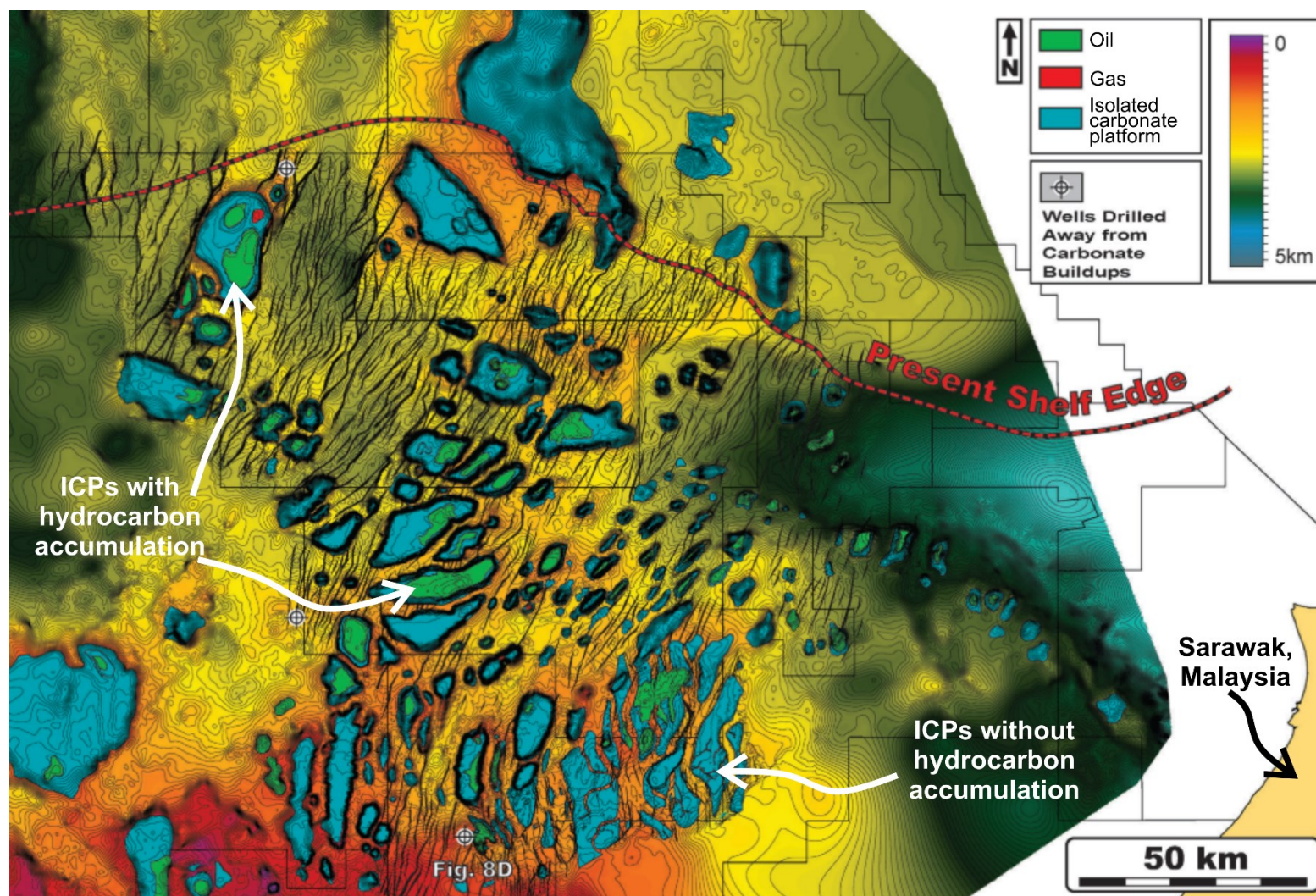


Figure 7.4. Middle Miocene regional map showing the distribution of isolated carbonate platforms in Central Luconia offshore Sarawak, NW Borneo. Note how densely faulted is the area, and that not all ICPs have hydrocarbon accumulation. Modified from Kosa et al. (2015).

Reservoir potential of Type 2 ICPs is expected to be high as it is associated with a relay ramp, providing a good scenario to fluid migration pathways. Furthermore, due to active fault propagation during high rates of carbonate growth, and a brittle internal structure, this type of ICP is expected to be highly fractured with enhanced rock permeability. A map differentiating different types of ICPS can provide a practical approach to facilitate the decision of selecting a structure/target to drill (Figure 7.3). Based on the analysis of seismic data and conceptual models, Type 2 ICPs are the preferred structures due to their extensive petroleum system (i.e. hydrocarbon migration, reservoir, trap, seal), followed by Type 3. Based on this classification, Type 1 ICPs have a lower petroleum potential.

Data analysed in the Bonaparte Basin is an excellent analogue to study similar settings. Central Luconia offshore Sarawak in Malaysia, is a suitable area to continue this study since it is a well-studied field with a robust dataset of seismic and borehole data. Figure 7.3 shows the ICP distribution and the presence of hydrocarbon accumulation in certain structures. A detailed map classifying each ICP into the specific ICP types proposed in this thesis, would provide a better understanding of the petroleum system in Luconia.

7.3.2 Fracture types and reservoir properties

The ICP prospect evaluation presented above is a useful tool to classify various types of ICPs that are expected to have different internal rock properties. Porosity and permeability depend on the interplay between matrix porosity, cementation and associated fractures with multiple sizes. Therefore, accurate estimates of these properties cannot be directly observed and measured from seismic data alone. The

resolution of a given dataset limits the way in which rock properties can be observed and quantified. For this reason, additional datasets are needed such as borehole data. However, as discussed in Chapter 5, there is an observational scale gap between seismic and borehole datasets that complicates the analysis of sub-seismic features (Figure 5.12).

Data from outcrop analogues provide a unique opportunity to assess three-dimensional geological features that are, otherwise, not detected in seismic and wellbore data. Outcrop analogues are a key tool for the creation of conceptual models that can be compared to subsurface observations. Nevertheless, reservoir analogues have to be used with caution because surface processes such as weathering, occurring at low confining pressures and low temperatures, can change outcropping units into volumes of rock that are quite different from their subsurface counterparts (Cerri et al., 2020). Some fractures observed at outcrop may have formed at depth and have now been uplifted but, in many other cases, outcrop surfaces have been overprinted by younger surface fractures. In order for the fracture sets at outcrop to be considered as analogous to deep reservoirs, the two sets of strata must have shared a similar burial history with similar fracturing episodes (Moore and Wade, 2013b).

Chapter 5 focussed on the importance of outcrop analogues as tools to understand reservoir fracture systems, since many aspects of fracture character are impossible to measure using subsurface data. A multi-scale analysis of the Messinian Fringing Reef Unit of Cariatiz in SE Spain was developed in this chapter, and it was established that fractures exist at all scales of observation (Figure 5.12). Significant data gaps

exist due to resolution issues; specific fracture types can only be observed at a certain scale of observation.

At Cariatiz, structural and depositional features are thought to have a potential impact on permeability and fluid flow. Five types of structural features were recognised (Figure 7.5). The first type comprises centimetre-long open fractures or joints (Figure 7.5c). These joints are present across the Reef Unit and show a broad distribution with no clear dominant orientation. Trace-lengths range from 1 cm to 150 cm with variable apertures. The second type are veins with a calcite infill that reveal similar geometries to joints (Figure 7.5d). A third fracture type is recognised from a section parallel to the platform margin (Figure 7.5a). These are vertical fractures oriented perpendicularly to the platform margin. They present trace-lengths with tens of metres that offset depositional facies boundaries, propagating from the reef crest (Figure 7.5a).

These first three fracture types are related to syn-depositional processes and slope instability as mentioned in Nooitgedacht et al. (2018). The fourth fracture type comprise large fracture swarms that are tens to hundreds of metres long. They are 20 m to 50 m wide and are composed of clusters with closely spaced fractures (Figure 7.5b). Fracture swarms display a clear orientation parallel to the platform margin, as also observed on LiDAR maps. The origin of these fracture swarms, given their size and orientation pattern, can be associated with tectonism during the Pliocene-Quaternary tectonic uplift of the platform (Braga et al., 2003; Van Tuyl et al., 2018). The last structural feature observed in the field are karst features (Figure 7.5a, e). Karsts are diagenetic features predominantly related to vertical fractures, creating centimetre and metre length caves, sink holes, bogaz and limestone pavements

(Monroe, 1970). Their origin can be linked to rock dissolution by acidic (CO₂-rich) meteoric waters during its current period of sub-aerial exposure.

Two main depositional features observed at Cariatiz are thought to influence porosity and fluid flow. A system of vertical *Porites* is the main component of the Reef Unit, together with microbial boundstones (Figure 7.5e). *Porites* are massive coral skeletons formed of vertical fused columns, which are cm long individually (Brachert et al., 2006). These *Porites* develop vertical lineations in between the columns, and moldic porosity. The skeleton exhibits fractures that were preferentially formed parallel to the contacts of the individual columns. This setting is common in this type of corals as described from Late Miocene reefs in central Crete, Greece, which can enhance rock permeability (Brachert et al., 2006). Cariatiz is a massive rock unit with no apparent bedding. However, the presence of chaotic and curved pseudo-bedding surfaces is noted throughout the study area (Figure 7.5f). These surfaces create blocky compartments within the Cariatiz Fringing Reef Unit. Obviously, the origin of these two last textures is related to the depositional and biological features developed during the deposition of the Cariatiz Fringing Reef Unit.

The combination of structural and depositional features observed at Cariatiz can affect the permeability of carbonate units. All these features can serve as fluid flow pathways, with the exception of the cemented veins that form barriers and baffles to fluid flow. In contrast, the best evidence for fractures being prone to fluid flow is the development of karst features and their subsequent enlargement.

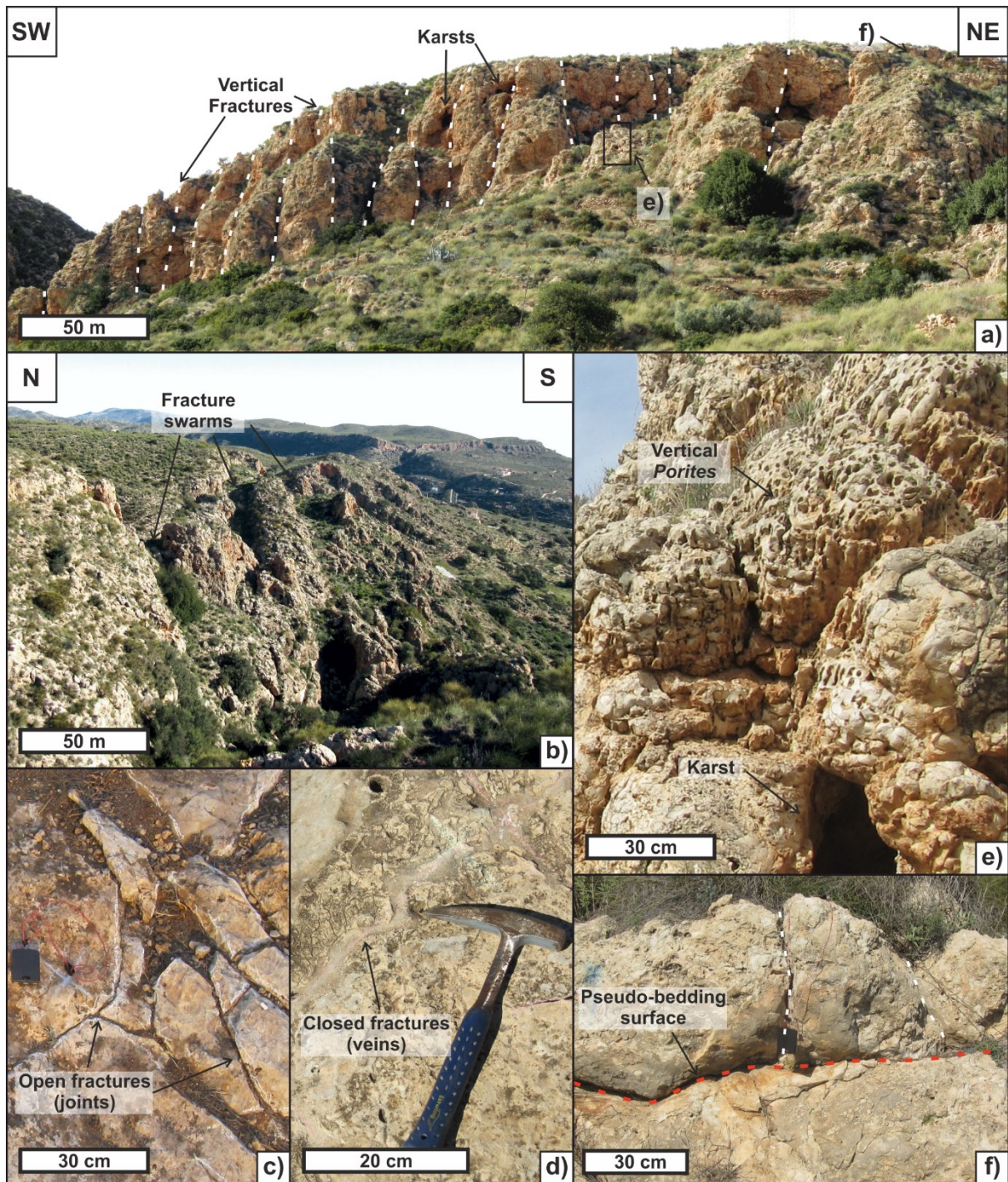


Figure 7.5. Types of structural and depositional fabrics at Cariatiz, SE Spain. a) Outcropping section of the Cariatiz Fringing Reef Unit showing large vertical fractures and karsts. b) Fracture swarms. c) Open fractures (joints). d) Closed fractures (veins). e) Vertical Porites and a small karst cave. f) Pseudo-bedding surfaces.

7.3.3 Importance of fracture types to fluid flow

It is known from oil and gas reservoirs that a combination of fracture types and depositional properties enhance fluid flow. In the Cantarell Field, Gulf of Mexico, fold- and fault- related tectonic fractures appear to be the most relevant (Ricoy et al., 2004; Ricoy-Paramo, 2005). In the Tengiz Field, Kazakhstan, syn-depositional fractures are the principal fractures that promote permeability in the field (Kenter et al., 2015). In the Ekofisk Field, North Sea, a combination between stylolite- and fold-related fractures appear to be the most important (Moore and Wade, 2013c, 2013b). However, there is not a specific fracture type that appears to favour fluid flow consistently in all reservoirs. Interestingly, a common characteristic that most reservoirs have, is the fact that many of the pre-existing fractures were affected by dissolution and enlargement at some point. This pattern is evident and can be observed in the surface, such as on exposed outcrops in the Paraná Basin, Brazil, in which enlarged tectonic fractures contain oil impregnations (Cerri et al., 2020, fig. 4 and 5). This is an exceptional example that allow us to recreate how oil flows in the subsurface. As a subsurface example, in the Tengiz reservoir, image logs show characteristic enlarged fractures and caverns (Narr and Flodin, 2013).

Another aspect that seems important in all reservoirs, is the fracture size. Large fractures, recognisable at seismic scale, appear to be the main contributors to fluid pathways. In Chapter 4, it was recognised how large fault arrays in the Timor Sea could generate considerable pathways to fluid flow due to the fault linkage and relay ramp development. At Ekofisk, a similar behaviour is observed, in which large faults control the early flow to the reservoir at a large scale (Moore and Wade, 2013b).

In contrast, at reservoir scale, smaller fractures are the main contributors to fluid flow and accumulation. Without small fractures, even if there is a good system of large faults, contributing to fluid migration, accumulation and fluid flow in a reservoir, would not be as good. Outcrop data in Chapter 5 recognised that small fractures at a cm scale display better connectivity, in comparison to large fault systems at a km scale. This observation confirms the fact that smaller fractures are, in many cases, the main contributors to permeability and fluid flow. However, fractures of different sizes have to be consistently analysed collectively to obtain a more comprehensive model of the fracture network, as suggested in the Ekofisk reservoir. As a conclusion, it can be said that the importance of fractures for reservoir potential and fluid flow relates to their size and degree of dissolution-enlargement for those fractures.

7.3.4 Structural and sedimentological controls on deep-water carbonate settings

Chapters 4 and 5 of this thesis emphasises the importance of structural patterns (i.e. faults and fracture networks) for reservoir characterisation on shallow-water carbonate depositional settings. In contrast, Chapter 6 emphasises the significance of sedimentological patterns on the analysis of deep- and ultra-deep-water depositional settings. This is interesting, as the assessment for reservoir potential in resedimented carbonate deposits seems to be dominated by sedimentological patterns, which demands carbonate explorationists to have a different mindset when working with deep-water systems.

7.3.4.1 Sediment type

Deep-water depositional systems are controlled by multiple processes that are closely related to the carbonate shelf. In general, a carbonate shelf or platform can produce distinctive types of sediment based on the margin type (Rankey, 2017). Flat-topped rimmed shelves and platforms with steep slopes commonly develop photozoan successions, which encompass photosynthetic organisms that require shallow waters (Rankey, 2017). Photozoans include corals and calcareous green algae. Examples of this setting are the isolated carbonate platforms in Tengiz and the Tuxpan Platform in the Gulf of Mexico. In contrast, platforms with steepened ramps such as in the PAMA Basin or in the Browse Basin, commonly develop heterozoan successions in which production of carbonate sediment is not dependent on light, allowing the carbonate factory to produce sediment across a range of water depths (Rankey, 2017). Heterozoan sediment includes calcareous grains produced by organisms such as coralline algae, molluscs, bryozoans and benthic foraminifera, which can form in shallow and deeper water depths (Rankey, 2017). In certain situations, such as the observed in the PAMA Basin, carbonate sediment can be mixed with siliciclastic material from river mouths or deltas.

Reservoir potential of deep-water systems relies on the type of sediment shed from the shelf or platform. For the case of flat-topped rimmed platforms such as Tuxpan and Tengiz, it is common to have a dispersed-flow system such as debris aprons. The material shed to the slope and basin varies from carbonate muds, skeletal grains and breccias, which ultimately have pervasive low matrix porosity; and permeability in this type of deposit is usually influenced by fractures (Loucks et al., 2011; Collins et al., 2014).

Contrasting with the previous settings, calciclastic focused-flow systems are known to resemble siliciclastic systems in which calcareous grains provide the main porosity and permeability (Goldstein et al., 2012). Focused-flow systems characterise to have coarse: fine facies volume ratios with a good sorting mechanisms of grains. Based on the previous examples analysed, focused-flow systems such as channel-levee systems are commonly found in steepened ramp margins. Although channel-like deposits can also occur in steep platform margins such as in Agua Amarga Basin, SE Spain (Goldstein et al., 2012). Reservoir potential in channel systems is closely related to the type of calcareous grains deposited in a confined system.

7.3.4.2 Palaeotopography and funnelling mechanisms

As recognised in Chapter 6, in adding to Payros and Pujalte (2008), a characteristic component and the most important to develop focused-flow depositional systems beyond the toe-of-slope, such as calciclastic submarine fans and channel-levee systems, is the presence of a pre-existing palaeotopographic features. Palaeotopography plays a key role in determining the development of focused- (i.e. point-sourced) versus dispersed-flow (i.e. line-sourced) deep-water systems (Goldstein et al., 2012). Palaeotopographic features can funnel sediment gravity flows from a long linear distance of a shelf or platform into a single confined channel, in essence transforming a line-source system into a point-source system (Goldstein et al., 2012).

There are many settings in which funnelling mechanisms can occur. Tributary gullies and canyons are often found on steepened ramps, such as the observed in the

PAMA Basin. Gullies are merged, leading to the development of a major channel transporting sediment off the platform. In terms of reservoir potential, palaeotopography can act as a good trapping system as the reservoir unit is confined within the channel system. For example, in the case of channel development by merging gullies such as in PAMA, the distance of the channel acts as a good sorting mechanism, in which the channel is filled with calcarenites that will have a good matrix porosity. And the channel is surrounded by calcareous mud and shale, trapping the reservoir.

7.3.4.3 Sea-level fluctuations

The classic stratigraphic model for photozoan carbonates emphasises on “highstand shedding”, suggesting that during high sea levels, flooded shallow flat shelves and platforms are prone to produce large volumes of sediment, which can be shed off shelves into deep waters. And during lowstands, when shelf areas are subaerially exposed and carbonate sediment is limited, the platform fails to transport carbonate sediment into deep-water channels, and instead, channel fill can be switched to siliciclastic sediment (Playton et al., 2010; Janson et al., 2012; Verwer et al., 2014).

As discussed in Chapter 6, there are various scenarios in which sea level changes can affect in a different way sediment deposition in deep waters. One is the presence of an heterozoan succession on a steepened ramp, such as the observed in the PAMA Basin and the Browse Basin. In this setting, carbonate production can move basinwards when there are drops in sea levels, maintaining an almost constant carbonate productivity. In addition, as observed in the PAMA Basin, existing

topography at the slope, such as terraces, can accumulate material shed during highstands, to then be transported during lowstands.

This combination of sedimentological and palaeotopographical patterns suggest that channels developed in such settings, like in PAMA and the Browse Basin, have an aggradational architecture, which makes them good targets for hydrocarbon exploration due to their large volume of sediment. In contrast, channels that do not aggrade and stop their development when there is a change in the sea level, are expected to have small volumes of sediment and therefore less hydrocarbon potential.

7.3.4.4 Oceanic currents

Oceanic currents are important components that influence the type and volume of sediment shed from the platform to the slope. As it was discussed in Chapter 6, oceanic current can transport siliciclastic sediment from the inner shelf to the outer shelf, creating a mixed calciclastic-siliciclastic setting, like in the PAMA Basin. This scenario is also observed in the Gulf of Papua, in which sediment is transported by a combination of wind-driven waves and tidal currents (Francis et al., 2008).

7.3.5 Deep-water exploration play types

Frontier evaluation of carbonate plays is commonly focused on platform-top, margin and upper slope facies (Winefield et al., 2011). Exploration for carbonate distal slope and basin-floor reservoirs is underdeveloped compared to carbonate-shallow-water and siliciclastic-deep-water depositional settings (Janson et al.,

2012). Multiple deep-water reservoirs worldwide have shown the reservoir potential of resedimented carbonate deposits. Examples include the Cretaceous Poza Rica Field in Mexico (Loucks et al., 2011), the Mississippian Tengiz Field in Kazakhstan (Collins et al., 2014), and several fields in the U.S. Permian Basin (Janson et al., 2007; Winefield et al., 2011); although these reservoirs are limited to debris apron deposits. Channel-levee systems are still underexplored targets, with examples such as the PAMA Basin suggesting a good potential, despite the limited data available up to date.

Outcrop studies and careful examination of wellbore data and 2D-3D seismic data have led to the development of new conceptual models of deep-water stratigraphic architecture (Playton et al., 2010; Janson et al., 2012). Slope and basin deposits reflect the growth, evolution and depositional conditions of the carbonate system in relation to platform-top deposits (Playton et al., 2010). However, their relationship is still not fully understood. Winefield et al. (2011) suggest that downslope resedimentation of carbonate material is in part controlled by the evolution of the parent platform margin, which in turn is best characterised in terms of various controlling processes such as carbonate factory type, tectonic setting, eustatic variations, and platform alignment relative to prevailing wind direction and ocean current patterns. Here, key controls and sedimentological patterns of deep-water depositional settings are discussed in relation to important hydrocarbon reservoirs, unique outcrops and seismic imaged deposits to assess the relationship with platform settings and their importance for reservoir potential.

Chapter 6 introduced the different types of carbonate deep-water depositional systems based on classifications by Payros and Pujalte (2008) and Playton et al.

(2010). Those classifications separate deep-water deposits depending on their spatial architecture, sediment type and platform margin type. This section presents a classification based on the position of deep-water deposits relative to the platform margin and slope as to facilitate reservoir evaluation. Based on the observations and analyses of different examples, two types of deep-water carbonate exploration plays can be recognised: (Type 1) attached carbonate slope play developed immediately adjacent to the carbonate platform and dominated by rockfall and platform collapse deposits or in situ boundstone; and (Type 2) detached carbonate slope play, deposited further from the platform margin via channelised turbidity currents and other mass-flow processes (Winefield et al., 2011) (Figure 7.6).

Type 1 has been relatively well studied, and includes slope apron deposits, such as the Tamabra Formation in the Poza Rica Field, Mexico (Loucks et al., 2011) and the late Viséan-Serpukhovian Tengiz Field, Kazakhstan (Collins et al., 2014), which accumulated at water depths of about 1,000 m extending more than 20 km and about 2-5 km into the basin, respectively. These types of deposits are generally line-sourced from the platform and have a dispersed-flow (Figure 7.6).

Type 2 is relatively less studied and includes the calciclastic submarine fans and channel-levee systems analysed in Chapter 6 from the PAMA Basin (Figure 7.6). Geomorphic analyses of calciclastic channel-levee systems presented in Chapter 6 display a degree of similarity to their siliciclastic counterparts. This suggests that reservoir characterisation for deep-water carbonates is dominated by the architecture and type of material being transported, such as in siliciclastic settings.

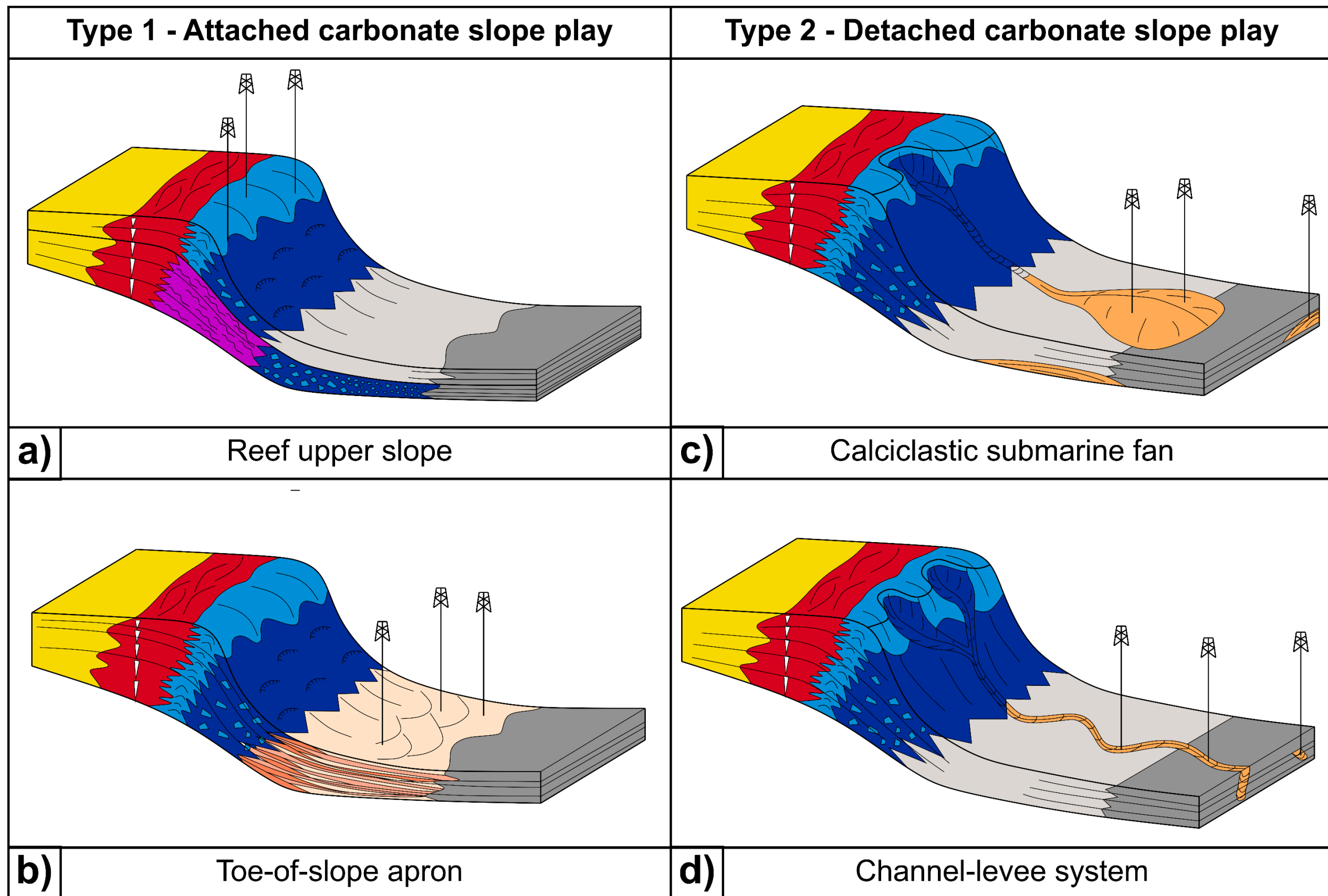


Figure 7.6. Schematic diagrams of redeposited carbonate play types. Type 1 include reef upper slope (a) and toe-of-slope apron (b). Type 2 include calciclastic submarine fans (c) and channel-levee systems (d). Modified after Janson et al. (2012).

7.4 Limitations of this research

The primary data type used throughout this thesis on the different study areas is seismic reflection data. For all the studies, a key limitation involves the quality and resolution of seismic datasets. Even though the 3D seismic volumes utilised in this thesis were of high-quality, there were still certain features that could not be resolvable at the seismic scale. In Chapter 4 it was mentioned that large fault arrays are created by the linkage of small fault segments, which in some cases, the fault segments could not be fully resolved with seismic data. Throw-depth and throw-distance maps of fault arrays proved to be useful to differentiate individual fault segments, generally larger than 500 m in length; with smaller fault segments not being clearly imaged. Chapter 5 in fact, explained in detail the limitations and challenges associated with resolution of different datasets; not just seismic data, but also outcrop mapping, LiDAR and wellbore data. Each type of data can only be useful to observe and measure a feature of a specific range in size. In Chapter 6, delineation of channel systems is also limited to the resolution of the seismic dataset.

Furthermore, seismic imaging underneath isolated carbonate platforms in the Bonaparte Basin (Chapter 4) was susceptible to artifacts related to the difference in acoustic impedance between the facies within the platform and the surrounding areas. Fault interpretation within these areas was problematic as there were shadows masking the stratigraphy, in addition to false “uplifted” strata. In the seismic volume from the Pernambuco Basin (Chapter 5), there is a high density of faults and fractures along the shelf margin, which in some instances resulted in a very dark image when calculating the variance attribute. A higher resolution seismic data would be useful to better delineate faults along the margin. The Pará-Maranhão

seismic volume utilised (Chapter 6) is located on the edge of the shelf margin, imaging mostly a portion of the continental slope and continental rise. Shelf strata is essentially not observable within the seismic volume and the upper slope is poorly imaged as it is present on the edge of the seismic volume. Acquisition of larger 3D seismic volume covering the full transition from the shelf to the basin would be beneficial to better understand the relationship between shallow- and deep-water deposits.

Another limitation is the accessibility to wellbore data, and the location of wells to obtain useful data for a specific analysis. In the Bonaparte Basin (Chapter 4) there are a couple of wells drilled within the study area adjacent to isolated carbonate platforms, which was useful to tie the stratigraphy of the area. However, there is no data providing information inside of those structures. Similarly, in the PAMA Basin there is only well data on the outer shelf, though relatively modern, and there are no wells drilled on the continental slope and continental rise, which limited the interpretations in this work.

For the case of Chapter 5, in which the topic of scale relationships between datasets is discussed, the major limitation was the availability of a comprehensive dataset including all scales of observation in the same geographical area. Ideally, a dataset including satellite imagery; seismic data; aerial, LiDAR, and drone imagery; outcrop mapping; core data; and wellbore data would be useful to better understand the fracture gaps that currently limit our understanding of fracture networks. However, having such dataset is not publicly available at present, and for that reason this thesis utilised analogue examples from two distinct areas (i.e., the Cariatiz Platform in SE Spain and the Pernambuco Platform in Brazil).

7.5 Future work

Over the course of this thesis, different study areas were investigated in which several theories and methods were proposed to better understand structural and depositional patterns of carbonate systems. In Chapter 4 it was revealed a relationship between relay ramps and the position of isolated carbonate platforms. This relationship was deemed important for hydrocarbon exploration as the presence of a relay ramp provides a good scenario for hydrocarbon migration, and the facies and geometrical architecture of the overlying isolated carbonate platform provides a good setting to accumulate hydrocarbons. Following the methods applied in this thesis to identify relay ramps based on fault-throw measurements, it would be of interest to investigate distribution of isolated carbonate platforms and their relation to relay ramps in other regions with more available data such as the ones in Central Luconia offshore Sarawak, NW Borneo. This would be beneficial to identify whether this relationship can be replicated and to confirm the proposed play scenario from a hydrocarbon-proven isolated carbonate platform.

A fracture network model in Chapter 6 shows a relationship between fracture size and fracture connectivity, being small fractures better connected than large fractures. As it was discussed, this relationship is key for reservoir evaluation. The study of other areas with different datasets would be useful to test the reliability of the proposed interpretations. Image logs and core data would complement interpretations at the small scale. Drone imagery and higher quality airborne LiDAR maps would improve our understanding of intermediate scale fractures. And higher resolution seismic data along with satellite imagery would enhance the model of large fractures. Moreover, it is critical to note that the fracture model presented in this thesis correspond to fractures developed along the carbonate platform margin.

An interesting work would be to perform a similar analysis on fracture networks developed on the slope. Cariatiz has a good exposure of slope fractures that can be measured, and it would be the ideal place to continue this study, in which drone imagery can be included to breach the gap between outcrop mapping and aerial LiDAR imagery. Other examples, such as Tengiz and the Canning Basin are also adequate to perform a similar analysis.

Geomorphic patterns of mixed calciclastic-siliciclastic channel-levee systems in Chapter 6 show a degree of similarities to their siliciclastic counterparts. The models proposed in this thesis are based on detail measurements from the PAMA Basin. However, a study from other areas with a similar setting such as in the Gulf of Papua, Nova Scotia or the Browse Basin would be useful to complement the results presented here. Additionally, as mentioned before, lithological data inside the channels is absent as there are no wells drilled beyond the shelf margin in PAMA. Based on the analysis presented here, calciclastic channel-levee systems have a positive potential to accumulate hydrocarbons. A well drilled in a channel would provide unique data to better understand these settings.

Chapter 8: References

- Abotalib, A.Z., Heggy, E., Scabbia, G., Mazzoni, A., 2019. Groundwater dynamics in fossil fractured carbonate aquifers in Eastern Arabian Peninsula: A preliminary investigation. *Journal of Hydrology* 571, 460-470. <https://doi.org/10.1016/J.JHYDROL.2019.02.013>
- Adler, P.M., Thovert, J.-F., 1999. Fractures and fracture networks. Springer Science & Business Media.
- Aguilera, O., Oliveira de Araújo, O.M., Hendy, A., Nogueira, A.A.E., Nogueira, A.C.R., Maurity, C.W., Kutter, V.T., Martins, M.V.A., Coletti, G., Dias, B.B., da Silva-Caminha, S.A.F., Jaramillo, C., Bencomo, K., Lopes, R.T., 2020. Palaeontological framework from Pirabas Formation (North Brazil) used as potential model for equatorial carbonate platform. *Marine Micropaleontology* 154, 101813. <https://doi.org/10.1016/j.marmicro.2019.101813>
- Aich, S., Gross, M.R., 2008. Geospatial analysis of the association between bedrock fractures and vegetation in an arid environment. *International Journal of Remote Sensing* 29, 6937-6955. <https://doi.org/10.1080/01431160802220185>
- Alavian, S.A., Whitson, C.H., 2005. CO2 IOR Potential in Naturally Fractured Haft Kel Field, Iran. International Petroleum Technology Conference. International Petroleum Technology Conference. <https://doi.org/10.2523/10641-MS>
- Almeida, N.M. De, Alves, T.M., Filho, F.N., Souza, A.C.B., Oliveira, K.M.L., Barbosa, T.H.S., 2020. A three-dimensional (3D) structural model for an oil-producing basin of the Brazilian Equatorial margin. *Marine and Petroleum Geology*.
- Almeida, N., Alves, T., Filho, N., Freire, S., de Souza, C., Leopoldino, K., Normando, M., Barbosa, T., 2018. Tectono-sedimentary evolution and petroleum system of a new deep-water exploration frontier: Mundaú sub-basin Equatorial Brazil.

- AAPG Bulletin 0, 20. <https://doi.org/10.1306/07151917381>
- Alsharhan, A.S., 1987. Geology and reservoir characteristics of carbonate buildup in giant Bu Hasa oil field, Abu Dhabi, United Arab Emirates. AAPG Bulletin 71, 1304-1318.
- Alves, T., Fetter, M., Busby, C., Gontijo, R., Cunha, T.A., Mattos, N.H., 2020. A tectono-stratigraphic review of continental breakup on intraplate continental margins and its impact on resultant hydrocarbon systems., Marine and Petroleum Geology. <https://doi.org/10.1016/j.marpetgeo.2020.104341>
- Alves, T.M., 2016. Polygonal mounds in the Barents Sea reveal sustained organic productivity towards the P-T boundary. 28, 50-59. <https://doi.org/10.1111/ter.12190>
- Alves, T.M., Abreu Cunha, T., 2018. A phase of transient subsidence, sediment bypass and deposition of regressive-transgressive cycles during the breakup of Iberia and Newfoundland. Earth and Planetary Science Letters 484, 168-183. <https://doi.org/10.1016/j.epsl.2017.11.054>
- Alves, T.M., Moita, C., Sandnes, F., Cunha, T., Monteiro, J.H., Pinheiro, L.M., 2006. MesozoicdashCenozoic evolution of North Atlantic continental-slope basins: The Peniche basin, western Iberian margin. AAPG Bulletin 90, 31-60. <https://doi.org/10.1306/08110504138>
- Andresen, N., Reijmer, J.J.G., Droxler, A.W., 2003. Timing and distribution of calciturbidites around a deeply submerged carbonate platform in a seismically active setting (Pedro Bank, Northern Nicaragua Rise, Caribbean Sea). International Journal of Earth Sciences 92, 573-592. <https://doi.org/10.1007/s00531-003-0340-0>

- Aquino da Silva, A.G., Amaro, V.E., Stattegger, K., Schwarzer, K., Vital, H., Heise, B., 2015. Spectral calibration of CBERS 2B multispectral satellite images to assess suspended sediment concentration. *ISPRS Journal of Photogrammetry and Remote Sensing* 104, 53-62. <https://doi.org/10.1016/j.isprsjprs.2015.02.011>
- Bachtel, Steven L, Kissling, Randal D, Martono, Dwi, Rahardjanto, Setya P, Dunn, Paul A, Macdonald, Bruce A, Bachtel, S L, Kissling, R D, Martono, D, Rahardjanto, S P, Dunn, P A, Macdonald, B A, 2004. Seismic Stratigraphic Evolution of the Miocene-Pliocene Segitiga Platform, East Natuna Sea, Indonesia: The Origin, Growth, and Demise of an Isolated Carbonate Platform.
- Back, S., Reuning, L., 2015. Channels in Carbonate Environments: 3-D-Seismic Characteristics Extracted From the Sedimentary Record. AAPG Annual Convention and Exhibition, Denver, Co.
- Baillie, P.W., Powell, C.M., Li, Z.X., Ryall, A., 1994. The tectonic framework of Western Australia's Neoproterozoic to Recent Sedimentary Basins. *The Sedimentary Basins of Western Australia: Proceedings of the Petroleum Exploration Society of Australia*, 45-62.
- Baker, E., Gaill, F., Karageorgis, A., Lamarche, G., Narayanaswamy, B., Parr, J., Raharimananirina, C., Santos, R., Sharma, R., Tuhumwire, J., 2016. Offshore mining industries. In: (UN), U.N. (Ed.), *The First Global Integrated Marine Assessment; World Ocean Assessment I*. New York, NY, USA.
- Bastesen, E., Rotevatn, A., 2012. Evolution and structural style of relay zones in layered limestone-shale sequences: Insights from the Hammam Faraun Fault Block, Suez rift, Egypt. *Journal of the Geological Society* 169, 477-488. <https://doi.org/10.1144/0016-76492011-100>

- Berkowitz, B., 2002. Characterizing flow and transport in fractured geological media: A review. *Advances in Water Resources* 25, 861-884. [https://doi.org/10.1016/S0309-1708\(02\)00042-8](https://doi.org/10.1016/S0309-1708(02)00042-8)
- Bertotti, G., Hardebol, N., Taal-van Koppen, J.K., Luthi, S.M., 2007. Toward a quantitative definition of mechanical units: New techniques and results from an outcropping deep-water turbidite succession (Tanqua-Karoo Basin, South Africa). *AAPG Bulletin* 91, 1085-1098. <https://doi.org/10.1306/03060706074>
- Betzler, C., Lindhorst, S., Eberli, G.P., Lüdmann, T., Möbius, J., Ludwig, J., Schutter, I., Wunsch, M., Reijmer, J.J.G., Hübscher, C., 2014. Periplatform drift: The combined result of contour current and off-bank transport along carbonate platforms. *Geology* 42, 871-874. <https://doi.org/10.1130/G35900.1>
- Betzler, C., Reijmer, J.J.G., Bernetà, K., Eberlià, G.P., Anselmetti, F.S., 1999. Sedimentary patterns and geometries of the Bahamian outer carbonate ramp (Miocene±Lower Pliocene, Great Bahama Bank). *Sedimentology* 46.
- Birch, F., 1966. SECTION 7: COMPRESSIBILITY; ELASTIC CONSTANTS. *Memoir of the Geological Society of America* 97, 97-173. <https://doi.org/10.1130/MEM97-P97>
- Blendinger, W., Bowlin, B., Zijp, F.R., Darke, G., Ekroll, M., 1997. Carbonate buildup flank deposits: an example from the Permian (Barents Sea, northern Norway) challenges classical facies models. *Sedimentary Geology* 112, 89-103. [https://doi.org/10.1016/S0037-0738\(97\)00025-0](https://doi.org/10.1016/S0037-0738(97)00025-0)
- Bolt, Bruce A, Bolt, Bruce Alan, 1982. *Inside the Earth: evidence from earthquakes.* WH Freeman San Francisco.
- Bonnet, E., Bour, B.O., Odling, N.E., Davy, P., Bour, O., Odling, N.E., Davy, P., Main, I., Cowie, P., Berkowitz, B., 2001. Scaling of fracture systems in geological

media. Reviews of Geophysics 39, 347-383.
<https://doi.org/10.1029/1999RG000074>

Bornhold, B.D., Pilkey, O.H., 1971. Bioclastic turbidite sedimentation in Columbus Basin, Bahamas. *Bulletin of the Geological Society of America* 82, 1341-1354.
[https://doi.org/10.1130/0016-7606\(1971\)82\[1341:BTSICB\]2.0.CO;2](https://doi.org/10.1130/0016-7606(1971)82[1341:BTSICB]2.0.CO;2)

Borromeo, O., Luoni, F., Bigoni, F., Camocino, D., Francesconi, A., 2010. Stratigraphic Architecture of the Early Carboniferous Reservoir in Karachaganak Field, Pri-Caspian Basin (Kazakhstan). *SPE Caspian Carbonates Technology Conference*. Society of Petroleum Engineers. <https://doi.org/10.2118/139887-MS>

Bosence, D., 2005a. Sedimentary Environments | Carbonate Shorelines and Shelves. *Encyclopedia of Geology* 501-513. <https://doi.org/10.1016/B0-12-369396-9/00178-7>

Bosence, D., 2005b. A genetic classification of carbonate platforms based on their basinal and tectonic settings in the Cenozoic. *Sedimentary Geology* 175, 49-72.
<https://doi.org/10.1016/J.SEDGEO.2004.12.030>

Bourbiaux, B., 2010. Fractured Reservoir Simulation: a Challenging and Rewarding Issue. *Oil & Gas Science and Technology-Rev. IFP* 65, 227-238.
<https://doi.org/10.2516/ogst/2009063>

Bourget, J., Ainsworth, R.B., Nanson, R., 2013. Origin of Mixed Carbonate and Siliciclastic Sequences at the Margin of a “Giant” Platform During the Quaternary (Bonaparte Basin, nw Australia). *Deposits, Architecture, and Controls of Carbonate Margin, Slope and Basinal Settings*. *SEPM Society for Sedimentary Geology*, 157-177. <https://doi.org/10.2110/sepmsp.105.17>

- Boyer, R.E., McQueen, J.E., 1964. Comparison of Mapped Rock Fractures and Airphoto Linear Features.
- Brachert, T.C., Reuter, M., Felis, T., Kroeger, K.F., Lohmann, G., Micheels, A., Fassoulas, C., 2006. Porites corals from Crete (Greece) open a window into Late Miocene (10 Ma) seasonal and interannual climate variability. *Earth and Planetary Science Letters* 245, 81-94.
<https://doi.org/10.1016/j.epsl.2006.03.005>
- Braga, J.C., Martín, J.M., 1996. Geometries of reef advance in response to relative sea-level changes in a Messinian (uppermost Miocene) fringing reef (Cariatiz reef, Sorbas Basin, SE Spain). *Sedimentary Geology* 107, 61-81.
[https://doi.org/10.1016/S0037-0738\(96\)00019-X](https://doi.org/10.1016/S0037-0738(96)00019-X)
- Braga, J.C., Martín, J.M., Wood, J.L., 2001. Submarine lobes and feeder channels of redeposited, temperate carbonate and mixed siliciclastic-carbonate platform deposits (Vera Basin, Almería, southern Spain).
- Braga, J.C., Martín, J.M., Quesada, C., 2003. Patterns and average rates of late Neogene-Recent uplift of the Betic Cordillera, SE Spain. *Geomorphology* 50, 3-26. [https://doi.org/10.1016/S0169-555X\(02\)00205-2](https://doi.org/10.1016/S0169-555X(02)00205-2)
- Brandão, J., Feijó, F.J., 1994. Bacia do Pará-Maranhão. *Boletim de Geociências Da PETROBRÁS* 8, 101-102.
- Brown, A.R., 2011. Interpretation of Three-dimensional Seismic Data, Seventh Edition, Seventh. ed, AAPG Memoir 42. Society of Exploration Geophysicists and American Association of Petroleum Geologists, Tulsa, Oklahoma, U.S.A.
[https://doi.org/10.1016/0191-8141\(91\)90111-u](https://doi.org/10.1016/0191-8141(91)90111-u)
- Buarque, B. V., Barbosa, J.A., Magalhães, J.R.G., Cruz Oliveira, J.T., Filho, O.J.C.,

2016. Post-rift volcanic structures of the Pernambuco Plateau, northeastern Brazil. *Journal of South American Earth Sciences* 70, 251-267. <https://doi.org/10.1016/J.JSAMES.2016.05.014>
- Buarque, B. V, Barbosa, J.A., Oliveira, J.T.C., Magalhães, J.R.G., Correia, O.J., Varela Buarque, B., 2017. Carbonate Buildups in the Pernambuco Basin, NE Brazil. *An Acad Bras Cienc* 89, 841-857. <https://doi.org/10.1590/0001-3765201720160544>
- Burchette, T.P., 2012. Carbonate rocks and petroleum reservoirs: A geological perspective from the industry. *Geological Society Special Publication* 370, 17-37. <https://doi.org/10.1144/SP370.14>
- Burgess, P.M., Winefield, P., Minzoni, M., Elders, C., 2013. Methods for identification of isolated carbonate buildups from seismic reflection data. *AAPG Bulletin* 97, 1071-1098. <https://doi.org/10.1306/12051212011>
- Bush, I., 2010. An integrated approach to fracture characterisation., *Oil Review Middle East Issue Two* 88-91.
- Cacas, M.C., Daniel, J.M., Letouzey, J., 2001. Nested geological modelling of naturally fractured reservoirs. *Petroleum Geoscience* 7, S43-S52. <https://doi.org/10.1144/petgeo.7.S.S43>
- Carannante, G., Esteban, M., Milliman, J.D., Simone, L., 1988. Carbonate lithofacies as paleolatitude indicators: problems and limitations. *Sedimentary Geology* 60, 333-346. [https://doi.org/10.1016/0037-0738\(88\)90128-5](https://doi.org/10.1016/0037-0738(88)90128-5)
- Carenzi, G., Cazzola, L., 2008. Final Report - AC/P-38 Time and Depth Re-processing Report 3D Karmt Seismic Survey.
- Carrillo, M., González, J.M., 2002. A new approach to modelling sigmoidal curves.

- Technological Forecasting and Social Change 69, 233-241.
[https://doi.org/10.1016/S0040-1625\(01\)00150-0](https://doi.org/10.1016/S0040-1625(01)00150-0)
- Cartwright, J., Bouroullec, R., James, D., Johnson, H., 1998. Polycyclic motion history of some Gulf Coast growth faults from high-resolution displacement analysis. *Geology* 26, 819. [https://doi.org/10.1130/0091-7613\(1998\)026<0819:PMHOSG>2.3.CO;2](https://doi.org/10.1130/0091-7613(1998)026<0819:PMHOSG>2.3.CO;2)
- Catuneanu, O., 2006. Principles of sequence stratigraphy. Elsevier.
- Cerri, R.I., Luvizotto, G.L., Tognoli, F.M.W., Warren, L.V., Okubo, J., Morales, N., 2020. Mechanical stratigraphy and structural control of oil accumulations in fractured carbonates of the Irati Formation, Paraná Basin, Brazil. *Brazilian Journal of Geology* 50, 1-13. <https://doi.org/10.1590/2317-4889202020190117>
- Chen, Y., Ma, G., Wang, H., 2018. Heat extraction mechanism in a geothermal reservoir with rough-walled fracture networks. *International Journal of Heat and Mass Transfer* 126, 1083-1093.
<https://doi.org/10.1016/J.IJHEATMASSTRANSFER.2018.05.103>
- Chiarella, D., Longhitano, S.G., Tropeano, M., 2017. Types of mixing and heterogeneities in siliciclastic-carbonate sediments. *Marine and Petroleum Geology* 88, 617-627. <https://doi.org/10.1016/j.marpetgeo.2017.09.010>
- Childs, C., Watterson, J., Walsh, J.J., 1995. Fault overlap zones within developing normal fault systems. *Journal of the Geological Society* 152, 535-549.
<https://doi.org/10.1144/gsjgs.152.3.0535>
- Chilès, J.-P., 2005. Stochastic modeling of natural fractured media: a review. *Geostatistics Banff 2004*. Springer, 285-294.
- Chopra, S., Marfurt, K.J., 2007. Seismic attributes for prospect identification and

reservoir characterization. Society of Exploration Geophysicists and European Association of Geoscientists and Engineers.

Choquette, P.W., Pray, L.C., 1970. Geologic nomenclature and classification of porosity in sedimentary carbonates. AAPG Bulletin 54, 207-250.

Clare, M.A., Vardy, M.E., Cartigny, M.J.B., Talling, P.J., Himsworth, M.D., Dix, J.K., Harris, J.M., Whitehouse, R.J.S., Belal, M., 2017. Direct monitoring of active geohazards: Emerging geophysical tools for deep-water assessments. Near Surface Geophysics 15, 427-444. <https://doi.org/10.3997/1873-0604.2017033>

Collins, J., Kenter, J., Harris, P., Kuanysheva, G., Steffen, D., 2006. Facies and reservoir-quality variations in the late Visean to Bashkirian outer platform, rim, and flank of the Tengiz buildup, Precaspian Basin, Kazakhstan. P.M. Harris and L.J. Weber, Eds., Giant Hydrocarbon Reservoirs of the World: From Rocks to Reservoir Characterization and Modeling: AAPG Memoir 88/SEPM Special Publication 55-95. <https://doi.org/10.1306/1215874M881469>

Collins, J., Narr, W., Harris, P.M., Playton, T., Jenkins, S., Tankersley, T., Kenter, J.A.M., 2014. Lithofacies, depositional environments, burial diagenesis, and dynamic field behavior in a carboniferous slope reservoir, tengiz field (republic of Kazakhstan), and comparison with outcropanalogs, SEPM Special Publications. <https://doi.org/10.2110/sepmsp.105.11>

Collins, J.F., Jones, G.D., Haffener, J., Mohammad, S.R., Nauryzgaliyev, M., Nursaidova, R., 2016. Origin of the Raised Rim in the Kashagan Buildup, Kazakhstan: A Hypothesis for Diagenesis Associated With Fractures and Burial Compaction*.

Coniglio, M., Dix, G.R., 1992. Carbonate Slopes. In: Walker, R.G., James, N.P. (Eds.),

- Facies Models-Response to Sea-Level Change. Geological Association of Canada, St. John's Newfoundland.
- Conneally, J., Childs, C., Walsh, J.J., 2014. Contrasting origins of breached relay zone geometries. *Journal of Structural Geology* 58, 59-68. <https://doi.org/10.1016/J.JSG.2013.10.010>
- Counts, J.W., Jorry, S.J., Vazquez Riveiros, N., Jouet, G., Giraudeau, J., Cheron, S., Boissier, A., Miramontes, E., 2019. A Late Quaternary record of highstand shedding from an isolated carbonate platform (Juan de Nova, southern Indian Ocean). *The Depositional Record* 5, 540-557. <https://doi.org/10.1002/dep2.57>
- Cowie, P.A., Knipe, R.J., Main, I.G., 1996. Introduction to the special issue. *Journal of Structural Geology* 18, v-xi. [https://doi.org/10.1016/S0191-8141\(96\)80038-1](https://doi.org/10.1016/S0191-8141(96)80038-1)
- Cox, D.R., Newton, A.M.W., Huuse, M., 2020. An introduction to seismic reflection data: acquisition, processing and interpretation. *Regional Geology and Tectonics: Principles of Geologic Analysis*. Elsevier, 571-603. <https://doi.org/10.1016/B978-0-444-64134-2.00020-1>
- Crevello, P.D., Schlager, W., 1980. Carbonate debris sheets and turbidites, Exuma Sound, Bahamas. *Journal of Sedimentary Petrology* 50, 1121-1148.
- Cross, N.E., Bosence, D.W.J., Lukasik, J., Simo, J.A., 2008. Tectono-sedimentary models for rift-basin carbonate systems. *Controls on Carbonate Platform and Reef Development*, SEPM, Special Publication 89, 83-105. <https://doi.org/10.2110/pec.08.89.0083>
- Cross, T.A., Lessenger, M.A., 1988. Seismic Stratigraphy. *Annual Review of Earth and Planetary Sciences* 16, 319-354. <https://doi.org/10.1146/annurev.ea.16.050188.001535>

- Cuevas Castell, J.M., Betzler, C., Rössler, J., Hüssner, H., Peinl, M., 2007. Integrating outcrop data and forward computer modelling to unravel the development of a Messinian carbonate platform in SE Spain (Sorbas Basin). *Sedimentology* 54, 423-441. <https://doi.org/10.1111/j.1365-3091.2006.00843.x>
- Da Silva, B., Ribeiro, H.J.P.S., 2018. Exploratory plays of Pará-Maranhão and Barreirinhas basins in deep and ultra-deep waters, Brazilian Equatorial Margin. *Brazilian Journal of Geology* 48, 485-502. <https://doi.org/10.1590/2317-4889201820180146>
- Da Silva, C.P., 2007. Estudo Sobre Foraminíferos e Radiolários do Cretáceo, Bacia Pará-Maranhão, Margem Equatorial Brasileira. Universidade Federal do Rio Grande do Sul.
- Damsleth, E., Sangolt, V., Aamodt, G., 1998. Sub-seismic Faults Can Seriously Affect Fluid Flow in the Njord Field off Western Norway - A Stochastic Fault Modeling Case Study. SPE Annual Technical Conference and Exhibition. Society of Petroleum Engineers. <https://doi.org/10.2118/49024-MS>
- Darros de Matos, R.M., 1999. History of the northeast Brazilian rift system: kinematic implications for the break-up between Brazil and West Africa. *Geological Society, London, Special Publications* 153, 55-73. <https://doi.org/10.1144/GSL.SP.1999.153.01.04>
- Davies, R.J., Stewart, S.A., Cartwright, J.A., Lappin, M., Johnston, R., Fraser, S.I., Brown, A.R., 2004. 3D Seismic Technology: Are We Realising Its Full Potential? *Geological Society Memoir* 29, 1-10. <https://doi.org/10.1144/GSL.MEM.2004.029.01.01>
- de Moraes, J.O., Ximenes Neto, A.R., Pessoa, P.R.S., de Souza Pinheiro, L., 2019.

- Morphological and sedimentary patterns of a semi-arid shelf, Northeast Brazil. *Geo-Marine Letters* 40, 1-8. <https://doi.org/10.1007/s00367-019-00587-x>
- De Souza, V., 2006. Radiolários Do Cretáceo Médio Das Bacias Do Pará-Maranhão E Barreirinhas, Margem Equatorial Brasileira Vladimir. Universidade Federal do Rio Grande do Sul.
- Dias, F.J.S., Castro, B.M., Lacerda, L.D., 2013. Continental shelf water masses off the Jaguaribe River (4S), northeastern Brazil. *Continental Shelf Research* 66, 123-135. <https://doi.org/10.1016/j.csr.2013.06.005>
- Ding, W., Li, J., Dong, C., Fang, Y., Tang, Y., Fu, J., 2014. Carbonate Platforms in the Reed Bank Area, South China Sea: Seismic Characteristics, Development and Controlling Factors. *Energy Exploration & Exploitation* 32, 243-261. <https://doi.org/10.1260/0144-5987.32.1.243>
- Ding, X., Bassinot, F., Guichard, F., Fang, N.Q., 2013. Indonesian Throughflow and monsoon activity records in the Timor Sea since the last glacial maximum. *Marine Micropaleontology* 101, 115-126. <https://doi.org/10.1016/J.MARMICRO.2013.02.003>
- Ditty, P.S., Harmon, C.J., Pilkey, O.H., Ball, M.M., Richardson, E.S., 1977. Mixed terrigenous-Carbonate sedimentation in the Hispaniola-Caicos turbidite basin. *Marine Geology* 24, 1-20. [https://doi.org/10.1016/0025-3227\(77\)90012-3](https://doi.org/10.1016/0025-3227(77)90012-3)
- Dominguez, G.C., Fernando, S. V., Chilingarian, G. V., 1992. Chapter 12 Simulation of Carbonate Reservoirs. *Developments in Petroleum Science* 30, 543-588. [https://doi.org/10.1016/S0376-7361\(09\)70135-9](https://doi.org/10.1016/S0376-7361(09)70135-9)
- Dondurur, D., 2018. Acquisition and processing of marine seismic data. Elsevier.
- Doornenbal, J.C., Kombrink, H., Bouroullec, R., Dalman, R.A.F., De Bruin, G., Geel,

- C.R., Houben, A.J.P., Jaarsma, B., Juez-Larré, J., Kortekaas, M., Mijnlief, H.F., Nelskamp, S., Pharaoh, T.C., Ten Veen, J.H., Ter Borgh, M., Van Ojik, K., Verreussel, R.M.C.H., Verweij, J.M., Vis, G.-J., 2019. New insights on subsurface energy resources in the Southern North Sea Basin area. Geological Society, London, Special Publications 494, SP494-2018-178. <https://doi.org/10.1144/SP494-2018-178>
- Dorobek, S., 2007. Carbonate-platform facies in volcanic-arc settings: Characteristics and controls on deposition and stratigraphic development. Formation and Applications of the Sedimentary Record in Arc Collision Zones. Geological Society of America Special Paper 436. [https://doi.org/10.1130/2008.2436\(04\)](https://doi.org/10.1130/2008.2436(04))
- dos Santos, E.J., Schmus, W.R. Van, Kozuch, M., Neves, B.B. de B., 2010. The Cariris Velhos tectonic event in Northeast Brazil. Journal of South American Earth Sciences 29, 61-76. <https://doi.org/10.1016/J.JSAMES.2009.07.003>
- Droxler, A.W., Schlager, W., 1985. Glacial versus interglacial sedimentation rates and turbidite frequency in the Bahamas. Geology 13, 799-802. [https://doi.org/10.1130/0091-7613\(1985\)13<799:GVISRA>2.0.CO;2](https://doi.org/10.1130/0091-7613(1985)13<799:GVISRA>2.0.CO;2)
- Dunham, R.J., 1962. Classification of carbonate rocks according to depositional textures.
- Dunlap, D., Janson, X., Sanchez Phelps, C., Covault, J., 2018. Carbonate Channel-Levee Systems Influenced by Mass-Transport Complexes, Browse Basin, Western Australia. AAPG ACE 2018.
- Dupraz, C., Reid, R.P., Braissant, O., Decho, A.W., Norman, R.S., Visscher, P.T., 2009. Processes of carbonate precipitation in modern microbial mats. Earth-

Science Reviews 96, 141-162.
<https://doi.org/10.1016/J.EARSCIREV.2008.10.005>

Eberli, G.P., Anselmetti, F.S., Betzler, C., Van Konijnenburg, J.H., Bernoulli, D., 2005. Carbonate platform to basin transitions on seismic data and in outcrops: Great Bahama Bank and the Maiella Platform margin, Italy. AAPG Memoir 207-250.

Eberli, G.P., Masferro, J.L., Sarg, J.F.R., 2004. Seismic Imaging of Carbonate Reservoirs and Systems. AAPG Memoir 81.

Eberli, G.P., Swart, P.K., McNeill, D.F., Kenter, J.A.M., Anselmetti, F.S., Melim, L.A., Ginsburg, R.N., 1997. A synopsis of the Bahamas Drilling Project: results from two deep core borings drilled on the Great Bahama Bank. In: Marin, J.A. (Ed.), Proceedings of the Ocean Drilling Program, Initial Reports. Ocean Drilling Program, Texas A&M University, 23-41.

Elliott, S., Hsu, H.H., O'Hearn, T., Sylvester, I.F., Vercesi, R., 1998. The giant Karachaganak field, unlocking its potential. Oilfield Review 10, 16-25.

Elvebakk, G., Hunt, D.W., Stemmerik, L., 2002. From isolated buildups to buildup mosaics: 3D seismic sheds new light on upper Carboniferous-Permian fault controlled carbonate buildups, Norwegian Barents Sea. Sedimentary Geology 152, 7-17. [https://doi.org/10.1016/S0037-0738\(02\)00232-4](https://doi.org/10.1016/S0037-0738(02)00232-4)

Etheridge, M., McQueen, H., Lambeck, K., 1991. The role of intraplate stress in tertiary (and mesozoic) deformation of the Australian continent and its margins: A key factor in petroleum trap formation. Exploration Geophysics 22, 123. <https://doi.org/10.1071/EG991123>

Fabianovicz, R., 2013. Pará-Maranhão Basin. Brasil 11th Round - Oil & Gas Bidding

- Rounds. National Agency of Petroleum, Natural Gas and Biofuels, Rio de Janeiro.
- Ferril, D.A., Morris, A.P., Waiting, D.J., Tsuneyama, F., Tamura, Y., Sims, D.W.,
2002. Relay Ramp Style in Massive Limestone: Examples from the Sierra del
Carmen, West Texas. AAPG Annual Meeting 2002.
- Figueiredo, J.D.J.P. De, Zalán, P.V., Soares, E.F., 2007. Bacia da Foz do Amazonas.
Boletim de Geociencias - Petrobras 15, 299-309.
- Fossen, H., Hesthammer, J., 1998. Structural geology of the Gullfaks Field, northern
North Sea. Geological Society, London, Special Publications 127, 231-261.
<https://doi.org/10.1144/GSL.SP.1998.127.01.16>
- Fossen, H., Rotevatn, A., 2016. Fault linkage and relay structures in extensional
settings—A review. Earth-Science Reviews 154, 14-28.
<https://doi.org/10.1016/J.EARSCIREV.2015.11.014>
- Francis, J.M., Daniell, J.J., Droxler, A.W., Dickens, G.R., Bentley, S.J., Peterson,
L.C., Opdyke, B.N., Beaufort, L., 2008. Deep water geomorphology of the mixed
siliciclastic-carbonate system, Gulf of Papua. Journal of Geophysical Research:
Earth Surface 113, 1-22. <https://doi.org/10.1029/2007JF000851>
- Friedman, M., 1975. Fracture in rock. Reviews of Geophysics 13, 352.
<https://doi.org/10.1029/RG013i003p00352>
- Fryar, A.E., 2021. Groundwater of carbonate aquifers. Global Groundwater 23-34.
<https://doi.org/10.1016/B978-0-12-818172-0.00002-5>
- Gallagher, S.J., Smith, A.J., Jonasson, K., Wallace, M.W., Holdgate, G.R., Daniels,
J., Taylor, D., 2001. The miocene palaeoenvironmental and palaeoceanographic
evolution of the gippsland basin, southeast australia: A record of southern ocean
change. Palaeogeography, Palaeoclimatology, Palaeoecology 172, 53-80.

[https://doi.org/10.1016/S0031-0182\(01\)00271-1](https://doi.org/10.1016/S0031-0182(01)00271-1)

Galvis, N.E.B., 2018. Geomechanics, Fluid Dynamics and Well Testing, Applied to Naturally Fractured Carbonate Reservoirs: Extreme Naturally Fractured Reservoirs. Springer.

Gawthorpe, R.L., Hurst, J.M., 1993. Transfer zones in extensional basins: their structural style and influence on drainage development and stratigraphy. *Journal of the Geological Society* 150, 1137-1152. <https://doi.org/10.1144/gsjgs.150.6.1137>

Gee, M.J.R., Gawthorpe, R.L., Bakke, K., Friedmann, S.J., 2007. Seismic geomorphology and evolution of submarine channels from the Angolan continental margin. *Journal of Sedimentary Research* 77, 433-446. <https://doi.org/10.2110/jsr.2007.042>

Giba, M., Walsh, J.J., Nicol, A., 2012. Segmentation and growth of an obliquely reactivated normal fault. *Journal of Structural Geology* 39, 253-267. <https://doi.org/10.1016/J.JSG.2012.01.004>

Gillespie, J.L., 1992. Late Quaternary carbonate-clastic sedimentation on a temperate shelf, offshore Wanganui, New Zealand.

Gillespie, P.A., Walsh, J.J., Watterson, J., Bonson, C.G., Manzocchi, T., 2001. Scaling relationships of joint and vein arrays from The Burren, Co. Clare, Ireland. *Journal of Structural Geology* 23, 183-201. [https://doi.org/10.1016/S0191-8141\(00\)00090-0](https://doi.org/10.1016/S0191-8141(00)00090-0)

Glaser, K.S., Droxler, A.W., 1993. Controls and Development of Late Quaternary Periplatform Carbonate Stratigraphy in Walton Basin (Northeastern Nicaragua Rise, Caribbean Sea). *Paleoceanography* 8, 243-274.

<https://doi.org/10.1029/92PA02876>

Gluyas, J.G., Swarbrick, R.E., 2021. Petroleum geoscience. John Wiley & Sons.

Goldstein, R.H., Franseen, E.K., Dvoretzky, R.A., Sweeney, R.J., 2012. Controls on focused-flow and dispersed-flow deepwater carbonates: Miocene Agua Amarga basin, Spain. *Journal of Sedimentary Research* 82, 499-520. <https://doi.org/10.2110/jsr.2012.46>

Gradstein, F.M., Ogg, J.G., Smith, A.G., 2005. A geologic time scale 2004, A Geologic Time Scale 2004. Cambridge University Press. <https://doi.org/10.1017/CBO9780511536045>

Greenlee, S.M., Lehmann, P.J., Sarg, J.F., Loucks, R.G., 1993. Stratigraphic framework of productive carbonate buildups. *Carbonate Sequence Stratigraphy: Recent Developments and Applications: AAPG Memoir* 57, 43-62.

Guerriero, V., Iannace, A., Mazzoli, S., Parente, M., Vitale, S., Giorgioni, M., 2010. Quantifying uncertainties in multi-scale studies of fractured reservoir analogues: Implemented statistical analysis of scan line data from carbonate rocks. *Journal of Structural Geology* 32, 1271-1278. <https://doi.org/10.1016/j.jsg.2009.04.016>

Gutmanis, J., Ardèvol i Oró, L., Díez-Canseco, D., Chebbihi, L., Awdal, A., Cook, A., 2018. Fracture analysis of outcrop analogues to support modelling of the subseismic domain in carbonate reservoirs, south-central Pyrenees. *Geological Society, London, Special Publications* 459, 139-156. <https://doi.org/10.1144/SP459.2>

Gutmanis, J.C., Ardèvol i Oró, L., 2015. Application of Pyrenean Fractured Carbonate Outcrops for Subsurface Reservoir Characterisation. 77th EAGE Conference and Exhibition 2015.

- Hart, B.S., 1999. Definition of subsurface stratigraphy, structure and rock properties from 3-D seismic data. *Earth-Science Reviews* 47, 189-218. [https://doi.org/10.1016/S0012-8252\(99\)00029-X](https://doi.org/10.1016/S0012-8252(99)00029-X)
- Hayton, S., Nelson, C.S., Hood, S.D., 1995. A skeletal assemblage classification system for non-tropical carbonate deposits based on New Zealand Cenozoic limestones. *Sedimentary Geology* 100, 123-141. [https://doi.org/10.1016/0037-0738\(95\)00071-2](https://doi.org/10.1016/0037-0738(95)00071-2)
- Hedley, J.D., Roelfsema, C., Brando, V., Giardino, C., Kutser, T., Phinn, S., Mumby, P.J., Barrilero, O., Laporte, J., Koetz, B., 2018. Coral reef applications of Sentinel-2: Coverage, characteristics, bathymetry and benthic mapping with comparison to Landsat 8. *Remote Sensing of Environment* 216, 598-614. <https://doi.org/10.1016/j.rse.2018.07.014>
- Held, A., 2011. Apport de la paléohydrologie dans la quantification des rôles respectifs du climat et de la tectonique des systèmes fluviatiles méandriformes fossiles : application à des systèmes oligo-miocènes d ' Europe occidentale To cite this version : HAL Id : paste, <http://www.theses.fr>. Paris, ENMP.
- Henry, S., Kumar, N., Danforth, A., Nuttall, P., Venkatraman, S., 2011. Ghana-Sierra Leone Lookalike Plays in Northern Brazil. *GeoExPro* 8, 36-41.
- Hermansen, H., Landa, G., Sylte, J., Thomas, L., 2000. Experiences after 10 years of waterflooding the Ekofisk Field, Norway. *Journal of Petroleum Science and Engineering* 26, 11-18. [https://doi.org/10.1016/S0920-4105\(00\)00016-4](https://doi.org/10.1016/S0920-4105(00)00016-4)
- Herron, D.A., 2011. *First Steps in Seismic Interpretation*. Society of Exploration Geophysicists, Tulsa, Oklahoma, U.S.A.
- Hongxing, G., Anderson, J.K., 2007. Fault throw profile and kinematics of Normal

- fault: conceptual models and geologic examples. *Geological Journal of China Universities* 13, 75-88.
- Hutchison, C.S., 2014. South China Sea carbonate build-up seismic characteristics.
- James, N., Jones, B., 2016. Origin of Carbonate Sedimentary Rocks. *American Geophysical Union* 465.
- James, N.P., 1997. The Cool-Water Carbonate Depositional Realm. *Cool-Water Carbonates* 1-20. <https://doi.org/10.2110/PEC.97.56.0001>
- James, N.P., Jones, B., 2015. Origin of carbonate sedimentary rocks. John Wiley & Sons.
- James, N.P., Mountjoy, E.W., 1983. Shelf-slope break in fossil carbonate platforms: an overview. In: Stanley, D.J., Moore, G.T. (Eds.), *The Shelfbreak: Critical Interface on Continental Margins*. SEPM Special Publication, 33. SEPM Society for Sedimentary Geology, 189-206. <https://doi.org/10.2110/pec.83.06.0189>
- Janson, X., Dunlap, D., Zeng, L., Sanchez Phelps, C., Covault, J., 2018. Carbonate Shelf to Basin Architecture and Slope Seismic Geomorphology, Lower Miocene, Browse Basin, Northwest Shelf of Australia. AAPG ACE 2018.
- Janson, X., Kerans, C., Bellian, J.A., Fitchen, W., 2007. Three-dimensional geological and synthetic seismic model of Early Permian redeposited basinal carbonate deposits, Victorio Canyon, west Texas. *American Association of Petroleum Geologists Bulletin* 91, 1405-1436. <https://doi.org/10.1306/05210705188>
- Janson, X., Kerans, C., Playton, T., Clayton, J., Winefield, P., Burgess, P., 2012. Stratigraphic Models and Exploration Plays of Slope and Basin-Floor Carbonates *. 50637, 511-532.

- Jonk, R., Biermann, C., 2002. Deformation in Neogene sediments of the Sorbas and Vera Basins (SE Spain): constraints on simple-shear deformation and rigid body rotation along major strike-slip faults. *Journal of Structural Geology* 24, 963-977. [https://doi.org/10.1016/S0191-8141\(01\)00107-9](https://doi.org/10.1016/S0191-8141(01)00107-9)
- Jorry, S.J., Droxler, A.W., Mallarino, G., Dickens, G.R., Bentley, S.J., Beaufort, L., Peterson, L.C., Opdyke, B.N., 2008. Bundled turbidite deposition in the central Pandora Trough (Gulf of Papua) since Last Glacial Maximum: Linking sediment nature and accumulation to sea level fluctuations at millennial timescale. *Journal of Geophysical Research: Earth Surface* 113, 1-15. <https://doi.org/10.1029/2006JF000649>
- Jorry, S.J., Jouet, G., Edinger, E.N., Toucanne, S., Counts, J.W., Miramontes, E., Courgeon, S., Riveiros, N.V., Le Roy, P., Camoin, G.F., 2020. From platform top to adjacent deep sea: New source-to-sink insights into carbonate sediment production and transfer in the SW Indian Ocean (Glorieuses archipelago). *Marine Geology*. <https://doi.org/10.1016/j.margeo.2020.106144>
- Kang, H., Meng, J., Cheng, T., Jia, H., Bai, B., Li, M., 2018. Characteristics of deep water depositional system in Campos basin, Brazil. *Petroleum Exploration and Development* 45, 99-110. [https://doi.org/10.1016/S1876-3804\(18\)30009-0](https://doi.org/10.1016/S1876-3804(18)30009-0)
- Katz, D., Playton, T., Bellian, J., Harris, P.M.M., Harrison, C.J., Maharaja, A., 2010. Slope Heterogeneity in a Steep-Sided Upper Paleozoic Isolated Carbonate Platform Reservoir, Karachaganak Field, Kazakhstan. *SPE Caspian Carbonates Technology Conference*. Society of Petroleum Engineers. <https://doi.org/10.2118/139960-MS>
- Kearey, P., Brooks, M., Hill, I., 2002. *An introduction to geophysical exploration*.

John Wiley & Sons.

Kendall, C.G.S.C., Schlager, W., 1981. Carbonates and relative changes in sea level.

Marine Geology 44, 181-212. [https://doi.org/10.1016/0025-3227\(81\)90118-3](https://doi.org/10.1016/0025-3227(81)90118-3)

Kenter, J., Harris, P., Collins, J., 2008. Facies and Reservoir Quality of the Tengiz Isolated Platform, Pricaspian Basin, Kazakhstan*.

Kenter, J., Harris, P.M., Collins, J.F., Weber, L.J., Kuanysheva, G., Fischer, D.J., 2015. Late Visean to Bashkirian Platform Cyclicity in the Central Tengiz Buildup, Precaspian Basin, Kazakhstan: Depositional Evolution and Reservoir Development. Giant Hydrocarbon Reservoirs of the World: From Rocks to Reservoir Characterization and Modeling. AAPG Memoir. <https://doi.org/10.1306/1215873M88374>

Kenter, J.A.M., 1990. Carbonate platform flanks: slope angle and sediment fabric. Sedimentology 37, 777-794.

Key, S.C., Agarwal, B., Søliland, G. V., Nielsen, H.H., 1999. Ekofisk Field redevelopment: improved reservoir management through cross-discipline technology and integration of three dimensional models. Geological Society, London, Petroleum Geology Conference Series 5, 1147-1155. <https://doi.org/10.1144/0051147>

Kim, Y.-S., Sanderson, D.J., 2005. The relationship between displacement and length of faults: a review. Earth-Science Reviews 68, 317-334. <https://doi.org/10.1016/J.EARSCIREV.2004.06.003>

Kindler, P., Wilson, M.E.J., 2010. Carbonate grain associations: their use and environmental significance, a brief review. International Association of Sedimentologists, Special Publication 35-48.

- Kleipool, L.M., de Jong, K., de Vaal, E.L., Reijmer, J.J.G., 2017. Seismic characterization of switching platform geometries and dominant carbonate producers (Miocene, Las Negras, Spain). In: Della Porta, G. (Ed.), *Sedimentology* 64, 1676-1707. <https://doi.org/10.1111/sed.12369>
- Kosa, E., Warrlich, G., Loftus, G., 2015. Wings, mushrooms, and Christmas trees: The carbonate seismic geomorphology of Central Luconia, Miocene-present, offshore Sarawak, northwest Borneo. *AAPG Bulletin* 99, 2043-2075. <https://doi.org/10.1306/06181514201>
- Kuznetsov, V.G., 1997. Oil and gas in reef reservoirs in the former USSR. *Petroleum Geoscience* 3, 65-71. <https://doi.org/10.1144/petgeo.3.1.65>
- Larsen, P.-H., 1988. Relay structures in a Lower Permian basement-involved extension system, East Greenland. *Journal of Structural Geology* 10, 3-8. [https://doi.org/10.1016/0191-8141\(88\)90122-8](https://doi.org/10.1016/0191-8141(88)90122-8)
- Laubach, S.E., 2003. Practical approaches to identifying sealed and open fractures. *AAPG Bulletin* 87, 561-579.
- Laubach, S.E., Olson, J.E., Gross, M.R., 2009. Mechanical and fracture stratigraphy. *AAPG Bulletin* 93, 1413-1426. <https://doi.org/10.1306/07270909094>
- Laugié, M., Michel, J., Pohl, A., Poli, E., Borgomano, J., 2019. Global distribution of modern shallow-water marine carbonate factories: a spatial model based on environmental parameters. *Scientific Reports* 2019 9:1 9, 1-14. <https://doi.org/10.1038/s41598-019-52821-2>
- Leeder, M.R., Gawthorpe, R.L., 1987. Sedimentary models for extensional tilt-block/half-graben basins. Geological Society, London, *Special Publications* 28, 139-152. <https://doi.org/10.1144/GSL.SP.1987.028.01.11>

- Lees, A., 1975. Possible influence of salinity and temperature on modern shelf carbonate sedimentation. *Marine Geology* 19, 159-198.
- Lees, A., Buller, A.T., 1972. Modern temperate-water and warm-water shelf carbonate sediments contrasted. *Marine Geology* 13. [https://doi.org/10.1016/0025-3227\(72\)90011-4](https://doi.org/10.1016/0025-3227(72)90011-4)
- Lemay, M., Grimaud, J.L., Cojan, I., Rivoirard, J., Ors, F., 2020. Geomorphic variability of submarine channelized systems along continental margins: Comparison with fluvial meandering channels. *Marine and Petroleum Geology* 115, 104295. <https://doi.org/10.1016/j.marpetgeo.2020.104295>
- Liu, R., Li, B., Jiang, Y., 2016. A fractal model based on a new governing equation of fluid flow in fractures for characterizing hydraulic properties of rock fracture networks. *Computers and Geotechnics* 75, 57-68. <https://doi.org/10.1016/j.compgeo.2016.01.025>
- Lohr, T., 2004. Prediction of sub-seismic faults and fractures - integration of 3D seismic data, 3D retro- deformation, and well data on an example of deformation around an inverted fault. *Seismic and Sub-Seismic Deformation on Different Scales in the NW German Basin* 35-48.
- Longley, I.M., Buessenschuett, C., Clydsdale, L., Cubitt, C.J., Davis, R.C., Johnson, M.K., Marshall, N.M., Murray, A.P., Somerville, R., Spry, T.B., 2002. The North West Shelf of Australia-a Woodside perspective. *The Sedimentary Basins of Western Australia 3: Proceedings of Petroleum Exploration Society of Australia Symposium* 27-88. <https://doi.org/10.1017/CBO9781107415324.004>
- Loucks, R., Kerans, C., Janson, X., Marhx, M.A., 2011. Lithofacies Analysis and Stratigraphic Architecture of a Deep-Water Carbonate Debris Apron: Lower

- Cretaceous (Latest Aptian to Latest Albian) Tamabra Formation, Poza Rica Field Area, Mexico. Mass-Transport Deposits in Deepwater Settings. *SEPM (Society for Sedimentary Geology)*, 367-389.
- Loza Espejel, R., Alves, T.M., Blenkinsop, T.G., 2019a. Distribution and growth styles of isolated carbonate platforms as a function of fault propagation. *Marine and Petroleum Geology* 107. <https://doi.org/10.1016/j.marpetgeo.2019.05.020>
- Loza Espejel, R., Alves, T.M.T.M., Blenkinsop, T.G.T.G., 2019b. Distribution and growth styles of isolated carbonate platforms as a function of fault propagation. *Marine and Petroleum Geology In Press*, 484-507. <https://doi.org/10.1016/j.marpetgeo.2019.05.020>
- Ma, B., Wu, S., Mi, L., Lüdmann, T., Gao, J., Gao, W., 2018. Mixed Carbonate-Siliciclastic Deposits in a Channel Complex in the Northern South China Sea. *Journal of Earth Science* 29, 707-720. <https://doi.org/10.1007/s12583-018-0830-4>
- Maerten, L., Gillespie, P., Daniel, J.-M., 2006. Three-dimensional geomechanical modeling for constraint of subseismic fault simulation. *AAPG Bulletin* 90, 1337-1358. <https://doi.org/10.1306/03130605148>
- Magalhães, J.R., Barbosa, J.A., Oliveira, J.T.C., Lima Filho, M.F., 2014. Characterization of the ocean-continent transition in the Paraíba basin and Natal platform region, NE Brazil. *Revista Brasileira de Geofísica* 32 (3), 481-496. <https://doi.org/10.1590/rbgf.v32i3.504>
- Mandujano, J.J., Khachaturov, R.V., Tolson, G., Duncan Keppie, J., 2005. Curvature analysis applied to the Cantarell structure, southern Gulf of Mexico: implications for hydrocarbon exploration. *Computers & Geosciences* 31, 641-647.

<https://doi.org/10.1016/J.CAGEO.2004.11.018>

Manzocchi, T., 2002. The connectivity of two-dimensional networks of spatially correlated fractures. *Water Resources Research* 38, 1-1-1-20.

<https://doi.org/10.1029/2000WR000180>

Manzocchi, T., Walsh, J.J., Bailey, W.R., 2009. Population scaling biases in map samples of power-law fault systems. *Journal of Structural Geology* 31, 1612-

1626. <https://doi.org/10.1016/J.JSG.2009.06.004>

March, R., Doster, F., Geiger, S., 2018. Assessment of CO2 Storage Potential in Naturally Fractured Reservoirs With Dual-Porosity Models. *Water Resources*

Research 54, 1650-1668. <https://doi.org/10.1002/2017WR022159>

Marfurt, K.J., Alves, T.M., 2015. Pitfalls and limitations in seismic attribute interpretation of tectonic features. *Interpretation* 3, SB5-SB15.

<https://doi.org/10.1190/INT-2014-0122.1>

Marshall, J., Davies, P., Mihut, I., Troedson, A., Bergerson, D., Haddad, D., 1994.

Sahul shoals processes: Neotectonics and Cainozoic environments-cruise 122: Post Cruise Report. Australian Geological Survey Organisation, Canberra 928, 929-930.

Martín, J., Braga, J.C., 1994. Messinian events in the Sorbas Basin in southeastern Spain and their implications in the recent history of the Mediterranean.

Sedimentary Geology 90, 257-268. [https://doi.org/10.1016/0037-0738\(94\)90042-6](https://doi.org/10.1016/0037-0738(94)90042-6)

Mattos, N.H., Alves, T.M., Omosanya, K.O., 2016. Crestal fault geometries reveal late halokinesis and collapse of the Samson Dome, Northern Norway:

Implications for petroleum systems in the Barents Sea. *Tectonophysics* 690, 76-

96. <https://doi.org/10.1016/J.TECTO.2016.04.043>
- Mauldon, M., Dunne, W.M., Rohrbaugh, M.B., 2001. Circular scanlines and circular windows: new tools for characterizing the geometry of fracture traces. *Journal of Structural Geology* 23, 247-258. [https://doi.org/10.1016/S0191-8141\(00\)00094-8](https://doi.org/10.1016/S0191-8141(00)00094-8)
- Mazzullo, S.J., Chilingarian, G. V., 1992. Chapter 4 Diagenesis and Origin of Porosity. *Developments in Petroleum Science* 30, 199-270. [https://doi.org/10.1016/S0376-7361\(09\)70127-X](https://doi.org/10.1016/S0376-7361(09)70127-X)
- McQuillan, H., 1985. Fracture-controlled production from the Oligo-Miocene Asmari Formation in Gachsaran and Bibi Hakimeh fields, southwest Iran. *Carbonate Petroleum Reservoirs*. Springer, 511-523.
- Medici, G., Smeraglia, L., Torabi, A., Botter, C., 2021. Review of Modeling Approaches to Groundwater Flow in Deformed Carbonate Aquifers. *Groundwater* 59, 334-351. <https://doi.org/10.1111/GWAT.13069>
- Medici, G., West, L.J., Banwart, S.A., 2019. Groundwater flow velocities in a fractured carbonate aquifer-type: Implications for contaminant transport. *Journal of Contaminant Hydrology* 222, 1-16. <https://doi.org/10.1016/J.JCONHYD.2019.02.001>
- Meijninger, B.M.L., Vissers, R.L.M., 2006. Miocene extensional basin development in the Betic Cordillera, SE Spain revealed through analysis of the Alhama de Murcia and Crevillente Faults. *Basin Research* 18, 547-571. <https://doi.org/10.1111/j.1365-2117.2006.00308.x>
- Michel, J., Borgomano, J., Reijmer, J.J.G., 2018. Heterozoan carbonates: When, where and why? A synthesis on parameters controlling carbonate production and

occurrences. *Earth-Science Reviews* 182, 50-67.
<https://doi.org/10.1016/j.earscirev.2018.05.003>

Michel, J., Laugié, M., Pohl, A., Lanteaume, C., Masse, J.-P., Donnadieu, Y., Borgomano, J., 2019. Marine carbonate factories: a global model of carbonate platform distribution. *International Journal of Earth Sciences* 2019 108:6 108, 1773-1792. <https://doi.org/10.1007/S00531-019-01742-6>

Milliman, J.D., 1993. Production and accumulation of calcium carbonate in the ocean: budget of a nonsteady state. *Global Biogeochemical Cycles* 7, 927-957.

Monroe, W.H., 1970. A Glossary of Karst Terminology. US Geological Survey Water Supply Paper. [https://doi.org/10.1016/0022-1694\(71\)90080-1](https://doi.org/10.1016/0022-1694(71)90080-1)

Moore, C.H., 1989. Chapter 2 The Classification and Nature of Carbonate Porosity, Carbonate diagenesis and porosity. *Developments in Sedimentology*. [https://doi.org/10.1016/S0070-4571\(08\)71056-2](https://doi.org/10.1016/S0070-4571(08)71056-2)

Moore, C.H., Wade, W.J., 2013a. The nature and classification of carbonate porosity. *Developments in Sedimentology* 67, 51-65. <https://doi.org/10.1016/B978-0-444-53831-4.00004-5>

Moore, C.H., Wade, W.J., 2013b. Natural fracturing in carbonate reservoirs. *Developments in Sedimentology* 67, 285-300. <https://doi.org/10.1016/B978-0-444-53831-4.00011-2>

Moore, C.H., Wade, W.J., 2013c. Summary of early diagenesis and porosity modification of carbonate reservoirs in a sequence stratigraphic and climatic framework, *Developments in Sedimentology*. <https://doi.org/10.1016/B978-0-444-53831-4.00009-4>

Morley, C.K., Nixon, C.W., 2016. Topological characteristics of simple and complex

- normal fault networks. *Journal of Structural Geology* 84, 68-84.
<https://doi.org/10.1016/J.JSG.2016.01.005>
- Mory, A.J., 1991. Geology of the offshore Bonaparte Basin, northwestern Australia. Geological Survey of Western Australia.
- Moscardelli, L., Ochoa, J., Hunt, I., Zahm, L., 2019. Mixed siliciclastic-carbonate systems and their impact for the development of deep-water turbidites in continental margins: A case study from the Late Jurassic to Early Cretaceous Shelburne subbasin in offshore Nova Scotia. *AAPG Bulletin* 103, 2487-2520.
<https://doi.org/10.1306/02151917318>
- Mulder, T., Ducassou, E., Gillet, H., Hanquiez, V., Principaud, M., Chabaud, L., Eberli, G.P., Kindler, P., Billeaud, I., Gonthier, E., Fournier, F., Leonide, P., Borgomano, J., 2014. First Discovery of Channel-Levee Complexes In A Modern Deep-Water Carbonate Slope Environment. *Journal of Sedimentary Research* 84, 1139-1146. <https://doi.org/10.2110/jsr.2014.90>
- Mulder, T., Ducassou, E., Gillet, H., Hanquiez, V., Tournadour, E., Combes, J., Eberli, G.P., Kindler, P., Gonthier, E., Conesa, G., Robin, C., Sianipar, R., Reijmer, J.J.G., François, A., 2012. Canyon morphology on a modern carbonate slope of the bahamas: Evidence of regional tectonic tilting. *Geology* 40, 771-774. <https://doi.org/10.1130/G33327.1>
- Munro, M.A., Blenkinsop, T.G., 2012. MARD-A moving average rose diagram application for the geosciences. *Computers and Geosciences* 49, 112-120.
<https://doi.org/10.1016/j.cageo.2012.07.012>
- Muraoka, H., Kamata, H., 1983. Displacement distribution along minor fault traces. *Journal of Structural Geology* 5, 483-495.

- Narr, W., Flodin, E., 2013. Fractures in steep-rimmed carbonate platforms: Comparison of Tengiz reservoir, Kazakhstan, and outcrops in Canning Basin, NW Australia. 2nd EAGE Workshop Naturally Fractured Reservoirs: Naturally Fractured Reservoirs in Real Life 20161. <https://doi.org/10.3997/2214-4609.20132005>
- Needham, T., Yielding, G., Fox, R., 1996. Fault population description and prediction using examples from the offshore U.K. *Journal of Structural Geology* 18, 155-167. [https://doi.org/10.1016/S0191-8141\(96\)80041-1](https://doi.org/10.1016/S0191-8141(96)80041-1)
- Nelson, C.S., Keane, S.L., Head, P.S., 1988. Non-tropical carbonate deposits on the modern New Zealand shelf. *Sedimentary Geology* 60, 71-94. [https://doi.org/10.1016/0037-0738\(88\)90111-X](https://doi.org/10.1016/0037-0738(88)90111-X)
- Nelson, R.A., 2001. *Geologic analysis of naturally fractured reservoirs*, 2nd Edition. Gulf Professional Pub.
- Nemčok, M., Henk, A., Allen, R., Sikora, P.J., Stuart, C., 2013. Continental break-up along strike-slip fault zones; observations from the equatorial Atlantic. *Geological Society Special Publication* 369, 537-556. <https://doi.org/10.1144/SP369.8>
- Neuhaus, D., Borgomano, J., Jauffred, J.-C., Mercadier, C., Olotu, S., Grtsch, J., 2004. Quantitative Seismic Reservoir Characterization of an Oligocene Miocene Carbonate Buildup: Malampaya Field, Philippines.
- Nicol, A., Walsh, J.J.J., Watterson, J., Gillespie, P.A.A., 1996. Fault size distributions - Are they really power-law? *Journal of Structural Geology* 18, 191-197. [https://doi.org/10.1016/S0191-8141\(96\)80044-7](https://doi.org/10.1016/S0191-8141(96)80044-7)
- Nixon, C.W., Sanderson, D.J., Bull, J.M., 2012. Analysis of a strike-slip fault network

- using high resolution multibeam bathymetry, offshore NW Devon U.K. *Tectonophysics* 541-543, 69-80. <https://doi.org/10.1016/j.tecto.2012.03.021>
- Nooitgedacht, C.W., Kleipool, L.M., Andeweg, B., Reolid, J., Betzler, C., Lindhorst, S., Reijmer, J.J.G., 2018. New insights in the development of syn-depositional fractures in rimmed flat-topped carbonate platforms, Neogene carbonate complexes, Sorbas Basin, SE Spain. *Basin Research* 30, 596-612. <https://doi.org/10.1111/bre.12239>
- Nordaunet-Olsen, E.M., 2015. Controls on upper Paleozoic carbonate build-up development in the South Central Norwegian Barents Sea.
- Nyberg, B., Nixon, C.W., Sanderson, D.J., 2018. NetworkGT: A GIS tool for geometric and topological analysis of two-dimensional fracture networks. *Geosphere* 14, 1618-1634. <https://doi.org/10.1130/GES01595.1>
- Odling, N.E., 1997. Scaling and connectivity of joint systems in sandstones from western Norway. *Journal of Structural Geology* 19, 1257-1271. [https://doi.org/10.1016/S0191-8141\(97\)00041-2](https://doi.org/10.1016/S0191-8141(97)00041-2)
- Odling, N.E., Gillespie, P., Bourguin, B., Castaing, C., Chiles, J.P., Christensen, N.P., Fillion, E., Genter, A., Olsen, C., Thrane, L., Trice, R., Aarseth, E., Walsh, J.J., Watterson, J., 1999. Variations in fracture system geometry and their implications for fluid flow in fractures hydrocarbon reservoirs. *Petroleum Geoscience* 5, 373-384. <https://doi.org/10.1144/petgeo.5.4.373>
- Oliveira, M.J.R., Santarem, P., Moraes, A., Zalán, P. V., Caldeira, J.L., Tanaka, A., Trosdorf, I., 2012. Linked extensional-compressional tectonics in gravitational systems in the equatorial margin of Brazil. *AAPG Memoir* 159-178. <https://doi.org/10.1306/13351552M1003532>

- Palaz, I., Marfurt, K.J., 1997. 1. Carbonate Seismology: An Overview. Carbonate Seismology 1-8. <https://doi.org/10.1190/1.9781560802099.ch1>
- Paumard, V., Zuckmeyer, E., Boichard, R., Jorry, S.J., Bourget, J., Borgomano, J., Maurin, T., Ferry, J.-N., 2017. Evolution of Late Oligocene - Early Miocene attached and isolated carbonate platforms in a volcanic ridge context (Maldives type), Yadana field, offshore Myanmar. *Marine and Petroleum Geology* 81, 361-387. <https://doi.org/10.1016/J.MARPETGEO.2016.12.012>
- Payros, A., Pujalte, V., 2008. Calciclastic submarine fans: An integrated overview., *Earth-Science Reviews*. <https://doi.org/10.1016/j.earscirev.2007.09.001>
- Payros, A., Pujalte, V., Orue-Etxebarria, X., 2007. A point-sourced calciclastic submarine fan complex (Eocene Anotz Formation, western Pyrenees): facies architecture, evolution and controlling factors. *Sedimentology* 54, 137-168. <https://doi.org/10.1111/j.1365-3091.2006.00823.x>
- Peacock, D.C.P., Knipe, R.J., Sanderson, D.J., 2000. Glossary of normal faults. *Journal of Structural Geology* 22, 291-305. [https://doi.org/10.1016/S0191-8141\(00\)80102-9](https://doi.org/10.1016/S0191-8141(00)80102-9)
- Peacock, D.C.P., Nixon, C.W., Rotevatn, A., Sanderson, D.J., Zuluaga, L.F., 2016. Glossary of fault and other fracture networks. *Journal of Structural Geology* 92, 12-29. <https://doi.org/10.1016/J.JSG.2016.09.008>
- Pettingill, H.S., 2006. Global Overview of Deepwater Exploration and Production. In: Weimer, P., Slatt, R.M., Bouroullec, R., Fillon, R., Pettingill, H., Pranter, M., Tari, G. (Eds.), *Introduction to the Petroleum Geology of Deepwater Setting*. American Association of Petroleum Geologists (AAPG). https://doi.org/10.1111/oet.2_12511

- Pickering, G., Bull, J.M., Sanderson, D.J., 1995. Sampling power-law distributions. *Tectonophysics* 248, 1-20. [https://doi.org/10.1016/0040-1951\(95\)00030-Q](https://doi.org/10.1016/0040-1951(95)00030-Q)
- Pickering, G., Peacock, D.C.P., Sanderson, D.J., Bull, J.M., 1997. Modeling tip zones to predict the throw and length characteristics of faults. *AAPG Bulletin* 81, 82-99.
- Piovesan, E.K., 2008. Ostracodes Cretáceos (Turoniano-Maastrichtiano) Da Bacia Do Pará-Maranhão: Aspectos Taxonômicos, Paleoecológicos E Paleobiogeográficos. Universidade do Vale do Rio dos Sinos.
- Playton, T.E., Janson, X., Kerans, C., 2010. Carbonate Slopes. In: James, N., Dalrymple, R.W. (Eds.), *Facies Models 4*. Geological Association of Canada, St. Johns, Newfoundland, 449-476.
- Pomar, L., 2020. Carbonate systems. *Regional Geology and Tectonics: Principles of Geologic Analysis* 235-311. <https://doi.org/10.1016/B978-0-444-64134-2.00013-4>
- Pomar, L., 2001. Types of carbonate platforms: a genetic approach. *Basin Research* 13, 313-334. <https://doi.org/10.1046/j.0950-091x.2001.00152.x>
- Pomar, L., Hallock, P., 2008. Carbonate factories: A conundrum in sedimentary geology. *Earth-Science Reviews* 87, 134-169. <https://doi.org/10.1016/J.EARSCIREV.2007.12.002>
- Posamentier, H.W., Laurin, P., Warmath, A., Purnama, M., Drajat, D., 2010. Seismic Stratigraphy and Geomorphology of Oligocene to Miocene Carbonate Buildups, Offshore Madura, Indonesia. *Cenozoic Carbonate Systems of Australasia*. SEPM (Society for Sedimentary Geology), 175-192. <https://doi.org/10.2110/sepmsp.095.175>

- Procter, A., Sanderson, D.J., 2018. Spatial and layer-controlled variability in fracture networks. *Journal of Structural Geology* 108, 52-65. <https://doi.org/10.1016/j.jsg.2017.07.008>
- Puga-Bernabéu, Á., Webster, J.M., Beaman, R.J., Reimer, P.J., Renema, W., 2014. Filling the gap: A 60ky record of mixed carbonate-siliciclastic turbidite deposition from the Great Barrier Reef. *Marine and Petroleum Geology* 50, 40-50. <https://doi.org/10.1016/j.marpetgeo.2013.11.009>
- Purdy, E.G., 1963. Recent calcium carbonate facies of the Great Bahama Bank. 2. Sedimentary facies. *The Journal of Geology* 71, 472-497.
- Questiaux, J.-M., Couples, G.D., Ruby, N., 2010. Fractured reservoirs with fracture corridors. *Geophysical Prospecting* 58, 279-295. <https://doi.org/10.1111/j.1365-2478.2009.00810.x>
- Rankey, E.C., 2017. Seismic architecture and seismic geomorphology of heterozoan carbonates: Eocene-Oligocene, Browse Basin, Northwest Shelf, Australia. *Marine and Petroleum Geology* 82, 424-443. <https://doi.org/10.1016/j.marpetgeo.2017.02.011>
- Rankey, E.C., Schlaich, M., Mokhtar, S., Ghon, G., Ali, S.H., Poppelreiter, M., 2019. Seismic architecture of a Miocene isolated carbonate platform and associated off-platform strata (Central Luconia Province, offshore Malaysia). *Marine and Petroleum Geology* 102, 477-495. <https://doi.org/10.1016/J.MARPETGEO.2019.01.009>
- Ravenne, C., Vially, R., Francaise, C., Valery, P., 1985. Deep Clastic Carbonate Deposits of the Bahamas – Comparison With Mesozoic Outcrops of the Vercors and Vocontian Trough.

- Reijmer, J.J.G., Andresen, N., 2007. Mineralogy and grain size variations along two carbonate margin-to-basin transects (Pedro Bank, Northern Nicaragua Rise). *Sedimentary Geology* 198, 327-350. <https://doi.org/10.1016/j.sedgeo.2007.01.018>
- Reijmer, J.J.G., Mulder, T., Borgomano, J., 2015a. Carbonate slopes and gravity deposits. *Sedimentary Geology* 317, 1-8. <https://doi.org/10.1016/j.sedgeo.2014.12.001>
- Reijmer, J.J.G., Palmieri, P., Groen, R., 2012. Compositional variations in calciturbidites and calcidebrites in response to sea-level fluctuations (Exuma Sound, Bahamas). *Facies* 58, 493-507. <https://doi.org/10.1007/s10347-011-0291-z>
- Reijmer, J.J.G., Palmieri, P., Groen, R., Floquet, M., 2015b. Calciturbidites and calcidebrites: Sea-level variations or tectonic processes? *Sedimentary Geology* 317, 53-70. <https://doi.org/10.1016/j.sedgeo.2014.10.013>
- Reolid, J., Betzler, C., Braga, J.C., Martín, J.M., Lindhorst, S., Reijmer, J.J.G., 2014. Reef slope geometries and facies distribution: controlling factors (Messinian, SE Spain). *Facies* 60, 737-753. <https://doi.org/10.1007/s10347-014-0406-4>
- Rexilius, J.P., Powell, S.L., 1999a. Micropalaeontological Analysis Fannie Bay-1, Permit AC-P16, Bonaparte Basin. Western Australia.
- Rexilius, J.P., Powell, S.L., 1999b. Micropalaeontological Analysis Paleogene Section Mandorah-1, Permit AC-P16, Bonaparte Basin. Western Australia.
- Rexilius, J.P., Powell, S.L., Howe, R., 1998a. Micropalaeontological Analysis Mandorah-1, Permit AC-P16, Bonaparte Basin. Western Australia.
- Rexilius, J.P., Powell, S.L., Howe, R., 1998b. Micropalaeontological Analysis

Ludmilla-1, Permit AC-P16, Bonaparte Basin. Western Australia.

Ricoy-Paramo, V., 2005. 3D seismic characterisation of the Cantarell Field, Campeche Basin, Mexico.

Ricoy, V., Cartwright, J., Kingdom, U., 2004. The Structural Evolution of The Giant Cantarell Field , Mexico : Implications for Modelling of a Fractured Carbonate Reservoir. 44, 2004.

Riding, R., Martin, J.M., Braga, J.C., 1991. Coral-stromatolite reef framework, Upper Miocene, Almeria, Spain. *Sedimentology* 38, 799-818.
<https://doi.org/10.1111/j.1365-3091.1991.tb01873.x>

Rinke-Hardekopf, L., Reuning, L., Bourget, J., Back, S., 2018. Syn-sedimentary deformation as a mechanism for the initiation of submarine gullies on a carbonate platform to slope transition, Browse Basin, Australian North West Shelf. *Marine and Petroleum Geology* 91, 622-630.
<https://doi.org/10.1016/j.marpetgeo.2017.12.034>

Roden, R., Smith, T.A., Santogrossi, P., Sacrey, D., Jones, G., 2017. Seismic interpretation below tuning with multiattribute analysis. *The Leading Edge* 36, 330-339.

Rohrbaugh, M.B., Dunne, W.M., Mauldon, M., 2002. Estimating fracture trace intensity, density, and mean length using circular scan lines and windows. *AAPG Bulletin* 86, 2089-2104.

Rossetti, D.F., Bezerra, F.H.R., Dominguez, J.M.L., 2013. Late oligocene-miocene transgressions along the equatorial and eastern margins of brazil. *Earth-Science Reviews* 123, 87-112. <https://doi.org/10.1016/j.earscirev.2013.04.005>

Ruig, M. de, 2000. Seismic Interpretation Report Karmt 3D Survey, Permit AC/P16

- (Bonaparte Basin, Timor Sea). 16.
- Rusciadelli, G., Shiner, P., 2018. Isolated Carbonate Platforms of the Mediterranean and their seismic expression - searching for a paradigm. *The Leading Edge*.
<https://doi.org/10.1190/tle37070492.1>
- Sánchez-Almazo, I.M., Braga, J.C., Dinarès-Turell, J., Martín, J.M., Spiro, B., 2007. Palaeoceanographic controls on reef deposition: the Messinian Cariatiz reef (Sorbas Basin, Almería, SE Spain). *Sedimentology* 54, 637-660.
<https://doi.org/10.1111/j.1365-3091.2006.00853.x>
- Sanderson, D.J., 2016. Field-based structural studies as analogues to sub-surface reservoirs. Geological Society, London, Special Publications 436, 207-217.
<https://doi.org/10.1144/SP436.5>
- Sanderson, D.J., Nixon, C.W., 2018. Topology, connectivity and percolation in fracture networks. *Journal of Structural Geology* 115, 167-177.
<https://doi.org/10.1016/j.jsg.2018.07.011>
- Sanderson, D.J., Nixon, C.W., 2015. The use of topology in fracture network characterization. *Journal of Structural Geology* 72, 55-66.
<https://doi.org/10.1016/j.jsg.2015.01.005>
- Sanderson, D.J., Peacock, D.C.P., Nixon, C.W., Rotevatn, A., 2019. Graph theory and the analysis of fracture networks. *Journal of Structural Geology* 125, 155-165. <https://doi.org/10.1016/j.jsg.2018.04.011>
- Santiago, E., Velasco-Hernández, J.X., Romero-Salcedo, M., 2014. A methodology for the characterization of flow conductivity through the identification of communities in samples of fractured rocks. *Expert Systems with Applications* 41, 811-820. <https://doi.org/10.1016/J.ESWA.2013.08.011>

- Saqab, M.M., Bourget, J., 2015a. Controls on the distribution and growth of isolated carbonate build-ups in the Timor Sea (NW Australia) during the Quaternary. *Marine and Petroleum Geology* 62, 123-143. <https://doi.org/10.1016/J.MARPETGEO.2015.01.014>
- Saqab, M.M., Bourget, J., 2015b. Structural style in a young flexure-induced oblique extensional system, north-western Bonaparte Basin, Australia. *Journal of Structural Geology* 77, 239-259.
- Sarkheil, H., Hassani, H., Alinia, F., 2013. Fractures distribution modeling using fractal and multi-fractal-neural network analysis in Tabnak hydrocarbon field, Fars, Iran. *Arabian Journal of Geosciences* 6, 945-956. <https://doi.org/10.1007/s12517-011-0400-x>
- Sattler, U., Immenhauser, A., Schlager, W., Zampetti, V., 2009. Drowning history of a Miocene carbonate platform (Zhujiang Formation, South China Sea). *Sedimentary Geology* 219, 318-331. <https://doi.org/10.1016/J.SEDGEO.2009.06.001>
- Savitzky, A., Golay, M.J.E., 1964. Smoothing and differentiation of data by simplified least squares procedures. *Analytical Chemistry* 36, 1627-1639.
- Schlager, W., 2005. Carbonate sedimentology and sequence stratigraphy. SEPM Soc for Sed Geology.
- Schlager, W., 2000. Sedimentation rates and growth potential of tropical, cool-water and mud-mound carbonate systems. Geological Society, London, Special Publications 178, 217-227. <https://doi.org/10.1144/GSL.SP.2000.178.01.14>
- Schneider, J.A., Senders, M., 2010. Foundation design: A comparison of oil and gas platforms with offshore wind turbines. *Marine Technology Society Journal* 44,

32-51. <https://doi.org/10.4031/MTSJ.44.1.5>

Sheriff, R.E., Geldart, L.P., 1995. Exploration seismology. Cambridge university press.

Soares, D.M., Alves, T.M., Terrinha, P., 2012. The breakup sequence and associated lithospheric breakup surface: Their significance in the context of rifted continental margins (West Iberia and Newfoundland margins, North Atlantic). *Earth and Planetary Science Letters* 355-356, 311-326. <https://doi.org/10.1016/j.epsl.2012.08.036>

Soares, E.F., Zalán, P.V., Figueiredo, J.J.P., Trosdorf Jr, I., 2007. Bacia do Pará-Maranhão. *Boletim de Geociências Da Petrobras* 15, 321-330.

Soares Júnior, A.V., 2002. Paleografia e evolução da paisagem do nordeste do estado do Pará e noroeste do Maranhão: cretáceo ao holoceno, Arsyad, Azhar,. Universidade Federal do Pará.

Soares Júnior, A.V., Hasui, Y., Costa, J.B.S., Machado, F.B., 2011. Evolução do rifteamento e paleogeografia da margem Atlântica Equatorial do Brasil: Triássico ao Holoceno. *Geociencias* 30, 669-692.

Soliva, R., Benedicto, A., Schultz, R.A., Maerten, L., Micarelli, L., 2008. Displacement and interaction of normal fault segments branched at depth: Implications for fault growth and potential earthquake rupture size. *Journal of Structural Geology* 30, 1288-1299. <https://doi.org/10.1016/J.JSG.2008.07.005>

Stanton Jr, R.J., 1967. Factors controlling shape and internal facies distribution of organic carbonate buildups. *AAPG Bulletin* 51, 2462-2467.

Steen, Ø., Sverdrup, E., Hanssen, T.H., 1998. Predicting the distribution of small faults in a hydrocarbon reservoir by combining outcrop, seismic and well data.

Geological Society, London, Special Publications 147, 27-50.
<https://doi.org/10.1144/GSL.SP.1998.147.01.03>

Strijker, G., Bertotti, G., Luthi, S.M., 2012. Multi-scale fracture network analysis from an outcrop analogue: A case study from the Cambro-Ordovician clastic succession in Petra, Jordan. *Marine and Petroleum Geology* 38, 104-116.
<https://doi.org/10.1016/J.MARPETGEO.2012.07.003>

Sylvester, Z., Pirmez, C., 2017. Latitudinal changes in the morphology of submarine channels: Reevaluating the evidence for the influence of the coriolis force. *SEPM Special Publications* 108, 82-92. <https://doi.org/10.2110/sepmsp.108.02>

Tao, Z., Alves, T.M., 2019. Impacts of data sampling on the interpretation of normal fault propagation and segment linkage. *Tectonophysics* 762, 79-96.
<https://doi.org/10.1016/J.TECTO.2019.03.013>

Telford, W.M., Geldart, L.P., Sheriff, R.E., 1990. *Applied Geophysics*. Applied Geophysics. <https://doi.org/10.1017/CBO9781139167932>

TerHeege, J.H., Osinga, S., Carpentier, S., 2018. The Geomechanical Response of Naturally Fractured Carbonate Reservoirs to Operation of a Geothermal Doublet.

Tesch, P., Reece, R.S., Pope, M.C., Markello, J.R., 2018. Quantification of architectural variability and controls in an Upper Oligocene to Lower Miocene carbonate ramp, Browse Basin, Australia. *Marine and Petroleum Geology* 91, 432-454. <https://doi.org/10.1016/j.marpetgeo.2018.01.022>

Torabi, A., Berg, S.S., 2011. Scaling of fault attributes: A review. *Marine and Petroleum Geology* 28, 1444-1460.
<https://doi.org/10.1016/j.marpetgeo.2011.04.003>

Tournadour, E., Mulder, T., Borgomano, J., Gillet, H., Chabaud, L., Ducassou, E.,
355

-
- Hanquiez, V., Etienne, S., 2017. Submarine canyon morphologies and evolution in modern carbonate settings: The northern slope of Little Bahama Bank, Bahamas. *Marine Geology* 391, 76-97. <https://doi.org/10.1016/j.margeo.2017.07.014>
- Trosdorf Junior, I., Zalán, P.V., Figueiredo, J. de J.P. De, Soares, E.F., 2007. Bacia de Barreirinhas. *Boletim de Geociencias - Petrobras* 15, 331-339.
- Van As, A., Jeffrey, R.G., 2002. Hydraulic fracture growth in naturally fractured rock: mine through mapping and analysis.
- Van Tuyl, J., Alves, T.M., Cherns, L., 2018. Pinnacle features at the base of isolated carbonate buildups marking point sources of fluid offshore Northwest Australia. *GSA Bulletin*. <https://doi.org/10.1130/B31838.1>
- Veevers, J.J., 1971. Shallow stratigraphy and structure of the Australian continental margin beneath the Timor Sea. *Marine Geology* 11, 209-249. [https://doi.org/10.1016/0025-3227\(71\)90026-0](https://doi.org/10.1016/0025-3227(71)90026-0)
- Verwer, K., Playton, T.E., Harris, P.M.M., 2014. Deposits, Architecture, and Controls of Carbonate Margin, Slope, and Basinal Settings—Introduction. *SEPM Society for Sedimentary Geology*.
- Vidal, J., Genter, A., 2018. Overview of naturally permeable fractured reservoirs in the central and southern Upper Rhine Graben: Insights from geothermal wells. *Geothermics* 74, 57-73. <https://doi.org/10.1016/J.GEOTHERMICS.2018.02.003>
- Vollmer, F.W., 2015. Orient 3: a new integrated software program for orientation data analysis, kinematic analysis, spherical projections, and Schmidt plots. *Geological Society of America Abstracts with Programs*. 49.
- Vollmer, F.W., 1995. C program for automatic contouring of spherical orientation

- data using a modified Kamb method. *Computers and Geosciences* 21, 31-49.
[https://doi.org/10.1016/0098-3004\(94\)00058-3](https://doi.org/10.1016/0098-3004(94)00058-3)
- Vollmer, F.W., 1990. An application of eigenvalue methods to structural domain analysis. *GSA Bulletin* 102, 786-791. [https://doi.org/10.1130/0016-7606\(1990\)102<0786:aaemt>2.3.co;2](https://doi.org/10.1130/0016-7606(1990)102<0786:aaemt>2.3.co;2)
- Walsh, J.J., Watterson, J., 1991. Geometric and kinematic coherence and scale effects in normal fault systems. Geological Society, London, Special Publications 56, 193-203. <https://doi.org/10.1144/GSL.SP.1991.056.01.13>
- Wang, Z., 1997. 3. Seismic Properties of Carbonate Rocks. *Carbonate Seismology* 29-52. <https://doi.org/10.1190/1.9781560802099.ch3>
- Watkins, H., Bond, C.E., Healy, D., Butler, R.W.H., 2015. Appraisal of fracture sampling methods and a new workflow to characterise heterogeneous fracture networks at outcrop. *Journal of Structural Geology* 72, 67-82. <https://doi.org/10.1016/J.JSG.2015.02.001>
- Watterson, J., Walsh, J.J., Gillespie, P.A., Easton, S., 1996. Scaling systematics of fault sizes on a large-scale range fault map. *Journal of Structural Geology* 18, 199-214. [https://doi.org/10.1016/S0191-8141\(96\)80045-9](https://doi.org/10.1016/S0191-8141(96)80045-9)
- Weimer, P., Slatt, R.M., 2004. Deepwater Reservoir Elements: Channels and their Sedimentary Fill. In: Weimer, P., Slatt, R. (Eds.), *Petroleum Systems of Deepwater Settings*. Society of Exploration Geophysicists and European Association of Geoscientists and Engineers. <https://doi.org/10.1190/1.9781560801955.ch4>
- Wencai, Y., 2013. *Reflection Seismology: theory, data processing and interpretation*. Elsevier.

- Whittam, D.B., Norvick, M.S., McIntyre, C.L., 1996. MESOZOIC AND CAINOZOIC TECTONOSTRATIGRAPHY OF WESTERN ZOCA AND ADJACENT AREAS. *The AAPG Journal* 36, 209. <https://doi.org/10.1071/AJ95012>
- Williams, G.P., 1986. River meanders and channel size. *Journal of Hydrology* 88, 147-164. [https://doi.org/10.1016/0022-1694\(86\)90202-7](https://doi.org/10.1016/0022-1694(86)90202-7)
- Willis, S., 2000. Mindil-1 Well Completion Report, Interpretive Data.
- Willis, S., 1999a. Mandorah-1 Well Completion Report, Interpretive Data.
- Willis, S., 1999b. Fannie Bay-1 Well Completion Report, Interpretive Data.
- Willis, S., 1999c. Lameroo-1 Well Completion Report, Interpretive Data.
- Willis, S., 1998. Ludmilla-1 Well Completion Report, Interpretive Data.
- Wilson, M.E., 1999. Prerift and synrift sedimentation during early fault segmentation of a Tertiary carbonate platform, Indonesia. *Marine and Petroleum Geology* 16, 825-848. [https://doi.org/10.1016/S0264-8172\(99\)00019-7](https://doi.org/10.1016/S0264-8172(99)00019-7)
- Wilson, M.E.J., Vecsei, A., 2005. The apparent paradox of abundant foramol facies in low latitudes: their environmental significance and effect on platform development. 69, 133-168. <https://doi.org/10.1016/j.earscirev.2004.08.003>
- Winefield, P., Burgess, P., Minzoni, M., Pierson, B., Playton, T., Janson, X., 2011. Deep-Water Resedimented Carbonate Exploration Play Types: Controls and Models *. AAPG Annual Convention and Exhibition: Search and Discovery Article 50502. [https://doi.org/10.1016/S0025-3227\(01\)00287-0](https://doi.org/10.1016/S0025-3227(01)00287-0).Eberli
- Woodall, M., 1990. Nancar-1/ST Well Completion Report, Interpretive Data.
- Wright, V.P., Burchette, T.P., 1998. Carbonate ramps: An introduction. *Geological Society Special Publication* 149, 1-5.

<https://doi.org/10.1144/GSL.SP.1999.149.01.01>

- Wu, Y., Li, P., Hao, Y., Wanniarachchi, A., Zhang, Y., Peng, S., 2021. Experimental research on carbon storage in a CO₂-Based enhanced geothermal system. *Renewable Energy* 175, 68-79. <https://doi.org/10.1016/J.RENENE.2021.04.139>
- Wunsch, M., Betzler, C., Lindhorst, S., Lüdmann, T., Eberli, G.P., 2017. Sedimentary dynamics along carbonate slopes (Bahamas archipelago). *Sedimentology* 64, 631-657. <https://doi.org/10.1111/sed.12317>
- Yilmaz, Ö., 2001. *Seismic data analysis: Processing, inversion, and interpretation of seismic data*. Society of exploration geophysicists.
- Yokoyama, Y., De Deckker, P., Lambeck, K., Johnston, P., Fifield, L., 2001. Sea-level at the Last Glacial Maximum: evidence from northwestern Australia to constrain ice volumes for oxygen isotope stage 2. *Palaeogeography, Palaeoclimatology, Palaeoecology* 165, 281-297. [https://doi.org/10.1016/S0031-0182\(00\)00164-4](https://doi.org/10.1016/S0031-0182(00)00164-4)
- Zalán, P.V., 2015. Re-Interpretation of an Ultra-Deep Seismic Section in the Para-Maranhao Basin - Implications for the Petroleum Potential of the Ultra-Deep Waters. *OTC Brasil 2015: The Atlantic: From East to West - An Ocean of Innovation*. 662-672. <https://doi.org/10.4043/26134-ms>
- Zalán, P.V., 2001. Growth Folding in Gravitational Fold-and-Thrust Belts in the Deep Waters of the Equatorial Atlantic, Northeastern Brazil. *Seventh International Congress of the Brazilian Geophysical Society*. AAPG Datapages/Search and Discovery. <https://doi.org/10.1306/61eed5a8-173e-11d7-8645000102c1865d>
- Zampetti, V., Schlager, W., van Konijnenburg, J.-H., Everts, A.-J., 2004. Architecture and growth history of a Miocene carbonate platform from 3D

-
- seismic reflection data; Luconia province, offshore Sarawak, Malaysia. *Marine and Petroleum Geology* 21, 517-534. <https://doi.org/10.1016/J.MARPETGEO.2004.01.006>
- Zarei, H.R., Uromeihy, A., Sharifzadeh, M., 2012. Identifying geological hazards related to tunneling in carbonate karstic rocks - Zagros, Iran. *Arabian Journal of Geosciences* 5, 457-464. <https://doi.org/10.1007/s12517-010-0218-y>
- Zeeb, C., Gomez-Rivas, E., Bons, P.D., Blum, P., 2013. Evaluation of Sampling methods for fracture network characterization using Outcrops. *AAPG Bulletin* 97, 1545-1566. <https://doi.org/10.1306/02131312042>
- Zeng, L.Y., 2020. Seismic-based geomorphology of a mixed carbonate siliciclastic shelf-to- basin submarine drainage system , Miocene , Browse Basin , Northwest Shelf of Australia APPROVED BY SUPERVISING COMMITTEE : The University of Texas at Austin.

Appendix A: Fracture branch length distribution histograms

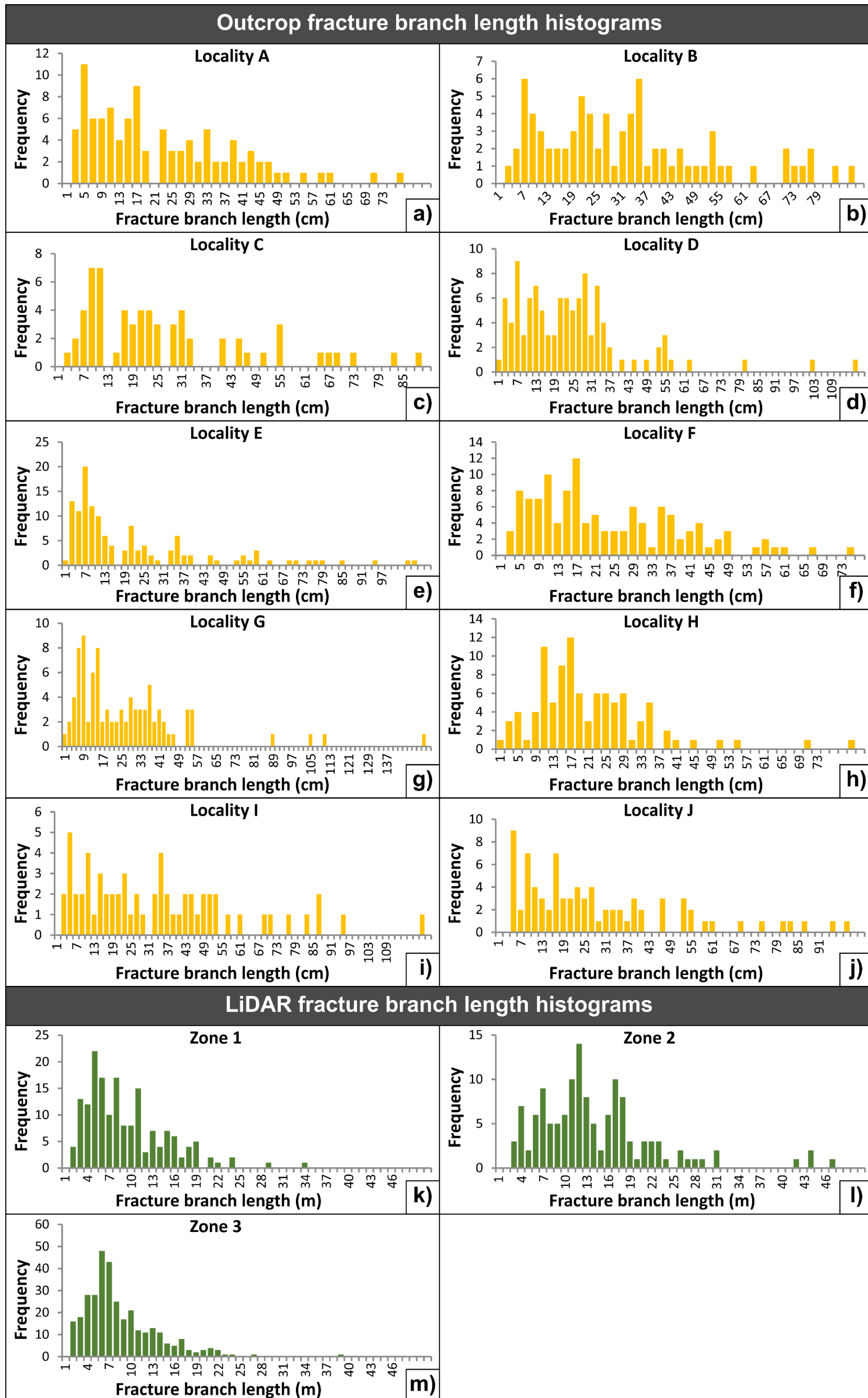


Figure A1. Fracture branch length histograms from the Cariatiz carbonate platform. a) to j) Histograms from outcrop localities. k) to m) Histograms from LiDAR zones.

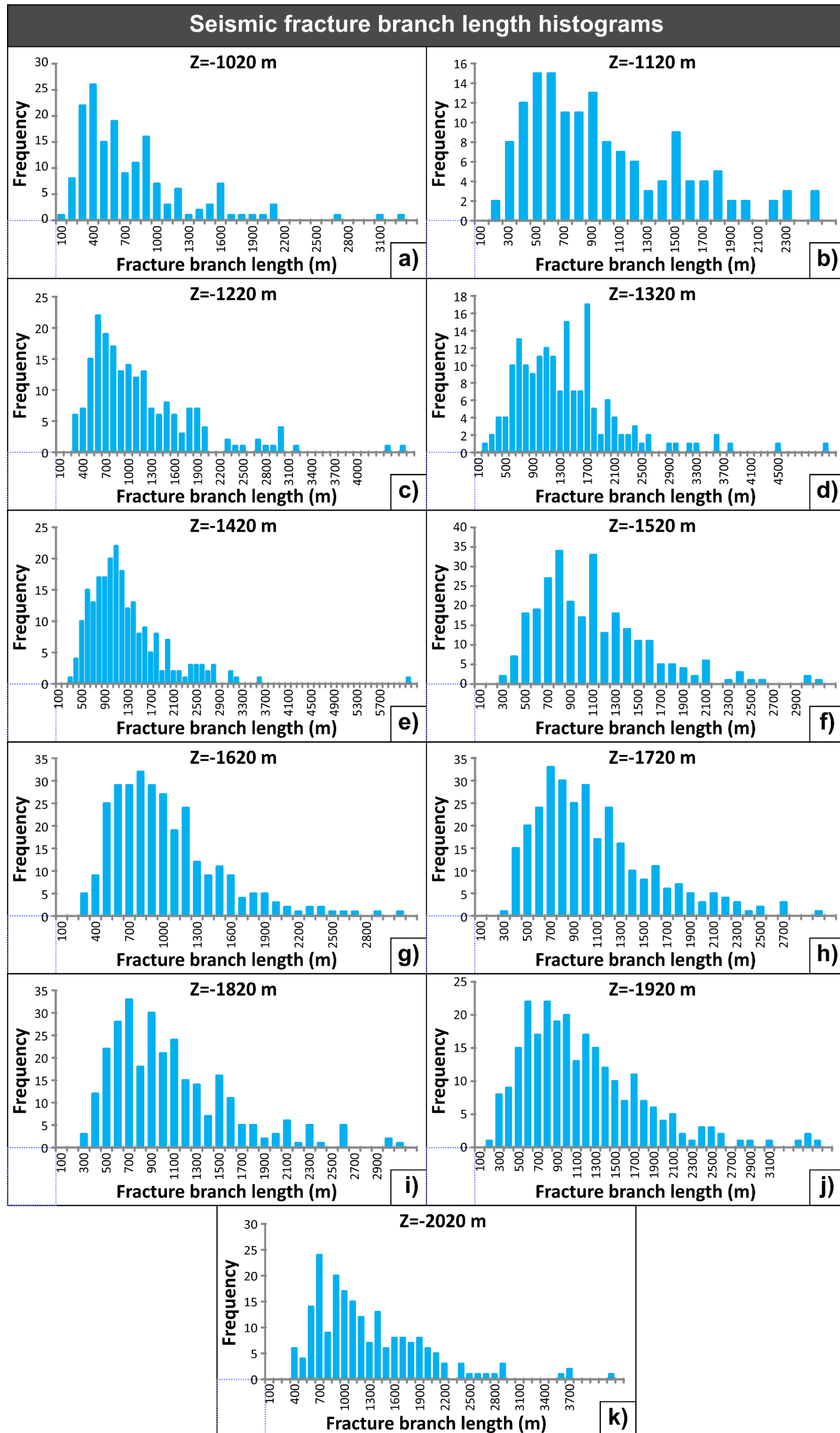


Figure A2. Fracture branch length histograms from seismic data (depth slices -1020 m to -2020 m) in the Pernambuco carbonate platform. Fracture branches at seismic scale are in the range of hundreds of metres.

Appendix B: Rose diagrams showing fracture branch orientation

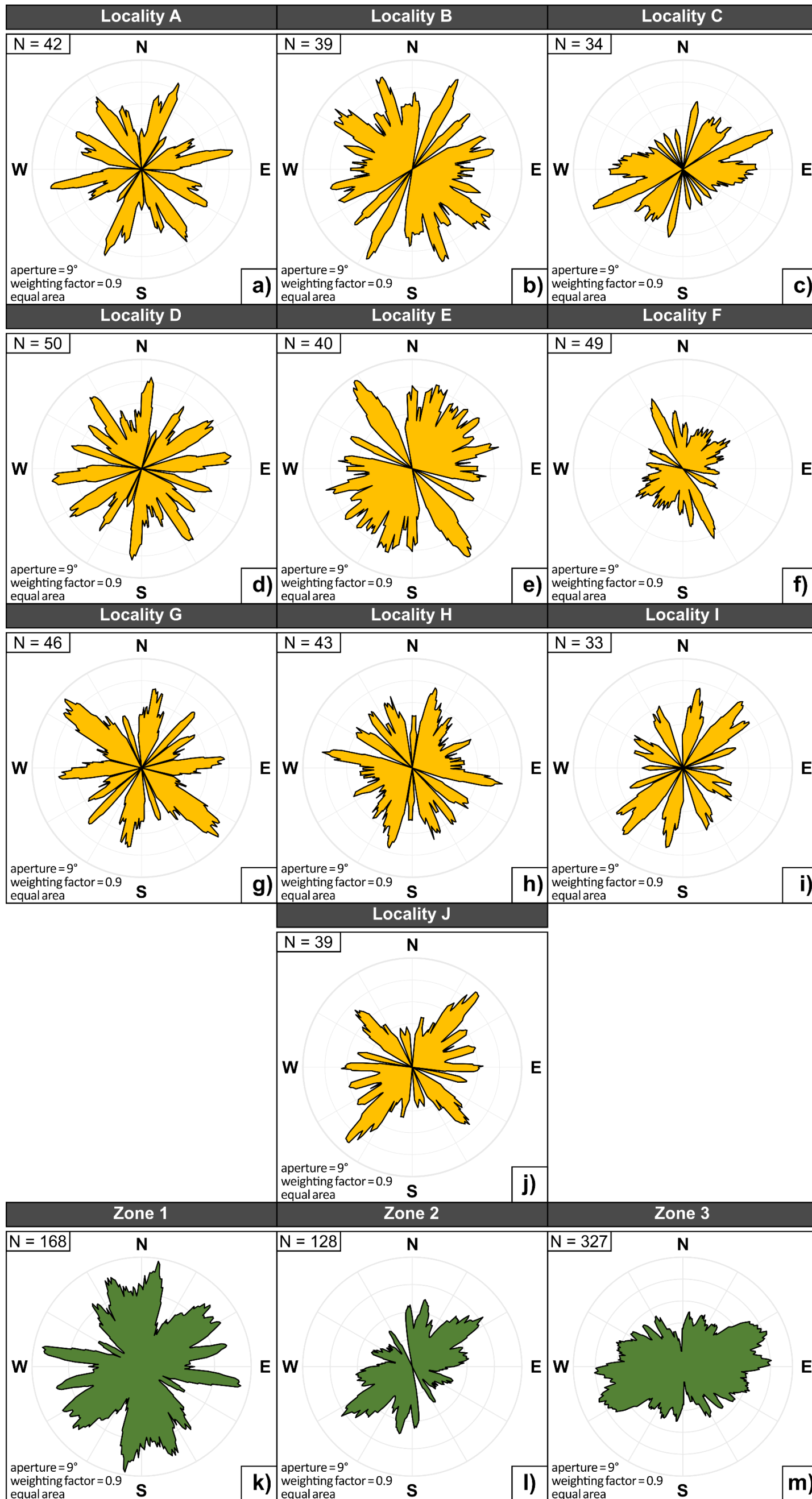


Figure B1. Bi-directional moving average rose diagrams showing fracture orientation from the Cariatiz carbonate platform. a) to j) Rose diagrams from outcrop localities. k) to m) Rose diagrams from LiDAR zones. Rose diagrams were generated as equal area with a weighting factor of 0.9 and aperture of 9°.

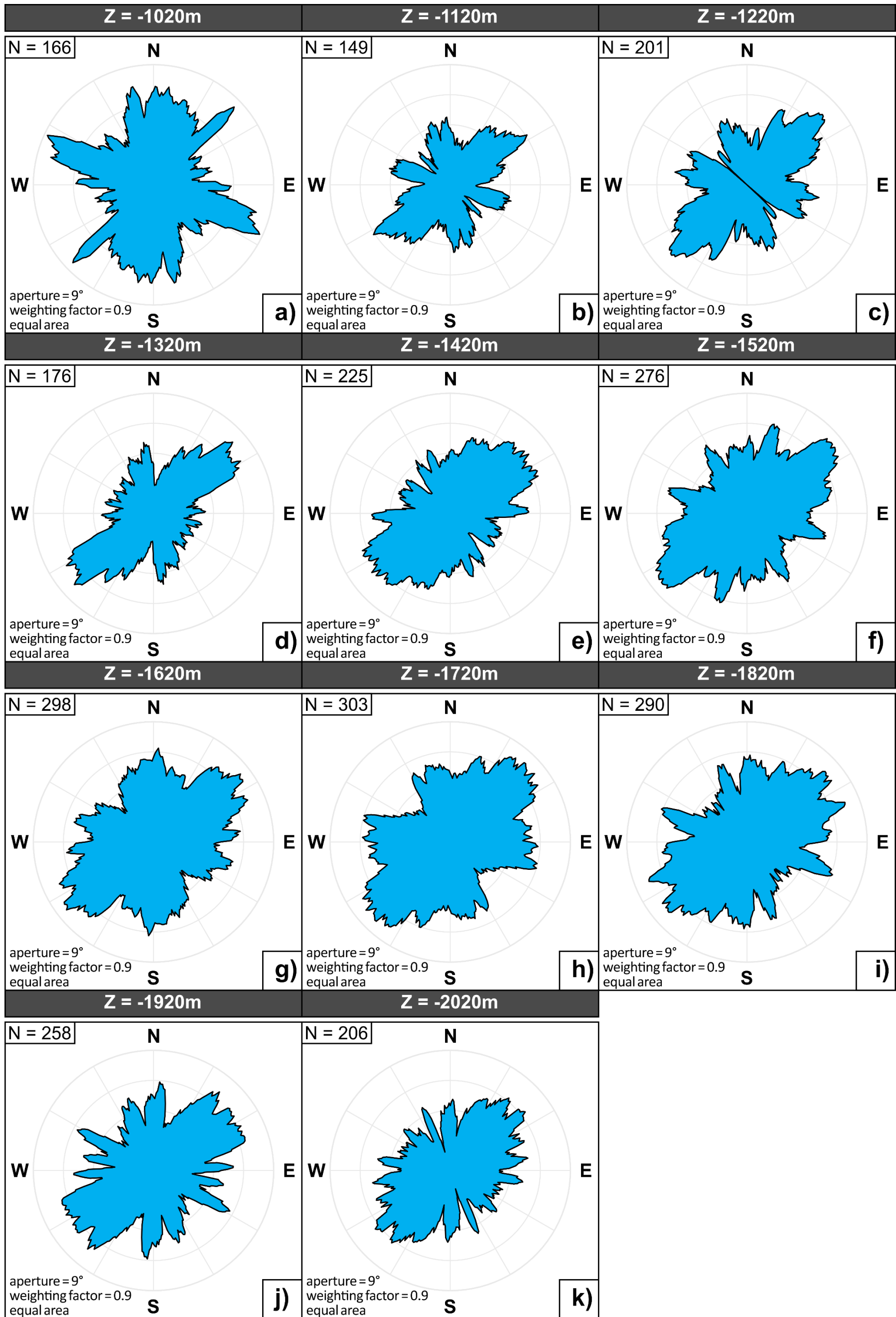


Figure B2. Bi-directional moving average rose diagrams showing fracture orientation from our study area in the Pernambuco carbonate platform at different seismic slices from Z= -1020 m to -2020 m. Rose diagrams were generated as equal area with a weighting factor of 0.9 and aperture of 9°.

Appendix C: Ternary plots showing detailed topological analyses

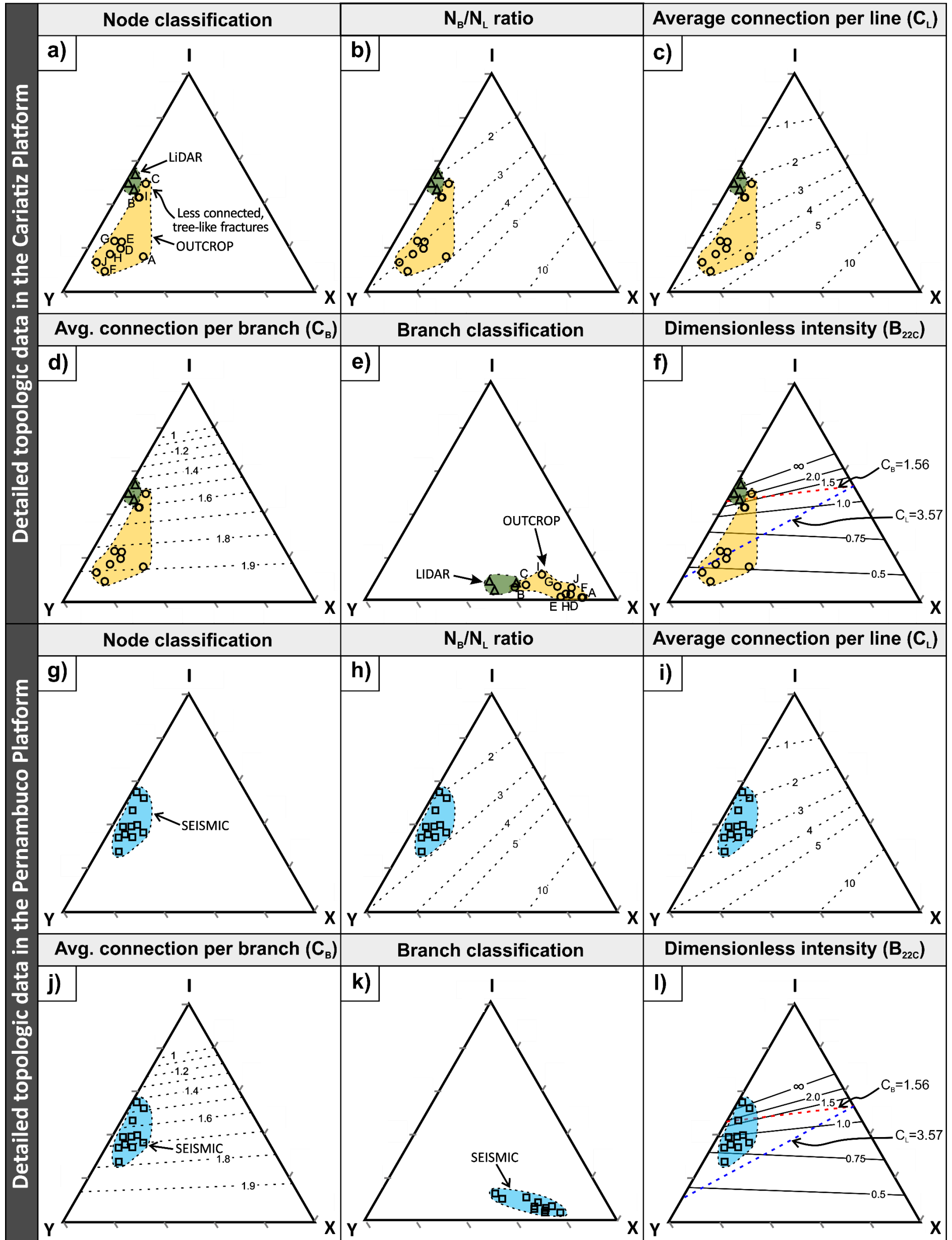


Figure C1. Triangular plots showing detailed topological analyses of nodes and branches from outcrop localities and LiDAR zones at the Cariatiz Fringing Reef (a to f), as well as seismic depth slices from the Pernambuco carbonate platform (g to l). Yellow, green and blue shapes represent the range of node and branch values at outcrop, LiDAR and seismic scale, respectively. a, g) Fracture network node classification. b, h) N_B/N_L ratio shows most of the points lying over N_B/N_L ratio value of 3 within the range of 2 and 4. c, i) Average number of connections per line (C_L) showing that in Cariatiz, at outcrop level, values range from 2 to 5. d, j) Average number of connections per branch (C_B). e, k) Branch classification with I-I isolated branches, I-C partly connected branches, and C-C doubly connected branches. f, l) Dimensionless intensity of branches (B_{22c}).

Appendix D: Fracture topological data

Table D1. Fracture topological results from field data (outcrop and LiDAR) and seismic data.

	Node count			Branch count			Number of lines or traces (NL)	Number of branches (NB)	Number of branches to traces ratio (NB/NL)	Total fracture length (FLT)	Average trace length (LL)	Average branch length (BL)	Connections per line or trace (CL)	Connections per branch (CB)	Proportion of nodes		Proportion of branches		
	NI	NY	NX	I-I	I-C	C-C									Isolated (PI)	Connected (PC)	Isolated (PII)	Singly connected (PIC)	Doubly connected (PCC)
Field data (Outcrop)										[cm]	[cm]	[cm]							
Site A	9	36	14	0	13	86	22.5	86.5	3.84	2232.17	99.21	25.81	4.44	1.90	0.0520	0.9480	0.0027	0.0493	0.8987
Site B	26	30	5	4	30	45	28	68	2.43	2436.43	87.02	35.83	2.50	1.62	0.1912	0.8088	0.0365	0.1546	0.6542
Site C	25	22	4	4	21	39	23.5	53.5	2.28	1661.31	70.69	31.05	2.21	1.53	0.2336	0.7664	0.0546	0.1791	0.5873
Site D	12	43	8	2	18	87	27.5	86.5	3.15	2519.18	91.61	29.12	3.71	1.86	0.0694	0.9306	0.0048	0.0646	0.8661
Site E	19	57	10	1	27	98	38	115	3.03	2761.9	72.68	24.02	3.53	1.83	0.0826	0.9174	0.0068	0.0758	0.8416
Site F	6	56	8	0	16	104	31	103	3.32	2749.91	88.71	26.70	4.13	1.94	0.0291	0.9709	0.0008	0.0283	0.9426
Site G	13	40	5	5	18	66	26.5	76.5	2.89	2357.84	88.98	30.82	3.40	1.83	0.0850	0.9150	0.0072	0.0777	0.8373
Site H	10	45	6	2	18	76	27.5	84.5	3.07	1999.34	72.70	23.66	3.71	1.88	0.0592	0.9408	0.0035	0.0557	0.8852
Site I	20	23	4	7	15	41	21.5	52.5	2.44	2096.67	97.52	39.94	2.51	1.62	0.1905	0.8095	0.0363	0.1542	0.6553
Site J	6	39	3	4	12	65	22.5	67.5	3.00	2250.83	100.04	33.35	3.73	1.91	0.0444	0.9556	0.0020	0.0425	0.9131
All outcrop	146	391	67	29	188	707	268.5	793.5	2.96	23065.58	85.91	29.07	3.41	1.82	0.0920	0.9080	0.0085	0.0835	0.8245
Field data (Lidar)										[m]	[m]	[m]							
Zone 1	83	87	8	12	60	92	85	188	2.21	1507.81	17.74	8.02	2.24	1.56	0.2207	0.7793	0.0487	0.1720	0.6072
Zone 2	74	74	0	6	63	66	74	148	2.00	1791.94	24.22	12.11	2.00	1.50	0.2500	0.7500	0.0625	0.1875	0.5625
Zone 3	207	175	6	28	153	147	191	378	1.98	2633.2	13.79	6.97	1.90	1.45	0.2738	0.7262	0.0750	0.1988	0.5274
Lidar	364	336	14	46	276	305	350	714	2.04	5932.95	16.95	8.31	2.00	1.49	0.2549	0.7451	0.0650	0.1899	0.5552
Seismic data										[m]	[m]	[m]							
-1020 m	97	78	11	15	67	83	87.5	187.5	2.14	119340.04	1363.89	636.48	2.03	1.48	0.2587	0.7413	0.0669	0.1918	0.5496
-1120 m	96	76	3	17	62	68	86	168	1.95	139308.08	1619.86	829.21	1.84	1.43	0.2857	0.7143	0.0816	0.2041	0.5102
-1220 m	78	106	15	9	60	132	92	228	2.48	220090.82	2392.29	965.31	2.63	1.66	0.1711	0.8289	0.0293	0.1418	0.6872
-1320 m	87	92	8	17	53	104	89.5	197.5	2.21	234830.78	2623.81	1189.02	2.23	1.56	0.2203	0.7797	0.0485	0.1717	0.6080
-1420 m	88	112	21	12	65	145	100	254	2.54	275457.57	2754.58	1084.48	2.66	1.65	0.1732	0.8268	0.0300	0.1432	0.6836
-1520 m	89	144	27	8	73	195	116.5	314.5	2.70	286638.22	2460.41	911.41	2.94	1.72	0.1415	0.8585	0.0200	0.1215	0.7370
-1620 m	76	176	23	8	60	228	126	348	2.76	288439.9	2289.21	828.85	3.16	1.78	0.1092	0.8908	0.0119	0.0973	0.7935
-1720 m	101	139	38	12	78	212	120	335	2.79	308308.35	2569.24	920.32	2.95	1.70	0.1507	0.8493	0.0227	0.1280	0.7212
-1820 m	95	170	14	16	64	208	132.5	330.5	2.49	296778.68	2239.84	897.97	2.78	1.71	0.1437	0.8563	0.0207	0.1231	0.7332
-1920 m	88	143	17	12	64	180	115.5	292.5	2.53	287458.13	2488.81	982.76	2.77	1.70	0.1504	0.8496	0.0226	0.1278	0.7218
-2020 m	84	122	9	15	54	132	103	243	2.36	254034.02	2466.35	1045.41	2.54	1.65	0.1728	0.8272	0.0299	0.1430	0.6842
All seismic	979	1358	186	141	700	1687	1168.5	2898.5	2.48	2710684.59	2319.80	935.20	2.64	1.66	0.1689	0.8311	0.0285	0.1404	0.6908